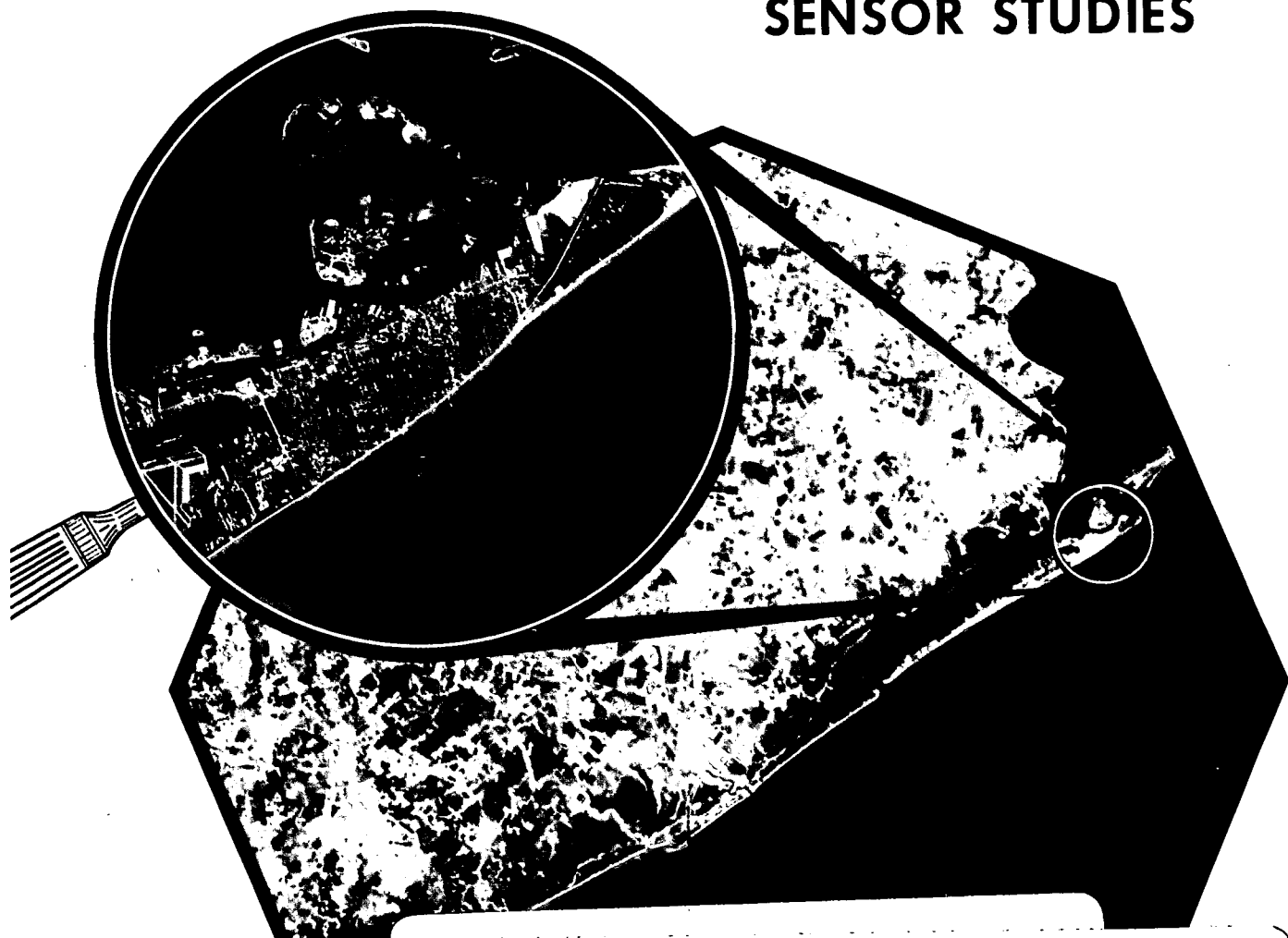


# THIRD ANNUAL EARTH RESOURCES PROGRAM REVIEW

## VOLUME II AGRICULTURE, FORESTRY, AND SENSOR STUDIES



N72-12269  
thru  
N72-12294  
Unclas  
09158

(NASA-TM-X-67404) THIRD ANNUAL EARTH  
RESOURCES PROGRAM REVIEW. VOLUME 2:  
AGRICULTURE, FORESTRY, AND SENSOR STUDIES  
(NASA) 1970 640 p CSCL 02B

G3/13

PAI (NASA OR OTHER OR NUMBER)

Presented at the  
NASA Manned Spacecraft Center  
Houston, Texas

December 1 to 3, 1970

Produced by  
NATIONAL TECHNICAL  
INFORMATION SERVICE  
Springfield, Va. 22151



## FOREWORD

A review of various aspects of the Earth Resources Program was held at the Manned Spacecraft Center, Houston, Texas, December 1, 2, and 3, 1970. Particular emphasis was placed on the results of analysis of data obtained with the Manned Spacecraft Center and other aircraft which have contributed data to the program.

The review was divided into the disciplinary areas of Geology, Geography, Hydrology, Agriculture, Forestry, and Oceanography. Program investigators presented the results of their work in each of these areas. The material presented is published in three volumes:

VOLUME I - GEOLOGY AND GEOGRAPHY

VOLUME II - AGRICULTURE, FORESTRY, AND SENSOR STUDIES

VOLUME III - HYDROLOGY AND OCEANOGRAPHY

The review provided a current assessment of the program for both management and technical personnel. Note that the material presented represented the current status of ongoing programs and complete technical analyses will be available at a later date.

Where papers were not submitted for publication or were not received in time for printing, abstracts are used.

ORIGINAL CONTAINS  
COLOR ILLUSTRATIONS

iii

PRECEDING PAGE BLANK NOT FILMED

CONTENTS OF VOLUME I

Section		Page
	FOREWORD . . . . .	iii
1	INTRODUCTORY COMMENTS ON THE USGS GEOGRAPHIC APPLICATIONS PROGRAM . . . . . By Arch C. Gerlach	1-1
2	CENSUS CITIES PROJECT AND ATLAS OF URBAN AND REGIONAL CHANGE . . . . . By James R. Wray	2-1
3	THE APPLICATION OF REMOTE SENSING TECHNIQUES TO SELECTED INTER AND INTRA URBAN DATA ACQUISITION PROBLEMS . . . . . By Frank E. Horton	3-1
4	CLIMATOLOGY OF URBAN-REGIONAL SYSTEMS . . . . . By Robert W. Pease	4-1
5	REGIONAL LAND USE STUDIES . . . . . By John L. Place	5-1
6	ENVIRONMENTAL APPLICATION OF REMOTE SENSING METHODS TO COASTAL ZONE LAND USE AND MARINE RESOURCES MANAGEMENT . . . . . By H. G. Goodell	6-1
7	EXPERIMENTAL APPLICATIONS OF MULTISPECTRAL DATA TO NATURAL RESOURCE INVENTORY AND SURVEY . . . . . By Harry J. Mallon	7-1
8	SPECIAL PROJECTS OF THE GEOGRAPHIC APPLICATIONS PROGRAM . . . . . By Gary W. North	8-1
9	GEOGRAPHY PROGRAM, DESIGN, STRUCTURE, AND OPERATIONAL STRATEGY . . . . . By Robert H. Alexander	9-1

Section		Page
10	PROCESSING OF MULTISPECTRAL DATA AND SIMULATION OF ERTS DATA CHANNELS TO MAKE COMPUTER TERRAIN MAPS OF A YELLOWSTONE NATIONAL PARK TEST SITE . . . . .	10-1
	By Harry W. Smedes, Margaret M. Spencer, and Frederick J. Thomson	
11	LINEAR GEOLOGIC STRUCTURE AND MAFIC ROCK DISCRIMINATION AS DETERMINED FROM INFRARED DATA . . . . .	11-1
	By T. W. Offield, L. C. Rowan, and R. D. Watson	
12	MULTISPECTRAL ANALYSIS OF LIMESTONE, DOLOMITE, AND GRANITE, MILL CREEK, OKLAHOMA . . . . .	12-1
	By L. C. Rowan and Kenneth Watson	
13	A THERMAL MODEL FOR ANALYSIS OF INFRARED IMAGES . . . . .	13-1
	By Kenneth Watson	
14	A STUDY OF PASSIVE MICROWAVE TECHNIQUES APPLIED TO GEOLOGIC PROBLEMS . . . . .	14-1
	By A. T. Edgerton	
15	GEOLOGIC INTERPRETATION OF APOLLO 6 STEREOPHO- TOGRAPHY FROM BAJA CALIFORNIA TO WEST TEXAS . . . . .	15-1
	By Stephen J. Gawarecki	
16	GEOLOGIC TERRAIN MAPPING FROM EARTH-SATELLITE AND ULTRA-HIGH AERIAL PHOTOGRAPHS . . . . .	16-1
	By R. B. Morrison	
17	REMOTE SENSING IN MARINE GEOLOGY: ARTIC TO CARIBBEAN . . . . .	17-1
	By Paul R. Carlson	
18	RELATIONSHIP BETWEEN VEGETATION REFLECTANCE SPECTRA AND SOIL GEOCHEMISTRY: NEW DATA FROM CATHEART MOUNTAIN, MAINE . . . . .	18-1
	By F. C. Canney, Sondra Wenderoth, and Edward Yost	

Section		Page
19	GROUND TRUTH VERSUS NO GROUND TRUTH . . . . .	19-1
	By Grover B. Torbert	
20	A REVIEW OF APPLICATION STUDIES ON INDIAN LANDS USING NASA AEROSPACE IMAGERY . . . . .	20-1
	By Arthur M. Woll	

CONTENTS OF VOLUME II

Section	Page
21      CARTOGRAPHY . . . . .	21-1 ✓
By Alden P. Colvocoresses	
22      AUTOMATIC CARTOGRAPHY TECHNIQUES FOR EARTH RESOURCES RESEARCH . . . . .	22-1 ✓
By Dean T. Edson	
23      SPECTRAL REFLECTANCE FROM PLANT CANOPIES AND OPTIMUM SPECTRAL CHANNELS IN THE NEAR INFRARED . . . . .	23-1 ✓
By William A. Allen, Harold W. Gausman, and Craig L. Wiegand	
24      AERIAL PHOTOGRAPHY FOR SENSING PLANT ANOMALIES . . . . .	24-1 ✓
By H. W. Gausman, R. Cardenas, and W. G. Hart	
25      REMOTE SENSING FOR DETECTION OF SOIL LIMITATIONS IN AGRICULTURAL AREAS . . . . .	25-1 ✓
By C. J. Frazee, R. D. Heil, and F. C. Westin	
26      RECOGNITION OF CROPS AND SOILS BY SPOT DENSITY MEASUREMENTS OF IMAGERY . . . . .	26-1 ✓
By Gerald D. Nelson	
27      THERMAL SCANNER DATA FOR STUDYING FREEZE CONDITIONS AND FOR AIDING IRRIGATION SCHEDULING . . . . .	27-1 ✓
By Jon F. Bartholic, Craig L. Wiegand, Ross W. Leamer, and Leo N. Namken	

Section		Page	
28	COMPUTER DISCRIMINATION PROCEDURES APPLICABLE TO AERIAL AND ERTS MULTISPECTRAL DATA . . . . .	28-1	✓
	By Arthur J. Richardson, Robert J. Torline, and William A. Allen		
29	THE APPLICATIONS OF REMOTE SENSING TO CORN BLIGHT DETECTION AND CROP YIELD FORECASTING . . . . .	29-1	✓
	By R. B. MacDonald		
30	A SEMI-OPERATIONAL AGRICULTURAL INVENTORY USING SMALL-SCALE AERIAL PHOTOGRAPHY . . . . .	30-1	✓
	By William C. Draeger and Lawrence R. Pettinger		
31	IMAGE RESOLUTION: ITS SIGNIFICANCE IN A WILDLAND AREA . . . . .	31-1	✓
	By Donald T. Lauer and Randolph R. Thaman		
32	IDENTIFICATION AND MEASUREMENT OF SHRUB-TYPE VEGETATION ON LARGE-SCALE AERIAL PHOTOGRAPHS . . . . .	32-1	✓
	By Richard S. Driscoll		
33	A VEGETATIONAL INVENTORY AND ECOLOGICAL RESOURCE ANALYSIS FROM SPACE AND HIGH-FLIGHT PHOTOGRAPHY . . . . .	33-1	✓
	By Charles E. Poulton, David P. Faulkner, and Barry J. Schrupf		
34	REMOTE DETECTION OF INSECT EPIDEMICS IN CONIFERS . . . . .	34-1	✓
	By Robert C. Heller		
35	MULTISPECTRAL SENSING OF MOISTURE STRESS . . . . .	35-1	✓
	By Charles E. Olson Jr. and Wayne G. Rohde		

Section		Page	
36	CLASSIFYING FOREST AND NONFOREST LAND ON SPACE PHOTOGRAPHS . . . . .	36-1	✓
	By Robert C. Aldrich		
37	SUMMARY OF MICHIGAN MULTISPECTRAL INVESTIGATIONS PROGRAM . . . . .	37-1	✓
	By Richard R. Legault		
38	USER ORIENTED DATA PROCESSING AT THE UNIVERSITY OF MICHIGAN . . . . .	38-1	✓
	By Frederick J. Thomson		
39	THE APPLICATION OF AUTOMATIC RECOGNITION TECHNIQUES IN THE APOLLO IX SO-65 EXPERIMENT . . . . .	39-1	✓
	By R. B. MacDonald		
40	THE DEVELOPMENT OF MACHINE TECHNOLOGY PROCESSING FOR EARTH RESOURCE SURVEY . . . . .	40-1	✓
	By D. A. Landgrebe		
41	REMOTE SENSING AT THE UNIVERSITY OF KANSAS IN RADAR SYSTEMS . . . . .	41-1	✓
	By Richard K. Moore		
42	DATA PROCESSING AT THE UNIVERSITY OF KANSAS . . . . .	42-1	✓
	By G. L. Kelly		
43	RECENT ADVANCES IN RADAR APPLICATIONS TO AGRICULTURE . . . . .	43-1	✓
	By Stanley A. Morain		
44	INTERACTIVE DISPLAY/GRAPHICS SYSTEMS FOR REMOTE SENSOR DATA ANALYSIS . . . . .	44-1	✓
	By W. G. Eppler, D. L. Loe, E. L. Wilson, S. L. Whitley, and R. J. Sachen		



Section		Page
45	RESULTS OF SCATTEROMETER SYSTEMS ANALYSIS FOR NASA/MSC EARTH OBSERVATION SENSOR EVALUATION PROGRAM . . . . .	45-1 ✓
	By K. Krishen, N. Vlahos, O. Brandt, and G. Graybeal	
46	PHENOMENOLOGICAL APPROACH TO SCATTER- OMETER DATA INTERPRETATION . . . . .	46-1 ✓
	By F. E. Alzofon	

CONTENTS OF VOLUME III

Section		Page
47	DETECTION AND IDENTIFICATION OF BENTHIC COMMUNITIES AND SHORELINE FEATURES IN BISCAYNE BAY USING MULTIBAND IMAGERY . . . . .	47-1
	By Milton C. Kolipinski and Aaron L. Higer	
48	REMOTE SENSING FOR DEFINING AQUIFERS IN GLACIAL DRIFT . . . . .	48-1
	By Victor I. Myers	
49	SUMMARY — REMOTE SENSING SOIL MOISTURE RESEARCH . . . . .	49-1
	By Fred A. Schmer, Hal D. Werner, and Fred A. Waltz	
50	MEASUREMENT OF PLANT COMMUNITY COVER FROM AERIAL PHOTOGRAPHS USING EKTACHROME INFRARED AERO FILM . . . . .	50-1
	By Raymond M. Turner	
51	EMMISSION CHARACTERISTICS OF SNOW AND ICE IN THE MICROWAVE RANGE . . . . .	51-1
	By Mark F. Meier and A. T. Edgerton	
52	MANAGEMENT APPLICATIONS FOR THERMAL IR IMAGERY OF LAKE PROCESSES . . . . .	52-1
	By J. M. Whipple and R. B. Haynes	
53	SPECTRAL REFLECTANCE CHARACTERISTICS AND AUTOMATED DATA REDUCTION TECHNIQUES WHICH IDENTIFY WETLAND AND WATER QUALITY CONDITIONS IN THE CHESAPEAKE BAY . . . . .	53-1
	By Dr. Richard R. Anderson	

Section		Page
54	DATA RELAY SYSTEM SPECIFICATIONS FOR ERTS IMAGE INTERPRETATION . . . . .	54-1
	By James F. Daniel	
55	THE ROLE OF REMOTELY SENSED AND RELAYED DATA IN THE DELAWARE RIVER BASIN . . . . .	55-1
	By Richard W. Paulson	
56	NOAA's OCEANOGRAPHY STUDIES UNDER THE EARTH RESOURCES SURVEY PROGRAM . . . . .	56-1
	By E. Paul McClain	
57	NOAA's HYDROLOGY STUDIES UNDER THE EARTH RESOURCES SURVEY PROGRAM . . . . .	57-1
	By E. Paul McClain	
58	REMOTE SENSING AND THE PELAGIC FISHERIES ENVIRONMENT OFF OREGON . . . . .	58-1
	By William G. Pearcy	
59	REMOTE SENSING OF OCEAN COLOR FROM AIRCRAFT . . . . .	59-1
	By G. L. Clarke and G. C. Ewing	
60	THE REMOTE SENSING NEEDS OF ARTIC GEOPHYSICS . . . . .	60-1
	By William J. Campbell	
61	MEASUREMENT OF WATER DEPTH BY MULTISPECTRAL RATIO TECHNIQUES . . . . .	61-1
	By F. C. Polcyn	
62	RADAR MONITORING OF OIL POLLUTION . . . . .	62-1
	By N. W. Guinard	
63	VISIBLE REGION REMOTE SPECTROSCOPY OF POLLUTED WATER . . . . .	63-1
	By Peter G. White	

Section		Page
64	LASER OBSERVATIONS OF WAVE GROWTH AND FOAM DENSITY FOR FETCH-LIMITED 25M/SEC WINDS . . . . .	64-1
	By Duncan B. Ross and Vincent Cardone	
65	WHITECAP COVERAGE FROM AERIAL PHOTOGRAPHY . . . . .	65-1
	By Roswell W. Austin	
66	ON THE USE OF A SINGLE BLUE BAND IN OCEANOGRAPHY . . . . .	66-1
	By John W. Sherman III	
67	THE VARIATION OF RADAR CROSS SECTION WITH WIND . . . . .	67-1
	By N. W. Guinard	
68	NANOSECOND RADAR OBSERVATIONS OF THE OCEAN SURFACE FROM A STABLE PLATFORM . . . . .	68-1
	By B. S. Yapple, A. Shapiro, D. L. Hammond, and E. A. Uliana	
69	PASSIVE MICROWAVE STUDIES . . . . .	69-1
	By James P. Hollinger	
70	THE INTEGRATION OF REMOTE SENSING DATA INTO GLOBAL WEATHER PREDICTION, WAVE FORECASTING, AND OCEAN CIRCULATION COMPUTER BASED SYSTEMS . . . . .	70-1
	By Willard J. Pierson, Jr.	

TABLES

Table		Page
25-1	CAMERA, FILM, AND FILTER DATA FOR OAHE SITES . . . . .	25-11
25-2	INTERPRETATION OF SPATIAL DATA ANALYSIS OF AN UNDULATING DRIFT PLAIN . . . . .	25-15
26-1	THE CLASSIFICATIONS ESTABLISHED FOR PATTERN RECOGNITION . . . . .	26-12
26-2	SAMPLE CONFUSION MATRIX . . . . .	26-13
26-3	CONFUSION MATRIX, 14 000 EKTACHROME INFRARED . . . . .	26-13
26-4	RANK ORDERING OF FEATURES . . . . .	26-14
26-5	CONFUSION MATRIX - 60 000 FEET . . . . .	26-15
26-6	CONFUSION MATRIX - 14 000 FEET . . . . .	26-15
26-7	CONFUSION MATRIX - 14 000 FEET . . . . .	26-16
26-8	CONFUSION MATRIX - 14 000 FEET . . . . .	26-16
26-9	CONFUSION MATRIX - 14 000 FEET . . . . .	26-17
27-1	THE DISTRIBUTION OF LETTERS REPRESENTING RESOLUTION ELEMENTS IN COMPUTER PRINTOUT . . . . .	27-14
28-1	REFERENCE GROUND PATTERN MEAN VECTORS AND COVARIANCE MATRIXES FOR OPTICAL DENSITY READINGS . . . . .	28-12
28-2	COMPARISON OF RECOGNITION RESULTS FOR THE MDM CLASSIFICATION MODELS . . . . .	28-13
28-3	COMPARISON OF RECOGNITION RESULTS FOR THE EBC CLASSIFICATION MODEL USING THE INDICATED GROUND PATTERN CATEGORIES WITH RED AND GREEN LIGHT EIR OPTICAL DENSITY MEASUREMENT AS CHARACTERISTIC FEATURE . . . . .	28-14
29-1	1970 CORN BLIGHT STUDY MISSIONS - AERIAL . . . . .	29-14
29-2	RATINGS AND DESCRIPTIONS FOR SOUTHERN CORN LEAF BLIGHT . . . . .	29-16

Table		Page
30-1	TABULATION OF THE TYPES OF IMAGERY OBTAINED THROUGH THE NASA EARTH RESOURCES SURVEY PROGRAM FOR THE PHOENIX TEST SITE DURING 1969 AND 1970 . . . . .	30-21
30-2	DETAILED SUMMARY OF NASA RB57F IMAGERY FOR THE PHOENIX, ARIZONA, TEST SITE . . . . .	30-22
30-3	ACREAGE ESTIMATES AND SAMPLING ERROR . . . . .	30-23
30-4	RATIO CORRECTION FACTORS . . . . .	30-23
30-5	SAMPLING ERROR OF INTERPRETERS . . . . .	30-23
30-6	INTERPRETATION TIME . . . . .	30-17
32-1	CORRECT SHRUB AND SMALL TREE IDENTIFICATION PERCENTS BY INTERPRETER AND FILM TYPE . . . . .	32-9
32-2	MEANS AND RANGES OF IMAGE DENSITY VALUES . . . . .	32-10
33-1	HIGHEST LEVEL OF GENERALIZATION IN A STANDARD SYMBOLIC NOTATION FOR IDENTIFYING AND CODING LAND USE ACTIVITIES . . . . .	33-7
33-2	A SYMBOLIC, TECHNICAL, AND DESCRIPTIVE LEGEND, PRIMARY RESOURCE AND LAND USE CLASS . . . . .	33-8
33-3	A SYMBOLIC, TECHNICAL, AND DESCRIPTIVE LEGEND, NORTH AMERICAN VEGETATIONAL PHYSIOGNOMIC TYPES . . . . .	33-9
33-4	A SYMBOLIC, TECHNICAL, AND DESCRIPTIVE LEGEND, MACRORELIEF CLASSES . . . . .	33-10
34-1	FILM-FILTER-SCALE COMBINATIONS EXPOSED DURING RB-57 FLIGHT MISSION 101 . . . . .	34-16
34-2	SPECTROMETER CHANNELS USED FOR TARGET RECOGNITION BY UNIVERSITY OF MICHIGAN AIRCRAFT . . . . .	34-17
36-1	CAMERA, FOCAL LENGTH, FILM-FILTER DATA, SCALE AND TYPE OF COVERAGE FOR APOLLO 9 FOREST INVENTORY STUDY SUPPORT PHOTOGRAPHY, APRIL 1969 . . . . .	36-19

Table	Page	
36-2	CAMERA, FOCAL LENGTH, FILM FILTER, AND PHOTOGRAPHIC SCALE FOR RB-57 (MISSION 131) PHOTOGRAPHY FOR SITE 217, ATLANTA, GEORGIA, JUNE 1970 . . . . .	36-20
36-3	LAND USE AND FOREST CONDITION CLASSIFICATION . . . . .	36-21
36-4	COMPARISON OF PERCENT FOREST AREA BY STUDY BLOCK, MEAN FOR ALL BLOCKS, AND TYPE OF PHOTOGRAPHY . . . . .	36-22
36-5	COMPARISON OF AREA FOR FOREST AND NONFOREST CLASSES USING THREE PHOTO SCALES . . . . .	36-23
37-1	RESULTS OF ESTIMATING PROPORTIONS (SIMULATION) . . . . .	37-10
39-1	FILM-FILTER COMBINATIONS USED IN SO-65 EXPERIMENT . . . . .	39-7
39-2	PRELIMINARY CLASSIFICATION RESULTS . . . . .	39-8
41-1	RADAR SYSTEM RESEARCH, FY70, UNIVERSITY OF KANSAS . . . . .	41-14
41-2	RADAR SYSTEMS . . . . .	41-15
41-3	PROJECTED 1975 SYNTHETIC APERTURE SPACE RADAR WITH DIGITAL PROCESSING . . . . .	41-16
43-1	SEGREGATION OF CROP GROUPS ON THE BASIS OF RADAR RETURN AND VIEWING ANGLE	
	a. ALL FIELDS . . . . .	43-23
	b. SELECTED FIELDS . . . . .	43-23
43-2	PERCENT CROP SEGREGATION ON SCATTERGRAMS AS A FUNCTION OF RADAR FREQUENCY AND DATE IN THE GROWING SEASON . . . . .	43-24
45-1	WAVEGUIDE INSERTION LOSSES . . . . .	45-6
45-2	MAXIMUM VALUE OF ERROR FOR SELECTED PARAMETERS . . . . .	45-15
45-3	VERTICAL VELOCITY ERROR . . . . .	45-25
45-4	ERROR CAUSED BY ROLL OF 4 DEGREES . . . . .	45-26

FIGURES

Figure		Page
21-1	A section of the Florida Keys from 60 000 feet as photographed with a 12-inch focal-length mapping camera in color infrared . . . . .	21-7
21-2	Coastal wetland area as photographed from 60 000 feet with a 6-inch focal-length mapping camera in color infrared . . . . .	21-8
21-3	1:250 000 scale line map compared with the line map combined with space image . . . . .	21-9
21-4	The manuscript (1:250 000 scale, Phoenix sheet) was compiled by USGS from all available (other) sources and was considered current as of March 1969 . . . . .	21-10
21-5	A coordinate reader superimposed on gridded 1:250 000 scale map . . . . .	21-11
21-6	Selected segment of exposure AS9-26C-3740, March 11, 1969, showing the Ouachita River in the Mississippi Valley at flood stage . . . .	21-12
21-7	Open water separated from land by photo- optical means . . . . .	21-13
22-1	Digital cartographic systems for earth resources research . . . . .	22-6
22-2	Reformatting of graphic data . . . . .	22-7
22-3	Scanning the graphic data . . . . .	22-8
22-4	Steps in processing line data . . . . .	22-9
22-5	Feature code assignment . . . . .	22-9
22-6	Terrain model generation . . . . .	22-10
22-7	Image correlator for precise point transfer . . . .	22-11
22-8	Photomechanical map symbol separation . . . . .	22-12



Figure		Page
23-1	Infrared photograph of agricultural scene at Texas A&M University Research and Extension Center, Weslaco, Texas . . . . .	23-7
23-2	Photograph of grapefruit orchard taken at 3000 foot elevation . . . . .	23-8
23-3	Infrared scanner image from Nimbus III . . . . .	23-9
23-4	Photomicrograph of typical dorsiventral cotton leaf transection . . . . .	23-10
23-5	Models of light interaction with leaves . . . . .	23-11
23-6	Percent transmittance of near infrared flux within a 250-cm high, Ithaca, New York, corn canopy September 13, 1963 . . . . .	23-12
23-7	Mean dispersion curve for 200 field grown cotton leaves . . . . .	23-13
23-8	Absorptance spectra of a typical leaf (solid line and open circles) . . . . .	23-14
23-9	Correlation coefficients of leaf reflectance . . . . .	23-15
24-1	Diffuse reflectance, transmittance, and absorptance surface of a mature orange leaf . . . . .	24-5
24-2	Three-dimensional drawing of a leaf structure that is similar to the structure of a citrus leaf . . . . .	24-6
24-3	Microphotographs of leaf transections of young and mature citrus leaves . . . . .	24-7
24-4	Diffuse reflectance of the upper surfaces of young and mature orange leaves . . . . .	24-8
24-5	Diffuse reflectance of upper leaf surfaces of healthy and salt-affected citrus leaves . . . . .	24-9

Figure		Page
24-6	Aerial photographs of plant anomalies with EIR film	
	a. Salt toxicity . . . . .	24-11
	b. Kinds of citrus trees . . . . .	24-11
	c. Foot rot . . . . .	24-11
	d. Sooty mold . . . . .	24-11
24-7	Effect of sooty mold on reflectance of leaves coated with varying amounts of the fungus . . . . .	24-13
25-1	Location of study area in Spink County, South Dakota . . . . .	25-16
25-2	Claypan limitation, Lake Dakota Plain . . . . .	25-17
25-3	Topography limitation, Lake Dakota Plain . . . . .	25-18
25-4	Soil areas without claypan, Lake Dakota Plain . . . . .	25-19
25-5	Undulating drift plain, Williams Loamy Plain . . . . .	25-20
25-6	Color coded representation of figure 25-2 . . . . .	25-21
25-7	Color coded representation of figure 25-3 . . . . .	25-22
25-8	Color coded representation of figure 25-5 . . . . .	25-23
26-1	Soils A and B - pattern recognition study used data measured with Macbeth densi- tometer and spatial data system . . . . .	26-18
26-2	National Aeronautics and Space Administration imagery taken on August 8, 1969, over South Dakota at an altitude of 60 000 feet . . . . .	26-19
26-3	Remote Sensing Institute imagery taken over South Dakota at an altitude of 14 000 feet . . . . .	26-20
26-4	Special purpose K-class classifier . . . . .	26-21

Figure		Page
26-5	Sample probability density function of soils A and B	
	a. Red and green filters . . . . .	26-22
	b. Neutral and blue filters . . . . .	26-23
26-6	Scatter plots of density measurements for soils A and B . . . . .	26-24
26-7	Spatial data black and white image of soils A and B with neutral filter on the vidicon . . .	26-30
26-8	Spatial data black and white image of soils A and B with a red filter on the vidicon . . . .	26-31
26-9	Classification results versus number of features . . . . .	26-32
26-10	Sample probability density functions for the four filters and six classes . . . . .	26-33
27-1	Thermal image produced in flight, A & I south grove . . . . .	27-15
27-2	Thermal image of analog magnetic tape displayed on CRT of same area as figure 27-1 . . . . .	27-15
27-3	Image transparency of figure 27-1 displayed on a color enhancing datacolor set . . . . .	27-16
27-4	Temperature versus digital counts showing the position of the blackbody cal-source temperatures . . . . .	27-17
27-5	Thermal image produced in flight showing the considerable thermal (irradiance) contrasts occurring in the agricultural scene overflown . . . . .	27-18
27-6	Relation of the difference between crop surface and air temperatures to solar radiation at various mean soil moisture tensions for the top meter of soil . . . . .	27-19

Figure		Page
27-7	Film density versus grey scale step voltage and blackbody temperature, RS-14 scanner . . . . .	27-20
27-8	Ektachrome IR picture of the research farm . . . . .	27-21
27-9	Thermal image obtained for the research farm . . . . .	27-21
27-10	Relationship between PRT-5 temperature measurements taken from the ground and temperatures obtained from RS-14 data . . . . .	27-22
27-11	Relation between cotton leaf emittance (8 - 14 $\mu$ m) measured with an RS-14 scanner and plant stress . . . . .	27-23
28-1	Positive reproduction of a 70-mm positive infrared transparency showing bare soil, cotton, and water conditions in the vicinity of the Rio Grande River . . . . .	28-15
28-2	Scatter diagram of red versus green optical density measurements for 160 mean transect readings . . . . .	28-16
28-3	Scatter diagram of red versus green light optical density measurements showing decision regions for the EBC classification model . . . . .	28-17
28-4	Scatter diagram of red versus blue light optical density measurements . . . . .	28-18
28-5	Scatter diagram of blue versus green light optical density measurements . . . . .	28-19
29-1	Southern corn leaf blight . . . . .	29-17
29-2	Corn plants	
	a. Healthy plants . . . . .	29-18
	b. Moderately infected plants . . . . .	29-19
	c. Severely infected plants . . . . .	29-20

Figure		Page
29-3	Effects of stalk rot on corn plants suffering from corn blight . . . . .	29-21
29-4	Ear rot resulting from southern corn leaf blight . . . . .	29-22
29-5	Indiana counties where severe corn blight damage occurred . . . . .	29-23
29-6	Corn production estimates	
	a. Indiana . . . . .	29-24
	b. United States . . . . .	29-25
29-7	Southern corn leaf blight flightline in Indiana flown in August 1970 . . . . .	29-26
29-8	Color photograph taken from an altitude of 10 000 feet . . . . .	29-27
29-9	Infrared photograph taken from an altitude of 10 000 feet . . . . .	29-28
29-10	Color infrared photograph taken from an altitude of 60 000 feet . . . . .	29-29
29-11	Conventional color photograph taken from an altitude of 60 000 feet . . . . .	29-30
29-12	Color infrared photograph taken from an altitude of 60 000 feet . . . . .	29-31
29-13	Low altitude color photograph . . . . .	29-32
29-14	Low altitude color infrared photograph . . . . .	29-33
29-15	Color coded computer classification of vidicon converted color infrared photograph . . . . .	29-34
29-16	Computer printout of the results of classi- fication of the spectral data collected . . . . .	29-35
30-1	Phoenix test site where the semioperational agricultural inventory was performed . . . . .	30-24

Figure		Page
30-2	Test images, ground data, and sample interpretation test results for 4-square mile test plot . . . . .	30-25
30-3	Portion of Maricopa County for which the semioperational survey was performed . . . . .	30-26
30-4	Coded fraction representing a typical field code as recorded by field crews gathering information pertaining to the sample plots . . .	30-27
30-5	Map of field data collected for 4-square mile plots in Maricopa County . . . . .	30-28
31-1	Multidisciplinary Test Site 29 at Phoenix, Arizona . . . . .	31-11
31-2	Cumulative results of photo interpretation, image 1 . . . . .	31-12
31-3	Cumulative results of photo interpretation, image 2 . . . . .	31-13
31-4	Cumulative results of photo interpretation, image 3 . . . . .	31-14
31-5	Cumulative results of photo interpretation, image 4 . . . . .	31-15
31-6	Cumulative results of photo interpretation, image 5 . . . . .	31-16
31-7	Ground truth key for overlay in figure 31-2 . . .	31-17
31-8	Interpretation results for each category expressed as percent correct and percent commission error . . . . .	31-18
31-9	Interpretation results for all categories individually expressed as percent correct identification . . . . .	31-19
31-10	Interpretation results for all categories individually expressed as percent commission errors . . . . .	31-20

Figure		Page
31-11	Interpretation results for combined categories expressed as percent correct and percent commission error . . . . .	31-21
31-12	Interpretation results for woody vegetation, grasslands, and water expressed as percent correct identification . . . . .	31-22
31-13	Interpretation results for woody vegetation, grassland, and water expressed as percent commission error . . . . .	31-23
31-14	Phenological growth stages of annual grasslands in California . . . . .	31-24
32-1	Aerial photograph showing the plot marking system for identification and measurement of shrub species . . . . .	32-11
32-2	Photographs showing errors in identification of various species . . . . .	32-12
32-3	Stereo pairs in color and color infrared of mountainmahogany at a scale of 1:1500 . . . . .	32-13
32-4	Rabbitbrush is difficult to identify in either color or color infrared stereograms even at photoscales of 1:600 . . . . .	32-14
32-5	Comparison of ground to photo measurements of percent cover of big sagebrush . . . . .	32-15
33-1	An ecosystem legend format for range resource and land use analysis from space and supporting aircraft imagery . . . . .	33-12
33-2	A portion of photomosaic map of Maricopa County, Arizona, showing natural vegetation resources, agricultural, and urban land use . . .	33-13
34-1	Flag shows location of Black Hills National Forest near Rapid City, South Dakota . . . . .	34-18
34-2	Oblique view of Black Hills beetle damage to ponderosa pine . . . . .	34-19

Figure		Page
34-3	Seasonal differences of tree stress caused by bark beetles	
	a. Normal color film . . . . .	34-20
	b. Infrared film . . . . .	34-21
34-4	Flight coverage of RB57F August 3 and 8, 1969 . . . . .	34-22
34-5	Views of 1.6- by 5- kilometer study area near Lead, South Dakota . . . . .	34-23
34-6	Aerial color photograph taken August 11, 1969, over study area, scale 1:8000 . . . . .	34-24
34-7	RB57F coverage of study area . . . . .	35-25
34-8	Hasselblad imagery over study area . . . . .	34-26
34-9	Detection success in locating infestations on study area by scale and by size of infestation . . . . .	34-27
34-10	Detection success in studying various films and filters on 1:220 000 scale Hasselblad photography over 1.6- by 5- kilometer study area . . . . .	34-28
34-11	Photo interpretation detection successes on well exposed color and color infrared film over study area . . . . .	34-29
34-12	Improved ground data instrumentation	
	a. Neutron probe to measure soil moisture . . . . .	34-30
	b. Aerial tramway to collect solar radiation and emission data continuously over the trees . . . . .	34-31
	c. Data logger digitizes and records 38 channels of biophysical data . . . . .	34-32
34-13	Target coding of study area according to small temperature differences . . . . .	34-33
34-14	Meteorological and tree physiological data collected at ground instrumented test site for period May 29 to 30, 1968 . . . . .	34-34



Figure		Page
34-15	Ground data collected at <u>Poria weirii</u> site on two dates at Wind River, Washington . . . . .	34-35
34-16	Thermal gray map of <u>Poria weirii</u> site constructed from digitized thermal analog tapes . . . . .	34-36
35-1	Leaf moisture content prediction equations for three tree species derived with stepwise multiple regression techniques . . . . .	35-12
35-2	Distribution of trees species at the University of Michigan Saginaw Forest near Ann Arbor, Michigan . . . . .	35-13
35-3	Recognition map of Saginaw Forest generated by the University of Michigan spectral analysis and recognition computer . . . . .	35-14
35-4	Recognition map of Saginaw Forest generated by the University of Michigan spectral analysis and recognition computer . . . . .	35-15
35-5	Needle cast on Scots pine was much more severe in 1969 than in 1970 as indicated by these photographs taken from 3000 feet . . . . .	35-16
35-6	Damage believed due to ozone became more severe in 1970 as indicated by these photographs taken from 3000 feet . . . . .	35-17
35-7	Simulated color IR image prepared from data obtained with the University of Michigan multispectral scanner . . . . .	35-18
36-1	Apollo 9 coverage for a portion of Atlanta Test Site 217 . . . . .	36-24
36-2	The Atlanta test site includes all or portions of 27 counties in Alabama and Georgia . . . . .	36-25
36-3	RB57F Mission 131 covered the Atlanta test site in seven flight lines . . . . .	36-26

Figure		Page
36-4	Interpreters used a Bausch and Lomb zoom 70 stereoscope at 7.5X to interpret satellite photography . . . . .	36-27
36-5	A forest-type land use map was constructed using a 28X enlargement of block 3 made from the Apollo 9 IR color as a base map . . . . .	36-28
36-6	A photometric data system microdensitometer coupled to a data acquisition system digitizer was used to scan the Apollo 9 and high-altitude RB57F photography . . . . .	36-29
36-7	Interpreters delineated forest type and land use along sample strips . . . . .	36-30
36-8	The mean red, green, and blue optical densities for 13 forest and nonforest classes on Apollo 9 IR color . . . . .	36-31
36-9	The mean red, green, and blue optical densities for 9 of 13 forest and non-forest classes . . . . .	36-32
36-10	The mean optical density (no filter) for 9 of 13 forest and nonforest classes . . . . .	36-33
36-11	Pulpwood cuttings	
	a. A pulpwood cutting that occurred sometime after the Apollo 9 mission, but before RB57F Mission 131, is shown detected by a microdensitometer scan . . . . .	36-34
	b. The pulpwood cutting shown on the density trace in figure 36-11a does not appear on the top photo taken in April 1969 . . . . .	36-35
36-12	Pipeline subject	
	a. A pipeline that was constructed sometime after the Apollo 9 mission, but before RB57F Mission 131, is shown detected by a microdensitometer scan . . . . .	36-36
	b. The pipeline shown on the density trace in figure 36-12a does not appear on the top photo taken in April 1969 . . . . .	36-37

Figure		Page
37-1	Video print of scanner data from Colorado grassland, 0.62 to 0.66 $\mu\text{m}$ . . . . .	37-15
37-2	Three dimensional plot of filtered scanner data from Colorado grasslands, 0.4 to 0.44 $\mu\text{m}$ . . . . .	37-16
37-3	Three dimensional plot of filtered scanner data from Colorado grasslands, 0.8 to 1.0 $\mu\text{m}$ . . . . .	37-17
37-4	Three dimensional plot of filtered voltage ratio from Colorado grasslands scanner data . . . . .	37-18
37-5	Altitude dependence of irradiances in a homogeneous atmosphere with a visibility of 23 km . . . . .	37-19
37-6	Altitude dependence of irradiances in a homogeneous atmosphere with a visibility of 2 km . . . . .	37-20
37-7	Normal spectral emissivity of rocks . . . . .	37-21
37-8	Discrimination of acidic silicates near Mill Creek, Oklahoma, sand quarry . . . . .	37-22
37-9	Surface temperature for 16 percent surface moisture for two soil types, Columbia Basin area . . . . .	37-23
37-10	Surface temperature for sandy loam at three different surface moisture percentages, Columbia Basin area . . . . .	37-24
37-11	Surface temperature for sandy loam at 11 percent surface moisture, Columbia Basin area . . . . .	37-25
37-12	Mixture of materials . . . . .	37-26
37-13	Reflectance spectra . . . . .	37-27
37-14	Reflectance spectra of mixtures . . . . .	37-28

Figure		Page
37-15	Calculated estimates of vegetational components of experimental plots	
	a. Plots without nitrogen amendments . . . . .	37-29
	b. Plots with nitrogen amendments . . . . .	37-29
37-16	Spectral adaptive recognition computer/hybrid, SPARC/H . . . . .	37-30
37-17	SPARC/H processing flow and timing chart . . . . .	37-31
38-1	Preprocessing transforms . . . . .	38-8
38-2	Ratio preprocessing transforms . . . . .	38-8
38-3	Spectral channel output versus scan angle for three materials showing the scan angle functions . . . . .	38-9
38-4	Transformed spectral channel output versus scan angle for three materials showing means of combined signatures . . . . .	38-10
38-5	Color coded digital recognition map of a portion of Yellowstone National Park . . . . .	38-11
38-6	Typical digital computer graymap of ponds, Woodworth study area, North Dakota . . . . .	38-12
38-7	Typical digital computer graymap of ponds, Woodworth study area, North Dakota . . . . .	38-13
38-8	Typical digital computer printout of pond statistics, Woodworth study area, North Dakota . . . . .	38-14
38-9	Typical digital computer printout of pond statistics, Woodworth study area, North Dakota . . . . .	38-15
38-10	Comparison of typical yawed and yaw corrected data	
	a. Video with yawed geometry . . . . .	38-16
	b. Video with yaw corrected geometry . . . . .	38-16

Figure		Page
38-11	Type I processing services . . . . .	38-17
38-12	Type II processing services . . . . .	38-17
38-13	Type I work completed - FY70 . . . . .	38-18
38-14	Type II work completed - FY70 . . . . .	38-18
39-1	A computer gray scale printout of the white light scan of the color infrared frame . . . . .	39-9
39-2	Apollo 9 computer map of Imperial Valley region . . . . .	39-10
39-3	Computer map of Imperial Valley vegetation, bare soil, and water . . . . .	39-11
39-4	Computer analysis of Apollo 9 multispectral photography, Dogwood Road . . . . .	39-12
39-5	Computer analysis of Apollo 9 multispectral photography, McCabe Road . . . . .	39-13
39-6	Soil identification map of an area near El Centro . . . . .	39-14
39-7	A computer map of the El Centro region . . . . .	39-15
39-8	Conventional geologic map of the area west of the Imperial Valley . . . . .	39-16
39-9	Computer derived geological map of the area west of the Imperial Valley . . . . .	39-17
40-1	Visible and thermal IR imagery . . . . .	40-12
40-2	Adaptive multispectral picture registration system . . . . .	40-13
40-3	Digital imagery registration system . . . . .	40-14
40-4	Border enhancement techniques . . . . .	40-15
40-5	Example of rotational distortion in multi- spectral airborne scanner imagery . . . . .	40-16

Figure		Page
40-6	Multitemporal analysis . . . . .	40-17
40-7	Image data registration . . . . .	40-18
40-8	Digital image display system . . . . .	40-19
40-9	Satellite based remote sensing system, block diagram . . . . .	40-20
40-10	Data with noise added . . . . .	40-21
40-11	Classification results, wheat only . . . . .	40-22
40-12	Classification performance versus noise . . . . .	40-23
40-13	GE/LARS data compression study . . . . .	40-24
40-14	GE/LARS data compression study, test results . . . . .	40-25
40-15	MSS data compression based on spectral correlation, block diagram . . . . .	40-26
40-16	MSS data compression based on spectral correlation, spectral bands for classification . . . . .	40-27
40-17	Spectral band selection values . . . . .	40-28
40-18	Spectral band selection classes . . . . .	40-29
40-19	Class separability measure, no maximum . . . . .	40-30
40-20	Class separability measure, maximum . . . . .	40-31
41-1	The remote sensing system . . . . .	41-17
41-2	Spectral responses of objects over octave bandwidths . . . . .	41-18
41-3	Comparison of monochromatic and panchromatic air photos with monochromatic radar image . . . . .	41-19
41-4	Acoustic side looking radar images of agricultural model demonstrating improve- ment of sensing with panchromatic illumination . . . . .	41-20

Figure		Page
41-5	Ultrasonically simulated polypanchromatic radar image . . . . .	41-21
41-6	Monochromatic images taken at slightly different frequencies . . . . .	41-22
41-7	Comparison of monochromatic and panchromatic images . . . . .	41-23
41-8	Comparison of monochromatic and panchromatic images . . . . .	41-24
41-9	Variance of received power versus averaging bandwidth . . . . .	41-25
41-10	Example of fading that causes speckle in radar images . . . . .	41-26
41-11	Fully focused synthetic aperture imaging over a boundary separating two fields whose nonstatistically distributed scattering cross sections differ by 9.54 decibels . . . . .	41-27
41-12	Use of multiple subapertures to improve grey scale . . . . .	41-28
41-13	True map of Rayleigh distributed scattering cross sections for two fields whose differential scattering cross sections differ by 9.54 decibels . . . . .	41-29
41-14	Radar shadow and layover versus angle . . . . .	41-30
41-15	Contour map to go with figure 41-16 . . . . .	41-31
41-16	Example of true ground range presentation in mountainous terrain . . . . .	41-32
41-17	Illustration of radar layover and shadow using different look angles for the same terrain and slant range presentation . . . . .	41-33
41-18	Optimum radar depression angles for geologic analysis, Western Hemisphere . . . . .	41-34

Figure		Page
41-19	Optimum radar depression angles for geologic analysis, Eastern Hemisphere . . . . .	41-35
41-20	Comparison of real and synthetic aperture DPD-2 images, Garden City, Kansas, 1970	41-36
43-1	K-band radar imagery near Tucson, Arizona . . . . .	43-25
43-2	Soil boundaries northwest of Tucson, Arizona . . .	43-26
43-3	Soil types of the Tucson region simplified from USDA soil survey map of 1931 . . . . .	43-27
44-1	Schematic diagram of precision color monitor . . . . .	44-15
44-2	Natural color display of multispectral scanner data . . . . .	44-16
44-3	Interactive method for entering ground truth areas . . . . .	44-16
44-4	Completed boundaries for ground truth areas . . . . .	44-16
44-5	Display showing color coded ground truth map . . . . .	44-16
44-6	Display showing computer derived land use map . . . . .	44-16
44-7	Errors in the computer derived land use map . . . . .	44-16
44-8	Multispectral scanner data represented as points in three dimensional measurement space . . . . .	44-17
44-9	Multidimensional histogram for soybean . . . . .	44-17
44-10	Multidimensional histogram for corn . . . . .	44-17
44-11	Classification space derived using L = 1.0 and D = 1000 . . . . .	44-18



Figure		Page
44-12	Classification space derived using L = 5.0 and D = 1000 . . . . .	44-18
44-13	Classification space derived using L = 1.0 and D = 15 . . . . .	44-18
44-14	Areas classified as soybean for D = 10 and D = 20 . . . . .	44-18
44-15	Soybean histogram on area classified as soybean . . . . .	44-18
44-16	Corn histogram on area classified as soybean . . . . .	44-18
44-17	Boresight path and sensor return for infrared radiometer . . . . .	44-19
44-18	Boresight path and sensor return for microwave scatterometer . . . . .	44-19
44-19	Microwave scatterometer signatures for three different flight path intervals . . . . .	44-19
45-1	13.3 GHz scatterometer system, block diagram . . . . .	45-31
45-2	13.3 GHz scatterometer, resolution cell geometry . . . . .	45-32
45-3	Klystron temperature stability . . . . .	45-33
45-4	Rolloff values for 13.3 GHz scatterometer . . . . .	45-34
45-5	$G_0^2 F'(\theta)$ values with 3 decibel beamwidth . . . . .	45-35
45-6	13.3 GHz single polarized scatterometer, blitz wheel test . . . . .	45-36
45-7	Digital program output of the blitz wheel test, plus Doppler data . . . . .	45-37
45-8	Digital program output of the blitz wheel test, minus Doppler data . . . . .	45-37

Figure		Page
45-9	13.3 GHz single polarized scatterometer, diagram showing channel phase shift . . . . .	45-38
45-10	Experimental results of phase shift study . . . . .	45-39
45-11	Geometry figures	
	a. Resolution cell geometry . . . . .	45-40
	b. Cross track geometry . . . . .	45-40
	c. Along track geometry . . . . .	45-40
45-12	Cross-section ratio of bandwidths . . . . .	45-41
45-13	Comparison of old and redop 1 modified beamwidths . . . . .	45-42
45-14	Comparison of antenna gains . . . . .	45-43
45-15	Cross track angle	
	a. Area of total transmitted/received antenna energy . . . . .	45-44
	b. Cumulative probability, percent of total power . . . . .	45-44
45-16	The value of beamwidth using various methods for redop 1 modified antenna patterns . . . . .	45-45
45-17	The value of $G_o^2 F'(\theta)$ using various methods for redop 1 modified antenna patterns . . . . .	45-46
45-18	Resolution cell geometry in the presence of roll variation . . . . .	45-47
45-19	Typical digital computer processed data plot for Mission 119 before program change . . . . .	45-48
45-20	Typical digital computer processed data plot for Mission 119 after program change . . . . .	45-49
45-21	Change in filter bandwidth due to change in aircraft velocity . . . . .	45-50

## CARTOGRAPHY

by

Alden P. Colvocoresses

INTRODUCTION

This paper is a condensation of the EROS Cartography Program's annual report to NASA for fiscal year 1970. It emphasizes the relationship between topographic activities of the U.S. Geological Survey and those of the NASA Manned Spacecraft Center.

This paper is divided into the following sections:

- o Objectives
- o Relationship to NASA aircraft program
- o Space photomapping
- o Support of ERTS
- o Thematic mapping
- o Conclusion

## OBJECTIVES

The program objectives are to:

1. Apply remote sensing of the earth (basically from space) to
  - a. Topographic and planimetric base mapping
  - b. Rapid thematic mapping of significant temporal phenomena, such as open water, snow, vegetation, and the massed works of man, and the sequential spatial changes of these phenomena.
  - c. Production of specially processed imagery from which useful information can be derived for a variety of disciplines associated with earth resources.
  - d. Rapid location and portrayal of unpredictable phenomena.

---

Publication authorized by the Director, U.S. Geological Survey.

2. Provide a user-oriented research facility in which data-processing techniques (principally analog) can be developed and tested in conjunction with various user groups associated with earth observations from space.

#### RELATIONSHIP TO NASA AIRCRAFT PROGRAM

High-altitude aircraft photography is of a continuing and vital interest to cartography. As early as 1965 a request was made to NASA for the simultaneous procurement of panoramic and mapping (frame) photo-coverage. Installation of the 12" focal-length mapping camera in the RB57 was also advocated. Although the simultaneous procurement of panoramic and mapping coverage has not been accomplished, the RB57 flights are of current operational value and their potential value to research and development is enormous.

The NASA RB57 program is producing photographic coverage of mapping quality with 6" and 12" cameras at about 60,000 feet, and the coverage is being applied within the Geological Survey to the following tasks as the films become available:

- o Flight planning (for low-altitude coverage) and field identification in southern Florida.
- o Field classification and possible direct use as a photobase for the Florida Keys. Figure 1 is a section of an RB57 12" color infrared photograph of the Keys (Bahia Honda).
- o Orthophoto compilation, field classification, and aerotriangulation in the San Francisco Bay area.
- o Experimental wetland categorization in the Chesapeake Bay area. Figure 2 is a 6" color infrared photo of the Chesapeake Bay area illustrating a clear demarcation of what presumably may be classified as wetlands.
- o Experimental production of color photomaps of both the Florida Keys and the Phoenix area.
- o Urban-area map revision and photomapping related to the "26-city" project.

Figures 1 and 2 demonstrate the value of the high-altitude air photos and also the information content of properly exposed color infrared film. No conflict with proposed space systems, or duplication of effort, is evident from this demonstration--in fact space and high-altitude aircraft systems appear to be highly complementary. The two primary national

mapping scales are currently 1:24,000 and 1:250,000, roughly a 10-fold difference. Consequently, obtaining images of the earth from altitudes of at least a 10-fold difference, say 20 kilometers and 200 kilometers, appears justified. Resolution is the dominant factor, but for similar sensors altitude is the key. A 10-fold difference in altitude (for the same sensor) means a 100-fold difference in the number of images. To the cartographer the representations are as different as the 1:24,000 and 1:250,000 scale maps, which are considered to be complementary in spite of their obvious differences. The cartographic program strongly supports the USGS recommendation that the complete high-altitude photo-coverage of the United States be obtained at the earliest practical date, and one of the reasons for the recommendation is that the photo-coverage will support and complement ERTS and other earth-imaging space systems.

#### SPACE PHOTOMAPPING

Sample photomaps at 1:250,000 and 1:500,000 scales were compiled, printed, and distributed. They cover areas in southern Arizona and adjacent States and were made from Apollo and Gemini photographs taken with Hasselblad and Maurer cameras, 80 mm and 76 mm focal length, at a nominal altitude of 125 nautical miles.

These products exemplify an effort to combine space images with conventional medium-scale line maps, with the potential of improving the content, currency, and even the accuracy of medium-scale maps. The photographs were rectified and scaled to the planimetric drawing of the existing line map. Although the photographs have neither the resolution nor the geometric fidelity that would be specified for a standard product, they were nearly orthographic after rectification and therefore could be reasonably well fitted to conventional map projections. The UTM grid was added for ease in scaling coordinates of map points. Some 3,000 copies of these photomaps were distributed to interested map users, with a request for comments. The comments received, which are in general highly favorable, will be considered in the development of a standard photomap rendition at medium and small scales. The comments of map makers, which as a whole are more critical, are also receiving full consideration as they reflect many technical problems that most map users are not aware of. Figure 3 illustrates the content difference between the line map and photomap, and figure 4 illustrates how currency and accuracy are both improved by the photoimage.

Color proofs at 1:1,000,000 scale were prepared from the same photographs, but a lack of adequate coverage and a suitable line base has postponed printing of a specimen photomap at this scale.

The application of ERTS to photomapping will be covered in the following section, but SKYLAB also promises some good source material for the photomapper. Experiment S190 (six 6" cameras recording on 70mm film) should provide ideal coverage for 1:250,000-scale photomaps, and because of the 50° orbit inclination could cover all the States but Alaska. However, the larger scales needed for many applications require a bigger camera. The USGS is recommending that the Hycon frame camera of 18" focal length developed for the Apollo program be flown on SKYLAB. The resulting photographs could be applied to a wide variety of map products at scales up to 1:100,000 or even larger.

#### SUPPORT OF THE EARTH RESOURCE TECHNOLOGY SATELLITE (ERTS)

Several tasks are underway in support of ERTS, as follows: (1) geometric analysis of the Return Beam Vidicon (RBV); (2) recommending format criteria for ERTS products and providing a map support system; (3) providing photoidentifiable ground control; and (4) definition of ERTS cartographic experiments.

All four of these tasks are covered in detail in the annual report of the EROS Cartography Program, but some highlights are summarized in the following paragraphs:

1. Precise positional measurements are being made of the 81 reseau marks on each RBV tube. When laboratory images are obtained and recorded with the RBVs, the reseaus are again measured on the images to obtain data for an analysis of distortions. This work is being performed in cooperation with NASA Goddard and RCA. A detailed report will be given at the 7th International Symposium on Remote Sensing of Environment (University of Michigan).
2. NASA has accepted the USGS recommendations for ERTS image format and annotations. The precision-processed images will be cast on the Universal Transverse Mercator (UTM) projection at 1:1,000,000 scale, to provide a photomap that can be directly correlated with line maps, such as those in the 1:250,000-scale series, since both will carry UTM grids. A metric coordinate reader, illustrated in figure 5, has been developed to facilitate measurement of grid coordinates on both gridded maps and precision-processed photos. Gridded 1:250,000-scale maps, currently a military product, are also being stocked by the USGS for "official use" and may be put on public sale if the demand warrants.
3. To produce precision-processed images, a sizeable bank of photoidentifiable ground control points is required. Points in the State of Missouri have already been filed, and negotiations are underway with NASA to enlarge the data bank to cover all 50 States.

4. Several cartographic experiments, at scales ranging from 1:250,000 to 1:5,000,000 are underway for ERTS. The areas of principal concern are the 50 States and the polar regions; and the projects concern planimetric photomapping, map revision, and thematic mapping (including change).

### THEMATIC MAPPING

The development of automated or semiautomated image-processing and information-extraction techniques is the immediate goal of this effort. Density slicing is being investigated on contract with Philco Ford and International Imaging Systems (I<sup>2</sup>S). In-house photoprocessing techniques have produced some enhanced images of potential value. Figure 6 is an enhanced image (produced by a sharp-mask technique) of the Ouachita River at flood stage as photographed on Apollo 9. The definitive separation of water from land areas is typical of the type of problem being attacked. Figure 7 illustrates the result of processing an Apollo S065 photograph of Georgia, to separate land and open-water areas. If the geometry and photometry of image acquisition and processing can be properly calibrated and controlled, the mapping of themes characterized by distinct spectral signatures should become a reality. Likewise, controlled sequential thematic mapping of the same area will provide the necessary input for the mapping of change. The present approach is to use photographic (optical) processing insofar as possible and to bring in scanners and the digital approach only as it becomes necessary. Since the most versatile computer in existence is the human brain, it will also be directly used in the thematic mapping process for a long time to come.

### USER RESEARCH FACILITIES

One of the basic objectives of the cartography program is to establish user-oriented research facilities. These facilities are primarily related to photographic processes although TV displays, scanners, and even a digital plotter are under development. The facilities are provided within the U.S. Geological Survey at Silver Spring, Md., except as otherwise noted. Instrumental developments are described in a separate paper, but the following is a list of the facilities available or in development:

- o A file of aircraft and space film
- o Precision enlargers, rectifiers, and viewers<sup>1</sup>
- o A three-band additive viewer<sup>2</sup>
- o A black-and-white and color<sup>3</sup> photoprocessing laboratory<sup>1</sup>

- o Cartographic facilities<sup>1</sup>
- o Density slicer (electronic)
- o BAI optical correlator<sup>4</sup>
- o Microdensitometer<sup>4</sup>
- o Automatic plotter<sup>4</sup>
- o Bendix Datagrid Digitizer<sup>4</sup>

- 1 Use is generally on a repay basis
- 2 On indefinite loan from the Air Force
- 3 Located in the GSA Building, Washington, D.C.
- 4 Located at the Research Center, McLean, Va.

In addition a precision color photographic laboratory is programmed for FY71.

#### CONCLUSION

Progress is being made and by the time ERTS flies, a system for image processing and dissemination should be operational. Several other sophisticated remote sensing systems will be in operation by 1972 and must be fully considered. But the view of the Cartography Program must also extend beyond 1972. At last year's meeting a geosynchronous system for earth sensing was suggested, and the USGS subsequently proposed such a system to NASA.

A few days ago the Program received a NASA Request for Research and Technology Objective and Plan for a Synchronous Earth Observation Satellite (SEOS-A), and this is most gratifying. The USGS is preparing to map the fixed and temporal features of the US and other areas from both space and aircraft. The various modes, which includes geosynchronous and film return systems as well as the ERTS type, must be fully tested so that optimum methods can be applied to the mapping tasks.



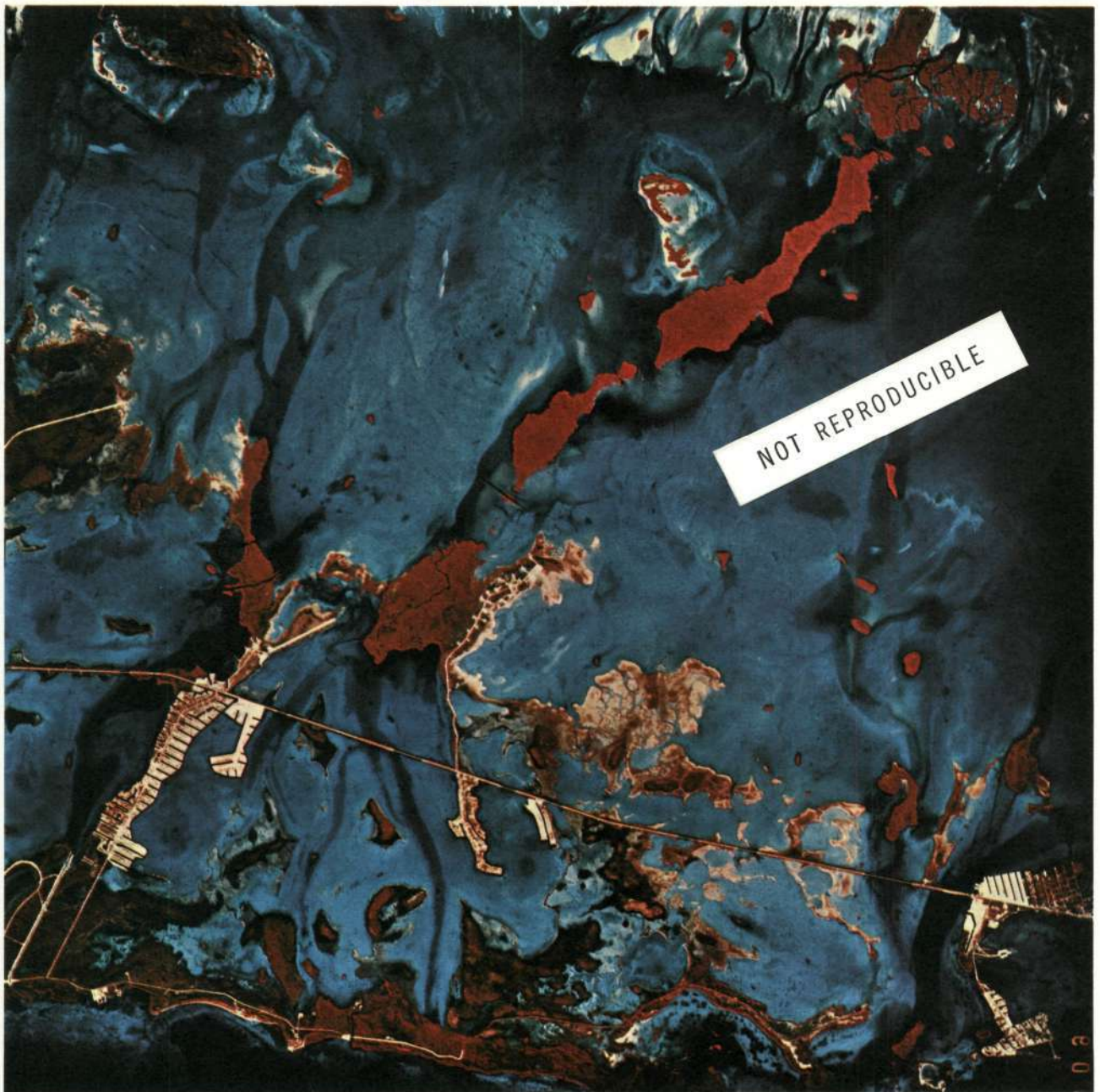


Figure 1--A section of the Florida Keys from 60,000 feet as photographed with a 12" focal-length mapping camera in color infrared (NASA photo).



Figure 2--Coastal wetland area as photographed from 60,000 feet with a 6" focal-length mapping camera in color infrared (NASA photo).

# 1:250,000-SCALE MAP – PHOENIX



**standard line map**

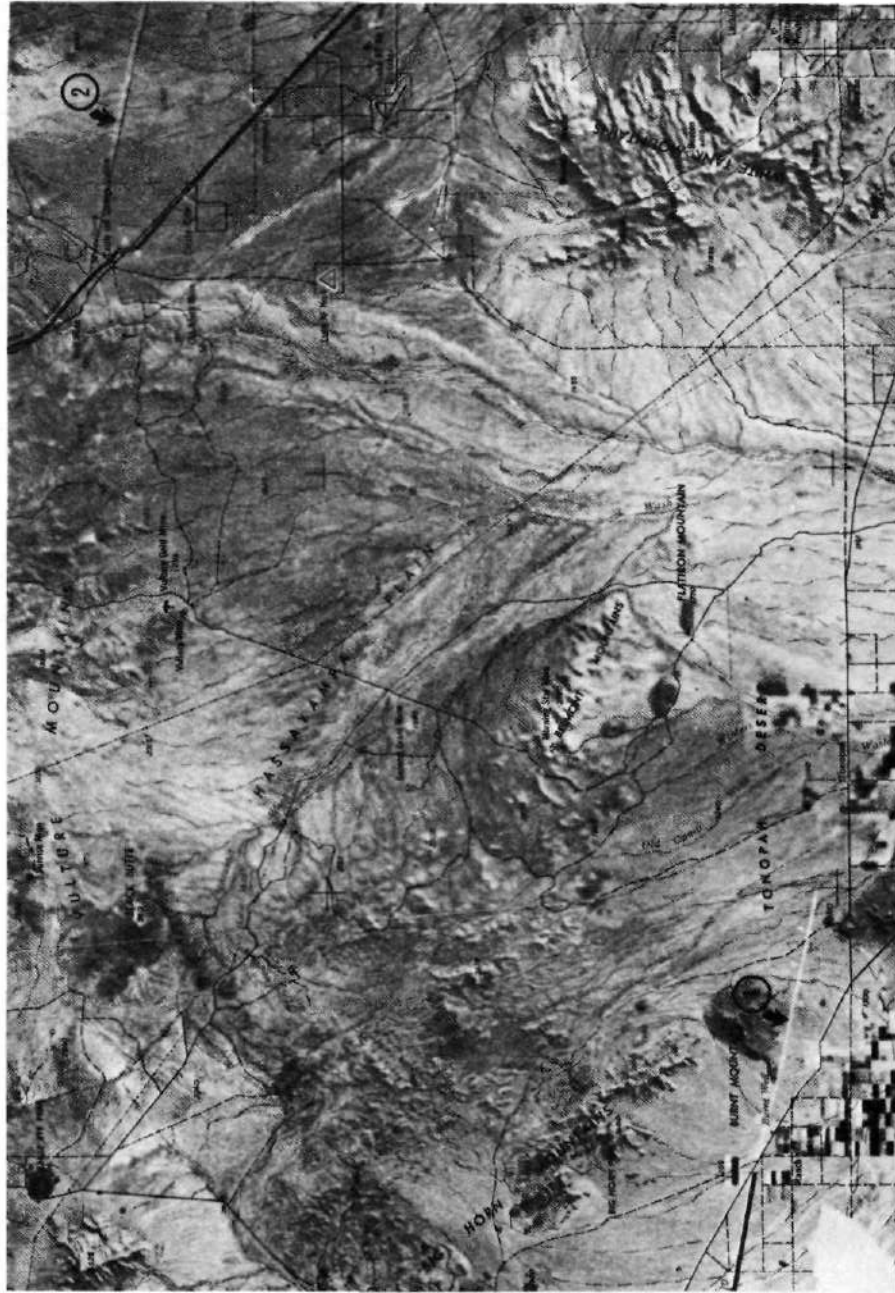
NOT REPRODUCIBLE



**...with space imagery base**

Figure 3.- 1:250,000-scale line map compared with the line map combined with space image.

1969 MANUSCRIPT REVISED BY 1969 SPACE (APOLLO) PHOTOGRAPHY

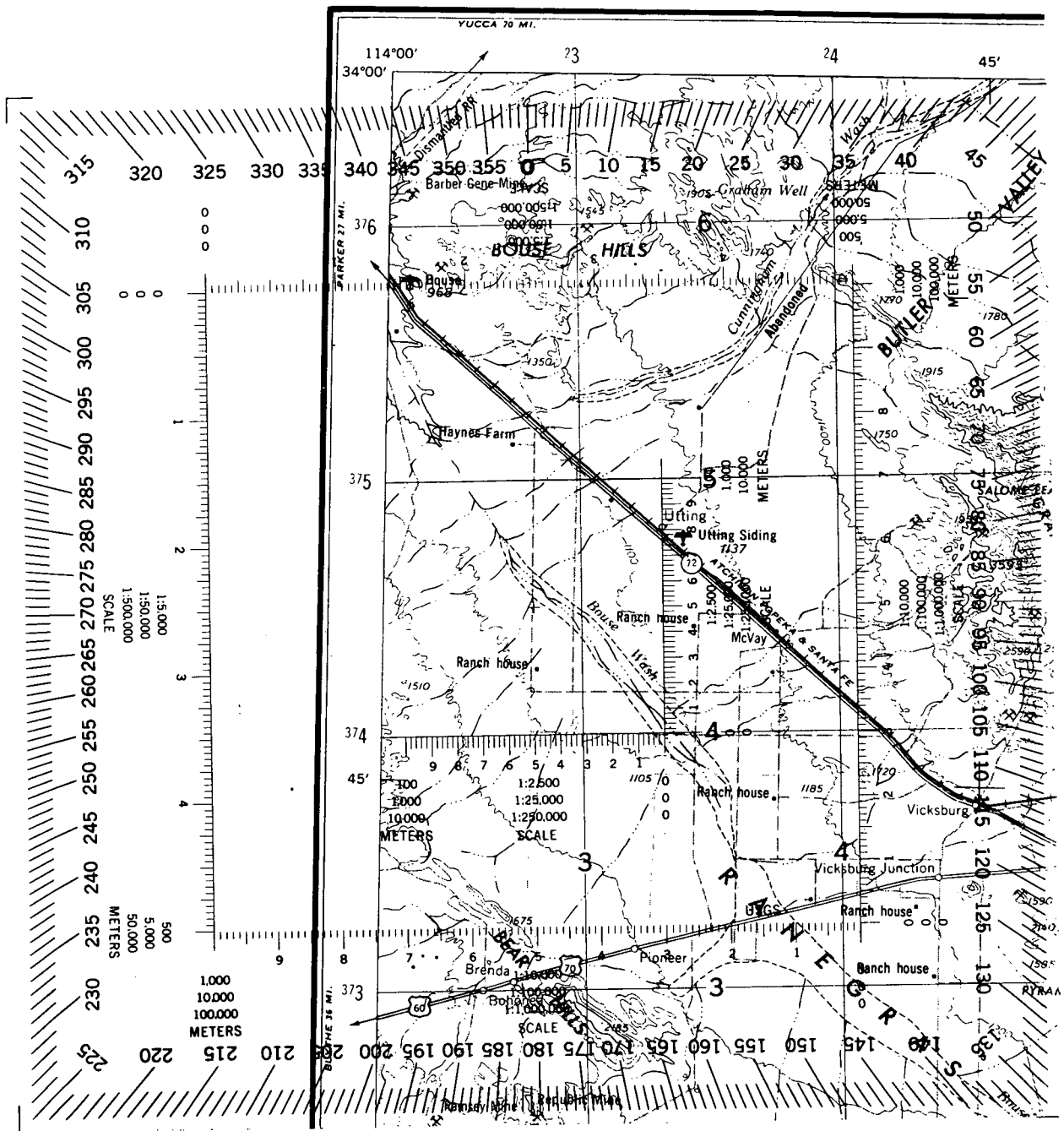


① EXTENSION TO INTERSTATE

② MISALIGNED ROAD

USGS

Figure 4.- The manuscript (1:250,000 scale, Phoenix sheet) was compiled by USGS from all available (other) sources and was considered current as of March 1969, which is the same date as the Apollo 9 (8065) space photograph. On this section of the space photo are indicated both additions and positional corrections to be made to the road net.



Metric Coordinate Reader

Figure 5.- A coordinate reader superimposed on gridded 1:250,000-scale map.

NOT REPRODUCIBLE

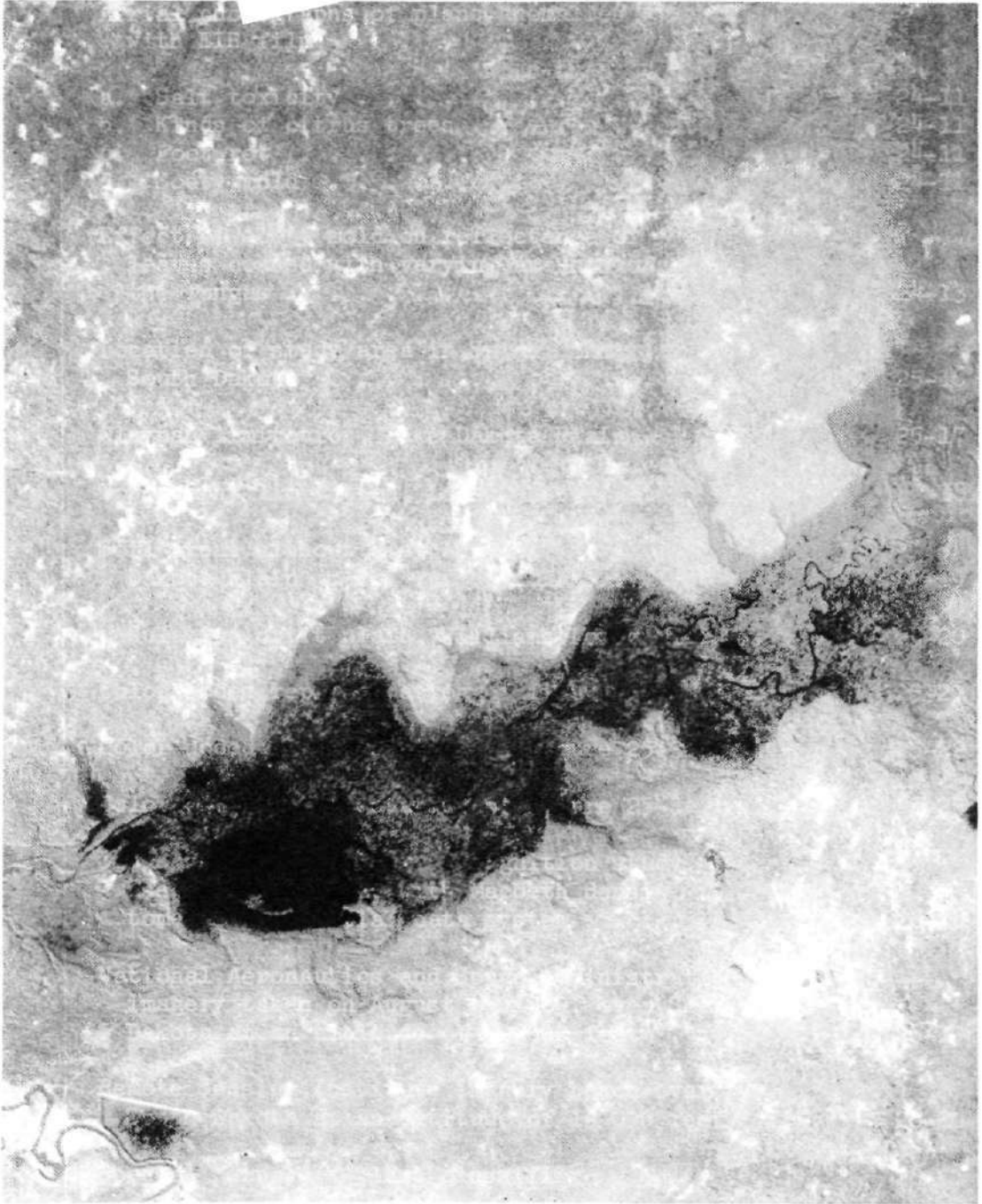


Figure 6.- Selected segment of exposure AS9-26C-3740, March 11, 1969 showing the Ouachita River in the Mississippi Valley at flood stage. Black-and-white enlargement was made from the IR (700-900 nm) band. A sharp-mask technique of image enhancement and exposure aimed at optimizing density differences were used.

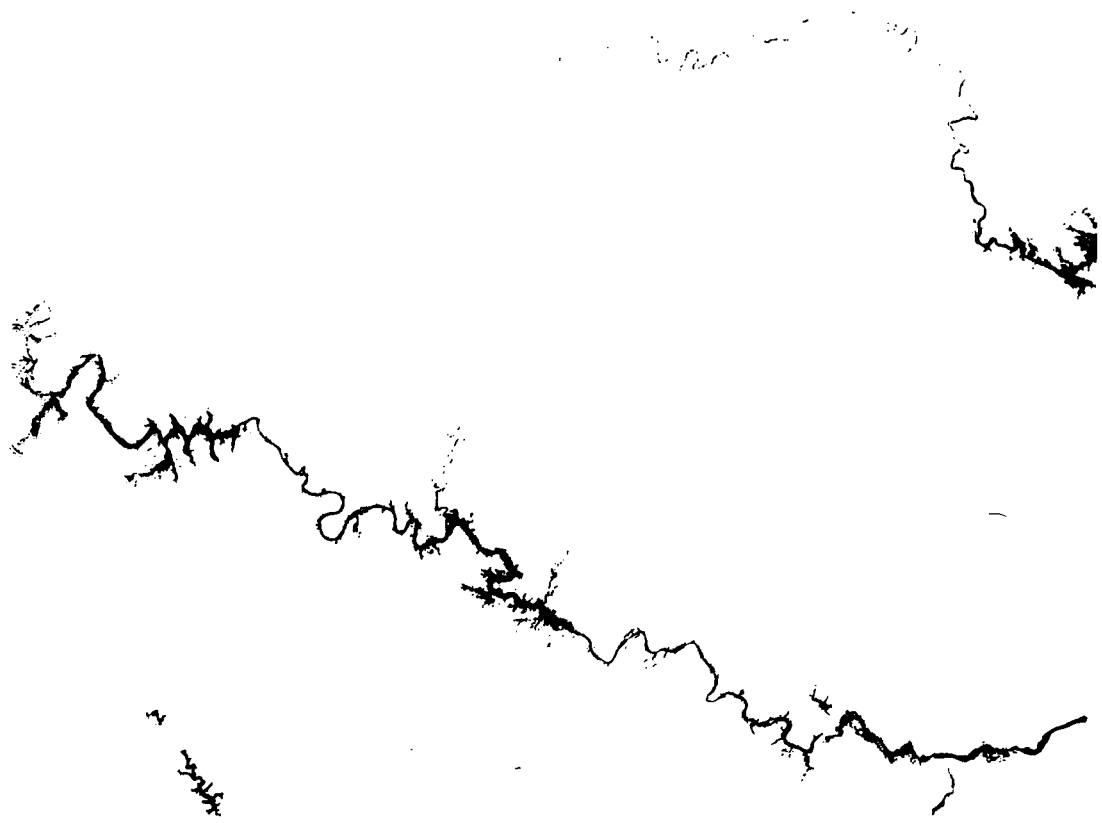


Figure 7.- Open water separated from land by photo-optical means (NASA Apollo photo).

AUTOMATIC CARTOGRAPHY TECHNIQUES  
FOR EARTH RESOURCES RESEARCH

by Dean T. Edson

ABSTRACT

One of the important requirements of the Earth Resources Observation Systems (EROS) program is to provide data users with adequate facilities and equipment for the interpretation and mensuration of photographic images and related graphics. This paper deals with the progress in developing instrumentation and software for the EROS user facilities. Significant progress has been made in developing the USGS binary-mode scanning digitizer which is described in detail. Other instrumentation and processes discussed include profile-generating techniques, a manual digitizer, image correlation systems, and some new photomechanical data-processing techniques.

## USER RESEARCH FACILITY

One of the major ongoing efforts in the Earth Resources Observation Systems (EROS) program is the development of a user research facility for studying cartographic applications of remote-sensed data. The equipment which is associated with the facility is presently located at the U.S. Geological Survey offices in Silver Spring, Maryland, and McLean, Virginia. Among the equipment items which are now assembled at these locations are a density slicer with TV output, a three-lens additive viewer, a graphic digitizer, a microdensitometer, and an image correlating and measuring system.

The Geological Survey is also developing a family of equipment for digital processing which will be used in automatic cartography techniques in both the EROS program and the topographic mapping research program. This equipment will include an x-y plotter of extremely high accuracy and resolution for cartographic use and a graphic scanner for converting binary graphic information to digital form. In its initial application, the scanner will be used for digitizing contours.

---

Publication authorized by the Director, U.S. Geological Survey.



For investigator support, a library of space and aircraft film is available with black-and-white photoprocessing facilities and an array of small viewers, enlargers, rectifiers, and other cartographic facilities for transforming imagery in both scale and geometric shape. A color photolab, which will be used for producing high-quality color imagery, is under development.

Figure 1 describes the interrelated functions of equipment being developed. The upper left box signifies a technique for generating profiles<sup>1</sup> which is being developed now at the research center in McLean, Va. This is an automatic photographic technique for recording terrain profiles from a stereoscopic model. The model is formed in a double-projection plotter with edge-enhanced photographs, one positive and the other negative. The two images counteract on each other at all intersections of corresponding rays and produce neutral-density traces of the profiles, which can be recorded on film. Research is underway to develop a method of extracting (possibly by density slicing) the profile traces from the images of the noncorresponding rays. The profiles, converted to digital form, could then be input to a terrain data base, shown in the upper right corner of figure 1.

The digitizing scanner, which is essentially a high-resolution Vidicon and imaging optical system under extremely fine control, will scan any binary graphic (for example, black and white) and record on magnetic tape the x-y raster address where data is detected. The scanner is being supported by a fairly extensive software project, which is nearly complete. The data resulting from this scanning will be input to the data base, and the data can be used to generate other cartographic material on an automatic coordinate plotter (USGS Cartoplot).

The manual digitizer, the third item on the left in figure 1, will generate auxiliary x-y data which can be superimposed on either the profile data or the scan data. This type of instrument generates a string of x-y coordinates at a high rate of speed as a graphic is traced manually with a cursor. For flexibility, this piece of equipment is being dovetailed into the system so that the data can be directed through two different routes to the graphic plotter. This approach permits the user to go either by way of off-line magnetic tape to the USGS computer, IBM System 360/65, located in Washington, D.C., or by way of paper tape in a teletype terminal to a time-sharing commercial computer. The time-sharing service route permits the user to convert, process, and plot data without any internal computer support and to maintain data files and programs which can be reached by commercial telephone.

## PROCESSING TERRAIN DATA

A process to convert existing graphic data to a map data base is being implemented. The first objective in this task is to convert contour information to a three-dimensional terrain model which could then be superimposed on remote-sensed data to aid in analyzing these data. A standard topographic map contour drawing is the first input document. Figure 2 demonstrates the method for reformatting a series of these documents to produce 10 X 10 km map blocks based on the Universal Transverse Mercator (UTM) Projection. It is noteworthy that the UTM has been adopted as the primary reference system for EROS data.

Once the input document is reformatted, it is divided into a 20 X 20 block array for scanning. Each block represents an area 500 X 500 m on the ground. A single block, which is approximately equivalent to an inch square at 1:24,000 scale, is imaged on the face of the photoemissive tube, as shown in figure 3.

A high-resolution Vidicon is used, and the scanning is under digital control. The resolution of this scanning process is over a million resolution points per square inch--1024 lines are scanned, and each line is sampled 1024 times. As the data are scanned, the x-y address of each data point is recorded on magnetic tape. A data point is defined as any resolution element which contains at least 50 percent of a line or other graphic object. Figure 4a is a computer printout with each X showing the x-y location of a data point. The first step in the computer program generates the center of gravity of the data-point array (shown in figure 4b as heavy black dots). The spacing of the rows and columns of x-y points in figure 4b represents 1-mil spacing on the original graphic. The next step, the filtering process, is fairly simple and results in a major reduction in the amount of data. In this process, the complexity of the line is analyzed, and only the information necessary to retain the character of that line is saved (fig. 4c). Only about 5 percent of the original data are finally stored.

The next step in the route from the contour map to the data base is the assignment of elevation numbers to the contours. A manual digitizer is used to assign a feature code or key, which represents an elevation number, to each contour, and the digitized keys are superimposed on the contour-line data. When the contour lines receive their proper identification, the data are then three dimensional (fig. 5). Next, a 10 m grid (ground scale) is superimposed over the data, and the most probable elevation of each grid intersection is generated (fig. 6). The 10 m grid, we feel, is fine enough to retain the accuracy of our most reliable data, and if we want to use contour information from small-scale maps, we can select a grid-cell size of 50 or 100 m, depending on the

reliability of the data. As indicated in figure 6, the array of elevations becomes a three-dimensional model that will be stored in the terrain data base by reference to the UTM grid. From this primary data base, users will be able to derive elevations, slopes, and other terrain information as required for analyzing remote-sensed data. Another planned application is the definition of drainage basins and subbasins. This scanner is scheduled to be delivered and should be in operation in May 1971.

Another very important application of this type of scanning is fast and accurate quantizing of any information developed by cartographic or photographic techniques, such as areal features isolated by density slicing. This binary scanning technique can be applied to many kinds of data derived from remote sensors.

#### IMAGE CORRELATION

The USGS, in cooperation with the BAI Corp., has developed an operational image correlating and measuring system (fig. 7).<sup>27</sup> Photometric and geometric control of the input imagery are major requirements for change detection. We feel that the use of this particular correlator provides the key to maintaining geometric control so that we can eventually superimpose corresponding images from different sensors or from time-variant exposures. We have used this equipment with images from the NASA SO 65 experiment to correlate multispectral frames, and we have obtained excellent results. The correlator has recently been modified so that we can now obtain a more responsive signature and a larger radius of signal acquisition.

#### MODIFYING GRAPHIC DATA

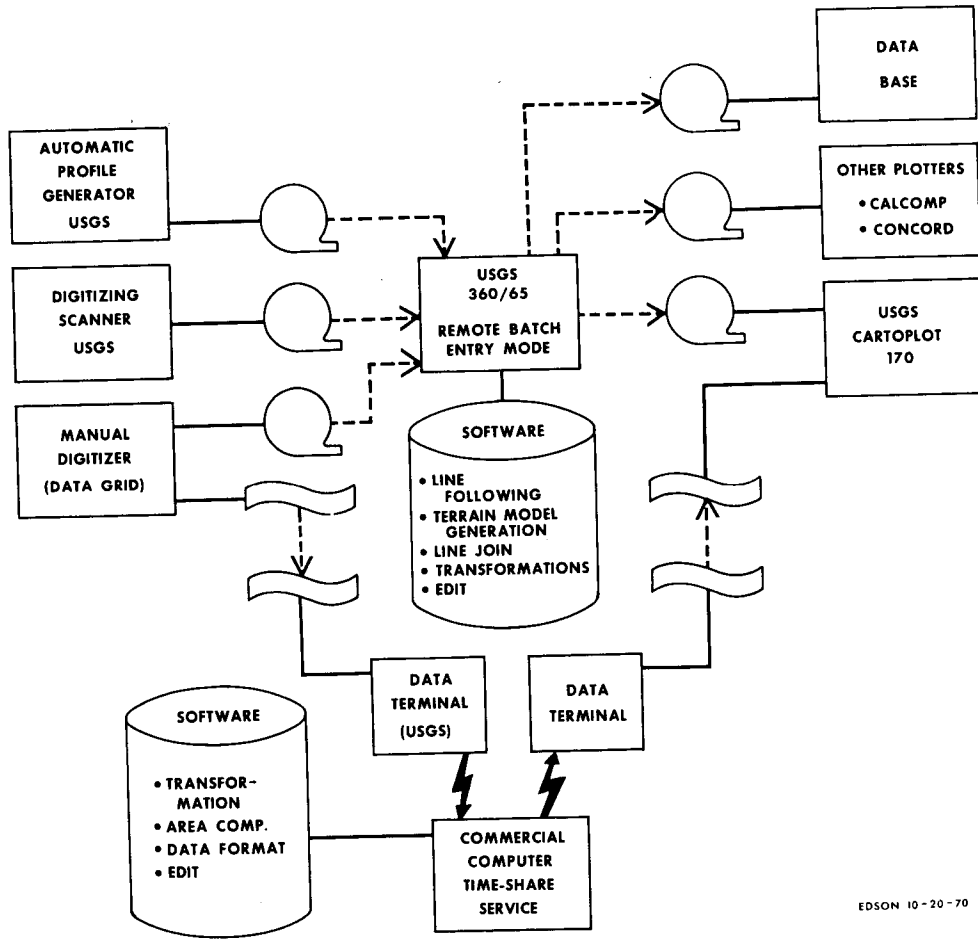
Finally, but by no means least important, research is being conducted in a field of data processing which incorporates optical, photographic, and mechanical techniques. Much of the existing ground truth is in graphic form, such as published maps and charts. The original manuscript material is on scale-stable films so that dimensional integrity is maintained as much as possible for future application. In digitizing selected graphic materials, many problems associated with sorting out various symbols and assigning symbol codes can be minimized by optically/mechanically separating symbols which appear on a single graphic. The topographic map black plate, for example, contains as many as 20 to 50 different symbol types (fig. 8a). The approach being developed, which is referred to as symbol dropout, employs a technique of controlling line widths in special reproduction processes.

Two results of the application of this technique are illustrated in figures 8b and 8c. In figure 8b all symbols 0.020 inch and larger

were isolated from the original plate, and in figure 8c the road symbols were isolated. The kind of graphic in figure 8b can now be scanned, digitized, and assigned a symbol code because the symbols all represent buildings. The line-width control technique has many other cartographic applications, such as the direct generation of slope maps and shaded relief overlays.

#### REFERENCES

1. Lewis, J. G., and Hughes T. A., Stereoscopic Profiling by Intersection of Ray Traces, paper presented at the ACSM-ASP Fall Technical Conference, Denver, Colo., Oct. 7-10, 1970.
2. Crabtree, J.S., and McLaurin, J. D., The BAI Image Correlator, Photogrammetric Engineering, vol. 36, no. 1, Jan. 1970, p. 70-76.



EDSON 10-20-70

Figure 1.--Digital cartographic systems for earth resources research.

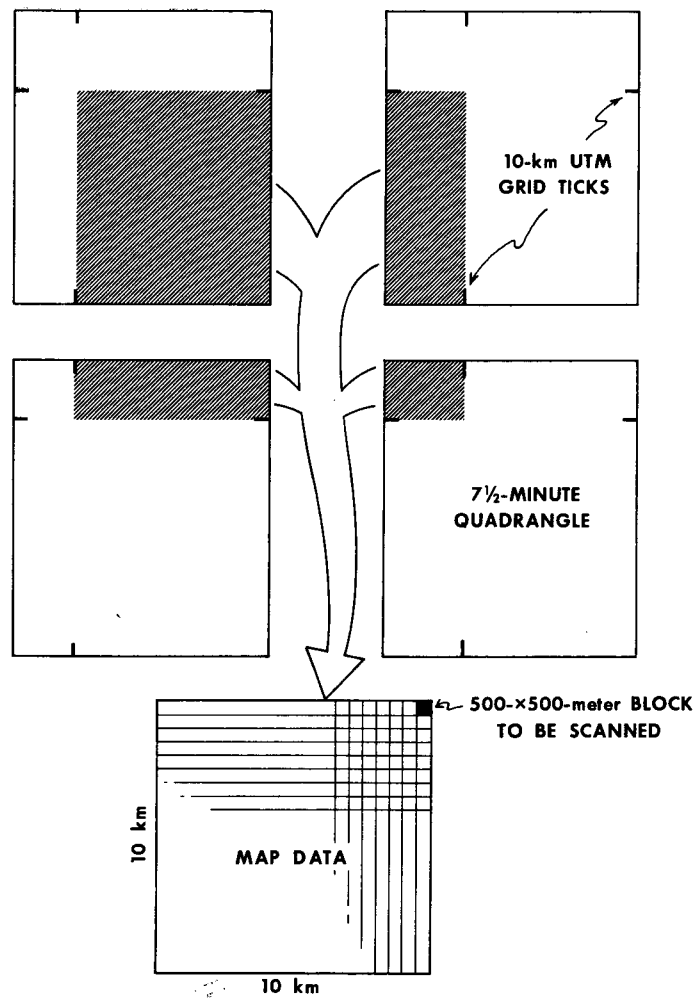


Figure 2.--Reformatting of graphic data.

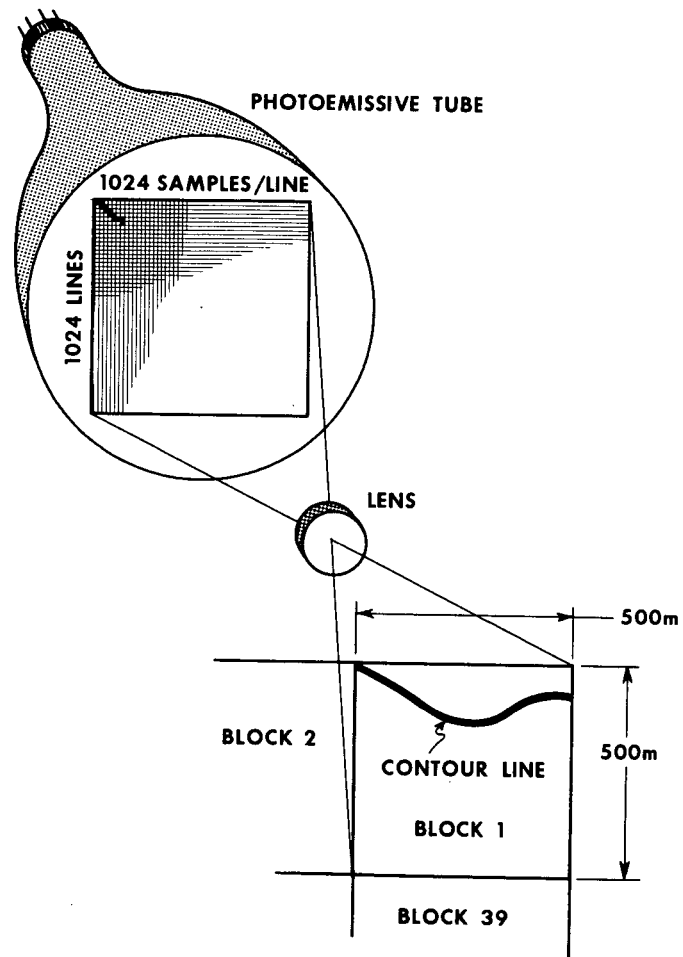
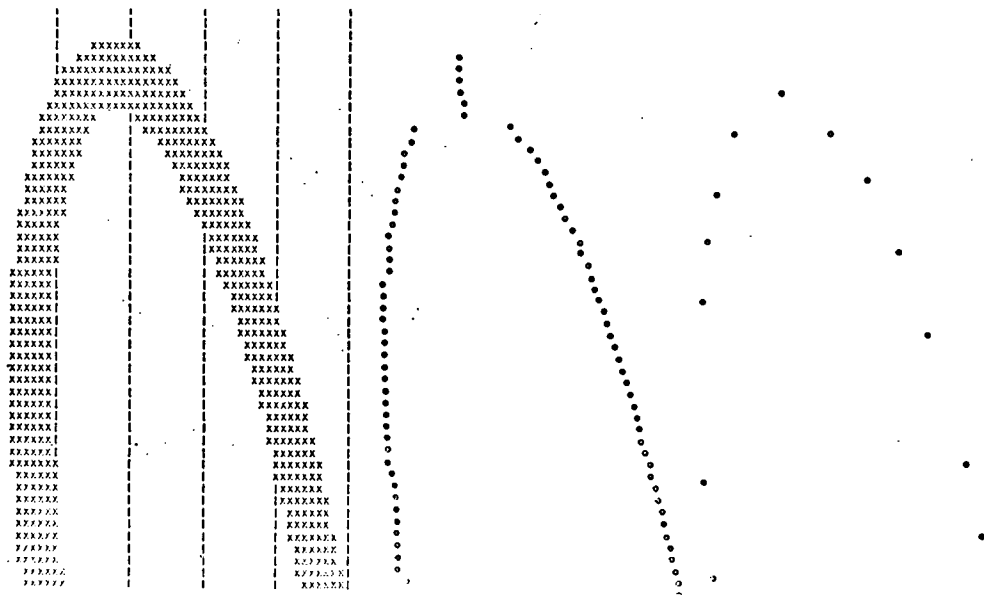


Figure 3.--Scanning the graphic data.



a. Data points resulting from a 0.007-inch line.      b. Processed for center of line.      c. Processed for line data compression.

Figure 4.--Steps in processing of line data.

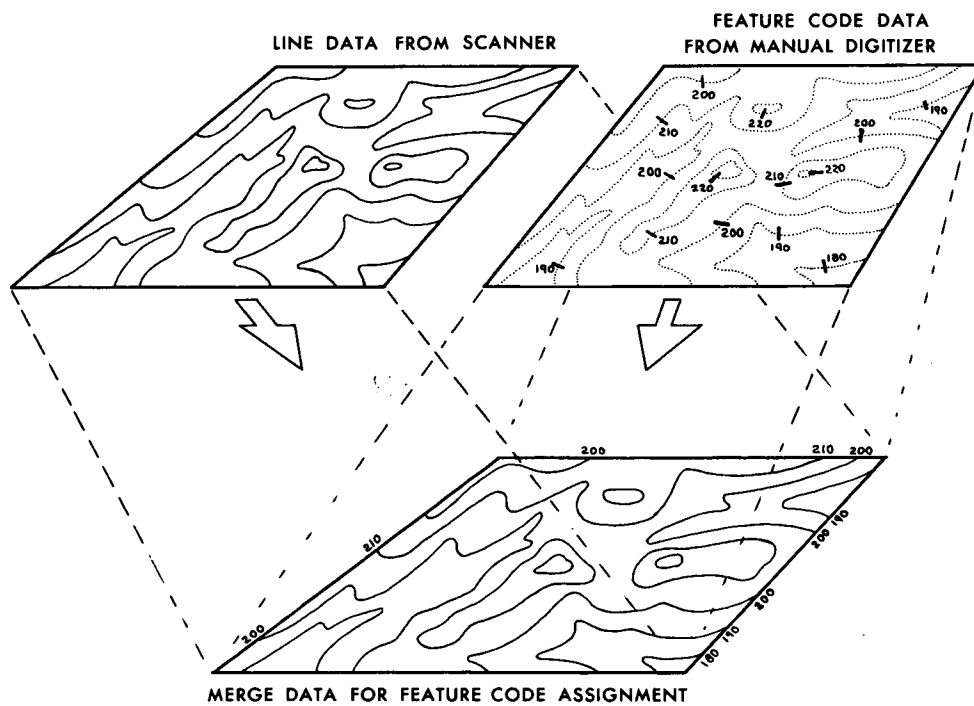
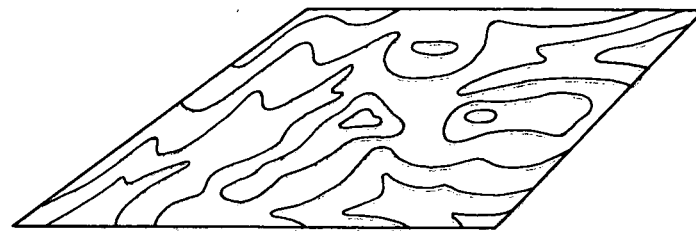
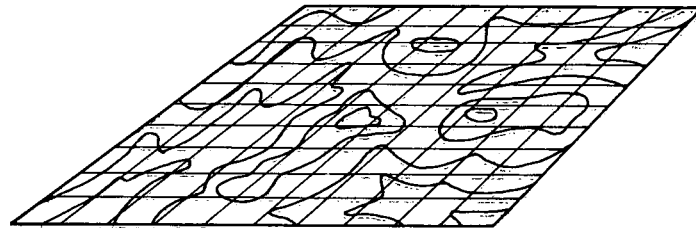


Figure 5.--Feature code assignment.



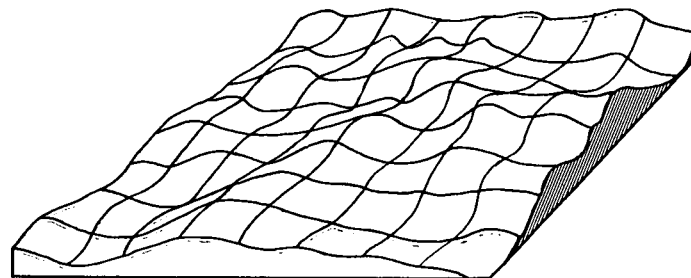


CONTOUR DATA IN DIGITAL FORM

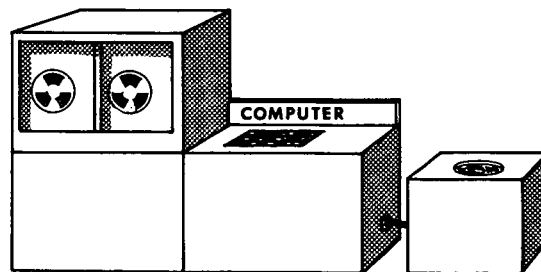


10-METER GRID OVER CONTOUR DATA

COMPUTE MOST PROBABLE ELEVATION FOR EACH GRID INTERSECTION



TERRAIN MODEL IN DIGITAL FORM



STORE IN DIGITAL FORM X, Y, Z VALUE FOR EACH INTERSECTION

Figure 6.--Terrain model generation.

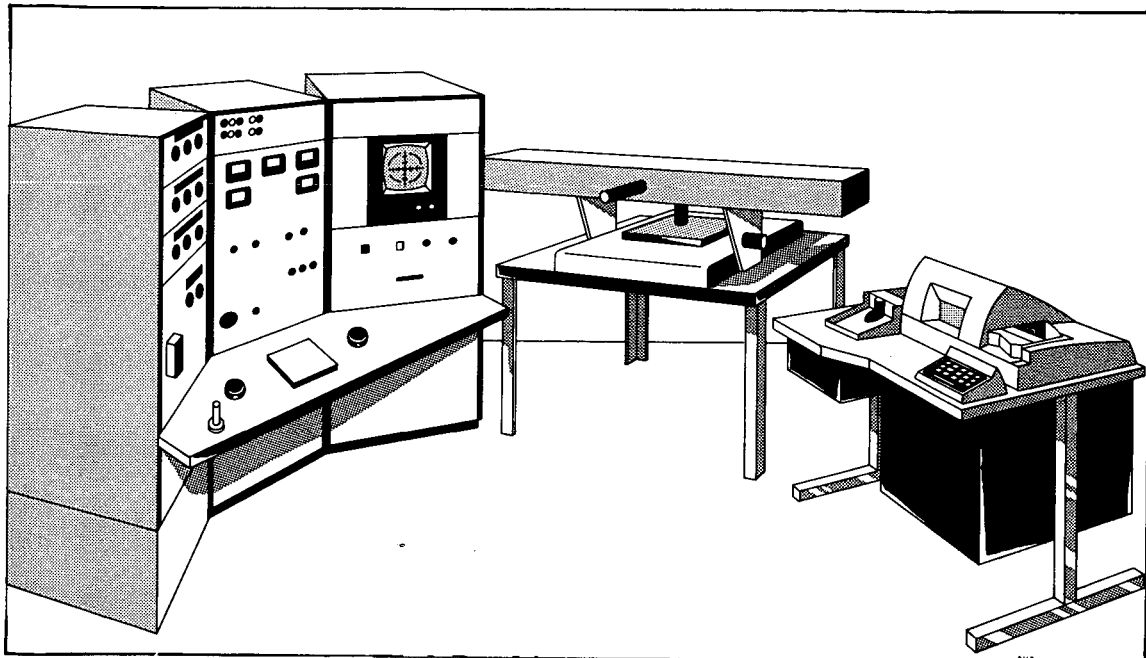
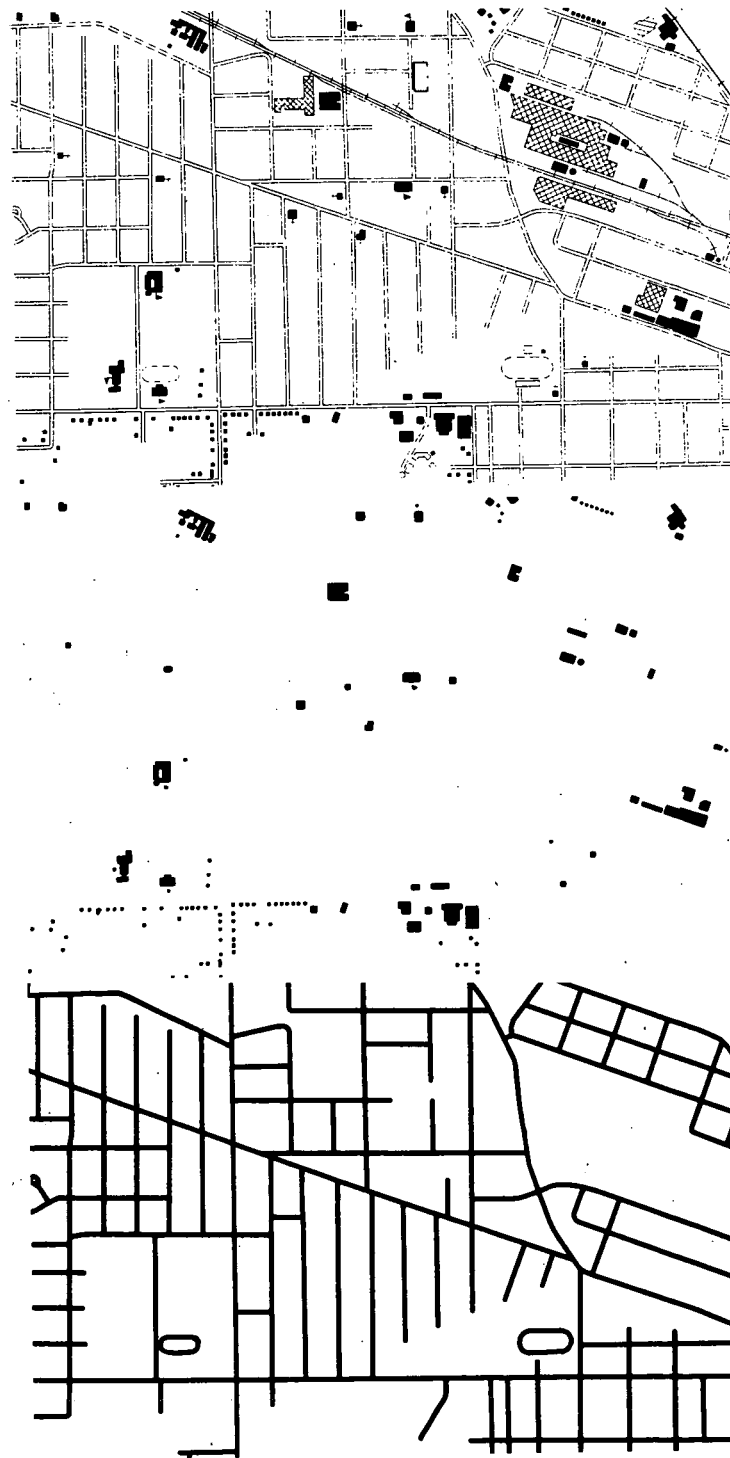


Figure 7.--Image correlator for precise point transfer.



a. Typical planimetric drawing

b. First-class buildings

c. Road pattern

Figure 8.--Photomechanical map symbol separation.

## SPECTRAL REFLECTANCE FROM PLANT CANOPIES AND OPTIMUM

## SPECTRAL CHANNELS IN THE NEAR INFRARED

by

William A. Allen, Harold W. Gausman, and Craig L. Wiegand  
Soil and Water Conservation Research Division  
Agricultural Research Service  
U. S. Department of Agriculture  
Weslaco, Texas

INTRODUCTION

This paper deals with the theoretical and experimental aspects of the interaction of light with a typical plant canopy. Both theoretical and experimental results will be used to establish optimum electromagnetic wavelength channels for remote sensing in agriculture. The spectral range considered includes half of the visible and much of the near-infrared regions.

Reflectance from a green plant under natural conditions is an integrated response from the plant reproductive structures, soil background, leaves, branches, dew, pesticide residue, dust, and innumerable other attributes. Most of the reflectance from vegetation, however, originates from the leaves. If the optical properties of the leaves are understood, the reflectance from plant canopies can be better interpreted. This paper is concerned with optical constants of leaves and the application of these constants to field conditions.

In practice, reflectance of a canopy is measured directly from an aircraft or spacecraft. Reflectance data can then be utilized to draw inferences regarding the nature, vigor, acreage, and maturity of the crop. This approach is empirical and is based upon the existence of extensive ground truth. Less ground truth would be required if the interaction mechanism between plant and light were better understood. That is the reason we address ourselves to the basic theory behind the physical measurements.

Remote sensing imagery in agriculture can be acquired on the ground, from aircraft, or at satellite altitudes. An example will be given for each case.

Figure 1 is an example of ground-acquired imagery. This is a near-infrared photograph of an agricultural scene that includes sugarcane, citrus trees, and palms. Reflectance from vegetation is about the same amplitude as that from the clouds. The appearance of vegetation in the near-infrared is similar to that of clouds or snow. The infrared reflectance for clouds, snow, and leaves is caused by the presence of water and the manner in which it is subdivided. The elementary scattering centers for clouds, snow, and leaves are water droplets, ice crystals, and plant cellular structure, respectively. The role of water in plant reflectance is obscured in the visible region of the spectrum by plant pigment absorption. In the near-infrared region, however, chlorophyll is highly transparent, and the effect of liquid water becomes dominant (1).

Figure 2 is an example of imagery obtained from an aircraft. This is a photograph of a grapefruit orchard. Note the white-appearing tree in the center. More will be said about this photograph by Dr. Gausman in a later paper.

Figure 3 was acquired from a satellite. This imagery was obtained August 1969 from an elevation of about 200 miles by means of a near-infrared scanner in Nimbus III. The Gulf coast is clearly visible. Vegetation and clouds are both expected to appear white in such imagery. The atmospheric disturbance north of the Yucatan Peninsula is Hurricane Camille. This was the most damaging hurricane, with respect to property, ever to hit the United States. The value of Nimbus III imagery, for purposes of agriculture, is seriously compromised by its 10-mile resolution. The Earth Resources Technology Satellite (ERTS), scheduled for 1972, has considerably improved ground resolution.

#### LEAF AND PLANT CANOPY MODELS

The reflectance of a dielectric object can be predicted, at least in principle, if its geometry and the optical constants of its constituents are known. The direct procedure to calculate reflectance of a given object involves tracing a representative bundle of light rays through the object, allowing for absorptance, and applying the Fresnel relations at all interfaces. The sum of all backscattered intensities, relative to incident intensity, is termed reflectance. In practice, however, the actual geometry of all but the most elementary objects is too complicated for exact mathematical analysis. Figure 4, for example, is a transection of a typical cotton leaf. The chloroplasts and spongy parenchyma cells have been accentuated by staining. The leaf contains a large number of different-sized intercellular air spaces in the mesophyll. Despite the complicated internal structure of such a leaf, its optical properties can be described accurately by means of a simple model--that is, a flat plate with rough surfaces.

A total of three different mathematical models (1, 2, 3) have proved applicable to individual leaves and plant canopies. Figures 5a and 5c are models of a plant canopy with light absorbing and light scattering leaves. The leaves are uniformly distributed and oriented, with dimensions much smaller than the height of the canopy. The models are assumed to have infinite lateral extension in order to eliminate canopy edge effects. The appropriate dimension is taken as the cumulative leaf area index  $n$  (LAI). The cumulative LAI at a given point is the total one-sided leaf area, per unit ground area, measured downward from the canopy top. The quantity  $N$  is the total LAI of the canopy and is measured at the soil. The plane  $n = 0$  is the illuminated canopy surface. Monochromatic light in the downward direction (Fig. 5a) is denoted  $I$ , while that in the upward direction is denoted  $J$ . The incident light  $I_0$  on the canopy is considered unity. The quantity  $R$  is the reflectance and  $T$  is the transmittance defined as the relative light intensity on the background.

Light passing through a layer of leaves is scattered and absorbed in direct proportion to a differential distance traversed, and in direct proportion to the amplitude of the light at that point. Absorbed radiation disappears from the models. Scattered radiation is merely changed in direction. Since the models are one-dimensional, the scattering must be either forward or backward. Light backscattered from  $I$  in Fig. 5a adjoins  $J$  and vice versa. The preceding discussion can be formulated into differential equations associated with the names Kubelka and Munk (K-M) (4).

Equations due to Duntley (5) have been generalized to provide values of irradiance within the plant canopy under specular light incident at various sun angles. The Duntley theory, illustrated by Fig. 5c, is based upon five optical parameters. An absorption coefficient, a back-scattering coefficient, and a forward-scattering coefficient are necessary to describe the interaction of specular light with a plant canopy. The unprimed quantities in Fig. 5c pertain to diffuse light generated by scattering. An absorption coefficient and a back-scattering coefficient apply to the diffuse light. There are two radiant fluxes, specular and diffuse, in the positive direction while the diffuse radiant flux in the negative direction is designated  $s$ . The specular flux incident on the canopy is designated  $I'_0$ . If  $I'_0$  is unity per unit horizontal area, the reflected light  $R'$  is designated reflectance and the transmitted light  $T'$  is designated transmittance.

Experiments have indicated that an actual plant canopy is characterized by diurnal effects. Attenuation within a plant canopy depends upon the sun angle. An argument of plausibility suggests that specular-light attenuation is a function of the slant range through the canopy; that is, the optical parameters for specular light are assumed to vary as the secant of the sun angle.

Figure 5b is a model of a compact plant leaf. The model, as mentioned before, is a flat plate with rough surfaces. Radiant flux  $I_0$  emanates from medium 1 and interacts with the interface between media 1 and 2 where it separates into two components. One component is reflected. The second component passes through medium 2 and interacts with the interface between media 2 and 3. The indicated multiple reflections produce an infinite number of rays that emerge eventually into both media 2 and 3. Total light emergence into medium 1 is designated reflectance  $r$  and total light emergence into medium 3 is termed transmittance  $t$ . Media 1 and 3 will be regarded as air. Medium 2 will be specified by its optical constants. The flat plate model of Fig. 5b can be generalized to simulate a non-compact leaf. In this case the leaf is assumed to consist of a stack of compact layers each separated by a layer of air.

### RESULTS

The K-M theory explains the reflectance and transmittance of stacked leaves in a spectrophotometer. Agreement between the observed and computed values is within the experimental uncertainties of the spectrophotometer used.

Figure 6 illustrates the Duntley equations fitted to near-infrared experimental transmission data obtained at Ithaca, New York within a 250 cm-high corn canopy (6). The three lines correspond to elevations 150, 100, and 50 cm within the corn canopy. Measurements were started in the morning and were continued until sundown. The standard deviation between the experimental and theoretical points is 3.2%--a value probably well within experimental error.

The generalized plate description of a typical, noncompact leaf has been applied to 200 mature, field-grown cotton leaves (7). Over the spectral range 1.4 - 2.5  $\mu\text{m}$ , the absorption spectra of leaves are not statistically different from that of pure liquid water. Leaf reflectance differences among the plant leaves over the 0.5 - 1.4  $\mu\text{m}$  range are caused principally by Fresnel reflections at external and internal leaf surfaces and by plant pigment absorption.

Figure 7 is the mean dispersion curve for 200 field-grown cotton leaves. The shaded area is bounded by 95% confidence bands. The dispersion curves of all other crop leaves are roughly similar.

Figure 8 is the absorptance spectra of a typical cotton leaf. The absorption curve can be regarded as a superposition of two independent absorption components: the first region, 0.50 - 0.75  $\mu\text{m}$ , is dominated by the plant pigments such as chlorophyll, and the second region, 1.4 - 2.5  $\mu\text{m}$ , is determined by the properties of liquid water. The intervening region, 0.80 - 1.40  $\mu\text{m}$ , is characterized by relative transparency of both plant pigments and water. The chlorophyll spectra and water spectra are relatively independent.

#### WAVELENGTH RECOMMENDATIONS

Inspection of Figs. 7 and 8 suggests that the bulk of existing information from leaf spectral reflectance must reside with the absorptance curve rather than with the dispersion curve. Figure 8 is plotted on semi-log paper because the absorption coefficient varies by orders of magnitude. The dispersion curve of Fig. 7, on the other hand, changes by only a few percent over the given spectral region.

The preceding physical considerations suggest that the three most useful spectral channels in the range 0.5 - 2.5  $\mu\text{m}$  would be those associated with chlorophyll, water, and a third region where both chlorophyll and water are transparent. Specifically, the three channels centered around the wavelengths 0.68, 0.85, and 1.65  $\mu\text{m}$  appear to be optimum. The first channel is in the visible region and the other two channels correspond to peaks of atmospheric windows I and IV.

The preceding discussion led to tentative consideration of three optimum wavelength channels where selection was based upon physical insight. Consider now the statistical analysis of laboratory measurements on single leaves. The leaves used in this analysis were collected in connection with an experiment to be reported elsewhere. Four crops--corn, cotton, peppers, and sorghum--were sampled at four separate stages of growth during the 1970 growing season in the Lower Rio Grande Valley of Texas. Reflectance and transmittance measurements were taken on single leaves, and were reduced to optical constants at each of 41 wavelengths over the spectral region 0.50, 0.55, ..., 2.50  $\mu\text{m}$ . Reflectance corresponding to an infinitely thick stack of such leaves was used in a correlation analysis. Figure 9 is an abstracted plot of the correlation reflectance matrix for all 41 spectrophotometric channels. The 100% correlation coefficients appear along the diagonal. All plotted coefficients were positive quantities. A few slightly negative correlation coefficients did appear in the extended calculations, but these values were treated as zero in Fig. 9. A low or poor correlation is considered to be in the range 0 - 25 and a high correlation is assumed to lie in the range 75 - 100. The region 20 - 75 will be regarded as intermediate correlations.



Figure 9 displays a high correlation for neighboring channels in chlorophyll region 0.5 - 0.7  $\mu\text{m}$  and a high correlation for neighboring channels in the water region 1.4 - 2.5  $\mu\text{m}$ . Correlation is also high for neighboring channels within the transparency region 0.7 - 1.4  $\mu\text{m}$ . The water absorption channels, 1.45  $\mu\text{m}$  and 1.95  $\mu\text{m}$ , are correlated weakly with all other channels. Inferences drawn from this correlation analysis support the previous finding that channels 0.68, 0.85, and 1.65  $\mu\text{m}$ , are optimum for vegetation since these channels are poorly correlated with each other.

#### REFERENCES

1. Allen, W. A., and Richardson, A. J. Interaction of light with a plant canopy. *J. Opt. Soc. Am.* 58:1023-1028. 1968.
2. Allen, W. A., Gausman, H. W., Richardson, A. J., and Thomas, J. R. Interaction of isotropic light with a compact leaf. *J. Opt. Soc. Amer.* 59:1376-1379. 1969.
3. Allen, W. A., Gayle, T. V., and Richardson, A. J. Plant canopy irradiance specified by the Duntley equations. *J. Opt. Soc. Amer.* 60:372-376. 1970.
4. Kubelka, P., and Munk, F. Ein Beitrag zur Optik der Farbanstriche. *Techn. Physik*, 12:593-601. 1931.
5. Duntley, S. Q. The optical properties of diffusing materials. *J. Opt. Soc. Amer.* 32:67-70. February 1942.
6. Allen, L. H., Jr., and Brown, K. W. Shortwave radiation in a corn crop. *Agron. J.* 57:575-580. 1965.
7. Allen, W. A., Gausman, H. W., Richardson, A. J., and Wiegand, C. L. Mean effective optical constants of thirteen kinds of plant leaves. *Appl. Opt.* 9:2573-2577. 1970.

This page is reproduced again at the back of this report by a different reproduction method so as to furnish the best possible detail to the user.

23-7



Figure 1.- Infrared photograph of agricultural scene at the Texas A&M University Research and Extension Center, Weslaco, Texas. Reflected light from both clouds and vegetation is scattered by dielectric interfaces where air is one of the media. Photograph taken at 11:30 A.M., 10 November 1969 with Kodak Infrared Aerographic Film 2424 and a Kodak Wratten Filter No. 89B. A 120 mm Hasselblad was used at f/8 and 1/250 sec. The spectral channel is about 0.69 - 0.90  $\mu\text{m}$ .

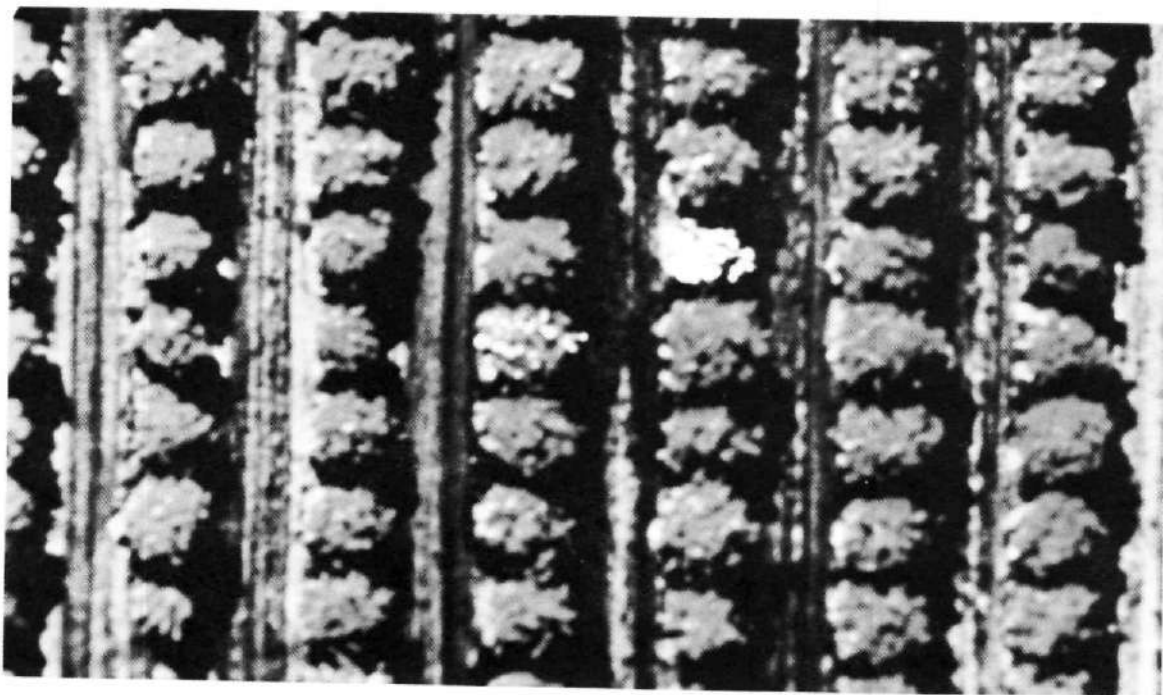


Figure 2.- Photograph of grapefruit orchard taken at 3,000 ft elevation.



Figure 3.- Infrared scanner image from Nimbus III. The atmospheric disturbance north of the Yucatan Peninsula is Hurricane Camille.

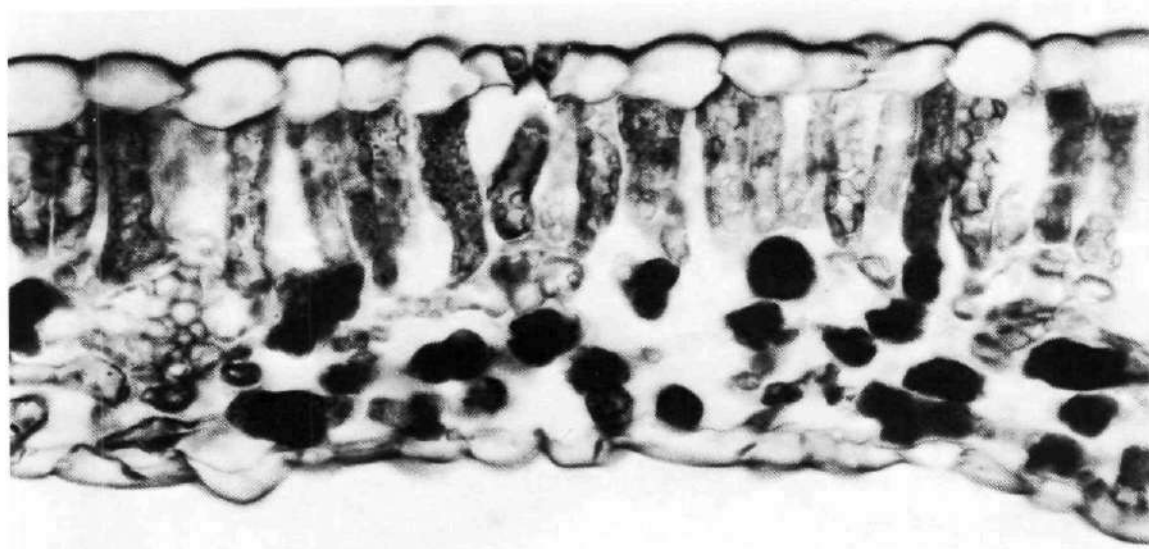


Figure 4.- Photomicrograph of typical dorsiventral cotton leaf transection.

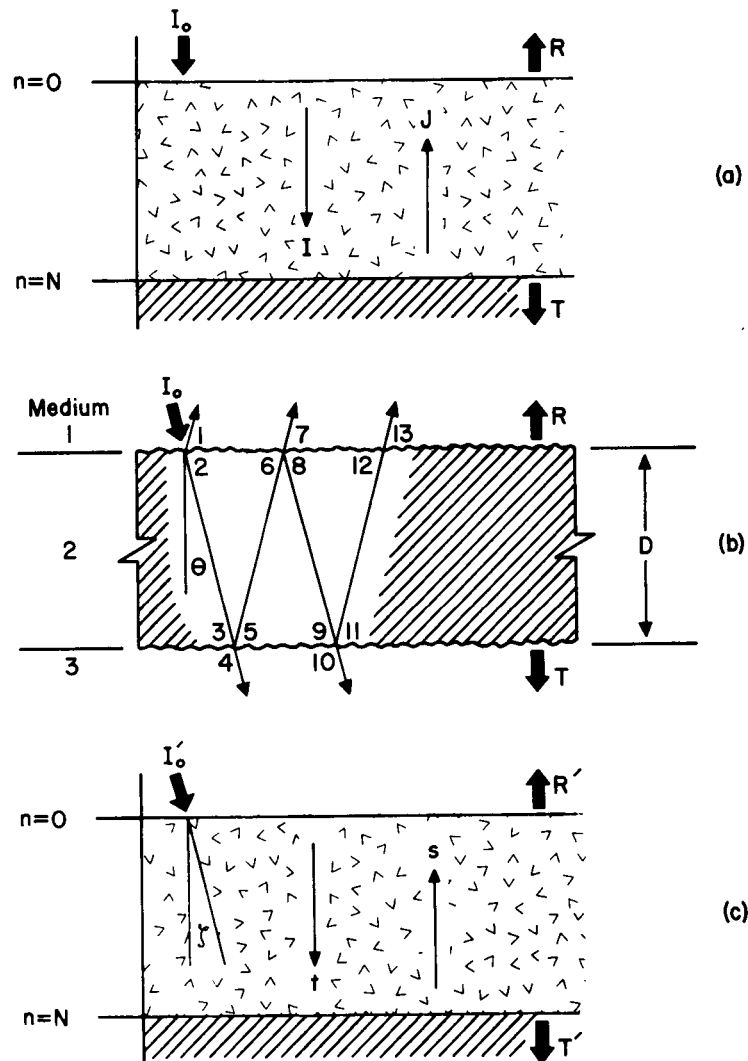


Figure 5.- Models of light interaction with leaves. The planes  $n = 0$  and  $n = N$  are the canopy surfaces and soil backgrounds. a) Diffuse light  $I_0$  impinging upon a plant canopy. Reflectance and transmittance are designated  $R$  and  $T$ . Diffuse light fluxes generated by scattering are designated  $I$  and  $J$ . b) Multiple reflections within a transparent plate with rough surfaces (a simulated compact plant leaf). Incident ray  $I_0$  impinges at angle  $\theta$ . Reflectance and transmittance are designated  $R$  and  $T$ . c) Specular light  $I_0$  at sun angle  $\zeta$  impinging upon a plant canopy. Reflectance and transmittance are designated  $R'$  and  $T'$ . Diffuse light fluxes generated by scattering are designated  $s$  and  $t$ .

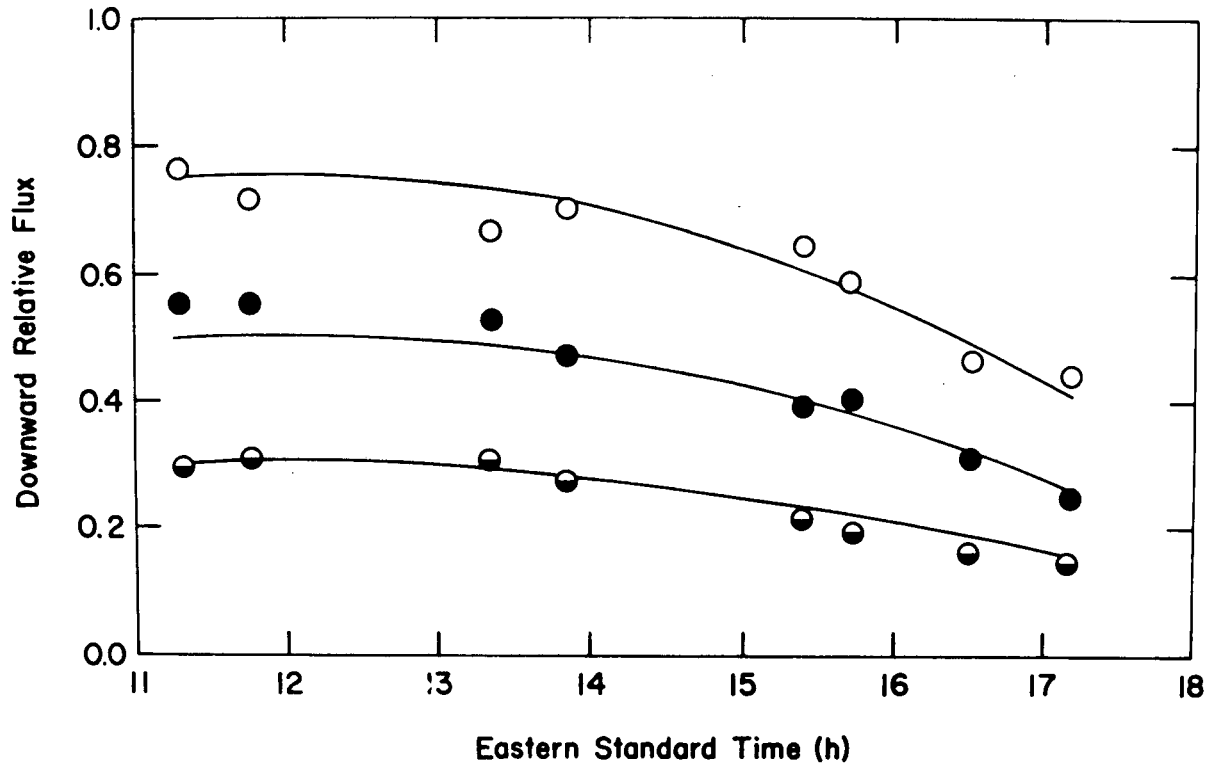


Figure 6.- Percent transmittance of near infrared flux within a 250-cm-high Ithaca, New York corn canopy on 13 September 1963. The curves; representing canopy heights 150, 100, and 50 cm. respectively; are theoretical predictions based upon the generalized Duntley equations. The data points are experimental values.

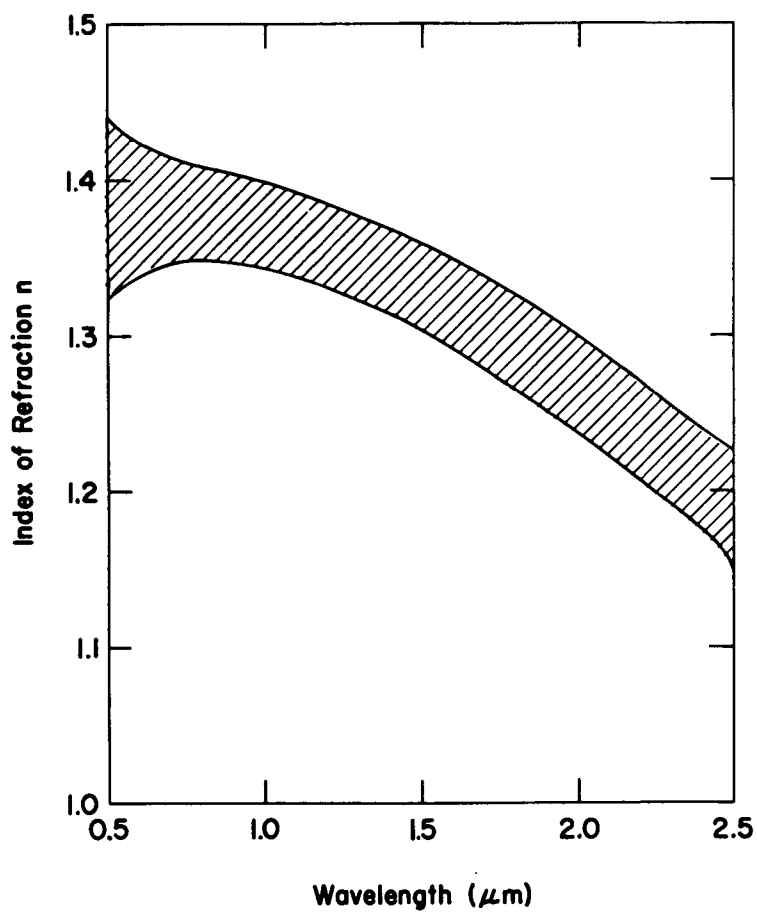


Figure 7.- Mean dispersion curve for 200 field-grown cotton leaves. The shaded area is bounded by 95% confidence bands.



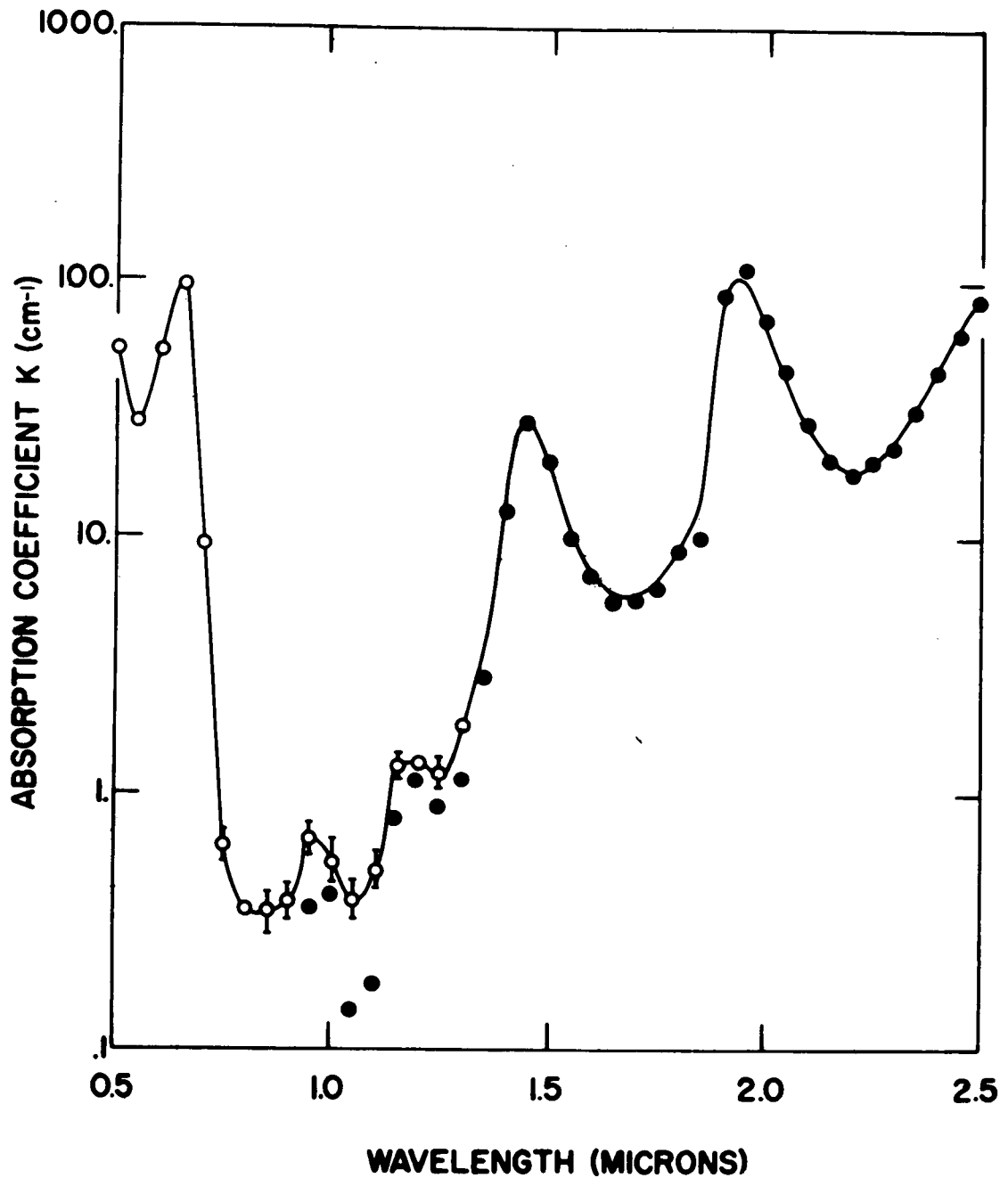


Figure 8.- Absorbance spectra of a typical leaf (solid line and open circles). The absorption curve can be regarded as a superposition of two independent absorption components. The first region is dominated by the plant pigments such as chlorophyll, and the second region is determined by the properties of liquid water. Properties of liquid water are indicated by closed circles.

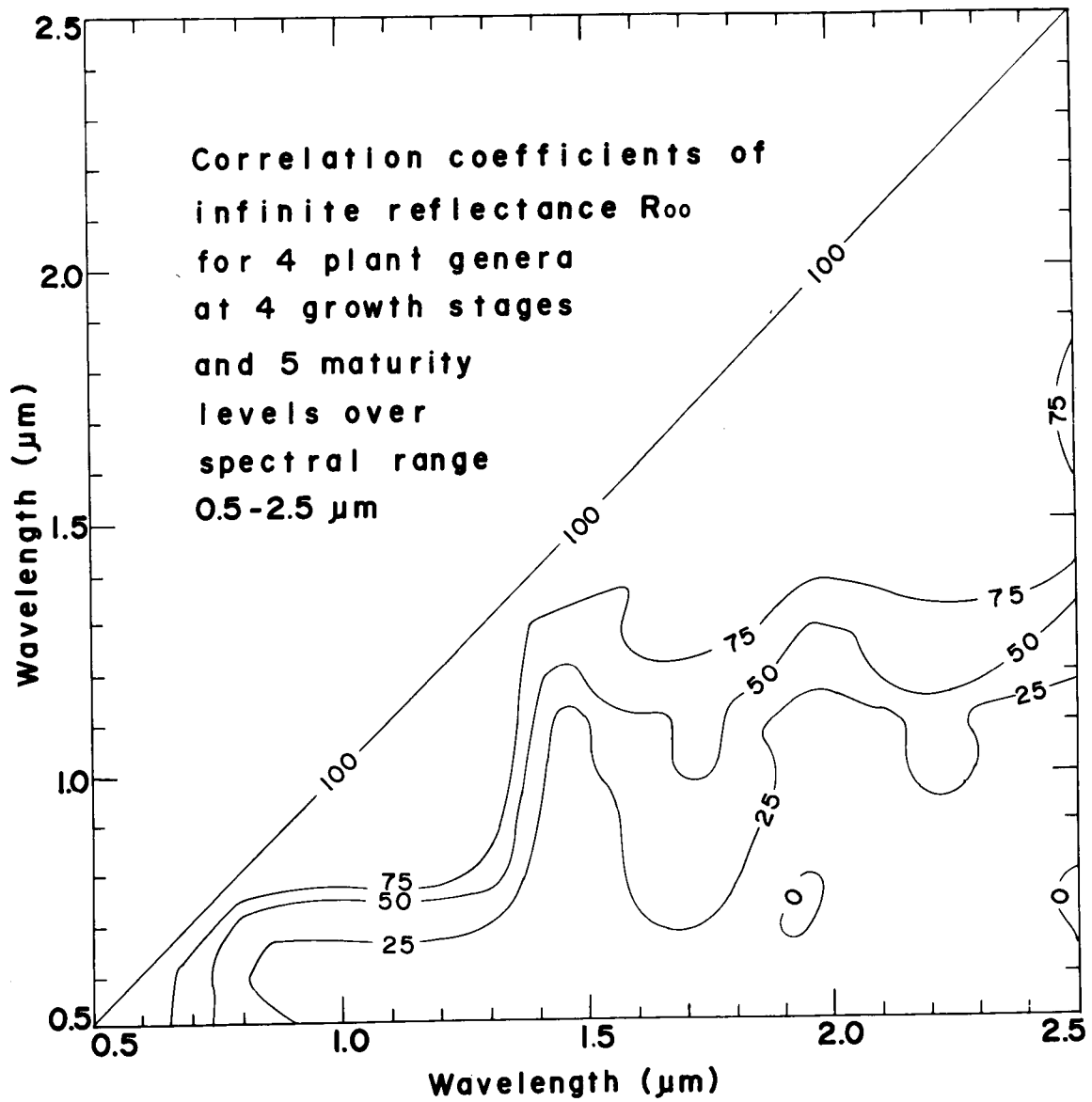


Figure 9.- Correlation coefficients of leaf reflectance.

## AERIAL PHOTOGRAPHY FOR SENSING PLANT ANOMALIES

by

H. W. Gausman and R. Cardenas  
Soil and Water Conservation Research Division  
Agricultural Research Service  
U. S. Department of Agriculture  
Weslaco, Texas

and

W. G. Hart  
Entomology Research Division  
Agricultural Research Service  
U. S. Department of Agriculture  
Weslaco, Texas

ABSTRACT

Changes in the red tonal response of Kodak Ektachrome Infrared Aero 8443 film (EIR) have been often incorrectly attributed solely to variations in infrared light reflectance of plant leaves, when the primary influence was a difference in visible light reflectance induced by varying chlorophyll contents. Assuming a relatively low cyan positive image density (high infrared light reflectance), a high compared with a low chlorophyll content reduces the reflection of visible light, the yellow and magenta positive images remain highly saturated, and the viewer has an impression of a darker red tone (higher red color saturation).

Comparisons are made among aerial photographic images of high- and low-chlorophyll foliage. New growth, foot rot, and boron and chloride nutrient toxicities produced low-chlorophyll foliage, and EIR transparency images of low-chlorophyll foliage were light red or white compared with dark-red images of high-chlorophyll foliage.

Deposits of the sooty mold fungus that subsists on the "honeydew" produced by brown soft scale insects, obscured the citrus leaves' green color. Infected trees appeared as black images on EIR film transparencies compared with red images of healthy trees.

The detection of brown soft scale infestations of citrus trees with EIR film is practical. Further work is planned to distinguish among photographic images produced by boron and chloride toxicities, iron deficiency, and foot rot of citrus trees. The new Kodak Aerochrome

Infrared 2443 film will be used, and it should give results superior to those of the EIR film.

## INTRODUCTION

The interpretation of false color imagery to detect spectral reflectance differences among plant genera and between healthy and abnormal plants is difficult and often requires an empirical procedure. Changes in the red tonal response of Kodak Ektachrome Infrared Aero 8443 film (EIR)<sup>1</sup> have been often incorrectly attributed solely to variations in infrared light reflectances of the subjects. Light- and dark-red tonal appearances on transparencies have been interpreted as indicating high and low infrared reflectances, respectively, when the primary influence may have been variations in visible light reflectances induced by different plant leaf chlorophyll concentrations.

This paper considers aerial photography with EIR film for sensing plant anomalies, and it stresses the importance of considering effects of different leaf chlorophyll concentrations, in addition to internal leaf structure, on the absorptance of visible light in interpreting false-color imagery. Examples are given where the plant foliage either differs widely in chlorophyll contents or the plant leaves' green color is obscured.

## REVIEW OF LITERATURE

### EIR AND AIR FILMS

EIR film (1) has three image layers individually sensitized to green, 500 to 600 nanometer (nm); red, 600 to 700 nm; and infrared radiation, 700 to 900 nm. A yellow filter is used on the camera to absorb the blue radiation, to which these layers are also sensitive. Upon processing, yellow, magenta, and cyan positive images are formed in the green-, red-, and infrared-light sensitive layers, respectively. The overall impression to an observer viewing the finished print or transparency will depend upon the positive images in the dye layers that predominate with respect to visual appearance. Because the eye sensitivity peaks in the green, the magenta layer generally contributes most to the subjective impression of lightness or darkness in a color

---

<sup>1</sup> Use of a company or product name by the Department does not imply approval or recommendation of the product to the exclusion of others that may also be suitable.

print or transparency. For example, healthy leaves, with high infrared compared with low infrared reflectance for unhealthy leaves, record red because a light-toned cyan image (less dense or less saturated) results, allowing the transmittance of more red light in the viewing.

Kodak has replaced the EIR 8443 film with a new emulsion series, Kodak Aerochrome Infrared Film 2443 (AIR). Interpretation of tonal responses of the new AIR film should be essentially alike the interpretation of the EIR film, except that the slower cyan dye layer of the AIR film compared with the EIR film should reduce the red saturation in the photography (2).

### Chlorophyll Effects on Red Saturation of EIR Film

Spraying cotton plants (Gossypium hirsutum L.) at the square stage of plant development with Cycocel [(2-chloroethyl) trimethylammonium chloride] (3), at 100 g/ha (0.545 lb/A) in enough water to produce run-off, increased the chlorophyll content of their leaves compared with leaves of plants sprayed with only the amount of water used for applying the Cycocel treatment (4). The Cycocel treatment increased absorbance 13% at the chlorophyll absorption band, 550 nm; and only 2 to 3% over the 750- to 1350-nm wavelength interval (WLI). Near-infrared light reflectance of upper surfaces of single leaves, measured with a spectrophotometer, was inversely related and visible light reflectance was directly related to the reflectivity of field plots of cotton recorded on EIR aerial photographs. The tonal response on EIR transparencies was darker red for Cycocel-treated plots than for untreated plots. This was caused by increased chlorophyll contents in leaves of Cycocel-treated plants.

High salt levels in the soil increased the chlorophyll contents of cotton leaves and produced a high red color saturation and appearance on EIR transparencies (5), compared with a light red appearance of cotton leaves from plants grown on a low salt soil. Also, young leaves near the top of a representative cotton plant photographed to give a darker green and deeper red appearance for conventional color (CC) and EIR films, respectively, than did lower mature leaves (5). Young leaves had more chlorophyll than the older leaves. High compared with low chlorophyll leaves absorbed more light within the visible spectrum (4,5), correspondingly reducing red light reflectance over the approximate 600- to 700-nm WLI. When less red light impinged on the EIR film, a magenta positive image was produced with high saturation. Transmission of the dark red-toned color of the magenta image contributed most to the viewer's impression of darkness in the EIR transparency or color print.

## PRESENTATION OF RESULTS

First, brief consideration will be given to the influence of internal leaf structure on light reflectance, transmittance, and absorptance. Next, physiological and environmental factors that affect citrus leaf light reflectance will be reviewed briefly and illustrated. Examples of plant anomalies that will be presented are: boron (B) and chloride ( $\text{Cl}^-$ ) nutrient toxicities, citrus species differences, sooty mold (fungus) deposits resulting from brown soft scale infestations, and foot rot (fungus) of citrus trees.

To facilitate ensuing discussions, the 500- to 2500-nm spectral range has been arbitrarily divided into: the 500- to 750-nm visible region dominated by pigment absorption (chlorophylls and carotenoids); the 750- to 1350-nm near-infrared WLI, a region of high reflectance and low absorptance that is affected primarily by internal leaf structure; and the 1350- to 2500-nm WLI, a region of high absorption by water--the strongest water absorption bands occurring at 1450 and 1950 nm.

### SPECTRA OF MATURE CITRUS LEAVES

The diffuse reflectance, transmittance, and absorptance of mature citrus leaves (orange, *Citrus sinensis* (L.) Osbeck) are portrayed in Fig. 1. The reflectance and transmittance spectra are each averages of measurements made on upper surfaces of 10 leaves. Measurements were made with a Model DK-2A spectrophotometer and its reflectance attachment. Data were corrected for the reflectance of the MgO standard to obtain absolute radiometric values (6). Absorptance was calculated as:  $[100 - (\% \text{ reflectance} + \% \text{ transmittance})]$ .

Figure 1 shows that reflectance, transmittance, and absorptance were 10, 2, and 90%, respectively, at the 550-nm green peak within the 500- to 750-nm visible WLI. Absorption in this region was primarily caused by pigments. Within the 750- to 1350-nm near-infrared range, there was approximately 55% reflectance, 40% transmittance, and 5% absorptance. Above 1350 nm, absorptance greatly increased because of water absorption of light energy.

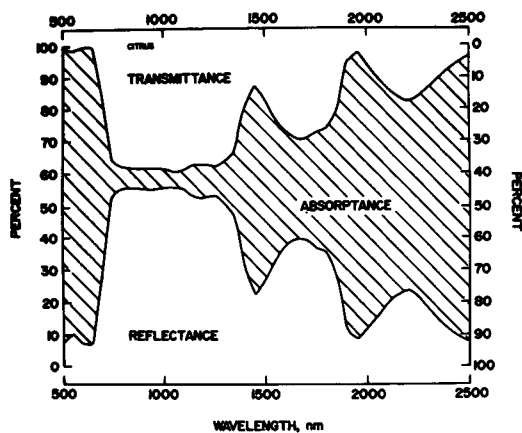


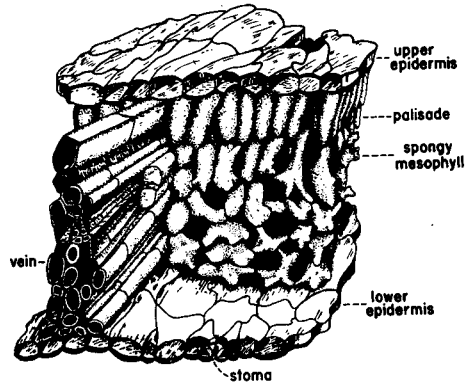
Figure 1.- Diffuse reflectance, transmittance, and absorptance [100 - (% transmittance + % reflectance)] of the upper (adaxial) surface of a mature orange leaf (Citrus sinensis (L.) Osbeck).

#### FACTORS AFFECTING CITRUS LEAF LIGHT REFLECTANCE

Citrus leaf light reflectance is affected by diseases, hormones, insects, leaf ages (maturation), phyllotaxis (leaf ontogeny relations), tissue water contents, nutrient deficiencies and toxicities, and spray residues. Of these factors, the influence of leaf ages, diseases, insects, and toxic nutrient levels will be considered below following a general review of leaf structure.

##### Internal Leaf Structure

A three-dimensional drawing (7) representing a leaf structure that is similar to a citrus leaf's structure is shown in Figure 2. The top layer of cells is the upper (adaxial) epidermis. The epidermal cells have a cuticular layer on their upper surfaces that diffuses but reflects very little light. The long narrow cells in the leaf mesophyll below the upper epidermis are palisade parenchyma cells. They house many



VAN NOSTRAND'S SCIENTIFIC ENCYCLOPEDIA  
COPYRIGHT, 1947

Figure 2.- Three-dimensional drawing of a leaf structure that is similar to the structure of a citrus leaf (redrawn from Van Nostrand's Scientific Encyclopedia, 1947).

chloroplasts with chlorophyll pigments that absorb some of the visible light, particularly at the 430-nm (blue) and 680-nm (red) wavelengths. The cells below the palisade cells are spongy parenchyma cells. The palisade and spongy parenchyma cells have many air spaces among them (intercellular air spaces). It is here that oxygen and carbon dioxide exchange takes place for photosynthesis and respiration. The lower (abaxial) epidermis is like the upper epidermis, except a stoma or port is present where gases enter and leave a leaf.

The air spaces in leaf mesophylls are important in remote sensing because hydrated cell wall - air faces scatter near-infrared light (8).

#### Leaf Age (Maturation)

The effect of leaf age on internal leaf structure is shown in Figure 3.



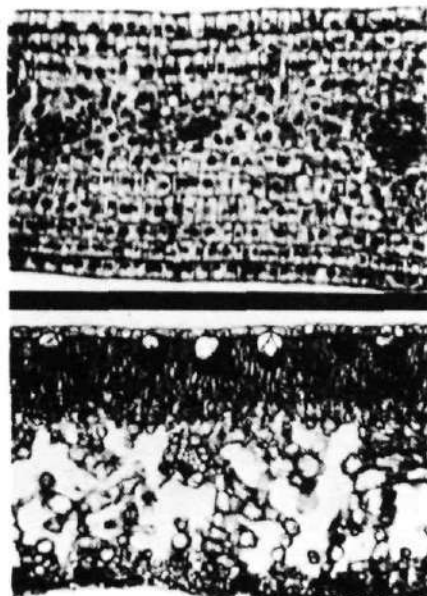


Figure 3.- Microphotographs of leaf transections of young (top, 125 X) and mature (bottom, 64 X) citrus leaves.

The top citrus leaf transection represents a very young citrus leaf (fifth leaf from apex of new growth flush, 125 X), and the transection at the bottom of the screen represents a mature citrus leaf (eighth leaf from apex of previous growth flush, 64 X). The young leaf is compact with few air spaces in its mesophyll, while the old leaf is "spongy" or has many air spaces. The young compact leaf has lower light reflectance than the mature leaf, Figure 4. The spongy mature leaf represented by the solid black line, compared with the compact young leaf represented by the dotted line, had about 5% and 15% more reflectance in the visible (500 to 750 nm) and near-infrared wavelength (750 to 1350 nm) ranges, respectively. The "spongy" effect in the mature leaf increases reflectance because there are more intercellular air spaces (8). Scattering of light within leaves occurs at cell wall (hydrated cellulose) - air cavity interfaces that have refractive indices of 1.4 and 1.0, respectively.

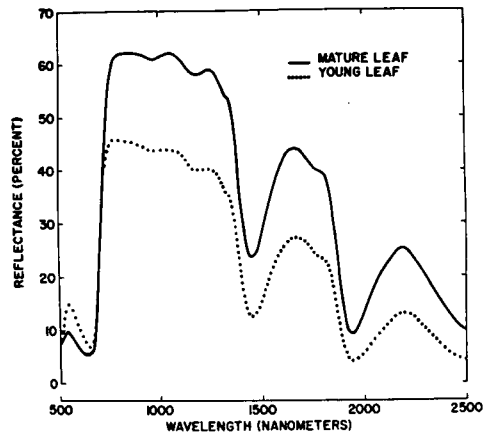


Figure 4. Diffuse reflectance of the upper (adaxial) surfaces of young (bottom dotted line spectrum) and mature (upper solid line spectrum) orange leaves (Citrus sinensis (L.) Osbeck).

#### Toxic Nutrient Levels

Too much salt in the soil or irrigation water affects physiological functions of plants and subsequently plants become stunted and toxicity symptoms become apparent in their foliage. Too much boron (B) produces citrus leaves with yellowish areas on their leaf surfaces, and too much chloride ( $\text{Cl}^-$ ) gives a brownish tip burn (9).

An experiment with toxic levels of B and  $\text{Cl}^-$  is being conducted on citrus trees by A. Peynado, Research Chemist, Crops Research Division, Weslaco, Texas, using an experimental design with four blocks (10). There are 16 Red Blush grapefruit (Citrus paradisi, Macf.) and 16 Valencia orange (Citrus sinensis (L.) Osbeck) trees within each block. The grapefruit and orange trees are each on 16 different rootstocks. Two treatments, that began in 1963, have been applied to the grapefruit and the orange trees within each block. Eight orange and eight grapefruit trees in each block have been irrigated with canal

water (control treatment); and eight orange and eight grapefruit trees in each block have been irrigated with irrigation water with 4,000 ppm sodium chloride (NaCl) and calcium chloride ( $\text{CaCl}_2$ ) and 6 ppm of boron (B) added (salt treatment).

Figure 5 shows that healthy compared with B- and  $\text{Cl}^-$ -affected leaves had about 3% less reflectance over the 750- to 1350-nm near infrared WLI.

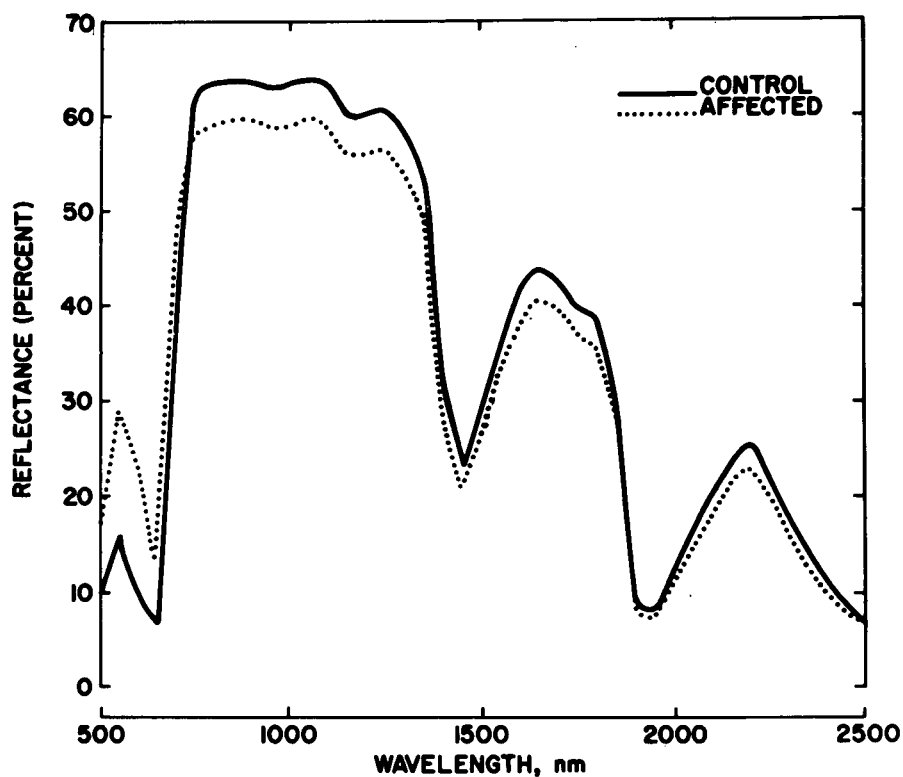


Figure 5.- Diffuse reflectance of upper (adaxial) leaf surfaces of healthy (control, solid line) and salt-affected (dotted line) citrus leaves.

This variation in reflectance was primarily caused by differences in leaf structure. Microscopic examinations of leaf transections indicated that healthy leaves had a more spongy mesophyll than affected leaves. However, the largest difference in reflectance between healthy and affected leaves was in the 500- to 750-nm WLI. Affected leaves were much lower in chlorophyll than healthy and had approximately 12% higher reflectance at the visible green reflectance peak of 550 nm.

Aerial photographs with EIR film (Figure 6 A) were taken of the experimental plots at an altitude of 3,000 ft with a 50-mm lens. Sixteen orange trees with no visual toxic salt symptoms and 12 grapefruit trees with rootstocks that were insensitive to the salt treatment photographed dark red; whereas grapefruit trees with the salt-sensitive Troyer citrange rootstock gave whitish-tree images on the EIR transparency. Thus it seems feasible that remote sensing with aerial photography can be used to detect the presence of salinity-stressed citrus trees.

### Species Differences

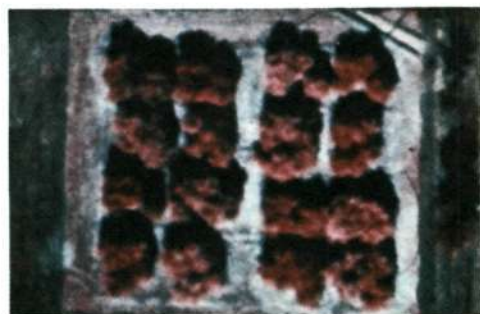
Aerial photographs were taken of an orchard of Red Blush grapefruit, Valencia and navel oranges, and Cleopatra tangerine trees at an altitude of 2,000 ft with a 50-mm lens (Figure 6 B). All trees had a new flush of growth except for the tangerine trees. The tangerine trees gave dark red images on the EIR transparency in contrast to lighter red colored images for the grapefruit and orange trees; because new foliage on citrus trees is lighter green in color (less chlorophyll) than the foliage of the previous flushes of growth. One of the main problems in the photographic remote sensing of citrus maladies is to distinguish them from new foliage growth that usually occurs five times per year.

### Citrus Foot Rot

Citrus foot rot is a fungal disease caused by Phytophthora citrophthora (Sm. & Sm.) and Phytophthora parasitica Dast. These fungi produce a gummy exudate at or near the graft union on citrus trees; wood rots underneath, leaves lose color, decline sets in, and eventually foot rot girdles the tree trunk and the tree dies. The foliage of foot rot-affected citrus trees lose their chlorophyll and become chlorotic (yellowish-white) in contrast to the dark-green foliage of healthy trees.

An overflight of a grapefruit citrus orchard, Citrus paradisi Macf., Nucellar - CES-3 selection of Red Blush on Citrus aurantium Linn. Sour Orange rootstock, near Monte Alto, Texas was made at an altitude of 2,000 ft (under cloudless skies with moderate haze), at 11:29 a.m., central standard time, December 5, 1968, in an easterly direction (10). Photographs were taken with a Zeiss, 6-in. focal length camera (scale 1:4,000), using 9-in. Kodak Ektachrome Infrared Aero 8443 film and a Zeiss D light-orange filter, approximate 100% absorption edge at 500 nm.

On EIR transparencies, healthy trees produced red images in contrast to white images for trees severely infected with foot rot (Figure 6 C).



A. Salt toxicity, photography scale 1/18,000, enlarged 20 X.



B. Kinds of citrus trees, photography scale 1/12,000, enlarged 2 X.



C. Foot rot, photography scale 1/4,000, enlarged 5 X.



D. Sooty mold, photography scale 1/10,000, reduced 0.5 X

Figure 6.- Aerial photographs of plant anomalies with EIR film.

A. Salt toxicity. Dark red trees are orange trees with no signs of being affected with boron and chloride salt additions, and grapefruit trees with salt insensitive rootstocks. (The trees in each block have grown together and cannot be individually identified in the photograph.) White images in each block are grapefruit trees with a salt sensitive rootstock.

B. Kinds of citrus trees. The two dark red trees on the bottom of the photograph, four rows in from the right, are tangerine trees with no new foliage (leaves dark green color, high chlorophyll). The remaining lighter colored trees are Red Blush grapefruit and orange trees with a new flush of foliage (leaves light green color, low chlorophyll).

## Figure 6.- Continued

C. Foot rot. The white tree in the center of the photograph has an advanced infection of foot rot, and the tree below it and to its left has an early case of foot rot. Healthy trees are red.

D. Sooty mold. Black trees are infested with brown soft scale, non-infested trees are red.

Figure 6 C is an EIR color photograph of foot rot-infected trees, and red images of healthy trees. Various degrees of white-appearing trees were detected among the red-appearing trees on the EIR color film. The white tree in the center of the photograph has an advanced infection of foot rot, and the tree below it and to its left has an early case of foot rot.

## Sooty Mold

Brown soft scale insects (Coccus hesperidum L.) start excreting large quantities of a sugary solution known as "honeydew" soon after establishment on the citrus leaf. The black sooty mold fungus, Capnodium citri, Berk. and Desm., develops rapidly on the leaf surface when the honeydew is abundant, and forms a dense black coating of interwoven filaments (hyphae). If the coating is heavy, it impairs plant growth and production. Light reflectance in the visible and near-infrared is considerably reduced (11). Figure 7 shows spectrophotometric measurements of diffuse reflectance of upper citrus leaf surfaces having varying amounts of sooty mold (11). Mature citrus leaves (spectrum 1) with no trace of sooty mold had reflectance values of 58 and 53% at 770 and 1300 nm, respectively. Leaves heavily coated with sooty mold (spectrum 4) had reflectance values of 9 and 23% at 770 and 1300 nm, respectively. A light sooty mold coating (spectrum 2) reduced reflectance 14 and 2 percentage points at the 770- and 1300-nm wavelengths, respectively.

Citrus trees coated with deposits of sooty mold photographed black with EIR film compared with red images of noninfested trees (Figure 6 D).

The detection of brown soft scale infestations of citrus trees with EIR film has been demonstrated (11). A commercial service to the growers is feasible at the present time. It could function as entomological ground surveys now function; that is, a commercial service would photograph the trees, ground check suspicious areas in groves, and make recommendations for spraying of the orchards. It is estimated that the cost of surveys could be reduced up to 50% with this technique (12).

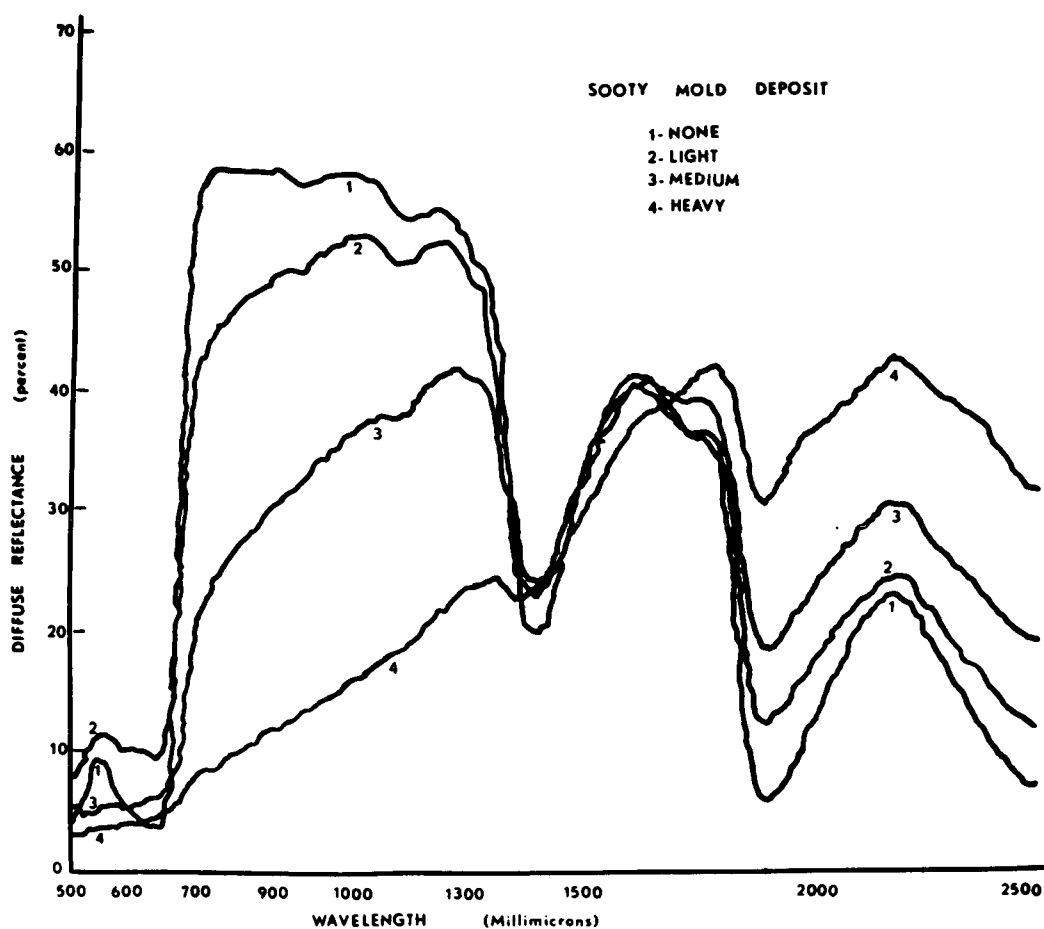


Figure 7.- Effect of sooty mold on reflectance (percent) of leaves coated with varying amounts of the fungus (reproduced from Hart and Myers, 1968).

#### FUTURE PLANS

Further work is planned for comparing film images of boron and chloride toxicities, iron deficiency, and foot rot of citrus trees. The new Kodak Aerochrome Infrared 2443 (AIR) film will be used, and it should give results superior to those of the EIR film. If visual interpretation among foot rot and the nutritional maladies is impractical, computer discrimination procedures (13) will be applied to densitometer readings on AIR film transparencies.

The detection of brown soft scale infestations of citrus trees with EIR film is practical. A commercial service to the growers is a possibility in the near future.

Research is in progress to detect insect damage on citrus trees with EIR films to assess the effectiveness of biological and chemical insect control applications.

#### ACKNOWLEDGEMENTS

The authors are indebted to Jean Ryan for stenographic assistance, Marcia Schupp for preparing leaf transections, Ron Bowen for photographic assistance, and Guadalupe Cardona and Armando Berumen for illustrative assistance.

#### REFERENCES

1. Fritz, N. L. 1967. Optimum methods for using infrared-sensitive color film. *Photogram. Eng.* 33:1128-1138.
2. Earth Observations Division Technical Bulletin TF6/TB1. 1970. NASA, Manned Spacecraft Center, Houston, Texas.
3. Tolbert, N. E. 1960. (2-Chloroethyl) trimethylammonium chloride and related compounds as plant growth substances. I. Chemical structure and bioassay. *J. Biol. Chem.* 235:475-479.
4. Gausman, H. W., W. A. Allen, V. I. Myers, R. Cardenas, and R. W. Leamer. 1969-1970. Reflectance of single leaves and field plots of Cycocel-treated cotton (*Gossypium hirsutum* L.) in relation to leaf structure. *Remote Sens. Environ.* 1:103-107.
5. Gausman, H. W., W. A. Allen, R. Cardenas, and R. L. Bowen. 1970. Color photos, cotton leaves, and soil salinity. *Photogram. Eng.* 36:454-459.
6. Sanders, C. L., and E. E. K. Middleton. 1953. The absolute spectral diffuse reflectance of magnesium oxide in the near infrared. *J. Opt. Soc. Am.* 43:58.
7. Van Nostrand's Scientific Encyclopedia. 1947. 2nd ed., D. Van Nostrand Co., Inc., New York. p 850.



8. Gausman, H. W., W. A. Allen, R. Cardenas, and A. J. Richardson. 1970. Relation of light reflectance to histological and physical evaluations of cotton leaf maturity (Gossypium hirsutum L.). Appl. Opt. 9:545-552.
9. Cardenas, R., A. Peynado, H. W. Gausman, A. H. Gerbermann, and R. L. Bowen. Photographic sensing of boron and chloride toxicities of citrus trees. Manuscript prepared for submission to 1971 Jour. Rio Grande Valley Hort. Soc.
10. Gausman, H. W., W. A. Allen, R. Cardenas, and R. L. Bowen. Detection of foot rot disease of grapefruit trees with infrared color film. Accepted for publication in 1970 Jour. Rio Grande Valley Hort. Soc.
11. Hart, W. G., and V. I. Myers. 1968. Infrared aerial color photography for detection of populations of brown soft scale in citrus groves. J. Econ. Entomol. 61:617-624.
12. Hart, W. G., and S. Ingle. 1969. Detection of arthropod activity on citrus foliage with aerial infrared color photography. Proceedings of the Workshop on Aerial Color Photography in the Plant Sciences. pp 85-88. Gainesville, Fla. March 5-7, 1969.
13. Richardson, A. J., R. J. Torline, D. A. Weber, R. W. Leamer, and C. L. Wiegand. Comparison of computer discrimination procedures using film optical densities. SWC Research Report 422, Weslaco, Texas.

REMOTE SENSING FOR DETECTION OF SOIL LIMITATIONS  
IN AGRICULTURAL AREAS

by

C. J. Frazee, R. D. Heil, F. C. Westin  
Soil Scientists  
Plant Science Department  
South Dakota State University  
Brookings, South Dakota

INTRODUCTION

Research is needed to establish remote sensing techniques for recognizing and mapping soil limitations in order to take full advantage of the imagery which will be transmitted back to earth from the earth resources satellite. Rapid automatic scanning procedures also must be developed in order to interpret the vast amount of data which can be obtained very quickly by remote sensing techniques.

As agriculture becomes more intense, as in irrigation, soil limitations become more restrictive. Approximately 84 percent of the 45.5 million acres expected to be irrigated by 1975 have soil limitations. These limitations may be evaluated according to (1) erosion susceptibility, (2) excess water, (3) adverse climate, and (4) unfavorable soil or rooting zone characteristics.

Information about soil limitations is needed by the users of soil survey data. In South Dakota, some of the agencies using this type of information are:

1. Soil Conservation Service for farm planning and conservation decisions,
2. Bureau of Reclamation for land classification and irrigation recommendations,
3. Bureau of Indian Affairs for land use planning,
4. U.S. Forest Service for recommendations about land use in forested and non-forested areas,
5. Department of Revenue for taxation purposes.

The value of the management decisions by the above users is determined by the quality of data available.

Agricultural areas throughout the world could be defined in terms of soil limitations. Remote sensing from spacecraft using broad survey methods and from aircraft using more detailed interpretations offers promise not only for identifying soil limitations but also for monitoring corrective measures.

The objectives of the study for this year are:

1. To establish remote sensing principals for identifying and mapping one or more soil limitations to land use in a potentially irrigable area.
2. To develop rapid scan, automatic identification techniques using color and multispectral photographic transparencies.

This report will deal mainly with the first objective. The second objective will be dealt with in another report entitled: "Pattern Recognition at South Dakota State University," by G. D. Nelson.

#### LOCATION AND DESCRIPTION OF STUDY AREA

The area selected for study spans the boundry between the proposed Oahe irrigation project and the adjacent glacial drift area (Fig. 1). The Oahe project encompasses most of the Lake Dakota Plain, the floor of a glacial lake late in the Wisconsinan glacial period. The ultimate size of the Oahe project is 495,000 acres.

The lake plain is rimmed by glacial deposits which in the study area occur as an undulating to rolling, loam, textured drift plain with complex slopes. Many closed depressions are present which collect most of the surface runoff. The elevation of the area ranges from 1300 to 1400 feet above sea level.

The crops grown in this area are determined by the climatic environment which is cool-temperature with irregular and usually deficient rainfall. The mean annual precipitation is 19.2 in. (Westin et al, 1954).

The study area may be divided into two broad physiographic units, the Lake Dakota Plain and the Williams Loamy Plain.

The soil limitations present in the soils of the study area are:

1. Unfavorable texture (claypan or sandy)
2. Topography
3. Shallow depth to lime
4. Saline conditions
5. Stoniness
6. Wetness
7. Slowly permeable substratum

Additional information about the study area may be found in Westin et al, 1954, and Westin, 1970.

### EXPERIMENTAL METHODS AND PROCEDURES

Initially three flight lines were established traversing typical soil areas in Spink County, South Dakota (Fig. 1). These flight lines were two miles wide. Flights made by the Remote Sensing Institute and the NASA RB-57 overflight for Mission 101, Site 195, are shown in Table I. Prints were made of selected areas.

Ground truth information was obtained for all flights. The information recorded on base maps is:

1. Plant type
2. Plant height
3. Row spacing
4. Row direction
5. Soil series
6. Soil moisture
7. Soil color
8. Condition of soil surface
  - a. Clod size
  - b. Amount of trash
9. Amount of weeds

In addition any other pertinent information is recorded. Interpretation of photographic and scanner transparencies was made with densitometers, visual methods, and an automatic color TV density slicing system (Spatial Data).

## RESULTS AND DISCUSSION

### SOIL PATTERNS

#### Bare Soil Surfaces

The soil patterns observed are different for the Lake Dakota and the Williams Loamy Plain. This difference is due to topography differences between the two physiographic units. The Lake Dakota Plain is extremely flat with simple slopes; whereas, the drift plain is undulating to rolling with numerous microdepressions and short complex slopes.

The soil limitations of the Lake Dakota Plain which can be identified are dense subsoil (claypan) (Fig. 2), unfavorable topography (convex sloping areas (Fig. 3) or depressional areas). The above are the major soil limitations to irrigation of the Lake Dakota Plain (Oahe project). The claypan areas are characterized by a pattern with a texture of different densities (Fig. 2) which is not present in soil areas which do not have this limitation (Fig. 4). This pattern is caused by varying amounts of the lighter colored (10YR6/1,dry) A2 horizon being mixed with the darker colored (10YR4/1,dry) Ap horizon by cultivation. The convex sloping areas are noted by a narrow band of lighter value along the slope change (Fig. 3). This lighter value is due to lighter colored calcareous material being exposed by water erosion or mixing with the overlying soil horizons. The soils occurring on these convex slope areas are usually very shallow. The depressional areas vary in size. They are somewhat circular in shape and if large enough, disrupt the normal field pattern. The depressions in cultivated areas are usually small and shallow. The small shallow depressions are associated with the claypan areas and may or may not be separable from the claypan areas.

The important soil limitations of the Williams Loamy Plain which can be observed are unfavorable topography (convex sloping areas or depressional areas) (Fig. 5). The topography of the drift plain is reflected by a random pattern of different densities. The areas of higher density are the soils on the flatter areas or in the concave areas which have darker colored A horizons. The areas of lower density are the eroded portions of the short complex slopes which are present. As with the lake plain the lighter colored areas are calcareous material close to the surface.

The depressional areas in cultivated areas appear as larger somewhat circular bodies with a density intermediate to the other topographic areas.

### Vegetated Areas

The soil patterns for vegetated and bare soil areas are the same until the vegetative cover masks the soil surface. The optical densities will be changed due to the effect of the growing vegetation. Once the vegetation covers the surface, the soil pattern is masked unless the crop is affected by the particular soil limitation present.

Under conditions of plant stress the crop in the claypan area reflects the pattern found in bare soil areas for claypan limitation. Similar conditions are true for the topographic limitation. The depressional areas show in vegetated areas as areas of different density than surrounding areas due to more vegetation or different type of vegetation because of the additional water collected in the depressional areas from runoff. Also, in the spring after heavy rainfall, these areas may have standing water present or may have the bare soil surface exposed if the crop has been drowned out.

### AUTOMATIC ANALYSIS OF SOIL PATTERNS

Two approaches for automatic analysis of the multi-spectral imagery listed in Table I have been utilized. The first was to measure optical densities of 9x9 inch EK-IR imagery with the four filter options available on the Macbeth optical densitometer. The other involves the use of an automatic color TV density slicing system (Spatial Data). The soil interpretations will be discussed in this part of the report while the details of obtaining the density data and classification problems are discussed in the report entitled: "Pattern Recognition at South Dakota State University," by G. D. Nelson.

The area selected for densitometer measurements consists of sandy soils ranging in drainage from excessively drained to poorly drained. The initial problem was to distinguish the poorly drained soils from the better drained soils. According to the confusion matrix generation by the pattern recognition group, this task could be accomplished 319 out of

320 times. The difference in the red chroma being the most important distinguishing factor. The Spatial Data system cannot make this separation without filters because it color codes only the value component of color. This type of analysis with the present equipment available is extremely slow because of the large amount of time needed to take the densitometer readings. Also, no stipulation for constructing a soil map is presently available.

Typical examples of soil limitations in the study area were analyzed by the Spatial Data system. A suitable map of a soil limitation can be made by photographing the color coded representation of differences of the value component of color of the area and making a contact print.

The claypan limitation of the Lake Dakota Plain (Fig. 2) may be mapped as shown in Figure 6. The yellow color represents areas of shallow depth to the claypan (<20cm.) whereas the blue color represents areas with greater depths to claypan (>20cm.). The black area is a depressional area which contained water at the time of flight.

Shallow soils on convex slopes (Fig. 3) are mappable also in some instances. Figure 7 shows the Spatial Data encoded image of Figure 3. The areas with erosion susceptibility are white.

On the Williams Loamy Plain, an undulating area with 3-5% slope, low round topped hills interspersed with areas of gentler slopes, flats, and swales was analyzed (Fig. 5). A Spatial Data representation with four colors is shown in Figure 8. The soils interpretation listed in Table II must be checked in the field.

The analyses of Table II indicate the great potential the automatic color TV density slicing system has for identifying and delineating areas of similar soil limitations or other groupings of similar soil. Not only can this type of system identify and map similar soil areas, but also the system can compute the area of each soil, which is extremely important as far as determining the composition of a soil mapping unit. Additional research is needed to define more precisely the uses and limitations of the Spatial Data system.

## FACTORS AFFECTING AUTOMATIC ANALYSIS OF SOIL LIMITATIONS

## Film-Filter Combinations

Evaluation of NASA RB-57 overflight on August 8, 1969,  
Mission 101, Site 195.-

## Quality of data:

The sensors employed are listed in Table I. Analysis of the film quality and exposure data for the film-filter combinations has been reported (Remote Sensing Institute, 1969). The important results from that report as well as additional points will be discussed here.

The analysis of the exposure data indicates that determining proper exposures is a serious problem which must be solved for multispectral sensing with photographic images. Hopefully, with better mission planning this problem can be eliminated.

The vignetting of all the imagery is so serious that the imagery cannot be used for quantitative density measurements. This problem is most serious for the RC-8 cameras and least serious for the Zeiss camera with the Hasselblad cameras being intermediate. The ranges in optical density due to vignetting cause density contrasts on the imagery that may be much greater than differences associated with vegetation and soil contrasts. Before photographic imagery of this type can be used for automatic data analysis this serious vignetting problem must be solved.

## Evaluation of imagery for detecting soil limitations:

Contact prints at scales approximating those used for soil surveys were made of the enlarged imagery for comparison and evaluation of the imageries for soil limitations.

For identifying and mapping soil limitations at this time of year (Aug. 8, 1969), the Ektachrome infrared imagery taken with the Zeiss camera is best. In order of excellence the black and white imagery (70 mm) are listed as follows:

<u>Film</u>	<u>Filter</u>	<u>Comments</u>
3400	58	Good target contrast and resolution
3400	25A	Less contrast than other B&W films and poor detail



<u>Film</u>	<u>Filter</u>	<u>Comments</u>
SO-246	89B	Good contrast, but very poor detail due to extreme graininess of enlargement

Usefulness of the 70mm color films may be ranked as follows:

<u>Film</u>	<u>Filter</u>	<u>Comments</u>
SO-368	2A	Detail limited by blue attenuation
SO-368	12	Detail poor
SO-180	15G	Overexposed, not suitable for use

The 9x9 inch color imagery taken with the RC-8 and Zeiss camera can be ranked as to usefulness as follows:

<u>Film</u>	<u>Filter</u>	<u>Comments</u>
SO-117	Zeiss "B"	Good detail, slightly underexposed
SO-117	500 Micro-meter/1.4AV	Detail good, but limited by slight overexposure
2448	HF3/2.2AV	Good detail for this film and time of year.

The above comments may apply only for the conditions for Site 195, Mission 101. Better exposure or different targets may alter the above observations. Additional studies on the above multispectral imageries and additional imagery for other conditions are needed to further answer the question of which film-filter combination is ideal for a particular condition.

#### Use of Mission 101 Imagery:

The transparencies may be used to make general maps of the study area, both physiographic and soil association maps, by visual analysis. Enlargements of any of the 9x9 inch color imagery to scales used in mapping soils provide a better base map for soil surveys than is presently being used.

The potential value of studying the multispectral imagery from NASA overflight lies in improving the accuracy of present surveys and in speeding up soil survey methods, the latter by permitting the soil surveyor to use remote sensing imagery to do a substantial amount of delineation and interpretation of soil boundaries in the office before going to the field.

#### Evaluation of RSI flight, Mission 104 on May 26, 1970.-

On May 26, 1970, the Remote Sensing Aircraft flew the Oahe #1 flight line with four 70mm sensors (Table 4) aboard

affording another opportunity for comparison of film-filter combinations. For the conditions of this flight, most spring grains emerging from the soil, the sensors may be ranked as follows:

<u>Film</u>	<u>Filter</u>	<u>Comments</u>
2448	HF3+4	Good detail in bare soil areas
8443	15G/30M	Comparable to 2448
8403	25A	Detail limited because of graininess
8403	58	Poor detail, underexposed

#### Summary of evaluation of film-filter combinations.-

The different target conditions of the August 8, 1969 and May 25, 1969 flights changed the ranking of usefulness of the films. From the above elementary analysis, it can be seen that the film-filter combinations selected for a mission will depend upon the target or time of year.

The film-filter combinations and their exposures need to be carefully selected for each mission according to the conditions of the agricultural scene to be sensed.

#### Scale

The scale of the image must be large enough to allow automatic analysis of an area. With present techniques, analyzing one field at a time because of vegetative differences, many cultivated areas on the 60,000 ft. 9x9 inch imagery from the NASA RB-57 are too small for analysis. The smallest element which presently can be analyzed is one-half inch square.

#### SUMMARY AND CONCLUSIONS

Establishing remote sensing principles for identifying and delineating soil limitations to land use in agricultural areas was the subject of research initiated in a potentially irrigable area in South Dakota. Representative patterns of claypan and topographical soil limitations can be identified on bare soil surfaces and on vegetated surfaces if the vegetation is subjected to a stress because of the soil limitation.

Automatic analysis of the soil limitations studied by an automatic color TV density slicing system was accomplished.

This system color codes the density range of the value component of color of an image. Maps of soil limitations or other similar soil groups may be produced by photographing the color coded representation of an area. These maps are comparable or may be superior to present day maps. The planimeter feature of the density slicing system can measure the area of each soil limitation providing information on the importance of a soil limitation in an area.

The results of this first year study suggest that an automatic color TV density slicing system has great potential not only for identifying and mapping similar soil areas, but also for indicating the percentage composition of an area.

TABLE I.- CAMERA, FILM AND FILTER DATA FOR OAHE SITES  
July 1, 1969 to June 30, 1970

Mission	Date	Altitude AGL Ft	Time of day	Sensor	Film Type	Filter	Wavelength $\mu$	Roll or Tape No.
27	7-25-69	2,000	11:53- 13:11	Thermal IR scanner			8-14	23,23,25
28	7-28-69	2,000	11:43- 12:44	Thermal IR scanner			4.5-5.5	26,27
36	8-7-69	14,000	15:06 15:42	Thermal IR scanner			4.5-5.5	37,38
				K-17 9x9in camera	EKIR	15G/30M	.510-F*	69-99
		6,500	16:02- 16:08	Thermal IR scanner			4.5-5.5	38
				K-17 9x9in camera	EKIR	15G/30M	.510-F*	69-99
101**	8-8-69	60,000	12:03- 1:18	Hass. 70mm camera A	EKMS	12	.495-F*	4
				Hass. 70mm camera B	Pana- tomic-X	58	.465-.620	6
				Hass. 70mm camera C	Pana- tomic-X	25A	.580-F*	7
				Hass. 70mm camera D	BW-IR	89B	.680-F*	4

69

TABLE I.- CONTINUED

Mission	Date	Altitude AGL Ft	Time of day	Sensor	Film Type	Filter	Wavelength $\mu$	Roll or Tape No
				Hass. 70mm camera E	EKIR	15G	.510-F*	3
				Hass. 70mm camera F	EKMS	2A	.405-F*	5
				RC-8 9x9in camera	EKMS	HF3/2.2AV	.375-F*	2
				RC-8 9x9in camera	EKIR	500 $\mu$ / 1.4AV	.500-F*	3
				Zeiss 9x9" camera	EKIR	Zeiss B	.470-F*	4
38	8-12-69	6,000	12:22- 13:01	Thermal IR scanner			4.5-5.5	44,45
				K-17 9x9in camera	EKIR	15G/30M	.510-F*	69-100
57	10-21-69	2,000	6:18- 7:41	Thermal IR scanner			8-14	62,63,64
60	10-23-69	8,000	10:50- 11:14	Thermal IR scanner			8-14	68
				K-17 9x9in camera	EKMS	HF3	.375-F*	69-139

TABLE I.- CONTINUED

Mission	Date	Altitude AGL Ft	Time of day	Sensor	Film Type	Filter	Wavelength $\mu$	Roll or Tape No
103	5-25-70	14,000	12:17- 12:29	Hass. 70mm camera A	Tri-X	58	.465-.620	70-144
				Hass. 70mm camera B	Tri-X	25A	.580-F*	70-145
				Hass. 70mm camera C	EKIR	15G/30M	.510-F*	70-146
				Hass. 70mm camera D	EKMS	HF3+4	.375-F*	70-147
104	5-26-70	14,000	14:56- 15:19	Hass. 70mm camera A	Tri-X	58	.465-.620	70-144
				Hass. 70mm camera B	Tri-X	25A	.580-F*	70-145
				Hass. 70mm camera C	EKIR	15G/30M	.510-F*	70-146
				Hass. 70mm camera D	EKMS	HF3+4	.375-F*	70-147
				K-17 9x9in camera	EKIR	15G/30M	.510-F*	70-157
112	6-25-70	14,500	12:48- 13:11	Hass. 70mm camera A	Tri-X	58	.465-.620	70-191

TABLE I.- CONCLUDED

Mission	Date	Altitude AGL Ft	Time of day	Sensor	Film Type	Filter	Wavelength $\mu$	Roll or Tape No
				Hass. 70mm camera B	Tri-X	25A	.580-F*	70-192
				Hass. 70mm camera C	EK-IR	15G/30M	.510-F*	70-193
				Hass. 70mm camera D	BW-IR	89B	.680-F*	70-194

\* F-sensitivity of film

\*\* Supplied by NASA RB57 flight, Mission 101, Site 195. All other data obtained by Remote Sensing Aircraft.

TABLE II.- INTERPRETATION OF SPATIAL DATA ANALYSIS OF AN  
UNDULATING DRIFT PLAIN.

---

---

<u>Color</u>	<u>Area %</u>	<u>Interpretation</u>
Yellow	5.6	Rolling, eroded, shallow soils. Excessively drained. Severe water erosion potential.
Green	34.0	Undulating, shallow soil, well drained, water erosion potential.
Red	49.6	Nearly level, well drained soils.
Blue	10.0	Concave to level, moderately well drained soil. Collect runoff from surrounding sloping areas.

---

---



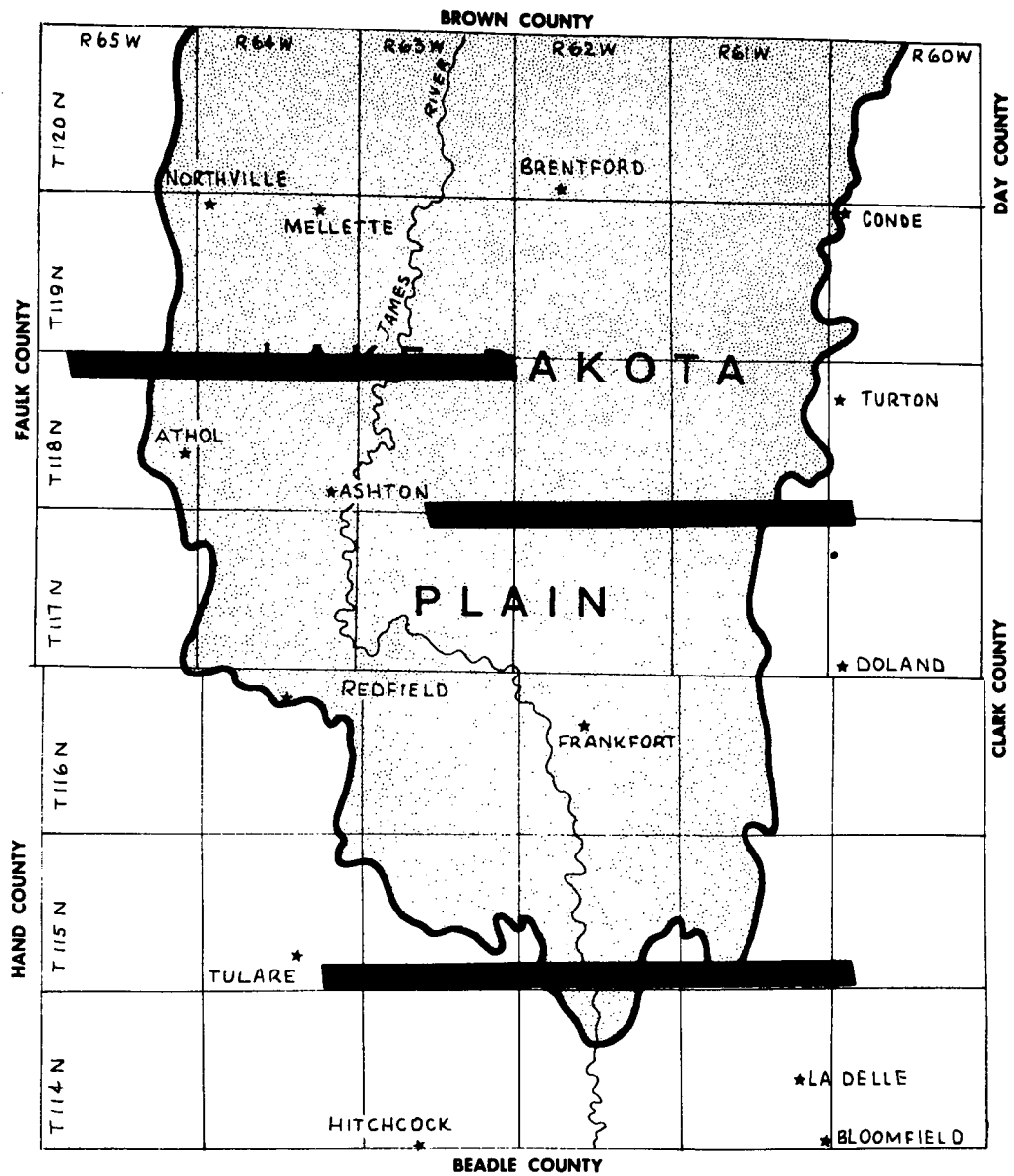


FIG. 1 LOCATION OF STUDY AREA IN SPINK COUNTY,  
SOUTH DAKOTA

NOT REPRODUCIBLE

25-17

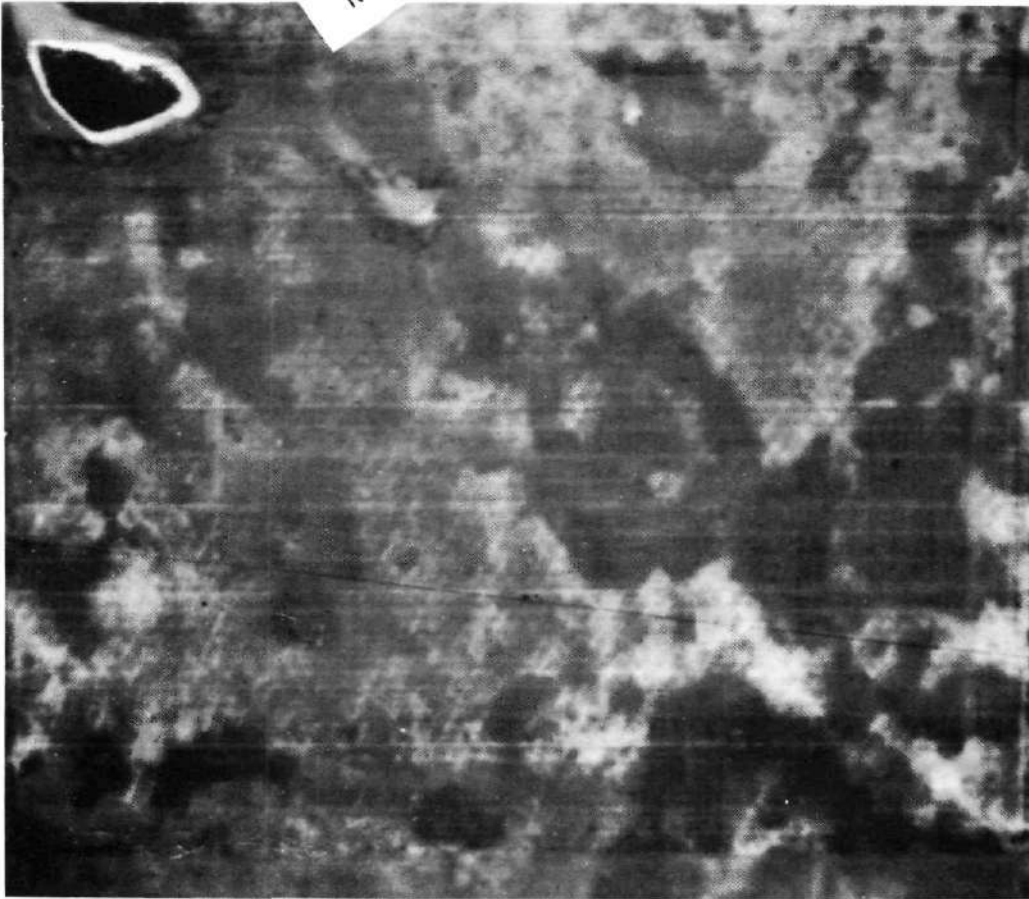


Figure 2. Claypan limitation, Lake Dakota Plain, T118N, R64W, Sec. 11, NE 1/4. RSI Mission 104. Scale - 1:4800. Crop is spring wheat, 5cm. high.

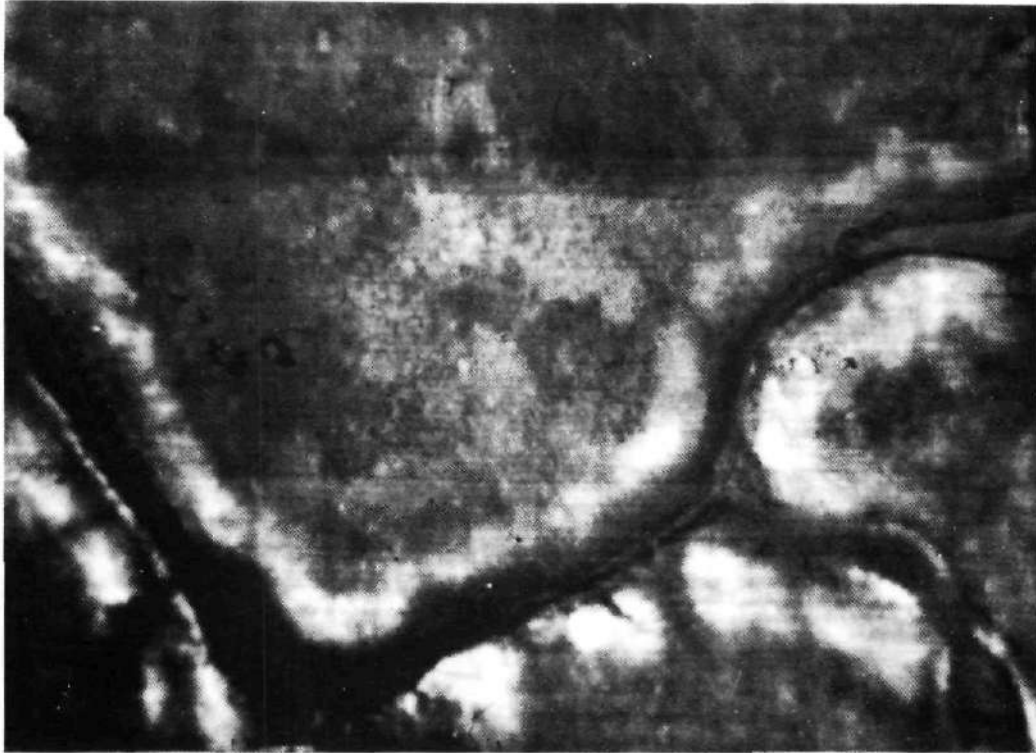


Figure 3. Topography limitation, Lake Dakota Plain, T118N, R63W, Sec. 10, SE 1/4, RSI Mission 104. Scale - 1:6000, Crop is spring wheat, 8cm high.

NOT REPRODUCIBLE

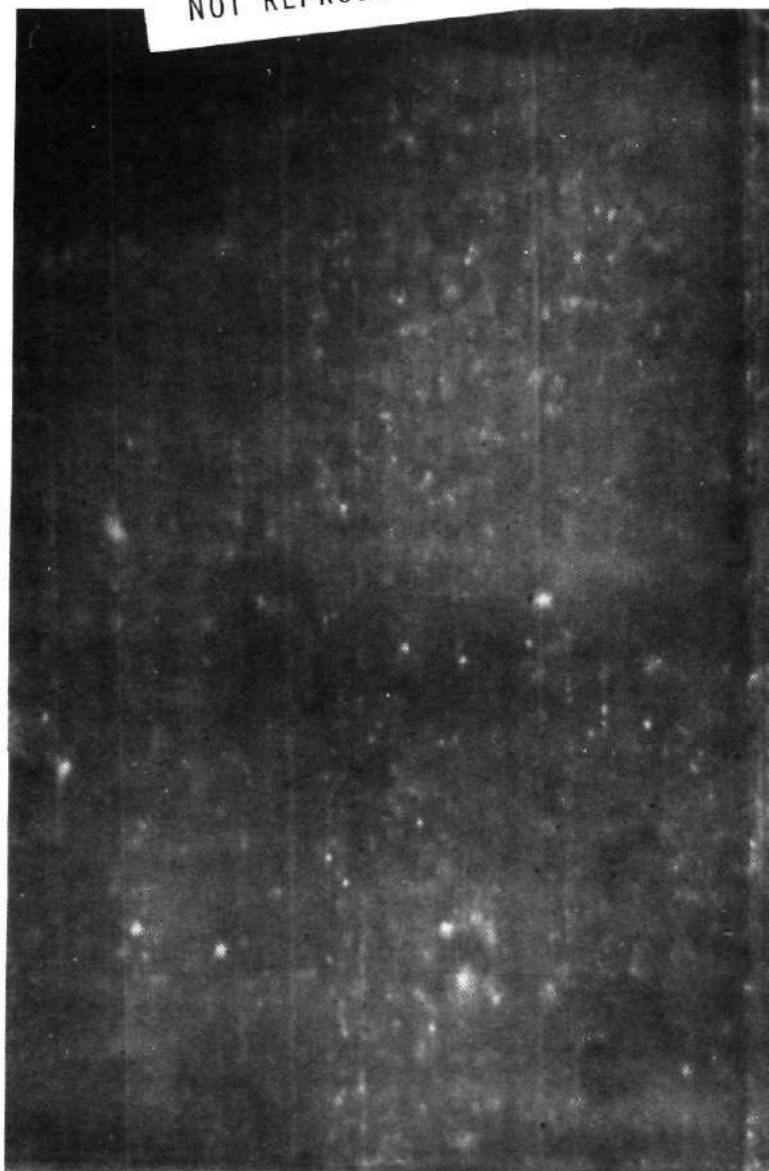


Figure 4. Soil areas without claypan, Lake Dakota Plain,  
T118N, R64W, Sec. 8, SE 1/4, RSI Mission 104. Scale - 1:6000  
Fallow field.

NOT REPRODUCIBLE

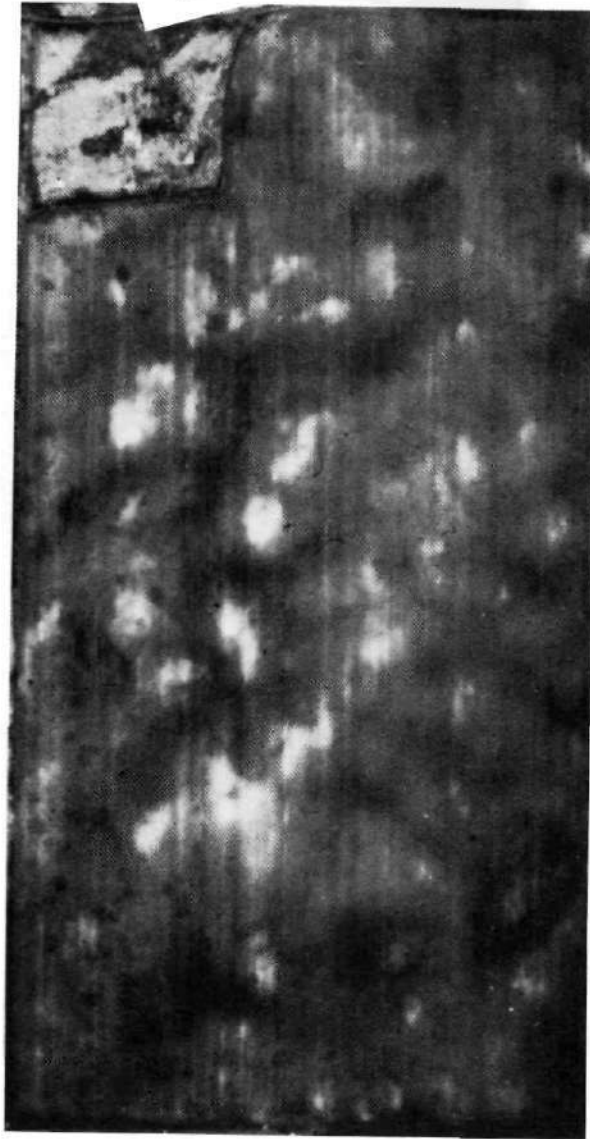


Figure 5. Undulating drift plain, Williams Loamy Plain, T118N, R65W, Sec. 3, NE 1/4. RSI Mission 104. Scale - 1:6000. Crop is spring wheat, 8cm high.

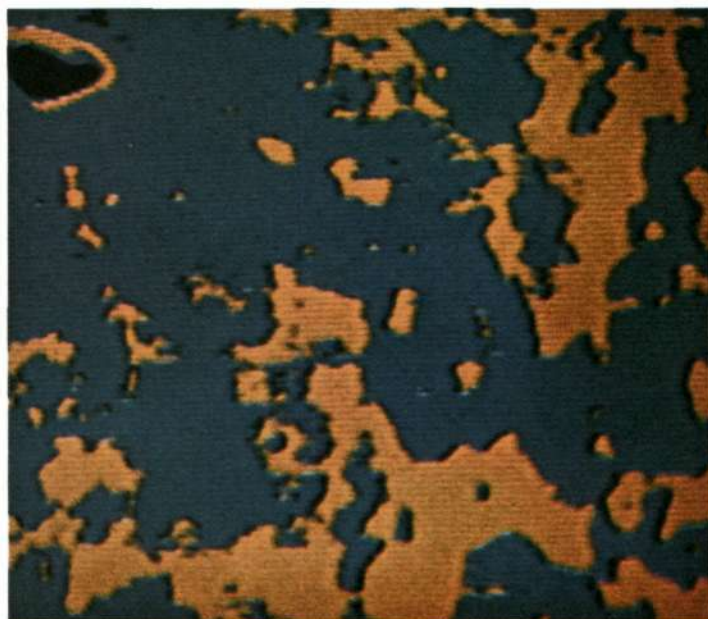


Figure 6. Color coded representation of Figure 2.

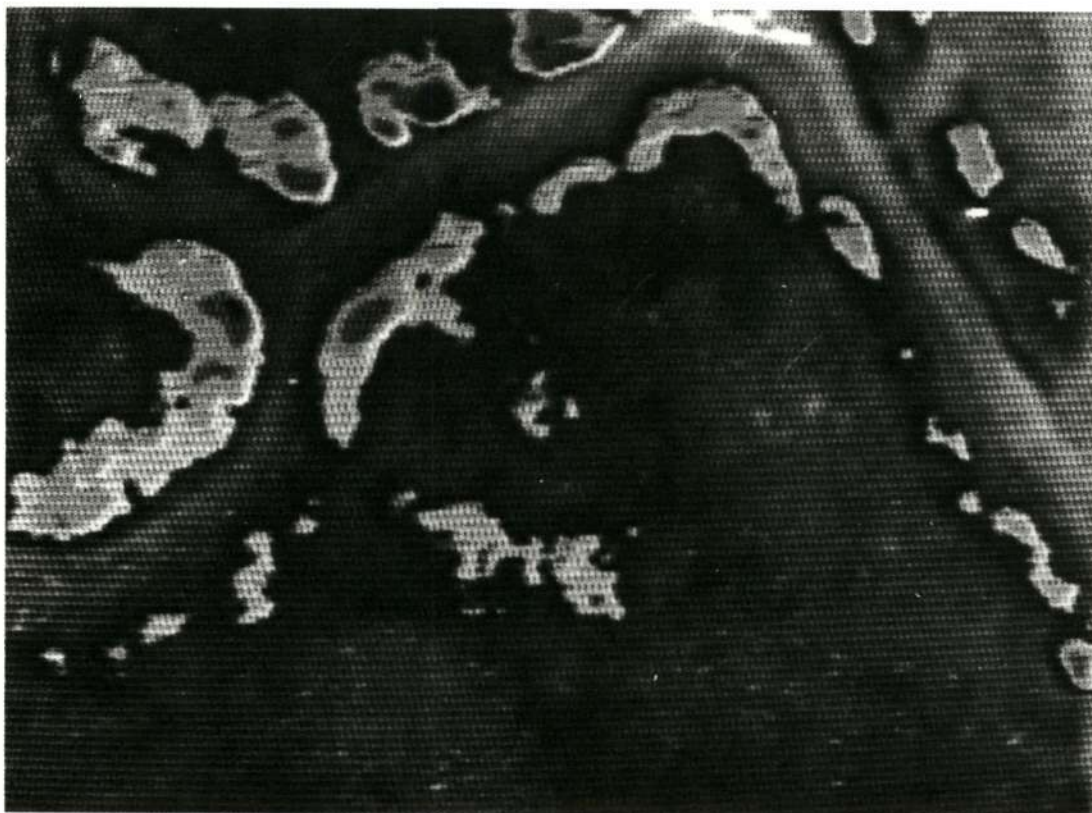


Figure 7. Color coded representation of Figure 3.

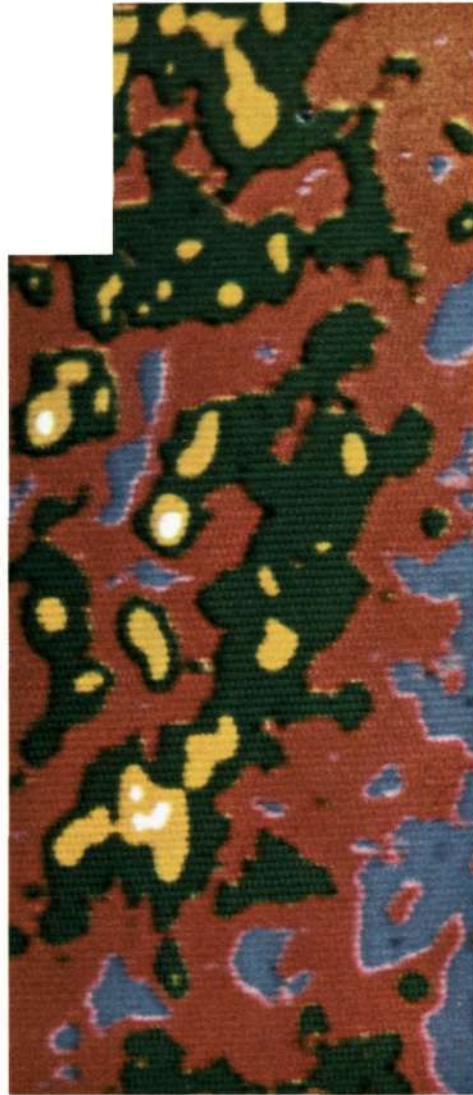


Figure 8. Color coded representation of Figure 5.



RECOGNITION OF CROPS AND SOILS  
BY SPOT DENSITY MEASUREMENTS OF IMAGERY

by

Gerald D. Nelson  
Remote Sensing Institute  
South Dakota State University  
Brookings, South Dakota

INTRODUCTION

The goals of the pattern recognition work in progress at the Remote Sensing Institute at South Dakota State University are:

1. To develop methods that are useful to the analyses, feature definition, feature selection, and classification of remotely sensed data, and
2. to determine the usefulness of spot density measurements of Ektachrome infrared film for use as features to classify crops from altitudes of 60,000 feet (NASA flight), and crops and soils from 14,000 feet (Remote Sensing Institute flight).

To develop automatic methods to aid as well as to classify the data resulting from imagery requires an extensive effort be supplied to feasibility studies. The pattern recognition feasibility study areas include:

Imagery measurements  
Data compression methods  
Feature definition  
Feature extraction  
Feature analysis  
Feature selection  
Classification  
Encoding of classification results  
Color display techniques

In order to develop a satisfactory pattern recognition system requires careful interfacing of all the feasibility study areas. Naturally, one recognizes this not as a new concept, but as a system approach to design which has significant merit.

The second goal is to determine the usefulness of spot density measurements of the imagery for different films and flight altitudes. The tasks encompassed have been all but the data compression, encoding of classification results and color display techniques. The feasibility study area results are discussed in this paper.

A major value of automatic or even semi-automatic pattern recognition techniques lies in the area of making repetitive measurements, numerical calculations and decisions without tiring as does the human. The trained human at the present time is still better qualified as a decision maker than any machine which uses density measurements as the features. Therefore, the research done in the area of pattern recognition for special tasks is still a search for reliable measurements which will provide adequate classification results to make the use of pattern recognition techniques economically feasible. It is also desirable that the results be as accurate as those of a good human photo interpreter. Implied, as a goal, in pattern recognition research is that the methods be computationally efficient.

### STUDY AREA

The description of the study area is presented by a set of three photos and their associated transparent overlays which outline the soils and/or crops. This set of three photos does not include all of the fields on which densitometer measurements were made.

The soil study at the present time has been restricted to two soils denoted as soil A and B. The two soils studied are outlined on the Ektachrome infrared photo contact printed from the transparency. This photo was taken at an altitude of 14,000 feet.

A study of the recognition of crops from altitudes of 60,000 feet and 14,000 feet were also conducted. The crop identification of fields from 60,000 feet is presented as Figure 2. Ektachrome infrared film was used.

The study of crops from an altitude of 14,000 feet is easier because the fields are larger and easier for the human to recognize. Also more measurements can be made per field. The identification of crops from 14,000 feet is presented as Figure 3.

## EXPERIMENTAL METHODS AND PROCEDURES

This section includes discussions of ground truth, densitometer measurements, pattern recognition computer programs, and a proposed hardware pattern classifier.

### GROUND TRUTH

A "ground-truth" mission was conducted on July 4, 1969. An identification of 533 fields in three separate flight coverage areas was made. For the pattern recognition studies, nineteen classes were assigned and are presented in Table I. This ground truth data has been mapped, coded, and field numbered to enable coordination of derived data from more than one source.

### DENSITOMETER MEASUREMENTS

The feasibility studies reported on within this report are based on the information contained in the measurements made with a densitometer with four different filters. The Macbeth densitometer was used with a one millimeter spot size. On the 14,000 foot imagery approximately 20 spot density measurements with each filter were made within a field, whereas only five spot density measurements were made with each filter within a field on the 60,000 foot imagery.

Another instrument, the Spatial Data system, can also be used to make density measurements. This is an instrument which uses a vidicon to sense the light transmitted through the film. The result is color encoded into as many as 32 colors. An advantage of this system is the speed at which the data is encoded.

### PATTERN RECOGNITION COMPUTER PROGRAMS

There exists a need to observe the structure of the density measurements which are the features. This can be done by generating a sample probability density function for each set of density measurements per crop or field. From these plots one can estimate the value of the feature for pairwise class or crop classification, but when trying to

interpret this data for a many-class problem one has difficulty.

When no single feature appears adequate, then it is desirable to use pairs of features to discriminate among the classes. A scatter-plot is useful to estimate the separability of classes by pairs of features. However, in the scatter plot the frequency of occurrence of each point is not presented, but can be determined by the list which is called the overprint record. The significant factor to be determined is the amount of overlap.

Another computer program which is helpful and should be used before a classification study is made determines the number of modes present in the data on a per class basis. Actually, the sample probability density function and scatter plots provide information as to the number of modes. However, the output of this program is more detailed than either of the other two. The output consists of the radius of each mode, the pairwise distance between crops or soils for each feature, and the total distance between crops for each of the features.

The classifier implemented as a computer program is based on determination of a matrix B which provides a least-squares mapping of the class vector estimate toward a set of orthonormal class vectors [1]. The minimization problem which is solved determines B by the minimization of the squared distance between the class orthonormal vectors and the class vector estimates.

An event or sample represented by the class vector estimate is assigned to that class whose class vector is closest, in a Euclidian sense, to the mapped feature vector which is

$$d = B x_A$$

where  $x_A$  is the  $n+1$  dimensional augmented feature vector

$$x_A = \begin{bmatrix} x_1 \\ \cdot \\ \cdot \\ \cdot \\ x_{n-1} \\ x_n \\ \hline -1 \end{bmatrix}$$

The decision rule is to select class  $i$

if  $d_i > d_j$  for all  $j \neq i$ .

The decision vector is also represented by the equation

$$d = [P_i] [\bar{x}^i - \bar{x}]_R^T \phi^{-1} [x - \bar{x}] + [P_i]$$

$$\text{where } [P_i] = \begin{bmatrix} p_1 & 0 & 0 \\ 0 & p_2 & \\ 0 & & p_k \end{bmatrix}$$

are the a priori probabilities of each class occurring or a set of weights since usually the a priori probabilities are unknown.

$\bar{x}^i$  is the mean vector of the  $i$ th class,  
 $\bar{x}$  is the mean vector of all classes,  
 $\phi$  is the sample covariance matrix and is calculated according to

$$\phi = [\overline{xx^T} - \bar{x}\bar{x}^T]$$

$\phi^{-1}$  is the inverse of the sample covariance matrix.

The normal process to determine the classifier structure is to supply a "training" set of feature vectors. From this "training" set  $\bar{x}^i$ ,  $\bar{x}$ ,  $[P_i]$ ,  $\phi$ , and  $\phi^{-1}$  are calculated. The only unknown term remaining in the equation for the decision vector is  $x$ , the feature vector. Therefore, at this point, the classifier is trained and either the training set or "testing" set of data is supplied to the classifier program. The decision vector is calculated for each feature vector and the classification result determined by selecting the subscript of the largest element of the decision vector as the correct class number. The result of this process is the confusion matrix which represents the score attained in the classification process. As an example consider Table II.

Ninety-five percent of the class three feature vectors were classified as class three, one percent were classified as class one, and four percent as class two.

SPECIAL CLASSIFICATION HARDWARE

The decision vector can also be written as in the next equation,

$$d = [P_i] [(\bar{x}^i - \bar{x})_R \phi^{-1} x - (\bar{x}^i - \bar{x})_R \phi^{-1} \bar{x} + 1]$$

$$d = Ax - A\bar{x} + 1$$

$$\text{where } A = [P_i] [\bar{x}^i - \bar{x}] \phi^{-1}$$

$$d = A(x - \bar{x}) + [P_i]$$

From the last equation it is obvious that to build a special purpose classifier once the training phase is completed is relatively easy. To build the hardware required to train the classifier is not so easy. A storage is required for the matrix  $[P_i]$  and the vector  $\bar{x}$ . The difference between the feature vector  $x$  and the average feature vector of all classes  $\bar{x}$  is formed and the result multiplied by the matrix  $A$ . To this product are added the weights  $[P_i]$  and then the largest element of the decision vector is determined and the decision recorded or announced by indicator lights. A block diagram of the classifier is shown in Figure 4.

This classifier is proposed as a slow speed system which could effectively demonstrate the decision at boundaries, or other selected spots on a film once the classifier was trained. The main advantages are that the density measurements do not have to be recorded, keypunched, verified, or positional information encoded so that the measurement spot can be located after the computer classification results are printed. The classification results could be determined as rapidly as the human can make them, and the human stores the positional information. In fact, the human acts as an adaptive sampler and determines results only at the location of special interest to him.

PRELIMINARY SOIL IDENTIFICATION EXPERIMENT

Two soils, referred to as soil A and B, were identified by Dr. Frazee on Ektachrome infrared film exposed at an altitude of 14,000 feet. To determine if density measurements could be used as features to recognize these soils the following tasks of the experiment were conducted.

1. Measurement of 160 spot density readings per soil type with a one millimeter aperture on the Macbeth densitometer. Each of the four filters were used, neutral or visible, red, green and blue.
2. Plot of the sample probability density function for all filters and each soil.
3. Plot of all two-dimensional scatter plots for the two soils.
4. Classification into two classes based on the four density readings per location.

The plot of the sample probability density function for each feature in Figure 5 indicates the best individual feature to discriminate between these soils is the red filter density measurement.

To determine the best pair of features to discriminate between these soils it is necessary to consider the scatter plots shown in Figure 6. There are several pairs of features that appear they could be used effectively. They are the blue-green and blue-red filters. These plots indicate that there is no overlap of the density measurements since there are no + signs indicated.

To classify the samples of a program K-class I was used and all four features were used. The confusion matrix or score matrix is presented as Table III. This result indicates that in the four-dimensional space the two soils are almost linearly separable.

The use of the Spatial Data system for quantizing or level slicing should be used with a red filter to get the best results for these soils with one filter. Figure 7 illustrates that a neutral filter on the vidicon does not separate the two soils, but Figure 8 indicates that a red filter does separate the two soils.

One of the major problems in pattern recognition work is to determine the procedure for the selection of features. In the present case since there are only four features, an exhaustive search for the best solution is feasible. The classification results for each of the fifteen combinations features the rank ordering of the classification results are presented in Table IV.

One should note that the two worst features separately, blue provides 53.75 percent and green 82.19 percent, if used together as a pair they provide a correct classification of 98.75 percent.

The classification results as a function of the number of features used, are presented in Figure 9.

### PRELIMINARY CROP IDENTIFICATION EXPERIMENTS

This preliminary study consisted of using Ektachrome infrared film exposed from 14,000 and 60,000 feet. As was the case with the soil study, spot density measurements were used. A one millimeter aperture on the MacBeth densitometer was used with four filters which included neutral or visible, red, green and blue.

#### 60,000 FEET, EKTACHROME INFRARED FILM

The classification results for the Ektachrome infrared film exposed at 60,000 feet are presented in Table V. The K-class I program was used to classify the crops. The low percentage of correct classification is believed to be due primarily to the large spot size used for imagery taken at 60,000 feet.

#### 14,000 FEET, EKTACHROME INFRARED FILM

The Ektachrome infrared film exposed at 14,000 feet appears to be more useful to study than Ektachrome infrared at 60,000 feet. Corn, fallow, harvested wheat, and pasture grass were classified 69.5 percent correct as shown in Table VI.

The classifiers based on the use of alfalfa, wheat, harvested oats, and harvested alfalfa; and sorghum, oats, and hayland do not yield results which are as good as the other 14,000 feet Ektachrome infrared imagery, as shown in Tables VII and VIII. The percent of correct recognition is 20 and 62, respectively.

A classifier for six classes which are corn, fallow, harvested wheat, roadways, trees, and water are determined. The confusion matrix is presented as Table IX. The correct recognition rate for all classes is 75.5 percent. However, the fallow class is difficult to recognize. This difficulty could possibly be traced back to the ground truth definition



of fallow which includes plowed and unplowed fields as well as fields with weeds. The poor classification results should be investigated by examination and comparison of the fields erroneously classified with those correctly classified.

The sample probability density functions for this six class problem are presented in Figure 10. I am sure that the human observer has a difficult time specifying the decision boundaries in this multi-class problem whereas in any two-class problem it may be quite easy. The classifier recognized 75 percent of these spot density measurements.

### SUMMARY AND CONCLUSIONS

Computerized techniques and methods have been developed which were used to conduct preliminary soil and crop identification experiments. They will also be used to continue the study of classification and/or identification methods. However, additional methods which are assured to provide better results than reported in this report are also being developed [2].

The soil identification experiment was conducted by making densitometer measurements on Ektachrome infrared film exposed at 14,000 feet. The density measurements were analyzed by plotting sample probability density functions, two-dimensional scatter plots, and the use of K-class I to determine the complete set of classification results for one, two, three and four features.

Due to the presence of nineteen classes, crop identification experiments were more difficult to formulate. This is partially due to the computer core size which limits the number of classes, features and/or samples. However, the classes of corn, fallow, harvested wheat, roadways, trees and water were classified 75 percent correct as reported in Table IX.

The amount of data used to make a decision has a definite effect on the quality of the decision. To use spot density readings of the film is probably the most elementary or basic measurement to be used to determine the decision. However, some of the results are encouraging even though one anticipates better classification results if more data is used.

One of the significant problems associated with classifiers is that they are sensitive to the subset of classes used as well as the subset of features.

## REFERENCES

- [1] N. Zagalsky, "A New Formulation of a Classification Procedure," M. S. Thesis, University of Minnesota, March 1968.
- [2] W. G. Wee, "On Feature Selection in a Class of Distribution - Free Pattern Classifiers," IEEE Transactions on Information Theory, Vol. IT-16, No. 1, pp 47-55, January 1970.

TABLE I.- THE CLASSIFICATIONS ESTABLISHED FOR  
PATTERN RECOGNITION

<u>Code</u>	<u>Identification</u>
1	Corn
2	Wheat
3	Oats
4	Alfalfa
5	Fallow
6	Sorghum
7	Pasture-grass
8	Barley
9	Harvested wheat
10	Harvested oats
11	Harvested alfalfa
12	Harvested barley
13	Slough
14	Brome
15	Hayland
16	Unknown
17	Roadways
18	Trees
19	Water

TABLE II.- SAMPLE CONFUSION MATRIX

	Number of Measurements	Percent	<u>Classified As</u>		
			1	2	3
1	100	99	99	1	0
<u>Known</u> <u>As</u> 2	100	98	0	98	2
3	100	95	1	4	95
Totals	300	97.33	Weights .333	.333	.333

TABLE III.- CONFUSION MATRIX, 14,000 EKTACHROME INFRARED

	Number of Measurements	Percent	<u>Classified As</u>	
			A	B
<u>Known</u> <u>As</u> A	160	99	99	1
B	160	100	0	100
Totals	320	99	Weights .500	.500

TABLE IV.- RANK ORDERING OF FEATURES

Individual Features

Red	99.375
Neutral	83.437
Green	82.187
Blue	53.750

Two Features

Neutral, Red	99.375
Neutral, Green	99.062
Red, Green	99.062
Green, Blue	98.750
Red, Blue	96.875
Neutral, Blue	94.062

Three Features

Neutral, Red, Blue	99.687
Red, Green, Blue	99.375
Neutral, Red, Green	99.375
Neutral, Green, Blue	98.750

Four Features

Neutral, Red, Green, Blue	99.687
---------------------------	--------

TABLE V.- CONFUSION MATRIX - 60,000 FEET  
Ektachrome Infrared Film

	Number of Measurements	Percent	Sorghum	Fallow	H. Oats	H. Alfalfa
Sorghum	65	32.3	<u>21</u>	29	11	4
Fallow	120	22.5	65	<u>27</u>	17	11
Harvested Oats	85	37.7	28	12	<u>32</u>	13
Harvested Alfalfa	50	24.0	15	16	7	<u>12</u>
Totals	320	28.7	Weights			
			.250	.250	.250	.250

TABLE VI.- CONFUSION MATRIX - 14,000 FEET  
Ektachrome Infrared Film

	Number of Measurements	Percent	Corn	Fallow	H. Wheat	Pasture Grass
Corn	200	93.5	<u>187</u>	0	10	3
Fallow	200	79.0	0	<u>158</u>	42	0
H. Wheat	200	81.5	13	4	<u>163</u>	20
Pasture Grass	200	23.0	48	33	73	<u>46</u>
Totals	800	69.5	Weights			
			.250	.250	.250	.250

TABLE VII.- CONFUSION MATRIX - 14,000 FEET  
Ektachrome Infrared Film

	Number of Measurements	Percent	Alfalfa	Wheat	H. Oats	H. Alfalfa
Alfalfa	100	36.0	<u>36</u>	0	61	3
Wheat	100	32.0	9	<u>32</u>	54	5
H. Oats	180	7.8	84	75	<u>14</u>	7
H. Alfalfa	160	16.3	44	52	38	26
Totals	540	20	Weights			
			.250	.250	.250	.250

TABLE VIII.- CONFUSION MATRIX - 14,000 FEET  
Ektachrome Infrared Film

	Number of Measurements	Percent	Sorghum	Oats	Hayland
Sorghum	100	65.0	<u>65</u>	25	10
Oats	80	68.7	1	<u>55</u>	24
Hayland	60	40.0	18	18	24
Totals	240	62	Weights		
			.333	.333	.333



TABLE IX.- CONFUSION MATRIX - 14,000 FEET  
Ektachrome Infrared Film

	Number of Measurements	Percent	Corn	Fallow	H. Wheat	Roadways	Trees	Water	
Corn	200	73.0	<u>146</u>	0	1	6	47	0	
Fallow	200	54.5	0	<u>109</u>	19	33	0	39	
H. Wheat	200	72.5	17	1	<u>145</u>	37	0	0	
Roadways	200	81.0	3	14	21	<u>162</u>	0	0	
Trees	200	89.0	21	0	1	0	<u>178</u>	0	
Water	200	83.0	3	29	1	1	0	<u>166</u>	
Totals	1200	75.5	Weights		.167	.167	.167	.167	.167

128

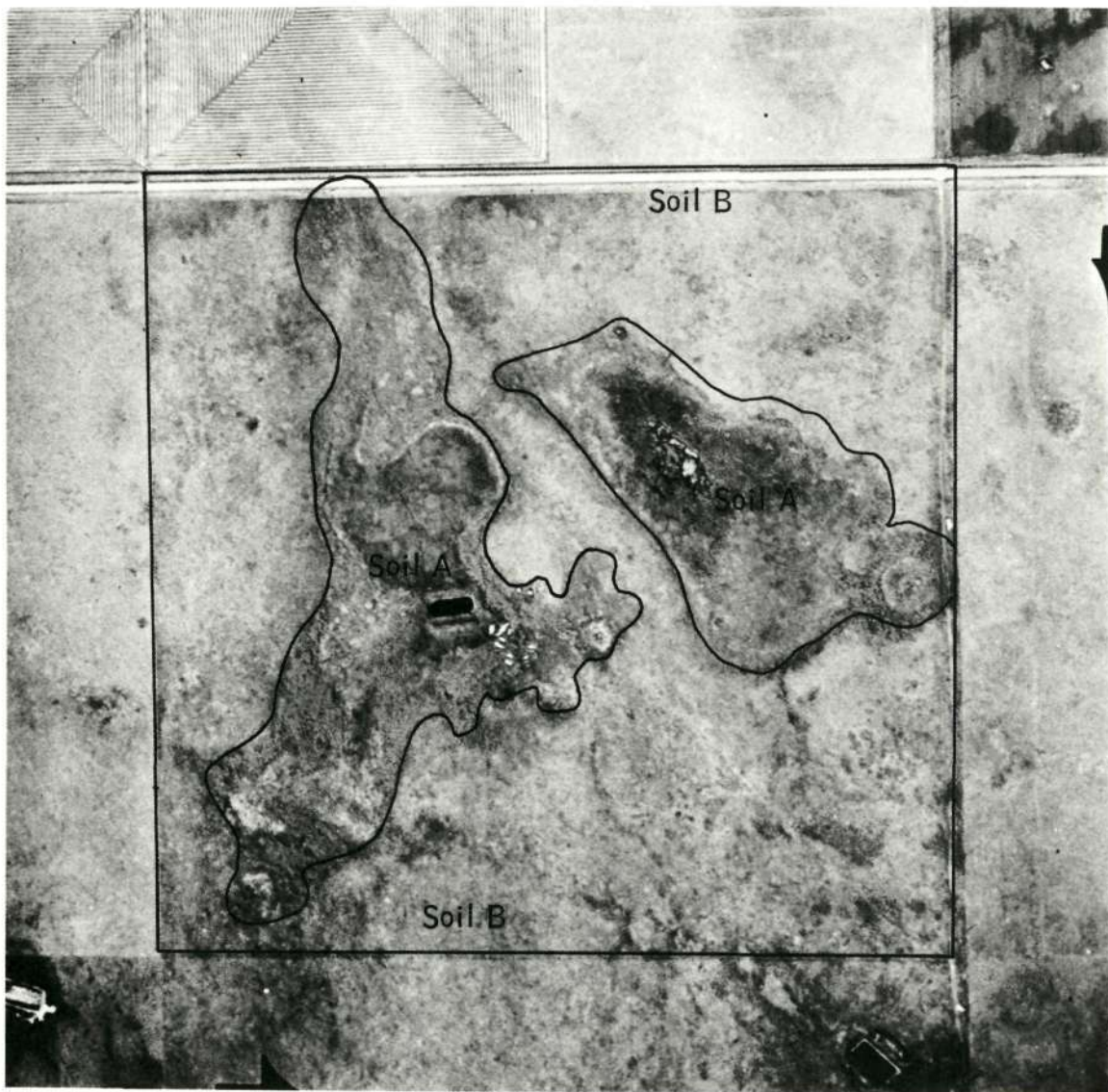


Figure 1. Soils A and B -- Pattern recognition study used data measured with Macbeth densitometer and Spatial Data system.

This page is reproduced again at the back of this report by a different reproduction method so as to furnish the best possible detail to the user.

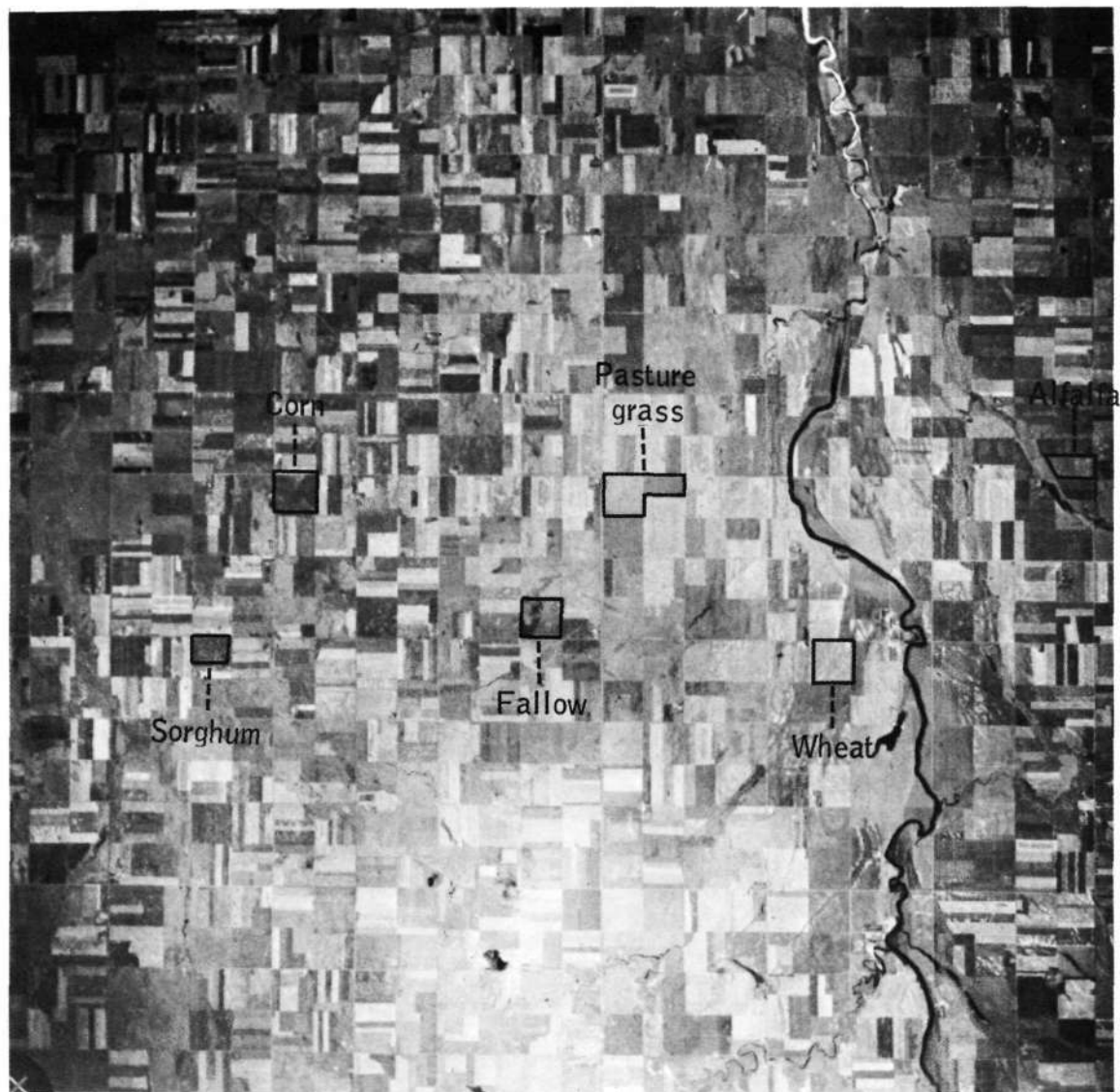


Figure 2. National Aeronautics and Space Administration imagery taken on August 8, 1969 over South Dakota at an altitude of 60,000 feet.

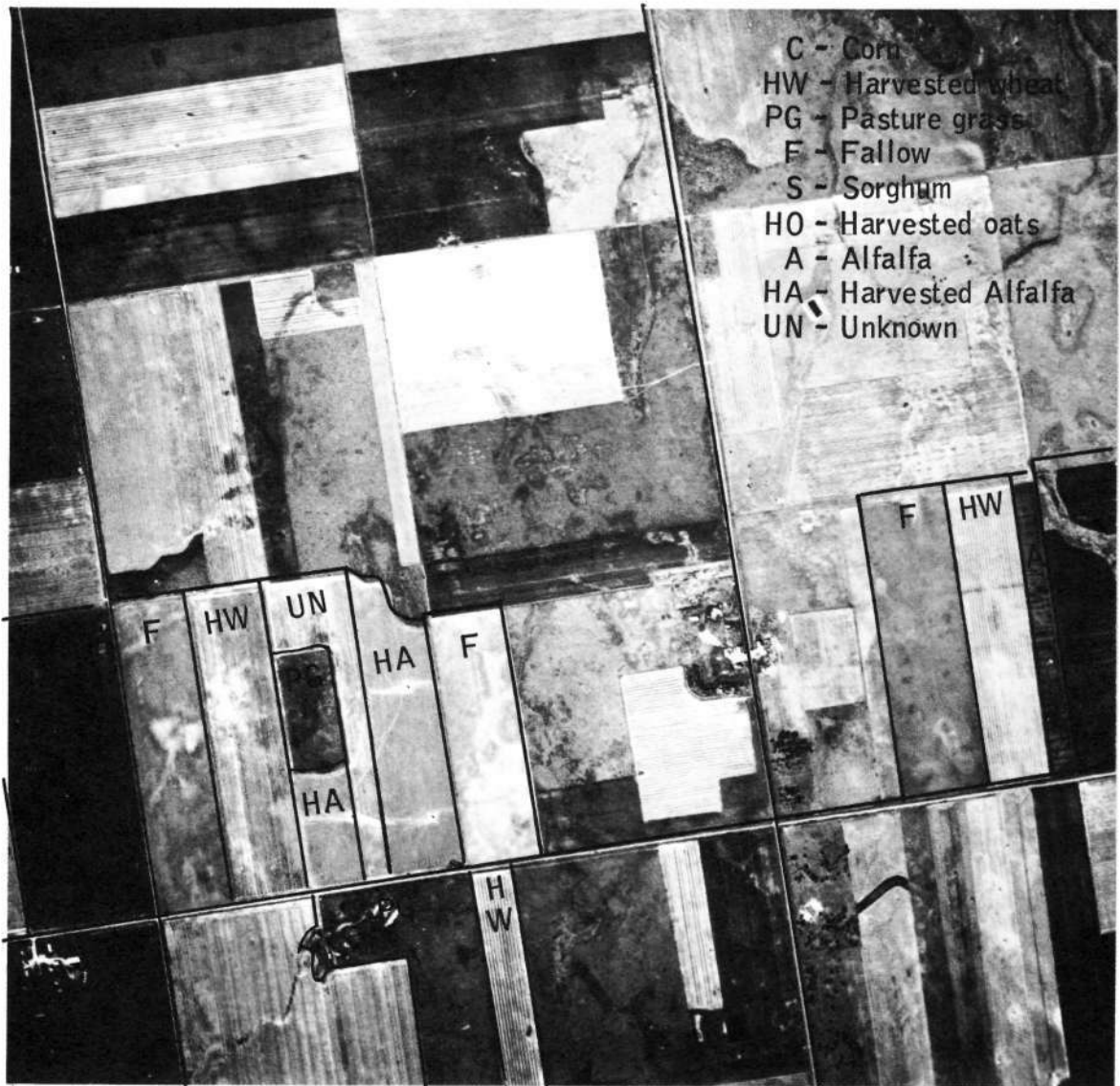


Figure 3. Remote Sensing Institute imagery taken over South Dakota at an altitude of 14,000 feet.

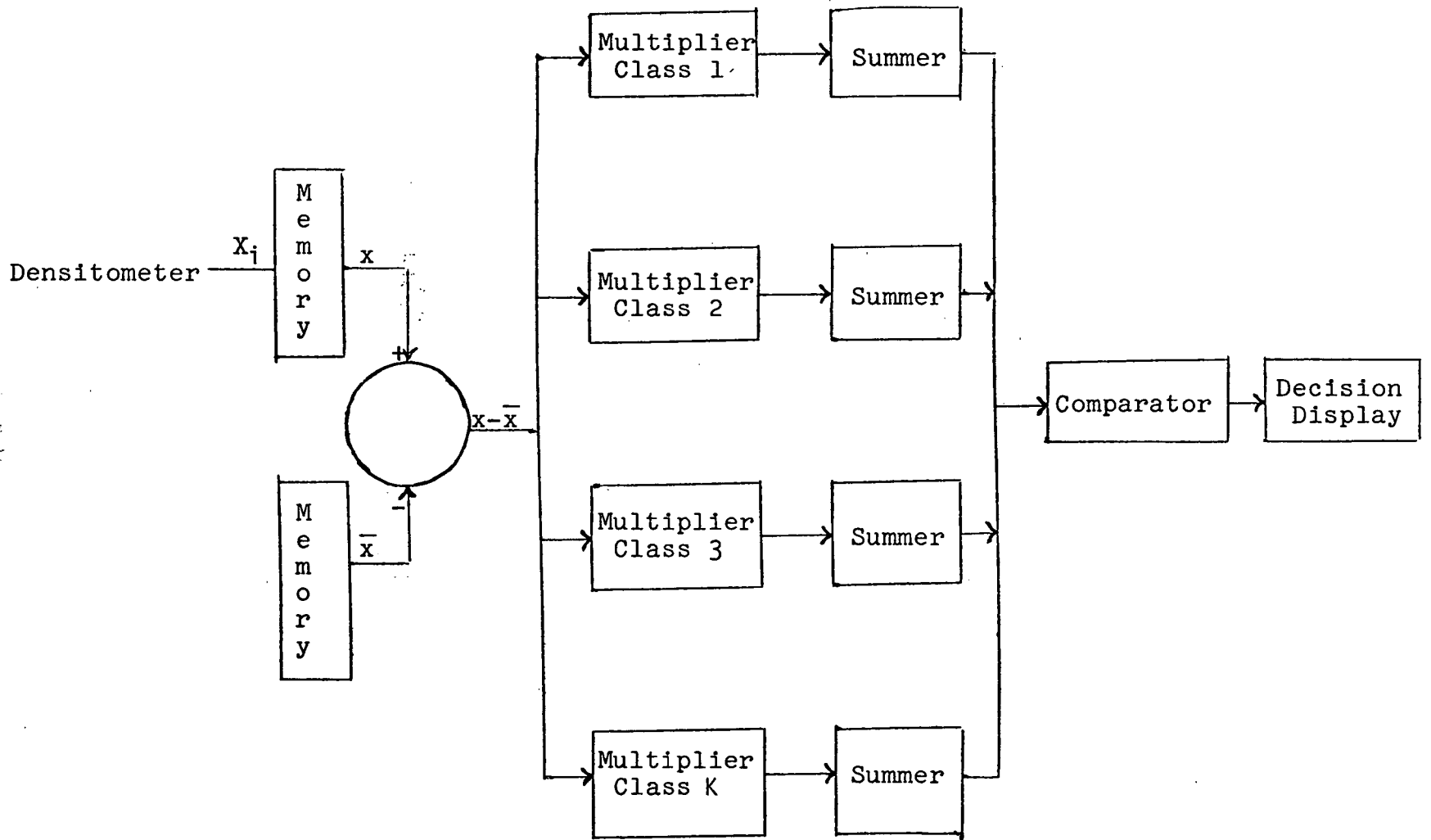
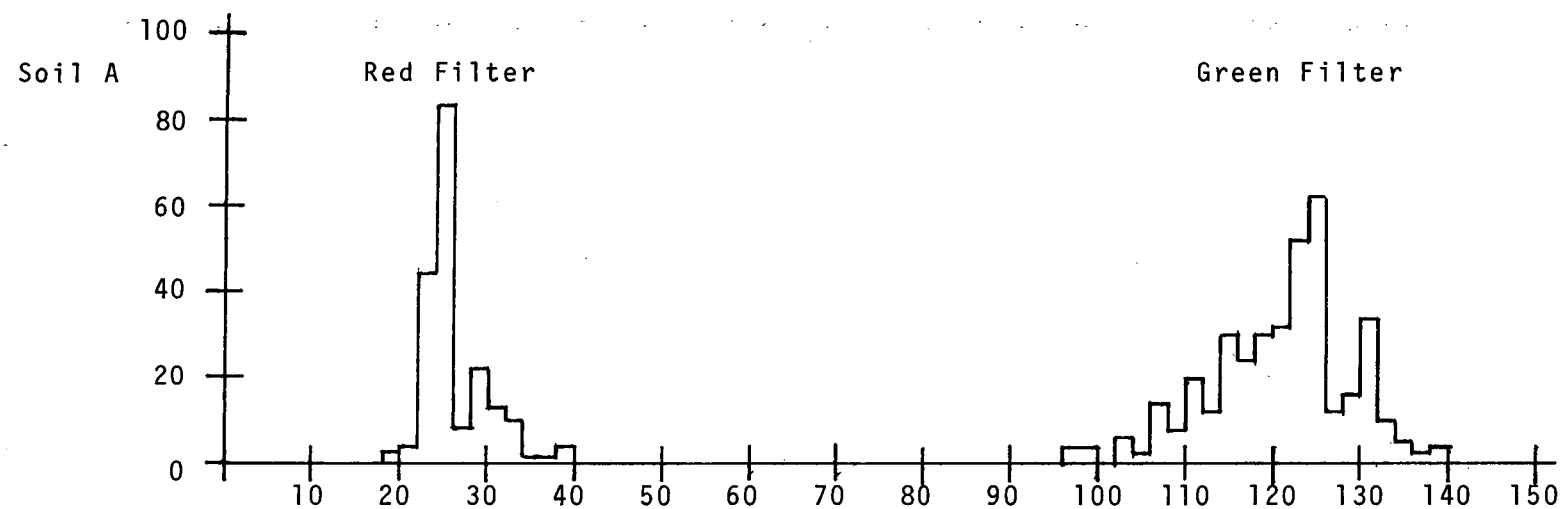


Figure 4. Special purpose K-Class classifier.



133

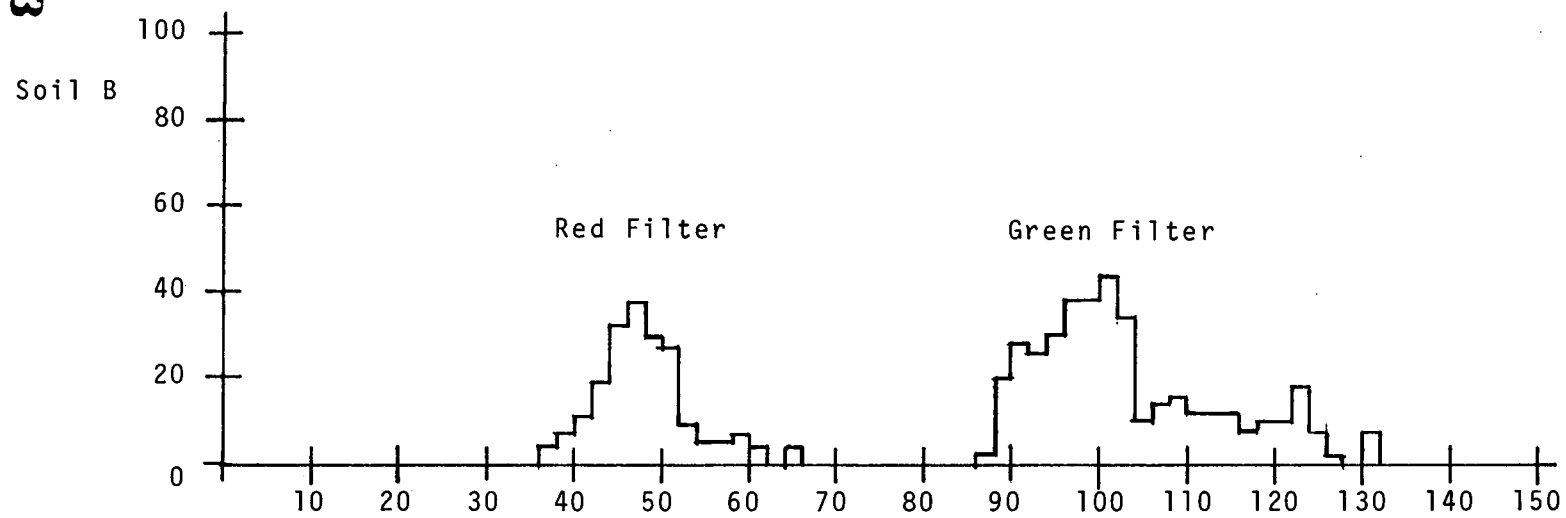


Figure 5a, Sample Probability Density Function of Soils A and B

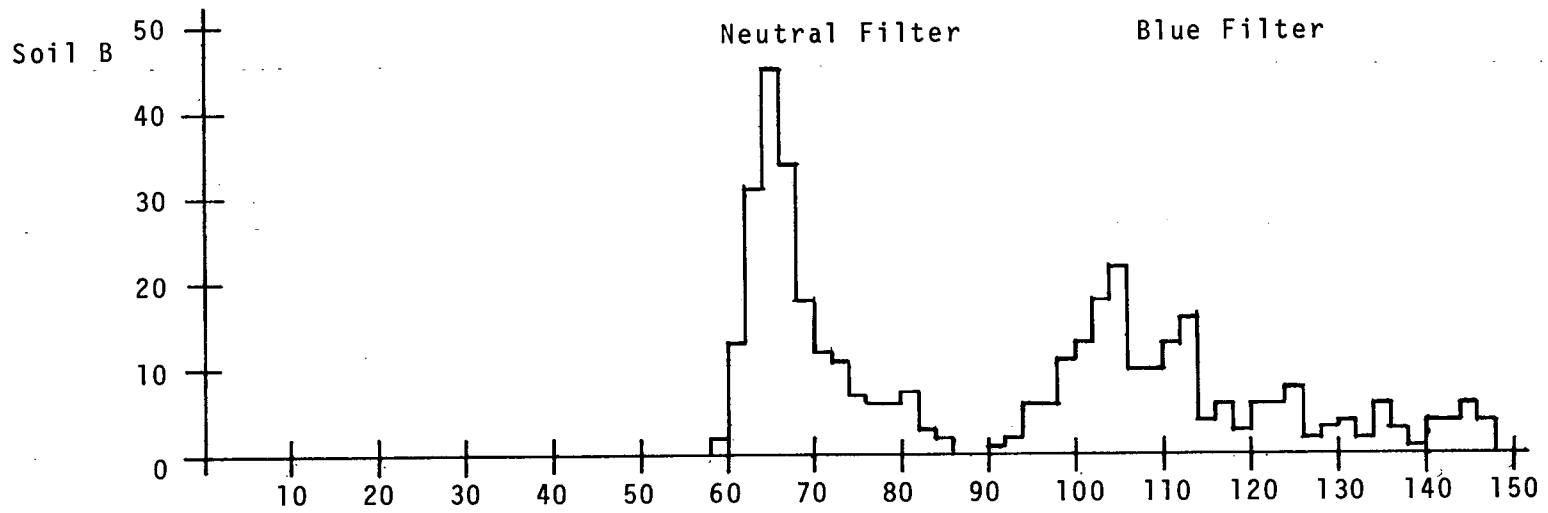
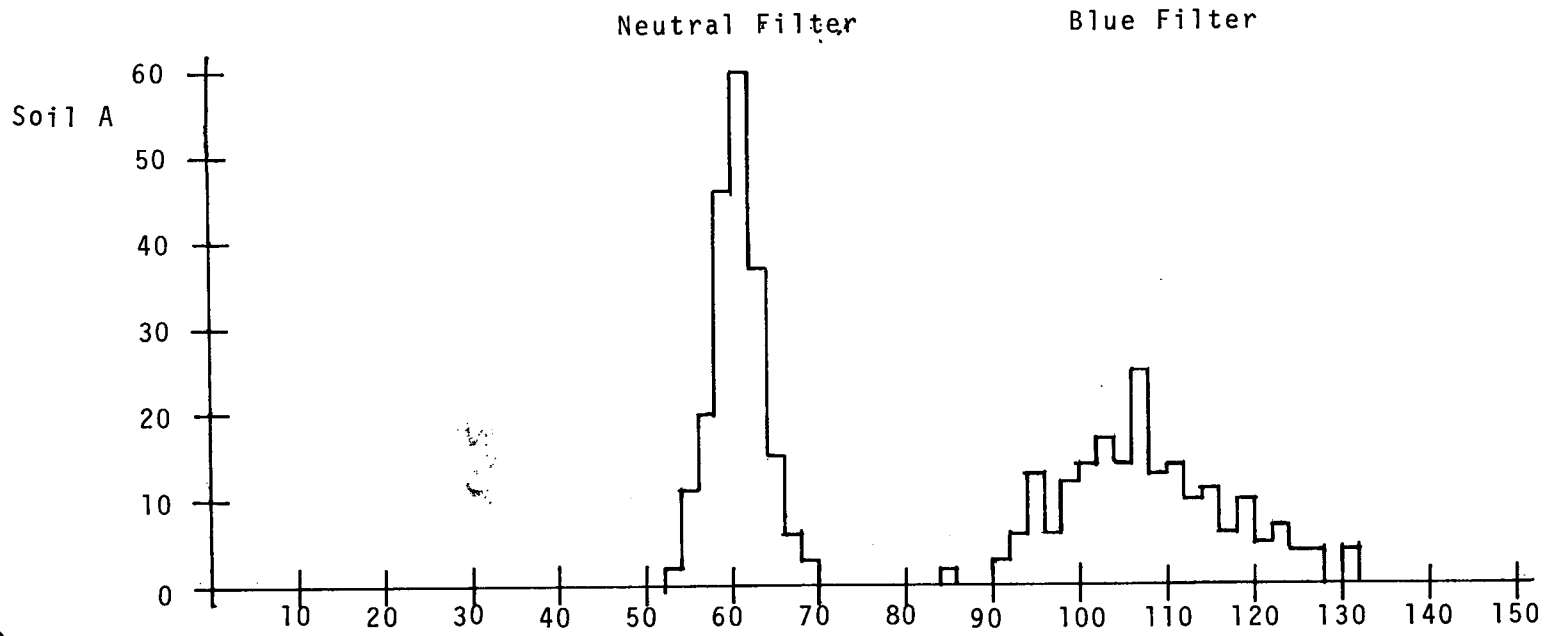
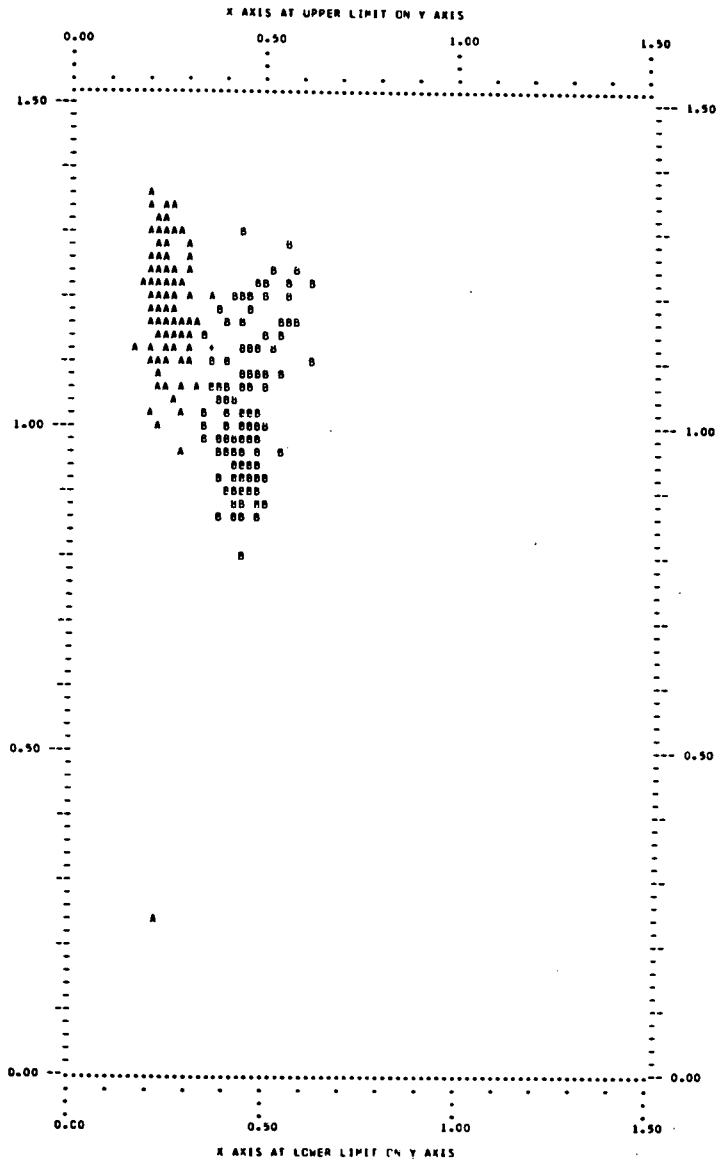


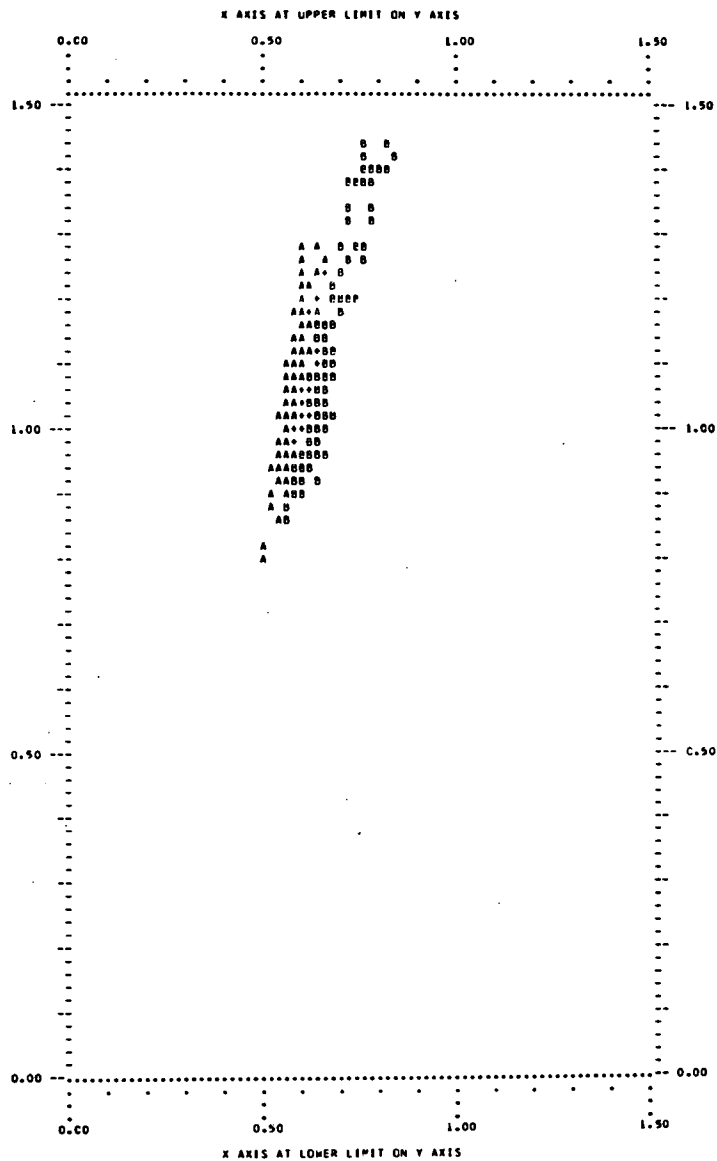
Figure 5b, Sample Probability Density Function of Soils A and B.



x-axis--red filter, y-axis--green filter EKIR

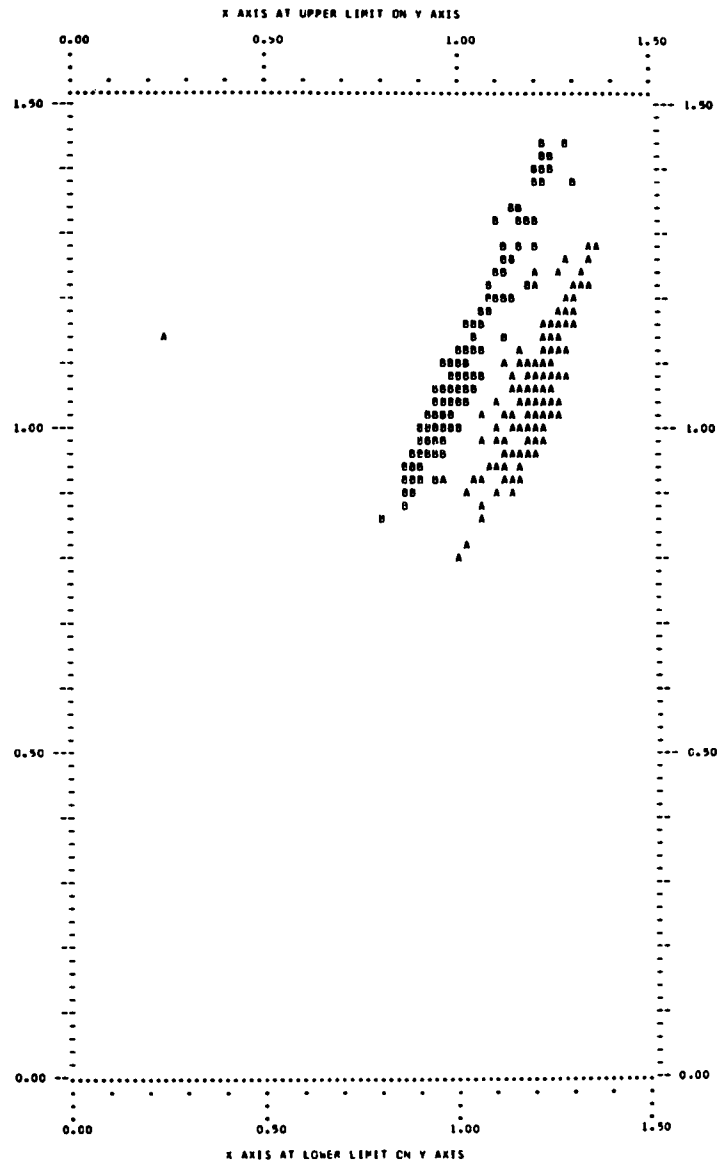
Figure 6. Scatter plots of density measurements for soils A and B.





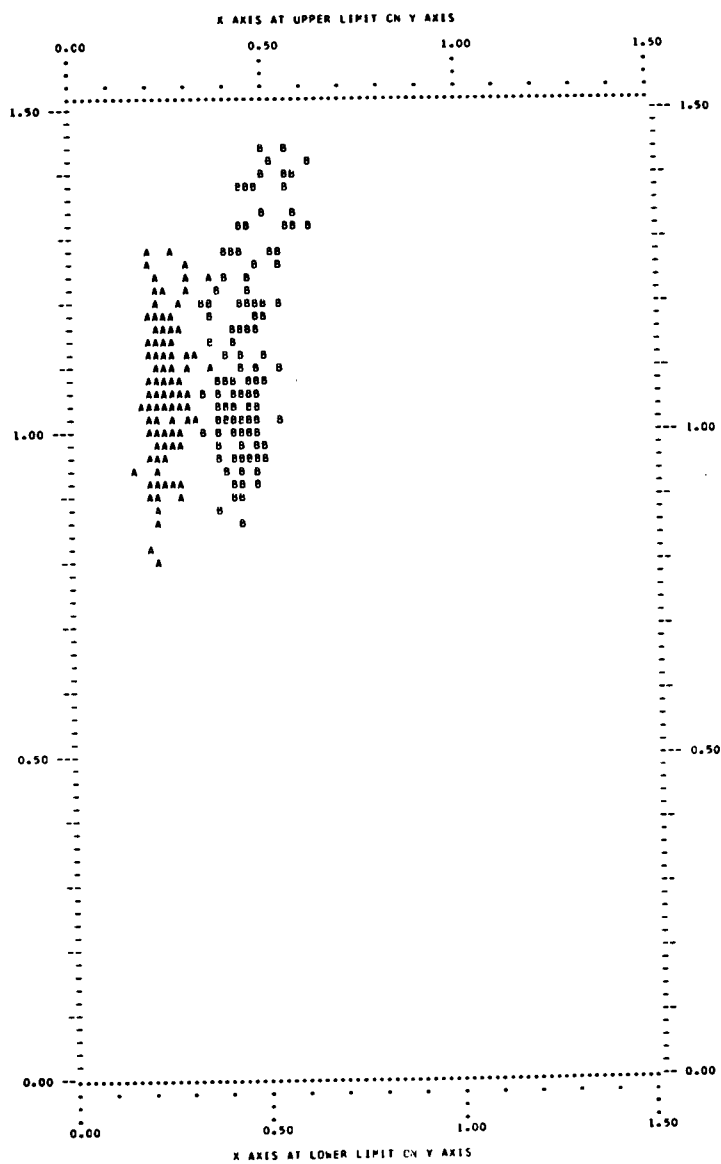
x-axis--neutral filter, y-axis--blue filter      EKIR

Figure 6. Continued.



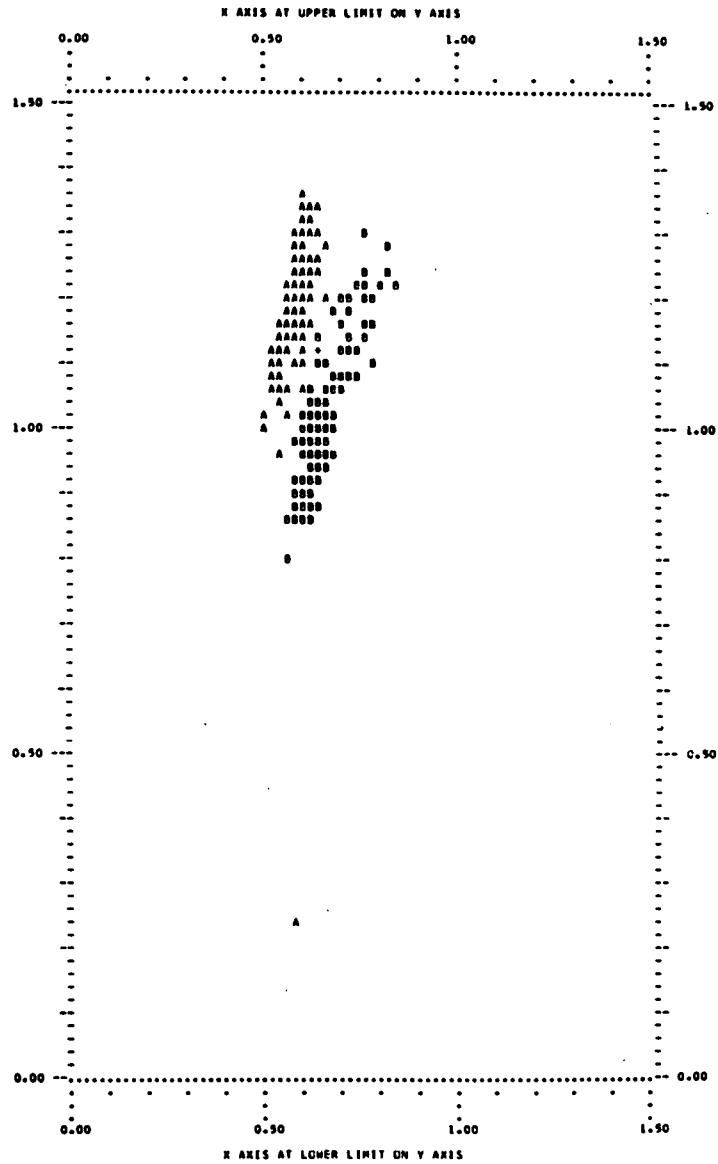
x-axis--green filter, y-axis--blue filter EKIR

Figure 6. Continued.



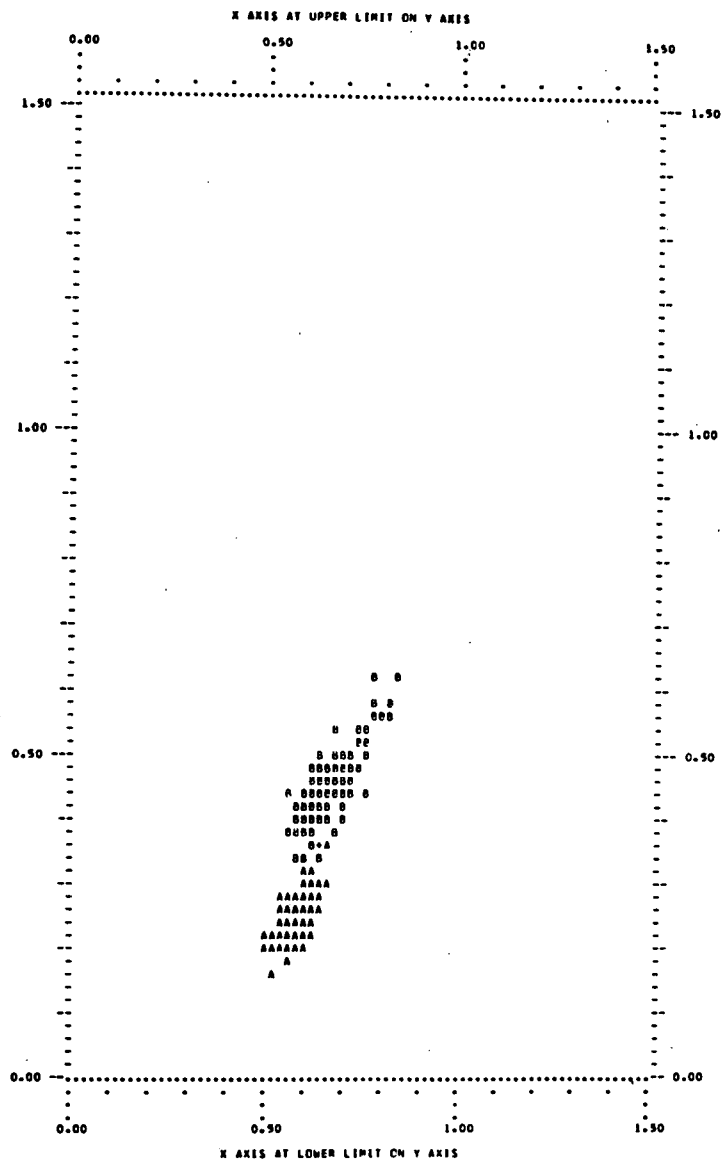
x-axis--red filter, y-axis--blue filter EKIR

Figure 6. Continued.



x-axis--neutral filter, y-axis--green filter EKIR

Figure 6. Continued.



x-axis--neutral filter, y-axis--red filter EKIR

Figure 6. Concluded.

NOT REPRODUCIBLE



Figure 7. Spatial Data black and white image of soils A and B with neutral filter on the vidicon. The classifier was only 83 percent correct.

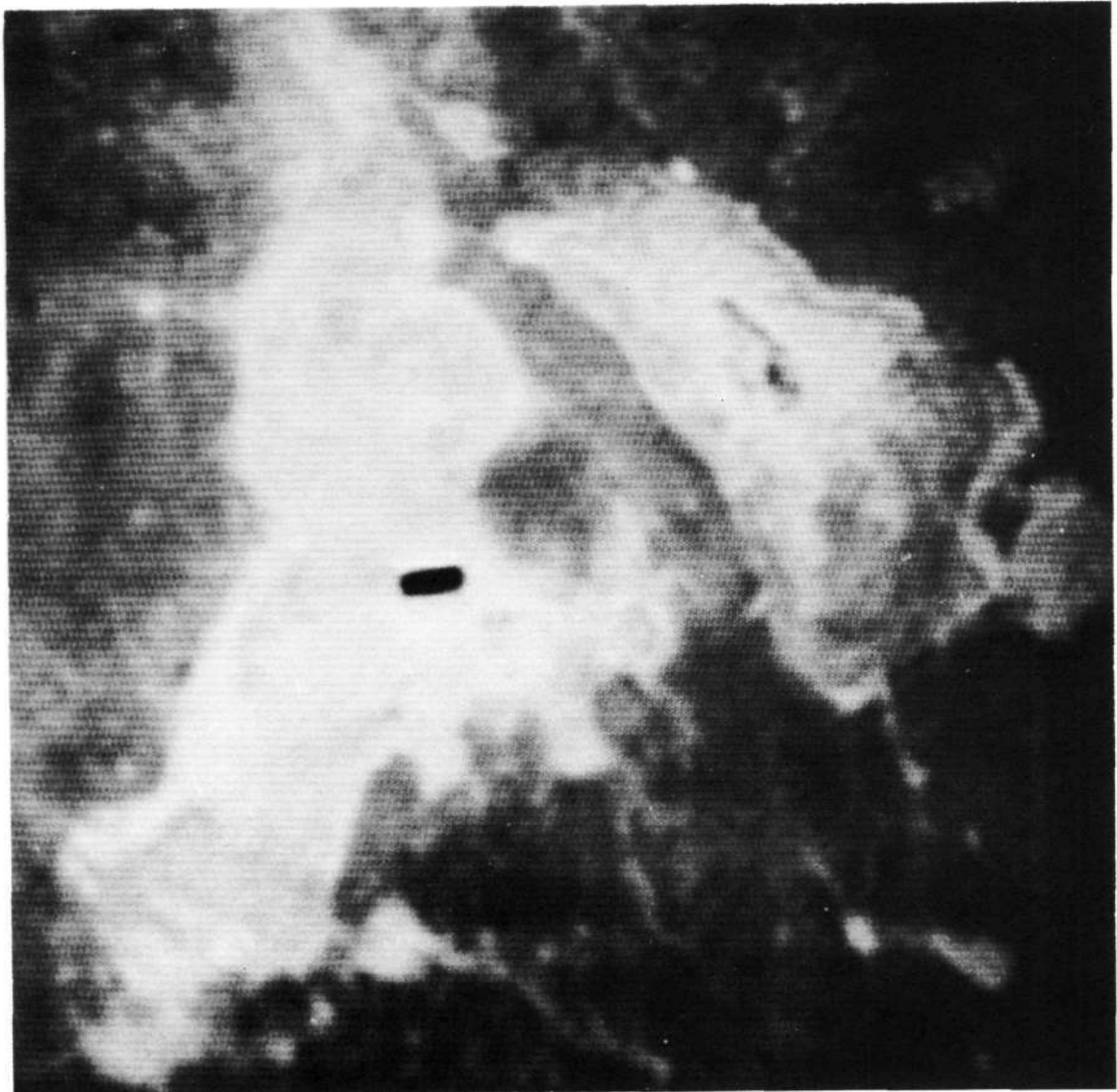


Figure 8. Spatial Data black and white image of soils A and B with a red filter on the vidicon. The classifier was 99 percent correct.

SOILS A AND B

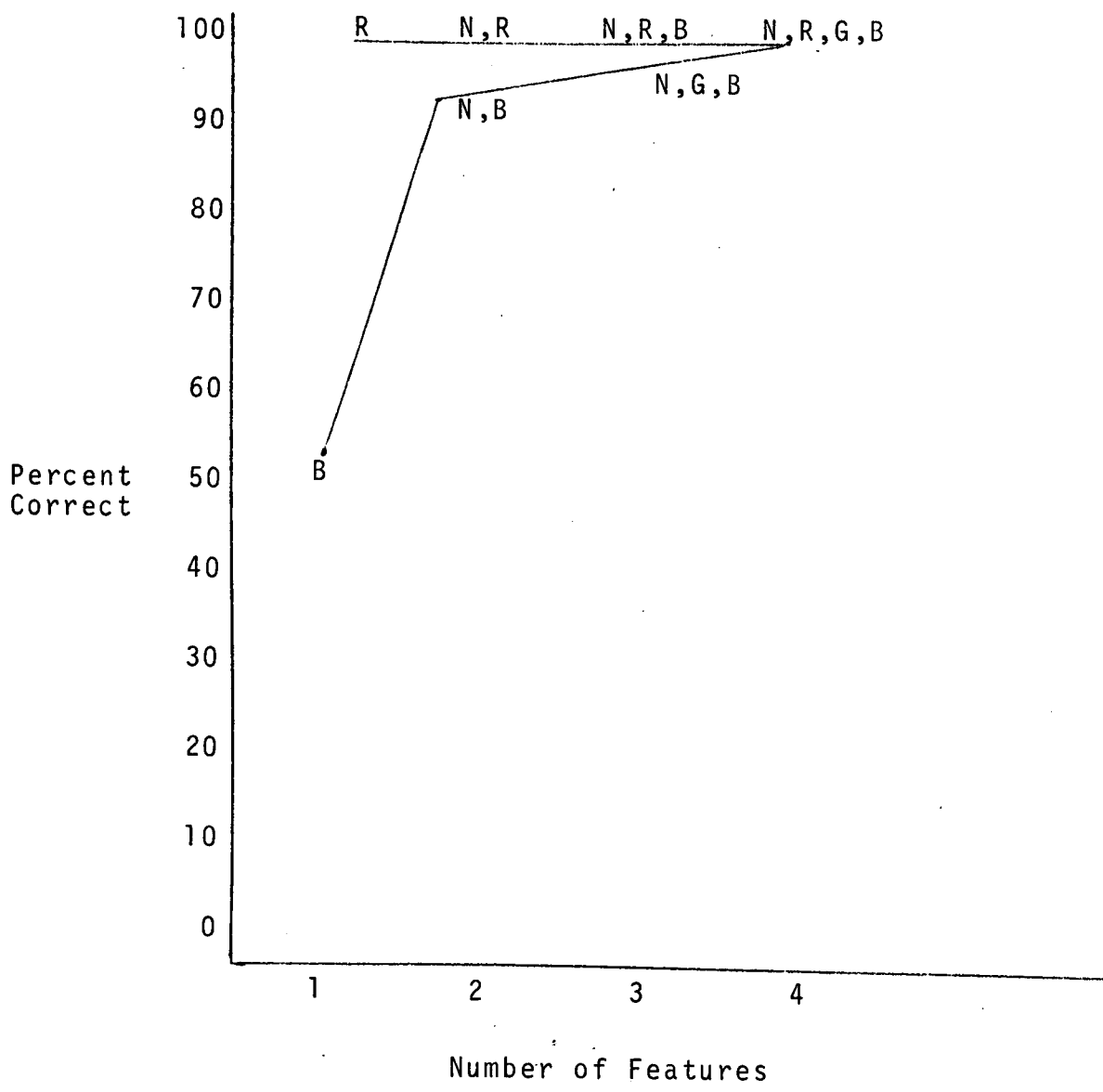


Figure 9. Classification results versus number of features.



144

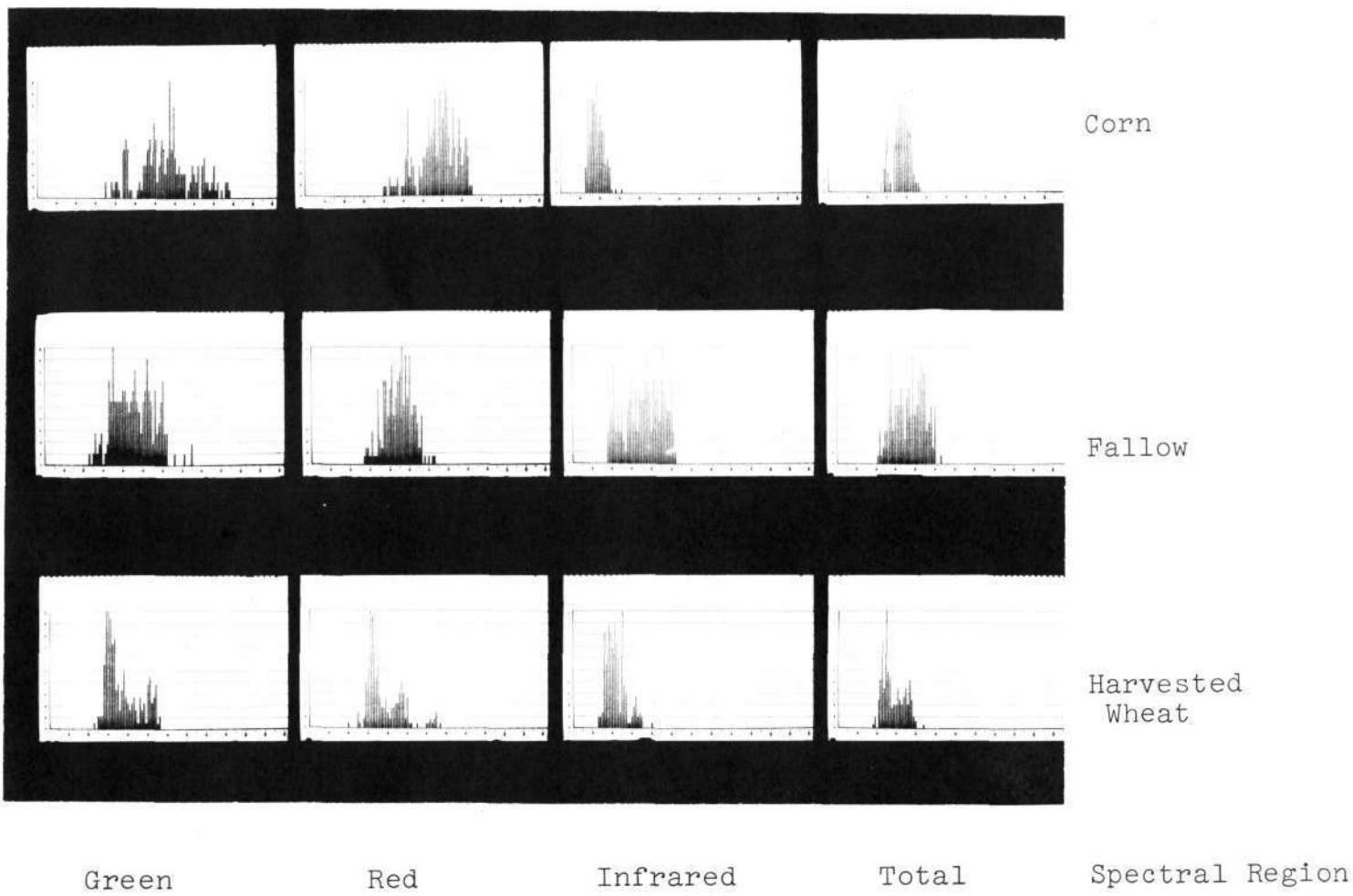


Figure 10. Sample probability density functions for the four filters and six classes. The classifier results are 88 percent correct.

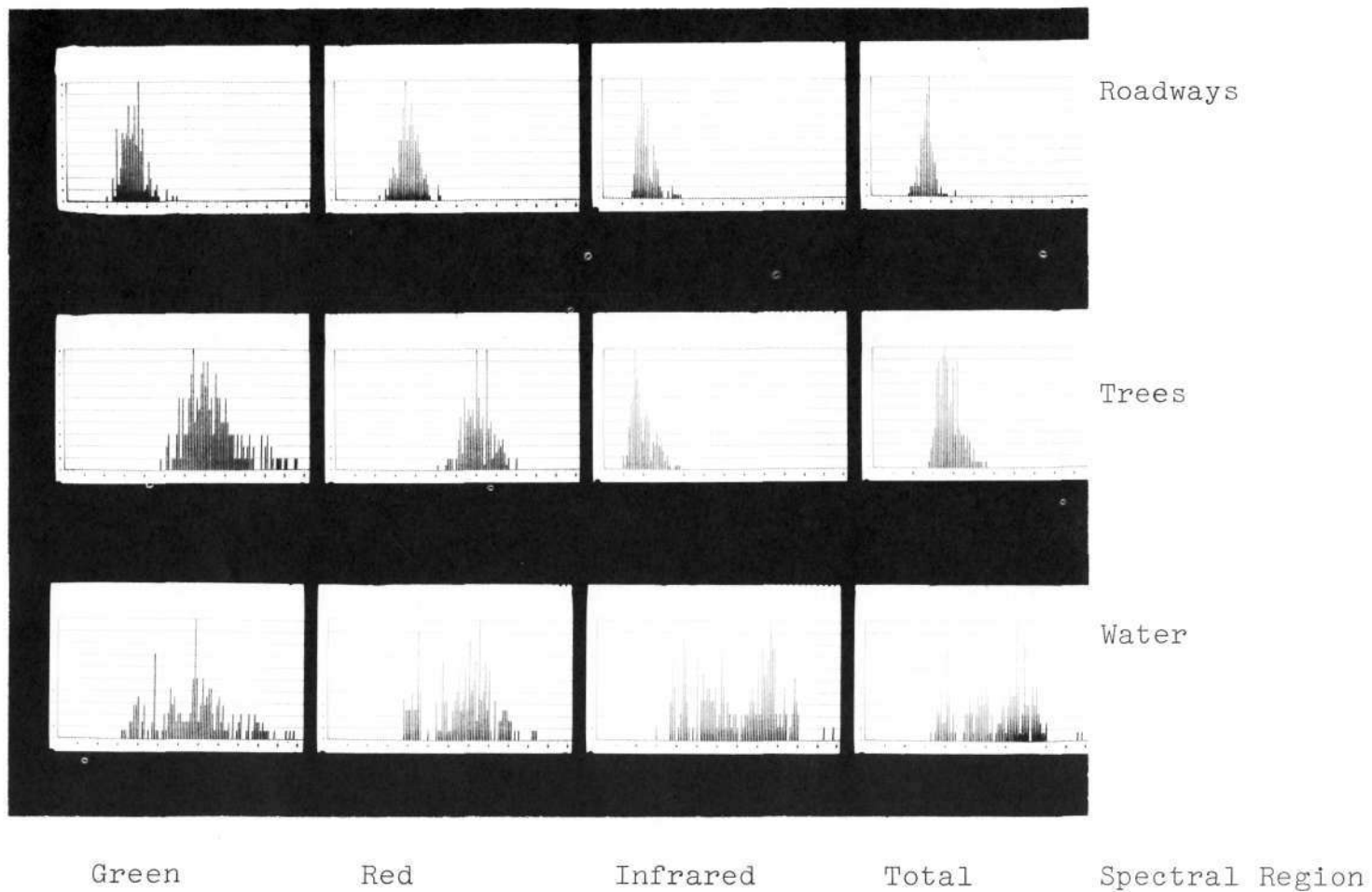


Figure 10. Concluded.

THERMAL SCANNER DATA FOR STUDYING FREEZE CONDITIONS  
AND FOR AIDING IRRIGATION SCHEDULING

by

Jon F. Bartholic, Craig L. Wiegand, Ross W. Leamer, and Leo N. Namken  
Soil and Water Conservation Research Division  
Agricultural Research Service  
U. S. Department of Agriculture  
Weslaco, Texas

PREFACE

There are many applications for infrared thermal scanners in Agriculture because they provide more complete thermal information than can be obtained using point measurements. The Recon IV scanner was used on Mission 117 during the night of January 7 and 8, 1970 under near freezing conditions when five different research agencies were conducting citrus grove heating experiments. Another experiment was conducted for determining plant canopy temperatures as an indicator of drought or need for irrigation. The RS-14 scanner<sup>1</sup> was flown early in July 1970 for this purpose. For ease of presentation, the paper will be divided into two parts, studies during freezing conditions being discussed first.

PART I - NASA MISSION 117 - THERMAL SCANNER RESULTS DURING A  
THREATENED CITRUS FREEZE

INTRODUCTION

When freezes severely injure citrus trees and other vegetation, the economy of an agricultural area is adversely affected for several years. In the Lower Rio Grande Valley of Texas severe freezes have occurred in 1930, 1949, 1951, and 1962. Although there is a 50% chance that a severe freeze will occur in the mid-Valley area once every 10 years, the time interval for a severe freeze has ranged from 2 to 19 years. Each of the 3 major freezes killed or severely damaged

---

<sup>1</sup> Trade names and company names used in this publication are included for the benefit of the reader and do not imply endorsement or preferential treatment of product by U. S. Department of Agriculture.

most of the bearing citrus trees. In the last major freeze (1962), the citrus industry in Texas lost over 17 million dollars, and in Florida the loss was in excess of one-half billion dollars (1).

Since there is no satisfactory method for freeze protection in the Lower Rio Grande Valley, research is needed on efficient ways of adding heat to a grove, of conserving energy contained in the grove, and of classifying land for freeze susceptibility. Information that is obtainable from aircraft-mounted thermal scanners would be very helpful in this type of work.

Freeze protection research is generally conducted in areas of 5 to 30 acres. Temperature is the key parameter, and it is difficult to take enough ground measurements with thermocouples, thermometers, diodes, and thermistors to adequately characterize the temperature in this large an area. On the other hand, a thermal scanner measures the thermal radiation (temperature) of an entire area.

A second need in freeze protection is to classify land areas as to their freeze susceptibility. This classification can be gained by experience through freezes, but it can be done routinely with thermal scanners since they provide information for thermal contouring. Thermal contours classify areas according to freeze susceptibility, show areas where cool air drainage is important, and suggest a means for diverting or modifying the flow of cool air.

A third area where temperature input is required is in determining temperatures throughout the Rio Grande Valley on nights when the freeze hazard is imminent. Temperature measurements are limited, and it is frequently difficult to extrapolate these measurements to large crop growing areas. Also, measurements are of air temperature, and the most important parameter is plant leaf temperature. Thermal scanner data obtained by aircraft flying during freeze hazard conditions could, with rapid data reduction, be used to tell grove managers when critical temperatures were reached, so freeze protection measures could be activated.

The use of infrared scanner information for 3 major purposes (freeze protection research evaluation, mapping freeze hazard areas, freeze protection activation systems) could minimize freeze losses and save millions of dollars.

## PURPOSE AND OBJECTIVES OF THE MISSION

Mission 117 was requested to obtain thermal scanner data under freeze conditions in the Lower Rio Grande Valley of Texas where winter freezes are an important crop production hazard. Flight lines were selected over citrus groves that various agricultural research agencies had chosen for heating tests. Temperature variations in other groves along the flight lines were expected as the result of differences in natural air drainage associated with topography, wind breaks, and different cultural practices in the groves. Previous experiments had relied on point temperature measurements in the groves, whereas scanner data offered the possibility of spatial integration of existing temperature conditions.

The specific objectives of the mission were:

- 1) To compare the temperature (irradiance) of a heated portion of a citrus orchard with an unheated portion of the same orchard.
- 2) To determine the effective area of an artificial fog for freeze protection, and the radiation characteristics of the fog.
- 3) To define the general thermal gradient along a 20 mile-long flight line from north to south across the middle of the Lower Rio Grande Valley.
- 4) To relate differences in ground conditions around trees (bare soil, grass sod, gravel mulch) with tree and ground temperatures (irradiance).
- 5) To determine how normal topographic variation and wind breaks affect citrus tree temperatures and air drainage.

PROCEDURE

## PREPARATIONS PRIOR TO MISSION

In preparation for the mission, scientists from Texas A&M University, Texas A&I University, Rio Farms, Inc., and the Crops Research and Soil and Water Research Divisions (USDA) met on December 19 to coordinate premission calibration of ground instruments (hygrothermographs, thermometers), deployment of ground instrumentation, establishment of a radio communication network, and the general conduct of 5 separate

freeze protection experiments that would be in progress during the night of the mission. Twenty-five user agency personnel were engaged in conducting the experiments the night the mission was flown.

Also, prior to the mission, the flight lines were overflown at 3,000 feet to take photographs with a 70 mm Hasselblad cluster. Photographic documentation was obtained using Plus-X black-and-white (8401), conventional aerial color (8442), Ektachrome infrared aero (8443), and black-and-white infrared (2424) films.

Extensive discussion took place with NASA and Lockheed (NASA contractor) personnel concerning operating characteristics of the Recon IV scanner, settings of the internal reference temperatures, preflight calibration of the scanner and PRT-5, and scanner imagery and its characteristics desired (linear portion of film gamma function).

#### CONDUCT OF THE MISSION

The mission was conducted the night of January 7 and 8, 1970 using the C130 aircraft and the Recon IV thermal scanner. Overflights were made at 2100, 2400, and 0300 hrs. Ambient temperature dropped through the evening to about 34°F at 0100 hrs. Around 0300 hrs the wind shifted and increased enough to arrest the temperature decline. The scheduled 0600 hr overflight was cancelled because landing gear trouble developed on the aircraft.

#### RESULTS AND DISCUSSION

##### RESULTS PERTAINING TO SPECIFIC OBJECTIVES OF THE MISSION

Objective 1: To compare the temperatures (irradiance) of a heated portion of a citrus grove with the unheated portion of the same grove.

Before extensive digitizing and print-out of digitized values were conducted, it was felt advisable to first intensively investigate one area. The area chosen is frequently referred to locally as A&I grove south. It was on flight line 2 and was overflown at 2,000 ft. Because of technical difficulties, this area was not flown at 2100 or 2400 hrs. However, on the second pass during flight 3 (0355 hrs), the area was overflown shortly after heating had been initiated in two different citrus plantings within the area. Heating consisted of burning 4-lb coke blocks, 2 per tree, in a 7-acre area, and return stack heaters, 40 per acre in an 8 1/2-acre area.

Figure 1 shows a thermal black-and-white photograph obtained from the film produced during the flight. The dark areas are warmer than the lighter-toned areas. The 2 heated citrus areas are designated by arrows. The RS represents the area with return stack heaters, while the other area is the petroleum coke-block-heated area labeled TH ("Tree Heet"). The 2 areas stand out quite clearly, and within each heated area there is considerable density contrast. This contrasting density is particularly noticeable in the return stack heated area, and is believed to be caused by 3 factors. First, the return stack heaters are much larger and burn hotter than the coke blocks. Therefore, there is a greater contrast among the heated areas directly around the heaters and those further away. Second, there is an AC-DC coupling problem that tends to give an overshoot when a warm element is followed by a cool element. Third, the RS heaters were located in the middles between the trees, whereas the TH heaters were located at the "skirts" (edge of the tree canopies). Consequently, tree foliage obscures many of the TH heaters.

Figure 2 shows a thermal photograph of the analog signal that was played onto a CRT scope with a variable Z axis. This picture was taken of the CRT screen by the Data Reduction Group of Lockheed, a NASA Houston subcontractor. This photograph is quite similar to the one produced during the flight. However, the light streak noted along the right side of Figure 1, believed to be caused by the bending of the film exposed in flight, is not observed in Figure 2, and it appears that the RS-heated area in Figure 2 does not have as high a contrast as the same area in Figure 1.

Of particular interest are 2 nonheated areas near the center of Figure 2 that are shown to be slightly warmer. These areas are relatively uniform, darker grey and rectangular in shape, compared with the surroundings. These 2 areas have different cultural practices than the citrus blocks around them. Thus the cultural practice appears to increase the temperature of trees in these 2 nonheated blocks compared with the temperature of trees in surrounding blocks.

Figure 3 is a color enhancement of the black-and-white negative thermal film. In this enhancement, dark blue, light blue, light green, dark green, olive, yellow, brown, red, magenta, violet, and black (grey) colors represent warmest to coolest temperatures in that sequence. In general, the return-stack-heated area shows a greater radiance as observed by the scanner than the area heated with TH. A north wind was blowing at about 1.5 m/sec at one meter above the trees during this overflight. There appears to be a warmer area south of the return-stack-heated area. This warmer area was probably caused by energy that moved downwind from the heated area. Further analysis is required to substantiate this interpretation of the color enhancement. Physically, however, it seems realistic, and thermographs in the downwind area showed a higher temperature than thermographs in a nonheated area east of the grove. Such a downwind effect can be expected from heat transfer theory.

Another warmer area of interest (IF) in the color enhancement, Figure 3, is in the northern part of the photograph. Prior to the flight, this area was irrigated in an attempt to eliminate freeze damage. The blue spot in the middle of the red flood-irrigated portion may have been caused by standing water, since it was the wettest portion of the field when it was examined after the flight.

Figure 4 shows a graph of temperature versus digital count values. The data were digitized by an 8-bit digitizer that gives 0 to 256 counts over a given voltage range. A line is drawn in this figure that connects the temperature from the 2 calibration (cal) sources on the Recon IV. These points are labeled BB1 (Blackbody 1) and BB2 (Blackbody 2). It was immediately obvious from observing the trace of a scan line on the scope, that the cal sources are at a considerably higher temperature than any of the ground truth data. This problem was anticipated, since the cal sources can only be heated and not cooled. However, there was no way to get the cal sources on the Recon IV to bracket the expected ground temperatures. Thus there was no alternative but to accept the blackbody temperatures available, one at near aircraft temperature and one that was slightly heated. Thus extrapolation from the cal source temperature range to the data range was necessary. Based on this extrapolation a great majority of the scanner resolution element temperatures surround 0°C. On Figure 4 the bins are indicated by the alphabetical letters A through O. The bins used in the 1st, 2nd, and 3rd Picout runs are shown. In the initial run, very few alphabetic letters were plotted since most of the data fell in the area where the blank symbol was used. Subsequently, in run 2, the counts corresponding to bins A and B were lowered so that much of the area was assigned symbols in the computer printout. Finally in run 3, the bins are moved down even further, and run 3 has been used to determine the average temperatures as seen by the scanner for the 2 heated areas.

Table 1 shows the distribution of the alphabetic letters for the RS and TH heated areas. In both cases the A's are the most frequently occurring letter as shown by 810 values in the TH area and 734 values in the RS area. The number of entries in the remaining bins decreases rapidly. It would seem to the authors that if the cal source temperatures could have been properly set, the majority of values would fall in the bins midway in the temperature range. With so many values falling in the 0 to a few count area, one has to worry about the statistical distribution of the data.

The number of values in each bin were counted, converted to temperatures, and averaged. The RS heated area corresponds in radiance to an average temperature of 1.1°C, while the TH heated area corresponds in radiance to a temperature of -.4°C. Thus, on the average, the temperature of the two areas differed by 1.5°C.



Objective 2: To determine the effective area of an artificial fog for freeze protection and irradiation characteristics of the fog.

This objective was investigated using both radiometers and Barnes thermal camera, and with aircraft data from the thermal scanner. Radiation instruments showed that the fog affected the radiation balance almost insignificantly, and extensive examination of the thermograms produced by the Barnes infrared camera revealed no grey scale variations. Visual observation showed that only a few wisps of the fog penetrated into the orchard from the foggers that were located about 40 feet upwind from the 1st tree row. The thermal film was examined by placing the negative produced during the flight on a Spatial Data Systems Datacolor system. Examination with various settings did not reveal any difference in film optical density (color difference on the TV screen) characteristics in the fogged area. It was concluded that on the particular night of the study the artificial fog produced did not significantly alter radiation characteristics of the area covered by the fog. Since this particular fog had a particle size of about 2  $\mu\text{m}$ , this finding can be anticipated from radiation theory which suggests that droplet size would have to be concentrated in the 5- to 20- $\mu\text{m}$  diameter range to be most effective.

Objective 3: To define the general thermal irradiance over a distance of 20 miles from north to south across the center of the Lower Rio Grande Valley.

This objective cannot be evaluated from this mission, even though the experiment was designed for this purpose, because two-thirds of the time the scanner was malfunctioning so that the data are discontinuous within flight lines. However, this type of information may be obtainable at some future time.

Objective 4: To relate differences in ground conditions around the trees (bare soil, grass sod, gravel mulch) with tree and ground temperatures (irradiance).

This experiment was to be conducted by use of the thermal scanner over the USDA Research Farm. Even though the Research Farm was overflown 3 times, no good imagery was obtained of that area. However, as mentioned under Objective 1, when discussing Figure 2, it appears that the effects of cultural practices can be evaluated. Figure 5 is included to show that imagery from the Recon IV is sufficiently detailed to show considerable contrast between fields observed below the plane. This figure shows that high contrast and good resolution can be obtained from

the agricultural scene. The outlines of fields are easily observable. Upon closer examination some warmer (darker) areas are observable within the fields in this figure. Thus it appears that thermal imagery could shed much light on this objective.

Objective 5: To determine how normal topographic variation and wind-breaks affect citrus tree temperatures and air drainage.

Further investigation into this objective may yield valuable information with the data obtained from this flight. Thus far, we have reached these preliminary conclusions. First, as is shown from Figures 1, 2, and most significantly in Figure 4, large temperature variations occur naturally from field to field, particularly where the fields change in cover such as from a bare soil to a cropped surface. Also, large irradiance changes occur even within a field when there is a moisture variable, since the higher ground may be dryer than the low ground. Low ground that is moist stores more heat during the day than higher dry ground. The lower ground, in this case, will be warmer than the higher areas, which is the reverse of what one would expect when significant cold air drainage is a factor. Another factor is that topographic variations are minor in the Lower Rio Grande Valley so that, except under extremely calm, strong radiation conditions, it may be difficult to pick up much thermal variation. There was not a strong temperature inversion the night of the mission. This variation caused by topography would most easily be detected in a large area of relatively uniform cover or cultural condition.

### CONCLUSIONS

This mission required the coordination of research by 5 agencies plus the flight by the C130 aircraft with the Recon IV thermal imager and PRT-5 in operation. The objectives laid out for the mission were numerous and challenging. Of key importance is that accomplishment of these objectives could demonstrate usefulness of thermal scanner data in improving our freeze protection techniques, forecasting our freezes, and mapping freeze hazard areas. Success in these 3 areas could save millions of dollars, and minimize the great financial and personal hardships experienced as a result of a severe freeze.

The mission as a whole went smoothly with all research agencies collecting valuable data. The data, particularly from the Recon IV and the PRT-5, however, were somewhat disappointing because of instrument malfunctions. Nevertheless, enough information from the scanner was obtained during the flight to advance our understanding significantly

on a number of the objectives. In particular, the scanner provided valuable information not obtainable any other way, on experiments conducted on various citrus grove heating methods.

Further analysis of the good data obtained and the experience gained relative to the capabilities of the scanner and the data reduction required, should enable future missions of this type to satisfactorily complete the objectives outlined.

PART II - RSI-1 MISSION WITH THE RS-14 THERMAL SCANNER TO  
EVALUATE PLANT WATER STRESS CONDITIONS

INTRODUCTION

From energy transfer theory it can be shown that as plant transpiration is reduced by drought, leaf temperature rises to increase heat transfer to the air and thermal radiation to the sky. The degree to which leaf temperature increases with increasing water stress is not clearly understood. Wiegand and Namken showed with a ground-based infrared camera that stressed plant temperatures were higher than nonstressed plants in the imagery (2). Horton, Namken and Ritchie (3) presented data showing (Fig. 6) that near field capacity, crop temperature seldom was more than 2°C above air temperature. However, when average water potential in the surface 1 m of soil was -5.4 bars, leaf temperature could be as much as 6°C higher than air temperature.

Based on this information about leaf temperature, it seems feasible to attempt detection of plant water stress by flying a thermal scanner over test areas where plants are under a variety of stresses. Ultimately this research might provide information to growers on when to irrigate. Proper timing of irrigations would help to provide a quality crop while minimizing water required.

DESCRIPTION OF APPARATUS

An RS-14 scanner was flown by Remote Sensing, Incorporated, Houston, at 2,000 feet over the test area at 1100, 1130 and 1400 on July 7, 1970 and at 1418 on July 8, 1970. Two other flight lines, 10 and 5 miles each were flown in non-test areas. With the exception of one flight, scanner data used to expose the film were from the 8-14  $\mu$ m channel. Both the 3-5 and 8-14 channels were recorded on analog tape. The scanner was set at 1 m field of view and 200 scan lines per second were obtained. The internal calibration blackbody sources were set at temperatures above and below that expected for the crops in the agricultural scene viewed.

### METHOD OF ANALYSIS

The data were reduced using a microdensitometer in which three main portions of the film were densitized. The areas densitized for each flight line were the cal sources, the grey scales and the field of interest. The fields of main interest were from our Research Farm. The entire 50-acre farm was scanned.

Figure 7 shows the manner in which film density was converted to blackbody temperature. The optical counts for the grey scale steps on the film were converted to film density; these film densities were then plotted versus the corresponding voltage level used to generate each grey scale. The voltages were used rather than using arbitrary numbers such as 1 through 10 for the grey scales, since equal voltage steps are not used (4). The cal source densities and their temperatures were then plotted as shown by the dashed lines. By placing these temperatures on a blackbody temperature scale as shown at the bottom of the figure, it was possible to obtain temperatures corresponding to each grey scale density. Using these sets of values a fourth-degree polynomial was fit to the curve.

The S-shaped curve results from the gamma function of the film. Though it might have been advantageous to have most of the densities shifted somewhat upward on this curve, they are nonetheless in a portion of the curve where temperature changes quite rapidly with film density.

The analog record obtained during the flight on magnetic tape is to be digitized. Once this is finished it will be possible to use programs such as Picout to plot the data. This will allow comparisons between the two methods of data reduction for both speed and accuracy.

### RESULTS AND DISCUSSION

Only data from the 7 July 1970 1400 flight of the Research Farm area will be presented. In general, findings from the 1400 flight are typical of those found during other flights.

Figure 8 is a black and white picture of the Research Farm. The research buildings are shown in the lower center portion of the figure. Crop areas are generally dark-toned while bare soil is grey. Cotton

under varying degrees of stress was the main test crop. Cotton plots had been irrigated at two weeks and five days prior to the flight and the third treatment had not been irrigated. In general, the cotton was planted on the south side of the farm and treatments had 3 bare rows between them. They can be seen in the area marked cotton in the upper right-hand portion of the film. Cotton in the lower right hand area has severe root rot. In this area data could be analyzed from only segments of each of the treatments. In the upper center portion of the picture, cotton was under investigation in a separate study (a diagonal line transects this area). The portion below the diagonal had been well irrigated while the upper portion was drier. Another area of particular interest is the lower bare field near the center of the photograph. The right side of this field is slightly darker than the remaining field. The difference is due to tillage underway during the flight.

Figure 9 shows the 1400 thermal film obtained of the Research Farm. In this film, the white areas are the warmest and dark areas are the coolest. It can be observed that the cotton root rot areas are warm since the scanner sees both hot soil and dead plants in those areas. In the cotton area in the upper right hand corner some differences in density are observable. These differences could be picked out very easily with the microdensitometer. Also the cotton field with the diagonal line shows less thermal radiation being emitted by the lower portion. A marked contrast exists in the bare field where the tractor was working. The soil turned up in tilling is cooler than the soil surface and remains cool as long as its water is readily available for evaporation.

An additional treatment in the thermal picture is of interest. This treatment is bare soil which had been irrigated at different intervals. It is just to the left of the cotton field with the diagonal line. We see a hot, intermediate and a cool area in Figure 9. The hottest area had not been irrigated. The middle area had been irrigated five days before the flight and the coolest area had been irrigated the day before the flight. There was no visible difference between the dry and the intermediate irrigation treatment. Thermal radiation differences are observable, however, in the thermal film.

During this flight, ground measurements were taken with thermocouples and a PRT-5. The PRT-5 was mounted on a truck and just before, during and after the flight, it was driven through the farm on a predetermined course to obtain temperatures from the 28 test fields.

These data are compared with that obtained from the thermal film in Figure 10. In Figure 10 if all the points fell on the dash line a one to one relation would exist. The points are observed to cluster close to the 45° line in the 29 to 37°C range. However, for the bare soils which generally had temperatures in the 50 to 60°C range, the scanner data gave temperatures several degrees higher than obtained with the PRT-5. The reason for this discrepancy is not yet clear. It does appear that a straight line could be drawn through the data as shown by the solid line.

We need to know how cotton temperatures obtained from the scanner vary with the moisture stress treatments. Figure 11 shows "crop temperature" as obtained from the thermal film compared with the leaf water potential in bars. Generally, well-watered crops have a water potential during midday of about -10 or -12 bars. Normally for cotton a potential of -20 bars is obtained in the afternoon when irrigation is required. It can be seen from this figure, that in this range of plant water stress, temperatures varied from 30° to 36°. Since there is both a low noise equivalent temperature for this scanner (0.5°C) and a good relation between temperature and stress conditions, it appears that temperature could be used to aid in irrigation timing.

#### CONCLUSION

The use of thermal imagery in connection with plant water stress appears to hold considerable potential, particularly with scanners such as the RS-14 where internal calibration sources can be adjusted to bracket the temperatures of interest.

The data from the thermal film are fairly easy to reduce; however, data reduction in 3 days or less would be required before it could be used in irrigation timing.

## REFERENCES

1. Cooper, W. C., Young, R. H., and Turrell, F. M. Microclimate and physiology of citrus: their relation to cold protection. Agr. Sci. Rev. Winter: 3-15. 1964.
2. Wiegand, C. L. and Namken, L. N. Influences of plant moisture stress, solar radiation, and air temperature on cotton leaf temperature. Agron. Jour. 58:582-586, 1966.
3. Horton, M. L., Namken, L. N., and Ritchie, J. T. Role of plant canopies in evapotranspiration. Presented at the Great Plains Agricultural Council Evapotranspiration Seminar, Bushland, Texas, March 23-25, 1970.
4. Mohr, Don M., Jr. Unique design of the RS-14 multispectral scanning system. Electro-optical Systems Design Conference Technical Paper. Texas Instruments, Inc.

Table 1.--The distribution of letters, representing resolution elements, in computer print-out for the third Picout run of the A&I south groves in which "Tree Heet" (TH)-4-1b petroleum coke blocks--and return stack (RS) heaters were burning at overflight time, 0355 hr.

Computer symbol	RS heated area		TH heated area		Bin temp range °C
	No. of elements	% of elements	No. of elements	% of elements	
A	810	57.46	734	81.92	-1.5 to -0.5
B	338	23.85	68	7.60	-0.5 to +1.0
C	55	3.88	18	2.01	1.0 to 1.5
D	38	2.68	16	1.79	1.5 to 2.0
E	17	1.20	15	1.67	2.0 to 2.7
F	17	1.20	9	1.00	2.7 to 3.2
G	10	.71	5	.56	3.2 to 4.2
H	8	.57	8	.89	4.2 to 5.0
I	24	1.69	5	.56	5.0 to 5.8
J	7	.50	3	.33	5.8 to 6.3
K	24	1.69	7	.78	6.3 to 8.4
L	20	1.41	5	.56	8.4 to 10.8
M	27	1.91	0	.00	10.8 to 12.5
N	12	.85	0	.00	12.5 to 14.5
O	6	.42	0	.00	14.5 to 15.4
P	4	.28	3	.33	> 15.4
Totals	1417	100.00	896	100.00	



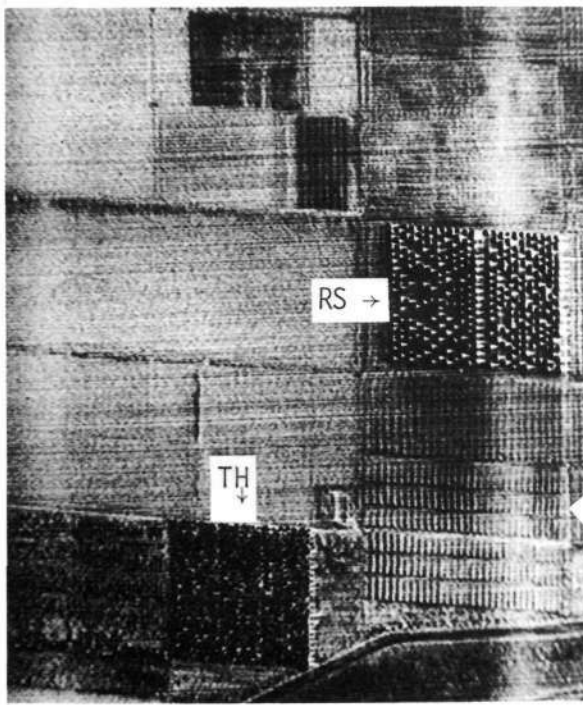


Figure 1.- Thermal image produced in flight, A&I south grove, 1/8/70, 0355 hours. (TH - area heated with Tree Heet, RS - area heated with return stack heaters.)

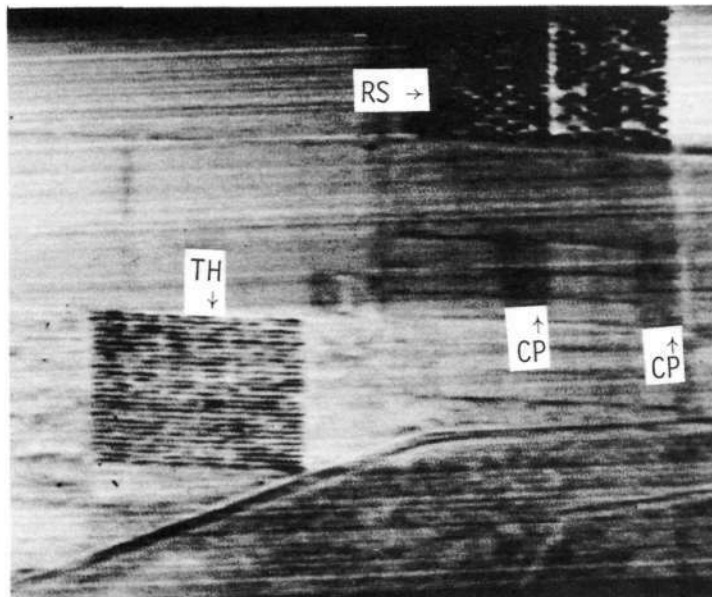


Figure 2.- Thermal image of analog magnetic tape displayed on CRT of same area as Fig. 1. (TH - area heated with Tree Heet, RS - area heated with return stack heaters, CP - cultural practice temperature effect.)

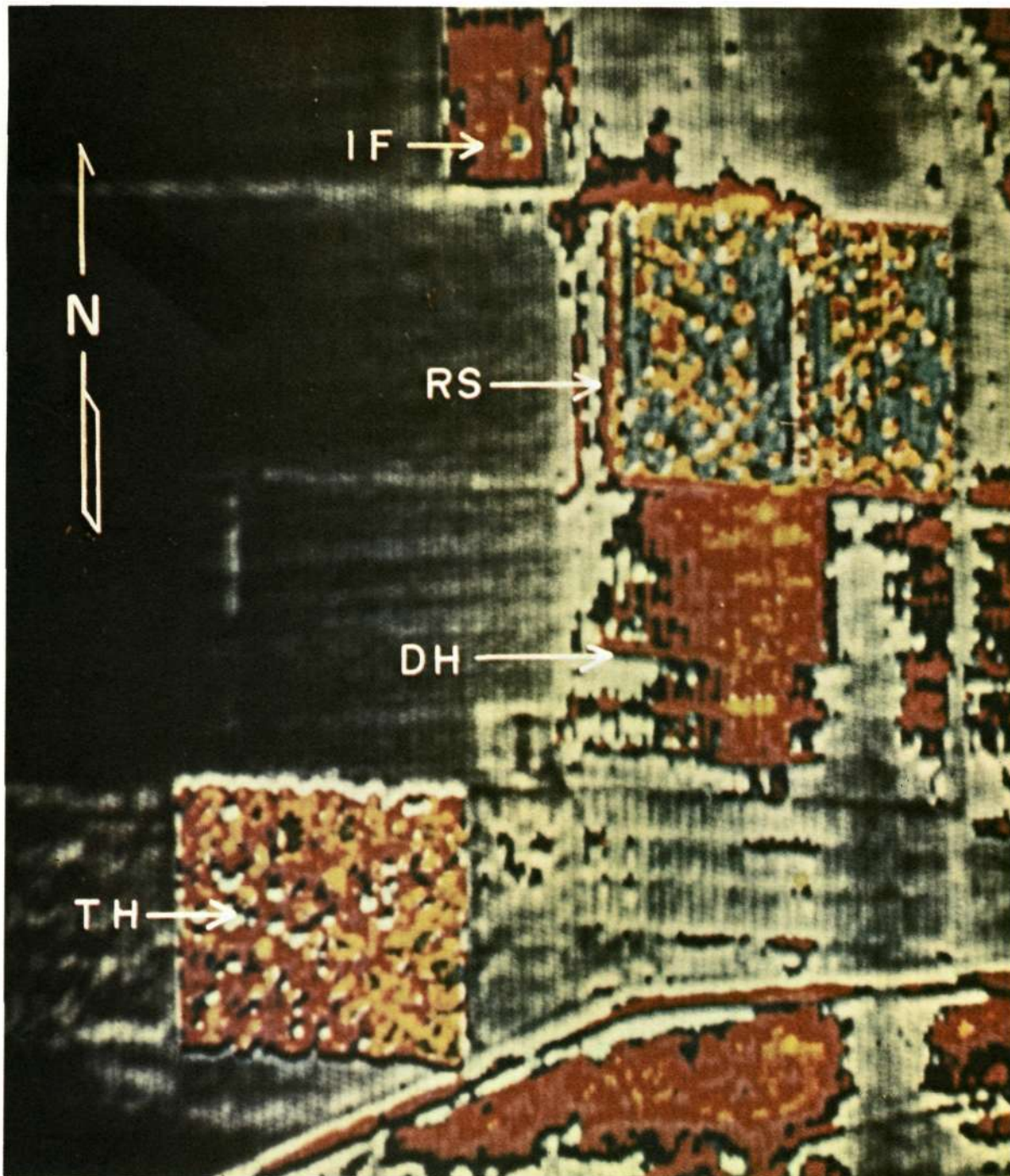


Figure 3.-Image transparency of Fig. 1 displayed on a color enhancing DATACOLOR SET. (TH - area heated with Tree Heet, RS - area heated with return stack heaters, DH - downwind heated area, IF - irrigated field.)

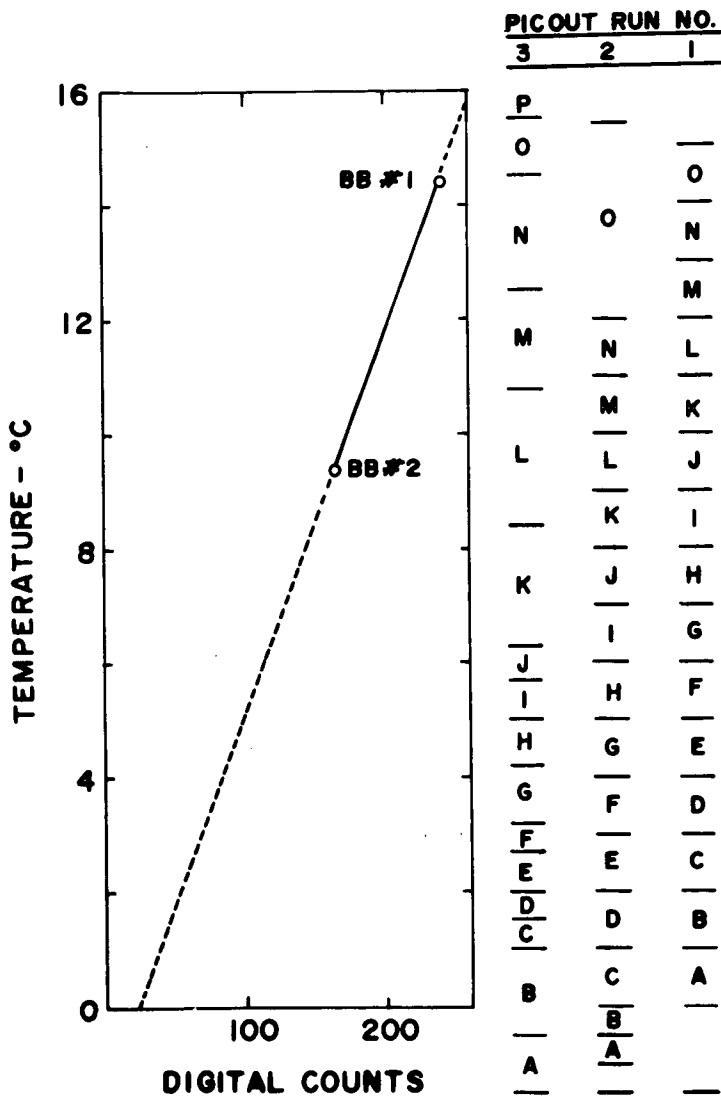


Figure 4.- Temperature versus digital counts showing the position of the blackbody (BB) cal source temperatures. Superimposed on the temperature scale are the symbols used for the computer printout of each bin in the Picout program for Picout runs 1, 2, and 3.

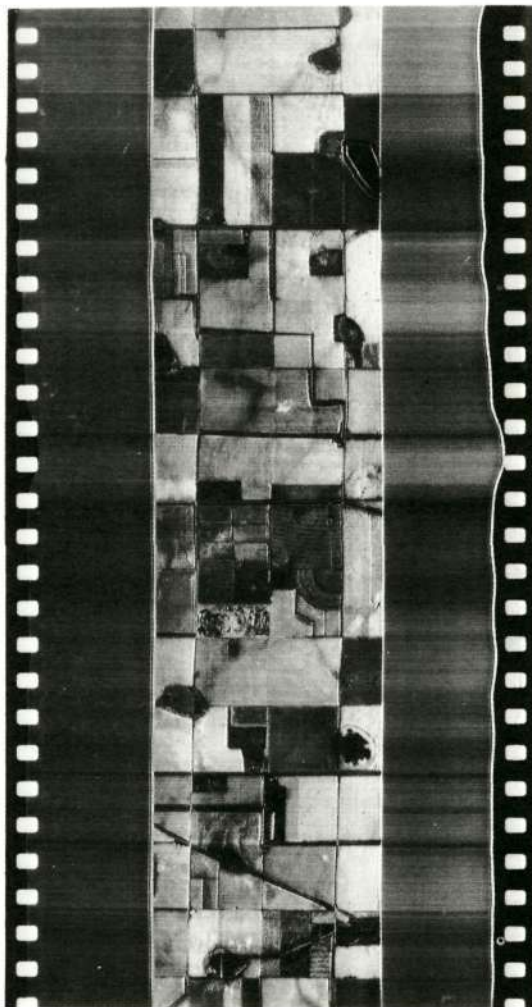


Figure 5.- Thermal image produced in flight (line 6, flight 2, 0000 hours, 1/8/70) showing the considerable thermal (irradiance) contrasts occurring in the agricultural scene overflown.

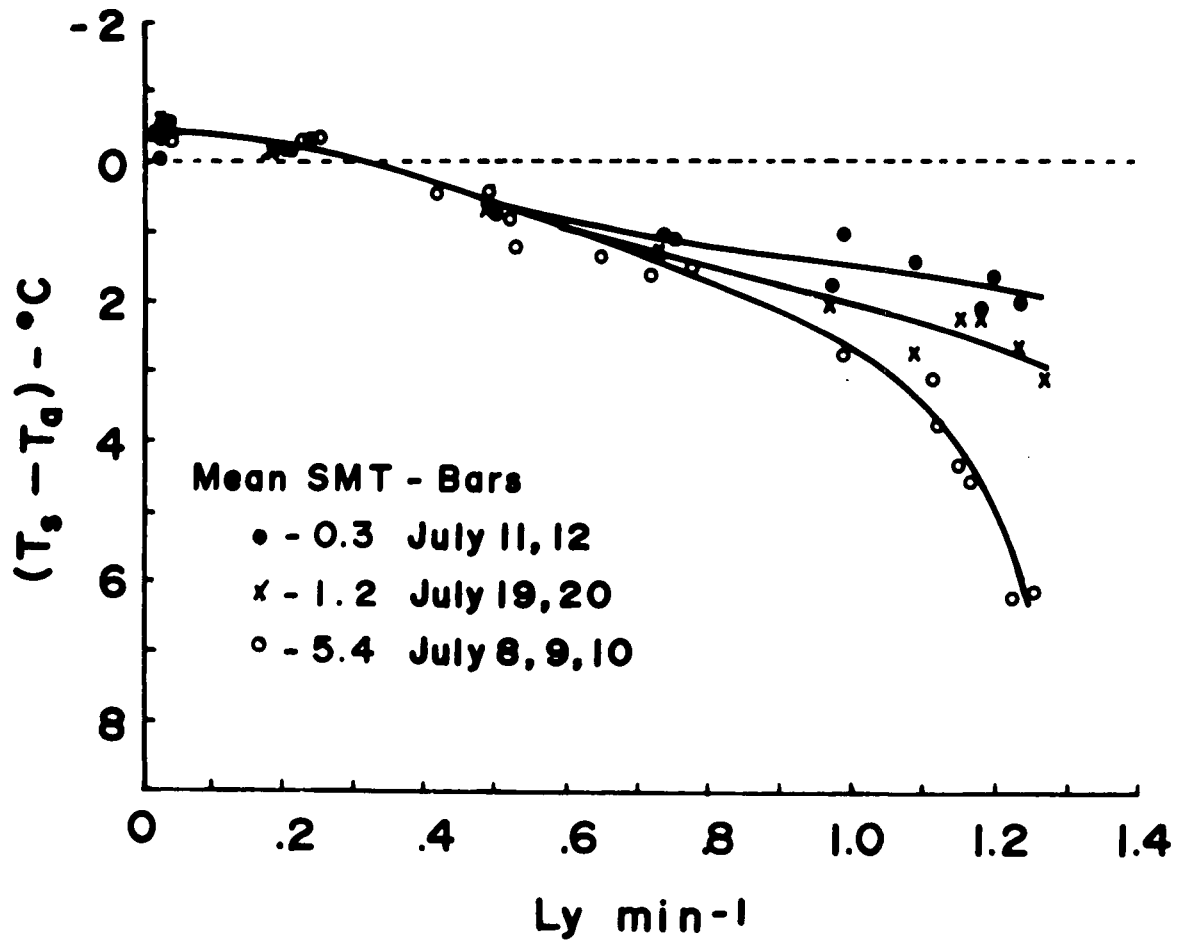


Figure 6.- Relation of the difference between crop surface and air temperatures ( $T_s - T_a$ ) to solar radiation at various mean soil moisture tensions (SMT) for the top meter of soil.

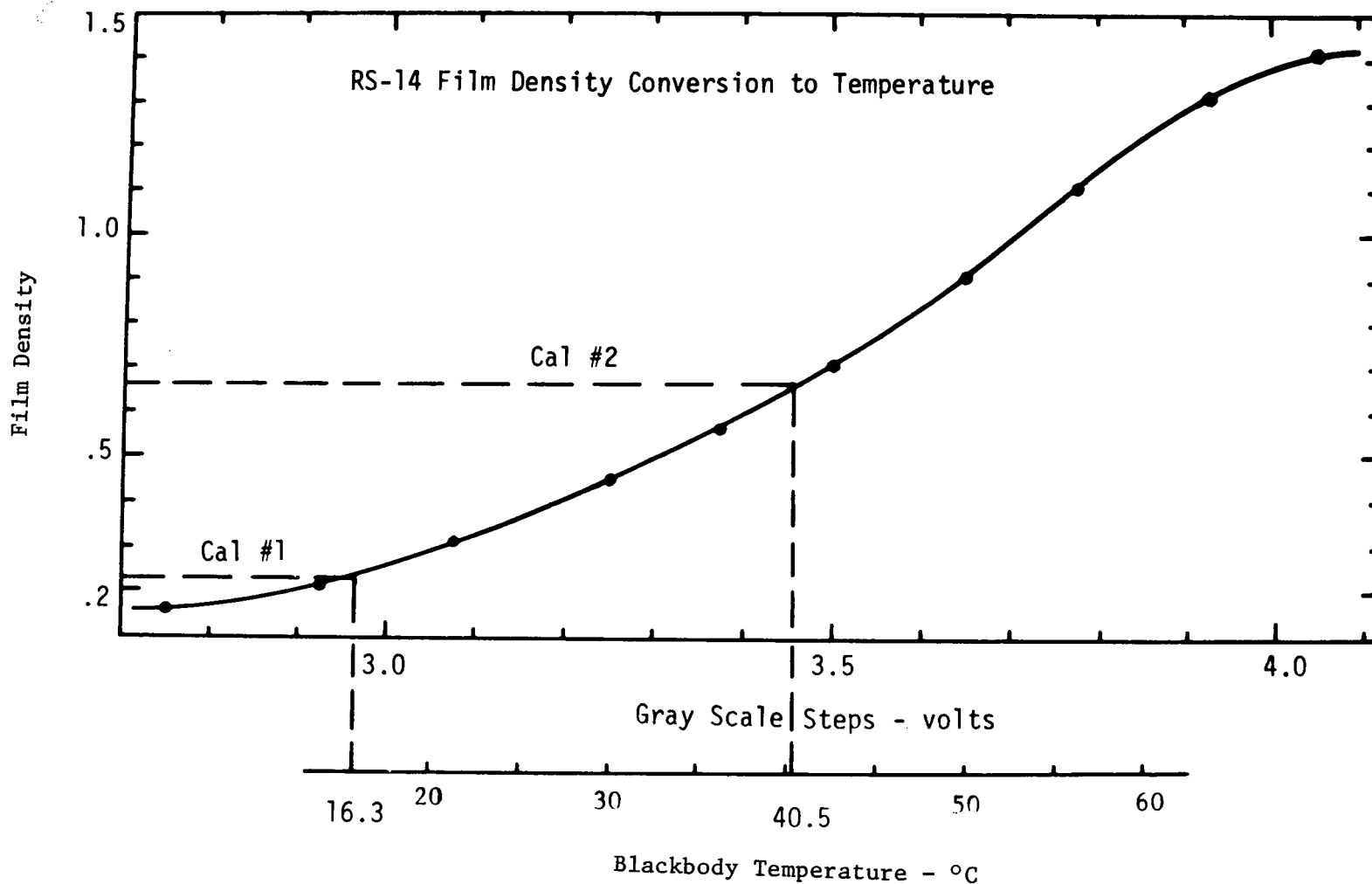


Figure 7.- Film density versus grey scale step voltage and blackbody temperature, RS-14 scanner. (Film density of the 10 grey scale wedges and the voltages of each were used to construct the curve. Then, using the measured density of the cal sources and their known temperature, a relation between film density and blackbody temperature was obtained.)

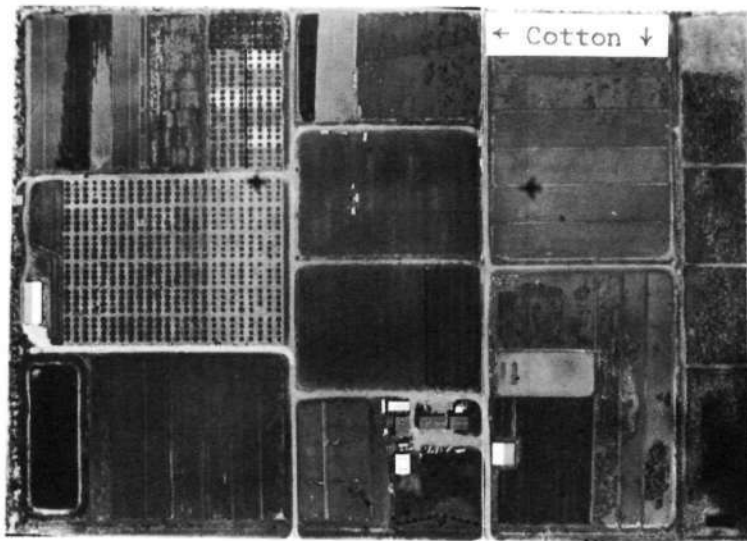


Figure 8.- Ektachrome IR picture of the Research Farm.

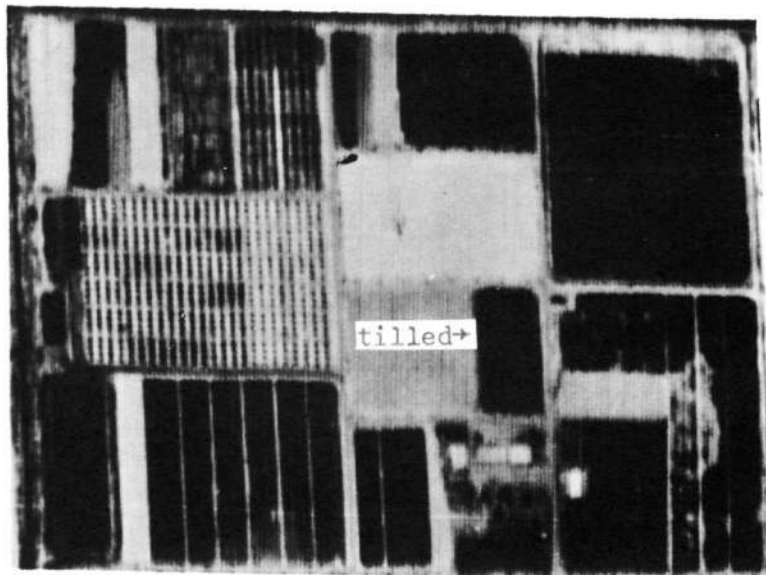


Figure 9.- Thermal image obtained for the Research Farm. Dark-toned objects are cool, light-toned objects are warm.

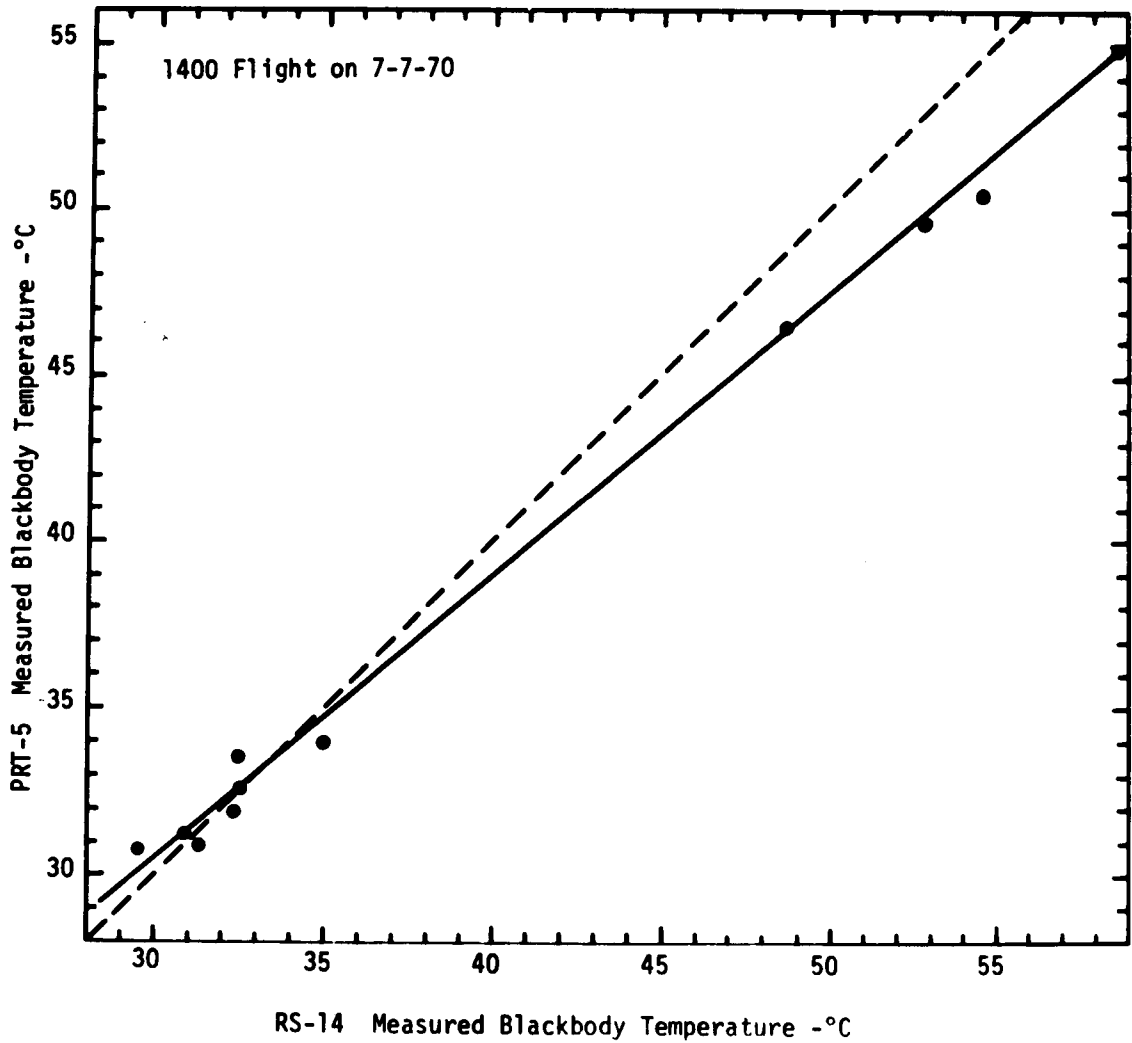


Figure 10.- Relationship between PRT-5 temperature measurements taken from the ground and temperatures obtained from RS-14 data.



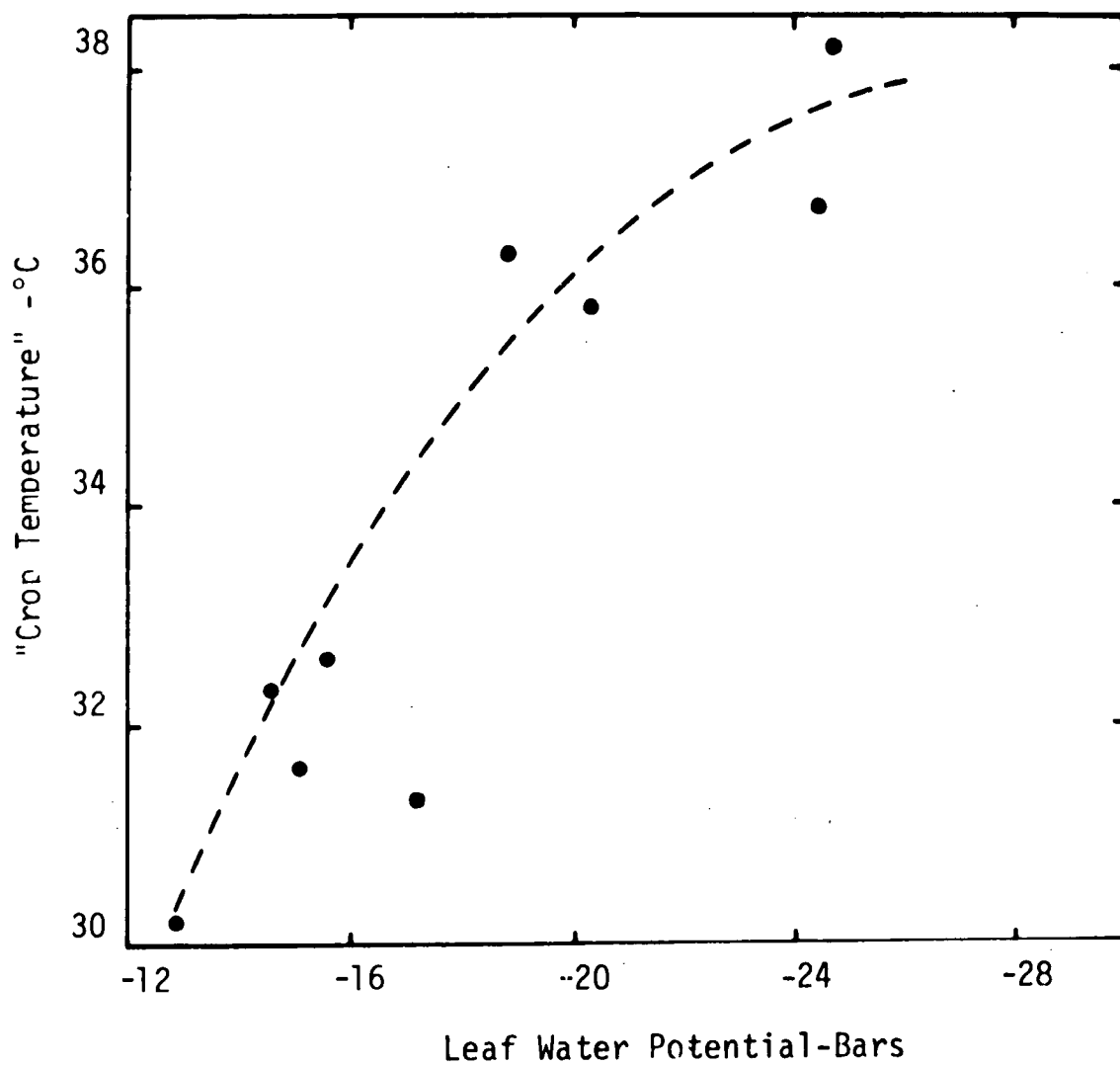


Figure 11.- Relation between cotton leaf emittance (8-14  $\mu\text{m}$ ) measured with an RS-14 scanner and plant stress.

COMPUTER DISCRIMINATION PROCEDURES APPLICABLE TO  
AERIAL AND ERTS MULTISPECTRAL DATA

by

Arthur J. Richardson, Robert J. Torline, and William A. Allen  
Soil and Water Conservation Research Division  
Agricultural Research Service  
U. S. Department of Agriculture  
Weslaco, Texas

ABSTRACT

Two statistical models are compared in the classification of crops recorded on color aerial photographs. A theory of error ellipses is applied to the pattern recognition problem. An elliptical boundary condition classification model (EBC), useful for recognition of candidate patterns, evolves out of error ellipse theory. The EBC model is compared with the minimum distance to the mean (MDM) classification model in terms of pattern recognition ability. The pattern recognition results of both models are interpreted graphically using scatter diagrams to represent measurement space. Measurement space, for this report, is determined by optical density measurements collected from Kodak Ektachrome Infrared Aero Film 8443 (EIR). The EBC model is shown to be a significant improvement over the MDM model.

INTRODUCTION

Earth ground patterns, represented by optical density feature measurement vectors were collected from Kodak Ektachrome Infrared Aero Film 8443 (EIR). Two statistical approximations of the distribution of these measurement vectors were developed. A feature measurement vector was constructed from EIR film optical density measurements to red, green, and blue light. Each optical density measurement was considered as an element (feature) of the feature measurement vector. Each element of the vector is a dimension of measurement space. A measurement vector with red, green, and blue light optical density measurements gives three dimensions to measurement space<sup>1</sup>.

Specific earth ground patterns most often investigated in agriculture are crops, water bodies, and bare soil (Fig. 1). These different kinds of earth ground patterns can be considered as categories to be recognized by a classification model. The recognition ability for a classification model will be dependent on its approximation, usually statistical, of the feature measurement vector distribution for each category.

The set of all possible ground pattern feature measurement vectors is called measurement space<sup>1</sup>. The distribution of these measurement vectors in measurement space result in a scattering of points. Each vector is represented by a point in measurement space. The natural groupings or clusters of optical density measurement vectors (points) for EIR film in measurement space can be associated with specific ground pattern categories. Proper classification of a candidate pattern can be regarded as identifying a point in measurement space belonging to a particular cluster (category) of points.

Part of the pattern recognition problem is to design classification models that partition measurement space into cells that correspond closely to the clusters associated with each ground pattern category. The other part of the pattern recognition problem is the selection of characteristic features used to construct measurement space which contains the ground pattern categories.

The elliptical boundary condition (EBC) and minimum distance to the mean (MDM) statistical classification models are compared in this report. The EBC model partitions measurement space into elliptical cells while the MDM model partitions measurement space into irregular polygonal cells. Recognition results of ground pattern categories on EIR film were determined for each model. Scattering diagrams, representing measurement space, were developed to explain recognition results obtained for each classification model.

#### DATA MANAGEMENT PROCEDURES

Ground patterns investigated in this report are shown in Figure 1. Water is shown in three modes of sun glinting defined as low reflecting (W), medium reflecting (M), and high reflecting (H). A cotton field (C) is shown with 90 to 100% vegetation cover. Bare soil is shown in dry (B) and disked (D) conditions. These ground patterns were randomly sampled for flight lines 1, 11, and 12 established by the United States Department of Agriculture, Weslaco, Texas to include as many agricultural conditions in the Rio Grande Valley as possible.

A Hasselblad camera with a 50 mm lens was used to obtain aerial photographs on EIR (8443) film (70 mm) from these three flight lines. The camera was mounted in a plane so that photographs could be taken directly above (1800 to 3000 feet) ground pattern areas. Each flight line was photographed with 60 percent forward overlap. Six rolls of film were used between July 14 and July 27 of 1968 between the hours of 1052 and 1457 CDT. A Tiffen 15G filter was used on all cameras. A typical exposure was 1/250 at f/10. All film processing followed the recommended times, temperatures, and solution concentrations recommended by Eastman Kodak's E-3 process.

Positive transparencies of selected ground pattern areas were mounted in a Joyce-Loibl microdensitometer. Three scans were made of transects running through ground pattern areas appearing in selected frames. A scan was made using a red filter (Wratten 92), green filter (Wratten 93), and a blue filter (Wratten 94) in both beams of the microdensitometer. Each scan produced 20 optical density readings for each filter along each transect. This is equivalent to 20 three-dimensional feature measurement vectors per transect. One transect was established for each ground pattern area appearing in a frame. The mean of the 20 readings per transect for each filter was determined and used in pattern recognition procedures. These mean transects are listed in Appendix I.

A total of 160 mean transects for seven ground pattern categories were sampled as follows, 52 for cotton, 46 for dry bare soil, 20 for sorghum, 19 for low reflecting water, 9 for disked bare soil, 8 for high reflecting water, and 6 for medium reflecting water. All mean transects from each ground pattern category were used to establish the reference mean of the MDM classification model and the reference operation constants for the EBC classification model. Recognition tests for both models were conducted using all transects.

Ground pattern areas on transparencies were selected on the basis of uniformity in visual appearance of their images. A grease pencil was used to mark the location of the transect on the transparency for microdensitometer measurements. This procedure gave ground pattern areas with homogeneous optical density characteristics. Other criteria used for selection of ground pattern areas were derived from ground truth considerations for each category as follows:

- a. Cotton selected was in the boll stage with 90 to 100% vegetation cover.
- b. Sorghum selected was near harvest stage with 90 to 100% vegetation cover.
- c. Bare soil (dry) represented a variety of dry soil surface conditions with 0 - 15% vegetation cover.
- d. Bare soil (disked) selected was wet or freshly tilled soil with 0 - 15% vegetation cover.
- e. Water selected was visually categorized into three levels of reflectance (low, medium, and high) depending on sun glinting (sun angle).

#### ERROR ELLIPSE THEORY

The mathematics associated with error ellipses evolves from the elliptical law of error<sup>2</sup>. This law provides a method for describing the distribution of accidental errors for experimental measurements involving many variables (features or dimensions) with elliptical curves.

In two dimensions (x, y) the law of error is expressed by the general equations:

$$\phi = R \exp -(ax^2+2bxy+cy^2) \quad (1)$$

where

$$ax^2 + 2bxy + cy^2 - H = 0. \quad (2)$$

Equation (1) is a probability function that expresses a two-dimensional distribution. Equation (2) are curves of like probability that are assumed not to diverge to infinity. There are an infinite number of values for H, and thus an infinite number of probability curves exist. Since equation (2) must be an ellipse, then

$$b^2 - ac < 0 \quad . \quad (3)$$

By rotation of the x, y plane about the origin, the equation of these ellipses may be written as

$$a' x'^2 + c' y'^2 - H = 0 \quad , \quad (4)$$

where the equations of translation are

$$\tan 2\theta = -2b/(c-a) \quad , \quad (5)$$

$$c' = \frac{1}{2}(a+c) \pm b \csc 2\theta \quad , \quad (6)$$

$$a' = \frac{1}{2}(a+c) \mp b \csc 2\theta \quad . \quad (7)$$

The major and minor axes of the ellipse,  $2\alpha$  and  $2\beta$ , respectively, may be determined as follows:

$$x'^2/\alpha^2 + y'^2/\beta^2 = 1 \quad , \quad (8)$$

where

$$\alpha^2 = H/a' \text{ and } \beta^2 = H/c' \quad . \quad (9)$$

The probability of a measurement falling outside an ellipse with  $H = H_0$  is

$$\int \exp (-H) dH = \exp (-H_0) \quad , \quad (10)$$

where the integration limits are  $\infty$  and  $H_0$ . If it is desired that 5 percent of the experimental points should fall outside the error ellipse, then

$$\exp(-H_0) = 0.05 \quad , \quad (11)$$

$$H_0 = 2.99573227 \quad . \quad (12)$$

To determine the coefficients, a, b, and c, of equation (2) the following equations are used:

$$a = \frac{\sum \epsilon_i^2 (n-1)}{2[\sum \delta_i^2 \sum \epsilon_i^2 - (\sum \delta_i \epsilon_i)^2]} \quad , \quad (13)$$

$$b = \frac{-\sum \delta_i \epsilon_i (n-1)}{2[\sum \delta_i^2 \sum \epsilon_i^2 - (\sum \delta_i \epsilon_i)^2]} \quad , \quad (14)$$

$$c = \frac{\sum \delta_i^2 (n-1)}{2[\sum \delta_i^2 \sum \epsilon_i^2 - (\sum \delta_i \epsilon_i)^2]} \quad , \quad (15)$$

where

$$\sum \delta^2 = \sum (x - \bar{x})^2 = \sum x^2 - (\sum x)^2/n \quad , \quad (16)$$

$$\sum \epsilon^2 = \sum (y - \bar{y})^2 = \sum y^2 - (\sum y)^2/n \quad , \quad (17)$$

$$\sum \delta \epsilon = \sum (x - \bar{x})(y - \bar{y}) = \sum xy - \sum x \sum y/n \quad . \quad (18)$$

The mathematics needed for the n-dimensional error ellipse is given below:

$$P_{ij} = \sum \frac{\delta_i \delta_j}{n_{ij}^{-1}} \quad , \quad (19)$$

$$a_{ij} = 1/2[P_{ij}^T]^{-1} \quad , \quad (20)$$

$$\delta_i \delta_j = (x_i - \bar{x}_i)(x_j - \bar{x}_j) \quad , \quad (21)$$

where

$$P_{ij} = P_{ij}^T \quad , \quad (22)$$

for a symmetrical matrix. The (T) notation indicates the transpose matrix operation.

The  $(a_{ij})$  matrix contains the coefficients for the general error ellipse for any dimension. The elements for the  $(a_{ij})$  matrix which correspond to the coefficients in the two dimensional general equation (2) are:

$$\begin{aligned} a_{11} &= a \quad , \\ a_{12} &= b \quad , \\ a_{22} &= c \quad . \end{aligned} \quad (23)$$

Expanding the  $(a_{ij})$  matrix equation (20) and combining with the feature measurement vector  $X$  produces the following general equation:

$$\begin{aligned} a_{11}x'_1 + 2a_{12}x'_1x'_2 + \dots + 2a_{1n}x'_1x'_n \\ + a_{22}x'_2x'_2 + \dots + 2a_{2n}x'_2x'_n \\ + \dots + a_{nn}x'_nx'_n \end{aligned} \quad (24)$$

$$- H = 0 \quad .$$

The primes on the  $x$  terms above mean that the feature measurement vector elements  $x_1, x_2, \dots, x_n$  must be translated before they can be used by equation (24) as follows:

$$\begin{aligned}
 x'_1 &= x_1 - \bar{x}_1 \\
 x'_2 &= x_2 - \bar{x}_2 \\
 &\dots \\
 x'_n &= x_n - \bar{x}_n
 \end{aligned}
 \tag{25}$$

#### EBC CLASSIFICATION MODEL FOR n-DIMENSIONS

For  $m$  ground cover pattern classes  $\omega_1, \omega_2, \dots, \omega_m$ ,  $m$  error hyper-ellipses in  $n$ -dimensional space can be generated using equations (19) through (25).

The classification rule for identification of a measurement vector  $X$  for  $m$  ground cover pattern classes may be formed as follows:

Classify candidate measurement vector  $X$  as belonging to pattern class

(ground cover category)  $\omega_L$  if:

$$\sum_{i=1}^n \sum_{j=1}^n a_{ijL} x'_{iL} x'_{jL} < \sum_{i=1}^n \sum_{j=1}^n a_{ijk} x'_{ik} x'_{jk}
 \tag{26}$$

for all  $k \neq L$  where the index  $k$  varies from 1 to  $m$  and excludes  $L$ .

A rejection class (threshold) for "everything else" may be constructed for the  $n$ -dimensional error hyper-ellipse. A candidate measurement vector  $X$  is classified as from class  $\omega_L$  if it meets the criterion in (26) and fulfills the following condition

$$\sum_{k=1}^n \sum_{j=1}^n a_{ijL} x'_{iL} x'_{jL} \leq H
 \tag{27}$$

#### MDM CLASSIFICATION MODEL

Using the EBC optical density measurement vectors  $m$  mean and standard deviation vectors ( $\bar{X}_i$  and  $S_i$ ) can be developed for  $m$  ground pattern classes (categories) ( $\omega_1, \omega_2, \dots, \omega_m$ ). If red (R), green (G), and blue (B), light density readings are used as characteristic features  $X_{1 ik}, X_{2 ik},$  and  $X_{3 ik}$ , respectively, constituting a sample from the  $i$ th ground pattern class and  $k$ th observation, then  $\bar{X}_i$  and  $S_i$  are defined as:



$$\bar{X}_i = \frac{1}{N_i} \sum_{k=1}^{N_i} X_{ik} = \begin{bmatrix} \frac{1}{N_i} \sum_{k=1}^{N_i} X_{lik} \\ \dots \\ \frac{1}{N_i} \sum_{k=1}^{N_i} X_{3ik} \end{bmatrix} = \begin{bmatrix} \bar{X}_{li} \\ \dots \\ \bar{X}_{3i} \end{bmatrix}, \quad (28)$$

$$S_i = \frac{\sum_{k=1}^{N_i} (X_{ik} - \bar{X}_i)^2}{N_i - 1} = \begin{bmatrix} S_{li} \\ \dots \\ S_{3i} \end{bmatrix}, \quad (29)$$

where  $k = 1, \dots, N_i$  number of observations for the  $i$ th ground cover pattern class.

The MDM classification rule for identification of a candidate measurement vector  $X$  for  $m$  ground cover pattern classes may be formed as follows:<sup>3</sup>

Classify measurement vector  $X$  as belonging to pattern class (category)  $\omega_L$  if

$$\sum_{j=1}^n [X(j) - \bar{X}_L(j)]^2 < \sum_{j=1}^n [X(j) - \bar{X}_i(j)]^2 \quad (30)$$

for all  $i \neq L$  where  $\bar{X}_i$  is  $m-1$  mean measurement vectors calculated for  $X$  from  $m-1$  pattern classes, excluding pattern class  $\omega_L$ , and  $\bar{X}_L$  is the  $L$ th mean measurement vector calculated for  $X$  from pattern class  $\omega_L$ . The index  $j = 1, \dots, n$  represents the number of elements (using optical density measurements to red, green, and blue light) formed  $X$ ,  $\bar{X}_L$ , and  $\bar{X}_i$  by each pattern recognition model.

A rejection class for "everything else" may be developed by employing standard deviations as threshold values. Mathematically a candidate measurement vector is classified as from class  $\omega_L$  if it meets the criterion from equation (30) and fulfills the following condition

$$\sum_{j=1}^n [X(j) - \bar{X}_L(j)]^2 \leq T_L \quad , \quad (31)$$

where  $T_L$  is the threshold for class  $\omega_L$  and is given by

$$T_L = \sum_{j=1}^n S_L(j)^2 \quad . \quad (32)$$

### EXPERIMENTAL RESULTS AND DISCUSSION

Scattering diagrams were developed to approximate two dimensional measurement space for all ground pattern categories used in this report. Scatter plots using the 160 mean transects of red versus green (Figure 2 and Figure 3), red versus blue (Figure 4), and blue versus green (Figure 5) light optical density measurements were constructed. For all four figures each of the 160 mean transect points are identified with a letter as cotton (C), dry bare soil (B), sorghum (S), low reflecting water (W), medium reflecting water (M), high reflecting water (H), and disked bare soil (D). In Figure 2 the partitioning of measurement space with cells for the MDM model is indicated with dashed lines that form irregular polygons. Partitioning with cells for the EBC model is indicated with solid lines that form ellipses in Figure 3. A circle with the appropriate letter identifies the mean for each circle. Table 1 contains the elliptical coefficients and means for all ground pattern categories used to construct Figures 2 and 3.

From Figure 5 it can be seen that the blue versus green scatter plot does not yield very good separation among ground pattern categories. The scatter plot in Figure 4 indicates better separation of ground pattern categories than Figure 5 but there is some confusion between the cotton and sorghum categories. The scatter plots in Figure 2 and Figure 3 show good separation among all ground pattern categories. For this reason the red versus green combination was used for tests comparing MDM and EBC classification models.

From casual inspection of Figure 2 and Figure 3 it should be immediately obvious that the EBC classification model will yield the best approximation of each ground pattern category. The clusters representing all ground pattern categories, except cotton, cross over MDM partitioning polygonal cells (Figure 2). The points that cross over represent those candidate measurement vectors that will be incorrectly classified by the MDM classification model. The elliptical cells can be tailored for close correspondence to each ground pattern category cluster with very few points of any cluster falling outside an elliptical cell (Figure 3).

A recognition test, using the mathematics developed for the MDM and EBC models, was conducted using the red and green optical density measurements in Appendix I. The results of this test is shown in Tables 2 and 3. Overall recognition by the EBC model (94.5%) was higher than the MDM model (80.6%).

### CONCLUSIONS

The theory of error ellipses, developed by Coolidge, was applied to the pattern recognition problem. The EBC classification model evolved from error ellipse theory yields better pattern recognition results (94.5%) than the MDM classification model (80.6%). Scatter diagrams show graphically (Figures 2 and 3) that the EBC model provides a much better description of ground cover category clusters than the MDM model does. These results indicate that the EBC model is more efficient than the MDM model for the pattern recognition problem.

Scatter diagrams provide a graphical method for determining those characteristic features that yield optimum discrimination results. For this report the scatter diagrams in Figure 2 through 5 indicated that optimum discrimination results could be obtained with the red versus green (Figures 2 and 3) optical density measurements. Ground pattern categories seemed to have better separation using red versus green density measurements as compared to using either the red versus green or the green versus blue density measurements.

REFERENCES

1. Haralick, R. M., and Kelly, G. L., "Pattern Recognition with Measurement Space and Spatial Clustering for Multiple Images," Proceedings of the IEEE, Vol. 57, No. 4, April 1969.
2. Coolidge, Julian L., "An Introduction to Mathematical Probability," Dover Publications, Inc., New York, N. Y. 1962.
3. Sebestyen, G. S., and Edie, J., "Pattern Recognition Research," Air Force Cambridge Research Lab., Bedford, Mass., Rept. 64-821 (AD 603 692), 1964.

Table I. Reference ground pattern mean vectors and covariance matrixes for optical density readings of red and green filters used for MDM and EBC classification models.

Ground pattern category	Mean vector elements		(a <sub>ij</sub> ) matrix elements		
	$\bar{X}_1$	$\bar{X}_2$	a <sub>11</sub>	a <sub>12</sub> & a <sub>21</sub>	a <sub>22</sub>
	Red Optical density	Green Optical density			
Cotton	0.2740	1.4907	276.21	-108.20	59.11
Bare Soil (Disked)	1.3171	1.4400	272.19	-394.00	582.10
Water (L.R.)	1.1678	0.8373	105.53	-116.90	137.70
Water (H.R.)	0.3851	0.3084	8374.50	-15730.00	29628.00
Bare Soil (Dry)	0.4366	0.5512	205.45	-182.90	219.05
Water (M.R.)	1.1375	1.0758	994.55	-1337.00	1919.70
Sorghum	0.5351	1.2910	93.45	-70.34	61.45

L. R. - Low Reflectance  
M. R. - Medium Reflectance  
H. R. - High Reflectance

Table II. Comparison of recognition results for the MDM classification models using the indicated ground pattern categories with red and green light EIR optical density measurements as characteristic features. A threshold class (T) for "every thing else" was used.

Ground pattern category	Number of observation	Ground Pattern classified as								Percent recognition
		C	B	S	W	D	H	M	T	
Cotton [C]	52	52								100.0
Bare Soil [B]	46		35	1			7	3		76.3
Sorghum [S]	20		1	17		2				85.0
Water (L.R.) [W]	19		4		9	4		2		47.3
Bare Soil (Disked) [D]	9					5		4		55.6
Water (H.R.) [H]	8		2				6			75.0
Water (M.R.) [M]	6							6		100.0

Overall percent recognition 80.6%

L. R. - Low Reflectance

H. R. - High Reflectance

M. R. - Medium Reflectance

Table III. Comparison of recognition results for the EBC classification model using the indicated ground pattern categories with red and green light EIR optical density measurement as characteristic feature. A threshold class (T) for "everything else" was used.

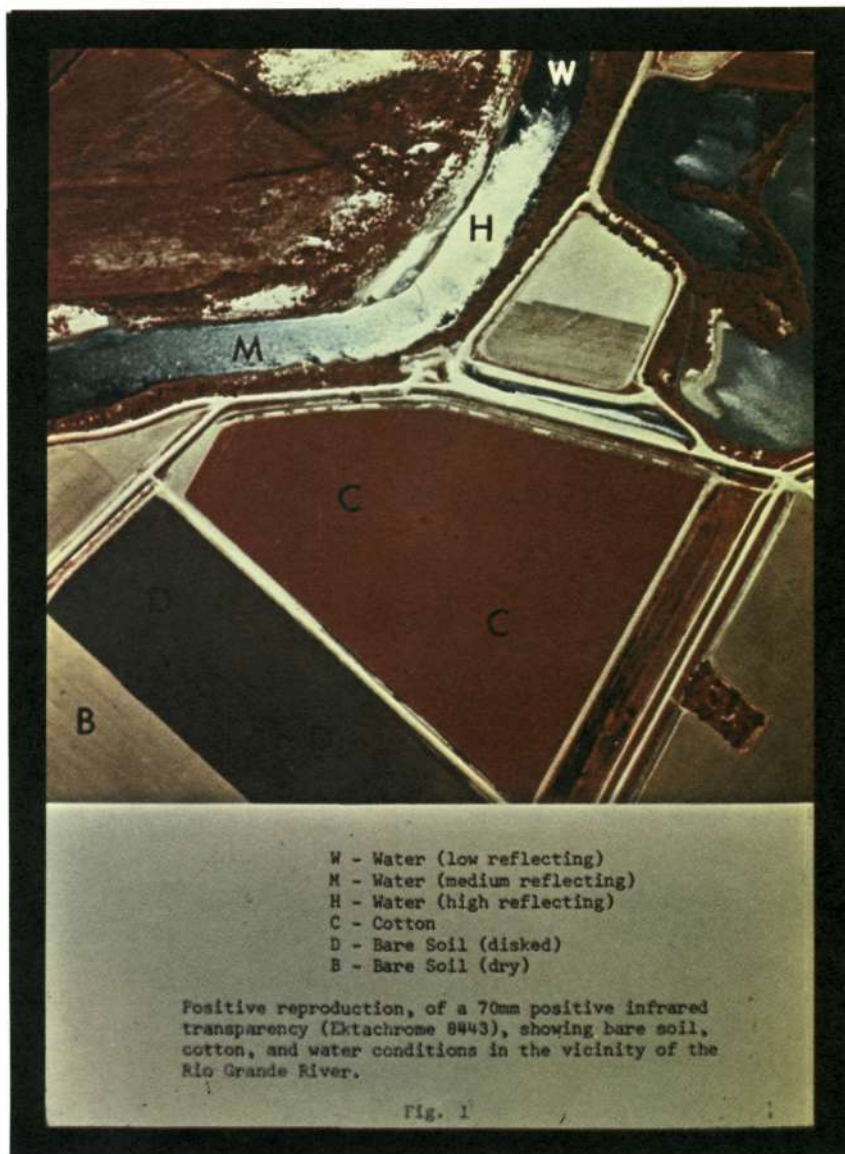
Ground pattern category	Number of observation	Ground Pattern classified as								Percent recognition
		C	B	S	W	D	H	M	T	
Cotton [C]	52	51							1	98.1
Bare Soil [B]	46		41			2			3	89.2
Sorghum [S]	20			19					1	95.0
Water (L.R.) [W]	19				19					100.0
Bare Soil (Disked) [D]	9					8			1	89.0
Water (H.R.) [H]	8				1		7			87.5
Water (M.R.) [M]	6							6		100.0

Overall percent recognition 94.5

L. R. - Low Reflectance

H. R. - High Reflectance

M. R. - Medium Reflectance





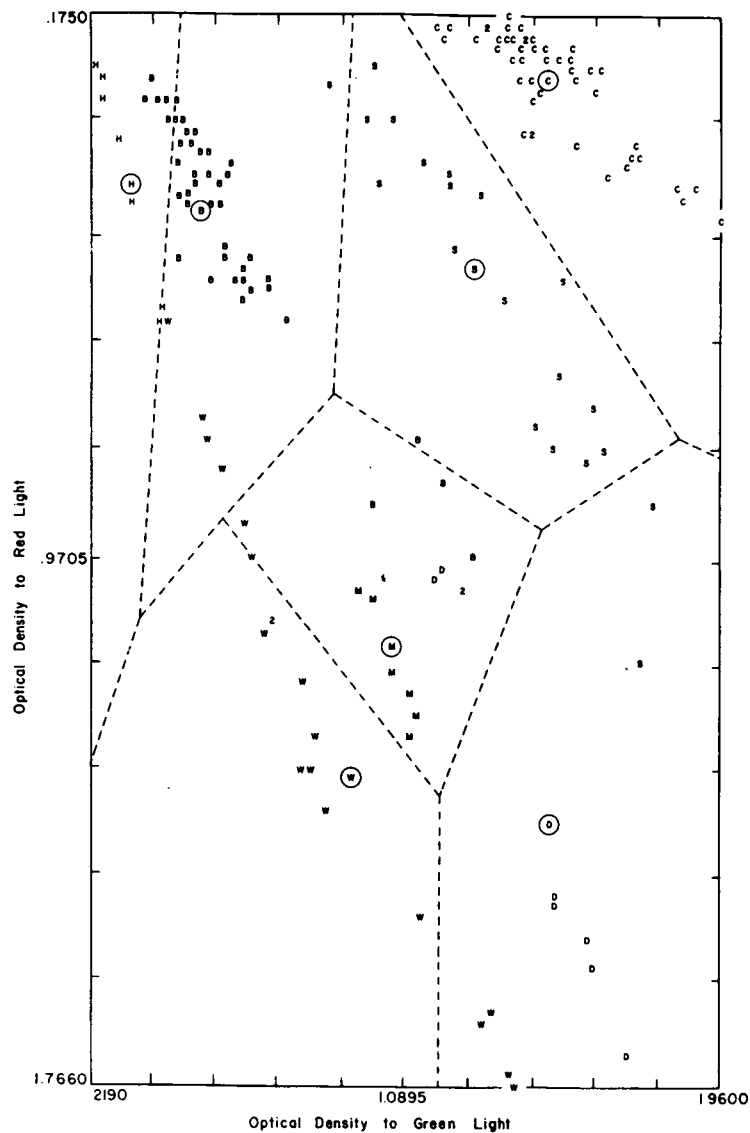


Figure 2.- Scatter diagram of red versus green optical density measurements for 160 mean transect readings. Decision regions for the MDM classification model appear as dashed lines. Appropriate letters indicate identity of points as cotton (C), bare soil (B), sorghum (S), low reflecting water (W), medium reflecting water (M), high reflecting water (H), and disked bare soil (D). The seven ground cover means appear as a circle with the appropriate letter.

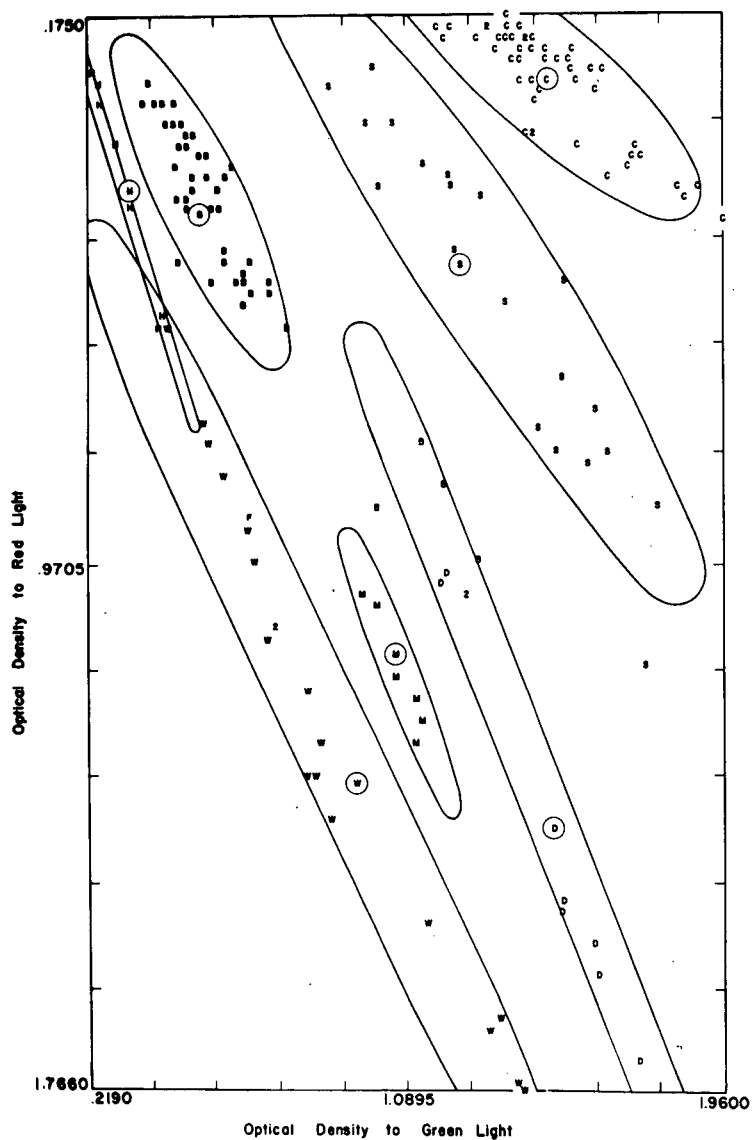


Figure 3.- Scatter diagram of red versus green light optical density measurements showing decision regions for the EBC classification model. Letter identification of points is the same as Fig. 2.

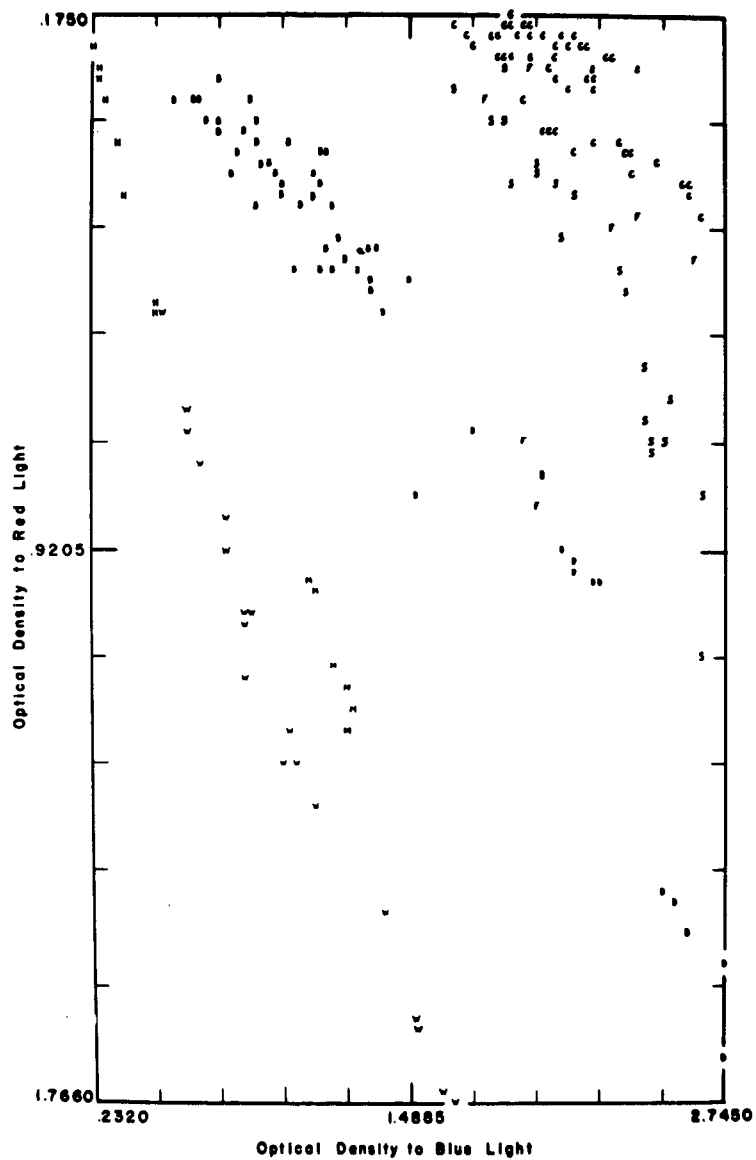


Figure 4.- Scatter diagram of red versus blue light optical density measurements. Letter identification of points is the same as Fig. 2.

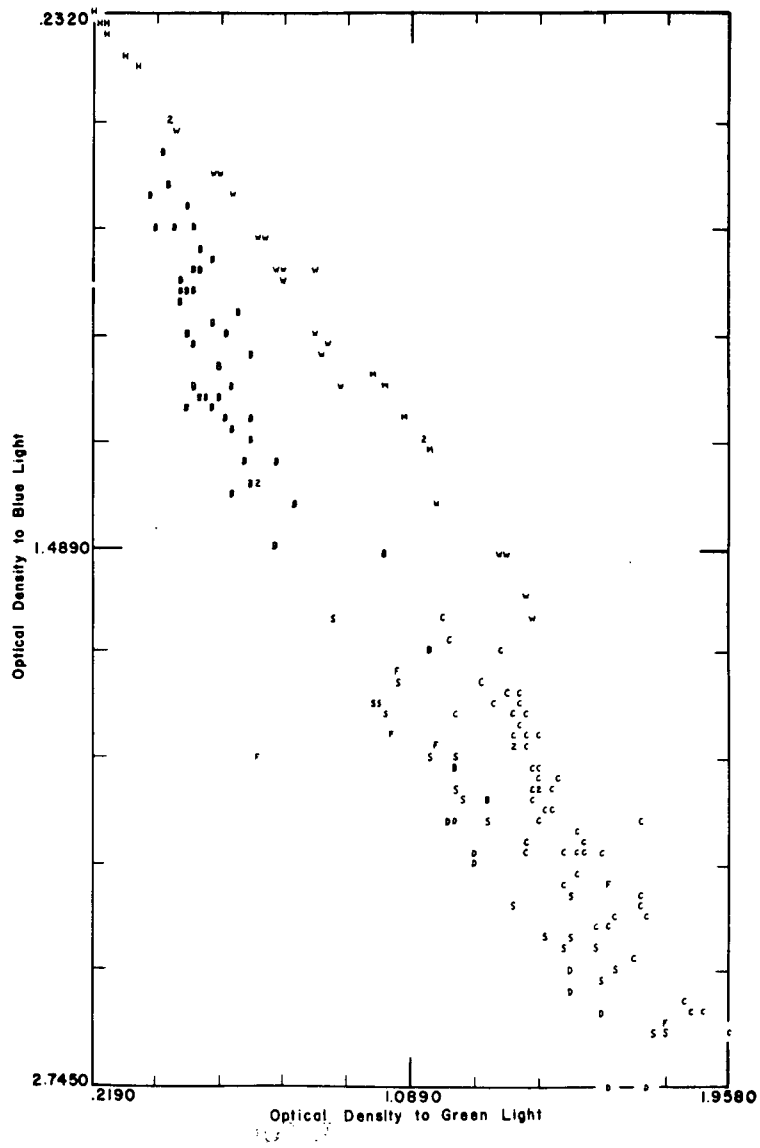


Figure 5.- Scatter diagram of blue versus green light optical density measurements. Letter identification of points is the same as Fig. 2.

APPENDIX I

Computer printout of 160 mean transect optical density measurements for Red, Green, Blue, and White Light.

- A Optical density measurements to red light
- B Optical density measurements to green light
- C Optical density measurements to blue light
- D Optical density measurements to white light
- E The average of red, green, and blue light optical density measurements
- F Identification number for each ground pattern category as follows:
  - 3 - Cotton
  - 2 - Bare soil (dry)
  - 19 - Sorghum
  - 23 - Water (low reflecting)
  - 4 - Bare soil (disked)
  - 8 - Water (high reflecting)
  - 13 - Water (medium reflecting)

A	B	C	D	E	F
0.236	1.377	1.848	1.136	1.154	3
0.235	1.398	1.886	1.157	1.173	3
0.235	1.381	1.869	1.159	1.161	3
0.236	1.405	1.974	1.174	1.205	3
0.252	1.480	2.044	1.212	1.259	3
0.261	1.620	2.399	1.294	1.427	3
0.211	1.362	1.964	1.150	1.179	3
0.208	1.341	1.848	1.133	1.132	3
0.230	1.535	2.159	1.246	1.308	3
0.209	1.425	2.010	1.173	1.215	3
0.214	1.435	2.134	1.186	1.261	3
0.212	1.420	2.082	1.174	1.238	3
0.223	1.428	2.066	1.181	1.239	3
0.245	1.537	2.256	1.250	1.346	3
0.235	1.506	2.295	1.210	1.345	3
0.258	1.508	2.226	1.224	1.331	3
0.277	1.400	2.229	1.185	1.302	3
0.228	1.400	2.182	1.162	1.270	3
0.259	1.596	2.400	1.270	1.418	3
0.407	1.651	2.367	1.364	1.475	3
0.397	1.695	2.474	1.383	1.522	3
0.366	1.561	2.205	1.299	1.378	3
0.201	1.199	1.719	1.023	1.040	3
0.198	1.167	1.673	1.003	1.013	3
0.211	1.380	1.914	1.121	1.168	3
0.206	1.280	1.816	1.075	1.101	3
0.195	1.205	1.903	1.029	1.101	3
0.265	1.551	2.198	1.241	1.338	3
0.375	1.708	2.136	1.376	1.406	3
0.474	1.958	2.657	1.544	1.697	3
0.433	1.882	2.598	1.499	1.638	3
0.424	1.837	2.581	1.470	1.614	3
0.442	1.855	2.595	1.490	1.631	3
0.376	1.730	2.375	1.381	1.494	3
0.382	1.716	2.337	1.384	1.478	3
0.373	1.722	2.311	1.381	1.469	3
0.296	1.439	1.929	1.216	1.222	3
0.233	1.477	2.067	1.216	1.259	3
0.225	1.469	2.129	1.206	1.275	3
0.282	1.453	2.119	1.217	1.284	3
0.259	1.541	2.210	1.252	1.336	3
0.272	1.434	2.060	1.205	1.255	3
0.282	1.612	2.210	1.317	1.368	3
0.230	1.339	1.743	1.140	1.104	3
0.357	1.435	2.044	1.247	1.279	3
0.355	1.416	2.058	1.250	1.276	3
0.346	1.431	2.009	1.246	1.262	3
0.175	1.374	1.896	1.121	1.149	3
0.186	1.365	1.946	1.130	1.166	3
0.186	1.374	1.972	1.127	1.177	3
0.190	1.400	1.950	1.148	1.180	3
0.187	1.308	1.861	1.072	1.119	3

A	B	C	D	E	F
0.557	0.653	1.046	0.706	0.752	2
0.558	0.662	1.179	0.727	0.799	2
0.409	0.520	0.781	0.564	0.570	2
0.628	0.769	1.394	0.834	0.930	2
0.521	0.679	1.334	0.758	0.845	2
0.556	0.716	1.277	0.763	0.850	2
0.415	0.555	0.973	0.589	0.648	2
0.593	0.660	1.337	0.750	0.863	2
0.468	0.574	1.059	0.661	0.700	2
0.542	0.659	1.229	0.737	0.810	2
0.888	1.027	1.515	1.099	1.143	2
0.443	0.493	1.106	0.586	0.681	2
0.522	0.486	1.170	0.612	0.726	2
0.462	0.496	0.885	0.568	0.615	2
0.552	0.560	1.127	0.646	0.747	2
0.399	0.470	0.899	0.547	0.589	2
0.519	0.598	1.356	0.698	0.824	2
0.577	0.724	1.501	0.803	0.934	2
0.514	0.600	1.202	0.676	0.772	2
0.565	0.666	1.344	0.747	0.859	2
0.559	0.635	1.284	0.722	0.826	2
0.446	0.477	0.977	0.563	0.633	2
0.790	1.132	1.746	1.144	1.223	2
0.856	1.208	2.013	1.218	1.359	2
0.965	1.293	2.084	1.307	1.447	2
0.468	0.582	1.181	0.653	0.744	2
0.377	0.539	1.148	0.608	0.688	2
0.388	0.552	1.156	0.615	0.699	2
0.338	0.471	0.873	0.522	0.561	2
0.361	0.500	0.999	0.565	0.620	2
0.359	0.482	0.890	0.547	0.577	2
0.310	0.465	0.859	0.520	0.545	2
0.269	0.387	0.723	0.448	0.460	2
0.348	0.489	0.736	0.527	0.524	2
0.306	0.403	0.566	0.434	0.425	2
0.416	0.606	1.105	0.665	0.709	2
0.378	0.549	0.812	0.578	0.579	2
0.354	0.514	0.829	0.554	0.566	2
0.332	0.472	0.682	0.511	0.495	2
0.296	0.430	0.633	0.456	0.453	2
0.396	0.624	0.929	0.651	0.650	2
0.332	0.448	0.743	0.512	0.508	2
0.423	0.581	0.998	0.632	0.667	2
0.299	0.384	0.649	0.445	0.444	2
0.424	0.515	1.126	0.607	0.688	2
0.356	0.505	0.847	0.560	0.569	2

A	B	C	D	E	F
0.416	1.213	1.995	1.102	1.208	19
0.341	0.989	1.877	0.982	1.069	19
0.248	1.003	1.860	0.947	1.037	19
0.825	1.586	2.433	1.477	1.615	19
0.425	1.026	1.884	1.000	1.112	19
0.279	0.882	1.668	0.858	0.943	19
0.559	1.526	2.315	1.353	1.467	19
0.694	1.528	2.426	1.400	1.550	19
0.804	1.639	2.494	1.511	1.646	19
0.894	1.791	2.637	1.650	1.774	19
0.747	1.603	2.516	1.482	1.622	19
0.586	1.360	2.344	1.313	1.430	19
1.133	1.745	2.654	1.656	1.844	19
0.779	1.451	2.425	1.397	1.552	19
0.811	1.505	2.434	1.441	1.583	19
0.517	1.230	2.088	1.145	1.278	19
0.330	1.051	1.804	0.980	1.061	19
0.439	1.291	2.138	1.171	1.289	19
0.398	1.139	1.988	1.060	1.175	19
0.433	1.216	2.062	1.128	1.237	19
1.086	0.730	0.825	0.752	0.880	23
1.284	0.831	0.981	0.864	1.032	23
1.281	0.843	1.026	0.881	1.050	23
1.354	0.905	1.102	0.944	1.120	23
0.849	0.601	0.653	0.621	0.701	23
0.972	0.693	0.756	0.708	0.807	23
1.068	0.742	0.823	0.758	0.878	23
1.248	0.861	1.011	0.887	1.040	23
0.791	0.559	0.617	0.582	0.656	23
0.769	0.550	0.600	0.566	0.639	23
1.070	0.740	0.848	0.764	0.886	23
1.660	1.349	1.520	1.343	1.510	23
1.744	1.397	1.610	1.405	1.584	23
1.667	1.339	1.518	1.341	1.508	23
1.766	1.413	1.666	1.423	1.615	23
1.160	0.832	0.824	0.798	0.939	23
1.504	1.159	1.377	1.156	1.347	23
0.615	0.453	0.515	0.456	0.528	23
0.922	0.663	0.751	0.666	0.779	23



A	B	C	D	E	F
0.979	1.212	2.130	1.264	1.440	4
1.009	1.188	2.140	1.244	1.446	4
1.020	1.264	2.215	1.306	1.499	4
1.017	1.269	2.236	1.313	1.507	4
1.720	1.732	2.742	1.808	2.065	4
1.543	1.614	2.600	1.676	1.919	4
1.487	1.530	2.485	1.605	1.834	4
1.494	1.518	2.543	1.595	1.852	4
1.585	1.633	2.745	1.700	1.908	4
0.304	0.261	0.279	0.271	0.281	8
0.443	0.335	0.358	0.345	0.379	8
0.617	0.431	0.481	0.443	0.510	8
0.607	0.427	0.484	0.442	0.506	8
0.217	0.219	0.232	0.227	0.225	8
0.247	0.238	0.247	0.247	0.244	8
0.273	0.246	0.259	0.258	0.259	8
0.373	0.310	0.324	0.311	0.335	8
0.304	1.050	1.798	1.001	1.050	6
0.248	1.152	1.961	1.041	1.120	6
0.536	1.779	2.628	1.489	1.648	6
0.491	1.624	2.283	1.394	1.466	6
0.472	1.596	2.384	1.372	1.484	6
0.816	1.032	1.953	1.107	1.267	6
0.909	0.672	1.996	1.171	1.192	6
1.020	0.986	1.080	0.993	1.029	13
1.139	1.074	1.193	1.061	1.135	13
1.237	1.121	1.241	1.112	1.200	13
1.211	1.137	1.265	1.120	1.204	13
1.042	1.011	1.112	0.997	1.055	13
1.176	1.126	1.248	1.114	1.183	13

## The Applications of Remote Sensing to

## Corn Blight Detection and

## Crop Yield Forecasting

by

R. B. MacDonald  
Laboratory for Applications of Remote Sensing  
Purdue University  
West Lafayette, Indiana

INTRODUCTION

The invasion of southern corn leaf blight throughout Indiana captured the attention of LARS researchers in mid-August. By the end of the 1970 crop year, 64 counties had been declared disaster areas by the U. S. Department of Agriculture. While early estimates forecasted corn production losses of a few percent, November 1 statistics showed a production decline of 20% in the state of Indiana. Similarly, nationwide forecasts for the corn crop went from a few percent in August to reductions of 15% by November.

During the week of August 17, a research project was initiated by Purdue University's Laboratory for Applications of Remote Sensing (LARS) in cooperation with NASA to investigate the feasibility of identifying various stages of the southern corn leaf blight using remotely sensed measurements. LARS and NASA were assisted during various phases of the project by industry, a U. S. Air Force research group at the Rome Air Force Development Center, Rome, New York and the Cooperative Extension groups at Purdue. Credit should be given to the various personnel who assisted LARS to rapidly organize and execute this timely research.

Much has been said and written about the applicability of remote sensing technology to outbreaks of disease in important agricultural crops. The primary motivation for this particular research was to take advantage of a naturally occurring situation to further explore the possibilities afforded by our existing capabilities in remote sensing.

The information which existed at the beginning of the project concerning the blight, such as its epidemiological characteristics and its affects over time on corn plants and yield, was relatively meager. Certainly, the electromagnetic radiation characteristics of infected plants were little known. While southern corn leaf blight has proven to be one of the most serious, if not the most serious, infections to

strike corn, the situation is believed to be generally typical of outbreaks of diseases that routinely strike cultural crops. It has become an occasion for the remote sensing community to test its present capabilities and to establish current deficiencies, thus providing guidelines for future program development.

## BACKGROUND

### PATHOLOGY

The southern corn leaf blight disease is caused by the fungus pathogen, Helminthosporium maydis. Evidently this species is composed of two physiologic races, which are morphologically similar, if not identical, in that the size, shape, number of crosswalls and color of the spores are the same in both races. A distinguishing feature of these two races is the unusually high virulence of one of them on corn containing "Texas Male-Sterile" cytoplasm. Additionally, the spores of this new race are rather large in size ranging from 75 to 80 microns in length. This new race, designated the "T" race is only mildly pathogenic on normal cytoplasm; usually so benign as to cause only small, hardly recognizable lesions.

The old race, designated the "O" race, has existed coincidentally with corn culture down through the centuries. This race attacks both "Texas Male-Sterile" corn and that bearing normal cytoplasm with equal facility but rarely causes any serious problems.

Both races are favored by warm, wet weather. Heavy dews are especially conducive to rapid multiplication of both races. The "T" race appears to be a prolific spore producer. In other words, the "T" race reproduces an abundance of inoculin in a warm, wet environment. The time between penetration of a leaf to production of spores on the dead tissue of the lesion can be as little as seven days under ideal conditions. It is though, exceedingly productive on corn containing "Texas Male-Sterile" cytoplasm.

The symptoms incited by the race are characterized by tan-to-brown elliptical lesions that are generally spindle-shaped and range in size up to about 1 X 1/2 inches. Usually these lesions appear first on the lower leaves. Eventually, more lesions are produced from successive infection of the upper leaves. Lesions are also formed on the husks, and from there the fungus penetrates through the successive shucks in the ear and on and within the kernels. Figure 1 is a photograph of leaves at six different stages of the infection. Stages range from healthy to a severely blighted condition. The leaves shown are repre-

sentative of the following stages:

0. No infection - no lesions present
1. Very mild - a few scattered lesions which appear mostly on the lower leaves with less than 10% of the lower leaf surface affected.
2. Mild - many lesions appearing on the lower leaves and a few scattered lesions on the upper half of the plant; 10-30% of the lower leaf surfaces and less than 10% of the upper leaf surfaces affected.
3. Moderately severe - lesions on the lower leaves to the extent that large areas of the leaves are non-functional with scattered lesions on upper leaves; 30-60% of the lower and 10-30% of the upper leaf surfaces affected.
4. Severe - lower leaves mostly killed with the upper leaves beginning to die; 60-90% of lower and 60-90% of upper leaves affected.
5. Very severe - nearly all leaves have become non-functional; more than 90% of total leaf surfaces affected.

Healthy corn plants are shown in Figure 2a. Figure 2b shows moderately infected plants and Figure 2c is a photograph of a field of severely infected plants.

The reduction of functional leaves from the disease predisposes the corn plant to stalk rot not only by Helminthosporium maydis, but also by other fungi of less aggressive capabilities. Figure 3 is a photograph of the effects of stalk rot on corn plants suffering from the blight. Such secondary invaders can also grow on or within kernels infected with Helminthosporium maydis. Corn ears suffering from such rotting are shown in Figure 4.

The disease appeared initially in southern Florida in 1970 where seedsmen were growing a winter crop of foundation stocks. From there, it spread to Alabama and Mississippi. The disease fanned out in a northerly direction and week by week progressed to the Corn Belt. Since then it has been recognized from Texas eastward to the Atlantic Coast and northward through Iowa, Ohio, Minnesota, Wisconsin, Michigan and southern Ontario in Canada. Figure 5 illustrates the counties in Indiana where severe blight damage occurred. Spores were evidently windborne and the northerly progression was in a stepwise manner. The pathogen can also be seedborne; seed treatment probably has little or no effect for control of the disease, since the fungus can be within the seed as well as on the surface.

Three major factors are of cardinal importance in the development of any plant disease, and these must act coordinately to bring about disease establishment. These factors are:

- virulent pathogen;
- a favorable environment for reproduction of the pathogen; and
- a susceptible host.

These three requisites have been operative in the production of the southern corn leaf blight in 1970 in that a new virulent race of the pathogen was wide spread, weather conditions in the gulf states and on up through the eastern half of the United States were conducive to rapid growth and development of this race of Helminthosporium maydis and, lastly, a very susceptible host with "Texas Male-Sterile" cytoplasm had been widely planted. It has been reported that some 80% of corn varieties planted in the U. S. in 1970 contained "Texas Male-Sterile" cytoplasm.

#### CROP MANAGEMENT - RECOMMENDATIONS AND CONTROL

In 1970, fungicide applications were started too late to be very effective; such treatments should have been started in mid-July and repeated weekly. However, most observers believe that fungicide applications did serve to check the spread of blight and so were justified. Producers were advised to harvest infected fields at as early a date as possible based on the development of ears and moisture content. This early harvest generally required that artificial drying or ensiling be utilized. Not much is known of how well kernels from blighted plants will store. It is generally thought that corn from infected plants can be used as feed without harmful effects to livestock.

While fungicide applications may be effective in 1971, control of this disease can be only satisfactorily accomplished by using hybrid with normal cytoplasm which are quite resistant to the blight. Next year it appears that 20% of the corn crop will be blight resistant, 40% will be blends only half of which are resistant and 40% of the seed will be of varieties which are again susceptible to the blight.

While it appears that Indiana suffered a windborne invasion in 1970, agriculturists say it may overwinter and strike earlier in the growing season next year. If it does overwinter in the north, then its spread earlier in the crop year could lead to more extensive damage to those susceptible varieties. By 1972, sufficient blight resistant varieties should be available for the producer.

#### ECONOMIC IMPLICATIONS

The immediate economic consequence of the blight would be an expected drop in production for the 1970 corn crop. The various production loss estimates obviously affected current and future corn prices. Any assessment of this price situation depends upon the accuracy of crop damage estimates, the resultant loss of production and the reduction in the quality of the 1970 crop.

Producers who harvested early and sold early realized prices which reflected estimates of the overall 1970 crop production at that time. A first major price increase attributable to the blight occurred on August 10. Upward pressure of the prices intensified after that date, with future prices on August 21 about 25¢ a bushel above August 1 level. With an expected 4.8 billion bushel corn crop, corn prices seemed destined to settle to a \$1 to \$1.10 level at harvest. On August 24, the change in crop prospect reflected a \$1.35 to \$1.40 level. Speculators report that yield reductions on the order of 15% could result in corn prices of \$1.60 per bushel. Estimates of expected production for Indiana and the U. S. at various dates are shown in Figure 6.

Blight damage also affects test weight and kernel damage. Price reductions are generally realized by producers when kernels are for any reason graded as distinctly low quality corn. Much of the blighted crop was so affected.

The blight is expected to have major influences on seed corn availability and prices. Corn seed production from the 1970 crop was reduced about in line with the overall crop reduction. Producers will be seeking feed supplies which are resistant to blight. Such seed will bring premium prices.

Additionally, the reduced corn crop and resultant higher corn prices boost livestock feed prices and are reflected in increasing prices of livestock.

#### RESEARCH OBJECTIVES

On August 17, 1970 a remote sensing research project was initiated in Indiana to investigate the feasibility of identifying the various stages of the disease infestation on a basis of measurements collected with aircraft together with a relatively limited quantity of ground truth. Ancillary studies were already underway by other groups to relate the degree of infestation at a specific stage of plant maturity to yield reduction.

The application objectives for remote sensing in this situation would include:

- finding foci of infection outbreaks and mapping spread to predict and advise (1) spray programs and (2) harvest practices
- determining number of fields infected, the degree of infection for use with current climatological data to predict damage i.e., yield reduction
- determining the epidemiology characteristics of this disease

Investigations were conducted to determine the ability to identify significant levels of infection from photography with different film filter combinations and from spectral measurements made with the University of Michigan and Bendix Corporation airborne spectrometers. Photographic data was to be processed with standard photo-interpretative techniques and digitized multiband photography was to be subjected to computer analysis using pattern recognition techniques. Multispectral measurements were to be analyzed using the same pattern recognition techniques.

These data were to be collected at 7 to 10 day intervals to permit investigations of the temporal characteristics of radiation from blight infected areas.

As a result of the stage of the growing season when this research was instituted, it was only possible to measure tasseled corn. However, measurements of infected plants were collected at different stages of maturity due to the rather wide range of geographic latitude of the flightline from Lake Michigan to the Kentucky-Indiana border at the southernmost tip of Indiana.

#### EXPERIMENT DESCRIPTION

Figure 7 illustrates the test site for this research. A flightline following highways U. S. 421, Indiana 43, U. S. 231 and Indiana 57 was established as a representative test site in Indiana. The flightline proceeds from near Michigan City in northern Indiana 260 miles south to near Evansville at the southern end of the state.

Within this site, six intensive study segments were selected. Each segment was 8 to 10 miles long and approximately 1 mile wide. Ground truth information was collected in 30 to 60 corn fields in each segment. These intensive study areas were designated as A, B, C, D, E and F. In addition an area southwest of West Lafayette along the Wabash River was used as a control area.

Table I lists the various dates on which aircraft data over the test sites were collected, the aircraft system used, the geographic portion of the test site covered and the altitude of the aircraft system and the type of data acquired. Data was first acquired on August 19 with the last data being acquired on September 11. By September 11 much of the corn crop was near its final stage of maturity prior to harvest.

Data were to be collected by the University of Michigan aircraft and the NASA RB-57F on three occasions at 7 to 10 day intervals beginning August 24 and ending on September 11. Additional data was acquired by the Purdue University light aircraft photographic system, a Bendix

Aviation Corporation light aircraft system equipped with the Bendix multispectral scanner and an Air Force C-131 aircraft system with a 9 lens 70mm camera system. On September 5 the University of Michigan aircraft flew three 25 mile flightlines in Tippecanoe County in addition to the corn blight test site. Tippecanoe County was also designated for intensive study since much remote sensing data have been collected over the area during the last few years.

Corn fields in each of the intensive study areas were visited near the time of each flight. Area Crop Extension agents and Purdue staff members collected ground truth data on these fields. In addition, they identified crops in all other fields in the intensive study areas. Each corn field was rated as to the degree of blight infestation. Information was collected on the following items: leaf damage, ear and stalk lesions, ear and stalk rot and plant maturity stage. Additional comments on such factors as fertility deficiencies and drought damage were requested.

The specific analysis goals were to evaluate the feasibility of detecting the southern corn leaf blight by each of several remote sensing techniques and further to determine the detectability of various degrees of blight infection with the better of these techniques. The techniques under consideration were:

- standard photo-interpretative techniques applied to various forms of aerial photography;
- automatic pattern recognition techniques applied to digitized multiband aerial photography; and
- automatic pattern recognition applied to multispectral measurements.

Photographic frames were to be digitized using standard television Vidicon systems and drum type microdensitometers. A comparison was also to be made of multichannel black and white photography with spectral data obtained through color separation of three emulsion transparencies.

Pattern recognition techniques to be applied to these data had been incorporated into the LARSYSAA computer software programs by researchers at IARS over the past several years.

#### ANALYSIS AND DISCUSSION

Figure 8 and Figure 9 are color and color infrared photographs taken simultaneously from an altitude of 10,000 feet. The fields designated by the letter "A" are relatively healthy corn fields. The fields designated by the letter "B" contain moderately infected corn plants. Fields designated by the letter "C" contain severely infected corn plants. The field designated by the letter "D" is a freshly plowed field. A field of soybeans is designated by the letter "F". Three classifications of corn are clearly discernible in this photography.



The 35mm and 70mm color and color infrared collected by IARS/Purdue has proven useful for distinguishing these three categories of corn: (1) healthy corn, little or no infection; (2) moderately infected corn turning brown due to other influences; and (3) blight-killed corn or early maturing corn. An interpreter sees a mixture of green vegetation and dry, brown vegetation, that is, green corn fields with various levels of brownness. Preliminary analysis of this photography has shown it to be difficult, perhaps impossible, to distinguish brownness due to corn blight from brownness due to other causes, such as natural senescence. However, an interpreter should be able to deduce abnormal senescence if the date of planting and variety are known.

The 9-inch RC-8 camera color and color infrared photography and the 9-inch Zeiss imagery in color infrared taken simultaneously have been given intensive photo-interpretive effort. Intensive study region "D", south of Worthington, Indiana was selected for this concentrated attention because of its diversity of blight infected corn fields and because it coincided with the portion of the scanner data receiving initial attention. Figure 10 is the photograph taken with color infrared film with an RC-8 camera over this area. Figure 11 was taken simultaneously with a second RC-8 camera using conventional color film. Figure 12 was taken simultaneously with the Zeiss camera utilizing color infrared film. An overlay was made for the frames to be analyzed. Each frame covers an area about 10 miles square. Thirty-nine fields for which ground truth was available were located and coded according to field number, leaf damage, maturity stage and estimated yield loss.

It was possible to classify fields into three categories based on the severity of blight infection. Again, these categories correspond to the brownness of the vegetation. Initially, keys in the form of charts were evaluated. Ground cover defined by the keys consisted of soybeans, pasture, hay crops, trees, bare soil and diverted acres. The diverted acres group was considered to be any responses not otherwise defined. Corn fields in area D ranged from the dough stage to the ready-to-harvest maturity stage. Blight levels ranged from mild to very severe (1 to 5). Preliminary results with these keys provided accuracies that ranged from as low as 60 to as high as 99% accuracy. Photographic keys are now being developed to replace the chart. It is believed that the photographic key will produce considerable more accuracy since they will be based primarily on relative color. Copies of photographic data received at IARS generally vary in density and image quality from mission to mission, but appear to be suitable for the present research.

Figures 10, 11 and 12 are photographs taken simultaneously from approximately 60,000 feet with the two RC-8 cameras and the Zeiss camera utilizing color infrared, color and color infrared respectively. The photographs are of area D and were collected on August 24. The following features are called to the readers attention: The area designated as "1"

is a power station. Fields designated "2" and "3" are soybeans. The area incorrectly classified and designated by the number "4" is a pasture. Field 8 is a field of corn with blight severity level 4 and of maturity stage 7. Field 9 is corn with level 1 blight and maturity stage 8. The field marked 5 is corn with infection level 2 and maturity stage 4. Field 6 is corn with level 3 infection and maturity stage 5. There is also a seed field that has a stripe pattern and is designated by 7. The owner-producer of this seed field reported that "the 6 female rows with T cytoplasm were making 50 bushels per acre while the 6 rows with normal cytoplasm were averaging 100 bushels".

A frame of the Zeiss photography from the RB-57F flight was selected for automatic analysis. The IBM Corporation's Houston Scientific Center at Houston, Texas volunteered their Vidicon camera computer system to color separate a color infrared frame and subsequently digitize the frame. The striped seed field designated by the number 7 in Figure 10 was selected for this initial analysis using the digitized Vidicon data. Figures 13 and 14 are low-altitude photographs using, respectively, color and color infrared film of this field. Figure 15 shows a color-coded computer classification of this Vidicon-converted color infrared photo. The frame was digitized with a 256 X 256 point raster. The initial results of this effort were most gratifying.

On the basis of this success, fields of a large area are to be similarly digitized and analyzed. Small scale 70mm multiband black and white are to be scanned, digitized and overlaid so that a three-band data storage tape is created which represents the photograph in digital form. In addition to the Vidicon digitizing technique, color infrared photographs will be scanned and digitized in two other ways. In one case, color separations are to be formed in a printing process and a scanning reflectometer will then be used to convert and digitize the data. Thirdly, color infrared transparencies will be converted through the use of a conventional color separation scanner.

The Vidicon conversion system has certain desirable characteristics in that it can be easily used in conjunction with a human interpreter. An operator can focus the optics of the Vidicon system on those fields designated as corn and the system can then digitize that area and convert it to a machine-compatible form in near real time. The operator could be provided with a quantitative analysis of the points within that field. Considerable work will be done in the near future with these data. While LARS scientists are optimistic at this point that such automatic data processing techniques will provide useful information with multichannel photographic data in this application, LARS researchers are doubtful that such data will provide the precision data that can be obtained from airborne scanning spectrometers.

Thus far, analysis of the multispectral airborne scanner data has proven most successful. Data collected on August 24, 1970 consisted of two passes over intensive study areas A through F. Due to marginal weather, data from the first pass is unusable. Similar conditions caused the two southernmost segments of the northbound pass to be unusable. Analysis of segments A, B and C were discouraging. The fields for areas were divided into classes according to blight severity levels. Histograms of the resulting classes were clearly unimodal; the statistics were input to the divergence processor to determine the separability of severity classes. It was found that the classes were non-separable, even when 11 channels were used. More significant improvement was obtained using the thermal infrared channels in conjunction with the visible and reflective infrared channels. These data were collected very late in the day - 6:20 p.m. over area A and it is speculated that the low light levels were responsible for the radiation characteristics of these data. Attention was then shifted to area D from the northbound pass. These data were designated "D2". This area contained a reasonable number of fields with ground truth and which were not obscured by cloud cover. The distribution of corn fields between blight severity levels was also quite satisfactory for the initial investigations. Fields for which ground truth data were available were divided into classes according to blight severity levels. The classes proved to be multimodal, and so were divided into subclasses on the basis of comparisons of histograms of the fields. The result was a total of 15 training classes distributed among five blight severity levels. Level 0 was not represented in this area. The divergence processor was used to determine the best 2, 3, 4, 5 and 11 channels out of 12 visible and reflective infrared channels. Results indicated that as few as three channels could be used to obtain separability between blight levels. A classification using all 12 reflective channels produced results which were qualitatively very satisfactory. Quantitative tabular results were not obtained for this classification. The classification map indicates that most corn fields were classified to a very high degree of accuracy. The majority of errors in the classification resulted from "other" cover types being incorrectly classified as corn. The greatest offenders in this respect were pastures which were mixtures of green and brown grasses.

The analysis has been extended to include a total of 17 channels of data including three middle infrared channels over the range of 1 to 2.5 microns and two thermal infrared channels over the range of 4.5 to 14 microns which have been overlayed on the reflective data. Interestingly the thermal infrared channels did not assist in recognizing corn blight. The latter result is somewhat surprising since the thermal characteristics of relatively healthy green vegetation are surely significantly different from the thermal infrared characteristics of dry, diseased vegetation. It may be that the late afternoon hour in which the data were collected affected the observed response substantially. Further investigation along this line is required.

Summarizing, the analysis of the August 24, 1970 mission data was somewhat limited due primarily to problems arising out of marginal weather conditions at the time of the mission. Results obtained appear to indicate that the southern corn leaf blight can be detected in multi-spectral scanner data. Preliminary indications from these data are that up to five levels of blight severity can be discriminated at this stage of the growing season, although severely blighted corn may be difficult to discriminate from normally mature corn late in the growing season. Data in the .4 to 1.0 micron region are reasonably effective in detecting blighted corn; additional yield can be gotten from the near and middle infrared (1.0-2.5 micrometers). It is not yet clear whether the thermal infrared data (4.5-14.0 microns) is of value.

Data from the September 5 flight over segment D was selected for the next analysis. Data from 3000 foot altitudes was displayed on gray-scale computer printouts in the .62 to .66 and .8 to 1.0 micron wavelength bands. Ground truth information on corn blight severity levels and corn crop maturity was added to the listing. For classifications, the 4.5 to 5.5 and 8 to 14 micron bands were included. When all bands were processed with \$DIVERG, the best set of four channels included the 8 to 14 micron band. The 4.5 to 5.5 band did not appear to be as valuable as the 8 to 14 band and it was not used in the classification. The spectral bands selected were .55 to .58, 1-1.4, 1.5-1.8 and 8 to 14 microns respectively. When the thermal channels were not included, \$DIVERG picked the following spectral bands: .44, .62-.66, 1.0-1.4 and 1.5 - 1.8 microns, respectively. In order to make direct comparisons between classification with or without thermal overlay, the data was restricted to the 40° field of view of the thermal scanner from the University of Michigan system. Clustering techniques were used to derive seven classes of corn. These classes were combined with three classes of soybeans, pasture, bare soil and trees to produce a set of statistics which was used with the \$DIVERG and \$CLASSIFY programs. Classification of corn and soybeans was improved by clustering the two cover types together. A total of 23 classes were defined with corn and soybeans having several subclasses. Corn blight severity level 2, three classes; corn blight severity level 3, four classes; corn blight severity level 4, five classes; soybeans, six classes; harvested corn, one class; and trees, one class. It was noted that only a slight overall increase of accuracy of the blight levels was obtained using thermal channels. Still LARS researchers do not feel these results are conclusive. Classification accuracy for corn vs. other cover types were 89.6% correct. Accuracy for blight level categories vs. other cover types were as follows: severity level 2 - 90.5% correct, severity level 3 - 81.2% correct, and severity level 4 - 74.5% correct recognition accuracy. Other cover types were close to 100% and heavy categories were classified with 84% recognition accuracies.

At the time of this writing, analysis is being conducted of the data

collected over Tippecanoe County on September 5. Preliminary results of these data are equally encouraging.

This analysis together with results of other efforts have indicated that many of the subclasses of categories as seen in the spectral data results from influences of such factors as sun angle, view angle, etc. Currently, LARS researchers are preparing software programs to transform spectral measurements to measures which are more invariant with such conditions. Initially, this transformation is to be comprised of taking the ratios of the energy in each band to the total energy in all bands for each instantaneous measurement. These new data are to be evaluated with data collected in the corn blight research program.

Figure 16 shows a computer printout of the results of classification of the spectral data collected on August 24 over area D on the northbound pass. There was generally good agreement between the ground truth (indicated by large numerals) and the letter C and classification results. Non-corn areas were designated by dashes. Note as an example, the field directly below the power station. It is designated "C3". The ground truth for this field indicated that it was at infection level 3 and was in maturity stage 6 which is the dent stage.

#### SUMMARY

Photography collected over the north-south flightline revealed the widespread and variable affects of southern corn leaf blight in Indiana. Three levels of severity of the infection could be discerned from good quality color and color infrared photography. As many as five severity levels appeared to be detectable and classifiable with multispectral scanner data and pattern recognition analysis. These conclusions are preliminary in nature, however, having been obtained from a limited amount of good quality scanner data collected over a small geographic area. The degree to which these results could be generalized to more significant areas remains to be seen. Analysis of these data in subsequent months are pointed towards this objective. Nevertheless, it is already clear that remote sensing technology is applicable to the corn blight situation. Remotely sensed measurements collected from aircraft in conjunction with limited amounts of ground truth can be combined to permit the analysis of a vast amount of measurements collectably from an aircraft system. Not only does the presence of blight appear to be detectable but considerable information as to its severity level is discernible. Certainly the results of these investigations warrant further investigations of the applicability of remote sensing to the corn blight. Already, a considerable amount of knowhow related to applying remote sensing to this real situation is being accumulated. Certain techniques developed in the past are proving to be extremely useful while the deficiencies of other techniques are being demonstrated.

LARS researchers in cooperation with other interested scientists will continue the analysis of the data collected this past summer and their final results are to be reported upon the conclusion of the work.

Table I. 1970 CORN BLIGHT STUDY MISSIONS - AERIAL.

<u>DATE</u>	<u>ORGANIZATION/PLANE</u>	<u>AREA COVERED</u>	<u>DATA TYPE</u>
8/19	Purdue Univ. Beechcraft	S. River Road	Photography: 35mm color & color IR
8/21	Purdue Univ. Beechcraft	S. River Road; study areas south of Lafayette	Photography: 70mm color; 35mm color and color IR
8/24	Purdue Univ. Beechcraft	S. River Road; study areas north of Lafayette	Photography: 70mm color; 35mm color and color IR
	University of Michigan	N/S flight line study areas, 2 passes (3000')	Multispectral scanner; Photography: black and white; color; color IR
8/26	NASA RB-57	N/S flight line, 2 passes (60,000')	Photography (RC-8): Color and color IR Photography Zeiss: Color IR Photography (Hasselblads): Various film/filter combs.
8/27	Air Force C-131	N/S flight line (20,000')	Photography: 9 lenses, 70mm format
8/28	Bendix Corporation	N/S flight line study areas	Multispectral scanner
9/5	University of Michigan	N/S flight line study areas (3000', 5000'); flight lines 21,23,24 in Tippecanoe Co. (3000')	Multispectral scanner: Photography; black and white

Table I. 1970 CORN BLIGHT STUDY MISSIONS - AERIAL (con't.)

<u>DATE</u>	<u>ORGANIZATION/PLANE</u>	<u>AREA COVERED</u>	<u>DATA TYPE</u>
9/9	NASA RB-57F	N/S flight line, 2 passes (50,000')	Same as above (8/26) except longer lens on Hasselblads
9/10	Air Force C-131	N/S flight line	Same as above (8/27)
9/11	Purdue Univ. Beechcraft	N/S flight line study areas (3000' - 9000')	Multispectral scanner; Photography; black and white

1970 CORN BLIGHT STUDY MISSIONS - GROUND TRUTH

<u>DATE</u>	<u>ORGANIZATION</u>	<u>AREA COVERED</u>
8/26-8/27	Purdue University	N/S flight line study areas
9/3-9/4	Purdue University	Study areas D, E and F
9/8-9/9	Purdue University	Study areas A, B, and C; and flight lines 21, 23, 24 in Tippecanoe County
9/12-9/15	Purdue University	N/S flight line study areas

207



Table II. Ratings and Descriptions for Southern Corn Leaf Blight

Leaf Damage

0. No infection - healthy, no lesions present
1. V. Mild - few scattered lesions, mostly on the lower leaves
2. Mild - lower leaves have many lesions, only a few scattered lesions on upper half of plant.
3. Mod. severe - many lesions to the degree where dead or dry areas appear on leaves of lower half of the plant, scattered lesions on upper half.
4. Severe - lower leaves mostly dead, upper leaves are beginning to dry up.
5. V. severe - nearly all leaves are dead (brown) or dry.

Ear & Stalk Lesions

0. None
1. Few - less than 25% of surface affected
2. Many - more than 25% of surface affected

Ear & Stalk Rot

0. None
1. Mild - less than 25% of ears or stalks infected
2. Many - more than 25% of surface infected

Plant Maturity Stage

- |  |  |
|--|--|
| <ol style="list-style-type: none"> <li>1. Tasseling</li> <li>2. Pollenation</li> <li>3. Blister</li> <li>4. Milk</li> <li>5. Dough</li> <li>6. Dent</li> <li>7. Mature</li> <li>8. Ready to harvest</li> </ol> | <u>Comment: Reason for drying of plants<br/>(if occurring) other than blight:</u> <ol style="list-style-type: none"> <li>1. Normal maturity</li> <li>2. Drought damage</li> <li>3. Fertility deficiencies</li> <li>4. Other blights or diseases</li> </ol> |
|--|--|

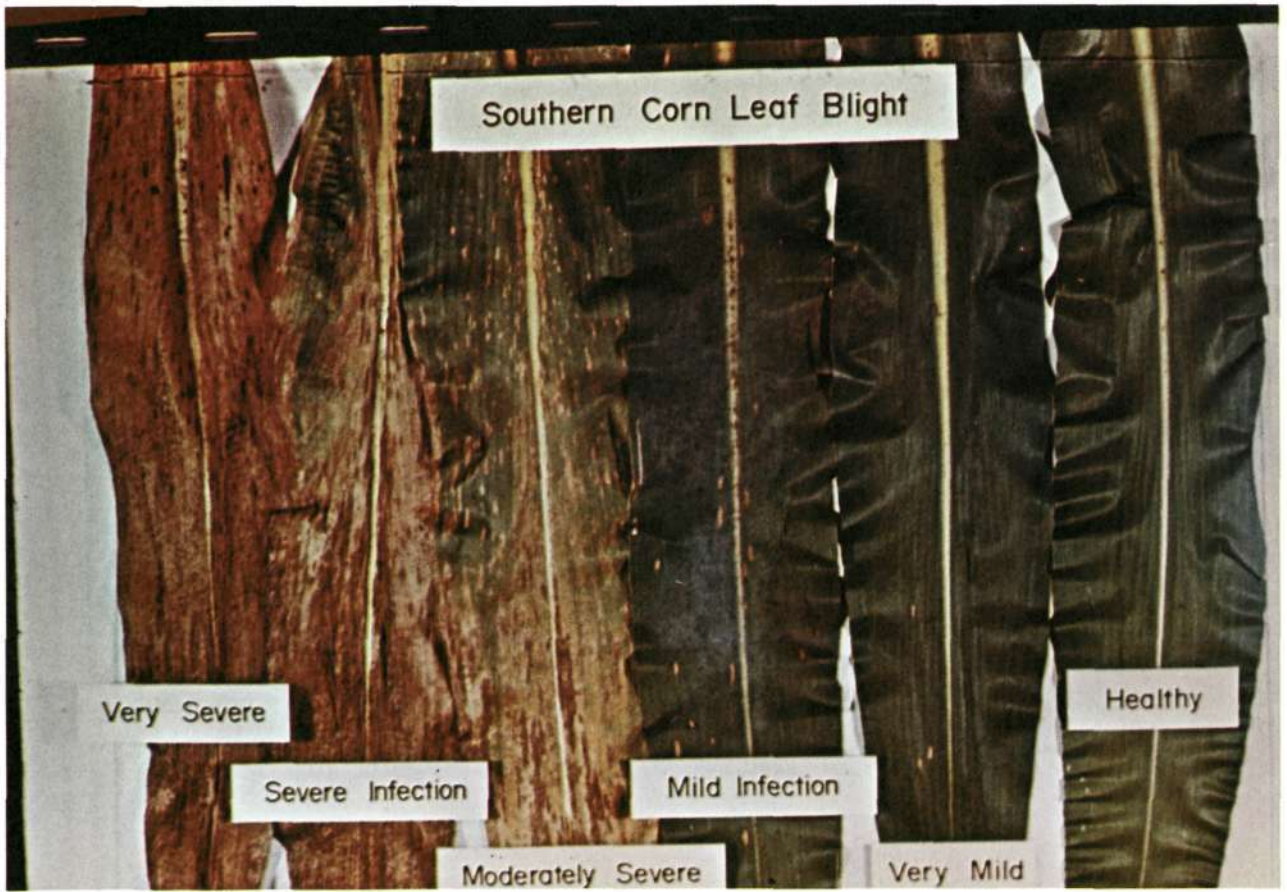


Figure 1



Figure 2a



Figure 2b



Figure 2c



Figure 3



111

Figure 4

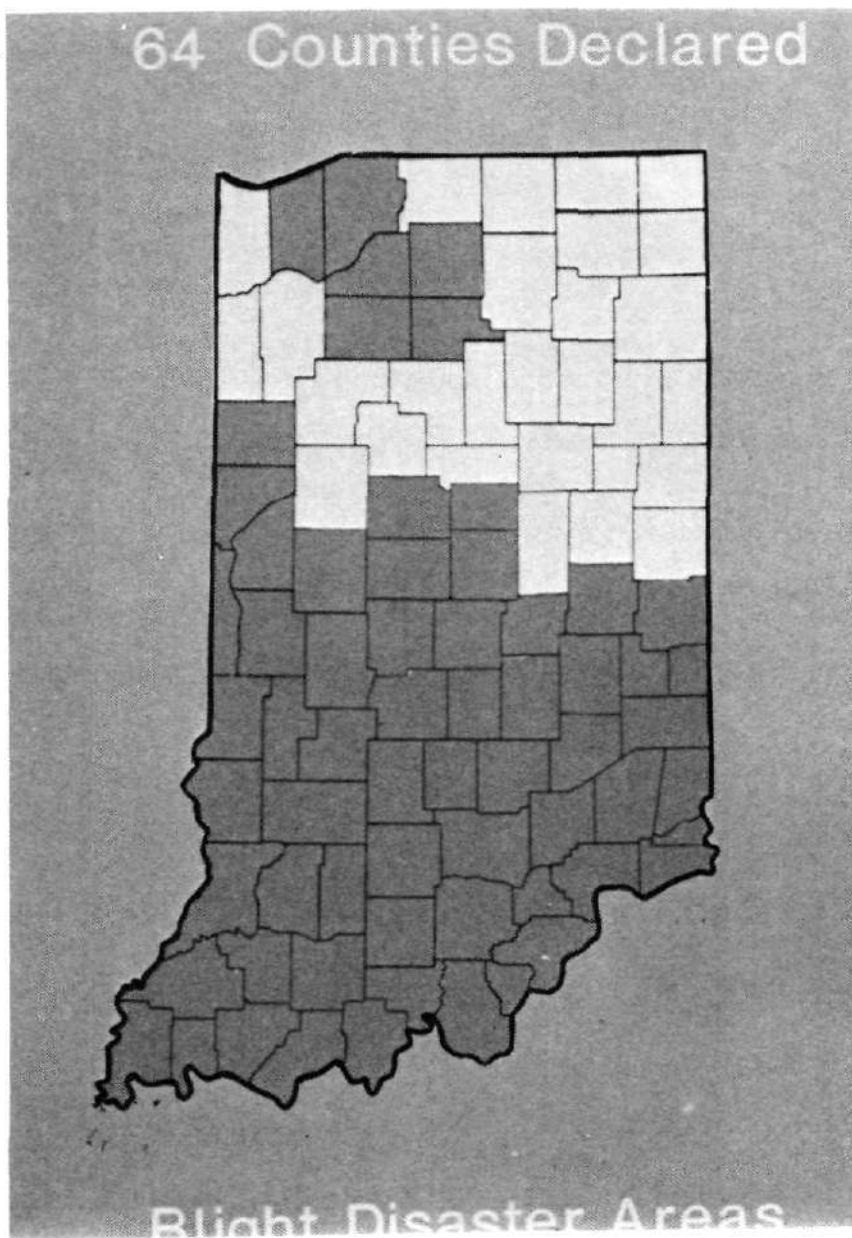


Figure 5



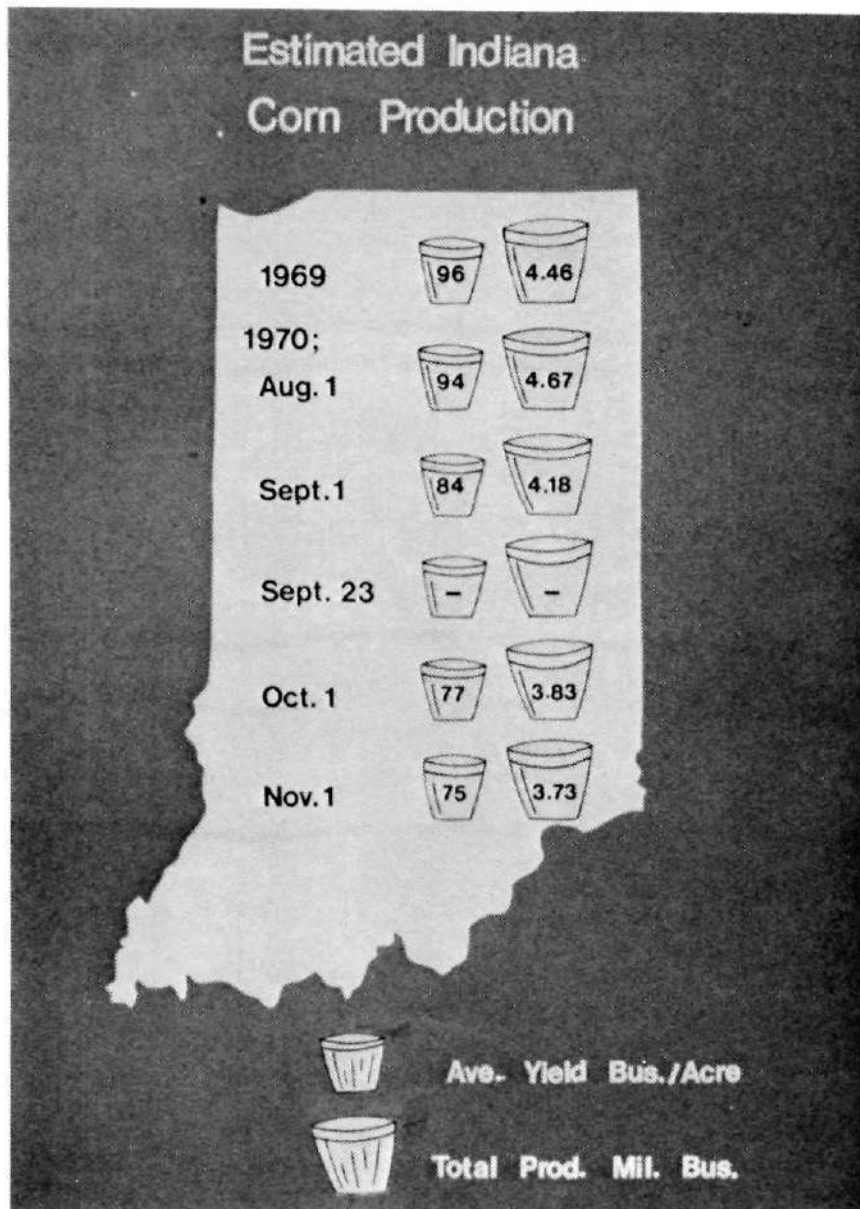


Figure 6a

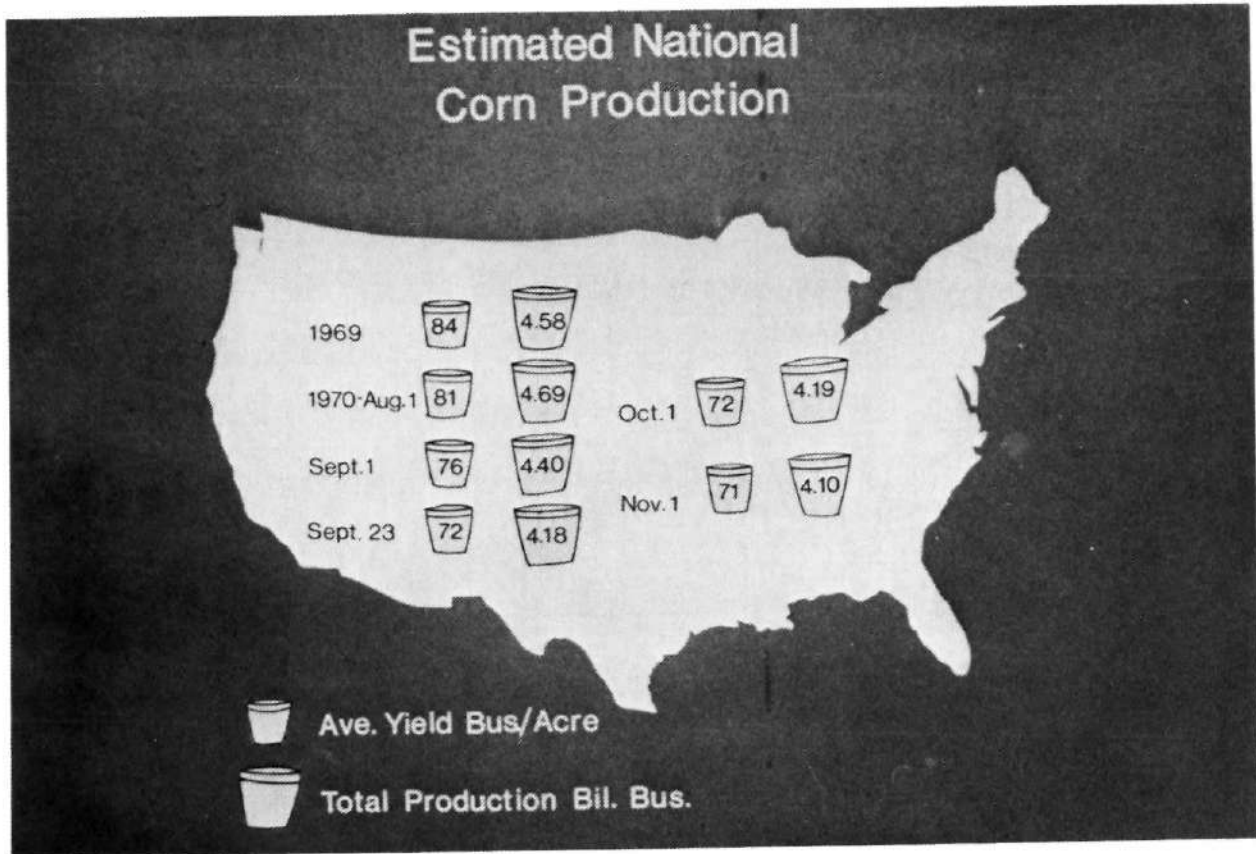


Figure 6b



Figure 7

Southern Corn Leaf Blight Flightline in Indiana flown in August, 1970 for the Laboratory for Applications of Remote Sensing (LARS) at Purdue University. Cross-hatched regions are intensive study areas.

619

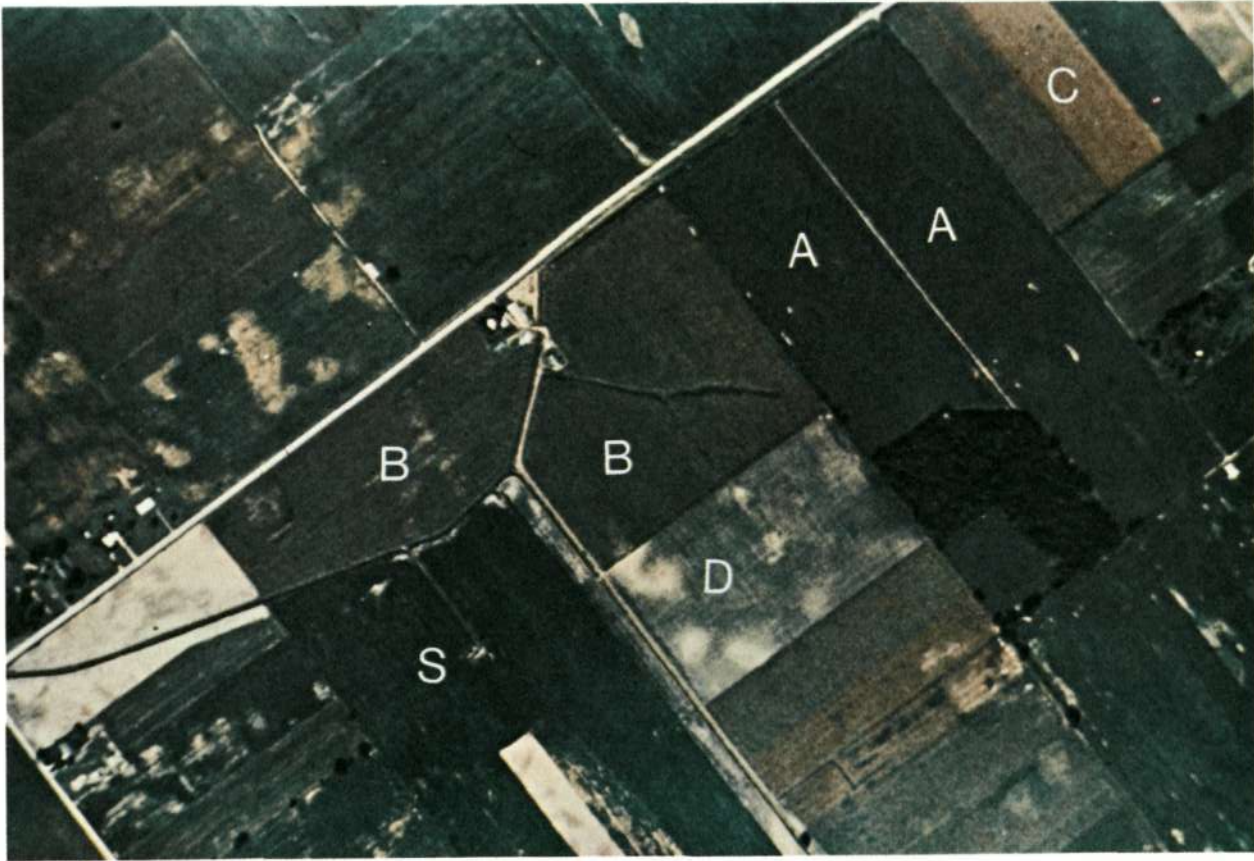


Figure 8

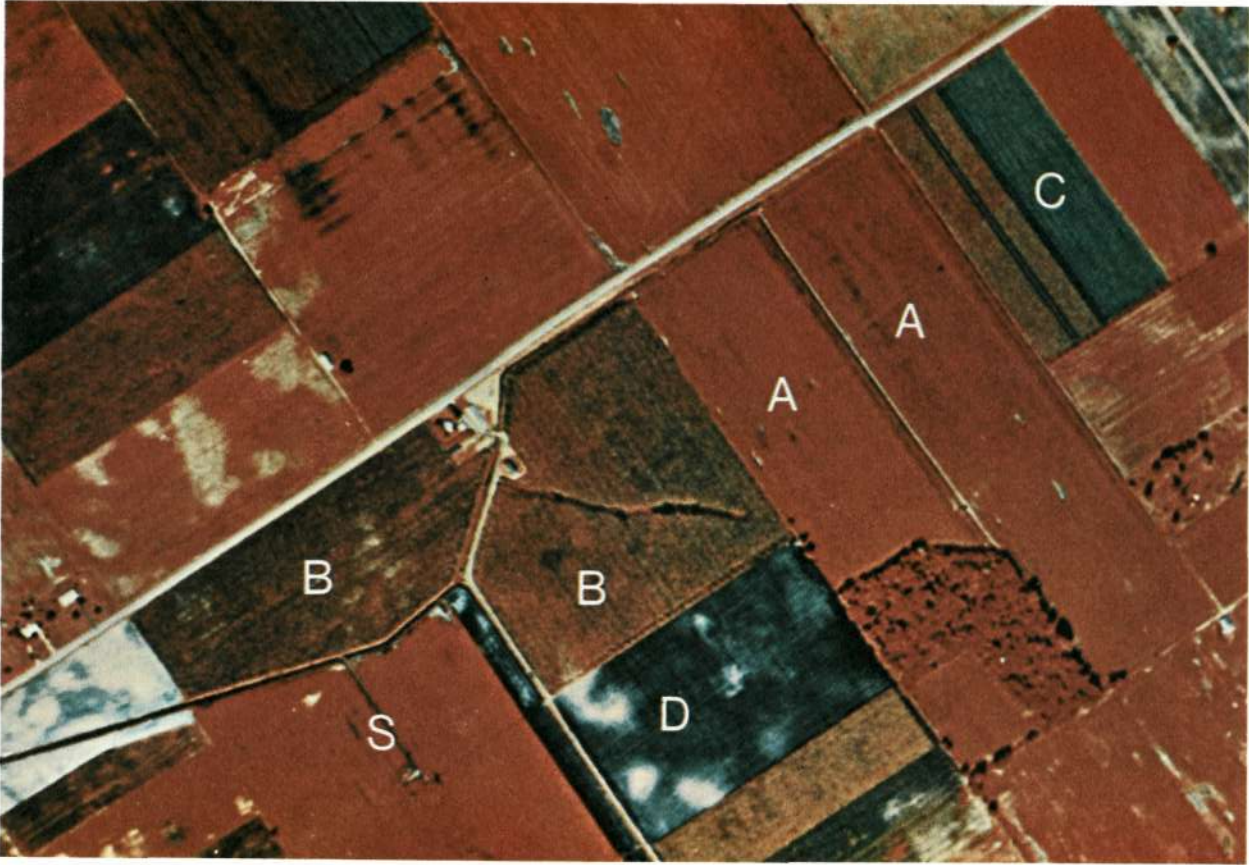


Figure 9

220



Figure 10



Figure 11



Figure 12





224

Figure 13

225

225

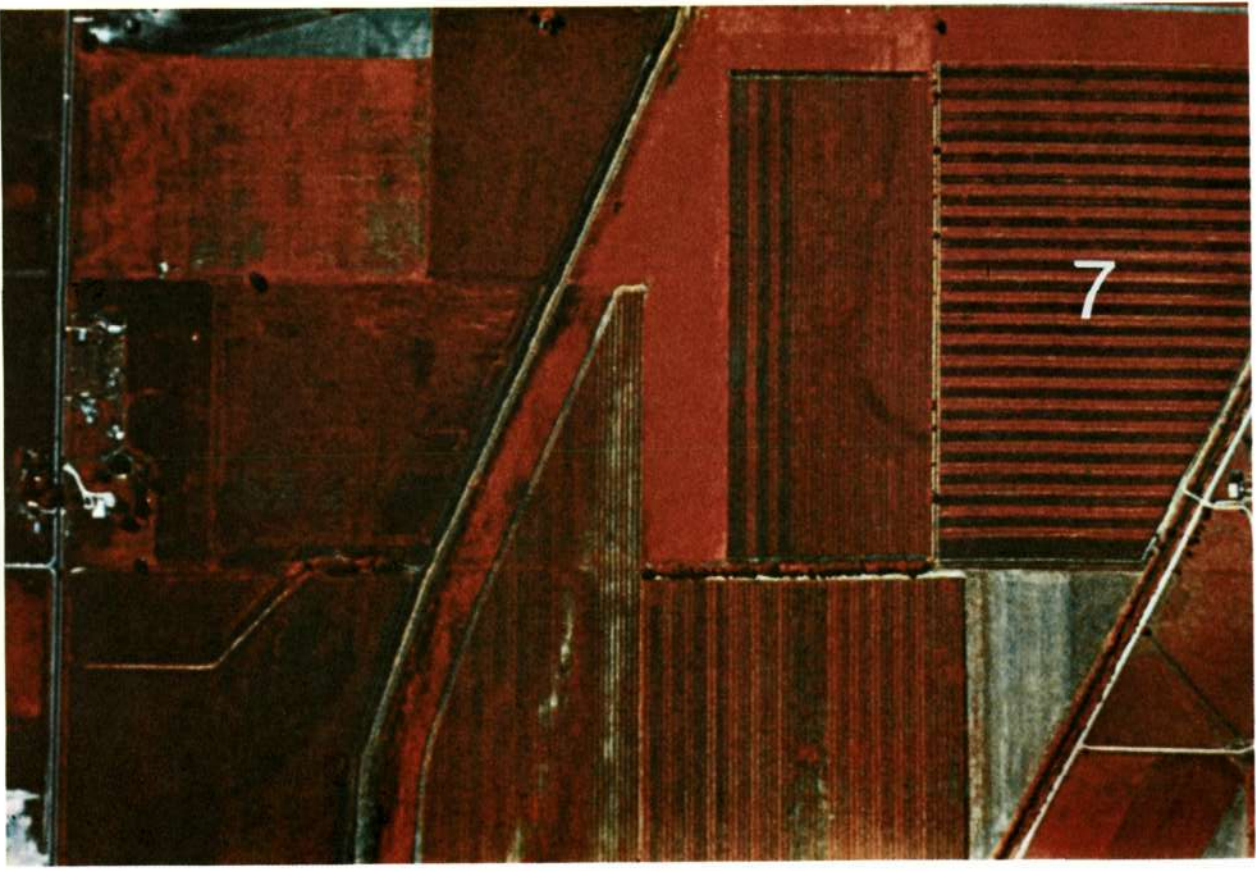


Figure 14

## Computer Analysis of Vidicon Digitized Color IR Film



Figure 15

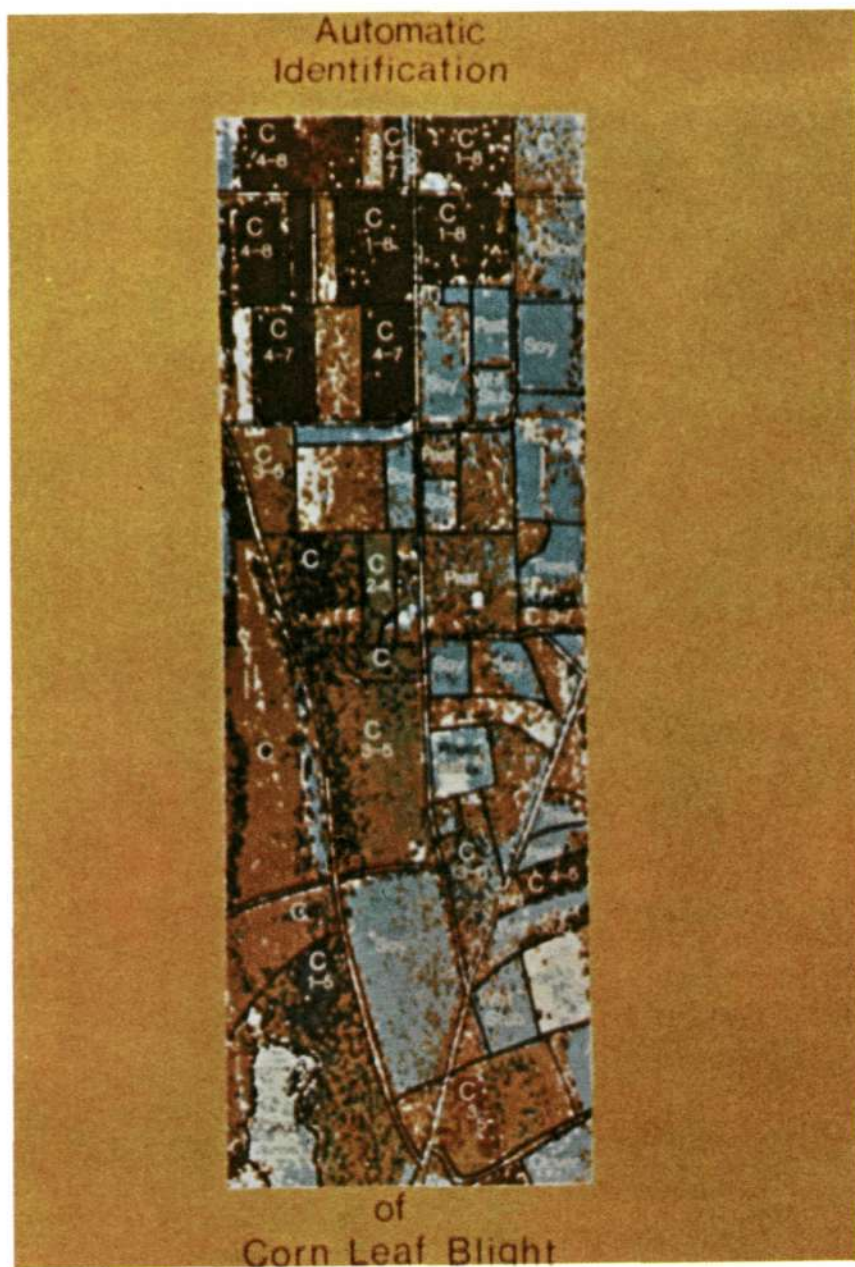


Figure 16

A SEMI-OPERATIONAL AGRICULTURAL INVENTORY  
USING SMALL-SCALE AERIAL PHOTOGRAPHY

William C. Draeger  
Lawrence R. Pettinger

Forestry Remote Sensing Laboratory  
School of Forestry and Conservation  
University of California  
Berkeley, California

INTRODUCTION

The photographic experiment performed by the Apollo 9 astronauts in March, 1969 provided the scientific community for the first time with high quality multiband space photography. These photos were obtained specifically for the purpose of developing improved capabilities for the inventory and evaluation of earth resources. One of the principal test sites for this experiment is Maricopa County, Arizona, chosen on the basis of its geographic location (proximity to existing remote sensing research centers and low latitude, which made vertical photography possible from the spacecraft), and the presence of numerous earth resources presenting intriguing possibilities for evaluation on small-scale imagery. The test site contains the urban complex comprising the city of Phoenix, extensive agricultural lands, and varied semi-arid desert and mountainous regions valuable as rangeland and watershed areas (see Figure 1).

In addition to the Apollo 9 photography, the site has been the subject of regular high altitude (60,000-70,000 feet flight altitude) multispectral aerial photographic missions made possible through the NASA Earth Resources Survey Program (Tables 1 and 2). These missions, the first of which coincided with the Apollo 9 experiment, have been flown at approximately monthly intervals during the ensuing year and a half.

It became apparent at the outset of the experiment that the nature of the photography which would be available -- i.e., broad aerial coverage on very small scale photos at regular intervals through a variety of seasonal conditions --

would make possible and, in fact, almost demand a regional-operational approach to the research. One of the primary advantages of using small scale aerial or space photography is that it affords a synoptic view of the earth's surface (i.e., large areas of land can be seen in their entirety on one or a very few images), suggesting a particular potential usefulness for conducting broad regional resource analyses. Furthermore, few actual resource inventories as presently undertaken limit themselves to a small area, but rather are usually geared to larger managerial or policy-formulation units such as entire watersheds, counties or states. Thus, most remote sensing surveys, when performed operationally, would probably also be geared to fairly large areas so as to provide maximum utility to the ultimate user. Finally, while the development of remote sensing techniques on small test sites is often quite useful, especially in the early experimental stage, findings of limited tests often cannot be directly applied to the larger operational case. In addition to the obvious problems stemming from increased interpreter fatigue and data handling requirements when large areas are the subject of surveys, the phenomenon of environmental variability often becomes a major factor to be dealt with in the design of information extraction techniques.

For these reasons, it seemed that one of the most meaningful experiments which could be performed with the imagery described above would be to attempt to make a survey of a particular resource for Maricopa County as a whole. By so doing, an attempt could be made to answer questions which would arise only in such a semi-operational survey and which must be solved before the full benefits which might accrue from the use of high altitude or space photography can be realized. In addition, it was hoped that such a study might provide some clues as to the procedures to be followed in evaluating synoptic imagery which will become available from the Earth Resources Technology Satellites, ERTS-A and ERTS-B, due to be launched in early 1972 and 1973, respectively, and the

manned Sky Laboratory, scheduled for launch in 1973.

While certainly any number of the varied resources of Maricopa County could be the subject of such a survey, none are more important or more amenable to the application of remote sensing techniques than agricultural crops. According to recent records, over 10 percent of the land in Maricopa County is under cultivation. The county provides roughly half of Arizona's agricultural crop production, and ranks third among all U.S. counties in gross value of such products. In addition, many of the crops grown contribute directly to the livestock and cattle feeding industry, in which Arizona ranks eighth nationally. The nature of agricultural cropland makes it especially well suited to such a study. By and large such land consists of discrete fields, each of which contains a fairly uniform stand of a particular type of vegetation that may vary quite rapidly in its phenological characteristics through a seasonal cycle. This characteristic presents an excellent opportunity for the development of techniques which could be quite valuable in their own right, and which hopefully could contribute to methods applicable to more variable wildland vegetation types. Finally, a very real need exists at the present time for inexpensive, accurate and up-to-date inventories of agricultural crops, as is evidenced by the extensive program carried out by the Statistical Reporting Service of the U. S. Department of Agriculture in cooperation with various state and county organizations. Thus it was decided that, at least initially, research efforts would be concentrated on the agricultural resources of the county.

#### PRELIMINARY TESTS

Detailed field studies were begun in two areas south of Mesa, Arizona in March, 1969 at the time of the Apollo 9 overflight. A 16 square-mile area containing more than 125 individual fields was chosen as the primary study area. This site was chosen because (1) it was contiguous, (2) it was easy to reach

for gathering crop data on a field-by-field basis, (3) it contained many of the important crop types found in the Phoenix area, and (4) it was imaged clearly on the Apollo 9 imagery as well as on most of the photos taken during subsequent aircraft missions. Additional data were also gathered during 1969 for another area of some 22 square miles (more than 250 fields) located in the same general region.

These two areas, totaling over 24,000 acres of agricultural land, were monitored at the time of each photo mission so that distribution and variability of crop type, crop development patterns, and crop signature could be adequately assessed. Coincident with each aircraft mission, each field was visited on the ground and notes were collected regarding crop type, condition, height of stand, and approximate percentage of ground cover.

An interpretation test was devised to establish whether crop type could be determined with greater accuracy using small scale Nikon aircraft photography than with Apollo 9 Hasselblad space photography. It was determined that overall interpretation results for crop identification were quite similar for both types of photographs (Carnegie, et al., 1969). Although the resolution of the high altitude photographs was greater than that of the space photographs of the same area, the improvement was not sufficient to permit detection of image detail which is necessary for increased accuracy of crop identification. For this reason, it is believed that valid inferences regarding the interpretation of crop type on space photography of Apollo 9 quality can be drawn from the conclusions based on studies of high altitude aircraft photography.

The most serious limitation to developing useful crop identification techniques lies in the variability of crop type and cropping practices. Any factor which affects the distribution, development and vigor of a crop will affect its photographic signature, and thus may influence the success with which that crop can be consistently identified. Thus some a priori knowledge



or assumptions regarding these factors is necessary before practical interpretation techniques can be developed. Our conclusions regarding these factors were as follows:

1. Crop type and distribution. It is generally true that agricultural practices in an area are relatively stable and that totally foreign crops are rarely introduced. For this reason, interpretation keys can be devised for particular crops in a specific area with little fear that certain crops will totally disappear or that new crops will suddenly be introduced in large number. These generalizations were found to be valid for the main crops grown in Arizona during a recent 4-year period.

2. Seasonal development. Documentation of the seasonal development of crops is important for determination of optimum times of the year for crop type discrimination. Both within-season and between-season variability will affect the specification of optimum dates for obtaining photography. Knowledge of crop sequences and of the variations which affect these sequences must be understood. For agricultural areas, the cyclic changes and the approximate dates when they occur are best summarized in a table or chart known as a "crop calendar." Tone values of individual fields (as seen on photographs of a given date) can be related to the stage of maturity of the crops on that date, as summarized in the crop calendar. The calendar can then be used to determine either (1) at what single date a particular crop type has a unique signature that could be discriminated from signatures of all other crops, or (2) what combination of dates for sequential photography would best permit identification of that crop type.

3. Crop signature. Since little field detail is discernible at the scale and resolution of the high altitude Nikon photographs which were studied during 1969, Photographic tone or color became the critical factor for identification. Either unique spectral signatures must exist at one date so that

individual crop type can be identified, or else sequential patterns of tone or color must exist such that crop type can be distinguished on the basis of changing patterns (i.e., bare soil to continuous cover crop to bare soil) at particular dates throughout the year.

Interpretation tests were administered to determine the value of multi-date and multiband photography obtained during 1969 for crop identification. The following conclusions are suggested by the results of these tests: (1) similar results were obtained from Apollo 9 and high altitude photographs, (2) better results were generally obtained from Infrared Ektachrome photos than from Panchromatic-25 photos, (3) improvement in percent correct identification resulted from the selection of specific date(s) for particular crops (e.g., May for identifying barley), and (4) the concurrent identification of crop types using March 12, April 23 and May 21 Infrared Ektachrome photographs produced the most substantial improvement in overall identification.

#### DEVELOPMENT OF THE SEMI-OPERATIONAL SURVEY

##### A. Determination of Film-Filter Combinations

As discussed earlier, and based on the above results, it was decided that a semi-operational countywide inventory of one or more particular crops would provide the most logical extension of the techniques initially developed for only one small portion of Maricopa County. The decision to perform this survey for barley and wheat was made for the following reasons: (1) small grains (of which barley and wheat are the only major varieties in Maricopa County) account for approximately 20% of the crop acreage in Maricopa County and thus are important crops for which agricultural statistics are currently prepared using conventional techniques, (2) these crops mature and are harvested within the first half of the calendar year, coincident with the time period for which monthly NASA aircraft missions were scheduled during 1970

and, (3) our previous results indicated that the highest percentage correct identification of any crop was achieved for barley (90% using Infrared Ektachrome photos and 91% using Pan-25 photos) by selecting the appropriate month (May) for conducting the test. For these reasons, it was felt that a survey for barley and wheat would provide the greatest opportunity for initial success using a previously untried technique. Plans for similar surveys for the other major crops will be undertaken in the future when the technique has been refined.

Previous studies of multiband high altitude Nikon aerial photographs of the Phoenix area (Carnegie, et al., 1969; Pettinger, et al., 1969) indicated that, of the 1969 photo dates available (March 12, April 23 and May 21), May photographs were best for identifying small grains; also, of the film/filter combinations available -- Infrared Ektachrome (8443)/15, Panatomic-X (3400)/25, Panatomic-X (3400)/58, and Infrared Aerographic (5424)/89B -- Infrared Ektachrome/15 and Panatomic-X/25 produced the best photo interpretation results. The following table summarizes the interpretation results obtained for the identification of barley in the 1969 study which used high altitude photography taken in March, April and May, 1969 (there were not enough wheat fields in the test area to design a valid test for that crop):

PHOTO INTERPRETATION TEST RESULTS FOR BARLEY IDENTIFICATION  
ON HIGH ALTITUDE PHOTOGRAPHY (1969)<sup>1</sup>

	Panatomic-X/25			Infrared Ektachrome/15		
	March 12	April 23	May 21	March 12	April 23	May 21
Percent Correct	34	31	91	33	57	90
Percent Commission	38	44	3	34	24	6

<sup>1</sup>Carnegie, et al., 1969.

In the table above, percent correct data indicate the percentage of actual barley fields in the test area that were correctly identified by the interpreters. Percent commission data indicate the percentage of the total number of fields

identified as barley which were actually some other crop type.

Studies of crop development patterns during early 1970 (data collected from FRSL field surveys and extracted from Arizona Crop and Livestock Reporting Service newsletters) indicated that the small grain crop was developing in a normal manner. Thus general conclusions based on crop calendar information, which indicate that small grains are mature and most easily distinguishable from other crops during the month of May, were held to be applicable for 1970.

Although barley could be consistently identified on May 21, 1970 photos, wheat and alfalfa were sometimes confused. It was discovered that the identity of fields in question usually could be established by noting the appearance of these same fields on June 28, 1970 photos. For this reason, photos taken on May 21 and June 28 were ultimately provided for the survey.

Previous conclusions regarding optimum film type were not totally acceptable in terms of the 1970 survey. In addition to the four film types tested using high altitude photos in 1969, a color film, namely Ektachrome MS (2448), was also available which had not previously been evaluated. Also, the scales of the RC-8 photos (1/120,000) and Hasselblad photos (1/500,000) which were to be used in the survey were different from the Nikon photos (1/950,000) obtained in 1969; the resolution of the 1970 imagery was also improved. Because of these differences, it was felt that a new test should be made, based primarily on May 21, 1970 photos, to determine the optimum film/filter combination for the identification of various types of crops.

The following film/filter combinations were tested:

<u>CAMERA</u>	<u>FILM/FILTER</u>	<u>SCALE</u>
RC-8	Ektachrome MS Aerographic (2448)	1/120,000
RC-8	Infrared Ektachrome (S0117)/15	1/120,000
Hasselblad	Plus-X Aerographic (2402)/25	1/500,000
Hasselblad	Plus-X Aerographic (2402)/58	1/500,000
Hasselblad	Infrared Aerographic (2424)/89B	1/500,000

It was realized at the outset that the scale differences between RC-8 and Hasselblad imagery would probably affect the success with which crop types could be distinguished. However, imagery at these two scales represented all that was available. The scale difference was accepted as another constraint within which the test must be administered.

Fifteen photo interpreters of equal ability were randomly placed in one of five three-man photo interpretation groups. Five four-square mile test plots were chosen from thirty-two sample plots located in the area (Figure 3). The photo interpretation tests were administered so that (1) each interpreter group would interpret each of the five film/filter types, (2) each test plot would be interpreted using each of the five film/filter types, and (3) no interpreter group would interpret a test plot more than once. Thus each plot was interpreted fifteen times for a total of seventy-five photo interpretation tests.

$$5 \text{ Test Plots} \times \frac{5 \text{ F/F Types}}{\text{Test Plot}} \times \frac{1 \text{ Interp. Group}}{\text{F/F Type}} \times \frac{3 \text{ Interpretations}}{\text{Interp. Group}} = 75$$

Four additional plots were chosen which would provide training and reference materials. These plots were selected from different parts of the test site and represented a sample of the variability which would be encountered during the test as well as during the semi-operational survey. These training plots were presented to the interpreters in pairs, so that one plot in each pair could be studied with ground data, for familiarization, and the second could be used as a "practice test" (without reference to ground data for that plot). Each interpreter corrected each of his own practice tests, thus learning where correct and incorrect identifications had been made. In each of the training plots, the identity of the crop type in each field was made known so that the interpreters could determine which other crop types were likely to be mistaken for barley and wheat. It is to be emphasized that all of the interpreters used in

this experiment were skilled photo interpreters who previously had worked with tests of this type. Hence each of them was asked to study the training material provided and decide for himself which criteria would be used for crop identification.

After each interpreter had trained himself to interpret a particular film/filter combination, he began the interpretation of the test plot assigned to him for that combination (each interpreter examined each of the five test plots on a different film/filter combination). Sample test results appear in Figure 2. That figure also contains (1) photo examples of each of the film/filter combinations, (2) the interpretation results for one of the three interpreters in the group assigned to the Ektachrome image, and (3) the correct identification of the fields in that plot.

For each of the five test plots, a map showing field boundaries was provided. Although a measure of the consistency with which interpreters can estimate field acreage would be needed to evaluate results from the semi-operational survey, it was decided that tests for identification would be separated from tests for acreage estimation. In addition, prior field delineation makes possible more rapid evaluation of crop identification per se, for the interpreter is interested only in identity of fields and not their measurement. Training in these two tasks would be given once the final team of interpreters (only three out of fifteen who took the tests) had been chosen for the semi-operational survey.

In order to ascertain the optimum film/filter combination for inventorying wheat and barley, the results of the tests were analyzed in three ways: (1) mean-of-ratio variance analysis, (2) analysis of variance for % correct, and (3) analysis of variance for % commission error.

Mean-of-Ratio Test: In the actual crop survey, the acreage estimates by the photo interpreters were to be adjusted by using a mean-of-ratio estimator.

This estimator is defined as:

$$R = \frac{\text{actual acreage of wheat (or barley)}}{\text{interpretation acreage estimate for wheat (or barley)}}$$

This estimator is calculated for each of the thirty-two sample plots, the mean of the ratios calculated, and the acreage estimation for the entire survey area adjusted by multiplying by this mean. The optimum film/filter type, therefore, is that in which the variance of ratios is lowest, (e.g., if the interpreter consistently interprets 60% correct, the adjusted total will be more accurate than if he fluctuates between 70% and 90%.

Variances of the ratios using each of the five film/filter types under consideration were tested at the 95% level of significance. No differences were found between the ratio variances for barley. For wheat, however, Ektachrome, Pan-25, and Pan-58 constituted a homogeneous sub-group of low variance, with Infrared Ektachrome and Infrared-89B showing significantly higher variances. Thus, either Ektachrome, Pan-25 or Pan-58 would be optimum for the operational survey under this criterion.

% Correct and % Commission Error Analyses: Analyses of variance were run to ascertain whether there were differences (at the 95% level of significance) between the film/filter types in terms of % correct acreage and % commission error. If significant differences were found, the types were to be ranked using the New Duncan's Multiple Range Test.

The film/filter types proved to be different in terms of both % correct and % commission error for both barley and wheat, and hence were ranked. The results are illustrated below. Percent correct is ranked with highest values at the top and % commission error with lowest values (and hence "best") at the top. However, types which are included within the same bracket are not significantly different according to Duncan's test at the 95% level of significance.

BARLEY INTERPRETATION

% Correct	% Commission Error
Ektachrome	Ektachrome
Infrared Ektachrome	Infrared Ektachrome
Pan-25	Pan-25
Infrared-89B	Pan-58
Pan-58	Infrared-89B

WHEAT INTERPRETATION

% Correct	% Commission Error
Infrared Ektachrome	Ektachrome
Ektachrome	Infrared Ektachrome
Pan-58	Infrared-89B
Infrared-89B	Pan-25
Pan-25	Pan-58

Based on the results of both the mean-of-ratio analysis and the analyses of % correct and % commission error, Ektachrome film was chosen as the film/filter type to be used for the operational survey. Although in some cases it was not significantly superior to other film types, it was the only type which was at least in the superior group in all tests.

B. Field Data and Sampling Rationale

Attempting to administer a photo interpretation survey involving the entire county immediately presented a number of problems not faced on the 16 square-mile study area. The principal questions raised were: (1) Will a sample provide a satisfactory estimate of crop acreage, or is 100% interpretation required? (2) Will stratification lead to a more accurate estimate? (3) How much ground information will be required for interpreter training and



for evaluation of the interpretation? In an attempt to answer several of these questions simultaneously, the agricultural area within the county was delineated into six strata based wholly on their appearance on the Infrared Ektachrome Apollo 9 photo. Thirty-two plots, each consisting of a square, two miles on a side, were allocated to the strata on the basis of proportional area, and plot centers were located randomly (Figure 3). Maps of each plot showing field boundaries were drawn based on their appearance on earlier high-flight photography, and each plot was visited by a field crew at the time of overflights for the months of April, May and June 1970.

Information gathered in this manner included the category of crop growing in each field, the condition of the crop, the percent of the ground covered by vegetation, crop height, and the direction of rows, if any (see Figures 4 and 5). The crop category code which was used, and which appears in Appendix II of this report, is an adaptation of a coding system originally developed by the U. S. Government for categorizing land use (U. S. Urban Renewal Administration, 1965) and subsequently refined for specific use in agricultural land use mapping by researchers at the University of California, Riverside (Johnson, et al., 1969).

In order to facilitate access to this information pertaining to each of the more than 2500 fields present in the thirty-two four-square-mile sample plots (comprising a total of more than 80,000 acres), field data were punched on computer cards. Programs were then written which made possible the compilation of data by stratum, cell, crop type, and date, and which provided for subdivisions or consolidations of fields over time. Thus data are available not only for each date of photography, but for the sequential changes in crop type and condition through the growing season as well.

Based on a knowledge of the distribution and variability of crop acreage thus obtained, tests were conducted regarding the value of stratification

based on gross appearance on space photography, and the possibility of sampling within the agricultural areas to obtain overall crop acreages for the county. Analyses of variance indicated that no significant differences existed between strata in terms of acreages of major field crops, thus indicating that stratification would not improve acreage estimates. In addition, calculations indicated that the acreage distribution of major crops was so variable that for any plot size, extremely large samples would be necessary in order to assure acreage estimates that would satisfy accuracy requirements. For example, in order to estimate the acreage of wheat with a standard error of  $\pm 10\%$  of the total acreage using a plot size of four square miles, a 75% sample would be necessary.

Thus, it was decided that the most efficient and realistic method of estimating crop acreage would entail a 100% photo interpretation of the agricultural areas, with ground data being gathered for thirty-two four-square-mile plots only. In this way photo interpretation results could be compared with the ground conditions on the field plots, and the overall photo interpretation results adjusted as appropriate using standard ratio sampling procedures.

Some problems were also encountered in the development of the method of compilation of photo interpretation data. First of all, in order to make a measure of interpretation accuracy, interpretation findings must be tied to some actual unit of land area. However, the preparation of detailed field boundary maps from small-scale photos by the interpreter, while possible, would constitute an extremely time consuming task. Also, the tabulation of interpretation data on the basis of numbers of fields is not necessarily indicative of accuracy of acreage estimates which in most cases is the item of interest to the ultimate user. Furthermore, to evaluate "number of fields" data, the researcher must assign arbitrary weight to "correct", "omission error" and "commission error" values, a task which in many cases might best be left to the discretion of the ultimate user of the information.

In order to avoid these problems while still collecting data which would be as meaningful as possible, it was decided to require the interpreter merely to grid agricultural areas into regular square-mile cells (thus making possible direct comparisons with ground data on the thirty-two sample plots) and to tabulate estimates of the acreage of barley and wheat in each cell without regard to the specific location of individual fields.

The agricultural areas within Maricopa County were divided into three nearly equal portions, with one interpreter assigned to each area. The interpreters, chosen on the basis of high scores on preliminary tests, were first trained using photos and ground data maps of areas which they would not interpret later. Training included both identification of wheat and barley, and estimation of field acreage. The interpreters were then supplied with Ektachrome photos for May 21 and June 16 (scale 1/120,000) of their test areas, as well as maps indicating township boundaries. Each township (nominally a six-mile square, but not invariably so because of ground survey errors made many years ago) was located on the test photography and interpreted as a unit, section by section. For each section the interpreter recorded total acreage of wheat, barley, and all cropland. (Deductions from cropland included farmhouse-barn complexes, freeways, major canals, and general urban and developed areas, but did not include secondary service roads or local irrigation ditches.) In addition, each interpreter was asked to interpret one township in another interpreter's area, as well as to repeat the interpretation of one township in his own area without reference to his earlier results.

## RESULTS

The results of the semi-operational survey were obtained in the following manner:

1. Each interpreter's estimates of acreage of barley, wheat, wheat and barley combined, and total cropland for the sample plots within his area

were compared with the actual acreages for each of the plots as determined by on-the-ground surveys.

2. Ratios of actual acreages to interpretation acreages for each category were calculated for each interpreter, and this ratio was used to adjust the results for the entire area as estimated by each interpreter by the formula

$$\hat{Y}_I = Y_{PI} \times R$$

where  $\hat{Y}_I$  = estimate of total acreage of category within an interpreter's area

$Y_{PI}$  = initial photo interpretation of acreage within an interpreter's area

$R$  = the correction ratio as derived from the sample plots.

3. The category estimates for the three interpreters were summed to form a total county estimate.

4. Sampling errors were calculated for the various category estimates by each interpreter as well as for the overall county estimates in order to give an indication of the accuracy of the crop estimates. In calculating the overall county statistics, each of the three interpreters' areas was handled as an individual stratum.

A summary of the survey results is presented below (Tables 3 through 6).

Note that sampling error is presented as a percentage figure calculated by:

$$\text{Sampling Error \%} = S_{\hat{Y}} / \hat{Y}$$

where  $S_{\hat{Y}}$  = standard error of the estimated acreage

$\hat{Y}$  = estimated acreage.

A correction ratio greater than 1 indicates that the interpreter underestimated the acreage of that category, while a ratio less than 1 indicates that he overestimated the acreage.

INTERPRETATION TIME

INTERPRETER	TRAINING TIME	INTERPRETATION TIME	AVERAGE TIME/TOWNSHIP
1	8 hr. 55 min.	26 hr. 20 min.	1 hr. 20 min.
2	7 hr. 30 min.	13 hr. 40 min.	1 hr. 03 min.
3	6 hr. 30 min.	28 hr. 05 min.	1 hr. 02 min.
TOTAL	22 hr. 55 min.	68 hr. 05 min.	1 hr. 08 min.

Table 6

The results of greatest interest are, of course, the estimated acreages of each category for the entire county, and their accuracies. In this case, however, there are no reliable statistics gathered in the conventional manner with which to compare these results. While the Statistical Reporting Service does publish monthly estimates of crop acreages for the U. S. as a whole and for individual states, their methods are such that no accurate estimates are available for specific counties until months after the time of harvest, and even then they are much less accurate than the state and national estimates. This, of course, only serves to emphasize the potential value of estimates obtained by means of the methods described here. It is possible, however, to discuss the accuracy of the estimates by reference to calculated measures of statistical reliability derived from the sample data.

The sampling error (standard error of the estimate expressed as a percent of the estimate) for barley was 11% and for wheat was 13%, while the figure for both barley and wheat combined was 8%, indicating that a good deal of error resulted from a confusion of the two small grain crops. This same phenomenon is evident in the correction ratio figures. In general, the interpreters underestimated barley and overestimated wheat, while they were only slightly low in their estimates of the two grains combined. These results indicate

that considerable improvement in the measurements could be realized if a more definite differentiation between the two small grains could be made. Nevertheless, the accuracies as shown are quite encouraging, especially considering the rapidity with which the data were produced, the relatively large area interpreted, and the lack of any other reliable estimates with which they could be compared.

In the table listing the individual interpreter's accuracy levels (Table 5) it can be seen that one of the interpreters had a significantly higher error for both barley and wheat than the other two interpreters, but all three were nearly equal for barley and wheat combined. This indicates that while this one interpreter had more trouble differentiating between the two crops, he did nearly as well as the others in distinguishing the two small grains from all other field conditions. Furthermore, the large differences in performance point up the importance of screening and training interpreters before undertaking operational surveys. The sampling error could have been significantly reduced if the performance of the one "inaccurate" interpreter had been equal to the other two. Also, all three interpreters indicated that their confidence in their interpretations increased as they progressed through the survey. Certainly any fully operational survey would include considerably more interpreter training than has been undertaken in this study.

#### CONCLUSION

The stated purpose of the experiment was to investigate the feasibility of performing inventories of agricultural resources using very small scale aerial or space photography. Further, it was hoped that by remaining cognizant at all times of the constraints that would be faced when carrying out an operational survey, findings would be more valuable than those resulting from the more usual limited-area tests.

Certainly the results to date are encouraging on two counts: (1) the questions posed initially are being answered, i.e., the very practical problems of

an operational survey are being faced and solutions are being found, and (2) it would seem that a fully operational agricultural inventory using space photography is not beyond the scope of present technology.

Probably the biggest problems that will be faced in establishing a functional inventory system are those concerning logistics and data handling. For example, it will be necessary to ensure that ground crews are at the proper place at the proper time over widely scattered areas in order to provide calibration data. Imagery must be obtained at specific times to permit differentiation among various crop types; interpretation of large areas must be performed rapidly to ensure that the information is not outdated before it is available; and interpretation results must be compared with calibration data and the necessary adjustments made before distribution.

Finally, data must be provided, not at those times and for those geographic units which lend themselves well to the data gathering techniques, but rather at times and for area units which are geared to user requirements as nearly as possible.

However, most of the data handling problems are not much more complex than those faced by government agencies gathering agricultural data by more conventional means at the present time. Furthermore, a number of systems are presently being developed which, it is hoped, will possess a capability to automatically extract image data from aerial or space photographs, perform crop identification functions, combine this information with other parameters keyed to the same geographic coordinate system, and produce graphical or tabular output in a wide variety of desired formats. It appears that such systems would lend themselves particularly well to agricultural surveys wherein nearly all the image interpretation is based on tone or color discrimination (a function much more accurately performed by a machine than a human interpreter) rather than complex deductive decisions. In fact, it is planned that further studies of agricultural inventory method by the Forestry

Remote Sensing Laboratory will involve an investigation of the extent to which automatic image interpretation and data handling methods can contribute to operational surveys of the type described in this report.

#### LITERATURE CITED

- Carneggie, D. M., et al. 1969. Analysis of earth resources in the Phoenix, Arizona area. In an Evaluation of Earth Resources Using Apollo 9 Photography. R. N. Colwell, et al. Final Report. NASA Contract No. NAS-9-9348. University of California, Berkeley.
- Johnson, C. W., et al. 1969. A system of regional agricultural land use mapping tested against small scale Apollo 9 color infrared photography of the Imperial Valley. University of California, Riverside. USDI Status Report III, Tech. Report V, Contract 14-08-0001-10674.
- Pettinger, L. R., et al. 1969. Analysis of earth resources on sequential high altitude multiband photography. Special Report Forestry Remote Sensing Laboratory, University of California, Berkeley. 31 December 1969.
- U. S. Dept. of Commerce, Urban Renewal Administration. 1965. Standard Land Use Coding Manual. January 1965.



SENSOR PLATFORM	APOLLO 9	HIGH ALTITUDE AIRCRAFT	NASA RB57F AIRCRAFT
ALTITUDE	126 NAUTICAL MILES	60,000 FEET	60,000 FEET
CAMERA SYSTEM	<u>70mm Hasselblad Cameras:</u> Pan-25, Pan-58, IR-89B, and IR Ektachrome-15 film-filter combinations (S065 Experiment)	<u>35mm Nikon Cameras:</u> Pan-25, Pan-58, IR-89B, and IR Ektachrome-15 film-filter combinations <u>70mm HyAc Cameras:</u> Pan-25 and IR Ektachrome- 15 film-filter combina- tions	<u>70mm Hasselblad Cameras:</u> Pan-25, Pan-58, IR-89B, and IR Ektachrome-15 film-filter combinations <u>RC-8 Cameras:</u> Ektachrome-HF3, and IR Ektachrome-15 film-filter combinations
DATE			
<u>1969</u> March 8-12 April 23 May 21 July 15 August 5 September 30 November 4 December 6  <u>1970</u> January 13 February 6-8 March 16 April 22 May 21 June 16 July 28	X	X* X X X X X X	X       X X X X X X X

\* 70mm Mitchell-Vinten cameras were substituted for 35mm Nikon cameras on this date only.

Table 1. Tabulation of the types of imagery obtained through the NASA Earth Resources Survey Program for the Phoenix test site during 1969 and 1970.

248

MISSION/DATE	Zeiss (1/60,000)	RC - 8 (1/120,000)				Hasselblad (1/500,000)					
	IR EKTA-15	EKTA	IR EKTA-15	IR-89B	PAN	PAN-25	PAN-58	IR-89B	EKTA-HF3	IR EKTA-15	OTHER
116/Dec. 6	S0117/D	S0278/2E	----	----	2402/12	3400	3400	----	2448/UV-17	S0180/15	----
118/Jan. 13	S0117/D	2448/HF-3	----	S0246	----	3400	3400	2424	2448/UV-17	S0180/15	----
120/Feb. 6-8	S0117/D (also S0278/2E)	S0278/2E	S0117/15	S0246	2402/12	3400	3400	2424	S0278/2E	S0180/12	3400/12
123/Mar. 16	S0117/D	2448/HF-3	----	S0246	----	2402	2402	2424	----	S0117/15 S0117/15 +CC30B	----
127/Apr. 22	S0117/D	2448/HF-3	----	S0246	----	2402	2402	2424	----	S0117/15	----
129/May 21	S0117/B	2448/HF-3	S0117/15	----	----	2402	2402	2424	S0278/3	S0117/15	----
131/Jun. 16	S0117/B	2448/HF-3	S0117/15	----	----	2402	2402	2424	S0278/3	S0117/15 S0117/15 +CC30B	----
139/Jul. 28	2443/15	S0-397/2E	2443/15	----	----	2402	2402	2424	S0168/2E	S0117/15 S0117/15 +CC30B	----

Table 2. Detailed Summary of NASA RB57F Imagery (by film-filter combination) Obtained Between December 1969 and July 1970 for the Phoenix, Arizona Test Site.

ACREAGE ESTIMATES AND SAMPLING ERROR

CATEGORY	TOTAL ESTIMATE (ACRES)	SAMPLING ERROR
Barley	50,044	11%
Wheat	41,714	13%
Barley and Wheat	92,207	8%
All Cropland	452,000	3%

Table 3

RATIO CORRECTION FACTORS

INTERPRETER	BARLEY	WHEAT	BARLEY AND WHEAT	ALL CROPLAND
1	1.1225	.9846	1.0481	.9913
2	1.1131	.9012	1.0352	.9809
3	1.1234	.9388	1.0309	1.0094

Table 4

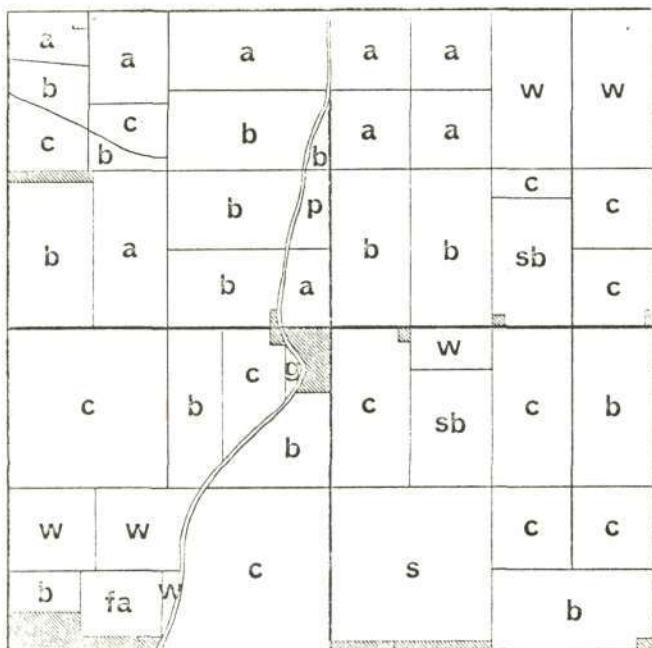
SAMPLING ERROR OF INTERPRETERS

INTERPRETER	BARLEY	WHEAT	BARLEY AND WHEAT	ALL CROPLAND
1	18%	17%	14%	5%
2	30%	32%	16%	3%
3	14%	21%	11%	6%
TOTAL AREA	11%	13%	8%	3%

Table 5



Figure 1. This enlargement of Apollo 9 Infrared Ektachrome frame AS9-26-3801 shows the Phoenix test site where the semi-operational agricultural inventory was performed. The city of Phoenix appears in the right center, surrounded by extensive agricultural lands and wildlands valuable as rangeland and watersheds.



Crop Type Map: Phoenix Plot 2-1  
Date: May 22, 1970

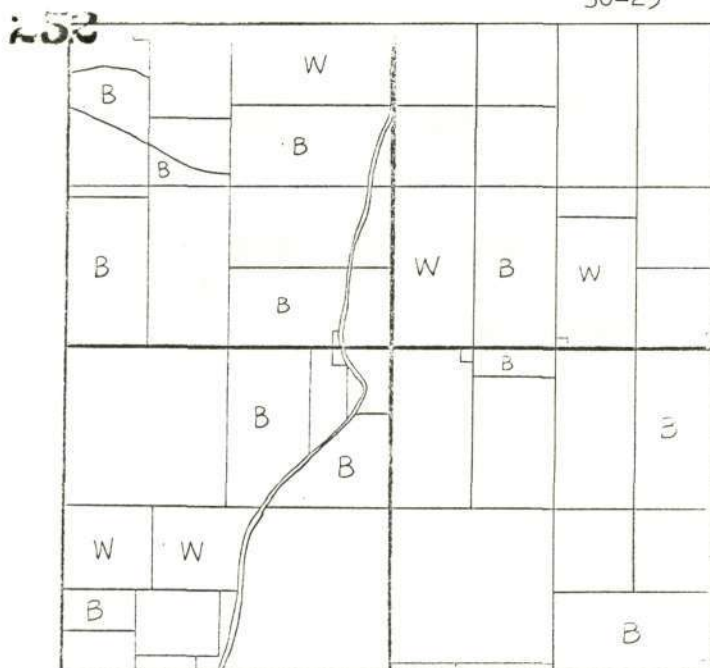
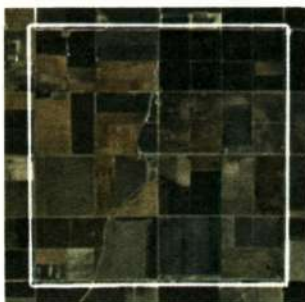


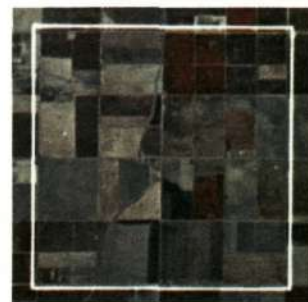
Photo Interpretation Answer Sheet  
Phoenix Plot 2-1

CROP SYMBOL KEY

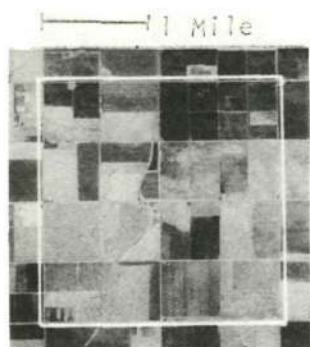
a = Alfalfa  
b = Barley  
c = Cotton  
fa = Fallow  
g = Grass  
p = Pond  
sb = Sugar Beet  
w = Wheat



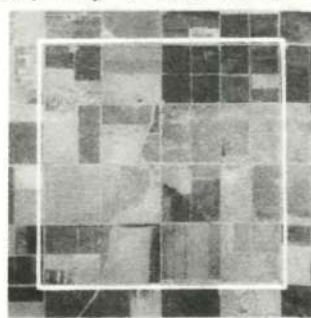
Ektachrome MS (2448)  
Filter: HF3 + 2.2 A.V.



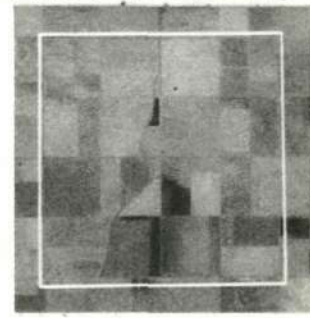
Infrared Ektachrome (S0117)  
Filter: Wratten 15



Plus-X Aerographic (2402)  
Filter: Wratten 25



Plus-X Aerographic (2402)  
Filter: Wratten 58

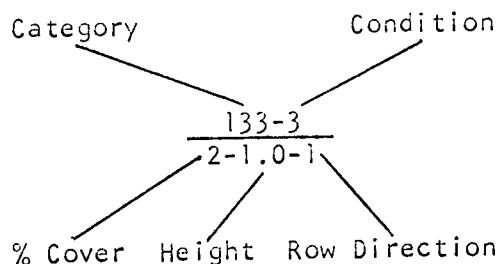


Infrared Aerographic (5424)  
Filter: Wratten 89B

Figure 2. Appearing in this figure are test images (obtained May 21, 1970), ground data, and sample interpretation test results for one 4-square-mile test plot. Ground data, top left, were collected in conjunction with the high altitude photo mission. The Ektachrome and Infrared Ektachrome photos above are reproduced at the same scale as the original transparencies. The black-and-white photos have been enlarged from their original scale (1/500,000) to match the color photos. Each of the test images was interpreted by a group of three photo interpreters. Results from the Ektachrome plot, as obtained by one interpreter (top right), are as follows (based on number of fields): barley - 85% correct, 8% commission; wheat - 40% correct, 33% commission.



Figure 3. This black-and-white enlargement of an Apollo 9 space photo shows the portion of Maricopa County for which the semi-operational survey was performed (compare with Figure 1). The location of each of the 32 4-square-mile plots selected for ground survey at the time of each NASA overflight is indicated on the overlay.

Condition Code

1 seeded  
 2 young  
 3 mature  
 4 dry (not harvested)  
 5 cut back (e.g., alfalfa)

% Cover Code

1 80-100%  
 2 50-80%  
 3 20-50%  
 4 5-20%  
 5 0-5%

Height: Indicate average  
 crop height in feet  
 and tenths.

Row Direction Code

1 N-S	
2 E-W	—
3 NW-SE	\
4 NE-SW	/

Figure 4. This coded fraction represents a typical field code as recorded by field crews gathering information pertaining to the sample plots. Field category codes appear in Appendix II of this report, while the coding system used for recording other field parameters is described above. The example shown here represents a mature alfalfa field one foot in height, with 50-80% ground cover and rows running in a north-south direction.

CELL 2-1  
 DATE 7-20-70  
 CREW SLW

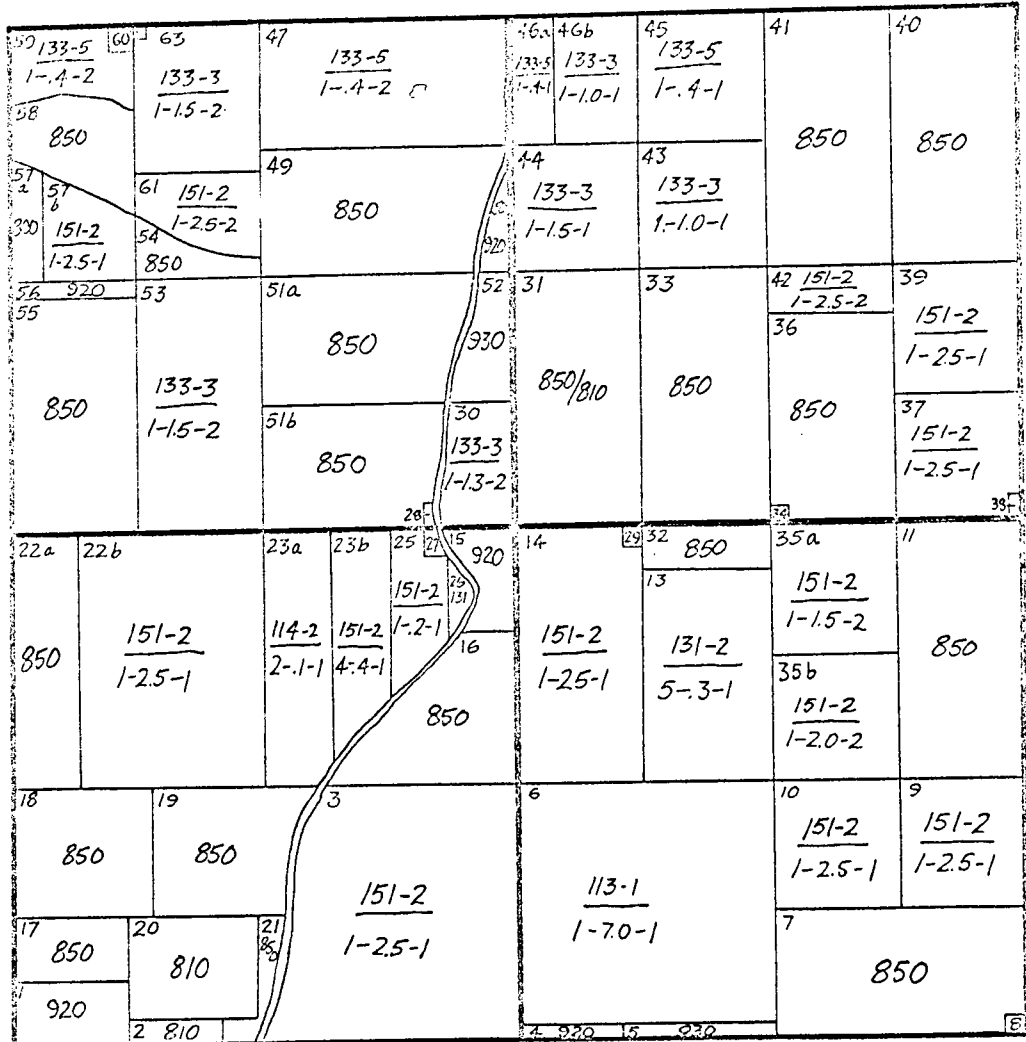


Figure 5. This map contains field data collected for one of the 4-square-mile plots in Maricopa County at the time of a NASA high altitude overflight. The coded fraction in each field is explained in Figure 4 (and a complete listing of the field category codes appears in Appendix II). Representative high altitude aerial photographs of this cell appear in Figure 2. Computer storage of survey data collected at the time of each flight on a field-by-field basis facilitates sequential analysis of crop patterns as well as evaluation of photo interpretation test results.



## IMAGE RESOLUTION: ITS SIGNIFICANCE IN A WILDLAND AREA

Donald T. Lauer  
Randolph R. Thaman

Forestry Remote Sensing Laboratory  
School of Forestry and Conservation  
University of California  
Berkeley, California

INTRODUCTION

An experiment has been carried out to determine the information content of simulated space photos as a function of various levels of image resolution. The study was performed using a series of images taken of the San Pablo Reservoir Test Site (NASA Test Site #48), each purposely degraded optically to a different level of ground resolvable distance (GRD). This research seeks to answer two questions. First, given low resolution ERTS data within the next few years, how well can a skilled image analyst identify the major vegetation-terrain types found to occur within the chaparral-hardwood-grassland cover type of California? Second, if certain vegetation/terrain types cannot be consistently identified on simulated low resolution imagery, what level of image resolution is required that would allow a skilled interpreter to discriminate between various types?

Until the recent series of Gemini and Apollo photographic experiments, remote sensing research regarding application of spaceborne imagery to earth science problems was based mainly on an analysis of airborne imagery. These studies, combined with conjectured reasoning, have led to a wide variety of opinions as to the usefulness of satellite imagery. Fortunately, the recently procured space photos are providing authentic data from which definitive experimental results can be derived. Experiments to date, however, suffer from two limitations: (1) existing and available spaceborne imagery as obtained by the Mercury,

Gemini and Apollo astronauts give coverage only of the lower latitudes of the United States -- due to the constraints of the orbital path -- thereby limiting the kinds of resource phenomena that might be studied, and (2) each study, to our knowledge, has simply sought to determine what kinds of useful information might be extracted from space photos with only minimal consideration to the informational requirements of users. The work reported herein not only applies to a resource inventory problem indigenous to the mid-latitude western United States but also approaches the resource inventory problem from a user's standpoint, i.e., given a particular problem, what kinds of spaceborne imagery (in this case, what level of resolution) is required so that useful information can be extracted from the imagery.

#### SIMULATED SPACE PHOTOGRAPHS

Probably the most common method of simulating synoptic view space photography is to prepare an uncontrolled photo mosaic from conventional vertical aerial photos of a large area and then reproduce the mosaic on a single sheet of film. Low resolution is obtained by greatly reducing photographic scale. Photographic tone, however, is disrupted throughout the final image due to haloing and fall-off common to each photo within the mosaic. This causes tonal mismatches in the mosaic that are easily confused with tonal differences between resource features. Since image tone or color, as opposed to image detail or stereo parallax, is the primary criterion used by the image analyst when interpreting low resolution space photos, a photo mosaic reduced in scale does not provide a realistic simulation of a space photo. Another method that is sometimes used is to enlarge or reduce the photo, as desired, with a projector that is purposely "out of focus" to the extent necessary to produce the desired image degradation. The problem which arises from this method is that linear features such as roads or boundaries between different vegetation types, because they are

out of focus, become displaced or spread out and if defocused enough will become double images taking up a greater areal extent on the resultant degraded image than they do on the original. To overcome such problems a technique has been developed for degrading aerial photography in such a way that image sharpness can be manipulated while image color or tone remains nearly unaltered. The technique entails reproducing an original high-altitude, small scale photograph with a flat diffusing plate of frosted acetate placed at various positions between the original photo and the copy camera (see Figure 1). In this manner, natural terrain features up to several hundred feet in size can be made to disappear or reappear on the copy photograph depending upon the distance between the acetate plate and the original photo. The scale of the copy photo is a function of copy camera focal length and distance from the copy camera lens to the original photo.

In this case, a single Ekta Aero Infrared photograph taken of the San Pablo Reservoir Test Site from an altitude of 15,000 feet above terrain by the NASA Convair 240 on June 1, 1968 was chosen for detailed analysis. More than 50 photo reproductions were made of this image, each time slightly changing the position of the diffusing screen thereby spanning the range of GRD from a few feet, as seen on the original photo, to several hundred feet on the most degraded image. Objects of known size seen on different backgrounds were examined on each image. In this way a resolution value in terms of ground resolvable distance was assigned to each image. A representative value was assigned to both high contrast features (e.g., dark toned tree crowns on a light toned grass background) and to low contrast features (e.g., dark toned tree crowns on a dark toned brush background). For testing purposes, five images ultimately were selected, each representing a distinct level or range of image resolution which was quite different from all others (see Figures 2, 3, 4, 5 and 6).

### INTERPRETATION TESTS

Tests were conducted using these five images to determine their information content in terms of portraying identifiable tonal and/or textural signatures for various terrain and vegetation types (i.e., Monterey pine, Pinus radiata; blue gum eucalyptus, Eucalyptus globulus; mixed hardwoods -- oak, bay, madrone, buckeye, chaparral -- coyote brush, poison oak; annual grasslands -- wild oats, soft chess, brome, ryegrass, fescue; water bodies -- reservoirs, lakes, ponds; and non-vegetated areas). Emphasis should be placed on the fact that these tests were oriented towards a single, well-defined user informational problem -- vegetation/terrain mapping. A group of 15 highly skilled photo interpreters was drawn from the pool of personnel working at the Forestry Remote Sensing Laboratory. These individuals were divided into five groups of three interpreters per group and each group analyzed a single image on which 100 randomly chosen points of known identity were to be identified. Consequently, three sets of data were generated for each image yet each interpreter analyzed only one image.

Prior to analyzing each of the test images the photo interpreters were trained in such a way as not to bias the test results. A photo interpretation key plus accompanying aids were carefully prepared in which the identifying characteristics of each vegetation/terrain type were presented in (1) a summary table, (2) a dichotomous word description and (3) selective photo illustrations. The several photo examples appearing in the key were selected from an adjacent but analogous area and enough examples were made of each type showing the range in tone or color variability exhibited by each type.

### INTERPRETATION TEST RESULTS

Interpretation results for the various images appear in tables below the corresponding images in Figures 2 through 6. These tables show the cumulative results of the three interpreters (data along rows for each type) along with the actual ground truth (data down the columns). For example, consider the case of

chaparral in Figure 2. First reading down the column marked (C), out of a total of 48 plots known to be chaparral, 41 were correctly identified, however, 5 were called mixed hardwoods and 2 non-vegetated, resulting in an omission error equal to 7. Reading across the row marked (C), out of a total of 59 plots called chaparral by the interpreter, 41 were correctly identified, however, 7 mixed hardwoods plots, 8 grassland plots and 2 non-vegetated plots were incorrectly identified as chaparral, resulting in a commission error equal to 18. Hence, of 48 chaparral plots, 41 were correctly identified yielding a percent correct rating of 86%. Percent commission error for chaparral is computed by dividing the number of chaparral commission errors made by the interpreter, 18, by the total number of plots called chaparral, 59; i.e., 33%. Interpretation results, expressed in percent, are presented in tabular form in Figures 8 and 11 and graphically in Figures 9, 10, 12 and 13.

#### DISCUSSION OF TEST RESULTS

The results presented here indicate that although there is definite decrease in interpretability as ground resolvable distance increases, some valuable information can be gained by using even the poorest photography. The greatest decrease in interpretability between two adjacent photographs (with respect to resolution) was between Image 1 and Image 2. On the best photography, Image 1 (5-10 ft. GRD), 90.3% of all plots were correctly identified whereas on Image 2 (50-100 ft. GRD) only 70.0% were correctly identified. This decrease seems to be due to an almost complete loss of shape, shadow, and textural differences on Image 2 which were present on Image 1. Due to color similarities, shape and textural differences are very important for the identification of Monterey pine (MP), eucalyptus (E), mixed hardwood (MH), and chaparral (C); MP and E both appear dark red in color and MH and C both appear bright red. It is interesting to note here that in a somewhat similar study conducted last year in the Phoenix area, it was concluded that no improvement was made in the

identification of agricultural crops on high altitude aerial photography (5-10 ft. GRD) versus Apollo 9 photography (200-300 ft. GRD). In that study, however, large homogeneous fields exhibiting unique tone signatures were interpreted, and those signatures, seen on both types of photography, were not significantly influenced by size, shape, shadow and texture characteristics of individual plants. Such identifying characteristics are useful only on extremely high resolution imagery, exhibiting a GRD of less than two feet.

The poorer results from the interpretation of Image 2 can be attributed for the most part to both omission and commission errors within the four above vegetation types. With the exception of MP, the percent correct for each of these four vegetation types decreased by amounts ranging from 28.6% for MH to 43.8% for C. The decrease in percent correct for MP was only 7.4% but the increase in percent commission for MP was 42.5% (from 3.6% to 49.0%) and for the remaining three types the increases in commission errors were as follows: MH - 22.3%, C - 31.8%, and E - 0.0% (no commission errors for E). As can be seen by the above figures (from Figure 8), the loss of shape and texture as identifying characteristics affected the interpreters' ability to correctly identify MP, E, MH, and C. The absolute values corresponding to the above mentioned omission and commission errors can be seen in Figures 2 to 6.

The interpretation results also are given in Figure 8 for the remaining vegetation and terrain types: annual grassland (G), water bodies (W), and non-vegetated areas (N). The interpretability of these types was not as affected by loss of textural evidence as that of MP, E, MH, and C. The percent correct and percent commission errors for these categories were not found to be significantly different for Images 1 and 2 at a .05 significance level. On the other hand, for both MH and C there was a significant difference for the percent correct between Images 1 and 2 at a .05 significance level and also a significant

difference in commission errors between the images for MP, MH and C at a .05 significance level. (A one sided t-test was used on the absolute values found in Figures 2 to 6.) Any assumptions based on the figures relating to eucalyptus probably have little significance because the sample size was quite small. The great variation for eucalyptus can be seen by the figures in Figure 8.

The above trends, i.e., the importance of shape and texture for the correct identification of broadleaf or coniferous vegetation types (MP, E, MH and C) and the relative unimportance of shape and texture for the identification of G, W and N are also shown in the graphs in Figure 9 and 10. In Figure 9 the steep drop in percent correct for E, MH and C can be seen whereas there is relatively little drop for G, W and N from Image 1 to Image 2. Figure 10 shows the very steep rise of commission errors for MP, MH and C and the relatively gradual rise of G, W and N.

Apart from the initial drop-off in percent correct between the first two images, the relative drop-off for percent correct for the next three images is more gradual. This gradual decrease in interpretability is to be expected, especially when trying to identify different types of woody vegetation. As resolution becomes worse the interpreter must rely almost entirely on color which makes differentiations such as that between mixed hardwood and chaparral, both which have a bright red tone, very difficult. In fact, these two vegetation types were the hardest to identify as soon as the images became more degraded. This is evidenced in Figure 8 where using Image 5 (300-500 ft. GRD) the interpreters were only able to correctly identify 21.4% of the MH plots and 29.2% of the C Plots. Monterey pine (MP) was also hard to identify with only 33.3% of the plots being correctly identified.

The annual grassland (G), the water bodies (W) and the non-vegetated areas (N) were more easily identified. The percent correct for W, 83.3%, would have

even been higher if the small one-acre pond at point 64 on Image 1, which was resolvable only on Image 1, had been eliminated.

It seems that difficulties are certain to arise when trying to differentiate between woody vegetation types such as MP, E, MH and C on low resolution photography. However, if these are combined into one group, i.e., "woody vegetation", and the interpreter is asked to interpret for woody vegetation, grassland and water bodies, the results might be improved. Figure 11 shows how the results might improve if these categories were used. The graphs in Figures 12 and 13 also show an improvement in results.

The accuracy of identification for the grassland (G) surely would have been much higher if the photography had been flown a month later, July 1 instead of June 1. At the time of the June 1 photography, some of the grassland area still had high reflectance in the reflective infrared portion of the electromagnetic spectrum and shows up pink or red (see point numbers 23 and 90 on Image 1) thus making it easy to confuse it with chaparral which is also pink or red at this time of year.

Although interpretability does fall off with increasing ground resolvable distance, very good results were obtained using the photography with the best resolution, and if a more general type of information such as the extent of woody vegetation versus grassland is desired, imagery of the quality obtainable from satellites may be of great utility especially if the optimum dates of photography are flown.

The examples in Figure 14 show a photograph taken on June 1, 1968 and one taken on July 17, 1969. In June the grasslands at "G" are still pink or red and easily confused with the chaparral at "C", but there is little confusion between the same points on the July photograph. There is also a greater contrast between the Monterey pines at "MP" and the mixed hardwoods at "MH" and the



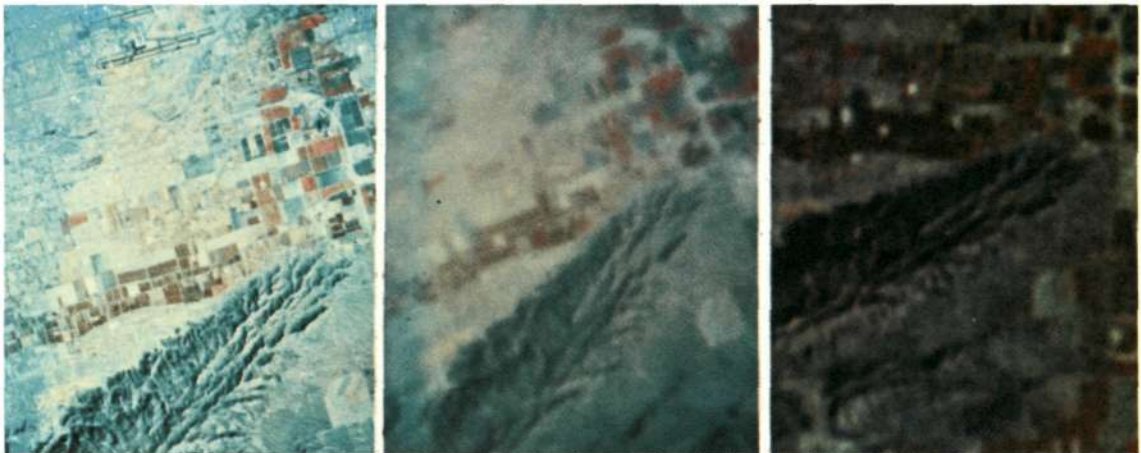
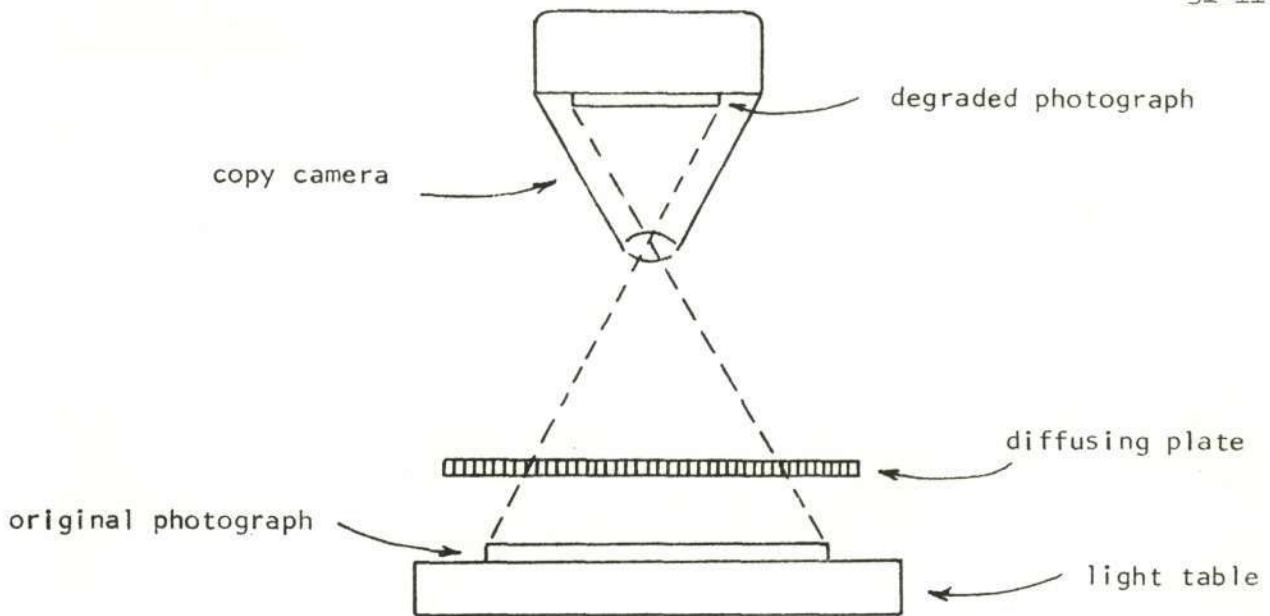
chaparral at "C" on the July photograph than there is on the June photograph. Thus by using photographs flown later in the year the results reported on herein could be improved upon considerably.

#### SUMMARY AND CONCLUSIONS

In summary, the results reported above help answer the two questions stated at the beginning of this paper. First, given (within the next few years) low resolution ERTS data taken of a chaparral-hardwood-grassland type, one could expect that a skilled image analyst could delineate and identify on these images woody vegetation and water bodies with better than 80% accuracy. In addition, annual grassland areas could also be identified with approximately the same accuracy provided the imagery is taken late in the growing season. (It is reasonable to assume that imagery will be available showing natural vegetation in nearly all seasonal states, since the ERTS vehicle will pass over the same point on the earth approximately every eighteen days.) However, the most interesting outcome of this research is in reference to the second question. Note that even if the image resolution capability of the proposed ERTS sensor system was improved from 400 feet GRD to 100 feet GRD, the imagery would remain inadequate for identifying the four primary types of woody vegetation found to occur in this area: Monterey pine, eucalyptus, mixed hardwoods and chaparral. Discrimination between these kinds of vegetative cover is done mainly by recognizing shape, size, texture and shadow characteristics within each type. To include these kinds of information, imagery must have a ground resolvable distance of at least 50 feet. In some instances the user might be satisfied with merely broad categorization; in other instances, however, either he or some other users might require detailed identifications as to individual species. Consequently, only by being able to thoroughly define user requirements can the usefulness of ERTS data, or for that matter, any data be determined. For

example in this case, if the user wants to discriminate between woody vegetation, grassland and water bodies, ERTS data exhibiting 400-500 feet GRD will contain a sufficient amount of information allowing such discriminations to be made. However, if the user desires additional information on the various types of woody vegetation, spaceborne data will have to be supplemented with higher resolution (i.e., > 50 ft. GRD) aircraft imagery on which individual tree crowns can be seen.

There is still another respect in which user requirements for information may differ. In some instances the user may need only to know the percentage or total acreage comprised by each vegetation or terrain type throughout the entire area that he seeks to manage. Such information is obtainable, as in the present experiment, merely through type identification at each of a suitably large number of selected spots. For any given type, the amount which it comprises throughout the entire area can then be assumed to be proportionate to its occurrence in the dot sample. However, in other instances the user may require a complete "in-place" delineation, showing the exact boundaries of each type, wherever that type may occur within the project area. In order for this second type of requirement to be satisfied, a higher order of image interpretability usually will be required. With respect to both types of problems, spaceborne and airborne data most certainly compliment one another in that an analysis of low resolution synoptic view space photos gives guidance to where and, more importantly, where not to procure supplementary aerial coverage.



GRD:	10-20'	200-300' (degraded)	200-300'
Scale:	1/300,000	1/300,000	1/300,000
Film Type:	Ekta Aero Infrared	Ekta Aero Infrared	Ekta Aero Infrared
Flight Altitude:	60,000' AMS	60,000' AMS	125 NM
Vehicle:	NASA RB57F	NASA RB57F	Apollo 9
Date:	March 8, 1969	March 8, 1969	March 8, 1969

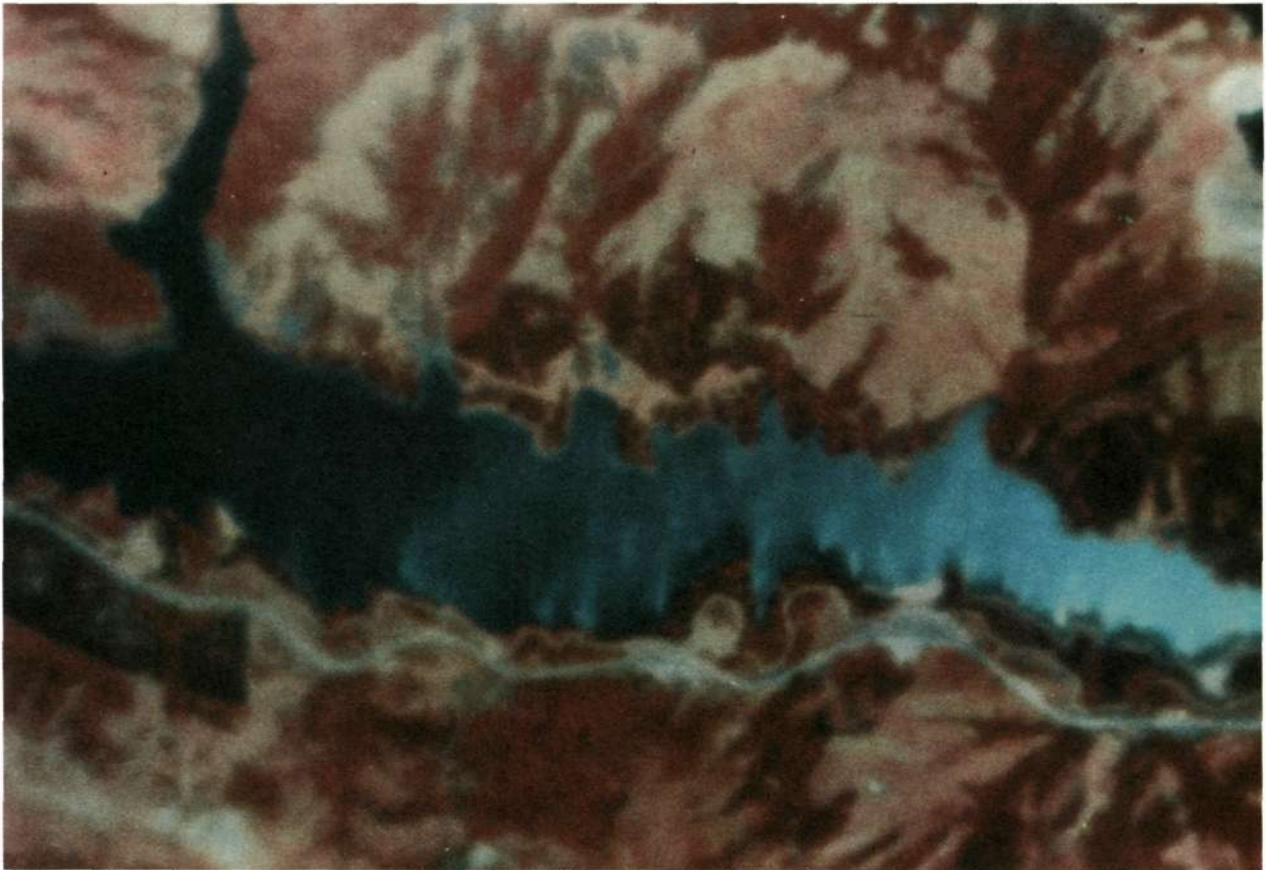
Figure 1. The three photos shown here are of the multidisciplinary test site at Phoenix, Arizona (NASA Test Site #29). In order to simulate low resolution space photography, high altitude small scale aerial photography was photographed through a diffusing screen made of frosted acetate. By degrading image sharpness without grossly affecting image tone or color, photography can be analyzed that exhibits 200-300 foot GRD, similar to the quality of existing Apollo and Gemini photography. In addition, by shifting the position of the diffusing screen, a photograph can be made with nearly any GRD desirable. (The differences in color balance between the RB57F and Apollo photos are due primarily to the exposure and processing of the original photography and not to the degradation process.)



		GROUND TRUTH						TOT. SEEN BY P.I.	COM. ERROR	
		MP	E	MH	C	G	W			N
PHOTO INTERPRETER'S RESULTS	MP	<b>27</b>	1					28	1	
	E		<b>11</b>					11	0	
	MH			<b>77</b>	5			82	5	
	C			7	<b>41</b>	8		3	59	18
	G					<b>67</b>		3	70	3
	W						<b>30</b>	30	0	
	N				2			<b>18</b>	20	2
TOTAL PLOTS		27	12	84	48	75	30	24		
OMIS- SION		0	1	7	7	8	0	6		

Figure 2. Three photo interpreters working with the above image produced the cumulative results shown here. A total of 100 randomly distributed points of known identity were used in this interpretation test. The numbers in the body of the array of results indicate the total number of plots identified by all interpreters. The numbers in the bold-faced diagonal row of boxes indicate the number of plots identified correctly.

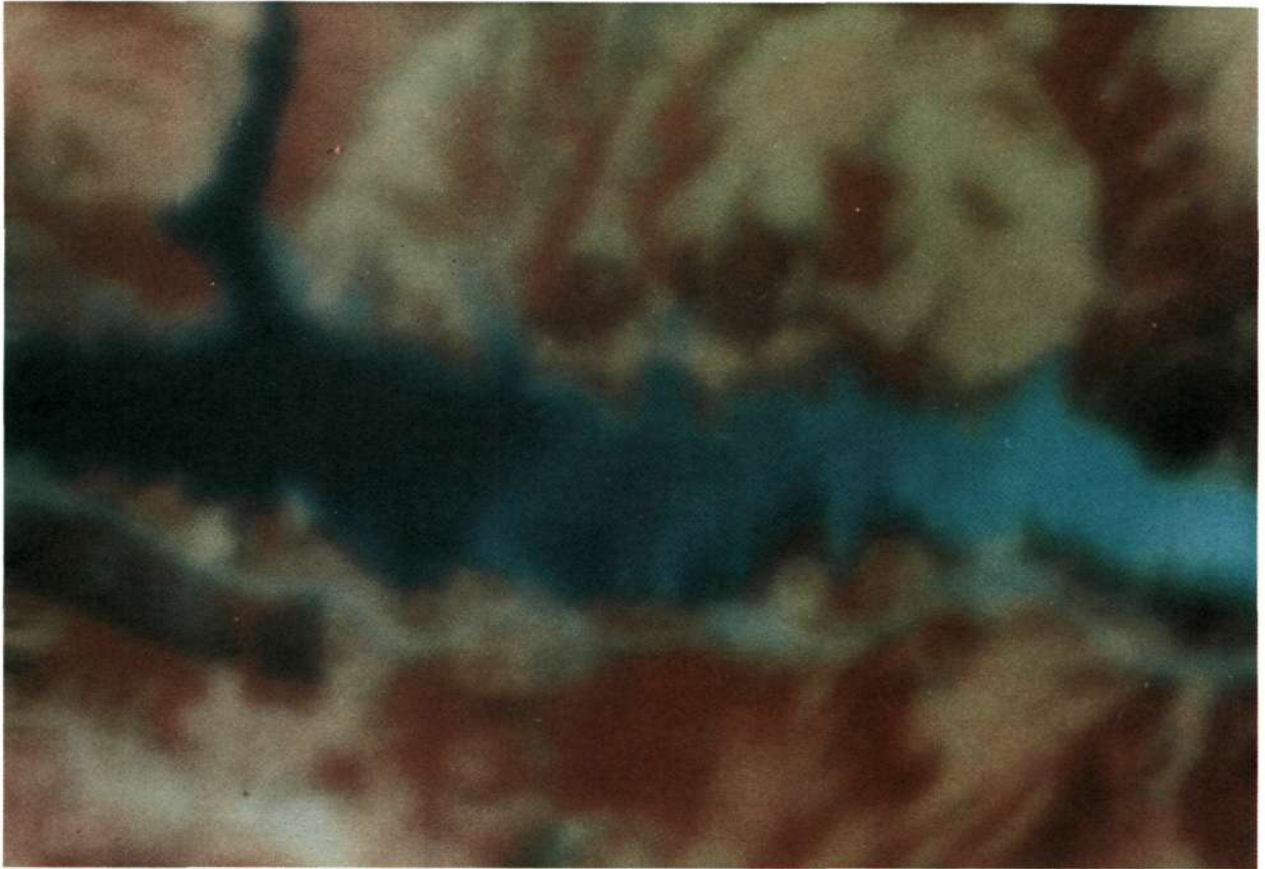
IMAGE 2: GROUND RESOLVABLE DISTANCE = 50-100 FEET



		GROUND TRUTH						TOT. SEEN BY P. I.	COM. ERROR	
		MP	E	MH	C	G	W			N
PHOTO INTERPRETER'S RESULTS	MP	<b>25</b>	5	9	10			49	24	
	E		<b>6</b>					6	0	
	MH	2		<b>53</b>	17	2		74	21	
	C		1	20	<b>20</b>	12		53	33	
	G			2		<b>60</b>		3	65	5
	W						<b>28</b>	3	31	3
	N				1	1	2	<b>18</b>	22	4
TOTAL PLOTS		27	12	84	48	75	30	24		
OMIS - SION		2	6	31	28	15	2	6		

268

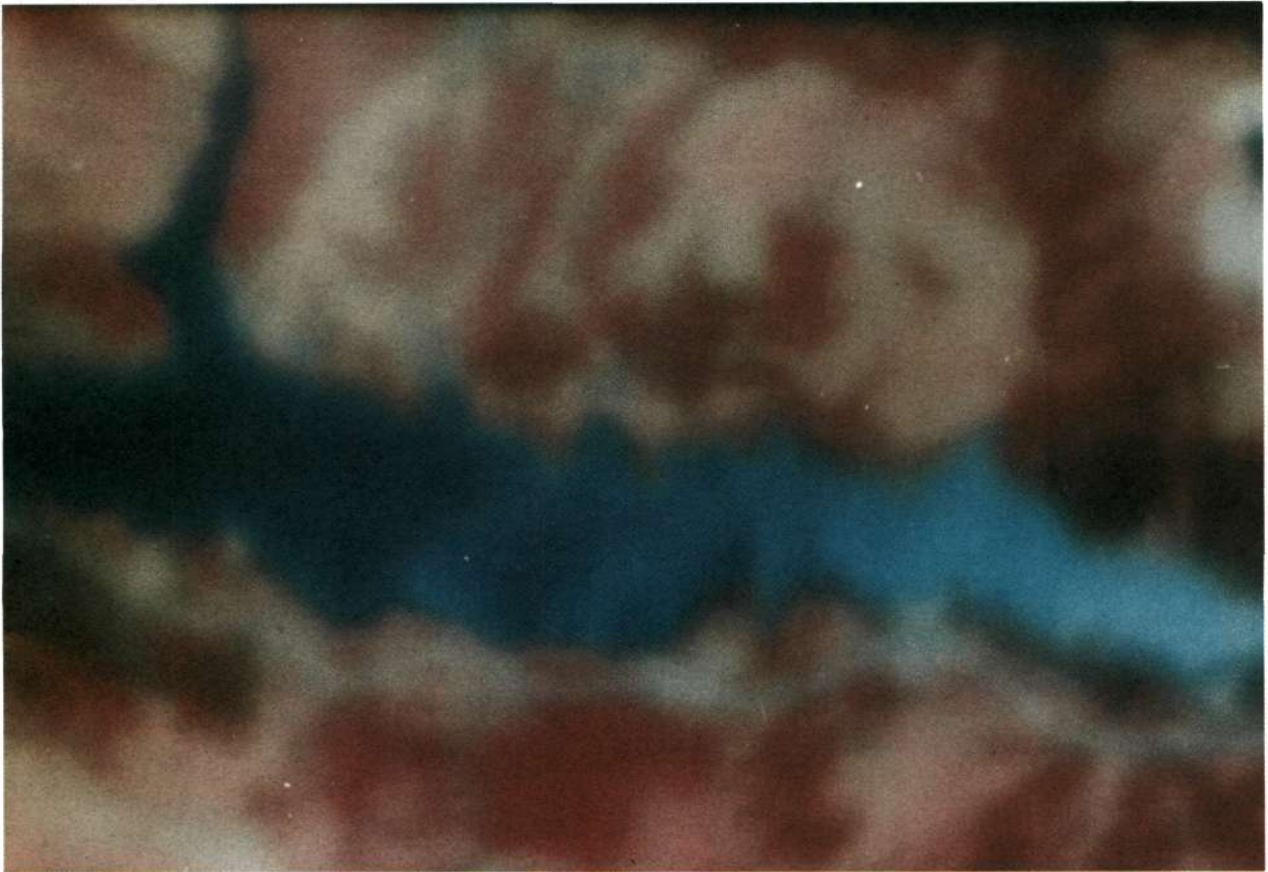
Figure 3. Three photo interpreters working with the above image produced the cumulative results shown here. A total of 100 randomly distributed points of known identity were used in this interpretation test. The numbers in the body of the array of results indicate the total number of plots identified by all interpreters. The numbers in the bold-faced diagonal row of boxes indicate the number of plots identified correctly.



		GROUND TRUTH						TOT. SEEN BY P. I.	COM. ERROR	
		MP	E	MH	C	G	W			N
PHOTO INTERPRETER'S RESULTS	MP	<b>21</b>	1	10	4				36	15
	E		<b>9</b>	1	2				12	3
	MH	3	1	<b>39</b>	16	3			62	23
	C	3	1	27	<b>22</b>	14			67	45
	G			4	2	<b>57</b>	3	8	74	17
	W					0	<b>27</b>	2	29	2
	N			3	2	1		<b>14</b>	20	6
TOTAL PLOTS		27	12	84	48	75	30	24		
OMIS - STON		6	3	45	26	18	3	10		

6072  
269

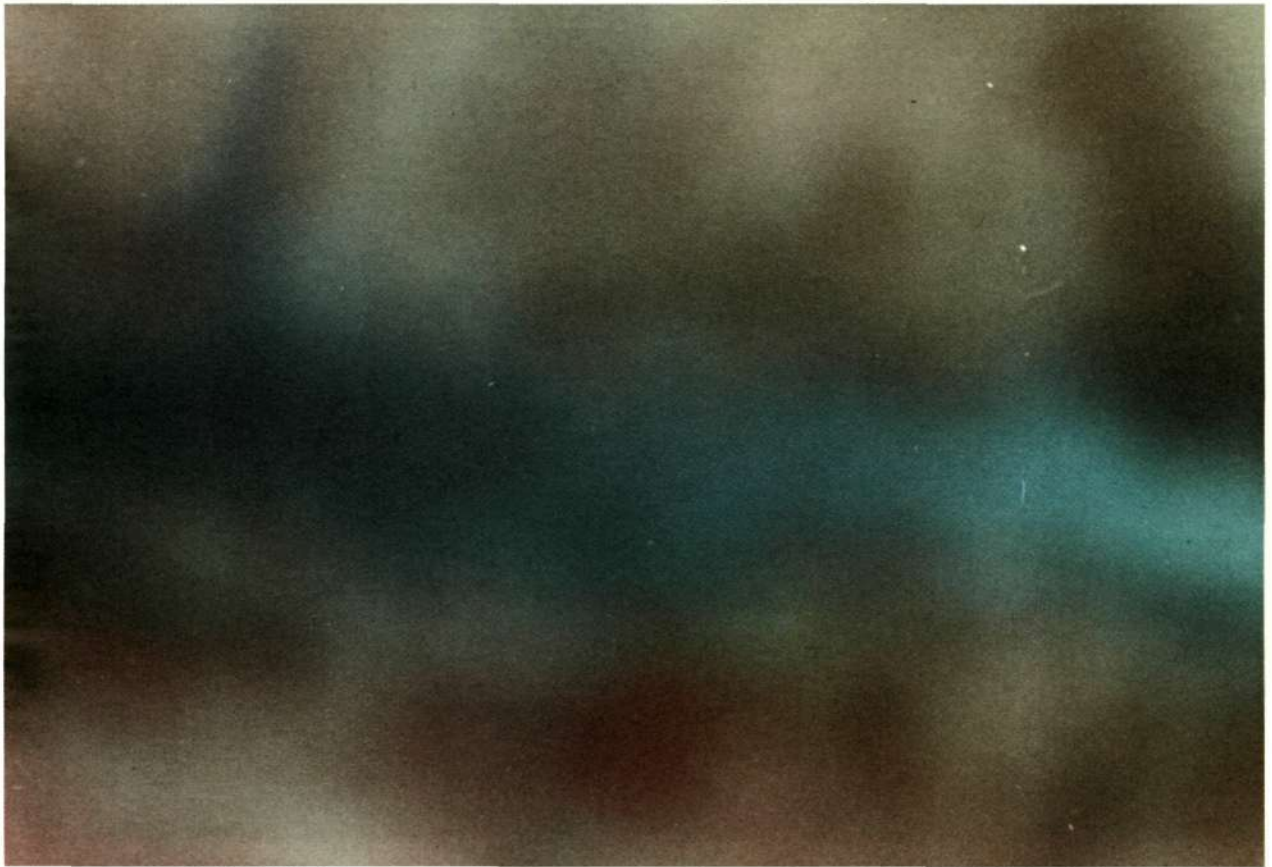
Figure 4. Three photo interpreters working with the above image produced the cumulative results shown here. A total of 100 randomly distributed points of known identity were used in this interpretation test. The numbers in the body of the array of results indicate the total number of plots identified by all interpreters. The numbers in the bold-faced diagonal row of boxes indicate the number of plots identified correctly.



		GROUND TRUTH						TOT. SEEN BY P. I.	COM. ERROR	
		MP	E	MH	C	G	W			N
PHOTO INTERPRETER'S RESULTS	MP	14	3	13	7	2			39	25
	E	3	6	3	4		2		17	10
	MH			22	11	2			36	13
	C	7	2	38	22	16		3	88	66
	G	3		7	3	52	3	6	74	22
	W						25		25	0
	N		1	1	1	3		15	21	6
TOTAL PLOTS		27	12	84	48	75	30	24		
OMISSION		13	6	62	26	23	5	9		

Figure 5. Three photo interpreters working with the above image produced the cumulative results shown here. A total of 100 randomly distributed points of known identity were used in this interpretation test. The numbers in the body of the array of results indicate the total number of plots identified by all interpreters. The numbers in the bold-faced diagonal row of boxes indicate the number of plots identified correctly.

IMAGE 5: GROUND RESOLVABLE DISTANCE = 300-500 FEET



		GROUND TRUTH						TOT. SEEN BY P.I.	COM. ERROR	
		MP	E	MH	C	G	W			N
PHOTO INTERPRETER'S RESULTS	MP	9	3	11	4	4			31	22
	E	5	8	5	6				24	16
	MH	2		18	15	6			41	23
	C	2	1	34	14	23			74	60
	G	2		14	6	33	3	11	69	36
	W	2					25		27	2
	N	5		2	3	9	2	13	34	21
TOTAL PLOTS	27	12	84	48	75	30	24			
OMIS-SION	18	4	66	34	42	5	11			

271

Figure 6. Three photo interpreters working with the above image produced the cumulative results shown here. A total of 100 randomly distributed points of known identity were used in this interpretation test. The numbers in the body of the array of results indicate the total number of plots identified by all interpreters. The numbers in the bold-faced diagonal row of boxes indicate the number of plots identified correctly.



1. G	21. C	41. G	61. G	81. G
2. MP	22. MP	42. W	62. N	82. G
3. C	23. G	43. MH	63. C	83. MH
4. MH	24. G	44. G	64. W	84. MH
5. MH	25. G.	45. G	65. W	85. C
6. MH	26. C	46. MH	66. W	86. G
7. C	27. N	47. C	67. N	87. C
8. C	28. W	48. C	68. W	88. MP
9. C	29. MP	49. C	69. MP	89. MH
10. G	30. MP	50. G	70. N	90. MH
11. G	31. MP	51. G	71. MP	91. G
12. G	32. MH	52. MH	72. G	92. MH
13. MH	33. E	53. G	73. E	93. MH
14. G	34. W	54. MH	74. G	94. MH
15. G	35. MH	55. MH	75. W	95. C
16. G	36. C	56. MH	76. MH	96. G
17. MH	37. MH	57. MH	77. N	97. MH
18. MP	38. W	58. E	78. MH	98. C
19. G	39. N	59. E	79. MH	99. MH
20. W	40. N	60. C	80. N	100. MH

Figure 7. Ground truth key for overlay in Figure 2.

CATEGORY	IMAGE RESOLUTION (FEET)				
	5-10	50-100	100-200	200-300	300-500
<u>COMPOSITE</u> (all types)					
Percent Correct	90.3	70.0	63.0	52.7	40.0
Percent Commission	9.7	30.0	37.0	47.3	60.0
<u>MONTEREY PINE</u> (MP)					
Percent Correct	100.0	92.6	77.8	51.9	33.3
Percent Commission	3.6	49.0	41.7	64.1	71.0
<u>EUCALYPTUS</u> (E)					
Percent Correct	91.7	50.0	75.0	50.0	66.7
Percent Commission	0.0	0.0	25.0	58.8	66.7
<u>MIXED HARDWOODS</u> (MH)					
Percent Correct	91.7	63.1	46.4	26.2	21.4
Percent Commission	6.1	28.4	37.1	36.1	56.1
<u>CHAPARRAL</u> (C)					
Percent Correct	85.4	41.6	45.8	45.8	29.2
Percent Commission	30.5	62.3	67.1	75.0	81.1
<u>ANNUAL GRASSLAND</u> (G)					
Percent Correct	89.3	80.0	76.0	69.3	44.0
Percent Commission	4.3	7.6	22.8	29.7	52.8
<u>WATER BODIES</u> (W)					
Percent Correct	100.0	93.3	90.0	83.3	83.3
Percent Commission	0.0	9.7	6.9	0.0	7.4
<u>NON-VEGETATED AREAS</u> (N)					
Percent Correct	75.0	75.0	58.3	62.5	54.2
Percent Commission	10.0	16.7	30.0	28.6	61.8

Figure 8. Interpretation results for each category expressed as percent correct and percent commission error.

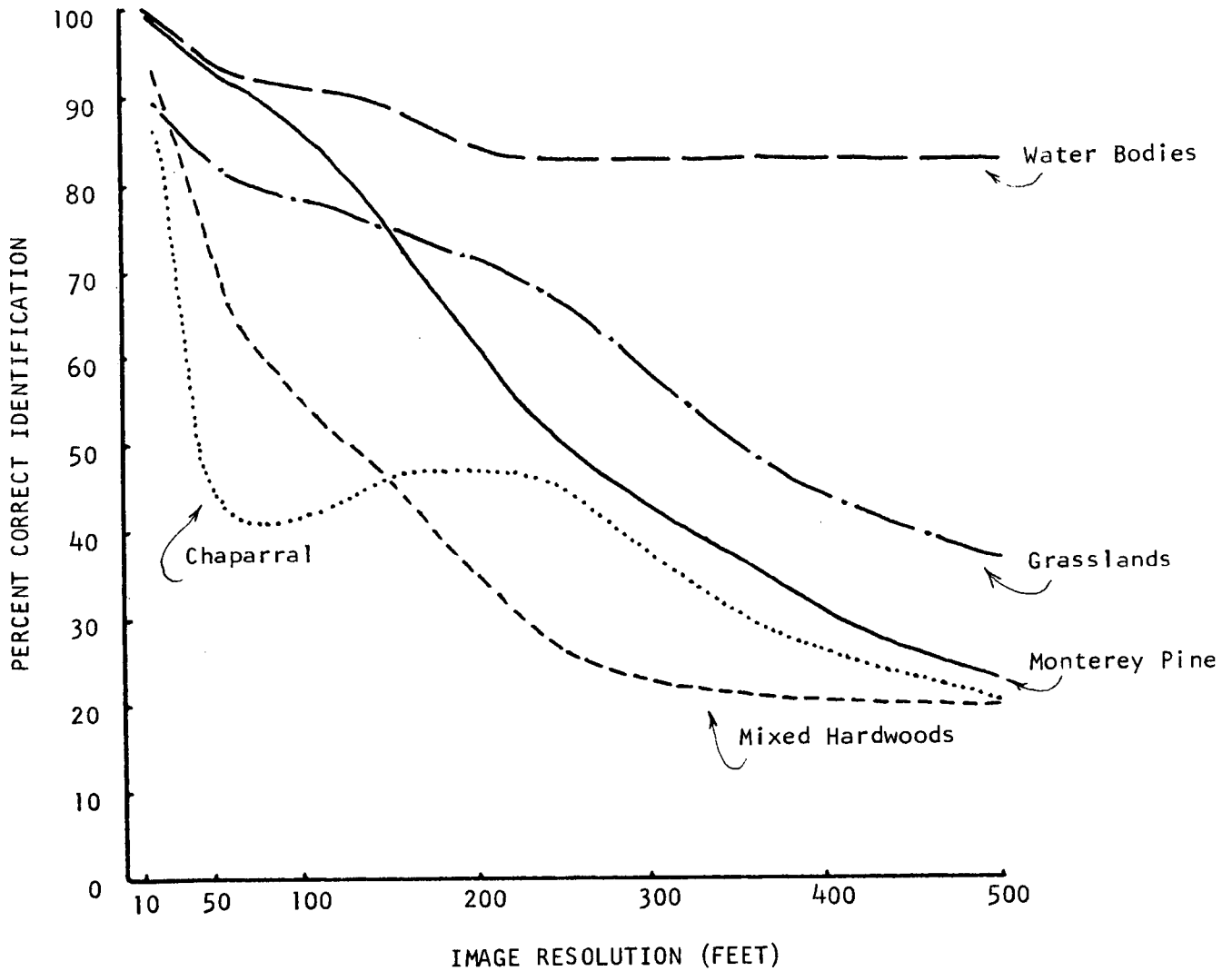


Figure 9. Interpretation results for all categories individually expressed as percent correct identification (data on eucalyptus and non-vegetated areas have been omitted due to an insufficient number of sample plots.)

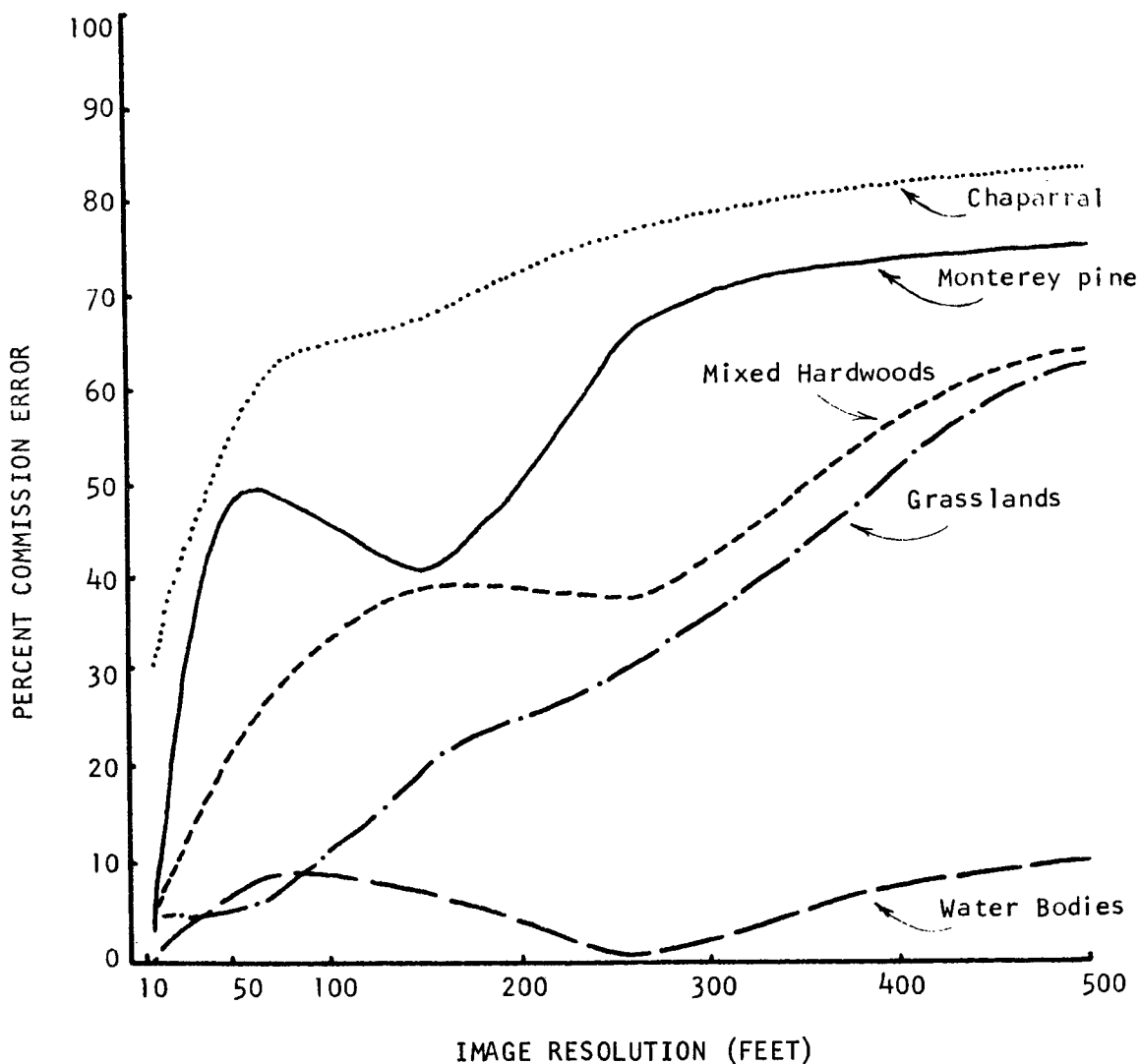


Figure 10. Interpretation results for all categories individually expressed as percent commission errors (data on eucalyptus and non-vegetated areas have been omitted due to an insufficient number of sample plots.)

CATEGORY	IMAGE RESOLUTION (FEET)				
	5-10	50-100	100-200	200-300	300-500
<u>WOODY VEGETATION</u> (MP, E, MH and C)					
Percent Correct	98.8	98.2	93.6	91.2	80.11
Percent Commission	4.4	7.7	9.6	13.9	19.4
<u>GRASSLAND</u> (G)					
Percent Correct	89.3	80.0	76.0	69.3	44.0
Percent Commission	4.3	7.7	23.0	29.7	52.2
<u>WATER BODIES</u> (W)					
Percent Correct	100.0	93.3	90.0	83.3	83.3
Percent Commission	0.0	9.7	6.9	0.0	7.4

Figure 11. Interpretation results for combined categories, expressed as percent correct and percent commission error.

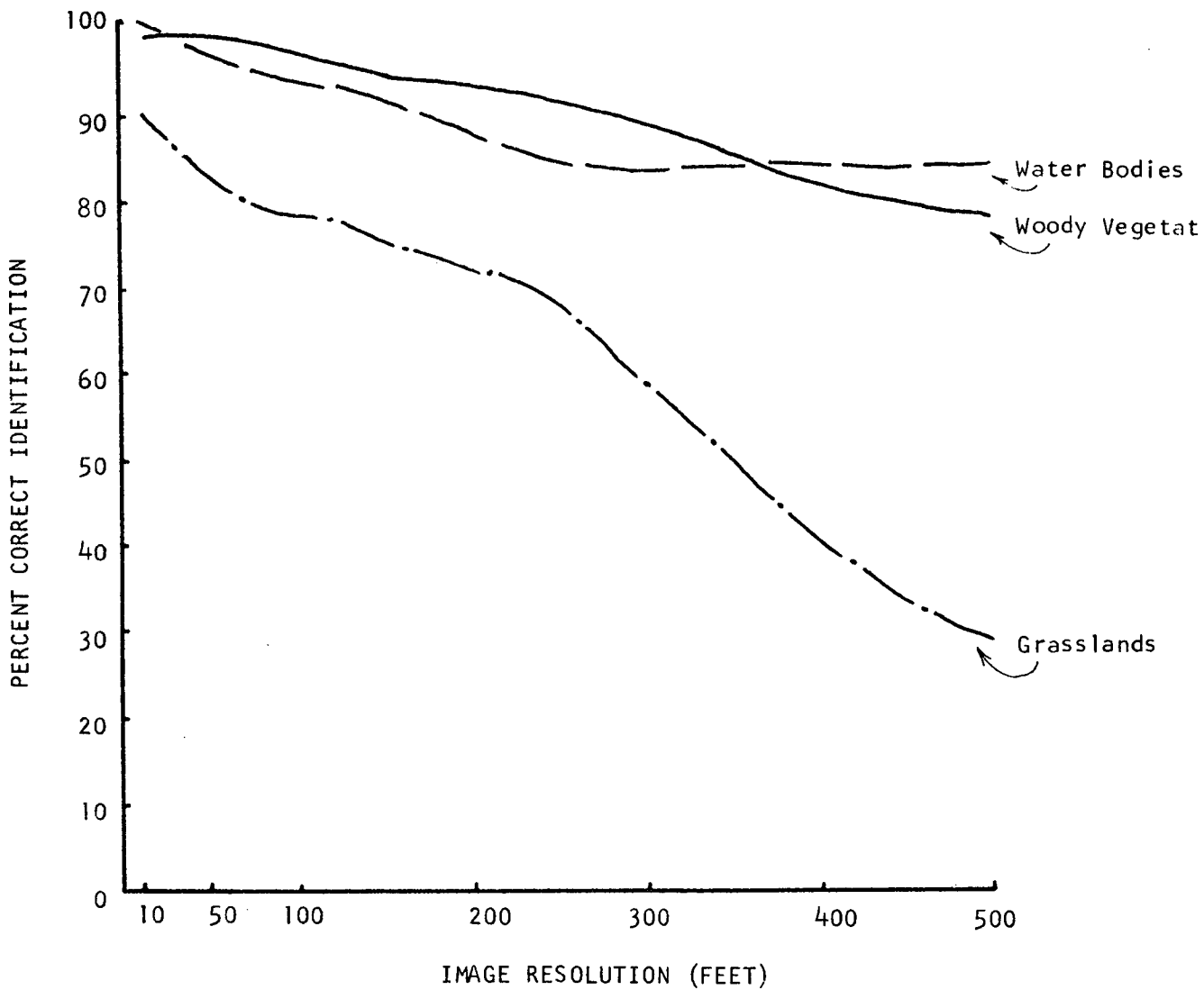


Figure 12. Interpretation results for woody vegetation, grasslands and water, expressed as percent correct identification.

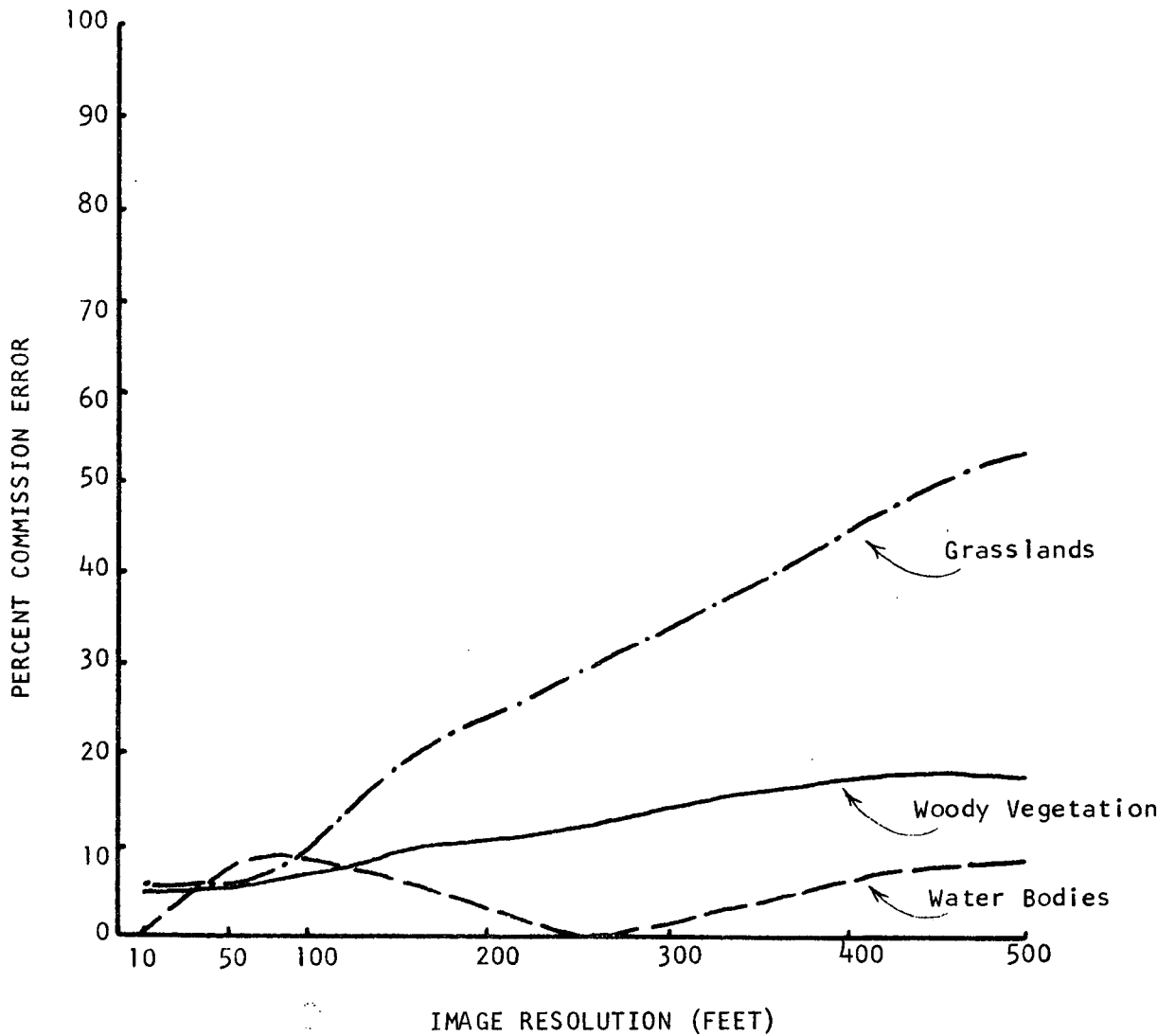
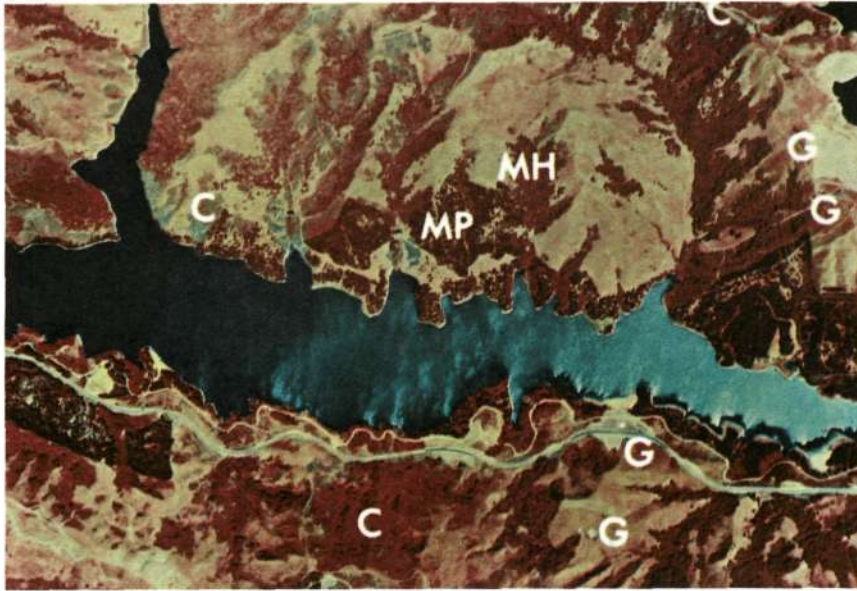
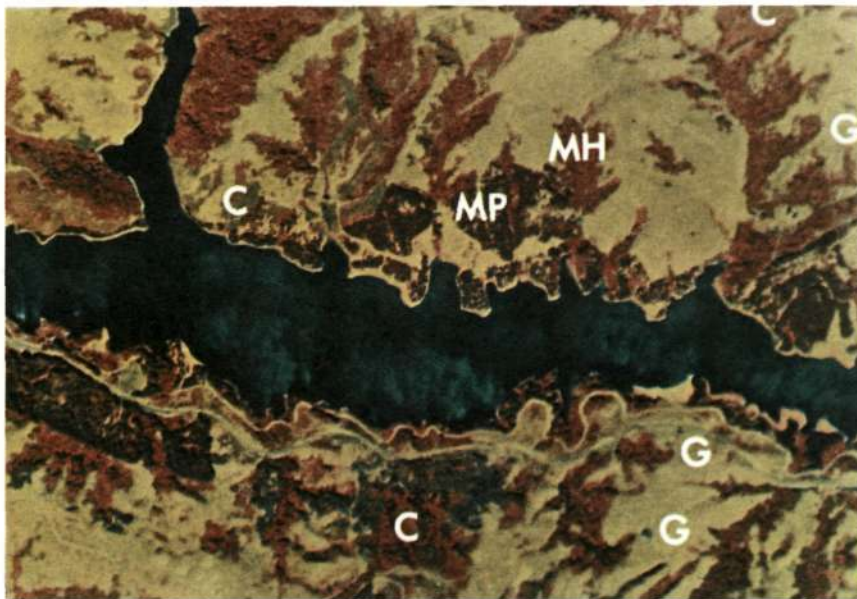


Figure 13. Interpretation results for woody vegetation, grassland and water, expressed as percent commission error.



Film: Ekta Aero Infrared  
 Aircraft: NASA Convair 240  
 Date: June 1, 1968



Film: Ekta Aero Infrared  
 Aircraft: NASA RB57F  
 Date: July 17, 1969

Figure 14. The accurate timing of image procurement greatly influences the interpretability of the resulting imagery. This example shows that in early June the phenological growth stages of annual grasslands in California are such that this cover type is often confused with adjacent woody vegetation. However, later in the year, the grasses have matured and dried and as a result the reflectance characteristics of grassland are quite different than those of hardwood vegetation. Consequently, the interpretation results reported here differentiating grasslands from other types might have been greatly improved if the analysis had been done on July imagery. (Annotations are explained in the text.)



## IDENTIFICATION AND MEASUREMENT OF SHRUB TYPE VEGETATION

## ON LARGE-SCALE AERIAL PHOTOGRAPHS

by

Richard S. Driscoll<sup>1/</sup>  
Rocky Mountain Forest and Range Experiment Station  
U.S.D.A. Forest Service, Fort Collins, Colorado

ABSTRACT

Important range-shrub species were identified at acceptable levels of accuracy on large-scale (1:600 to 1:1,500) 70 mm color and color infrared aerial photographs (positive transparencies). Identification of individual shrubs was significantly higher, however, on color infrared. Eight of 11 species were identified correctly more than 80 percent of the time on color infrared and two species were correctly identified 100 percent of the time. Six species were identified more than 80 percent correctly on color photographs but none were identified 100 percent correctly. Photoscales smaller than 1:2,400 had limited value except for mature individuals of relatively tall species, and then only if crown margins did not overlap and sharp contrast was evident between the species and background. Larger scale photos (1:800 or less) were required for low-growing species in dense stands. The crown cover for individual species was estimated from the aerial photos either with a measuring magnifier or a projected-scale micrometer. Photo measurements were significantly correlated with ground measurements. These crown cover measurements provide techniques for earth-resource analyses when used in conjunction with space and high-altitude remotely procured photos.

INTRODUCTION

The Nation's rangelands include approximately one billion acres of land not suitable for cultivated crop production. They produce forage for domestic and wild grazing animals, and provide recreational and intangible natural beauty benefits. They include the drainages of many river systems from which domestic and commercial water supplies are derived. These wildland areas, especially in the West, are relatively inaccessible due to topographic constraints or lack of access routes by land vehicles.

---

<sup>1/</sup> Project Leader and Principal Plant Ecologist in charge of Remote Sensing Research.

The range resources of these lands need to be more frequently inventoried and evaluated as a basis for developing national policies and programs for integrated rangeland use. Such an inventory would provide periodic data on quantity and quality of the resource. Inventories, including the extent and composition of plant communities, have been conducted by ground sampling for decades, but only a small fraction of the range area has been covered in detail. Because ground sampling requires considerable time, the relative composition of the communities may change due to natural phenology changes. Consequently, data interpretation is complicated and the results may produce a false image of the resource.

Aerial and space photographs (the scale depending on information needs) will potentially provide the data base required for a dynamic range resource inventory and information system. It has been demonstrated how space and high-flight aerial photographs can be used to locate, map, and determine the areal extent of plant communities (Poulton, Driscoll and Schrupf, 1969). The next level of information needed for this kind of a resource inventory is the identity of the plant community components as well as some measure of quantity.

The purpose of this paper is to review results and progress on use of color and color infrared aerial photographs to identify and measure species components of plant communities dominated by shrubs. It deals with large-scale (1:600-1:2,400) 70 mm aerial photographs. Increased ability to interpret data from such photos will help us to better interpret space or high-flight aircraft photographs.

#### AERIAL PHOTOGRAPHY AND GROUND DATA

Three areas were selected for this research, all in Colorado:

(1) A high-mountain grassland in which two shrub species, shrubby cinquefoil and Parry rabbitbrush, were widely distributed within heterogeneous herbaceous communities. (2) A pygmy forest with pinyon pine and juniper as the major species; true mountain mahogany, big sagebrush, and some bitterbrush occurred in the understory. (3) An area with a heterogeneous stand of shrubs including big sagebrush, alkali sagebrush, bitterbrush, Douglas rabbitbrush, snowberry, and broom snakeweed.

Aerial photographs were taken from the Forest Service Aero Commander assigned to the Remote Sensing Research Project at the Pacific Southwest Forest and Range Experiment Station, Berkeley, California. The camera package consisted of two Maurer KB-8 70 mm cameras mounted in a single frame to provide simultaneous photographs with two film/filter combinations. Film used was color infrared (Ektachrome Infrared Aero Type 8443) filtered with a Wratten 12 filter, and normal color (Ansco D-200 Type 7230) filtered with a Wratten 1-A skylight filter.

Photo missions were flown four times during the growing season to determine when during different plant growth stages the species previously mentioned could most accurately be identified in the resultant photographs. Various photoscales ranging from 1:600 to 1:4,800 were obtained each time to determine the resolution threshold for identifying the various plant species at an acceptable level of accuracy.

Ground data were obtained from a series of 6-meter-square plots aligned near the center of the flight lines at each location (Fig. 1). Within and around these plots, individual shrubs were marked and identified so they could be located and positively identified in the aerial photographs. In addition the position of four line transects were marked within the plots so they could also be identified in the aerial photographs. Foliage or crown cover of each shrub species was measured on the ground by a line intercept technique (Canfield 1947). These ground data were compared against cover estimates of individual shrub species measured on the line transects directly on the aerial photographs. The photo measurement devices used are defined in a subsequent section.

## RESULTS AND DISCUSSION

### SPECIES IDENTIFICATION

Detailed interpretation of the aerial photographs revealed that we could extract the greatest amount of information from photographs taken in early July. This does not mean that this photography provided the "best" information for the identification of all species. The selection was based on the inference that if an investigator, because of budgetary or other constraints, had to limit efforts to a single time for data gathering, early July would provide the most useful information.

Image characteristics used to develop a dichotomous photointerpretation key for the nine shrubs and two small trees included relative size, shadow, crown margin, crown shape, foliage pattern, texture, and color. At least 10 replicates were selected for nine of the species; more than six for the other two species, for a photointerpretation test. Four image analysts with varying degrees of experience and knowledge of the areas photographed completed the test. The results of the test, primarily with 1:600 to 1:1,500 scale photos, were as follows:

1. Identification of individual shrubs was significantly higher ( $P = .01$ ) on color infrared positive transparencies, regardless of interpreter experience or shrub species.

2. There was a significant difference ( $P = .01$ ) among interpreters for identifying the species which depended on photointerpretation experience and knowledge of the area imaged in the photos.

3. Identification of larger species was significantly better ( $P = .01$ ) regardless of film type or interpreter.

In general, 82 percent of the total 456 test specimens were correctly identified on the color infrared photos; 76 percent were correctly identified on color (Table I). Eight of the 11 species were identified at acceptable levels of accuracy ( $> 80$  percent) on color infrared; two of them were identified 100 percent by all interpreters. Six species were identified correctly more than 80 percent of the time on color photos, and none were identified 100 percent correctly by all interpreters.

Greatest differences in species identification between film types were for bitterbrush, snowberry, and mountainmahogany. Bitterbrush and snowberry had very similar colors both on the ground and in the color aerial photos. Consequently, identifications of these species were frequently confused. Greater color contrasts between the images of these two species in the color infrared photos improved identification (Fig. 2).

Mountainmahogany was frequently confused with small pinyon pine in the color photographs, especially when the apparent morphological characters as viewed in the film were similar. In the color infrared photos, color differences between the two species were sufficiently contrasting that errors in identification of the species were very unlikely (Fig. 3).

Image character differences among snowberry and the two species of rabbitbrush were so subtle that the species were hard to distinguish, regardless of film type or photoscale used (Figs. 2, 4). The most experienced interpreter identified these species in the color infrared photos correctly 90, 92, and 92 percent, respectively.

Differences among interpreters were related to interpretation experience and knowledge of the area. The image analyst with the most experience and knowledge of the area scored highest on the photointerpretation test. The least experienced analyst with least knowledge of the area or the species scored lowest.

With the camera system used for this research, mature plants of relatively tall species such as mountainmahogany and big sagebrush were readily identified with photoscales at 1:1,500. Photoscales to 1:2,400 proved satisfactory provided plant crown margins did not overlap and there was relatively high contrast between the species and background. Ability to identify individual species in heterogeneous shrub communities where plant crowns intermingled deteriorated rapidly at photoscales smaller than 1:950.

Multiseasonal photography remains important, however, to gain the most information about individual species. When to secure data about individual species can be patterned after determining the seasonality of the species of interest. For example, some species such as rabbitbrush, gain full vegetational development late in the growing season. Others, such as bitterbrush, are fully developed relatively early in the growing season. Photoidentification of these species was improved by using either late season photography (rabbitbrush) or early season photography (bitterbrush). Some species, including sagebrush, shrubby cinquefoil, and mountainmahogany, contrast sufficiently with associated vegetation that they can be identified, using the proper photoscale, with acceptable accuracy at any time during the growing season.

We attempted to develop automated species identification using a GAF Model 650 scanning microdensitometer in cooperation with the Remote Sensing Research Project, Pacific Southwest Forest and Range Experiment Station. We used the aerial color infrared positive transparencies for this work because of the manual photointerpretation success with this film type. The instrument senses image optical density in the transparencies by means of a light beam passed through the film onto a photocell. A strip-chart recorder is activated to produce a continuous density trace of a predetermined scan line marked in a transparency.

Although the mean image densities of selected species appear to separate, the density ranges among individual species indicate this method is not yet feasible for automatic image interpretation if several species occur in the same plant community image (Table II). However, if photographs are of communities in which the two species of sagebrush are the only shrubs, the technique is potentially useful. The image density differences between bare soil and live vegetation cover indicate the system is capable of automatically separating these two categories. The technique has potential; additional research is needed to define machine aperture mode and light filtration for acceptable automated interpretation.

#### MEASUREMENTS

Two kinds of measuring devices were used to relate photo measurements to ground measurements of foliage and crown cover of shrubs. One device was a simple 7-X measuring magnifier scaled for 0.1 mm (100 microns) measurements. The other was a projected-scale micrometer which, when attached to a Zoom 70 stereoscope, measures distance on aerial photographs directly to 0.00001 foot (3 microns).

The scale of each of these instruments was aligned along transect markers visible in the color infrared aerial transparencies. Crown cover of individual shrubs was estimated by determining the distance each shrub crown image covered along the scale line between the transect markers. These estimates were related to ground estimates by correlation and regression.

Our data for big sagebrush (Fig. 5) indicate that both measurement techniques provide acceptable information for relating photo to ground measurements of foliar cover of individual shrubs. Similar relationships existed for the other three species included in this work.

In all cases for all species, the correlation coefficients were highly significant ( $P = .01$ ). In all cases, the correlation coefficients of data obtained using the measuring magnifier were greater than 0.86, whereas for the projected-scale micrometer they were slightly less. However, the projected-scale micrometer yields close to a one-to-one relationship ( $b = 1$ ) between photo and ground measurements (Fig. 5). This instrument might therefore be selected for this photo measurement technique, except that its cost is 25 times that of the measuring magnifier, which provides equally acceptable information within the data range used for this work.

We discovered that the cost ratio of ground/photo measurements is in the magnitude of 10:1. This means that it costs 10 times as much to measure a transect on the ground as compared to the same transect imaged in the aerial photography. Therefore, we have defined an initial cost savings capability which, through multiple sampling techniques relating ground to photo measurements, will provide acceptable data about some parts of the range resource for large areas at less cost than ground sampling alone.

#### CONCLUDING REMARKS

We have developed a way of measuring ground vegetation, at least shrubby species, using large-scale color infrared aerial photographs. The technique provides at least partially quantified information about the mapping units defined on space or high-flight aircraft photographs for use in range resource inventory. It has the advantage of complementing the multistaged sampling procedure and data handling system defined by Langley, Aldrich and Heller (1969). Additional research is needed, however, before such a data system is implemented to inventory range resources. These needs include:

1. We must develop the capability to extrapolate the research results we now have to other land areas of similar vegetation for species identification and measurement from aerial photographs.

2. We need to further define, develop, and refine multiple sampling techniques, including multistage sampling, to relate ground data to space or high-flight aircraft photography for range resource inventory and evaluation.

3. We need to develop automated interpretation techniques controlled by sample data of absolute information in order to transfer raw remote sensor data to the user of the information as rapidly as possible.

LITERATURE CITED

1. Poulton, C. F., R. S. Driscoll and B. J. Schrupf  
1969. Range resource inventory from space and supporting aircraft photography. Second Annu. Earth Resour. Aircraft Program Status Rev., Vol. II, Agr./Forest. and Sens. Stud., Section 20, NASA Manned Spacecr. Cent., Houston, Tex., Sep. 16-18.
2. Canfield, R. H.  
1942. Sampling ranges by the line interception method; plant cover--composition--density--degree of forage use. USDA Forest Serv. Southwest. Forest and Range Exp. Sta., Res. Rep. 4, 28 p. Tucson, Ariz. [reprinted 1950, 1957].
3. Langley, P. G., R. C. Aldrich and R. C. Heller  
1969. Multi-stage sampling of forest resources by using space photography---an Apollo 9 case study. Second Annu. Earth Resour. Aircraft Program Status Rev., Vol, II, Agr./Forest. and Sens. Stud., Section 19, NASA Manned Spacecr. Cent., Houston, Tex., Sep. 16-18.



TABLE I.- CORRECT SHRUB AND SMALL TREE IDENTIFICATION PERCENTS BY INTERPRETER  
AND FILM TYPE

Species	Interpreter <sup>1/</sup>								Mean		
	A		B		C		D				
	EIR <sup>2/</sup>	D-200 <sup>3/</sup>	EIR	D-200	EIR	D-200	EIR	D-200	EIR	D-200	
Alkali sage	100	100	100	100	100	90	100	100	100	100	98
Big sagebrush	100	80	90	90	70	100	100	100	100	90	93
Mountainmahogany	100	100	100	100	100	100	100	67	100	67	92
Parry rabbitbrush	92	100	50	50	42	42	58	33	60	56	56
Green rabbitbrush	92	67	50	42	54	33	25	58	56	50	50
Snakeweed	90	90	100	100	100	80	80	80	93	88	88
Juniper	100	92	100	100	83	83	100	100	96	94	94
Pinyon pine	100	92	100	92	77	92	92	85	92	90	90
Bitterbrush	90	40	80	80	70	60	70	20	78	50	50
Cinquefoil	100	100	83	83	83	67	67	67	83	79	79
Snowberry	90	70	60	70	40	30	50	40	60	55	55
Mean	95	85	84	81	72	68	71	70	83	76	76

<sup>1/</sup> A = Skilled interpreter familiar with the area

B = Skilled interpreter unfamiliar with the area

<sup>2/</sup> Ektachrome Aero Infrared (Type 8443)

<sup>3/</sup> Anscochrome D-200 (Type 7220)

C = Medium experienced interpreter unfamiliar with the area

D = Inexperienced interpreter unfamiliar with the area

TABLE II.- MEANS AND RANGES OF IMAGE DENSITY VALUES FROM 70 MM  
 COLOR INFRARED POSITIVE TRANSPARENCIES EXPOSED IN  
 JULY OF FOUR SHRUBS, TWO SMALL TREES, AND BARE SOIL,  
 SCALE 1:1,100

Species or Object	Image Density Values	
	Mean	Range
<u>Cercocarpus montanus</u>	3.676	3.15-4.42
<u>Pinus edulis</u>	3.655	3.26-4.12
<u>Juniperus scopulorum</u>	3.266	3.04-3.56
<u>Purshia tridentata</u>	3.169	2.97-3.53
<u>Artemisia tridentata</u>	2.805	2.56-3.00
<u>Artemisia longiloba</u>	2.768	2.62-2.72
Bare Soil	2.497	2.44-2.58

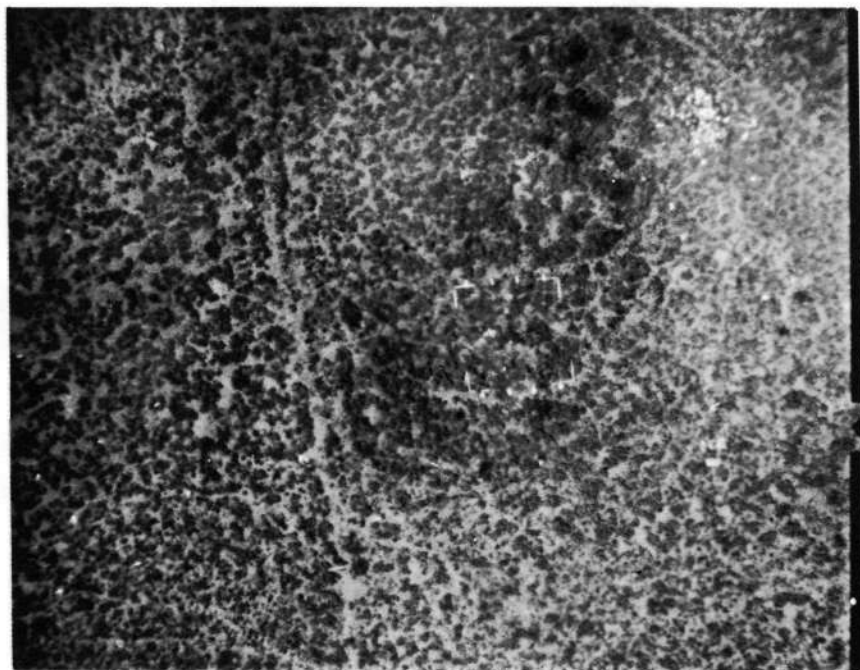


Figure 1.- A reproduction of an aerial photograph showing the plot marking system for identification and measurement of shrub species. The 6-meter-square plot is in the right center. Transect markers for measuring shrub crown cover are visible on the upper and lower boundaries of the plot. Markers identifying the location of individual shrub species are visible within the plot boundaries and in the lower left center.

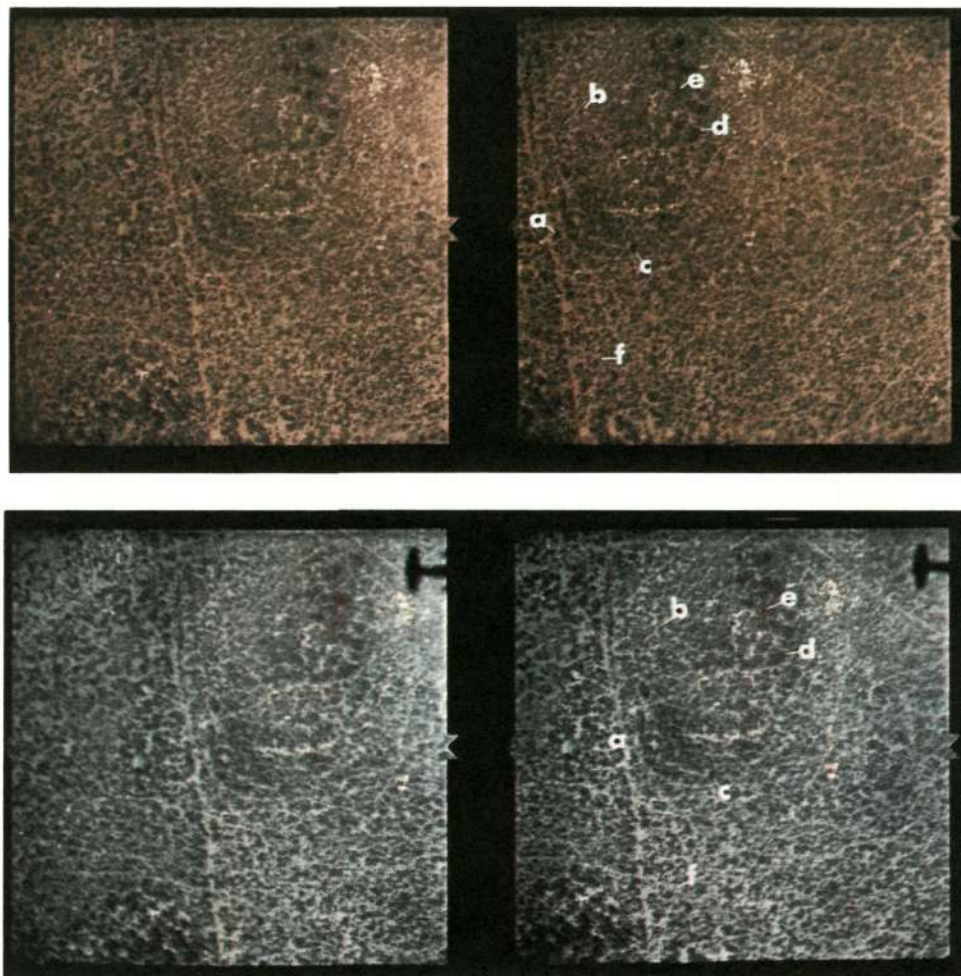


Figure 2.- Top--Ansochrome D-200; Bottom--Ektachrome Infrared stereograms at a scale of 1:800. Errors in identification of snowberry (d) and bitterbrush (e) were high in the color photos. Identification of the two species was improved in the color infrared. Other species indicated are: (a) big sagebrush, (b) alkali sagebrush, (c) green rabbitbrush, and (f) broom snakeweed.

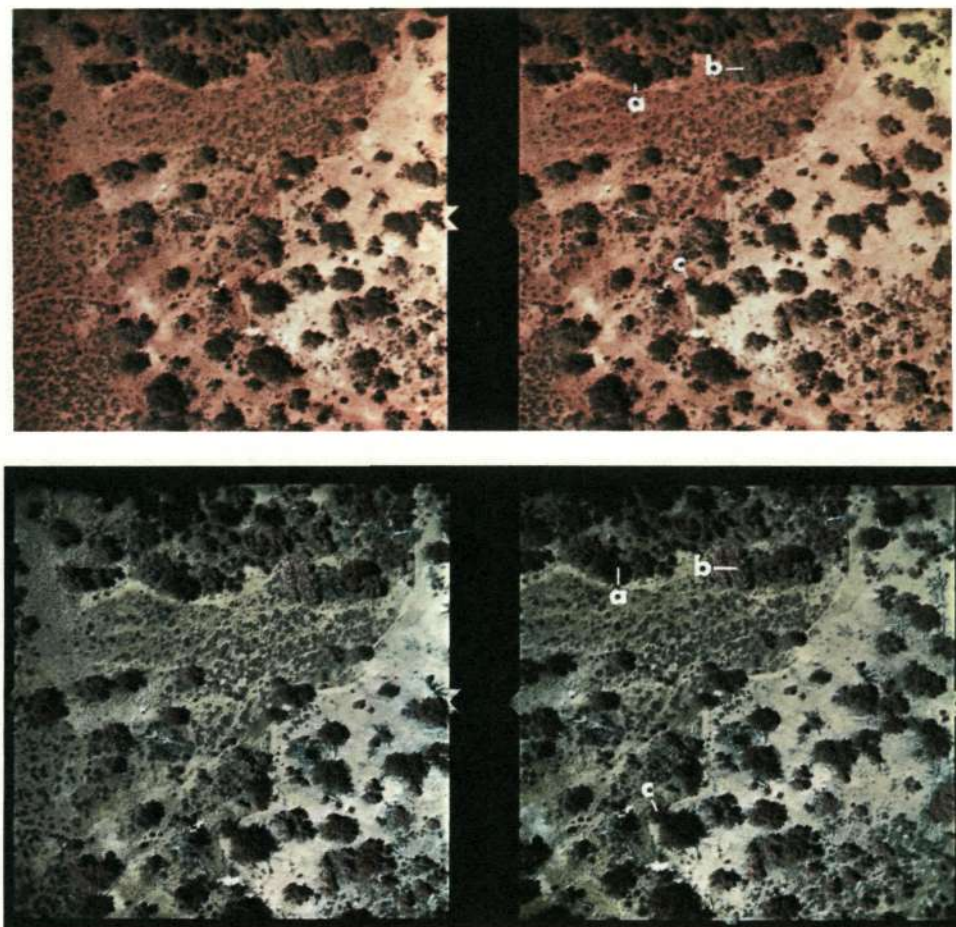


Figure 3.- Stereo pairs in color (top) and color infrared (bottom) of mountainmahogany (c) at a scale of 1:1,500. Color contrasts between this species and all others were sufficient in the color infrared to provide 100 percent correct identification. Some commission errors occurred between this species and small pinyon pine in the color photos, although not of sufficient magnitude to warrant complete rejection of color photos for identifying the species. Other plant species indicated are (a) pinyon pine and (b) juniper.

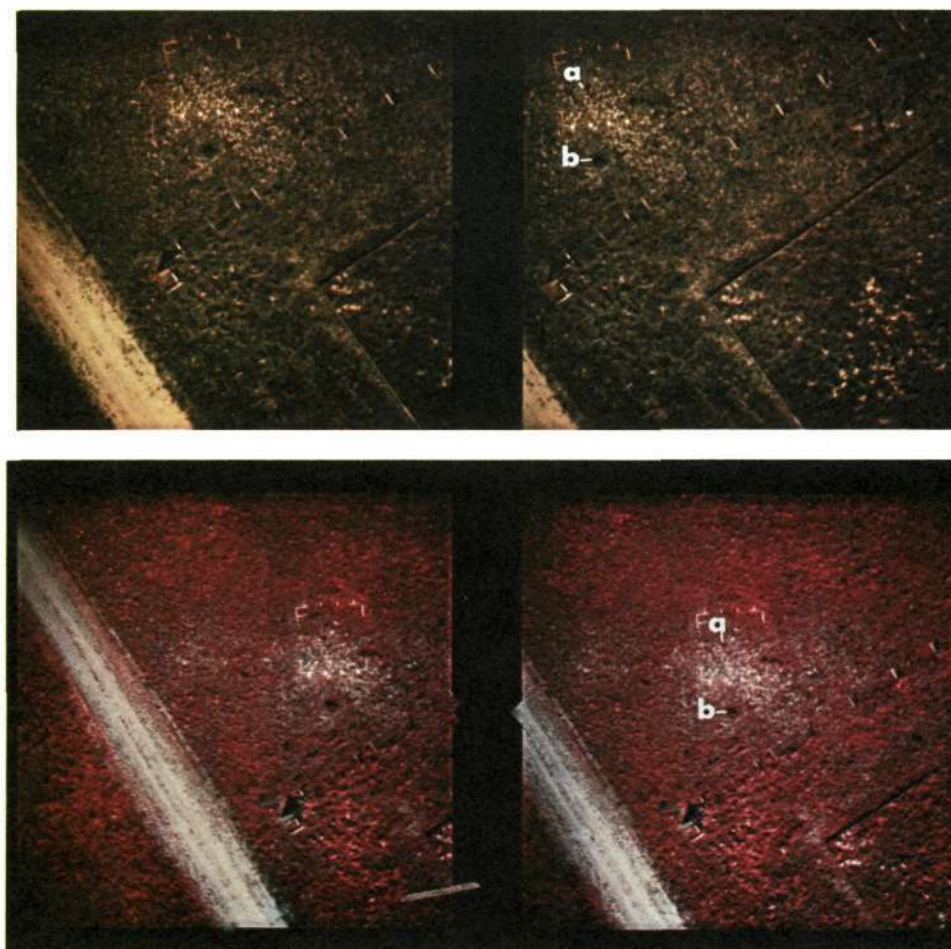


Figure 4.- Rabbitbrush (a) is difficult to identify in either color (top) or color infrared (bottom) stereograms even at photoscales of 1:600. Unless an interpreter knew that rabbitbrush was the only shrub species in the area imaged, commission errors were high, especially among the two species of rabbitbrush and snowberry. The other species indicated is cinquefoil (b). See Figure 2 (d) snowberry and (c) rabbitbrush for comparisons among the species.

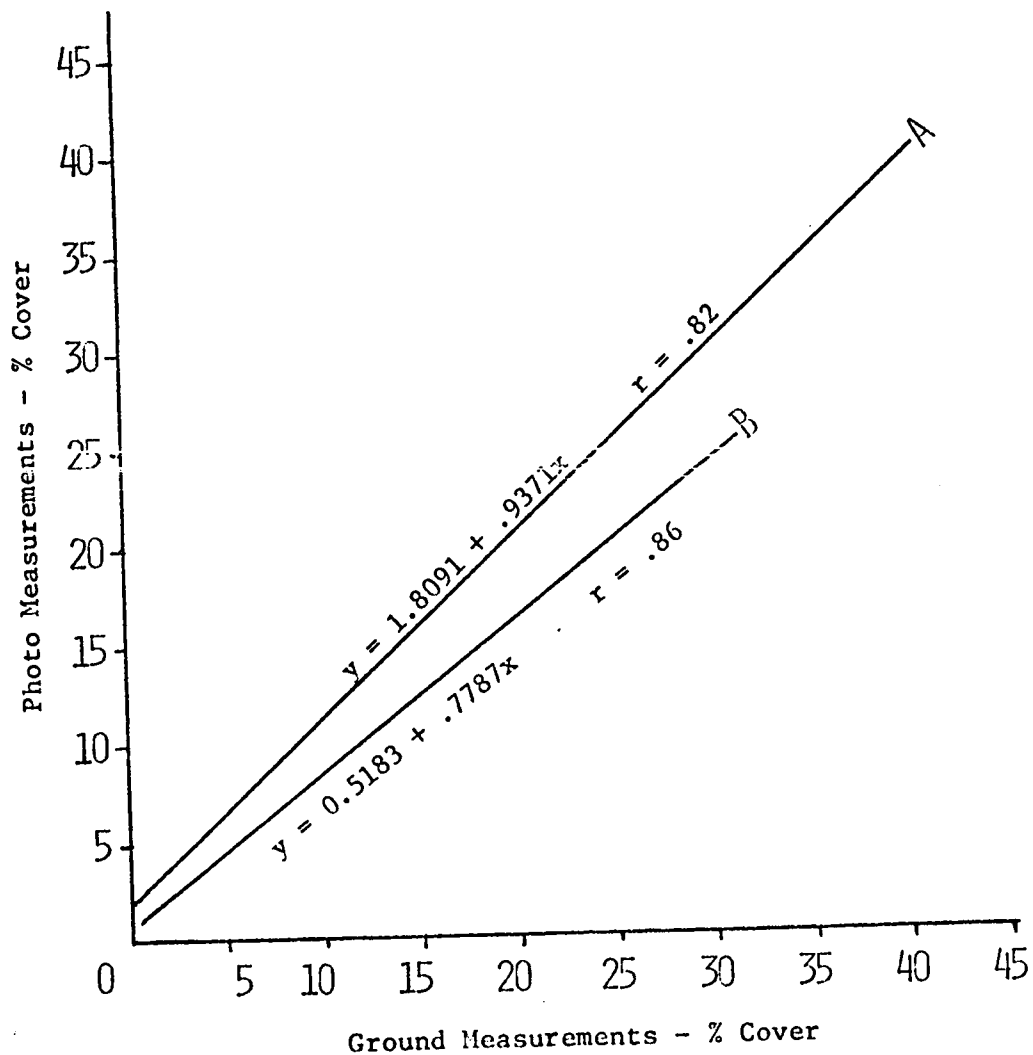


Figure 5.- Comparison of ground to photo measurements of percent cover of big sagebrush. (A): projected-scale micrometer; (B): measuring magnifier.

A VEGETATIONAL INVENTORY AND ECOLOGICAL RESOURCE ANALYSIS  
FROM SPACE AND HIGH FLIGHT PHOTOGRAPHY

by

Charles E. Poulton, Professor of Range Ecology  
David P. Faulkner, Research Assistant  
Barry J. Schrupf, Graduate Research Assistant  
Department of Range Management  
Oregon State University  
Corvallis, Oregon

Remote sensing data have limited value until someone uses the information to make a decision or to facilitate action that benefits man. This cannot be achieved until data are converted to information or intelligence, and this in turn relayed to an ultimate user in a comprehensible and useable form. Our attention has been heavily directed to problems of achieving this information flow.

The advent of space and high-flight synoptic photography brought a new need and dimension to renewable resource inventory and analysis. That is, the requirements for (1) an hierarchial classification of vegetation and related resources that is applicable across broad regions as well as adaptable to detailed inventories in restricted areas, and (2) a symbolic legend for the annotation and description of these resource classes.

In meeting these two requirements, the native vegetation worker, in contrast to the agricultural interpreter, must first determine, "what are the subject classes, what are their character and differentiating features, and how are the classes related?" Such an ecological classification provides the only biologically valid basis for making diverse land-use interpretations needed for policy, broad planning, and integrated resource development.

Our work on the classification of ground-truth data from native landscapes led naturally to development of a legend system that contributes significantly to solution of the information transfer problem.

The most familiar land use code is the one by the U.S. Department of Transportation (1969). The broadest classes they use are given in Table I. Their symbol 8 designates the resource production and extractive land uses under which subordinate categories for agriculture, range, and forest resources are found. For the natural resource disciplines, category 9 (undeveloped land and water areas) is both



misleading in name and redundant with some classes under category 8. While agricultural crops have been broken down in great detail, range and pastures are thrown into a single category, 8191, regardless of their nature, productivity level, or land use potential. Johnson (1969), University of California at Riverside, has provided a slight modification of caption 8191 by adding a fifth digit to separate range from grassland pastures. However, this lacks the specificity we need for ecological resource analysis.

Based on the same numerical symbolization concept, we have developed a similar, symbolic legend that progresses from the general to the specific as one moves from left to right through the symbol (Figure 1). This provides for three hierarchical levels of vegetational classification and three levels of classification of the environmental features associated with each vegetational class.

The primary resource and land use classes which we recommend are shown in Table II. These should have world-wide applicability in a legend system. This legend gives equal hierarchical levels to Barren Land, 1; Water Resources, 2; Natural Vegetation, 3; Agricultural Lands, 4; and Urban and Industrial Lands, 5. The majority of the classes in the Department of Transportation legend will be found under the latter class. The only change is to add the initial digit 5. The highest hierarchical level of natural vegetation classes we have described are shown in Table III. Our colleagues at the Forestry Remote Sensing Laboratory, Berkeley, are taking responsibility for the amalgamation of the agricultural legend into one universally applicable system that treats both cultured and non-cultured vegetation. It is being adapted to preserve the logic and detail of the Department of Transportation legend.

Table IV shows macrorelief classes, the highest level of generalization among the physical environment features. These features are consistently related to vegetation within given ecological provinces. Their recognition provides some associated evidence to narrow choices in the recognition of resource features through photo interpretation.

From space photography it is easy to map these landform classes and relate them to broad vegetational and soil characteristics. We have prepared such maps on enlargements of Apollo 9 color infrared photography, and they are included in our annual report for fiscal 1970 (Poulton *et al.* 1970). Even at the high hierarchical levels of classification used to make these "space maps," more vegetational resource detail is shown than is presently available, to our knowledge, on any single map of Maricopa County, Arizona. Comparisons with a county soil association map show close and meaningful relationships between vegetation and soils information at these scales.

We have also constructed a photo mosaic from RB57 high flight photography covering 63% of the county. We are in the process of transferring a slightly more detailed inventory of the vegetational resources, land-use patterns and potentials onto this photo map.

Figure 2 is a black-and-white copy of a 1:120,000 photo-scale treatment of the area north of the Whitetank Mountains and west of Phoenix. At this scale, more mapping detail is feasible. The specific units of vegetation that mirror unique productive capacities, environment factors, and land use potentials and limitations are interpreted according to our legend. Land uses that have strongly modified the natural landscape, plus the landform types that are ecologically relevant, can also be interpreted at this working photo scale.

To illustrate what some of these legend symbols mean, specific examples are given. First, on the high flight photo (Figure 2) note that the initial digit signifies a major class according to Table II. The digit 2 in the tens position also occurs on all native vegetation delineations. This indicates that in the bottomlands, valley fills, bajadas, and hills, desert vegetation is found—in this case, Sonoran Desert. The "1" in the units position, or "321," indicates that this is microphyll desert commonly with cacti.

What kind of land and vegetational resources are indicated in the extensive area designated by 321.11? This symbol identifies an open stand of creosote bush. It produces an understory of annual grasses and forbs when weather conditions are favorable. It occurs on flat macrorelief, in this instance dissected flat macrorelief; and the landform is usually valley fill and occasionally lower bajadas.

Symbol 321.21, appearing in the medium gray toned areas just below the hills on the high flight photo, represents plant communities identified by bursage, saguaro, and paloverde. This vegetation is typical of the upper bajadas, fans, and terraces, and is most commonly found on flat, but occasionally on undulating, macrorelief.

Symbol 321.22 indicates the vegetation common to the hills. The "21." shows that it still belongs to the Sonoran microphyll-cactus Desert. This vegetation type is identified by brittlebush, but with bursage, saguaro, and paloverde persisting. It is most commonly associated with hilly macrorelief, class 3. It is normally found on landforms we chose to call slopes, but also occasionally on strongly undulating uplands.

The final native vegetational delineation that appears on the high flight photo is designated 321.94. It is characterized by its location in drainageways and floodplains, usually on flat to slightly

dissected lands. The vegetation is variable, but usually includes foothill paloverde, mesquite, ironwood, and/or tamarisk.

This is only an abbreviated example of our legend and its use. We have had occasion now to carry this legend concept successfully in application from the Ft. Huachuca test area, where it was first developed, to the Phoenix test area. In October of this year, we had an opportunity to test the legend in cooperation with the Bureau of Land Management in Southern California. There, as in the Phoenix area, we found it necessary to add some additional vegetational indicator units at secondary and tertiary levels. We also dropped a few, but the broad legend classes in both numerator and denominator fit these areas very well, thus attesting to the region- and possibly the continent-wide application of the legend concept and the broader classes.

Now consider the practical value of this kind of resource mapping as a basis for land use planning and policy. Notice in Figure 2 how agricultural cropland conversion is moving into vegetational unit 321.11, comprising 18% of our intensive study area. This indicates a kind of land well suited to agricultural development, the best of the potentially irrigable land. It is from these areas, the creosote bush types, plus the broad-bottomland riparian types 321.94, that most of the good cropland has been carved in the Sonoran Desert.

In contrast, agricultural development has tended not to move into the areas designated by 321.21 suggesting that these latter area, which comprise 43% of the study area, are not well suited to agricultural development.

Space photography vividly and accurately shows how urban sprawl is eating into the choicest of the agricultural land in the area. The legend designator 519.14 indicates new suburban areas being developed as small acreages. In the upper right-hand corner of the high flight photo (Figure 2), two such areas are being developed in the 321.11 type (choice potential agricultural land). Other such areas are being developed well within the 321.21 type (in NE quadrant of Figure 2) where they more appropriately belong. Had such land classifications been recognized prior to development, urban growth could have been more appropriately encouraged or discouraged.

Other stories may be told to illustrate the relationship between ecological resource analysis and land use planning. Such knowledge gives a truly ecological basis for setting policy, planning, and zoning for the optimum use of the resources in a specified region. It is through ecological classification and relating of natural ecosystems to land use, development, and management that we will be able better to guide man's use of his environment and provide for a secure future by

designing legislation, policy, regional plans, and resource management programs that are compatible with the biological dictates of each kind of resource area. It is in providing the ground work for this kind of approach that ecological resource analysis and remote sensing from space and high flight can be successfully teamed in operational programs to help man meet his environmental challenges of today and tomorrow.

## REFERENCES

1. Johnson, C. W. 1969. A System of Regional Agricultural Land Use Mapping Tested Against Small Scale Apollo 9 Color Infrared Photography of the Imperial Valley. University of California, Riverside. USDI Status Report III, Tech. Report V, Contract Number 14-08-0001-10674.
2. Poulton, C. E., J. R. Johnson, D. A. Mouat, B. J. Schrupf. 1970. Inventory of Native Vegetation and Related Resources from Space Photography. Annual Report for Earth Resources Program, OSSA/NASA. Range Management Staff, Oregon State University, Corvallis, Oregon. 32 pp.
3. U.S. Department of Transportation. 1969. Standard Land Use Coding Manual. Government Printing Office (reprint of 1965 ed.). 111 pp.

TABLE I.- HIGHEST LEVEL OF GENERALIZATION IN A STANDARD SYMBOLIC NOTATION FOR IDENTIFYING AND CODING LAND USE ACTIVITIES <sup>1</sup>

<u>Code</u>	<u>Category</u>
1	Residential
2	Manufacturing
3	Manufacturing
4	Transportation, Communication and Utilities
5	Trade
6	Services
7	Cultural, Entertainment and Recreational
8	Resource Production and Extraction
9	Undeveloped Land and Water Areas

---

<sup>1</sup>Abstracted from Standard Land Use Coding Manual (Dept. of Transportation, 1969).

TABLE II.- A SYMBOLIC, TECHNICAL, AND DESCRIPTIVE LEGEND,  
PRIMARY RESOURCE AND LAND USE CLASS

<u>Mapping Symbol</u>	<u>Technical Legend</u>	<u>Descriptive Legend</u>
100	Barren Lands	The prominent features of barren lands are bare mineral soils and/or rocks. Vegetation is lacking or so widely scattered that the overall aspect is of a denuded area. Barren lands do not include temporarily denuded lands such as those caused by cultivation or plowing. Man-made barren lands created by urbanization or industry are found within the 500 class.
200	Water Resources	Only those areas perennially covered by water and lacking surface vegetation are classed as water resources. Vegetated water zones should be designated 380.
300	Natural Vegetation	Areas in which successional processes give an aspect of natural vegetation, even though the area may at one time have been strongly altered by man, are considered naturally vegetated. Areas such as logged-over forests or burns left to successional processes fit in this class.
400	Agricultural Lands	Agricultural lands are those which are characterized by man's relatively constant manipulation of the vegetation and micro-environment; the presence of feed, food, or fiber crops; and the general control of both placement and growth of vegetation.
500	Urban and Industrial Lands	Those lands which have been altered by man for living, manufacture, transportation and related activities are considered urban and industrial lands. Because of the nature of some of these land uses, they do not necessarily obscure classes 100, 200, or 300, in which case mapping units may contain these classes along with one or more 500 class.

TABLE III.- A SYMBOLIC, TECHNICAL, AND DESCRIPTIVE LEGEND,  
NORTH AMERICAN VEGETATIONAL PHYSIOGNOMIC TYPES

<u>Mapping Symbol</u>	<u>Technical Legend</u>	<u>Descriptive Legend</u>
300	Natural Vegetation	
320	Deserts	Deserts are typified by sparse vegetation and are located in the more arid regions of the Southwestern U.S. and Northern Mexico.
330	Steppes	Within steppes, the herbaceous layer, including both perennial grasses and forbs, is usually prominent. Low to medium height shrubs are scattered or lacking except in some grazing disclimax situations--notably among Great Basin shrub-steppe types.
340	Shrub/ Scrub Lands	Medium to tall shrubs or small trees (scrub) are the prominent vegetation. These usually form a closed layer so that the herbaceous layer is completely subordinate. The herbaceous vegetation is highly variable but can be important.
350	Savannas	Dense stands of herbs overlain by scattered individuals of tall shrubs or trees.
360	Wooded and Forested Lands	The tree layer forms the prominent vegetational feature. This layer often forms a closed canopy over a variety of subordinate vegetation.
370	Alpine and Arctic Tundra	Tundra is characterized by cold temperatures and short growing seasons. The vegetation is usually low and lacks distinct layers.
380	Vegetation of Aquatic Environments	The vegetation of aquatic environments appears above the perennial water cover.



TABLE IV.- A SYMBOLIC, TECHNICAL, AND DESCRIPTIVE LEGEND,  
MACRORELIEF CLASSES <sup>1</sup>

<u>Mapping Symbol</u>	<u>Technical Legend</u>	<u>Descriptive Legend</u>
1	Flat Lands	A generally flat landscape with prominent slopes less than 10 percent.
1a		The landscape is essentially smooth. Dissection is minimal. The regional slope in this class is nearly always between 0 and 3 percent.
1b		The landscape is relatively flat; however, dissection has progressed to a noticeable point. Dissection is either sharp and widely spaced (in which case side slopes may be over 10 percent), or gently rolling and more closely spaced. Where side slopes exceed 10 percent, microrelief is generally less than 10 percent.
2	Rolling and Moderately Dissected Lands	A rolling or moderately dissected landscape with prominent slopes 10 to 25 percent (side slopes may exceed that figure in the case of dissected planar surfaces).
2a		The landscape is rolling or hilly; a regional slope is not readily apparent - or - a regional slope of 10 to 25 percent is present.
2b		The landscape consists of a moderately to strongly dissected planar surface (i.e., pediment, bajada, valley fill, etc.). The regional slope is <u>generally</u> between 2 and 6 percent; side slopes must be steeper than 10 percent. If side slopes are steeper than 25 percent, relief must be less than 100 feet. The drainage network is finer than that of 1b.

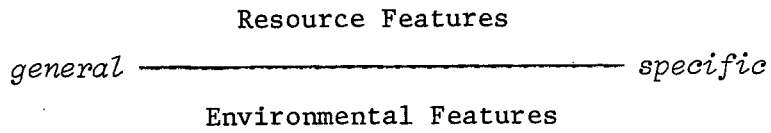
---

<sup>1</sup>Mapping legend for macrorelief adapted to fit the geomorphology of southern Arizona.

TABLE IV.- Concluded

<u>Mapping Symbol</u>	<u>Technical Legend</u>	<u>Descriptive Legend</u>
3	Hilly Lands	The landscape is hilly to submountainous; slopes are moderate to steep, predominantly exceeding 25 percent. Relief is generally over 100 feet but less than 1000 feet. Where relief approaches 1000 feet, the landform system appears to be relatively simple - with smooth slopes. Drainage systems generally have the same base level.
4	Mountainous Lands	The landscape is mountainous, having high relief, usually over 1000 feet. Slopes are moderate to steep, frequently exceeding 50 percent. The landform and drainage systems are usually complex, with drainage networks having base levels quite independent of one another.

GENERALIZED FORM:



SPECIFIC FORM:

Resource Classes Based on Vegetational Indicators

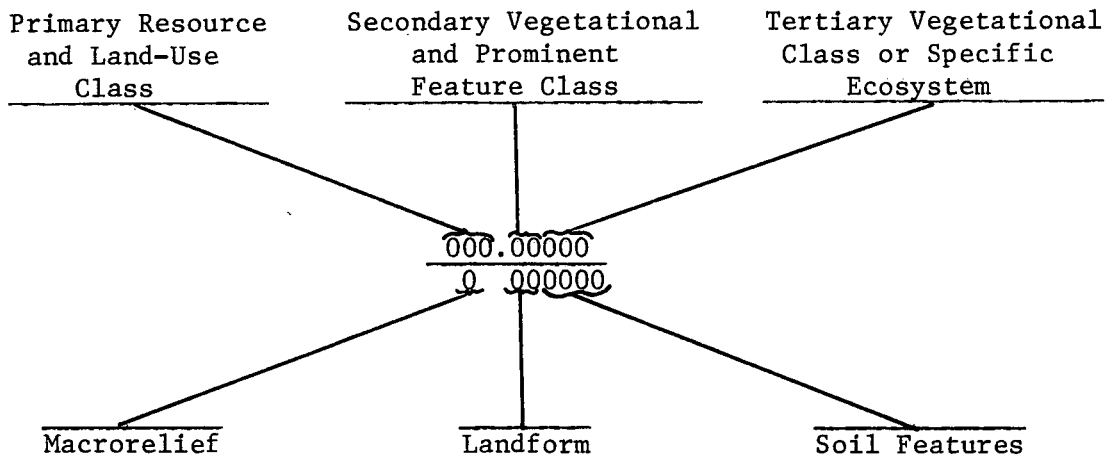


Figure 1.- An ecosystem legend format for range resource and land use analysis from space and supporting aircraft imagery.

Figure 2.— A portion of photo mosaic map of Maricopa County, Arizona, showing natural vegetation resources, agricultural, and urban land use. Mapped on high flight photography.

## SYMBOLIC LEGEND

## TECHNICAL LEGEND

## Native Vegetation

321.11	Creosote bush often with annuals
321.21	Bursage, saguaro, paloverde
321.22	Brittlebush, bursage, saguaro, paloverde
321.94	Mixed vegetation in desert drainage ways

## Agricultural

400	Mixed agriculture
-----	-------------------

## Urban &amp; Industrial

510	Residential area
519.1	Small acreage suburban residences
519.14	Developing small acreage suburban residences
545.1	Freeways
545.82	Graded and graveled roads
567.5	Military bases

## Macrorelief

1a	Undissected flat land
1b	Dissected flat land
3	Hilly land
4	Mountainous land

## Landform

B	Bottomland
Ca	Bajadas and fans
Cb	Valley fills
F	Slopes



Figure 2.

## REMOTE DETECTION OF INSECT EPIDEMICS IN CONIFERS

by

Robert C. Heller <sup>1/</sup>INTRODUCTION

The detection and location of timber lost to destructive agents in the forest is best done by a remote sensing technique of some kind. Most stress, whether it be caused by insects, disease, soil salinity or water deficiency, causes a change in foliage color. This discoloration can be seen better from an aerial platform than by making systematic ground surveys. Some of the early insect surveys by Forest Service entomologists showed that there was more than a 100 times improvement in efficiency by using aerial observation methods as compared with ground methods. Later work has shown still greater improvement in detection success by using color photography at medium scales (1:8,000).

Bark beetles are one of the nation's most serious killers of coniferous timber. Beetles also induce stress faster than any other damaging agent--excluding fire. In the Black Hills of South Dakota there has been a continuing epidemic of the Black Hills beetle (*Dendroctonus ponderosae*, Hopk.) in ponderosa pine (*Pinus ponderosa*, Laws.). The Black Hills (Fig. 1) extend about 64 by 160 kilometers and are covered mostly by ponderosa pine. In this vast green area, beetle attacks and associated blue stain fungus cause the affected trees to change color from green to green-yellow, yellow, and yellow-red as the season progresses. Figure 2 is an example of the

---

<sup>1/</sup> Pacific Southwest Forest and Range Experiment Station,  
Forest Service, U. S. Department of Agriculture, Berkeley, California

high contrast in August between healthy trees and those dying from bark beetle attack. A bare area in the foreground of this photograph is a tailings pile caused by gold mining at the turn of the century in the Black Hills. This pile of bare earth measures 80 meters (250 feet) and can be used as a point of reference for the reader when viewing the sample multiscale photographs described later.

I would like to describe two facets of our stress studies in this report--aerial photography and multispectral sensing for previsual detection. In connection with aerial photography, we are interested in optimum combinations of films, filters, and scales which are most effective in detecting stressed-discolored timber. Because the discolored infestations shown in Figure 2 vary in size from 3 to 200 meters, we are afforded natural resolution targets of varying sizes. By obtaining small-scale photographs from our own aircraft and by the NASA RB-57, we were able to study the effect of film and scale on resolution and the expected detectability on ERTS imagery. The second facet of our work involves previsual detection of stressed pine trees. In this case, we would like to determine the best sensor for detecting trees which are infested and dying but which have not yet discolored. If this phase of the work is successful, it will permit timber managers to greatly reduce their cost of insect control measures by permitting them to locate beetle-infested trees, remove them from the woods, and reduce the likelihood of an epidemic continuing and of additional resource losses.

SEASONAL, FILM, AND ALTITUDE EFFECTS  
ON INFESTATION DETECTION BY AERIAL PHOTOGRAPHY

SEASONAL AND FILM EFFECTS

While bark beetles induce stress more rapidly than most other destructive agents, the slowdown of the tree's metabolism usually requires about nine months before any visible signs of foliage discoloration begin in the Black Hills. For example, when adult beetles attack pine trees in August, it requires almost a full year for new broods to develop and emerge from those trees. The rate at which the trees die depends upon several factors, such as the number of beetles attacking, amount of blue stain fungus development within the xylem, and the susceptibility and vigor of individual pine trees. The drying out of pine foliage is what causes visible discoloration--chloroplasts die and other pigments--carotin and xanthophyll--become visible. Usually a ground observer cannot see the change in foliage color until almost nine months after beetle attack. This is usually in May in the Black Hills. In the South the rate of foliage discoloration from the southern pine beetle can occur in six weeks during the summer months.

We monitored several infestation spots by taking color and color infrared aerial photographs once a month from May through August (Figs. 3A and 3B). From our ground inspection of this site we know that 40 trees of the more than 200 tree images in these photos have been attacked; this infestation measures 36 meters (120 feet) in diameter. In May, only about 10 trees are visible on either the color or color infrared photos; the lighter yellow trees on the color photo (Fig 3A) are those which are



beginning to discolor first. On the color infrared (Fig 3B) in May, the same trees appear as a lighter pink. More and more trees discolor as the season progresses through June, July, and August. In August, all 40 trees were visible and detected by the photo interpreters. As a result of these studies we have found that color or color infrared film does not act as a previsual sensor. These films, then, are useful for detecting discolored trees only. We also learned that maximum contrast and maximum discoloration occurred in August.

#### ALTITUDE AND RESOLUTION EFFECTS

The Earth Resources Technology Satellite (ERTS) is expected to be put in orbit in March 1972. While no one can predict exactly the kind of spectral response and resolution qualities that the return-beam vidicon and four-channel multispectral scanner will produce, the expectations are that resolution will probably be no better than 100 meters. In August 1969, we attempted to obtain aerial photography of vegetative stress which closely approximates the spectral band widths which will be used on the television camera or multispectral scanner. These band widths are listed as follows:

Spectral Band Width (micrometers)		
Channel or Camera	Multispectral Scanner	RBV Camera
1	0.5 - 0.6	0.475 - 0.575
2	0.6 - 0.7	0.580 - 0.680
3	0.7 - 0.8	0.690 - 0.830
4	0.8 - 1.1	

While not all of the filters used in aerial photography coincide with the multispectral scanner channels or the RBV cameras, some of the Wratten filters approximate these spectral band widths. For example, the Wratten 58 filter is close to the first channel of the multispectral scanner and the first camera of the RBV, and the A25 Wratten filter approximates channel 2 and camera 2 of these ERTS subsystems. Similarly, the Wratten 89B filter used with infrared aerial film approximates channels 3 and 4 of the multispectral scanner and the third camera in the RBV subsystem. These combinations of filters and other color films were requested to be flown from the RB-57 aircraft in August 1969. The actual cameras and filters flown on this flight are listed in Table 1.

#### RB-57 Flight - Mission 101

Two flights were made by the RB-57--one on August 3, and the second on August 8, 1969. Photographs from the August 3 flight were not usable because the area was more than 80 percent cloud covered. The plotted flight lines of the August 8 flight are shown on Figure 4. Three flight lines were requested to be flown which cover the northern part of the Black Hills National Forest. This figure shows the actual location of the flight lines flown on both August 3 and August 8. Unfortunately, the predicted flight line location did not coincide with the actual location, and we were unable to get the coverage desired. Flight line orientation within the Black Hills is particularly difficult because of lack of landmarks; if any future high-altitude flights are made, we would suggest extending

the beginning and ending points of the flight lines so that flight line location is properly identified.

The purpose of the requested RB-57 coverage was to make a comparison of color photography taken at a scale of 1:8,000 at predetermined flight strip locations throughout the northern Black Hills. We had hoped to develop a relationship between 10 sample strips (1.6 by 16 kilometers) covered by large-scale (1:8,000) color photographs and the RB-57 color and color infrared photographs (1:110,000). The estimates of mortality derived by using probability sampling from the large-scale color photography strips are reported by Heller and Wear (2). Examination of the flight map (Fig. 4) shows that only four of the ten large-scale strips were covered by all scales of the RB-57 flight.

We fortunately obtained complete large- and small-scale photographic coverage of a 1.6 by 6.0 kilometer study area (Fig. 5) which contained 211 discolored infestations (or variable-size resolution targets). The sizes of each infestation were measured carefully on the ground, located on aerial photographs, and the numbers of trees counted within each infestation. Data from this ground survey, then, were used to rate photo interpretation efficiency. All subsequent sample photography can be oriented to this study area; the gold mine tailings pile described earlier in Figure 2 can be seen in Figure 6 which is representative of the Zeiss color photography (1:8,000) taken along our sample strips. Only the portions of the 9-inch format photography (Zeiss 12-inch focal length and RC-8 6-inch focal length cameras)

which cover the study area are shown in Figure 7. Similarly, examples of 3 of the Hasselblad photos are shown in color, infrared color, and color film taken through a minus blue filter in Figure 8; they also cover the same study area.

Almost all RB-57 aerial photography exposed over the Black Hills was underexposed from one to one-and-one-half diaphragm stops. This was true for all large-format photography and for four of the six Hasselblad cameras. The only properly exposed films were the color film exposed through the minus blue filter and the Ektachrome infrared film with the Wratten 15 filter with two of the Hasselblad cameras. Reflectance can be two to four times lower over a dense forest as compared with open farm land which surrounds the Black Hills. Exposures over farm land looked quite good. We would suggest the installation of automatic exposure controls on the diaphragms of all NASA cameras since it is impossible to make manual diaphragm adjustments once the RB-57 leaves the ground. Underexposure causes the duplicate transparencies to be excessively dark; small targets are not resolved, and shadows along north-facing slopes are so dark that even high-contrast targets are obscured. Thus, definite conclusions on best film, filter, and scale combinations are difficult to determine from these particular photographs.

Despite the fact that most of the film was underexposed, we interpreted all images over the study site. As might be expected, the larger the scale, the greater the accuracy. Also, as the infestations or targets became larger, the infestation accuracy improved (Fig. 9).

In comparing the films used on the Hasselblad cameras, all at a scale of 1:220,000, we obtained a similar trend as far as infestation size is concerned (Fig. 10). In this case the films which rated the highest were the color infrared, the color film with the minus blue filter, and the Panchromatic film with a 25A filter. The color film with a minus blue filter rated fairly high probably because it was one of the better exposed films of the lot.

The results of our own moderately small-scale photography over the study area compares just two color films (color and false color), but by infestation size in meters (Fig. 11). Again, as infestation size (or resolution size) becomes large, detection success improves; however, detection success is acceptable only on the larger infestations (over 30 meters in size and more than 20 trees) when scales as small as 1:174,000 are used. For determining stress in the early stages of an epidemic, it is apparent that we will need good resolution capabilities--probably 5 meters (16 feet). For discovery of stress in very remote areas, we may be able to detect discolored timber with resolution capabilities of 30 to 50 meters (100 to 200 feet). Based on the expected resolution (100 meters) of the two ERTS sensors--the return-beam vidicon and four-channel line scanner--it seems unlikely that we will be able to detect any but the largest discolored areas.

PREVISUAL DETECTION WITH MULTISPECTRAL SCANNERS

## BIOPHYSICAL MEASUREMENTS TAKEN ON HEALTHY AND INFESTED TREES

A great many techniques were developed and improved over the course of this study. Most of these methods have been described in detail by Weber (5) and Heller (3), but the ones which have been added during the past year and which have helped us derive our ground truth information more quickly are listed below:

Soil moisture data are now being collected by a neutron probe (Fig. 12A). This device measures a differential bombardment of neutrons from a nuclear source through moist and dry soils to a detector. It replaces the Coleman soil moisture meter which we had used previously.

Solar radiation and net radiation will now be monitored by aerial tramways which travel above the tops of the trees on wires supported between tall towers (Fig. 12B).

In the early stages of our study, most of the data were collected independently on separate recording instruments and analyzed separately-- a slow, tedious process. In 1970, we used a data logger and the moving tramway described by Wear and Weber (4) on their *Poria weirii* study to collect up to 38 channels of data, digitize them, and store them on magnetic tape (Fig. 12C). This system, now being erected on the Black Hills test site number 149, permits rapid access to the data and is in computer-compatible form. It saves up to one year on the analysis of the energy budget data. Now we can log internal needle temperatures, net and total

radiation, and wind velocity and direction continuously. We have developed computer programs which will recover these data the day after they are recorded.

#### Optical-mechanical Scanning Imagery

In a NASA-sponsored flight in July 1969, the University of Michigan multispectral line scanner was flown over our instrumented test site. (number 149). It used the discrete channels shown in Table 2. Data were collected at four time periods--early morning, midmorning, early afternoon, and late afternoon. These periods coincided with maximum change in tree metabolic activity as determined from our field measurements. We used handy-talky radios for ground-to-air communications, primarily to inform the operator of the thermal scanner about the range of apparent temperatures in ground targets. This information permitted him to adjust his temperature-controlled reference plates on the thermal line scanner.

We received analog printouts of each of the channels listed in Table 2 about one month after the July flight. Because our target size is relatively small for training the processor in the tape-loop training system of combining channels, we had to devise special adaptations of programs developed by Hasell, Le Gault, and Thomson (1).

Our training sets consisted of four classification models--healthy ponderosa pine, nonfaded infested ponderosa pine, discolored and dying ponderosa pine, and old-killed trees. In using the SPARC (Spectral Processing and Recognition Computer) processor and associated digital

computer, we first determined the optimum channel selection for the above four classifications. We found that little improvement of channel combining beyond five channels occurred and that the 0.8 to 1.0 micrometer meter band was the most efficient band in separating pine trees from all other classes of targets. The 0.40 to 0.44 spectral band was the most efficient in separating the old-killed trees from healthy and green infested trees.

Both the maximum likelihood ratio analysis and Euclidian distance analysis techniques were used at several voltage threshold levels. The combined target signature transparencies were made into color Ozalids to produce color mosaics for the selected flight periods during the day. We received the processed data from the Willow Run Laboratories in November 1970.

Several attempts were also made to separate targets by "thermal contouring". In this processing technique, one can adjust a limited temperature range of objects so that they may be expanded over a wide gray scale range. Since flights were made at three altitudes above terrain (450, 900, and 1350 meters), we were able to process the best single flight run for each altitude. The selection of the best flight run was done very carefully and only after consideration was given to the maximum temperature ranges between the healthy and affected trees occurring on the ground at the time of the flight. Figure 13 is an example of a 17° C. (Celsius) spread of target temperatures which occurred on July 22 at 1325 hours; this was a 900 meter-altitude flight using the 8.2 to 13.5 micrometer waveband. This color mosaic was compared carefully with the 1:8,000 scale color photographs taken



34-12

with a Zeiss camera over the study area. There is good agreement on many of the general classifications such as separation of grass from hardwoods, from pure conifers, and from exposed rock and soil. Some of the affected pine trees were confused with the nonaffected, but in general, classification accuracies are much improved over what was done one year earlier.

An example of the complex physical and biophysical factors which affect the emission of healthy and insect-infested trees can be seen in Figure 14. Note particularly the third graph down from the top where emission temperatures are shown. On this particular day, the greatest difference in temperature occurred between the healthy and attacked trees about 1500 hours; however, measurable differences began to show up after 1200 hours. In general, ground emission temperatures have been fairly sizeable--2° to 6° C. (Celsius)--on bark beetle-attacked trees. However, we have not been able to show a marked temperature difference for Douglas-fir trees infected with a *Poria weirii* root rot disease in Washington. A similar graph of data has been made in the disease case on two dates--May and July 1970 (Fig. 15); note again that the emission temperatures of the infected and healthy Douglas-fir trees are almost identical. It is therefore unlikely that any kind of thermal sensor would be successful in detecting the differences between these two classes of trees. A digital gray map was made from the analog scanner data at the University of Michigan and is shown in Figure 16. The objects on this gray map which are warm appear darker in tone; the cooler trees and shadows are very light in their representation of lower temperatures. Note that there is an almost uniform representation

of temperature of the trees located under the towers where the tramway-collected thermal data were made. These data support the null hypothesis that there is no temperature difference in the case of disease-infected trees, and therefore sensing with an airborne thermal scanner would be useless, at least in the case of *Poria weirii* (Fig. 16).

#### CONCLUSIONS

1. With properly exposed color or infrared color film, we can expect to detect discolored foliage caused by insect infestations in ponderosa pine on moderately small-scale photographs (1:32,000) with acceptable accuracies of all but the smallest infestations--less than 6 meters in diameter.

2. Black and white photographs taken from the RB-57 with Hasselblad cameras which matched the wavebands of the ERTS multispectral scanner were combined into one additive color photo. This imagery was not as useful as photographs taken on color, color infrared, or color film with a minus blue filter. Underexposure of the black and white Hasselblad imagery is the probable reason for this.

3. Based on the high-altitude color and color infrared photos which we have obtained to date, it is likely that only insect infestations larger than 100 meters in diameter will be detectable on ERTS imagery.

4. Multispectral preprocessing and processing procedures developed at the Willow Run Laboratories of the University of Michigan have improved over the past year; however, SPARC-processed data from the multispectral

scanner indicate that there are more commission errors than we are willing to accept for accurate detection of beetle infestations.

5. Processing of thermal data by thermal contouring is another technique which shows promise, but it, too, does not discriminate green infested trees from the discolored infested trees to acceptable accuracy levels.

6. It is unlikely that we will be able to improve previsual detection until an instrument is available which combines the thermal, near infrared, and visible channels. We look forward to testing a single aperture multi-spectral scanner and feel that it will provide us with the most powerful sensing device for previsual detection.

#### LITERATURE CITED

1. Hasell, P. G., R. Le Gault, and F. J. Thomson. 1968. Investigations of spectrum matching techniques for remote sensing in agriculture. Interim report, Volumes 1 and 2 (Report 8725-13-P). Willow Run Laboratories of the Institute of Science and Technology, University of Michigan, Ann Arbor, Michigan.
2. Heller, R. C., and J. F. Wear. 1969. Sampling forest insect epidemics with color films. Sixth International Symposium on Remote Sensing of Environment Proc. 1969:1157-1167.
3. Heller, R. C. 1968. Previsual detection of ponderosa pine trees dying from bark beetle attack. Fifth Symposium on Remote Sensing of Environment Proc. 1968:387-434.

4. Wear, J. F., and F. P. Weber. 1969. The development of spectro-signature indicators of root disease impacts on forest stands. Fourth Annual Report. Available in microfiche from NASA, Washington, D.C. Scientific and Technical Aerospace Reports.
5. Weber, F. P. 1969. Remote sensing implications of water deficit and energy relationships for ponderosa pine attacked by bark beetles and associated disease organisms. Ph. D. Thesis. University of Michigan, Ann Arbor, Mich. 143 pp. Available in microfiche from University of Michigan.

Table 1. Film-filter-scale combinations exposed during RB-57  
Flight Mission #101 - August 3 and 8, 1969.

Film	Filter	Camera	Focal Length	Scale	Format
Color IR (SO 117)	Zeiss "B" (15)	Zeiss	304 mm.	1:55,000	210 mm.
Color (2448)	HF-3	RC-8	152 mm.	1:110,000	210 mm.
Color IR (SO 117)	15	RC-8	152 mm.	1:110,000	210 mm.
Color (SO 368)	2A	Hasselblad	76 mm.	1:220,000	70 mm.
Color (SO 368)	12	Hasselblad	76 mm.	1:220,000	70 mm.
Color IR (SO 180)	15g	Hasselblad	76 mm.	1:220,000	70 mm.
Panchromatic (3400)	58	Hasselblad	76 mm.	1:220,000	70 mm.
Panchromatic (3400)	25A	Hasselblad	76 mm.	1:220,000	70 mm.
Panchromatic IR (SO 246)	89B	Hasselblad	76 mm.	1:220,000	70 mm.

Table 2 Spectrometer channels used for target recognition  
by University of Michigan aircraft and processing  
unit and their respective spectral colors

SPECTRAL COLOR	WAVELENGTH (Micrometers)	CHANNEL NUMBER
Violet	.40 - .44	1
	.44 - .46	2*
Blue	.46 - .48	3
Blue-Green	.48 - .50	4*
Green	.50 - .52	5
	.52 - .55	6
Yellow-Green	.55 - .58	7
Yellow	.58 - .62	8
Light Red	.62 - .66	9
	.66 - .72	10
Deep Red	.72 - .80	11
	.80 - 1.0	12
Reflective Infrared	1.0 - 1.4	13
	1.5 - 1.8	14
	2.0 - 2.6	15
Thermal Infrared	4.5 - 5.5	16
	8.2 - 13.5	17

\* Not used in the course of this study.

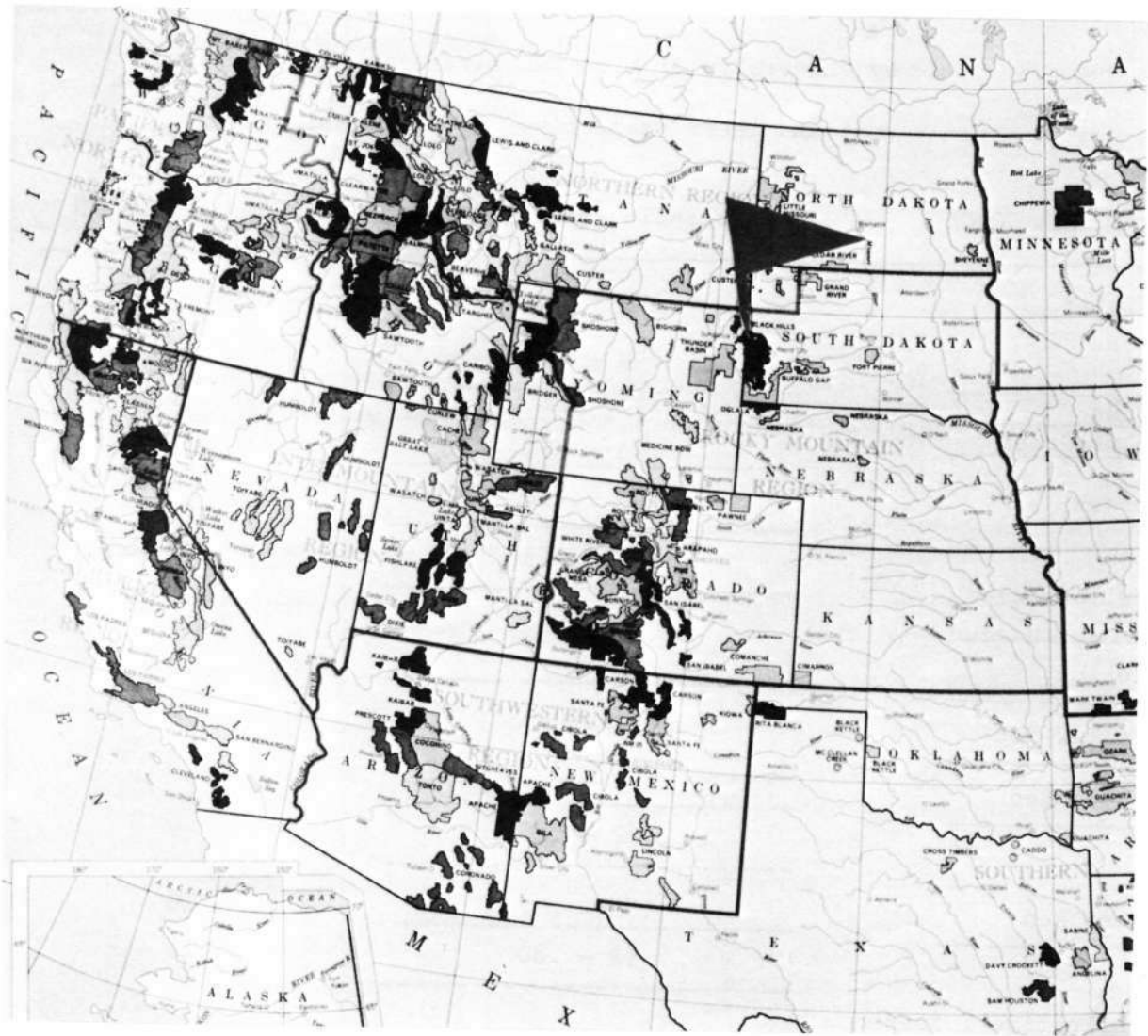


Figure 1.--Flag shows location of Black Hills National Forest near Rapid City, South Dakota.



Figure 2.--Oblique view of Black Hills beetle, *Dendroctonus ponderosae*, Hopk., damage to ponderosa pine, *Pinus ponderosa*, Laws. Yellow to yellow-red trees are most recently killed and offer greatest contrast to healthy pines. Note the mine tailings in foreground; it measures 80 meters (250 feet) and can be seen in small-scale imagery taken by RB-57 (Figures 7 and 8).



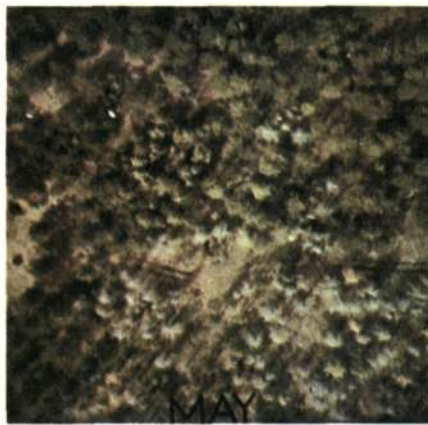
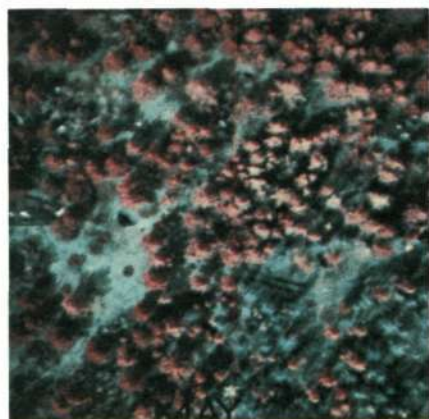
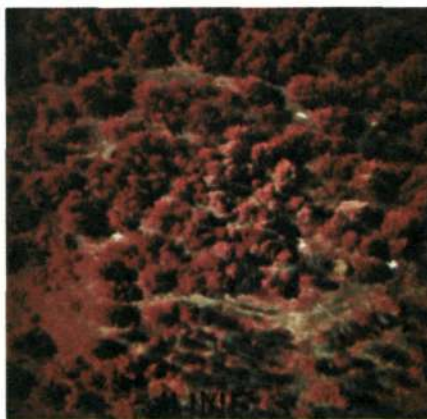


Figure 3A. Normal color film - Anscochrome D/200. Seasonal differences of tree stress caused by bark beetles. Forty infested ponderosa pine trees occur on these transparencies. Note the rate of foliage discoloration in May, June, July, and August--scale 1:1,600.



MAY



JUNE



JULY



AUGUST

Figure 3B. Kodak Ektachrome Infrared Aero - type 8443. Seasonal differences of tree stress caused by bark beetles. Forty infested ponderosa pine trees occur on these transparencies. Note the rate of foliage discoloration in May, June, July, and August--scale 1:1,600.

CHART OF DESIGNATED FLIGHT LINES AND COVERAGE OBTAINED  
 BY NASA RB-57 FLIGHT, AUGUST 3 & 8, 1969.

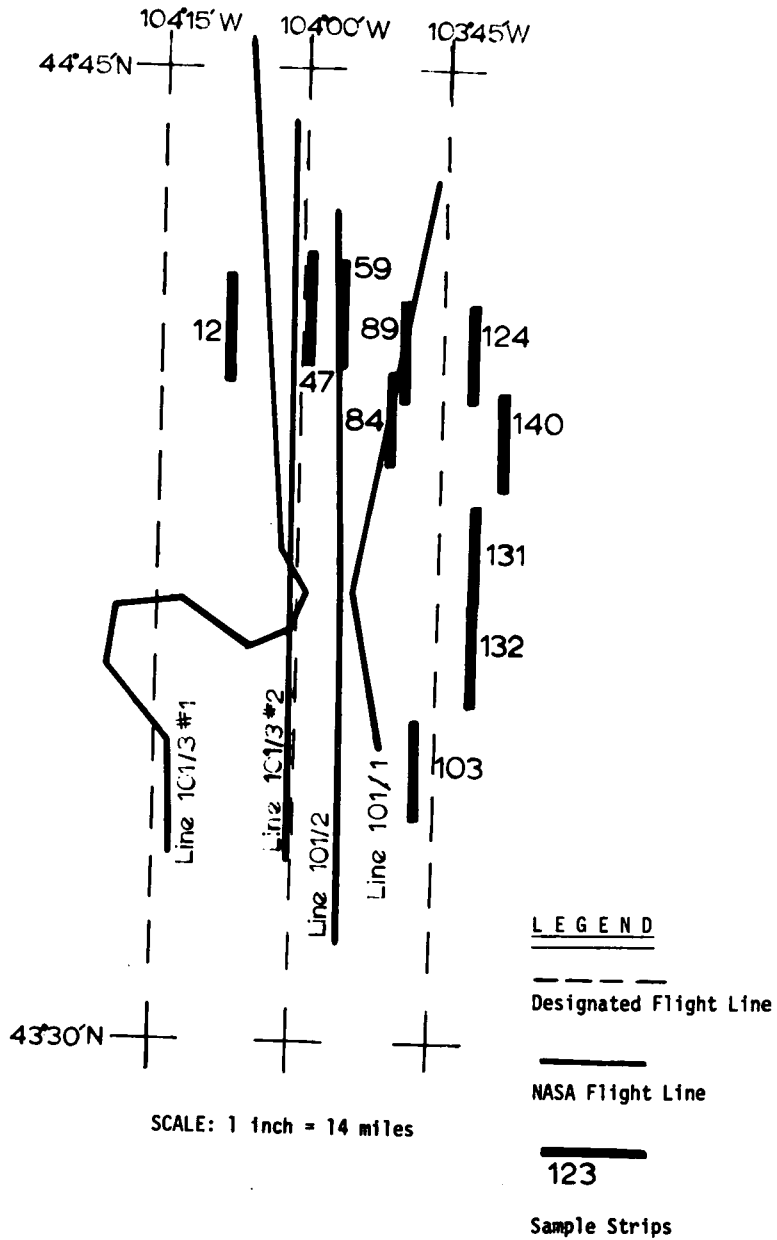


Figure 4.--Flight coverage of RB-57 on August 3 and 8, 1969. Dashed lines show expected flight line location. Heavy lines show 10 samples--each 1.6 by 16 kilometers, taken on color film--scale 1:8,000.

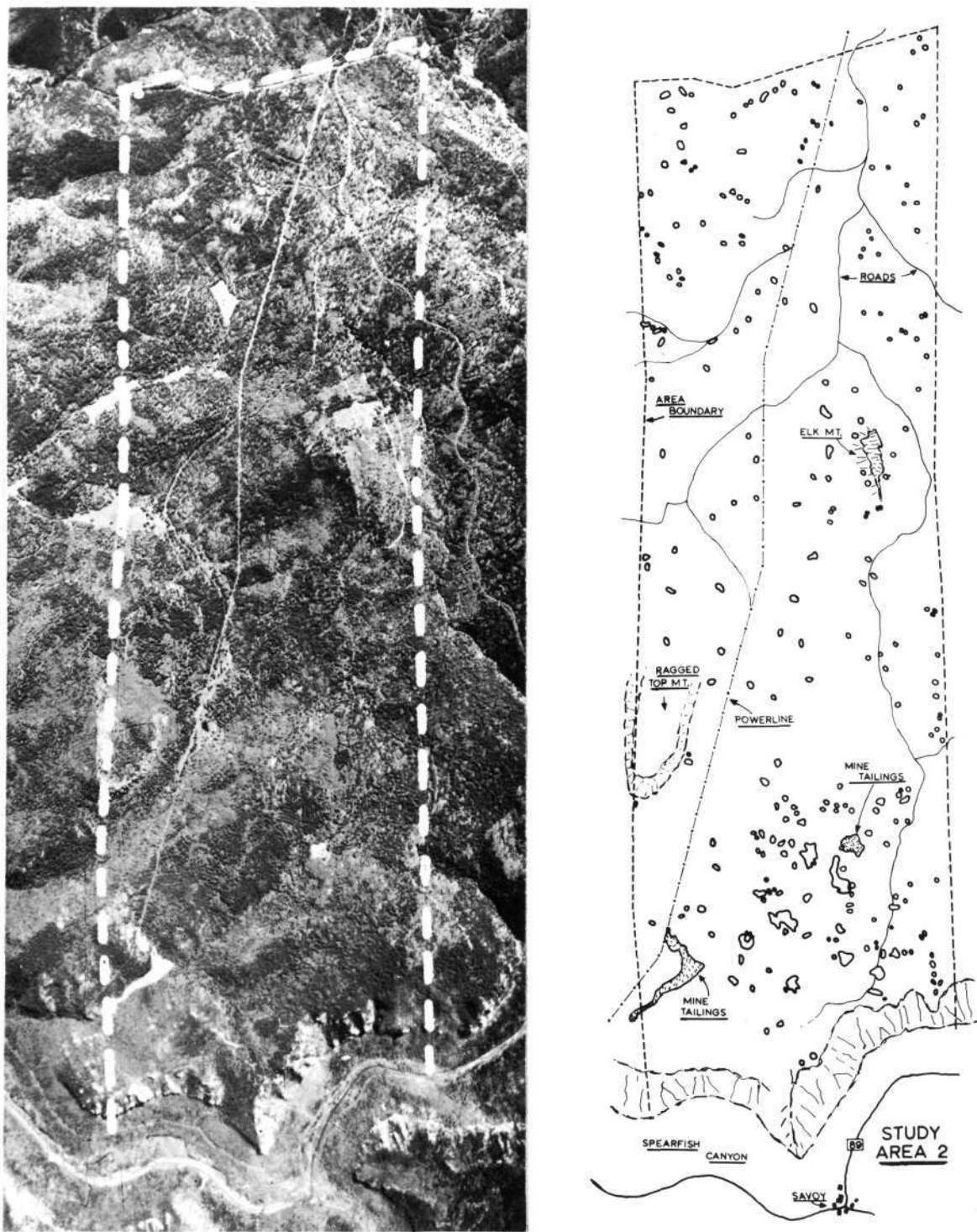


Figure 5.--Aerial mosaic on left of 1.6 by 5 kilometer study area near Lead, South Dakota. On right, 211 infestations of various sizes (3 to 200 meters) are plotted at the same scale.

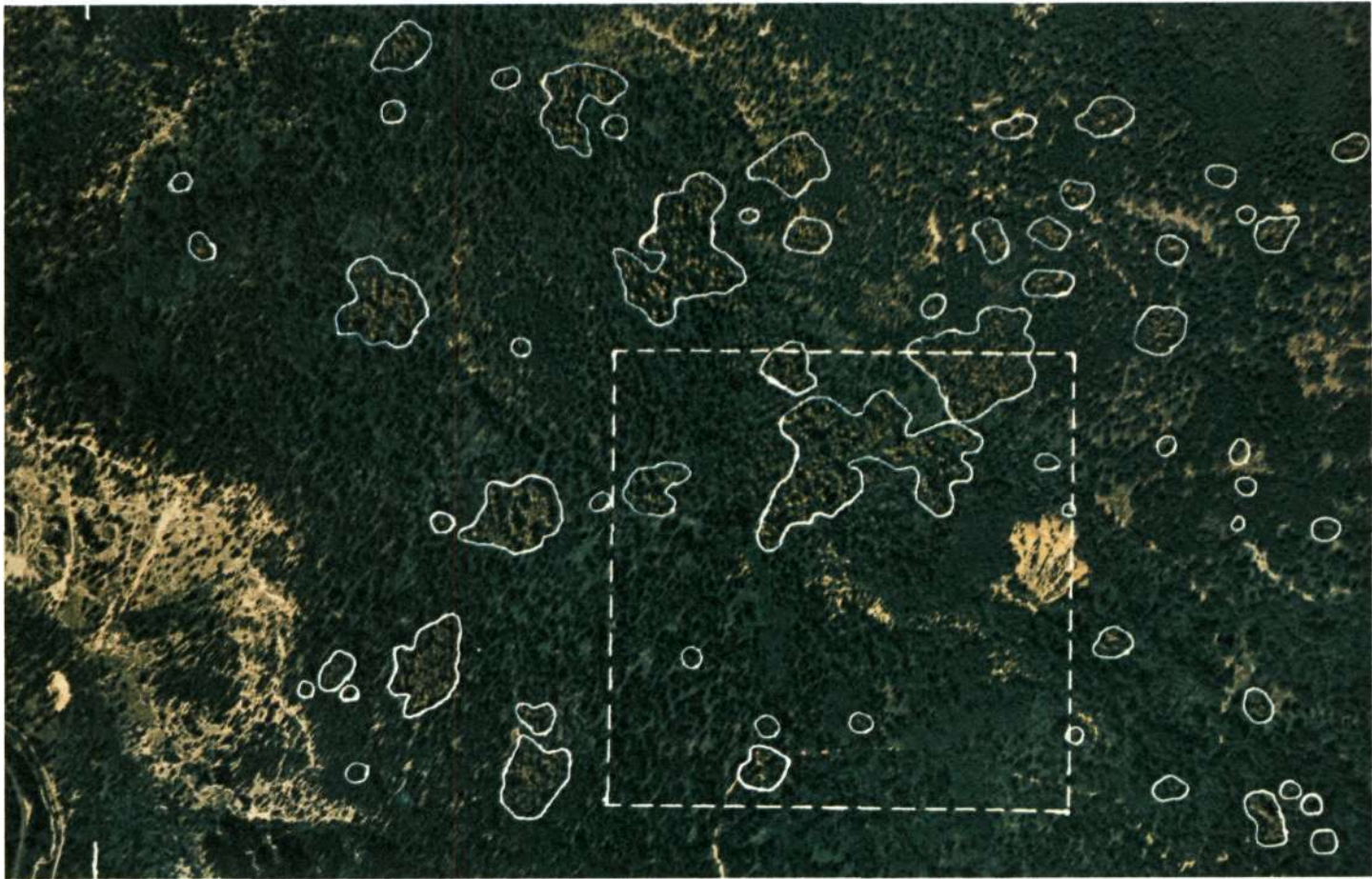


Figure 6.--Color photograph taken on August 11, 1969, with Zeiss 21/23 aerial camera over study area--scale 1:8,000. Infestations are outlined in white. Note high contrast of tailings pile shown on oblique (Figure 2). While several infestations are larger, target contrast is lower because of grassy ground cover.



(A) 1:110,000



(B) 1:110,000



(C) 1:55,000

Figure 7.--RB-57 coverage of study area. (A) RC-8 152 mm. Ektachrome (2448) + HF-3. (B) RC-8 152 mm. Ektachrome Infrared (SO 117) + 15. (C) Zeiss 304 mm. Ektachrome Infrared (SO 117) + "B" (15). Most forested areas were underexposed one to two times.



(A) 1:220,000



(B) 1:220,000



(C) 1:220,000



(D) 1:220,000

Figure 8.--Hasselblad imagery over 1.6 by 5 kilometer study area. Note size of tailings pile (80 meters). (A) Color (SO 368 + 2A). (B) Color IR (SO 180 + 15). (C) Color (SO 368 + 12). (D) Composite infrared photo prepared from the green, red, and infrared black-and-white transparencies; no additional benefits in detection of infestations could be found in this recombination.

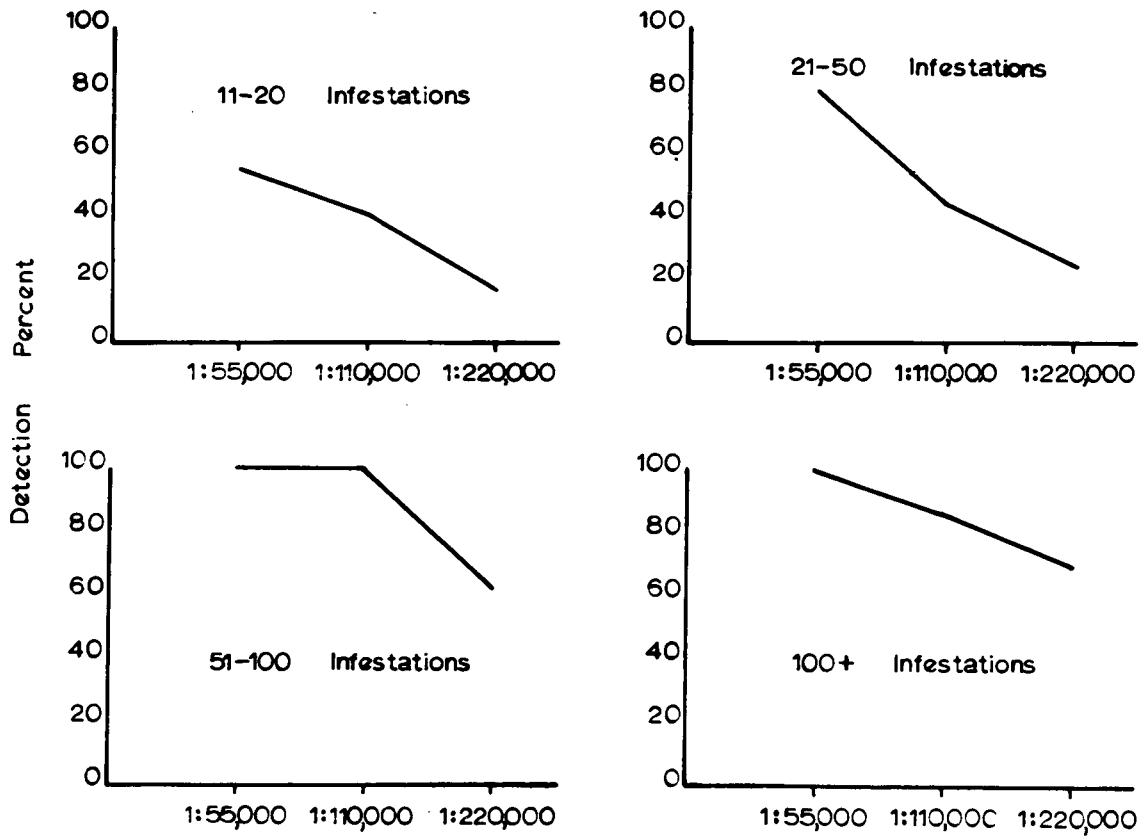


Figure 9.--Detection success in locating infestations on study area by scale and by size of infestation.



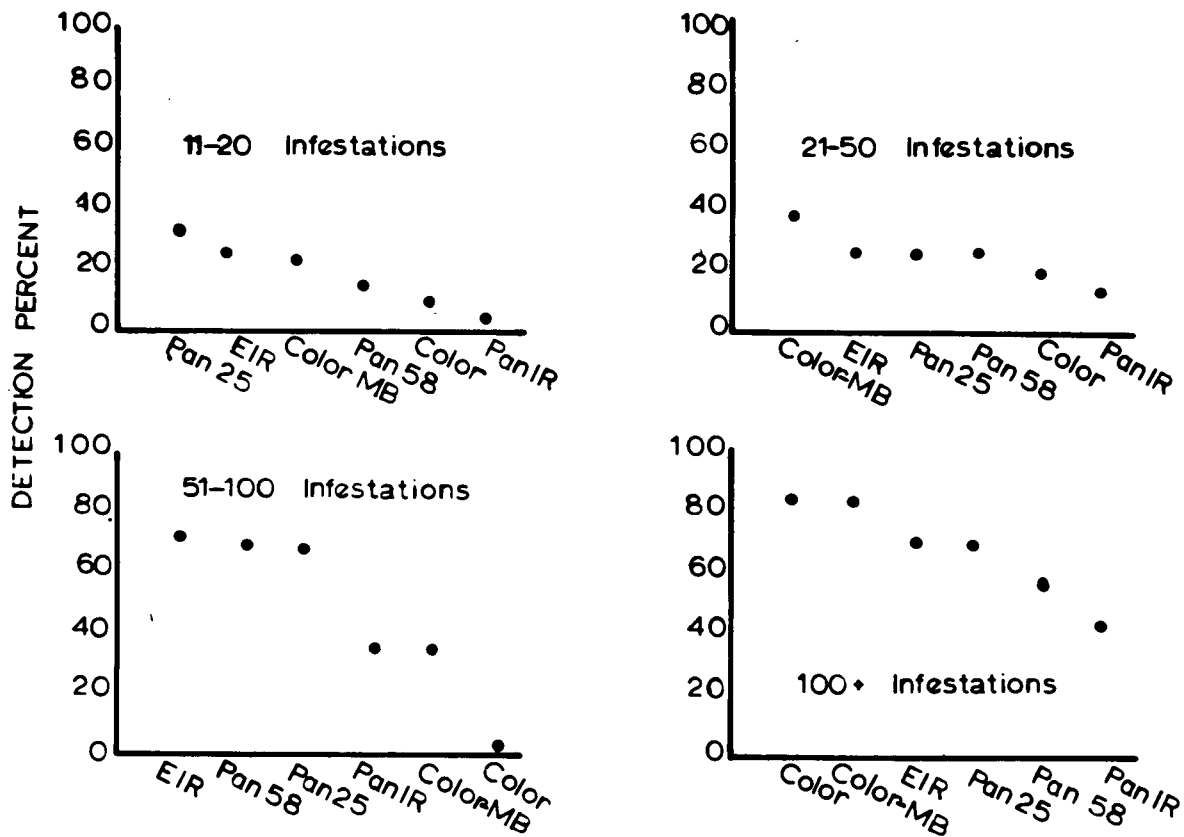


Figure 10.--Detection success in studying various films and filters on 1:220,000 scale Hasselblad photography over 1.6 by 5 kilometer study area.

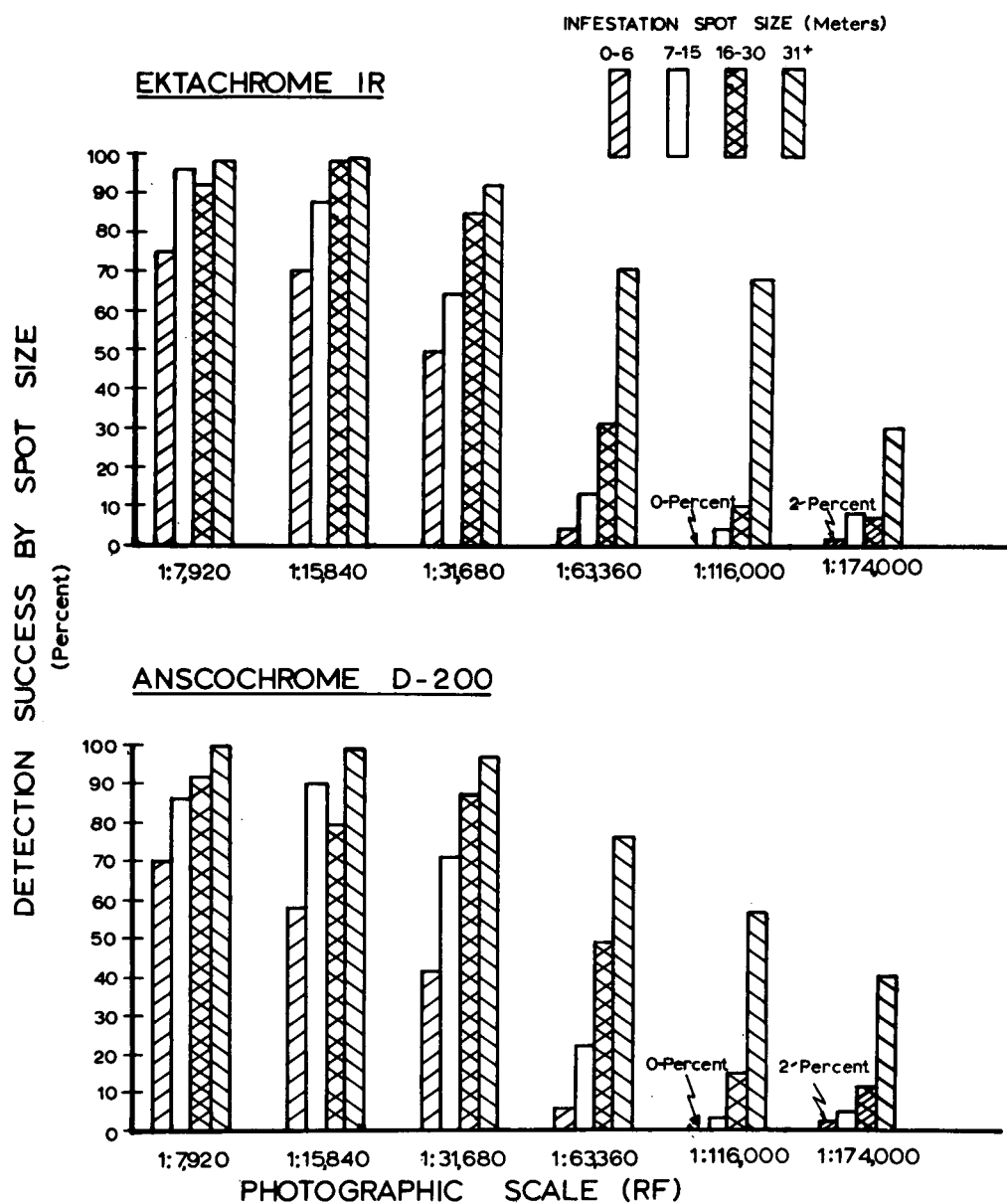


Figure 11.--Photo interpretation detection successes on well-exposed color and color infrared film over study area. Infestations were grouped into four target size classes. Best scale for detection is 1:31,680, but even at 1:174,000 larger infestations can be discerned.

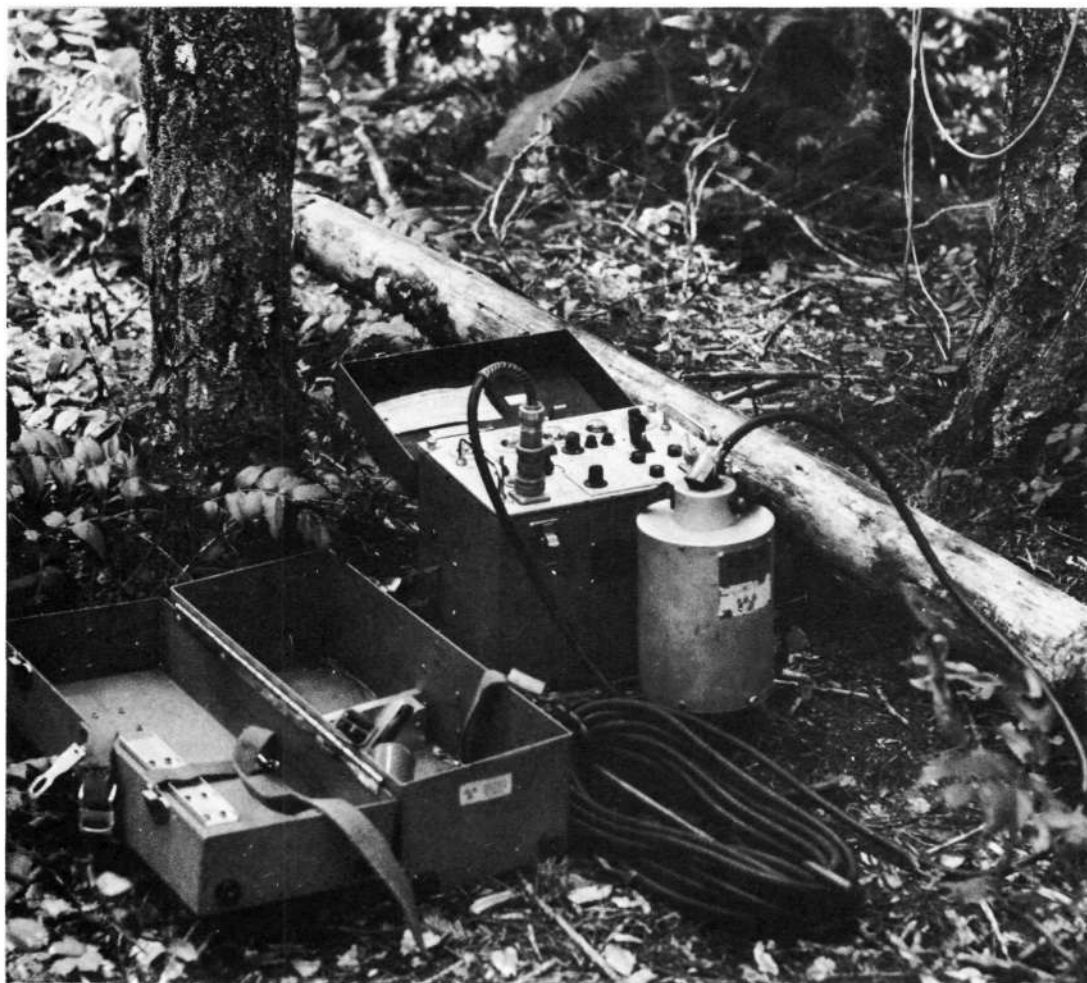


Figure 12A. Improved ground data instrumentation. Neutron probe to measure soil moisture.



Figure 12B. Improved ground data instrumentation. Aerial tramway to collect solar radiation and emission data continuously over the trees.



Figure 12C. Improved ground data instrumentation. Data logger digitizes and records 38 channels of biophysical data.



Figure 13.--(A) Black and white analog at top of study area. (B) Thermal contouring from 8.0 - 13.5 micrometer waveband, 1,500 meters above terrain; targets are coded according to small temperature differences.

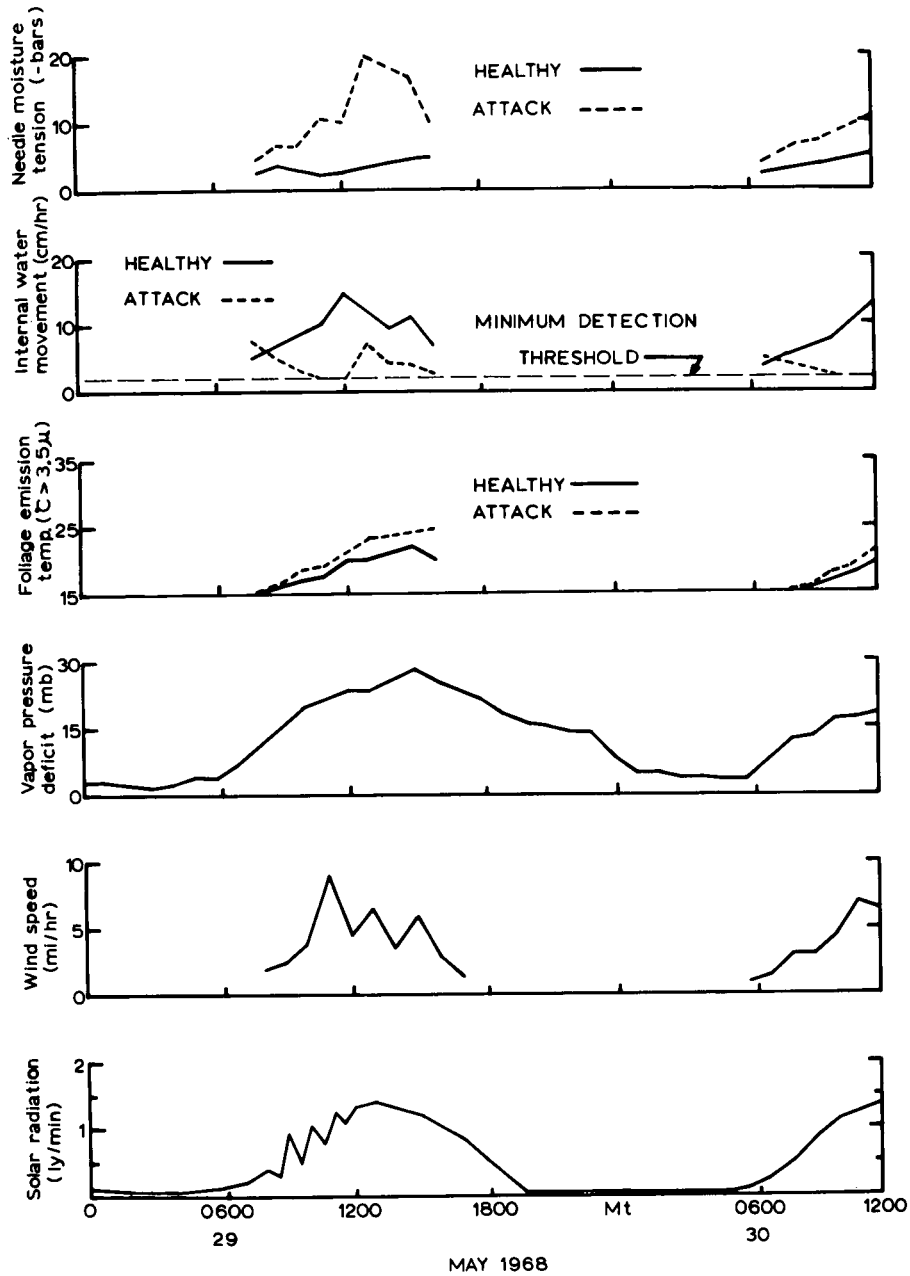


Figure 14.--Meteorological and tree physiological data collected at ground instrumented test site for period May 29 to 30, 1968. Note clear-cut apparent scene radiance difference during period when overflights were made by Michigan C-47 aircraft equipped with multispectral scanner.

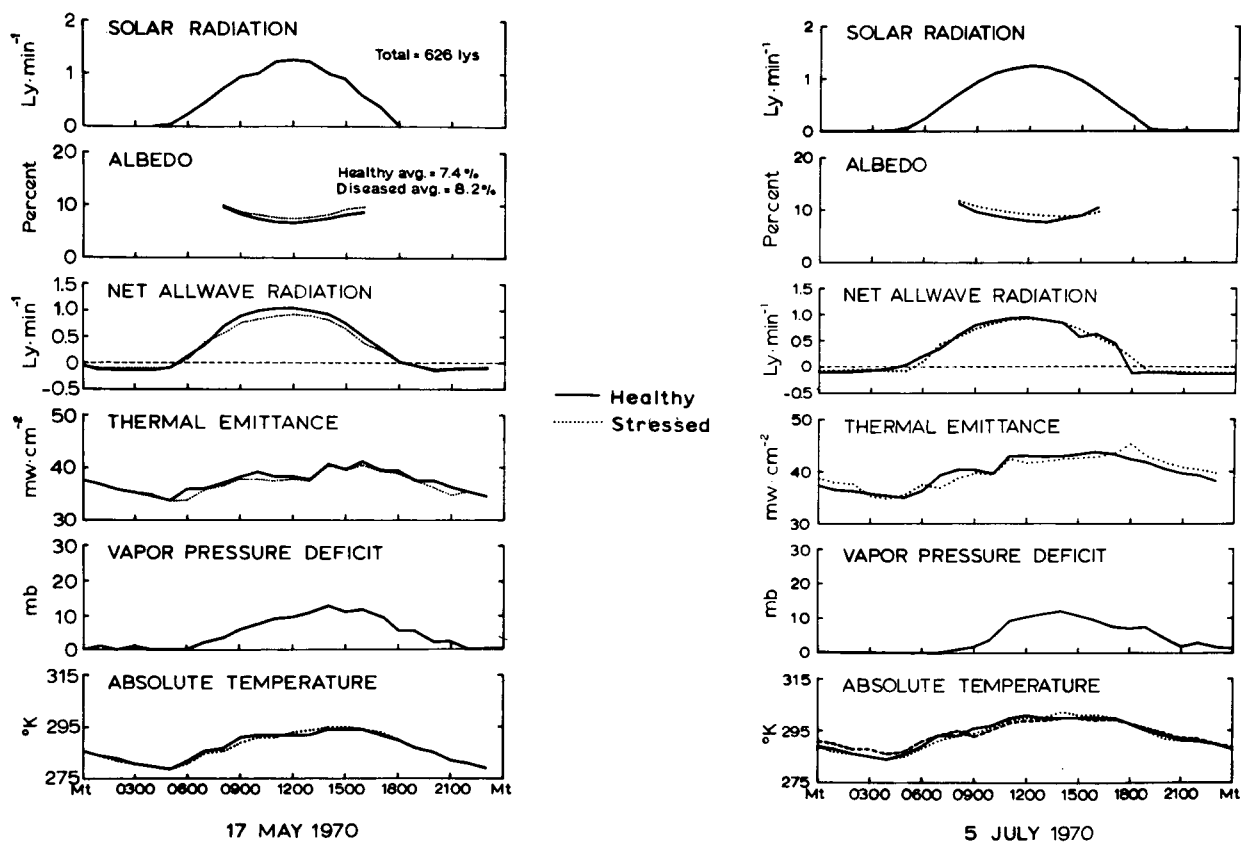


Figure 15.--Ground data collected at *Poria weirii* site on two dates at Wind River, Washington. Compare the thermal radiance graphs with those shown in Figure 14. No apparent scene radiance difference showed up on disease-infected trees as compared with insect-infested trees.



NOT REPRODUCIBLE

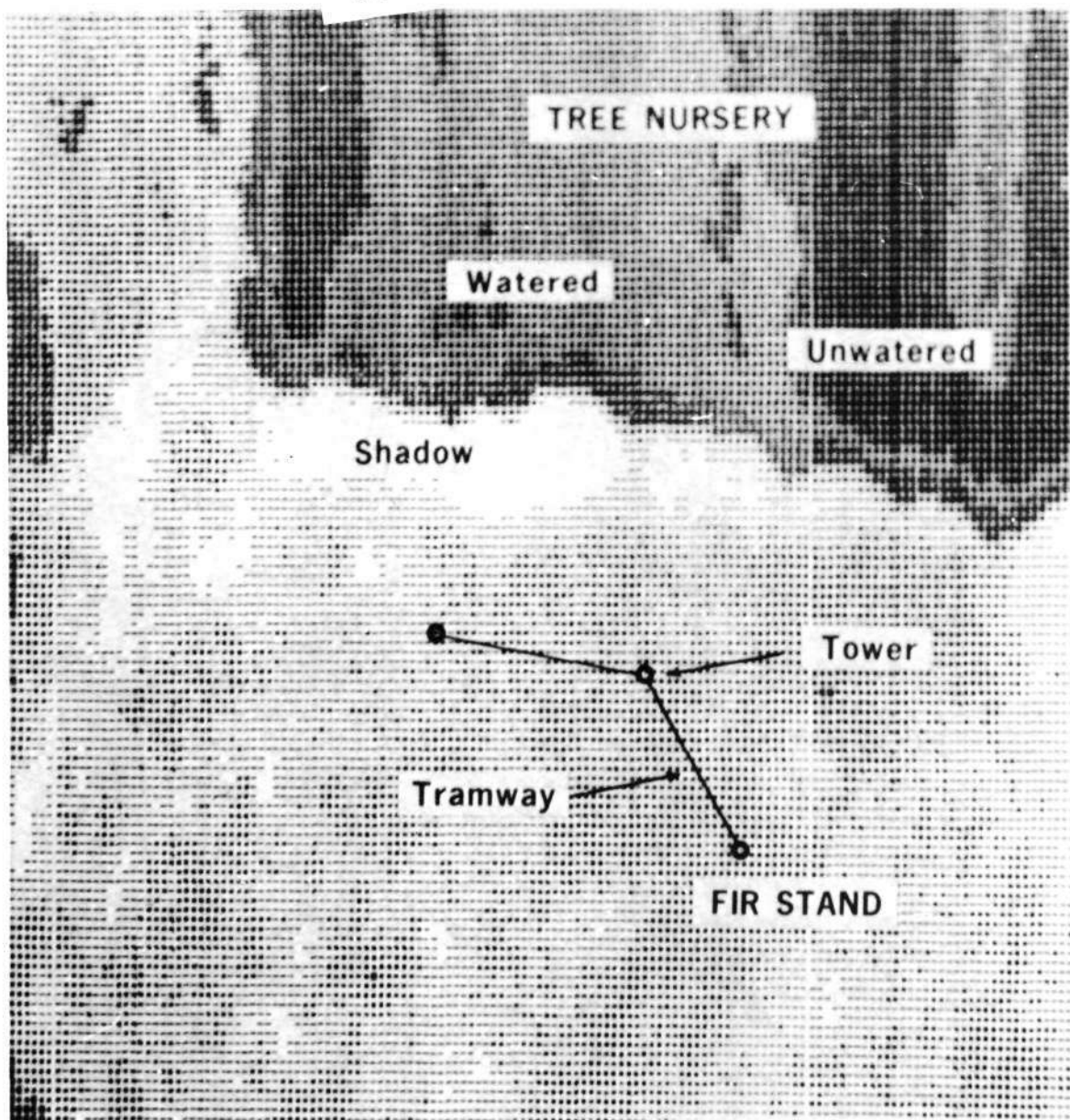


Figure 16.--Thermal gray map of *Poria weirii* site constructed from digitized thermal analog tapes. Data originated from University of Michigan multispectral scanner. No density printout difference occurs around known healthy or infected trees. Warm objects appear dark on this printout.

## MULTISPECTRAL SENSING OF MOISTURE STRESS

by

Charles E. Olson, Jr.  
and  
Wayne G. Rohde  
School of Natural Resources  
The University of Michigan  
Ann Arbor, Michigan

INTRODUCTION

Multispectral sensing is an effective tool for acquiring spectral signature data which permit recognition of several kinds of environmental phenomena. Ongoing research at the University of Michigan School of Natural Resources has identified moisture stress as a major factor affecting spectral signatures of woody plants. Laboratory studies have revealed consistent changes in foliar reflectance and emittance characteristics when plants are subjected to high moisture stresses. Many of these changes occur at wavelengths too long, or at threshold levels too low, to be detected by the human eye. Existing remote sensors can record these wavelengths, and have considerably lower thresholds than human interpreters.

During 1969 and 1970 tests were conducted at the Ann Arbor Test Site (NASA Site 190) with multispectral camera and line-scan systems to evaluate the field applicability of previously acquired laboratory data relating moisture stress and reflectance characteristics. In assessing the importance of the results, it is important to remember that moisture stress can result from any of several independent factors, including species differences, insect or disease attacks, leakage of natural gas, and variations in available soil moisture. Furthermore, the interaction of wind, relative humidity, temperature, and incoming solar radiation with plant foliage may result in large, but short term, water stresses. Since symptoms of moisture stress are similar regardless of cause, moisture stress is not a positive indicator of a particular damaging agent. Nevertheless, detection of differences in moisture stress may be

a first step in identifying tree species, and in previsual detection of attacks by many types of damaging agents.

### MOISTURE STRESS: A DESCRIPTION

Water in plants is part of a continuum extending from the foliage, down through the stem and roots, and out into the soil where it exists as capillary films among the soil particles. When water is lost at one point, moisture film adjustments occur that equalize the effects of the loss throughout the entire system. As the amount of water in the system decreases, moisture films become thinner and the forces holding the water to soil particles and walls of conducting cells reduce the rate at which moisture film adjustments can occur. Under drought conditions, these forces produce a tension in the water film which can exceed -35 bars (tension is expressed as negative pressure, and 35 bars is approximately 500 pounds per square inch). This tension is directly related to the level of moisture stress in the plant.

Moisture film adjustments occur slowly in a soil-plant system and differential stresses exist within the system until the adjustments are completed. During daylight, plants lose copious amounts of water through transpiration and increasing moisture tensions develop in their foliage. Transpiration slows in late afternoon and ceases at night, permitting slow moisture film adjustments from soil to root to replace water in the plant tissues faster than it is lost. Under very dry conditions the adjustment rate may be so slow, however, that equilibrium in the foliage is not attained before dawn; and, even if attained, equilibrium may be reached at an appreciable tension. Plants then begin the new day already under stress.

### MEASURING MOISTURE STRESS

The ideal way to measure moisture stress would be to measure the water tension within the plant. Because of the difficulties in accomplishing this, indirect estimates of moisture stress based upon measurements of soil moisture

have been, and are being used extensively. The usefulness of such measurements is dependent upon the degree to which moisture release characteristics of the soil are known. Estimates based solely on total moisture content of the soil are apt to be badly misleading, for they ignore the water content and water deficits in the plant.

The ability of plants to extract water from the soil is limited and some soil water is so tightly held that it is unavailable to plants. Much of the unavailable water is held closely to the surface of the soil particles, and the greater surface area of fine-textured soils makes more of the water in them unavailable than is true of coarse-textured, sandy soils. Soil texture may change markedly with small changes in depth and careful analysis of the soil profile in the root zone is needed to determine the amount of available water present at any given time.

The fact that moisture stress exhibits a diurnal rise and fall makes standardization of the time of measurement important when long-term trends are of concern. The period just before dawn would be ideal, for at this time the soil-plant-water system is most apt to be at equilibrium. Measurements at other times of day may more nearly represent actual stress levels at the time remote sensor data are acquired, however.

The above discussion suggests that considerable advantages are gained by direct measurement of internal moisture tensions. Such a method was proposed by Dixon (1914) but was not used until the apparatus needed was assembled by Scholander et. al. (1965). A good description of the method, and a diagram of the apparatus, is presented by Kramer (1969). The method requires cutting one leaf, or a twig, from the plant and inserting it into a pressure cylinder so that only the cut end of the stem is exposed. Nitrogen is bled slowly into the cylinder until water is forced back out of the cut end of the stem. The pressure in the cylinder when this first occurs is considered equal, but opposite in sign, to the tension in the water conducting tissues at the time the leaf was cut from the plant. Measurements are considered accurate to within  $\pm 1$  bar. When the necessary apparatus is available, this method is faster, cheaper, and more accurate than any other method now in use for determining levels of moisture stress in woody plants.

## REFLECTANCE AND MOISTURE STRESS

Reflectance characteristics of leaves are more strongly affected by moisture stresses at the time the leaves form and unfold than by moisture stresses existing at the time the reflectance is measured (Weber and Olson, 1967; Olson, Ward and Rohde, 1969; Olson, 1969). Leaves which form during periods of high moisture stress are significantly less reflective at all wavelengths between 0.4 and 2.5 micrometers than are leaves which form during periods of low stress. Leaves which form and grow to essentially full size under low stress conditions show a slight increase in reflectance (or no change) when the plants are subsequently subjected to high moisture stresses.

Some species produce new leaves (flush) only at the beginning of the growing season while others flush almost continuously throughout the growing season. Continuous leaf flushing results in crowns whose outer, more visible, leaves are formed under moisture conditions existing only a few days earlier. For those species in which flushing occurs only once, the outer, more visible, leaves maintain reflectance characteristics typical of moisture conditions at the time the leaves formed, and this may have been five months earlier. Differences in leaf flushing patterns result in differences in the way that reflectance of plants changes as moisture stresses develop. Leaf flushing patterns are closely related to the structure and arrangement of the water conducting cells in the stem, and it is easier to predict the effects of moisture stress on plant reflectance when this structure is known and considered.

Woody plants of the temperate zone can be grouped into three classes based upon the type and arrangement of their water conducting cells. The conifers with their non-porous conducting systems form one class. The two distinct arrangements of the water conducting vessels in broad-leaved, woody plants provide the other two classes. These are referred to as ring-porous and diffuse-porous because the vessels are concentrated in a narrow band in the spring-wood of the former, but dispersed through the entire annual ring of the latter. With few exceptions, ring-porous

species flush only at the beginning of the growing season, while diffuse-porous species usually flush continuously. Since foliar reflectance characteristics are largely controlled by moisture conditions at the time the leaves form, it is easier to detect moisture stress in diffuse- than in ring-porous species.

#### ACKNOWLEDGEMENTS

The work described in this paper is part of a continuing series of studies of the effects of morphological and physiological changes on remote sensing of trees under stress. Work was begun at the University of Illinois in 1959, with sponsorship of the Office of Naval Research, and shifted to the University of Michigan in 1963. Since 1966 primary financial support has been provided by the National Aeronautics and Space Administration as part of the Earth Resources Survey Program in Agriculture/Forestry (Contract No. R-09-038-022). The current work is a cooperative undertaking of the Forest Service, U. S. Department of Agriculture, and the School of Natural Resources, University of Michigan. Flight and data processing services were provided by NASA directly, and through terms of facilities contracts with the University of Michigan, Willow Run Laboratories.

Laboratory studies have been centered at the University of Michigan Botanical Gardens and the generous support of its director, Dr. Warren H. Wagner, Jr., and staff is gratefully acknowledged.

#### PROCEDURES

During the 1969 and 1970 growing seasons multispectral data were collected over areas of known vegetation stress within the Ann Arbor Test Site. The University of Michigan C-47, with four 70mm cameras and multispectral scanner, provided low altitude (1,500 to 9,000 feet) coverage of selected parts of the Site; and the NASA RB57F, with three 9 x 9 and six 70mm cameras, provided high altitude (40,000 to 60,000 feet) coverage of the entire Site.

## THE ANN ARBOR TEST SITE

The Ann Arbor Test Site (NASA Site 190) is located on morainal topography and includes both upland and lowland sites supporting a diverse mixture of natural and planted forest stands interspersed with active and abandoned agricultural fields. Data on land use and stand growth go back to 1903 for some locations. The Site is located approximately 40 miles west of Detroit, Michigan, and includes the active urban-rural tension zones adjacent to Ann Arbor and several smaller cities.

Active infection centers of a number of tree diseases are present and have been monitored for several years. Infestations of Fomes annosus, an important root-rotting fungus of conifers, and at least two needle cast diseases caused by fungi imperfecta, are included. In 1970, tip-burn damage, believed caused by ozone, was discovered within the Test Site. All of these disease centers were monitored during each overflight.

## CALIBRATION MEASUREMENTS

Foliar reflectance of healthy and stressed trees was measured with a Beckman DK-2a spectrophotometer for both greenhouse-grown and field-grown plants. Emittance data were collected for the same plants with Barnes PRT-10 or IT-3 radiometers. Levels of moisture stress were determined with a pressure cylinder similar to that described by Kramer (1969). These data were used in determining optimum wavelength bands for subsequent processing with the University of Michigan Spectral Processing and Recognition Computer (SPARC).

## DATA PROCESSING

Data from the multichannel scanner were used to prepare simulated normal-color and infrared-color imagery for comparison with the actual color and false-color photographs from the cameras carried by both aircraft. The

relative value of the simulated and real photography in detecting tree diseases was determined with conventional photographic interpretation techniques.

An attempt was made to obtain automatic recognition of tree species on the basis of naturally occurring differences in moisture stress. On the basis of laboratory reflectance data and visual inspection of imagery from individual channels of the scanner, six spectral bands were selected for use in the SPARC processor. The 0.58-0.62, 0.62-0.66, 0.72-0.80, and 0.80-1.0 micrometer channels were used in all cases; supplemented by the 0.40-0.44 and 0.55-0.58 micrometer bands for separation of broadleaved species, and the 0.46-0.48 and 0.52-0.55 micrometer bands when separation of coniferous species was desired.

As a side-line to the 1970 field tests, detailed statistical analyses were made of the relationship between reflectance and moisture content for 356 leaves. Step-wise regression techniques were used with several types of transformations in an attempt to derive a means of evaluating moisture content of fine forest fuels which would be of value to forest fire control organizations.

## RESULTS AND DISCUSSION

Results of the step-wise regression analyses provide substantial confirmation of the importance of changes in moisture conditions on foliar reflectance. Because previous work (Olson, 1969) had shown that the slope of the infrared reflectance plateau between 0.8 and 1.1 micrometers changes as a leaf unfolds and enlarges to full-size, ratioed combinations of reflectances at several wavelengths were tested. Two such combinations were found to improve predictive capability and the final regression equations (Figure 1) were based on three variables:

$A = R(1.00)$  or the reflectance at 1.00 micrometer.



$$B = \frac{R(2.00) + R(2.19) + R(2.30) + R(2.60)}{R(1.64) + R(1.75) + R(1.78)}$$

$$C = \frac{R(1.64) + R(1.75) + R(1.78)}{R(0.80) + R(0.90) + R(0.96) + R(1.00)}$$

We believe that these transformations can be accomplished as a preprocessing technique with data from a multispectral scanning system.

The high multiple correlation coefficients obtained with the three regression equations shown in Figure 1 (0.98, 0.94, and 0.92) support the hypothesis that the relationship between moisture content and foliar reflectance is significant. Even if these equations do not prove valuable in airborne remote sensing, they do provide a non-destructive method of estimating moisture content of plant foliage which should be of value in other research.

#### AUTOMATIC RECOGNITION OF TREE SPECIES

Automatic recognition of tree species was attempted with the SPARC for the 80-acre Saginaw Forest property controlled by the University of Michigan School of Natural Resources, and located within the Ann Arbor Test Site. This property contains several broadleaved and several coniferous plantations (Figure 2). Because available reflectance data supported the hypothesis that moisture stress effects are different for ring- and diffuse-porous species, the first test of the SPARC was an evaluation of its capability for separating ring-porous, diffuse-porous, and coniferous species. The results were highly successful (Figure 3). In subsequent tests successful separation of the major broadleaved species present on the property was achieved, including separation of red oak from white oak with an accuracy of about 70 percent (Figure 4). Although not perfect, results of this test of the SPARC's

ability to identify tree species represent at least an order of magnitude improvement over previous attempts which were not based on moisture stress considerations.

#### SIMULATED vs. REAL COLOR FILMS

This phase of the data analysis is not complete. To date, no consistent superiority has been found for either simulated or real color films. Both seem to have their place.

Analysis of the needle cast infestation on Scots Pine demonstrates the importance of repetitive coverage in assessing severity of damage. The disease is readily apparent in the low altitude color photography obtained in August 1969, but is not apparent in either the color or false-color photography obtained in July 1970 (Figure 5). Ground data confirmed that the disease was much less severe in 1970 than in 1969.

The false-color photograph in Figure 5 illustrates one consistent abnormality observed between the low (C-47) and high (RB57F) altitude photography obtained in both 1969 and 1970. At low altitudes the pine stands (P) and the broadleaved stands (B) appear in nearly equal red tones. From high altitude the conifers appeared distinctly blue-green rather than red.

Figure 6 provides another example of the value of sequential coverage in assessing changing severity of damage symptoms. The slight browning of several trees in the color photography from June 1970 went unnoticed until it had become more obvious in July. Subsequent comparison of the June and July imagery revealed the rapidly increasing severity of the damage symptoms, believed due to the effect of an abnormally high ozone concentration of undetermined origin.

Figure 7 presents both a real false-color photograph and a simulated false-color image prepared from the scanner data. The apparent enhancement of the Fomes annosus infection centers (the small pock-mark like openings in the crown canopy) in the simulation may be due to shadow

enhancement or to more sensitive recording of differences in moisture stresses. Further analysis of this imagery is in process.

#### CONCLUDING REMARKS

Laboratory reflectance data, and field tests with multispectral remote sensors at the Ann Arbor Test Site during 1969 and 1970, provide support for this hypotheses that differences in moisture content and water deficits are closely related to foliar reflectance from woody plants. When these relationships are taken into account automatic recognition techniques, such as those utilized with the University of Michigan Spectral Processing and Recognition Computer, become more powerful than when they are ignored. Evidence is increasing that moisture relationships inside plant foliage are much more closely related to foliar reflectance characteristics than are external variables such as soil moisture, wind, and air temperature. Short term (often diurnal) changes in water deficits seem to have little influence on foliar reflectance, however. This is in distinct contrast to significant short-term changes in foliar emittance from the same plants with changing wind, air temperature, incident radiation, or water deficit conditions.

REFERENCES

1. Dixon, H. H. 1914. Transpiration and the Ascent of Sap in Plants. MacMillan. London. 216 pp.
2. Scholander, P. F., H. T. Hammel, D. Bradstreet, and E. A. Hemmingsen 1965. Sap pressure in vascular plants. Science 148:339-346.
3. Kramer, P. J. 1969. Plant and Soil Water Relationships: A Modern Synthesis. McGraw-Hill. New York. 482 pp.
4. Weber, F. P. and C. E. Olson, Jr. 1967. Remote sensing implications of changes in physiologic structure and function of tree seedlings under moisture stress. Annual Progress Report. Forestry Remote Sensing Laboratory. Berkeley, California. 60 pp.
5. Olson, C. E., Jr., J. M. Ward, and W. G. Rohde 1969. Remote sensing of changes in morphology and physiology of trees under stress. Annual Progress Report. Forestry Remote Sensing Laboratory. Berkeley, California. 43 pp.
6. Olson, C. E., Jr. 1969. Seasonal change in foliar reflectance of five broadleaved forest tree species. Ph.D. dissertation. The University of Michigan. Ann Arbor. 112 pp.

**Sugar maple (Acer saccharum)**

$$r = .94$$

$$\log \text{ M.C.} = 8.4181 - 3.1378 \log A + 1.9490 \log B - 1.7609 B^2$$

**Yellow birch (Betula alleghenensis)**

$$r = .98$$

$$\log \text{ M.C.} = 1.5872 + 7.6537 B^2 + 67.8304 C^2$$

**White ash (Fraxinus americana)**

$$r = .93$$

$$\log \text{ M.C.} = 7.5649 - 2.6119 \log A - 0.6581 B^2 - 1.4915 C^2$$

M.C. - leaf moisture content

r - multiple correlation coefficient

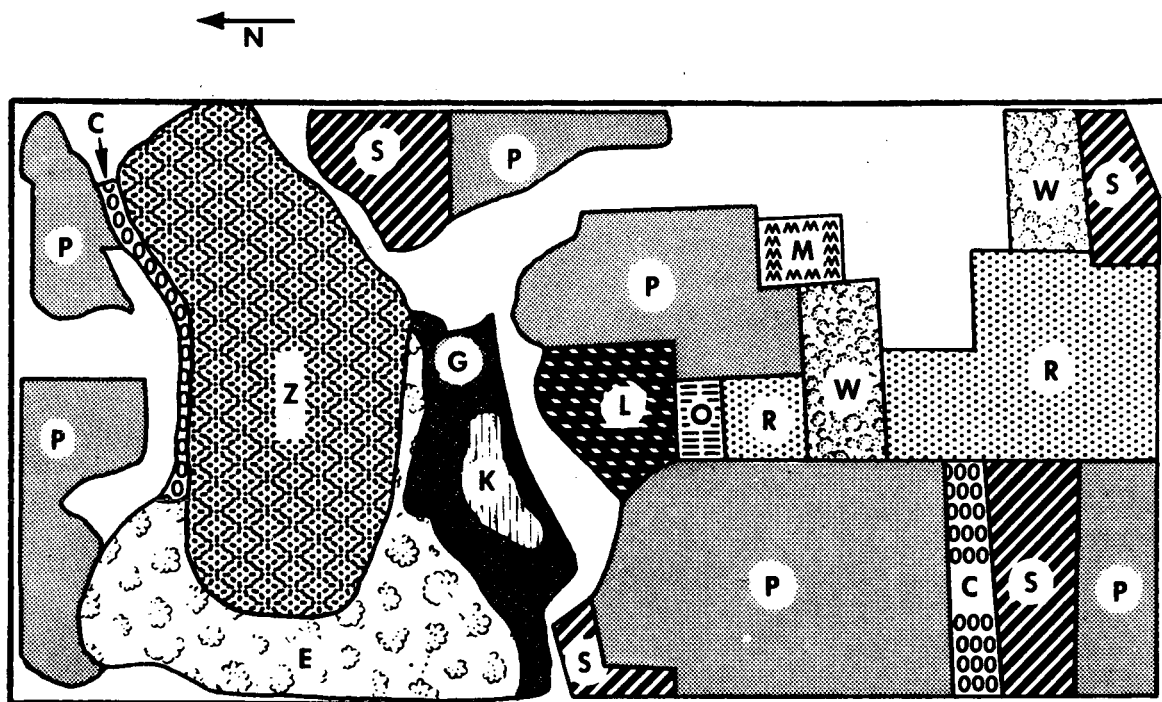
R - reflectance

$$A = R_{(1.00 \mu\text{m})}$$

$$B = \left[ \frac{R_{(2.00 \mu\text{m})} + R_{(2.19 \mu\text{m})} + R_{(2.30 \mu\text{m})} + R_{(2.60 \mu\text{m})}}{R_{(1.64 \mu\text{m})} + R_{(1.75 \mu\text{m})} + R_{(1.78 \mu\text{m})}} \right]$$

$$C = \left[ \frac{R_{(1.64 \mu\text{m})} + R_{(1.75 \mu\text{m})} + R_{(1.78 \mu\text{m})}}{R_{(0.80 \mu\text{m})} + R_{(0.90 \mu\text{m})} + R_{(0.96 \mu\text{m})} + R_{(1.00 \mu\text{m})}} \right]$$

Figure 1. Leaf moisture content prediction equations for three tree species derived with stepwise multiple regression techniques.



**C - Cottonwood, Aspen, Willow**

**E - Elm, Red Maple**

**G - White Cedar**

**K - Swamp**

**L - Black Locust**

**M - Sugar Maple**

**O - White Oak**

**P - Pine**

**R - Red Oak**

**S - Spruce**

**W - Black Walnut**

**Z - Lake**

Figure 2. Distribution of trees species at the University of Michigan Saginaw Forest near Ann Arbor, Michigan.



Figure 3. Recognition map of Saginaw Forest generated by the University of Michigan Spectral Analysis and Recognition Computer (SPARC). Conifers are shown in green, ring-porous species in red, and diffuse-porous species in black.



Figure 4. Recognition map of Saginaw Forest generated by the University of Michigan Spectral Analysis and Recognition Computer. Conifers are shown in green, red oak in red, white oak in orange, black locust in gold, black walnut in light blue, and sugar maple in pink.





Figure 5. Needle cast on Scots Pine was much more severe in 1969 than in 1970 as indicated by these photographs taken from 3,000 feet. The brown trees in the August 1969 photo are severely infected. Note that the broadleaved (B) and pine (P) trees in the Color IR photo show nearly equally red tones.

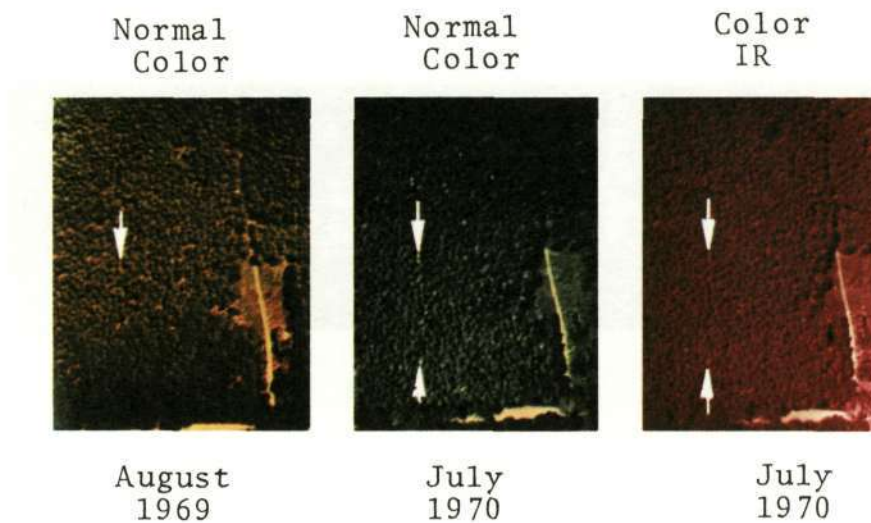


Figure 6. Damage believed due to ozone became more severe in 1970 as indicated by these photographs taken from 3,000 feet. Arrows point to affected trees.



Figure 7. Simulated Color IR image prepared from data obtained with the University of Michigan multispectral scanner. The small holes in the crown canopy indicated by arrows are centers of infection by Fomes annosus.

## CLASSIFYING FOREST AND NONFOREST LAND ON SPACE PHOTOGRAPHS

Robert C. Aldrich, Principal Research Forester  
Pacific Southwest Forest and Range Experiment Station  
Forest Service, U. S. Department of Agriculture  
Berkeley, California

INTRODUCTION

One important function of the Nationwide Forest Survey<sup>1/</sup> is to keep forest area, volume and growth statistics up to date for the 509 million acres of commercial forest land in the United States. The present 5- to 10-year schedule for resurveys of the forest resources by states is too infrequent to keep up with the rapid changes that are occurring. Another handicap is the fact that regardless of inventory schedules, new forest statistics are never available for the entire Nation or for an entire state at one time. In other words, we have a continuous forest inventory system. Space-age remote sensing could help to keep these statistics up to date by monitoring the forest for changes--land-use changes or forest disturbances that affect timber volume and growth.

Before we can use new concepts in remote sensing on extensive forest surveys, dependable predictors of forest area, timber volume, and condition classifications must be developed. But this is really not a new problem--predictors have been used with panchromatic or infrared aerial photographs ever since they were first used on a timber survey more than thirty years ago. The difference is that today we have a wider variety of sensors,

---

<sup>1/</sup> The Forest Survey is a branch in the Division of Forest Economics and Marketing Research, Forest Service, U. S. Department of Agriculture, Washington, D. C. The Forest Survey was authorized by the McSweeney-McNary Forest Research Act of May 22, 1928.

including color, infrared color, and multiband photography, which require new ideas and a completely different approach to image analysis.

Because of this need, the Forest Service Remote Sensing Research Project at Berkeley, California, began a program to seek solutions to forest inventory problems using new remote sensing tools. This research is supported by funds from the Forest Service, U. S. Department of Agriculture and the National Aeronautics and Space Administration. Our objectives were: to determine the limits of accuracy for forest area estimation on space photography, to determine the feasibility of using space photography to detect and outline disturbances in forest communities, and to develop spectral signatures for forest and land-use classes that may be related to Earth Resources Technology Satellites (ERTS) data. Some of the most significant results of this study will be reported here.

#### THE STUDY AREA

The study area is located southwest of Atlanta, Georgia, and is one of two areas used in the forest inventory study reported by Langley (1) a year ago (Fig. 1). We selected this area for several reasons, not the least of which is the excellent photographic coverage provided by Apollo 9 in March 1969. Another important reason is the geographic location. This area lies in one of the best timber growing regions of the country with diversified forest types and many different growing conditions. Furthermore, a wide variety of industries, including manufacturing, agricultural cash crops, livestock, and forest industry support the local economy. As a result, many land-use patterns and land-management practices present a challenge to remote sensing. The nearness of Atlanta, the transportation hub

of the South, makes this area extremely accessible and subjects the area to changes created by a growing urban environment.

Our final reason for selecting this area was the result of our 1969 multistage forest inventory study. By studying this area in greater depth, we hope to improve predictions for volume stratification on space photographs which will lead to greater sampling efficiency.

This area is located in the southern piedmont land resources sub-region (2). It is about 60 percent forested, mainly in farm woodlands. The elevations range from about 250 meters (800 feet) in the southeast to 400 meters (1300 feet) in the northwest. The topography is gently rolling to hilly and is cut by many narrow stream bottoms. Mean annual rainfall is approximately 125 centimeters (50 inches). The soils are primarily red and yellow podzolics. Major forest types in this region are loblolly-shortleaf pine and oak-pine (2). In addition to loblolly (*Pinus taeda*), shortleaf (*Pinus echinata*), and other southern pines, several oaks (*Quercus* sp.), hickories (*Carya* sp.), yellow poplar (*Liriodendron tulipifera*), black gum (*Nyssa sylvatica*), and sweet gum (*Liquidambar styraciflua*) are plentiful in a variety of mixtures.

#### REMOTE SENSOR DATA ACQUISITION

Since March 1969 we have accumulated an assortment of remote sensor data to support this study. These data range all the way from 1:2,000 color transparencies to the Apollo 9 space photographs. A review of these data seems essential at this time.

FOREST SERVICE PHOTOGRAPHY

In April 1969 the Forest Service remote sensing aircraft flew multi-scale photography for five 6.4-kilometer (4-mile) square blocks used in the 1969 inventory study (Fig. 2). This consisted primarily of 70 mm. photography for randomly selected sample strips. The photographic data are shown in Table 1. The high-quality large-scale color photographs have been useful in establishing land use and forest classifications at the time of the Apollo 9 flight. Small-scale Polaroid and Aero Neg color have been useful for planning and directing field crews to ground locations.

In March of this year, almost one year following the Apollo 9 flight, we rephotographed each of the five study blocks using Ektachrome infrared color film (8443) at a 1:32,000 scale. We also photographed one of the random sample strips with Eastman Aero Neg color film at a 1:12,000 scale. Ten additional 6.4-kilometer (4-mile) square blocks were selected at random and photographed at this same time. These new blocks will be used in the next phase of the study to test interpretation training models as they are developed.

The 1:32,000 IR color photography and ground observations are being used to check photo classification made by both manual and automated interpretation techniques on small-scale simulated space photography provided by RB-57 high-altitude flights.

NASA RB-57 PHOTOGRAPHY

In June 1970 we acquired our first coverage of the Atlanta test site by an RB-57 high-altitude flight (Mission #131). The entire test site was

covered in seven flight lines (Fig. 3). For this mission we requested and received the data described in Table 2.

Copies of the Mission 131 data were received on July 30--8 weeks following the flight. In terms of coverage the flight was successful. Of the fifteen 6.4-kilometer (4-mile) square study blocks, all but one was completely covered by the smallest scale photography. Unfortunately, this block was one of five intensive study blocks to be used in developing training models. Four of the five blocks were covered by the 1:120,000 scale RC-8 Ektachrome photography. Only one block was entirely covered by the largest scale Zeiss photography; but this was to be expected due to the limited side lap with this camera.

Of all the data received, only the RC-8 Ektachrome film taken with a 425 m $\mu$  filter and the panchromatic and B/W infrared Hasselblad films were completely acceptable for our purposes. Poor filter selection and poor film manufacture can be blamed for the failures of the Ektachrome with a 450 m $\mu$  filter and the infrared color films taken with both the Zeiss and Hasselblad cameras.

#### PHOTO ANALYSIS

Both satellite and small-scale aerial photography require special techniques for data analysis. In this section we will discuss some of the techniques we used to overcome the problems of interpreting coarse resolution imagery.

#### FOREST AREA PREDICTIONS

The Apollo 9 space photographs were taken in March and provided some helpful characteristics to separate forest land from nonforest land (3).



First, the deciduous tree species (hardwoods) were without leaves. This resulted in a distinctive bluish green color that allows interpreters to evaluate where deciduous trees predominate. The contrast between bluish green deciduous forest and medium to dark purplish red evergreen (pine) forest separates these two pure types and helps to identify where mixtures of both pines and hardwoods occur. Another advantage to March photography is the absence of crops on the greater part of the active agriculture land. Although fields had been plowed in preparation for planting, it was evident that few crops other than overwintering grains and pasture were present. This made it possible to separate forest from a large portion of the nonforest land.

One important limitation of space photographs is the poor ground resolution. On the Apollo 9 IR color we found that the resolution was approximately 91 meters (300 feet). Thus, small fields in dark forested areas and small farm woodlots in lighter toned agricultural areas were not resolved. Although the human eye cannot resolve these small features, there is hope that microdensitometers may detect minute differences in color density and recognize spectral signatures for land-use classification (4) (5).

Another limitation of satellite photography taken in March is the high ground water level resulting from winter and spring rains. High soil moisture and extremely high humus content of bottomland soils cause darker than normal images that may be mistaken for forest.

Using these criteria for interpretation, photo interpreters estimated the forest area within the five random 6.4-kilometer (4-mile) square study blocks on the Apollo 9 IR color film. Because of the small image size (6.4 kilometers equals 2.7 mm. on the photo), a Bausch and Lomb Zoom 70 stereoscope was used with 7.5X magnification (Fig. 4). Although there is little or no stereoscopic effect, we viewed images on adjacent photographs simultaneously. The two images viewed together complemented one another and aided the interpretation.

To check forest area predictions made on the space photograph, photo interpreters estimated the area of forest and other land-use classes on conventional medium-scale photography. Two sets of photographs were interpreted--the latest 1:20,000 Department of Agriculture (ASCS) panchromatic photography and 1:32,000 IR color photographs. The estimates were made using dot grid templates constructed to sample at an intensity of approximately 6.4 hectares (16 acres) per dot. This is more than 10 times the intensity used by the U. S. Forest Service to estimate forest area on their nationwide forest survey. An Old Delft scanning stereoscope was used to aid in this interpretation.

#### FOREST MAPPING

We selected one block (Block 3) to check the Apollo 9 forest proportion and to explore the possibility of mapping broad forest types and nonforest classes on low-resolution photography. We examined Block 3 on the Apollo 9 IR color transparency using 7.5X magnification. Then using a 28X panchromatic print enlargement made from the same photograph as a base map,

we constructed a forest-type land-use map (Fig. 5). A dot grid was constructed to sample approximately 6.4 hectares (16 acres) per dot. Using this grid, the percent forest was estimated in three broad types: pine, upland hardwood, and bottomland hardwood. The percentage of the area in nonforest and water was also calculated. These data have been compared with estimates made on medium-scale conventional photography.

#### FILM DENSITY CLASSIFICATION

A Photometric Data Systems microdensitometer was used to measure and record optical density along randomly selected sample strips on the Apollo 9 IR color transparency (Fig. 6). The strips were first located on the 1:32,000 IR color transparencies taken in March 1970. These strips are between 6.4 kilometers (4 miles) and 8 kilometers (5 miles) long and will be used to develop signatures to be used in interpretation training models. Well-defined beginning and ending points were selected for each strip so that they could be transferred to both the Apollo 9 transparency and 1:400,000 scale photography supplied by NASA's high-altitude aircraft.

Two interpreters classified and delineated nine nonforest and four forest classes along each of the fourteen lines, Table 3. These delineations were marked on a transparent overlay as shown in Figure 7. An Old Delft scanning stereoscope with 4X magnification was used to assist in the classification. We also estimated crown closure for forest in three classes, and forest disturbances were classified into 10 classes. To help detect disturbances we compared each strip with the 1:12,000 photography

taken in April 1969. When completed, the total length of line and length of each land-use segment along the line was measured and recorded to the nearest 100th millimeter. There were over 800 segments delineated on over 96 kilometers (60 miles) of line.

We selected 107 segments from all forest and agricultural categories for ground observations. The number selected in each category was arbitrarily set to obtain a representative sample of each. Ground observations were made between June 8 and June 18, 1970. Forest points were given a type designation based on an estimate of basal area per acre by tree species. Crown closure (density) was assigned to each point by ocular estimate, and stand size was based on an estimated number of sawtimber, pole, and seedling and sapling size trees. In addition, each part of the forest floor was examined and classified into seven classes. Munsell color standards<sup>2/</sup> were used for soil color classification. If we found a point that had been disturbed since March 1969, this was identified and recorded by cause.

Agricultural points were examined and classified by crop type and maturity, soil color, and erosion. Pasture land, idle land, and abandoned agriculture were classified by broad vegetation types, degree of grazing, erosion, and soil color. Both a 35 mm. color and infrared color photograph were taken on each forest and agricultural point to illustrate the conditions that we described.

---

<sup>2/</sup> Munsell Color Company. Munsell Book of Color. Ed. 1920-60. Baltimore, Md.

Using ground truth, the photo interpretation along the sample strips was adjusted to give a true picture of ground conditions. These adjusted photo data are known as our ground truth and are used to develop optical density signatures with an automatic scanning microdensitometer.

Using the microdensitometer, we scanned the 14 strips on Apollo 9 IR color frames 3791 and 3792. Because of the extremely small scale of this photography, we found that it was difficult to position the sample strips precisely for scanning. For this reason we developed a different technique. First we read the X and Y coordinates for the starting and ending points that we had selected and recorded them on tape. Then we programmed the microdensitometer to block-scan an area that included these two points. We used an effective aperture area of  $18.67 \mu\text{m}$  and the microdensitometer was programmed to read at  $9 \mu\text{m}$  intervals on scan lines  $9 \mu\text{m}$  apart. The density readings along our sample line were determined by computer programming. The red, green, and blue mean densities and their standard deviations were computed for each land-use class by strips, blocks, and the sum of all blocks. These densities have been plotted for comparison.

We have not attempted to detect forest disturbances using the microdensitometer and automatic data processing. However, we did run a test on two areas with known disturbances. One is a stand of pine pulpwood that was cut sometime between April 1969 and March 1970. The other is a natural gas pipeline that was constructed during the same period. First, we selected beginning and ending points for scan lines that would pass through these two areas. These points had to be recognizable on a small-scale

Apollo 9 IR color and June RB-57 Hasselblad imagery. Then these two films were scanned and density read using red, blue, and green cutoff filters.

#### RESULTS

When forest area predicted on Apollo 9 photographs was compared with forest area estimated on medium-scale aerial photographs, we found some interesting relationships. Despite the differences in scales, estimates of forest area made on the Apollo 9 photograph are correlated to some degree with estimates on 1:32,000 IR color made a year later (Table 4). Only in Blocks 3 and 4 does the difference exceed 10 percent. On Block 4, the difference can be explained in part by the lack of full coverage on the 1:32,000 photography. Unfortunately the western quarter of the block was not covered.

The forest area in Block 3 was underestimated. This was verified by comparing the prediction with the mean of the other three estimates--the mean is 85 percent or 12 percent above the Apollo 9 prediction. To check this, a dot count was made on a forest-type land-use map constructed from the Apollo 9 photograph. This new prediction resulted in a forest area estimate of 80 percent and compares more favorably with the mean for the other three methods.

When we compare Block 3 area percentages by broad forest types there is some correlation between the Apollo 9 and the other two estimates (Table 5). All three scales resulted in bottomland hardwood estimates within one percent. Water estimates are extremely close. The estimate

of pine type on the 1:32,000 IR color and Apollo 9 IR color were closer than we expected; the space photograph underestimated pine type by 15 percent. The estimate of pine type on the 1:20,000 panchromatic photography has obviously been affected by poor type discrimination on this film. Also, of the three estimates this was made by the least experienced interpreter. Better instruments for viewing and drawing maps directly from this extremely small-scale photography should improve these results.

Figure 8 shows a comparison of optical density for the thirteen forest and nonforest classes on Apollo 9 IR color photography. There were 4,985 data points involved in this analysis; 3,425 forest and 1,560 non-forest. Since we have used separate scans for red, green, and blue optical density this means that three times this number of data points were analyzed in the experiment.

Using density alone, our data indicate that at a confidence limit of one standard deviation (68 percent) we can discriminate between forest land and agricultural crops, plowed fields, pasture land, idle land, orchards, and turbid water. None of the three bands (red, green, or blue) appears to be better than another. Although at first glance the red band appears to have greater differences, the standard deviations for red density are greater than either green or blue. This would compensate for the greater density range shown in the curves.

Forest types cannot be separated based on density alone. The standard deviations about the means for density in all three bands overlap and reduce the probability of correct interpretation. However, the data do suggest

that it may be possible to develop signatures for forest types, abandoned agriculture, urban and clear bodies of water using a combination of nine variables. These would include density, differences in density, and density ratios. For instance, the relationship of red density to blue and green density appears to provide a signature for recognizing forest from crops, plowed fields, idle, abandoned, orchard, urban areas and turbid water.

Phenological development of vegetation and sun altitude will affect spectral reflectance and the response of film emulsions. Thus, it is important to study these effects so that imagery from the Earth Resources Technology Satellites (ERTS), in 1972, can be selected to provide the type of information desired. The Earth Resources Program at NASA's Manned Spacecraft Center in Houston, Texas, is providing high-altitude multiband imagery for studies of this nature.

We have just begun to process multiband imagery taken from 18,288 meters (60,000 feet) by high-altitude aircraft from NASA's Manned Spacecraft Center in Houston. This is the first in a series of photographic flights that will include early summer, late summer, fall, and winter conditions. The first films to be processed were taken in June 1970. Only one (Block 5) has been completed. Since this block is 90 percent forested it is not a good example for land-use discrimination. However, it does show discrimination possibilities between forest types.

We processed the IR color film with a red, green, blue, and clear filter only using the same scanning procedure as described for the Apollo 9



films. The only difference is that we used a 99.17  $\mu$  effective aperture size to scan approximately the same strip width in terms of ground resolution. Our data were collected at 51  $\mu$ m intervals of scans 51  $\mu$ m apart.

Figure 9 shows a comparison of red, green, and blue optical density measured on 1:420,000 infrared color film. Comparing these results with densities from Block 5 on the Apollo 9 infrared color film shows some interesting differences. The three-month difference in vegetation development between photography dates accounts for the big increase in red density levels (infrared response). Obviously, June photography with greater leaf cover should have a higher red density than March photography when deciduous trees are leafless, most vegetation is still dormant, and solar radiation is still rather low by comparison. It is interesting to note the similarity in shapes of the two sets of curves. Although these data are encouraging, we can attach very little significance to them because the RB-57 IR color film was of such poor quality. However, our conclusions based on these data are the same as those for the Apollo 9 density scans. That is, density alone may discriminate forest from several nonforest classes, but to discriminate forest, forest types, and all nonforest classes will require combinations of density and between-density relationships.

The microdensitometer scans made on three different B/W infrared and panchromatic film and filter combinations resulted in the mean densities plotted in Figure 10. We do not show the densities for infrared film with a Wratten 12 filter and panchromatic film with a Wratten 12

filter because they appear to provide very little information for this study. It is obvious from the three curves that the infrared film with a Wratten 89B filter shows limited value for forest-nonforest discrimination by itself. Future analyses may show, however, that this film, when coupled with infrared color film, will aid in differentiating between bodies of water and forest. Although we have no data at present to support this point, an examination of the photographs shows that bodies of water are enhanced on this film. This has been a weakness of the IR color film taken from space. Bodies of water in dark forested backgrounds are not resolved.

Of the two panchromatic film-filter combinations shown, only the panchromatic with a 25A filter indicates any potential for land-use classification. Here again, the discrimination of urban areas may be aided if this film is used in concert with the IR color film. The better resolution capabilities of this film-filter combination may aid in resolving narrow urban features such as highways, pipelines, and power lines that are not resolved on the infrared color taken from space altitudes.

Detecting and measuring changes in the forest environment created by urban development and other manmade and natural causes is important to keep forest information up to date. The microdensitometer scans in Figure 11 are meant to demonstrate the feasibility of automatic scanning microdensitometers to detect a pulpwood cutting by repetitive satellite imagery. We used red density on the Apollo 9 IR color and blue density on the RB-57

IR color because they appeared to show the best discrimination.

The photographs in Figure 11 show the pulpwood stand before cutting and after the cutting. Some of the differences in the shapes of the two curves can be attributed to film resolution as well as seasonal responses for vegetation on IR color film. Despite these differences, there is certainly a noticeable response at the site of the pulpwood cutting.

Figures 12A and 12B show a similar demonstration for a pipeline location. Although we have much to learn about how to interpret these data by data processing, it does show some hope for detecting areas of forest change even on satellite imagery.

#### CONCLUSIONS

Although the research reported here is in its preliminary stages, we can make four rather broad statements regarding the results of this work.

1. Infrared color film is the best single multiband sensor available at the present time.

2. There is very good possibility that we can separate forest from all nonforest land uses by microimage evaluation techniques on IR color film coupled with B/W infrared (Wratten 89B filter) and panchromatic film (Wratten 25A filter).

3. Discrimination of forest and nonforest classes may be possible by either of two methods: (1) interpreters with appropriate viewing and mapping instruments might simultaneously view enlarged multiscaled images and map forest types and land uses for estimating acreages or (2) programmable automatic scanning microdensitometers and automatic data processing

techniques may be used to make land-use decisions based on optical densities, density differences and density ratios.

4. Results show the importance of procuring the best possible remote sensor data that are possible. Without good data our efforts can be of little significance.

Our plans for the next year include continued efforts to develop optical density signatures for forest and nonforest classes on Apollo 9 photography. Signatures developed for IR color, panchromatic (Wratten 25A filter), and B/W infrared (Wratten 89B filter) will be compared with signatures developed for RB-57 high-altitude photography for three seasons and 1:32,000 IR color taken in March 1970. We will also study the use of several pattern recognition techniques using these density signatures.

#### ACKNOWLEDGEMENTS

The work reported here would not have been possible without the assistance of Wallace Greentree, forester, who was responsible for the precise microdensitometer measurements and who ably assisted in all phases of the photo interpretation and field work; Mrs. Nancy X. Norick who provided guidance in the statistical approaches to image recognition; and Miss Marilyn Wilkes who did the computer programming.

## LITERATURE CITED

1. Langley, P. G. R. C. Aldrich and R. C. Heller. 1970. Multi-stage sampling of forest resources by using space photography--an Apollo 9 case study. Second Annual Earth Resources Aircraft Program Status Review. Vol. 2. NASA, Manned Spacecraft Center, Houston, Texas. 28 pp., illus.
2. U. S. Forest Service. 1969. A forest atlas of the South. Southern Forest Experiment Station, New Orleans, La., and Southeastern Forest Experiment Station, Asheville, N. C. 27 p., illus.
3. Aldrich, R. C. 1970. Space photographs separate land use and aid in forest inventories. Paper presented at the 1970 joint annual meeting of ACSM and ASP, Washington, D. C. Submitted for publication in Photogramm. Engng. 30 pp., illus.
4. Doverspike, G. E., F. M. Flynn, and R. C. Heller. 1965. Microdensitometer applied to land use classification. Photogramm. Engng. 31(2):294-306.
5. Richardson, A. J., R. J. Torline, D. A. Weber, R. W. Leamer, and C. L. Weigand. 1970. Computer discrimination procedure comparisons using film optical densities. SWC Research Report 422. Rio Grande Soil and Water Research Center, Soil and Water Conservation Research Division Agricultural Research Service, U. S. Department of Agriculture, Weslaco, Texas. 39 pp., illus.

Table 1. Camera, focal length, film-filter data, scale and type of coverage for Apollo 9 forest inventory study support photography; April 1969.

Camera	Focal Length (mm.)	Film	Filter	Scale	Coverage
Crown Graphic	75	Polaroid 400	Wratten 12	1:60,000	Block (5)
Maurer KB-8	38	Eastman Aero Neg	HF-3	1:120,000	Block (5)
Maurer KB-8	228	Ekta IR color	Wratten 15	1:20,000	Strip (5)
Maurer KB-8	38	Eastman Aero Neg	HF-2	1:12,000	Strip (10)
Maurer KB-8	228	AnSCO D/200	1A	1:2,000	Strip (174 sample triplets)

Table 2. Camera, focal length, film-filter, and photographic scale for RB-57 (Mission 131) photography for site 217, Atlanta, Georgia; June 1970.

Camera	Focal Length (mm.)	Film	Filter	Approximate Scale
RC-8	152	Ektachrome SO-397	450 m $\mu$ .	1:120,000
RC-8	152	Ektachrome SO-397	425 m $\mu$ .	1:120,000
Zeiss	305	Ektachrome IR SO-117	530 m $\mu$ .	1:60,000
Hasselblad	40	Panchromatic 2402	Wratten 25A	1:420,000
Hasselblad	40	Panchromatic 2402	Wratten 58B	1:420,000
Hasselblad	40	Panchromatic 2402	Wratten 12	1:420,000
Hasselblad	40	B/W IR, 2424	Wratten 89B	1:420,000
Hasselblad	40	B/W IR, 2424	Wratten 12	1:420,000
Hasselblad	40	Ektachrome IR SO-117	Wratten 15	1:420,000

Table 3. Land use and forest condition classification

Land Use	Code	Forest Condition	Code
<u>Forest</u>		<u>Forest Density</u>	
Pine (51-100% pine)	01	75-100 percent	1
Pine-Hardwood (25-50% pine)	02	25-75 percent	2
Bottomland Hardwood (0-25% pine)	03	0-25 percent	3
Upland Hardwood (0-25% pine)	04	<u>Forest Disturbance</u>	
<u>Agriculture</u>		No disturbance	01
Crops	05	Cutting - heavy	02
Plowed fields	06	Cutting - light	03
Pasture	07	Land clearing	04
Idle	08	Insect damage - heavy	05
Abandoned	09	Insect damage - light	06
Orchard	10	Disease damage - heavy	07
<u>Urban</u>	11	Disease damage - light	08
<u>Water</u>		Fire damage - heavy	09
Turbid	12	Fire damage - light	10
Clear	13		



Table 4. Comparison of percent forest area by study block, mean for all blocks, and type of photography.

Photography	Percent Forest Area					Mean
	Block					
	1	2	3	4	5	
	Percent					
Panchromatic <sup>1/</sup> (1:20,000)	77	36	81	45	85	65
Polaroid <sup>2/</sup> (1:60,000)	69	25	87	51	93	65
IR Color <sup>1/</sup> (1:32,000)	83	39	86	68	86	72
Apollo 9 <sup>2/</sup> (1:2,430,000)	80	35	73	55	96	68

<sup>1/</sup> Estimated from a count of over 600 photo points systematically located within each block.

<sup>2/</sup> Ocular estimate.

Table 5. Comparison of area for forest and nonforest classes using three photo scales<sup>1/</sup> --Block 3.

Photography	Pine	Hardwood		Nonforest	Water
		Upland	Bottomland		
			Percent		
Panchromatic (1:20,000)	17.0	54.1	9.8	18.9	0.2
IR Color (1:32,000)	59.4	16.7	10.1	13.2	0.6
Apollo 9 (1:2,430,000)	44.8	24.2	10.7	19.7	0.6

<sup>1/</sup> Estimated from a count of over 600 photo points.

NOT REPRODUCIBLE

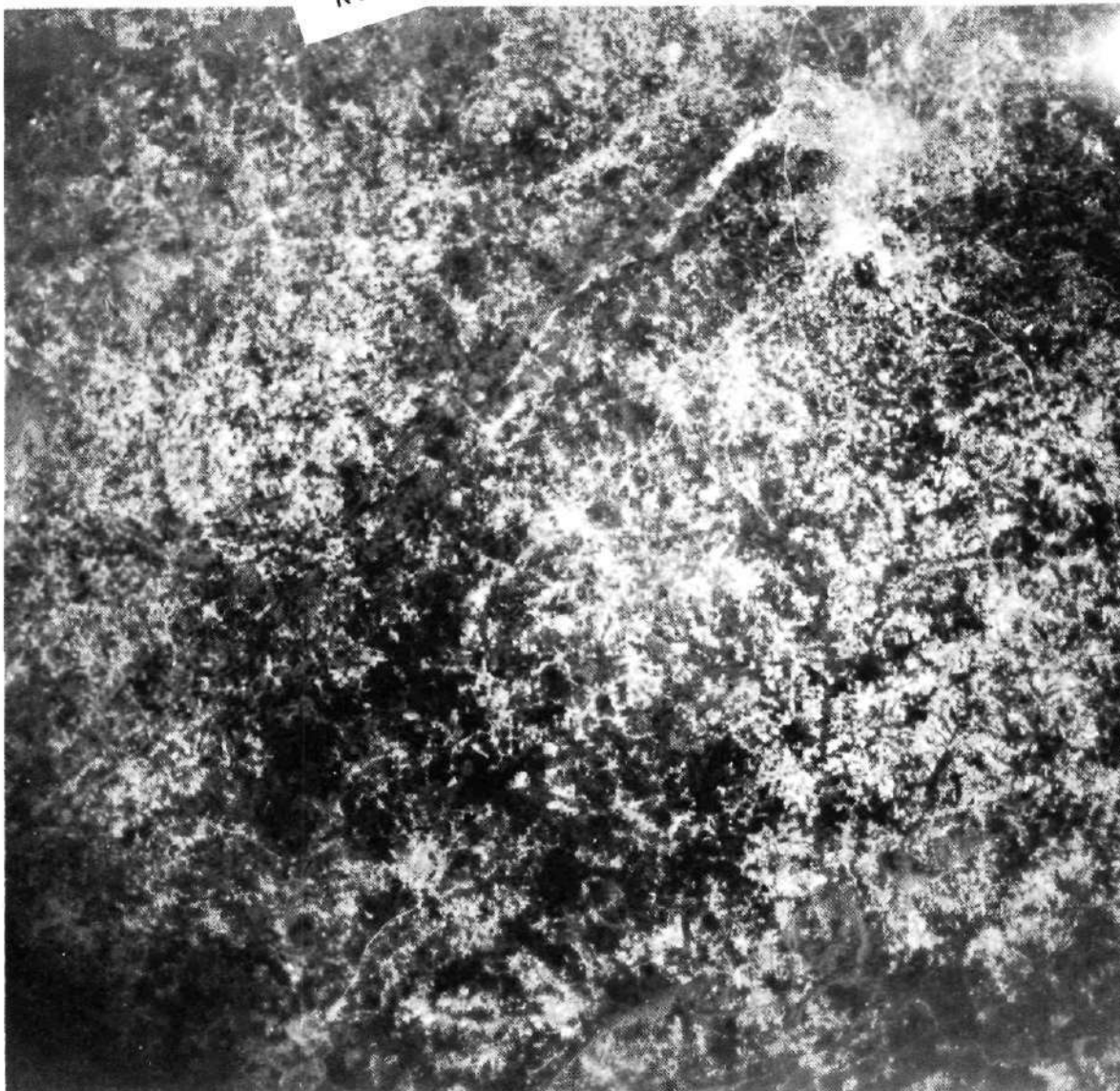


Figure 1.--Apollo 9 coverage for a portion of the Atlanta test site (Site 217). The light gray area in the upper right corner is Atlanta, Georgia. This photo was made from an IR color transparency.

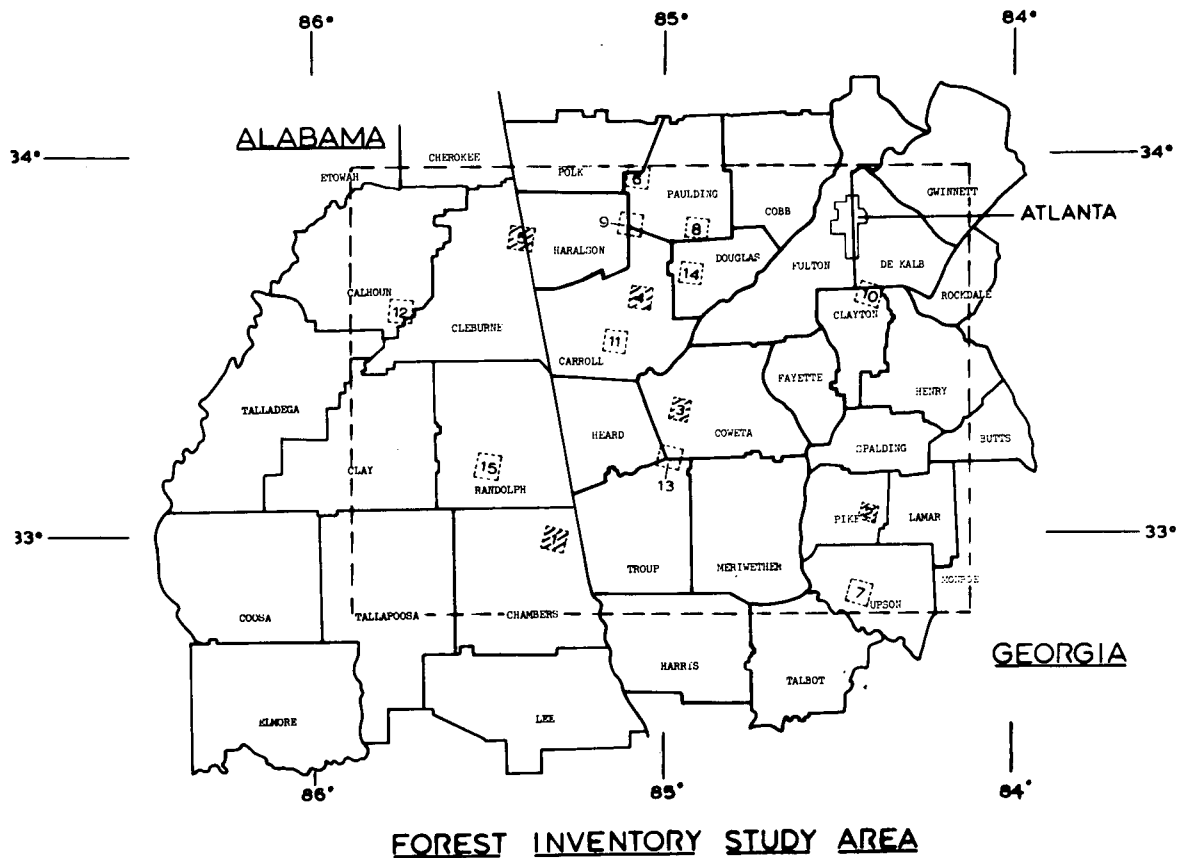


Figure 2.--The Atlanta test site includes all or portions of 27 counties in Alabama and Georgia. Five intensive study areas are shown with hatch marks. The 10 additional squares will be used to test interpretation models in another phase of this study.

NOT REPRODUCIBLE

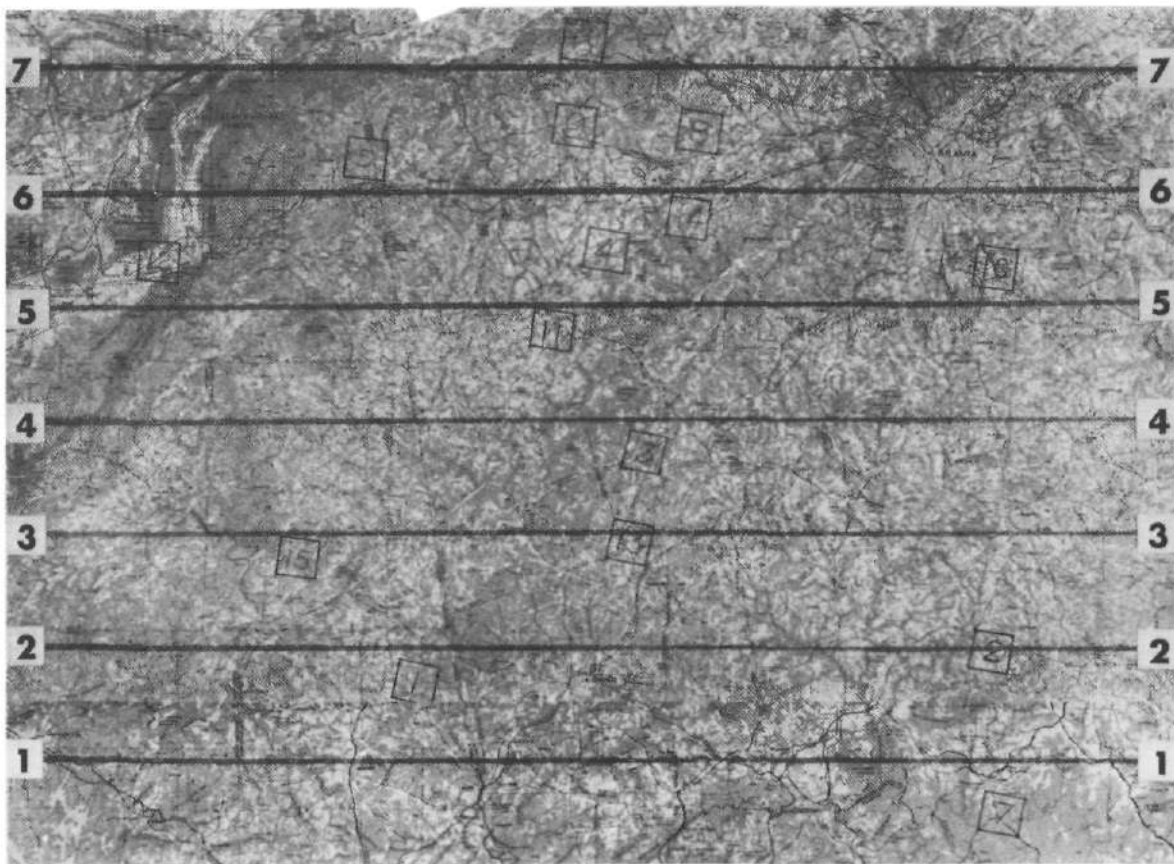


Figure 3.--RB-57 Mission 131 covered the Atlanta test site in 7 flight lines.

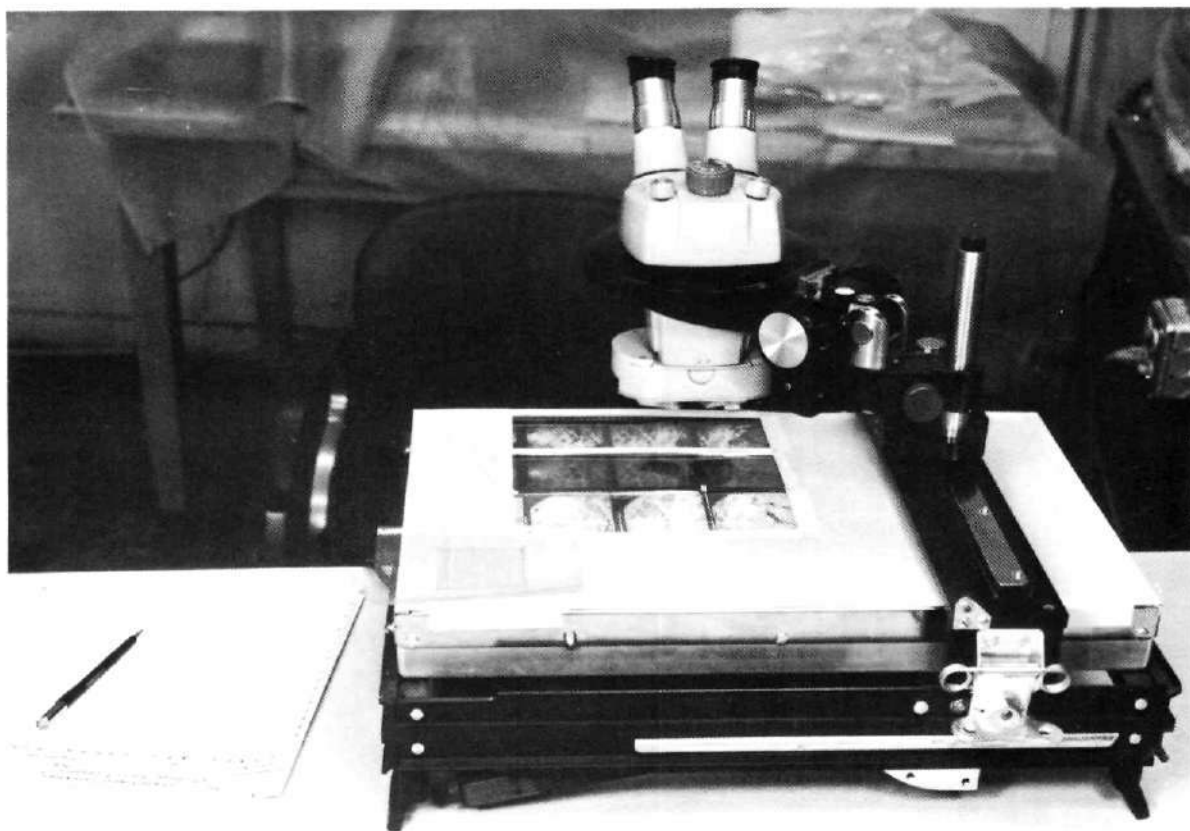


Figure 4.--Interpreters used a Bausch and Lomb Zoom 70 stereoscope at 7.5X to interpret satellite photography.

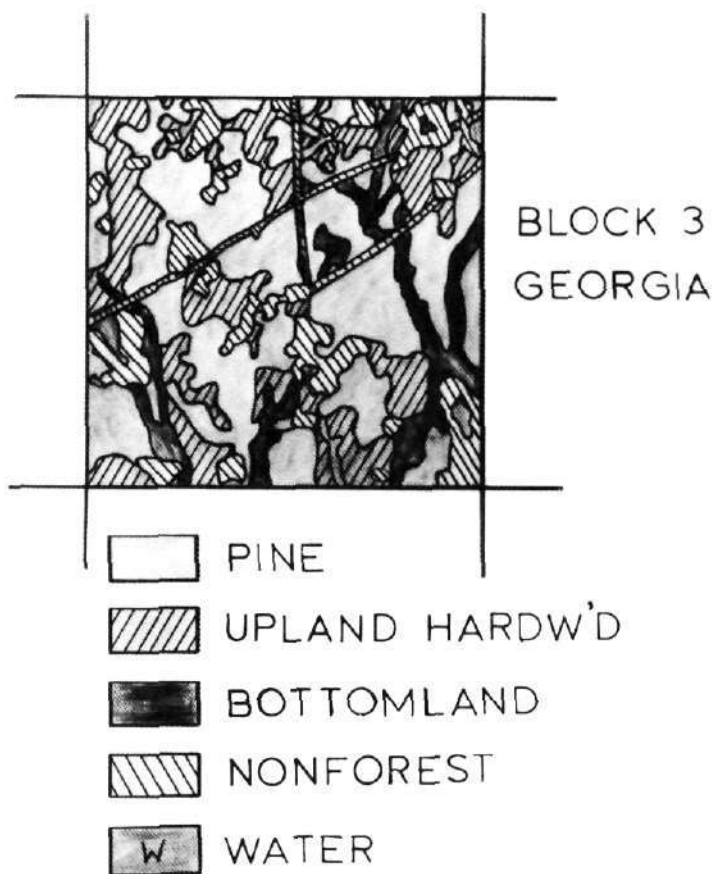


Figure 5.--A forest-type land-use map was constructed using a 28X enlargement of Block 3 made from the Apollo 9 IR color as a base map.

This page is reproduced again at the back of this report by a different reproduction method so as to furnish the best possible detail to the user.

36-29



Figure 6.--A Photometric Data Systems microdensitometer coupled to a Data Acquisition System digitizer was used to scan the Apollo 9 and high-altitude RB-57 photography.



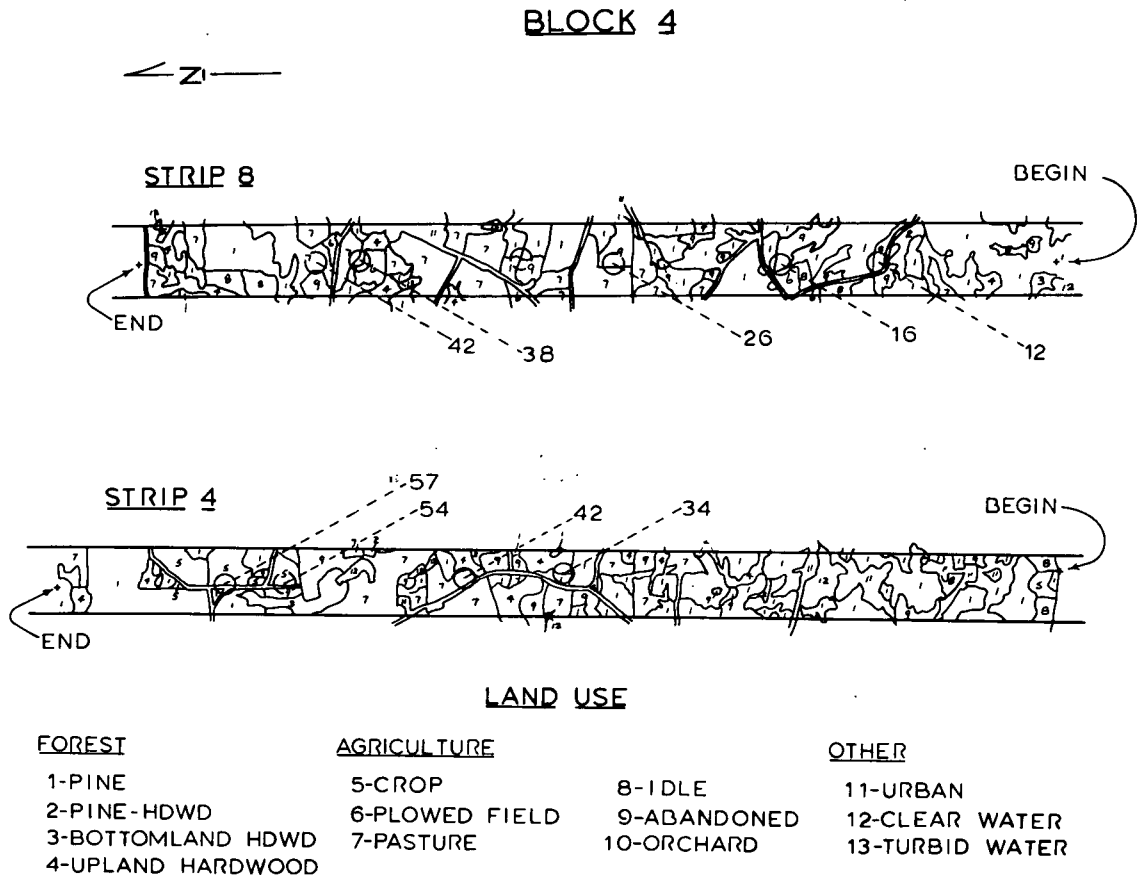


Figure 7.--Interpreters delineated forest type and land use along sample strips. These strips, adjusted by ground observations, are used as ground truth for microdensitometer scans on satellite and small-scale aerial photographs. Note beginning and ending points for the microdensitometer scans.

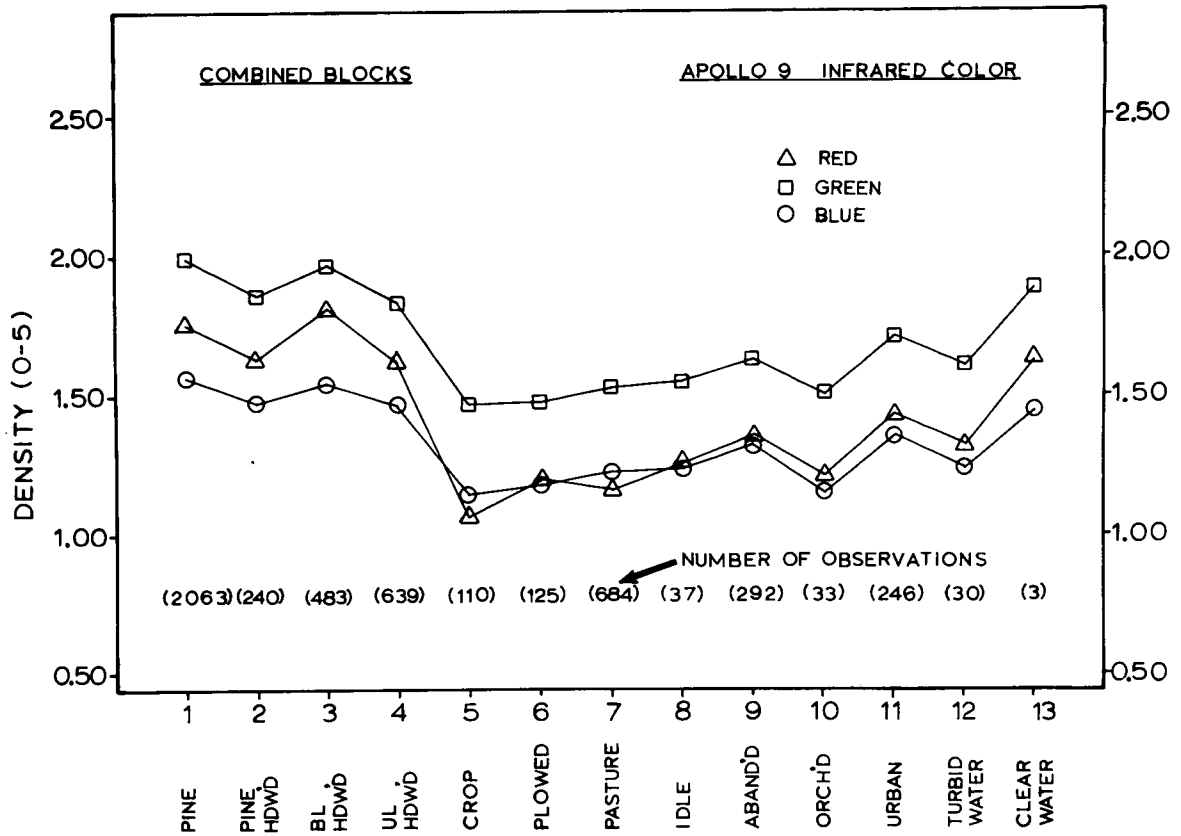
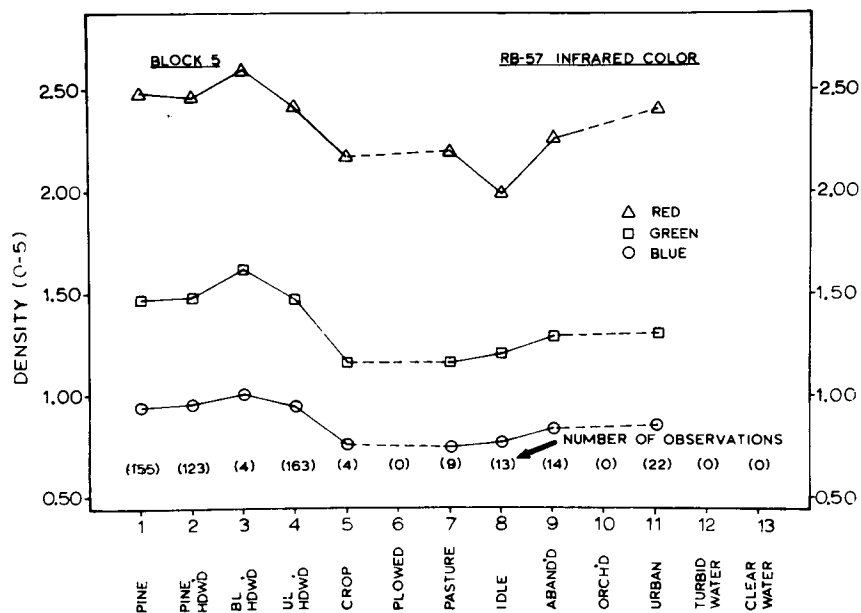


Figure 8.--The mean red, green, and blue optical densities for 13 forest and nonforest classes on Apollo 9 IR color--combined for all blocks.

A



B

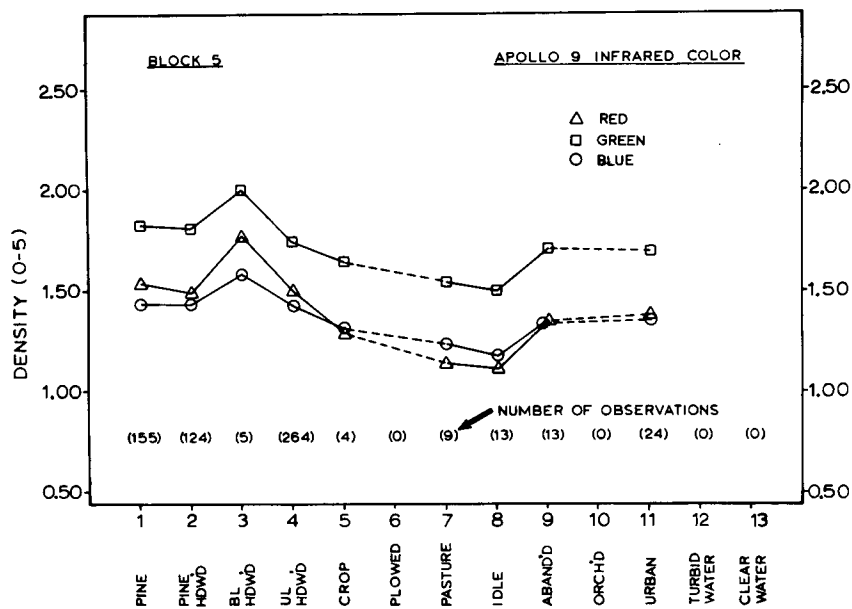


Figure 9.--The mean red, green, and blue optical densities for 9 of 13 forest and nonforest classes: (A) 1:420,000 IR color high-altitude photography, (B) Apollo 9 IR color--Block 5 only.

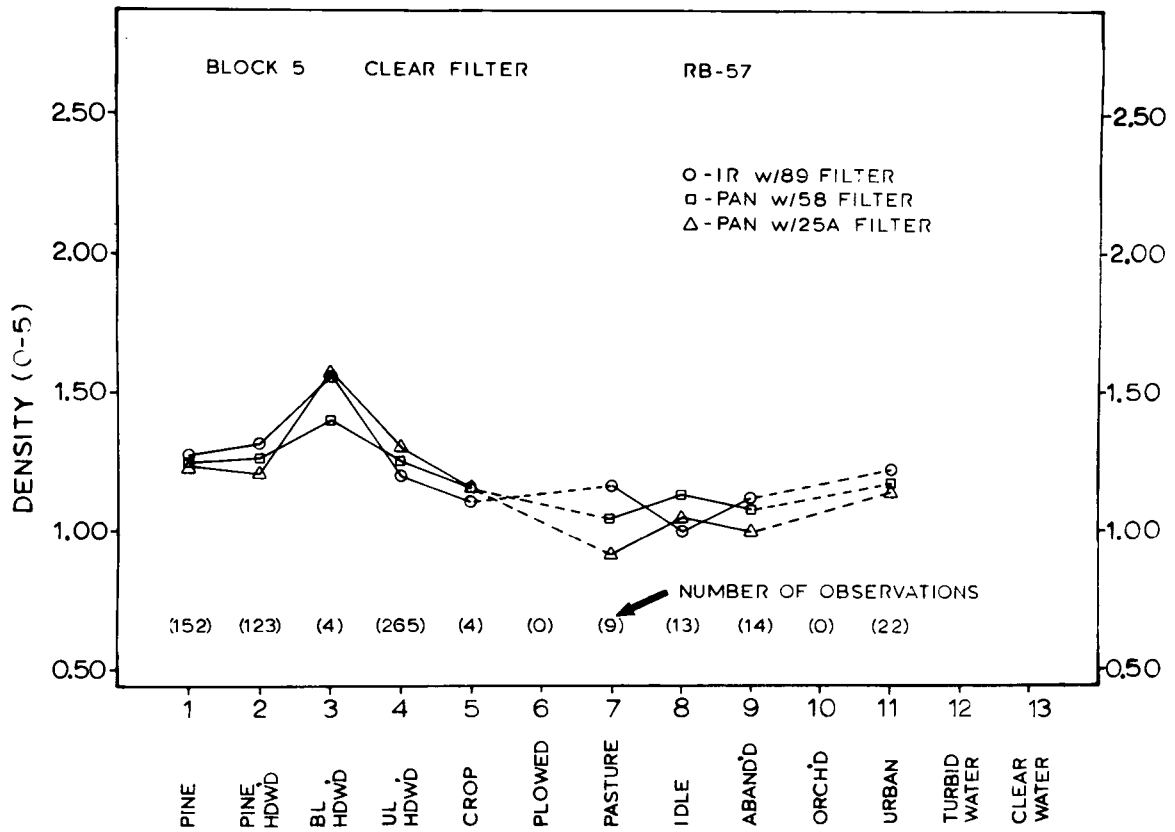


Figure 10.--The mean optical density (no filter) for 9 of 13 forest and nonforest classes on panchromatic (Wratten 25A), panchromatic (Wratten 58B), and B/W infrared (Wratten 89B)--Block 5 only.

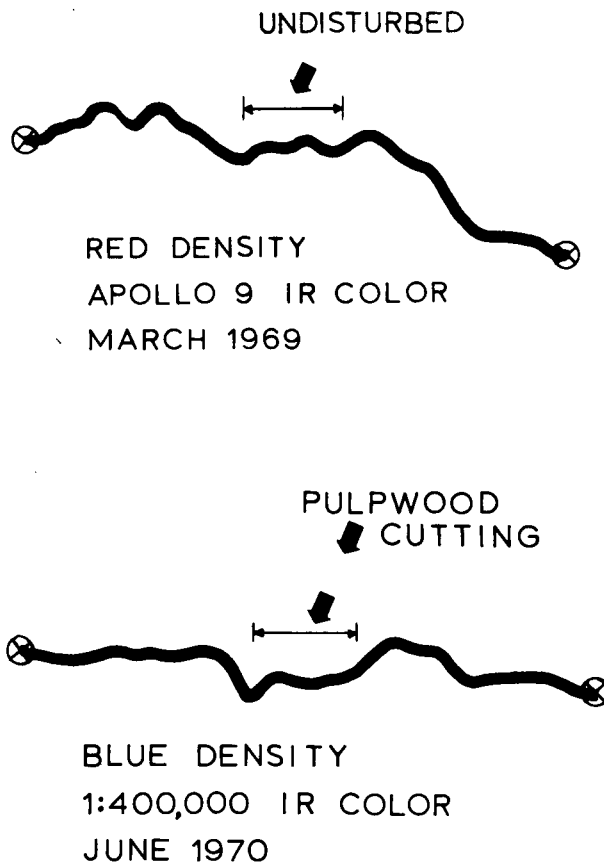


Figure 11A.--A pulpwood cutting that occurred sometime after the Apollo 9 mission, but before RB-57 Mission 131, is shown detected by a micro-densitometer scan. The upper density trace was made using a red filter on the Apollo 9 IR color photograph. The lower density trace was made using a blue filter on the 1:420,000 scale IR color taken on the RB-57 Mission 131.

BEFORE CUTTING      APRIL 1969



AFTER CUTTING      MARCH 1970



NOT REPRODUCIBLE

Figure 11B.--The pulpwood cutting shown on the density trace in Figure 11A does not appear on the top photo taken in April 1969. A photograph (IR color) taken in March 1970, one year following Apollo 9, shows the pulpwood stand has been cut.

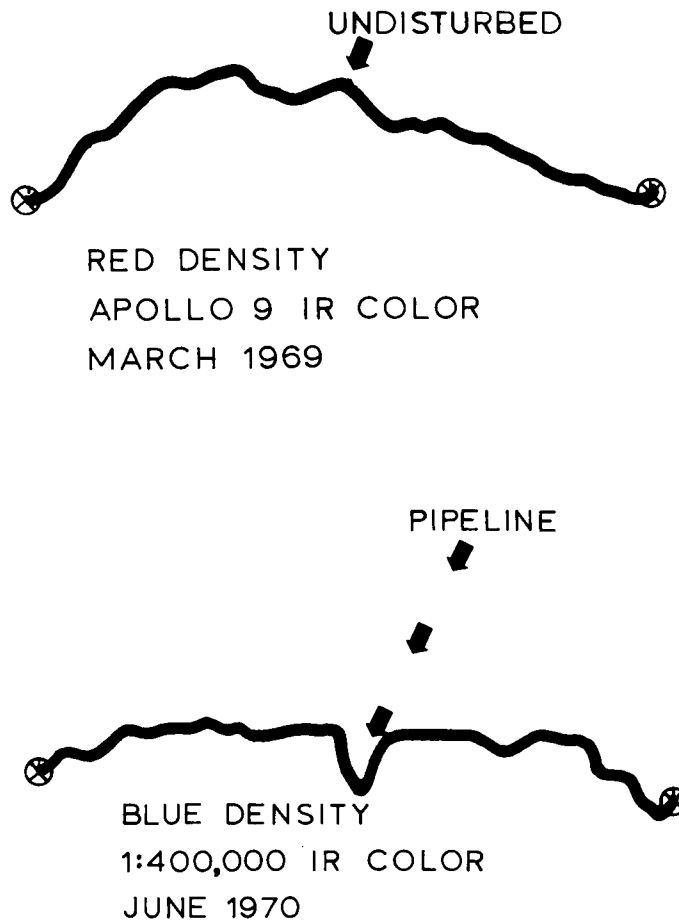


Figure 12A.--A pipeline that was constructed sometime after the Apollo 9 mission, but before RB-57 Mission 131, is shown detected by a micro-densitometer scan. The upper density trace was made using a red filter on the Apollo 9 IR color photograph. The lower density trace was made using a blue filter on the 1:420,000 scale IR color photograph taken on RB-57 Mission 131.

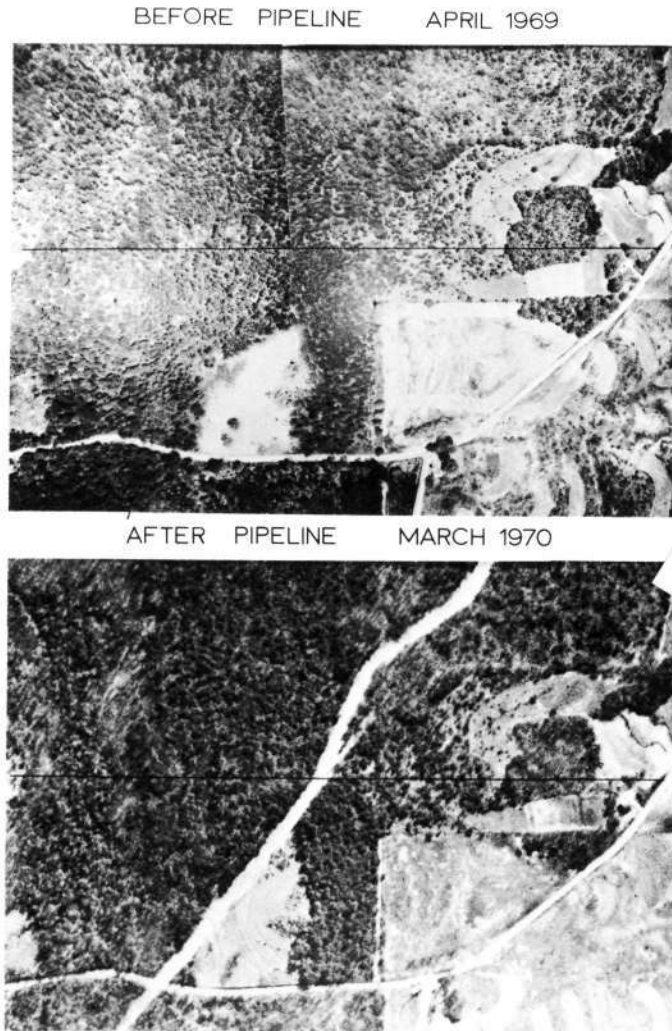


Figure 12B.--The pipeline shown on the density trace in Figure 12A does not appear on the top photo taken in April 1969. A photograph (IR color) taken in March 1970, one year following Apollo 9, shows the pipeline very clearly.



SUMMARY OF MICHIGAN MULTISPECTRAL  
INVESTIGATIONS PROGRAM

by

Richard R. Legault  
Willow Run Laboratories  
The University of Michigan  
Ann Arbor, Michigan

INTRODUCTION

This paper is a summary of the NASA supported activities at The University of Michigan's Willow Run Laboratories in the area of multispectral remote sensing. The objectives of this program are to improve and extend the techniques for multispectral recognitions of remotely sensed objects. The program has two major areas of activity. The first is a series of investigations directed in improving the techniques; the second is a series of programs with various users to extend the usefulness of these techniques and to show their practical application. In this paper, I shall summarize the activities of the past year in the development of multispectral techniques. The paper following will discuss the exploitation of the techniques developed in previous years, as well as those developed in this last year.

The primary thrust of last year's activities has been the development of techniques to extend spectral signatures in space and time. The fundamental barrier to the multispectral signature extension has been variations in the environment. These variations are differences, both spatially and temporally, in atmospheric transmission, illumination of the scene, and backscatter components. In previous years we pointed out that there are three ways one may hope to obtain such signature extensions. The first is by making suitable transformations on the remotely collected multispectral data; the intent of these transformations is to make the data invariant despite variations in transmission, illumination and backscatter. The second possible method is to employ ancillary sensors in the data collection platform which, in fact, do measure the illumination, transmission and backscatter. An example of such an ancillary sensor is the sun sensor now flown in the Michigan C47 aircraft. The third technique is to select in-scene references, which provide a calibration or reference source in the scene that permit us to correct the data.

The second area of effort has been the development of data upon which spectral signatures can be based. The data referred to here is laboratory data of the spectral reflectance and transmission of various materials. In addition, models of various types of problems have been constructed and, as we shall show later, are exploited to investigate various problems in remote sensing. This effort has resulted in the compilation of data and methods for retrieving this data for the remote sensing community as a whole.

The third effort has been the development of techniques which show some promise of enabling us to determine the composition of spatially unresolved scene elements. We shall treat the subject in fair detail later.

The fourth area of effort has been an investigation of the problems of multispectral data processing. Our attention has been directed towards practical speeds for such computations. We shall treat this subject in some detail as it has been a matter of some discussion in past meetings. This discussion has centered around the relative merits of digital and analog computation in the past. We will show that, in fact, both techniques have their place in an operational system.

Finally, some attention has been paid to problems of multispectral instrumentation. We shall not discuss the work we have done in this area in this paper.

Twelve reports will be issued on the work of this past year. During the course of the summary, I shall refer to these reports so that those interested in more detail than we have time to present here can have the required reference.

#### SIGNATURE EXTENSION

Spectral signatures are obtained today in the following manner. The objects to be recognized are identified in image form and from these areas the statistics for defining the spectral signatures are obtained. The problem at present is that the signatures obtained in this fashion usually do not hold for areas very far distant from the original learning set or for times very much different than the original collection time. A consequence of this is that a considerable amount of ground truth has to be collected in order to make effective use of spectral recognition techniques. Despite this rather obvious shortcoming, spectral recognition has played a role and undoubtedly will continue to do so, but perfection of the technique will require methods which allow us to extend the signature in both space and time. Equation (1) presents the rather unusual expression for the signal in the  $i^{\text{th}}$  spectral channel obtained by a multispectral remote sensor.

$$S(\lambda_i, \theta) = [H(\lambda_i)\tau(\lambda_i, \theta)\rho(\lambda_i, \theta) + b(\lambda_i, \theta)]K_i \quad (1)$$

where  $S(\lambda_i, \theta)$  = signal from instrument  
 $\lambda_i$  = spectral interval  
 $\theta$  = parameters of observation, direction, and distance  
 $H(\lambda_i)$  = irradiance (direct and diffuse sunlight)  
 $\tau(\lambda_i, \theta)$  = transmission  
 $\rho(\lambda_i, \theta)$  = material reflectance  
 $b(\lambda_i, \theta)$  = backscatter  
 $K_i$  = instrument response

The term that carries the information about the material in the expression is of course the reflectance of the material,  $\rho(\lambda_i, \theta)$  and its variation in this reflectance from one material to another that permits an identification. One is all too well aware, however, that we may expect variations in the irradiance or illumination  $H(\lambda)$ , transmission or visibility  $\tau(\lambda)$  and in the backscatter component  $b(\lambda)$ . These variations of illumination, transmission and backscatter are a primary source for the variation of the remotely sensed spectral signature and are a major contributor to the dilemma we face today in terms of signature extension.

That illumination, transmission and backscatter should vary from one area to another or from one time to another is not surprising, and considering that our present method for processing the data is to accept these variations, it is again not surprising that we have difficulty in establishing spectral signatures that will hold for very large areas or for very long periods of time.

One method for obtaining a spectral signature that is, in fact, invariant under variations in these environmental factors of illumination, transmission, and backscatter, is the transformation of the remotely sensed spectral data to obtain a new set of values which are hopefully invariant. Last year, we reported on some of the ratioing or normalizing transformations and illustrated their success under certain circumstances. Tabulated below are some of the multispectral transformations that we have tried.

$$\frac{S(\lambda_1, \theta)}{S(\lambda_2, \theta)} \dots\dots\dots, \frac{S(\lambda_{11}, \theta)}{S(\lambda_{12}, \theta)}$$

$$\frac{S(\lambda_2, \theta)}{S(\lambda_1, \theta)} \dots\dots\dots, \frac{S(\lambda_{12}, \theta)}{S(\lambda_{11}, \theta)}$$

$$\frac{S(\lambda_2, \theta) - S(\lambda_1, \theta)}{S(\lambda_2, \theta) + S(\lambda_1, \theta)} \dots\dots\dots, \frac{S(\lambda_{12}, \theta) - S(\lambda_{11}, \theta)}{S(\lambda_{12}, \theta) + S(\lambda_{11}, \theta)}$$

The reader is referred to Reference 1 to see some of the successes that were obtained. Now, these transformations essentially assume that we can ignore the backscatter component. They further assume that the ratio of illumination and transmission for two adjacent channels is essentially a constant.

$$\frac{H(\lambda_i)\tau(\lambda_i,\theta)}{H(\lambda_{i+1})\tau(\lambda_{i+1},\theta)}$$

The above expression is a constant for all atmospheric conditions and for all wavelengths. These techniques have been partially successful. In our view, the major failure of these techniques has been in their inability to adequately compensate for variations in the angles of observation.

These angular effects are illustrated in Figures 1, 2 and 3. In Figure 1, we have a video print of scanner data of Colorado grassland. Figure 2 is a three dimensional representation of the signal amplitude for a scanner strip of this area in the 0.4 to 0.44  $\mu\text{m}$  regions; in Figure 3 a similar strip of the same area is shown in the 0.8 to 1  $\mu\text{m}$  band. The reader can get a rough impression of the general slope or angular dependence by looking at the latter two figures. It should be apparent that the angular effects are, in fact, wavelength dependent by comparing the two figures. The very prominent dip in both of these figures is a cloud shadow, and in Figure 4 we will show a rather interesting method for detecting cloud shadows in the imagery.

In Figures 2 and 3, the horizontal dimension represents the flight path and the vertical dimension represents the scan dimension and is denoted in subsequent descriptions of the scan angle variations. If one looks closely at this data, one sees that if we average over local variations, a fairly well defined scan angle variation is sensible. This correction factor for scan angle is essentially obtained by averaging in the flight path dimension for a fixed scan angle and fixed spectral interval. This averaging process is represented in equation (2) below:

$$f(\lambda_i, \theta) = \frac{1}{T} \int_0^T S(\lambda_i, \theta, T) dT \quad (2)$$

where T = flight path dimension

$\theta$  = scan angle

The primary question, of course, is the interval over which such averaging should take place; in other words, how long a path length T should we take for finally determining the value of  $f(\lambda_i)$  for a fixed value of  $\theta$ . The inverse of the correction function  $f(\lambda_i, \theta)$  is then used to correct the remotely sensed data for angular effects. This technique is fairly obviously a combination of the transformed techniques discussed

earlier as well as the employment of in-scene references. In the particular scene in which this has been exploited so far, the various different elements have been randomly scattered with respect to the scan angle. Thus, we have a fairly unbiased estimate of the angular effects exploiting this averaging. Reference 1 covers in more detail this technique and some of the other work on transformation techniques that we have done during the past year, and reference 2 discusses the application of that technique to some actual data. The second paper will cover in more detail the results of this exploitation of the technique.

Figure 4 is a ratio of the 0.4 to 0.44  $\mu\text{m}$  bands to the 0.8 to 1  $\mu\text{m}$  band. It is rather interesting to note that the cloud shadow becomes very obvious in this ratio presentation. The reason I think is fairly clear, that the cloud shadow is relatively darker in the 0.8 to 1  $\mu\text{m}$  band than it is in the 0.4 to 0.44  $\mu\text{m}$  band, the difference largely due to the fact that the short wavelength 0.4 to 0.44  $\mu\text{m}$  band is primarily direct sunlight. The identification of cloud shadows and the subsequent correction of the data for cloud shadows detected in this manner is another way to extend the spectral signatures.

A second method for extending the spectral signatures is to employ ancillary sensors in the remote sensor platform to measure illumination, transmission and backscatter. At the present time, the Michigan C47 aircraft carries a sun sensor which measures the total downward irradiance at the aperture of the sun sensor. We have found that normalization of the remotely sensed multispectral data by the sun sensor data collected in each channel during the dead time of the scan has enabled us to extend the spectral signatures significantly. However, the simple normalization techniques have not accomplished all that we might desire. Consequently, we have initiated investigations into the calculation of the signals received by various types of sun sensors and the relationship to the backscatter, transmission and ground irradiance or illumination values. Figures 5 and 6 are the results of some of these calculations for albedos at the ground plane of 0. Figure 5 shows computations for visibility range of 23 km and Figure 6 for visibility range of 2 km, a quite significant difference in the atmospheric conditions.

The first impression that one receives in looking at this data is the fact that the total downward radiation which is currently being measured by our sun sensor is not nearly as sensitive to variations in the atmospheric conditions as is the diffuse downward component. This is hardly surprising since the diffuse component as measured from the aircraft platform (provided it is well within the atmosphere) should, in fact, be a fair measure of the atmospheric conditions. The real test of the importance of this is seen in the following tabulation.

	Visibility	
	<u>2 km</u>	<u>23 km</u>
Diffuse Sun Sensor	42	24
Total Sun Sensor	186	185
Total Ground $H(.55)$	168	178
Backscatter $b(.55)$	9	5
Transmittance	.23	.83
$H(\lambda)\tau(\lambda)$	38.6	148.7

#### Sun Sensor Estimates of Illumination and Transmittance

Here we have assumed the sensor platform is flying at 2 km and have tabulated the signal in milliwatts per square meter per micrometer for a diffuse sun sensor, the total sun sensor, the illumination of the ground plane in the 0.55  $\mu\text{m}$  band, the backscatter and the transmittance. The factor that we really have to consider is in fact not the total illumination of the ground plane or the transmittance separately, but the product of the two, the last line in the above tabulation, and it is apparent that the variations in the signal received by the diffuse sun sensor under the two visibility or atmospheric conditions described is much closer to defining the variability that we see in the product of transmittance and illumination  $H(\lambda)\tau(\lambda)$ . Both the diffuse and total sun sensors are inversely related to the product  $H(\lambda)\tau(\lambda)$  and the diffuse sun sensor outputs are a fair representation of the backscatter component, while the total sun sensor signal is a fair representation of the total ground illumination  $H(\lambda)$ . However, if we were forced to use a single sun sensor output, and since the factor that we wish to eliminate is the product of transmittance and total ground illumination, we would be forced to use the diffuse sun sensor signal.

There is, of course, no need to limit ourselves to either the total or diffuse measurement. We have, in fact, incorporated into the C47 system a diffuse sun sensor along with the total sun sensor so that more adequate normalization procedures can be employed. We believe it is possible to develop correction factors exploiting the diffuse and total sun sensor signals to more accurately measure transmittance, backscatter and ground illumination than is done by simple normalization by the diffuse and total sun sensor signals. Our next task in this area is to develop these correction procedures.

#### SPECTRAL SIGNATURES

The basis for multispectral detection as we have noted before are variations in the reflectance and emittance of various materials. In order to define the data processing, it is desirable to have available the

reflectivities and emissivities of various materials so that the potential false alarms as well as detection probabilities may be calculated before expensive operational tests of the detection procedure are made. To this end, we have compiled the available spectral reflectance and emittance data; this data compilation is reported in reference 3. The spectral signature data has, in addition, been digitized and retrieval programs have been generated. This retrieval and analysis program is described in reference 4. The digitized data are also available to the remote sensing community from either Houston or The University of Michigan. The available spectral data are far from complete; the data gaps are identified in reference 5. It is our hope that the remote sensing community will collaborate with us in filling these gaps and we hope that this document will be of use to other organizations in planning their measurement programs.

We have in addition exploited this data to some newer applications for remote sensing techniques. As most of you are aware today, our operations are limited to the 0.32 to 1  $\mu\text{m}$  region. In the very near future we shall have common aperture multispectral sensors from 0.32 to 14  $\mu\text{m}$  and it seems very obvious that we should start considering the use of multispectral thermal or infrared data. Figure 7 is a composite plot of the emission spectra of various silicon dioxide based rocks. It is well known that the emissivity dip in the 9 to 10  $\mu\text{m}$  region is due to the reststrahlen of silicon dioxide. The minimum of this reststrahlen dip for acidic rocks occurs at a shorter wavelength (roughly 9.4  $\mu\text{m}$ ) than does the minimum for ultra basic rocks (roughly 10.2  $\mu\text{m}$ ). It should then not be surprising that one might attempt to define the acidity of various rock types on the basis of multispectral data collected in the 9 to 11  $\mu\text{m}$  region. Some manipulation of these data convinced us of the potential of this technique.

A recently developed laminar detector was made available to us. The top layer of this detector was sensitive in the 8.2 to 10.9  $\mu\text{m}$  range and the bottom detector was sensitive in the 9.4 to 12.3  $\mu\text{m}$  range. A brief glance convinces one that there is some hope that by taking the ratio of these two bands, the acidity of the rock type might be determined. While the spectral bands encompassed by this detector are not optimal for this task by any stretch of the imagination, it is the first common aperture multispectral data available to us in the 8 to 14  $\mu\text{m}$  band.

In Figure 8 we show the images collected in the two bands respectively as well as the ratio. If the ratio of the 8.2 to 10  $\mu\text{m}$  channel to the 9.4 to 12.1  $\mu\text{m}$  channel is small, we would tend to say that acidic rock is present. In the ratio image of Figure 8, we see fairly dim areas around a silicate quartz sand quarry in Mill Creek, Arizona. In the two images separately, a body of water is noted in the lower central portion of the image. In the ratio image a dark outline for these areas indicates the sand shores of this body of water. Subsequently, Dr. Kenneth Watson of USGS and his colleagues have walked this area and identified all the

dark portions of this particular scene as being high acidic, silicon-dioxide-based rocks. While they have not investigated all the other portions of this scene, they have not found any other silicon-dioxide-based rocks that were not detected by this ratio technique. This work is reported in reference 6.

The spectral signatures work in the past year has also included some modeling of the radiation characteristics for various phenomena. One of the tasks undertaken was an attempt to determine whether ground water could be detected in thermal imagery. This work was in support of some data interpretation for the Columbia Basin area. There was some indication that thermal patterns in the scene were associated with varying depths of water table in this particular area. Consequently, calculations were made to determine whether the temperature as measured at the surface could be used as an indicator of the water table. The environmental conditions, relative humidity, temperature, time of the year and wind velocities for the period of data collection were used in these calculations. We used a one dimensional thermal model which allows us to assume various types of materials in layered structures.

In Figure 9 is plotted the diurnal cycle for temperature variations for two soil types. It should be noted that at certain times of the day, the differences of soil types do in fact produce different temperatures which would be detectable by an IR scanner. In Figure 10, different moisture contents for a single soil type were assumed and once again for optimal times of day detectable temperature differences are present.

In Figure 11, we considered a structure for the terrain with the water table at varying depths but with identical surface moistures and soil types. It is apparent that no detectable temperature differences for the environmental conditions postulated (in this particular example, they were in the late fall) are detectable. If underground water is going to be detected, it is likely that it will be by one of three means — either differences in vegetation types present at the surface where underground water is present, differences in soil moisture (which is very likely to occur), or differences in soil types probably related to permeability of the soil. While there still remains some hope for detection of underground water based upon remotely sensed infrared radiation, more work on the mechanism of such detection seems warranted at this time. It is also clear that both the time of day for this detection process and time of year will play an essential role.

#### DETECTION OF SPATIALLY UNRESOLVED OBJECTS

Much has been said to date of the problems associated with the limited spatial resolution capabilities of the first generation satellite-borne remote sensors. These remote sensors have concentrated on spectral coverage



rather than spatial coverage. That this concentration is warranted is partially demonstrated in the following work that was done during the last year. At first glance, it would seem impossible to identify objects that are spatially unresolved. This is certainly true if we are considering single spectral channel systems. However, the ability to measure the spectral distribution of radiance does offer us the possibility to resolve the elements within a resolution element -- in other words, the capability of identifying spatially unresolved objects. One example is the percent ground cover of an agricultural crop which is indicative of stage of growth and vigor. In Figure 12, we have such a classical problem, viz. the detection of the amount of weeds and bare soil in a corn field. Now let us consider this particular corn field as being a composite of corn plant reflectance spectra, the reflectance spectra of weeds and the reflectance spectra of bare soil. There is a certain percentage of each one of these pure types of materials in an individual resolution element. Very few sensors at almost any aircraft altitude are able to tell us very precisely what these percentages are. However, if we consider the multispectral signature of each individual type of materials (weeds, corn plant and soil) as vertices of a convex mixture, then the particular field we are looking at contains percentages of each of these types. In Figure 13, we have the reflectance spectra of bare soil and corn. These are pure spectral signatures of each of the materials. Now suppose a particular resolution element contains equal amounts of corn and bare soil while another resolution element contains 20% corn and 80% bare soil. We expect to see differences in the reflectance spectra for the various resolution elements and, in fact, we do as a scene in Figure 14. We are in fact able to take this composite spectrum and determine the percent of various elements that are within the resolution element.

A model for this detection is follows:

#### MODEL

Signature of Type  $i$  Material is Gaussian Distribution with Mean  $A_i$  and Covariance Matrix  $M_i$ . If Proportion of Type  $i$  Material in Mixture is  $X_i$ , Signature of Mixture Has Mean  $A_x$  and Covariance Matrix  $M_x$  Given by:

$$A_x = \sum_i X_i A_i$$

$$M_x = \sum_i X_i M_i$$

The procedure that we follow is to first identify the pure signatures that we expect to see in the resolution element. Of course, the expectation may not be realized for all of the elements, but they have to be sufficient in number to cover the possibilities that might be there. Secondly, we examine our data sample and estimate the proportions of each of the pure signatures that are present in the particular data sample representing the resolution element. The algorithms required for this estimation are developed and defined in reference 7 (along with some applications of the convex mixture algorithms to actual data). There is one practical problem in doing this work. At the present time, we have very little ground truth information which allows us to estimate the correct proportions of various materials within resolution elements or, for that matter, within various agricultural type fields. This lack of appropriate ground truth data for such things as percent ground cover has prohibited us from making very accurate tests of techniques developed. Hopefully within the coming year, such data will become available and we shall be in a position to properly validate the models. However, we have been able to obtain statistics from pure strains of various materials and simulate the statistics of these strains in such a way as to test out the validity of the convex mixture algorithm. Table I presents the results of such a simulation.

TABLE I. RESULTS OF ESTIMATING PROPORTIONS  
(SIMULATION)

<u>Material</u>	<u>True Value of Proportion</u>	<u>Estimated Value of Proportion</u>	<u>Error</u>
Sugar Beets	0.5500	0.5375	-0.0125
Weeds	0.2500	0.2397	-0.0103
Bare Soil	0.2000	0.2085	0.0085
Alfalfa	0.0000	0.0004	0.0004
Barley	0.0000	0.0139	0.0139

The basic data upon which the pure spectral signatures of sugar beets, weeds, bare soil, alfalfa and barley are based on data collected in the Imperial Valley during the spring of 1968. The simulation, therefore, is realistic in the sense that it is based upon actual data, but the proportions and the variations of the spectral signatures are the factor simulated. The results given in Table I are remarkably accurate. For example, the true proportion of sugar beets in our simulated area was 0.55, and we estimate 0.54. Such results are sufficiently encouraging to lead us to continue pursuing this work, particularly in light of the practical importance of developing such techniques for the first generation satellite remote sensors.

The only practical application of this technique made to date has been over a Colorado grasslands area where various nitrogen fertilizer treatments were applied. While once again we had inadequate ground truth to determine the percentages of tall, mid-length and short grasses on the various plots investigated, it was possible to at least quantitatively determine whether the algorithm was working properly. In Figure 1, we have a panchromatic image of the Colorado grassland area where the nitrogen treatments were applied. The treatments were applied at various times so that data was available on the height of the grass from the time of treatment. As we can see in Figure 15, the algorithm predicts more tall grass for the nitrogen treated plots than for plots receiving no treatments and that the rate of growth of the grass is greater for the nitrogen treated plots, as we might expect. In this particular case, we have specified percentages of the three grass heights that were involved. The best that we can say is that the results agree with what our intuition would be. As we have said before, there is no ground truth to support the results of these estimations. Various problems with the computational algorithms have been identified and work is currently going on to correct them. The technique will be exploited with more airborne data during the coming year.

#### DATA PROCESSING

Multispectral processing of remotely sensed data has proven effective in many applications related to earth resources studies. However, these applications usually require timely processing of large quantities of data and today this processing is several orders of magnitude beyond our capabilities. For example, if the U.S. and its coastal waters were overflowed twice a year with presently planned equipment, the data collected would require a conventionally organized digital computer with a cycle time of  $10^{-10}$  seconds to keep pace with the data collection rates. This cycle time is a factor of  $10^4$  faster than that obtainable with presently available digital computers. Alternative methods of computations are available. A parallel-channel, hard-wired analog computer system at The University of Michigan (SPARC) does in fact meet this data rate. However, there are drawbacks with this type of system. The set up of such an analog computer is extremely slow and its versatility is somewhat limited, whereas the digital computer is a much more versatile device. It seems, then, fairly clear that the type of operational data processing system that we will ultimately be led to combines the best features — program ability primarily of the digital computer, and the high throughput calculation rate of hard-wired, parallel-channel analog facilities.

During the past year, we have investigated the possible design alternatives for such a hybrid multispectral data processing facility. The results of these investigations are given in detail in references 8 and 9. Essentially these investigations began by considering some of the limitations

of the current analog systems. The major problems with the current analog systems are the time involved in setting up the problem for computation and the difficulty in optimizing the recognition procedure. It became fairly clear that an improved system should utilize a digital facility in the problem set up and the process optimization, and rely on the parallelism of the analog portion of the system for the bulk computation. Thus, we have a fairly standard hybrid where the digital computation system acts as a controller for the analog processor which does the high speed parallel channel computation.

In Figure 16, we have a component diagram for such a system which indicates the various types of units that are involved. We have data inputs and data primarily from magnetic tape, tape buffer storages, interfaces between both display and digital computer for the analog processor, pre-processor and the analog recognition processor. The recognition output is then interrogated by the digital system for determining whether it is operating according to plan. In Figure 17, we see the various functions that are performed and some estimate in terms of factors of real time for these various functions. The proposed hybrid system gives an effective reduction of a factor of 32 in the time for processing multispectral data. The type of equipment proposed here is, of course, prototype and there is little doubt that with more engineering work that hybrid facilities could, in fact, be designed to meet real time.

### INSTRUMENTATION

During the past year, three small studies of multispectral instrumentation have been performed. The results of these investigations are given in references 10, 11 and 12. We shall not discuss these reports in any detail. Very briefly, we considered the utilization of detectors in line scanners, some optical transfer techniques for multispectral orbital scanners, and some problems of calibrating multispectral scanners. These problems had arisen during the design and fabrication of the 24-channel multispectral scanner for aircraft use and the 10-channel Skylab sensor. These studies were an integral part of the engineering support we furnished NASA, Houston during the fabrication of the 24-channel and Skylab sensors.

### CONCLUSIONS

I should like to be able to report that our work on the spatial and temporal extension of multispectral signature had been completed. I cannot. A complicated multispectral recognition problem that required 219 learning sets last year can now be done with 13 learning sets. Signatures that were

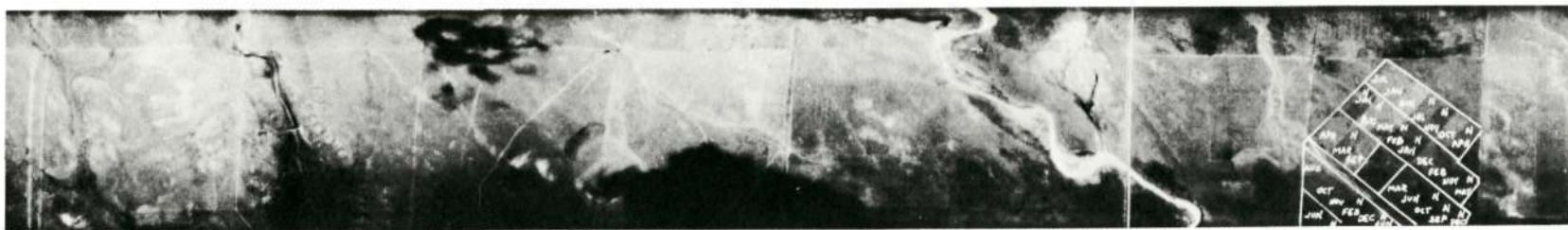
valid for 30 miles last year have been extended for 129 miles using transformation and sun sensor data. But there are still cases where our techniques will not work. We have sorted out most of the problems of signature extension and expect next year to be able to define the limits of signature extension and how the extension should be attained.

Spectral reflectance and emittance data are now available to the remote sensing community. This data can be used to define the approach to many multispectral remote sensing problems. All too often multispectral recognition is based on spectral differences which appear in a set of remotely sensed data without our being able to explain why such differences should be present. Consequently, we are unable to state with any certainty whether the recognition experiment can be repeated. An explanation of the observed differences based on the optical properties of the materials gives us some confidence of the recognition experiment's repeatability. We hope that the successful use of signature data reported will persuade the remote sensing investigators to make more extensive use of such data.

The most exciting new development is the possibility of recognizing spatially unresolved scene elements using multispectral data. These techniques are in their infancy but show considerable promise. A new factor must now be considered when defining required spatial resolutions. If spatially unresolved elements can be identified in some cases using multispectral data, we should have a new look at the remote sensing problems requiring high spatial resolution to determine whether or not they can be solved with the new multispectral recognition techniques for unresolved spatial elements.

## REFERENCES

1. STUDIES OF SPECTRAL DISCRIMINATION, W. A. Malila, R. Turner, R. Crane, C. Omarzu, Report No. 3165-22-T, in publication.
2. INVESTIGATIONS RELATED TO MULTISPECTRAL IMAGING SYSTEMS FOR REMOTE SENSING, J. Erickson, Report No. 3165-17-P, in publication.
3. THE NASA EARTH RESOURCES SPECTRAL INFORMATION SYSTEM: A DATA COMPILATION, V. Leeman, et.al., Report No. 3165-24-T, in publication.
4. EXPANDED RETRIEVAL ANALYSIS SYSTEM FOR THE NASA EARTH RESOURCES SPECTRAL INFORMATION SYSTEM, V. Leeman, et.al., Report No. 3165-22-T, in publication.
5. DATA GAPS IN THE NASA EARTH RESOURCES SPECTRAL INFORMATION SYSTEM, R. Vincent, Report No. 3165-25-T, in publication.
6. REMOTE SENSING DATA ANALYSIS PROJECTS ASSOCIATED WITH THE NASA EARTH RESOURCES SPECTRAL INFORMATION SYSTEM, R. Vincent, et.al., Report No. 3165-26-T, in publication.
7. INVESTIGATIONS OF MULTISPECTRAL SENSING OF CROPS, R. Nalepka, et.al., Report No. 3165-30-T, in publication.
8. A PROTOTYPE MULTISPECTRAL PROCESSOR WITH HIGH THROUGHPUT CAPABILITY, F. Kriegler, R. Marshall, Report No. 3165-23-T, in publication.
9. DATA PROCESSING DISPLAYS OF MULTISPECTRAL DATA, F. Kriegler, R. Marshall, Report No. 3165-28-T, in publication.
10. DETECTOR UTILIZATION IN LINE SCANNERS, Leo Larsen, Report No. 3165-29-T, in publication.
11. CALIBRATION OF MULTISPECTRAL SCANNERS, J. Braithwaite, Report No. 3165-27-L, in publication.
12. INVESTIGATION OF SHALLOW WATER FEATURES, F. Polcyn, et.al., Report No. 3165-31-T, in publication.

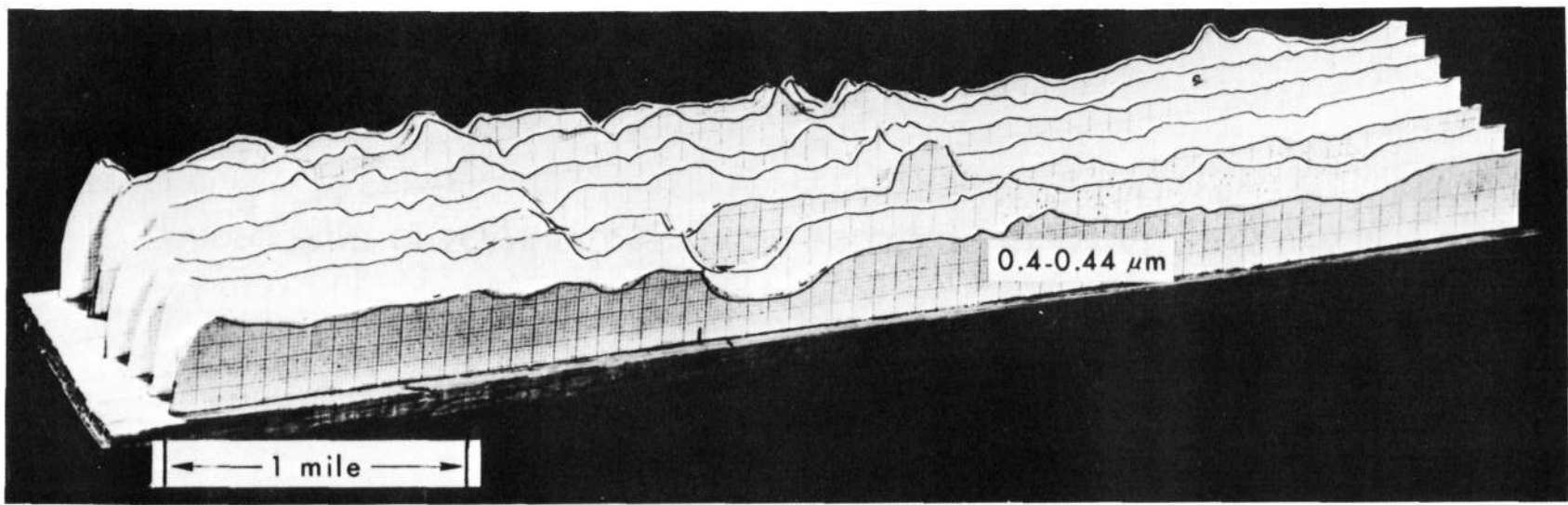


VIDEO PRINT OF SCANNER DATA FROM COLORADO GRASSLAND 0.62-0.66  $\mu$ m.



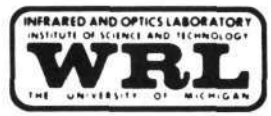
Figure 1

415

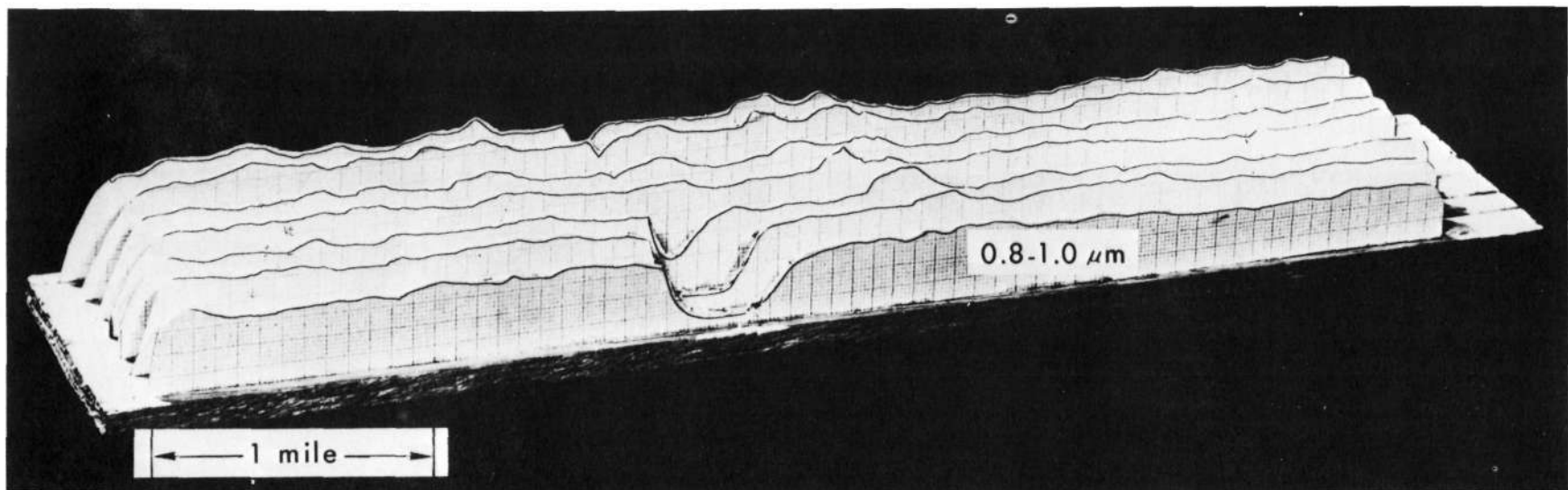


THREE DIMENSIONAL PLOT OF FILTERED SCANNER DATA FROM  
COLORADO GRASSLANDS, 0.4-0.44  $\mu\text{m}$

Figure 2

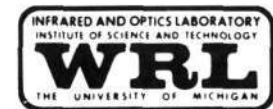


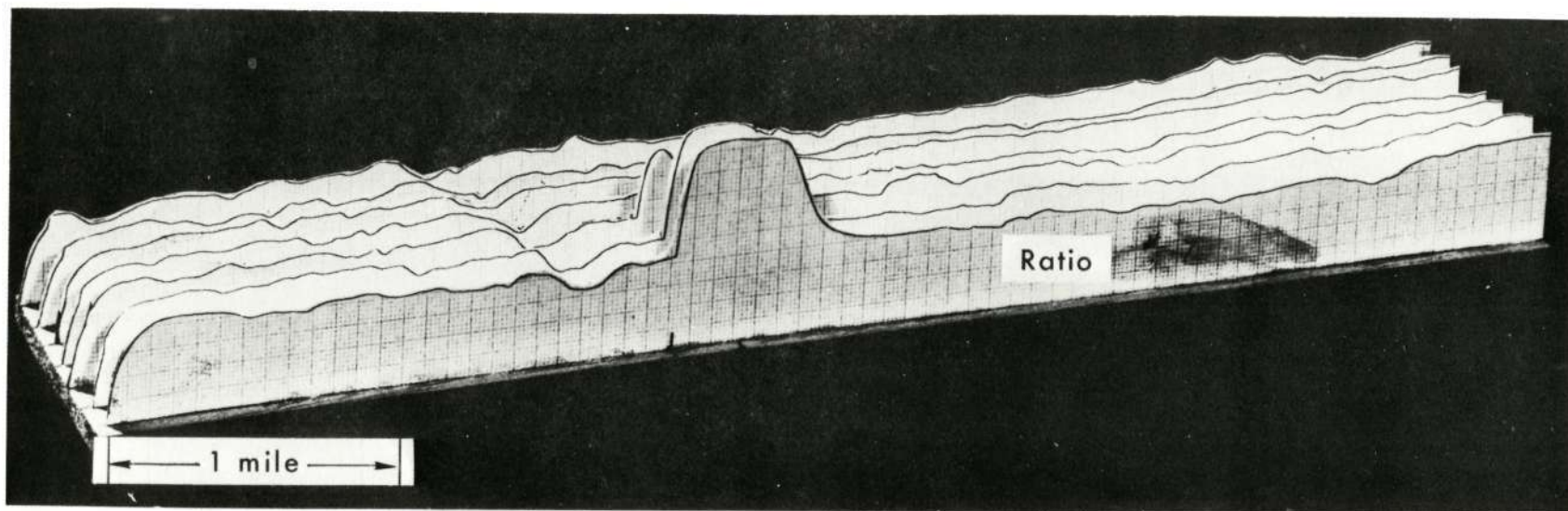




THREE DIMENSIONAL PLOT OF FILTERED SCANNER DATA FROM  
COLORADO GRASSLANDS, 0.8-1.0  $\mu\text{m}$

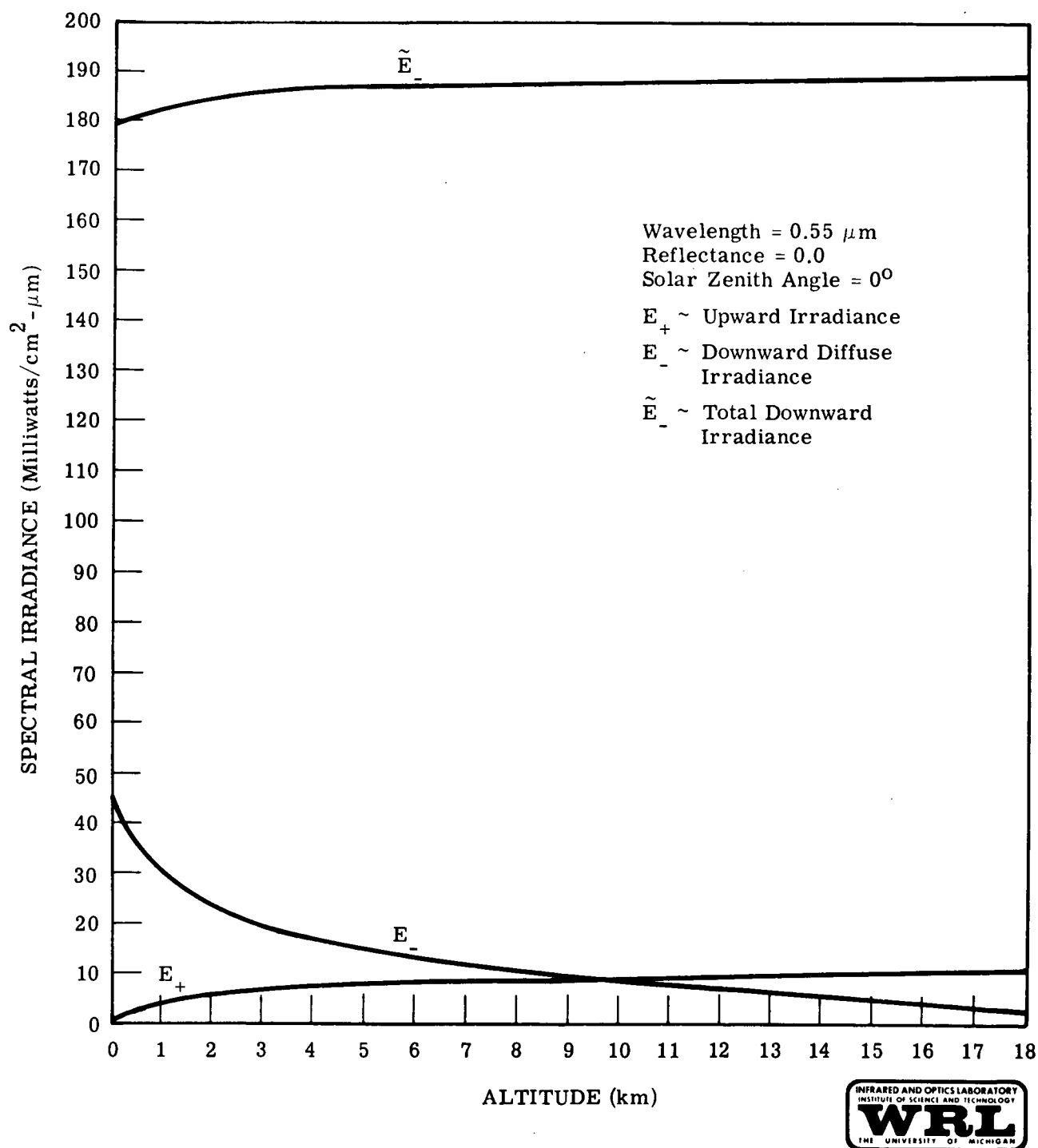
Figure 3





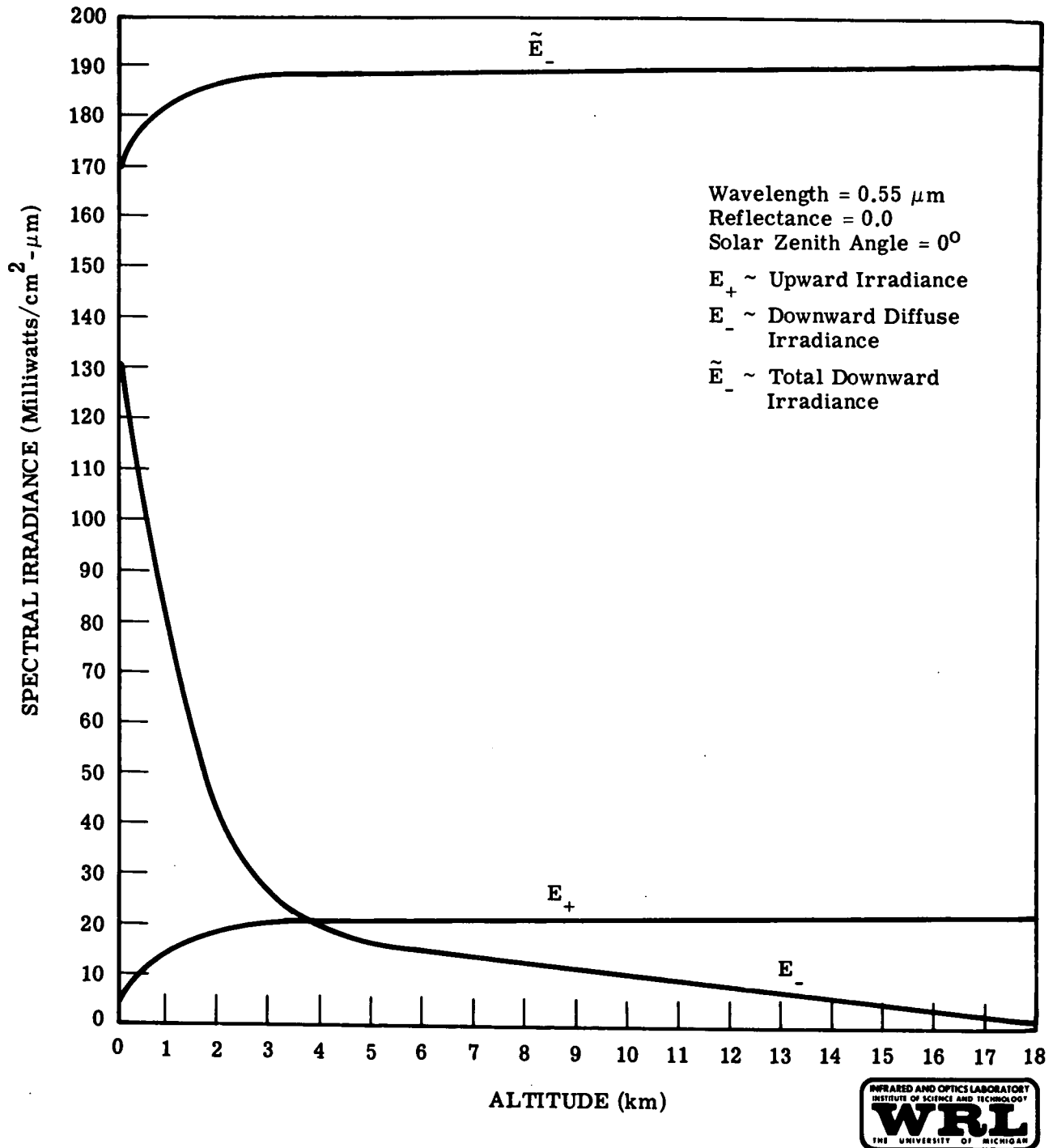
THREE DIMENSIONAL PLOT OF FILTERED VOLTAGE RATIO,  $V_{\downarrow 0.4-0.44} / V_{\downarrow 0.8-1.0}$ ,  
FROM COLORADO GRASSLANDS SCANNER DATA

Figure 4



ALTITUDE DEPENDENCE OF IRRADIANCES IN A HOMOGENEOUS ATMOSPHERE WITH A VISIBILITY OF 23 km

Figure 5



ALTITUDE DEPENDENCE OF IRRADIANCES IN A HOMOGENEOUS ATMOSPHERE WITH A VISIBILITY OF 2 km

Figure 6

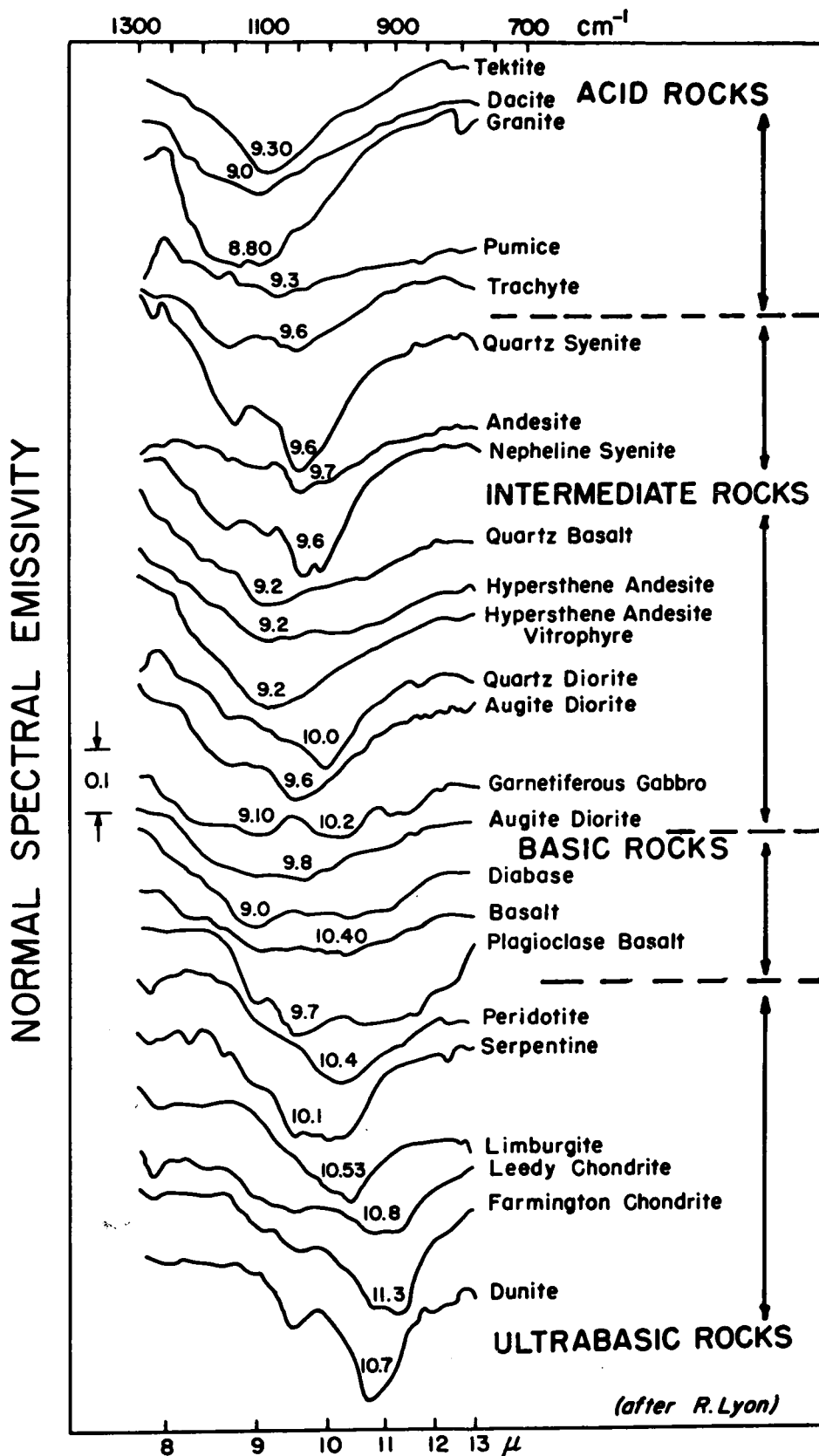
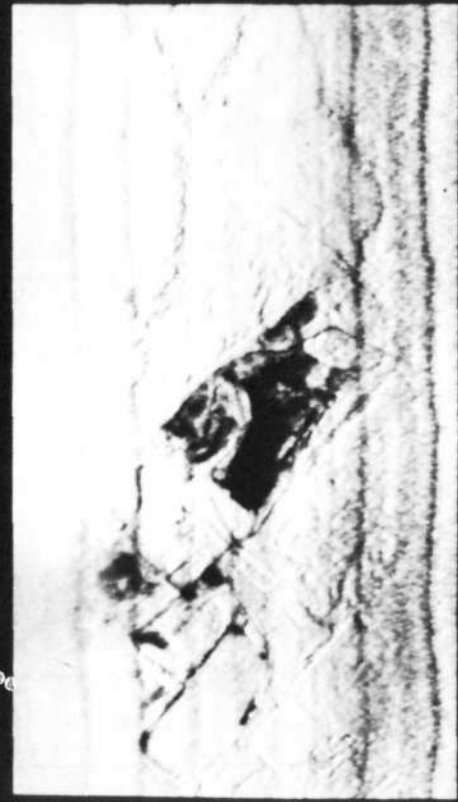
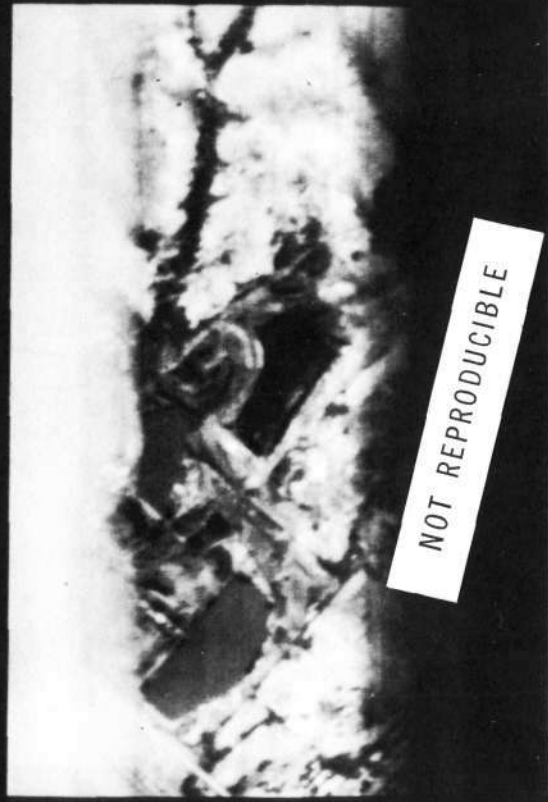


Figure 7

8.2-10.9  $\mu\text{m}$

9.4-12.1  $\mu\text{m}$

Ratio

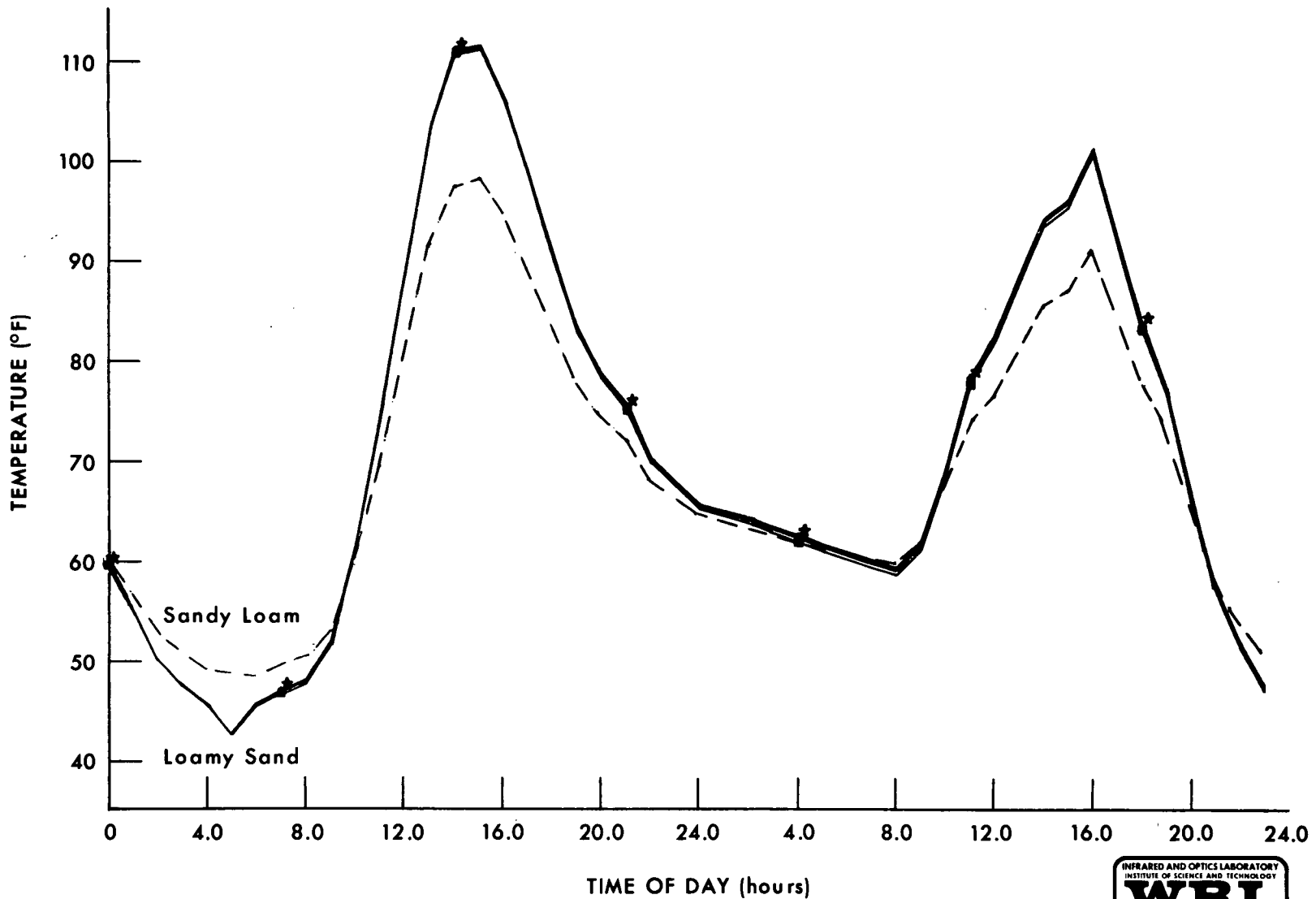


DISCRIMINATION OF ACIDIC SILICATES NEAR MILL CREEK, OKLAHOMA  
(Sand Quarry)

Figure 8

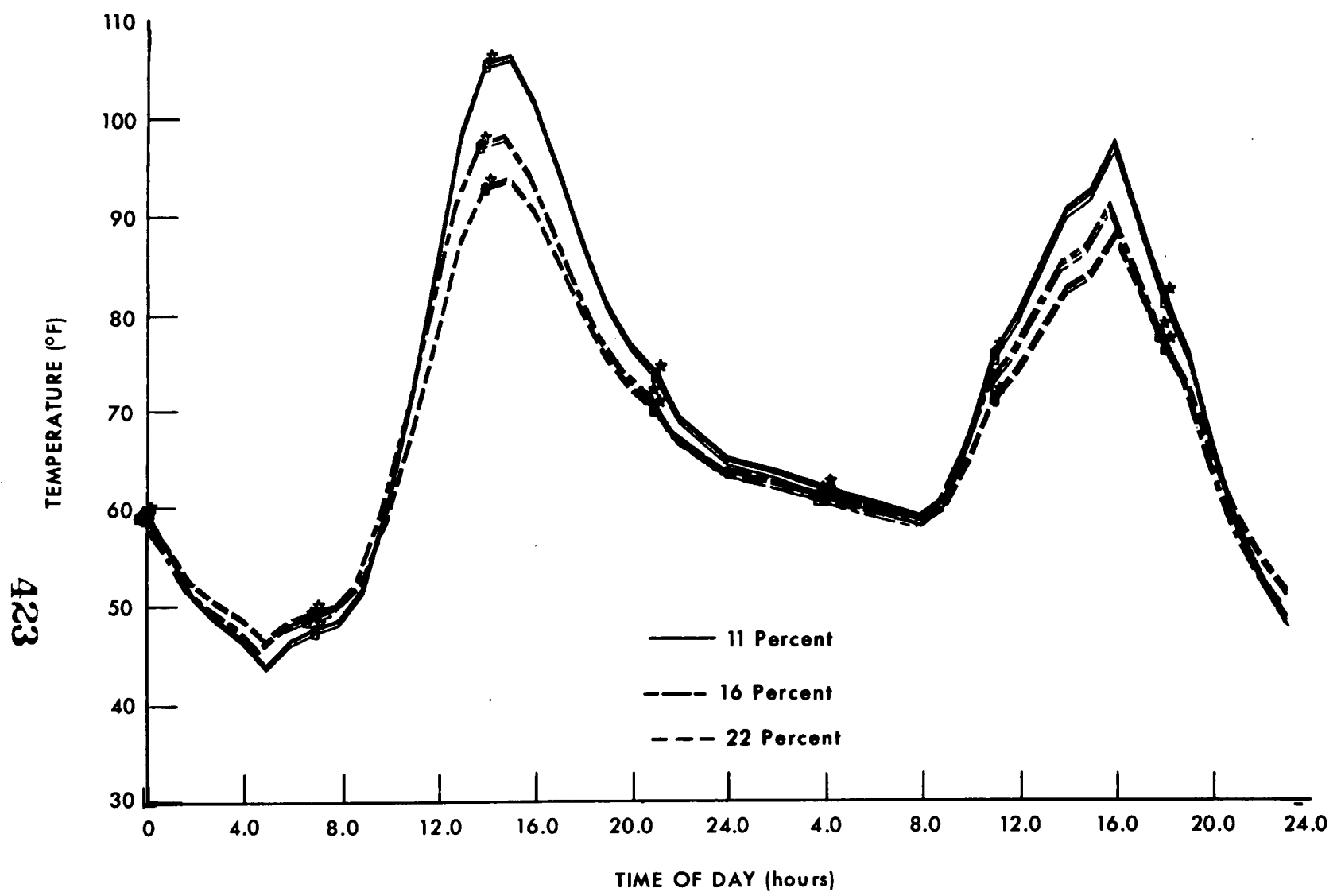


422



SURFACE TEMPERATURE FOR 16 PERCENT SURFACE MOISTURE FOR 2 SOIL TYPES  
Columbia Basin Area

Figure 9



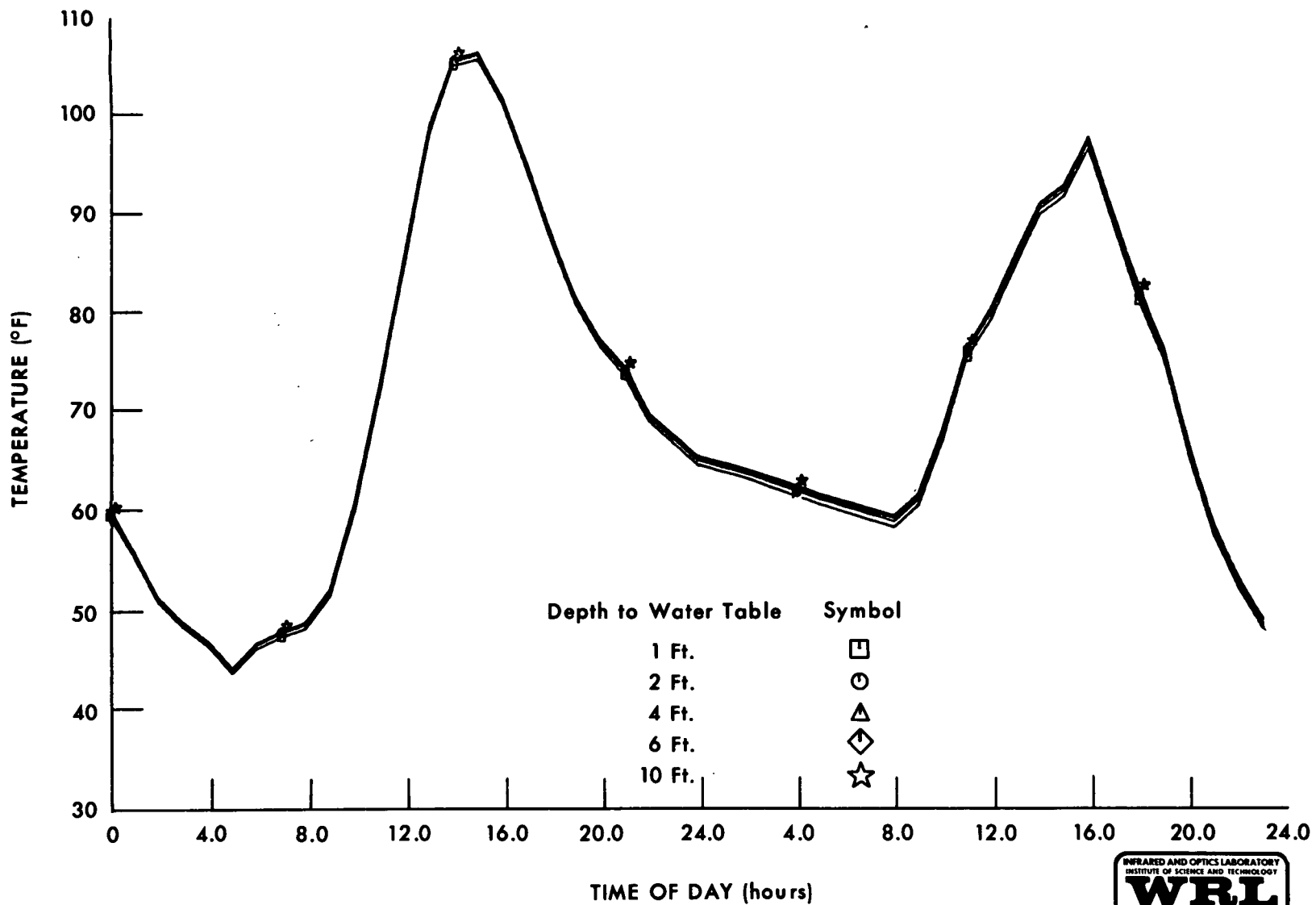
**SURFACE TEMPERATURE FOR SANDY LOAM AT 3 DIFFERENT  
SURFACE MOISTURE PERCENTAGES**  
Columbia Basin Area



Figure 10



424



**SURFACE TEMPERATURE FOR SANDY LOAM AT 11 PERCENT SURFACE MOISTURE  
Columbia Basin Area**

Figure 11

425

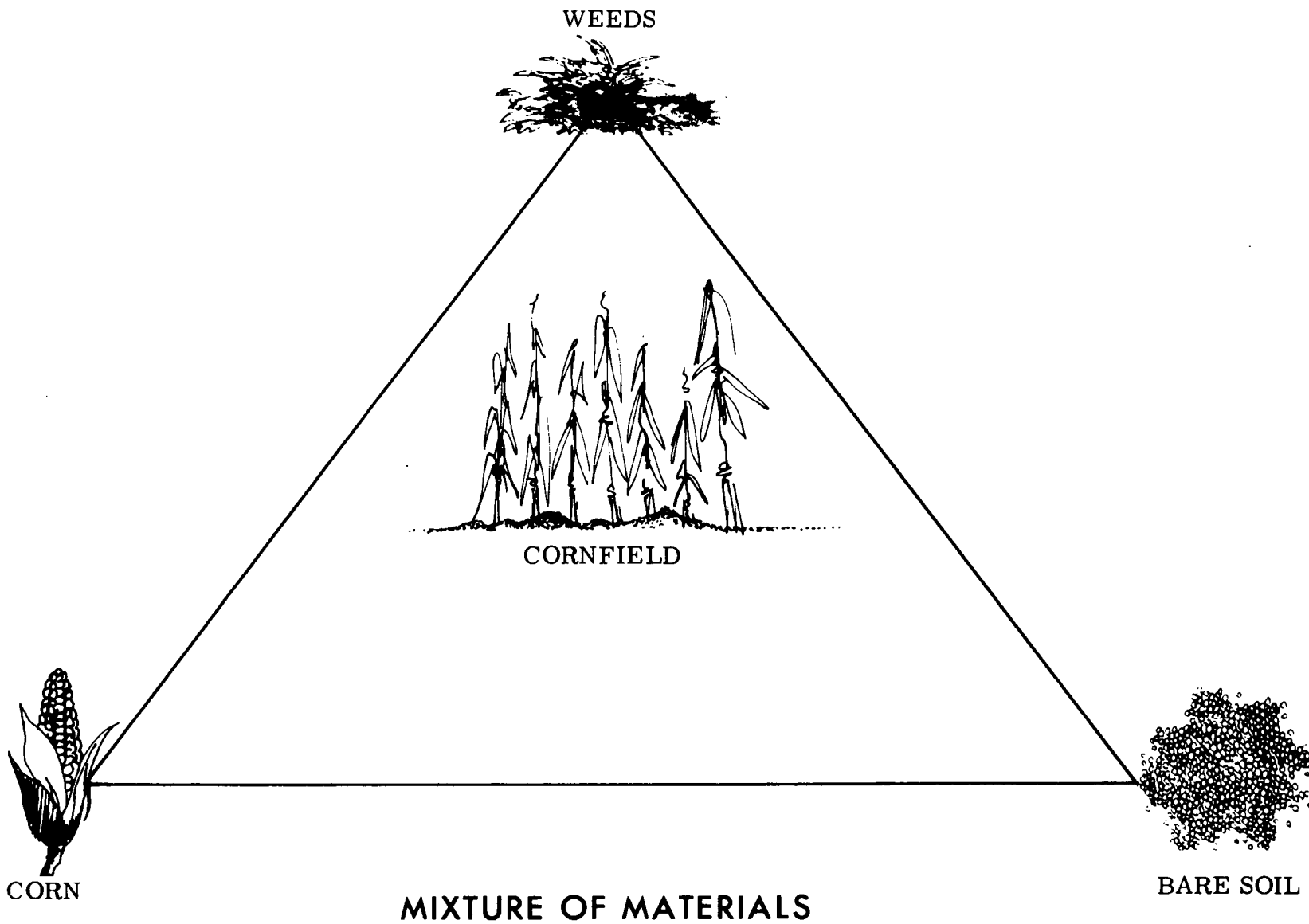
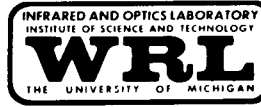
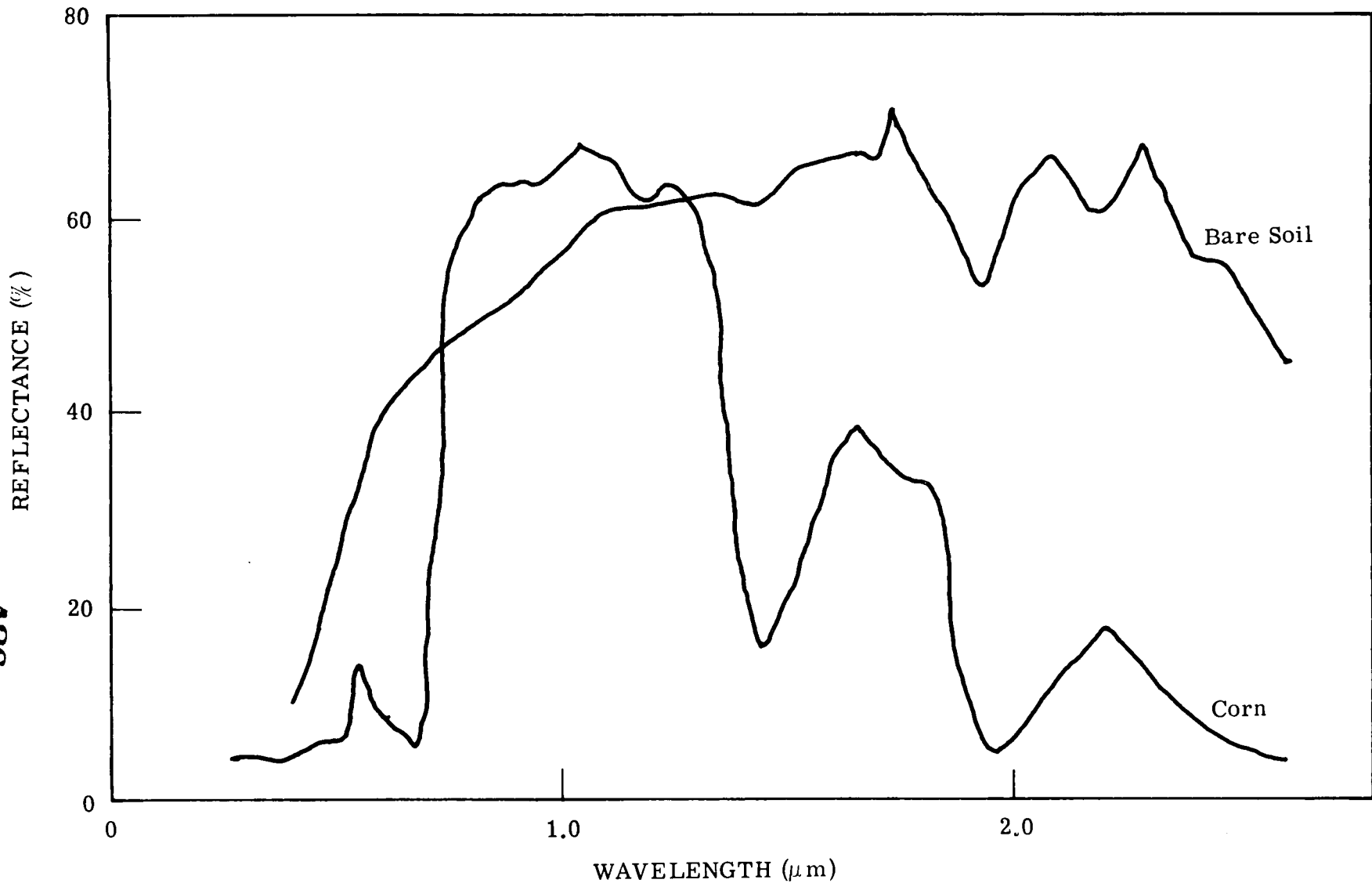


Figure 12



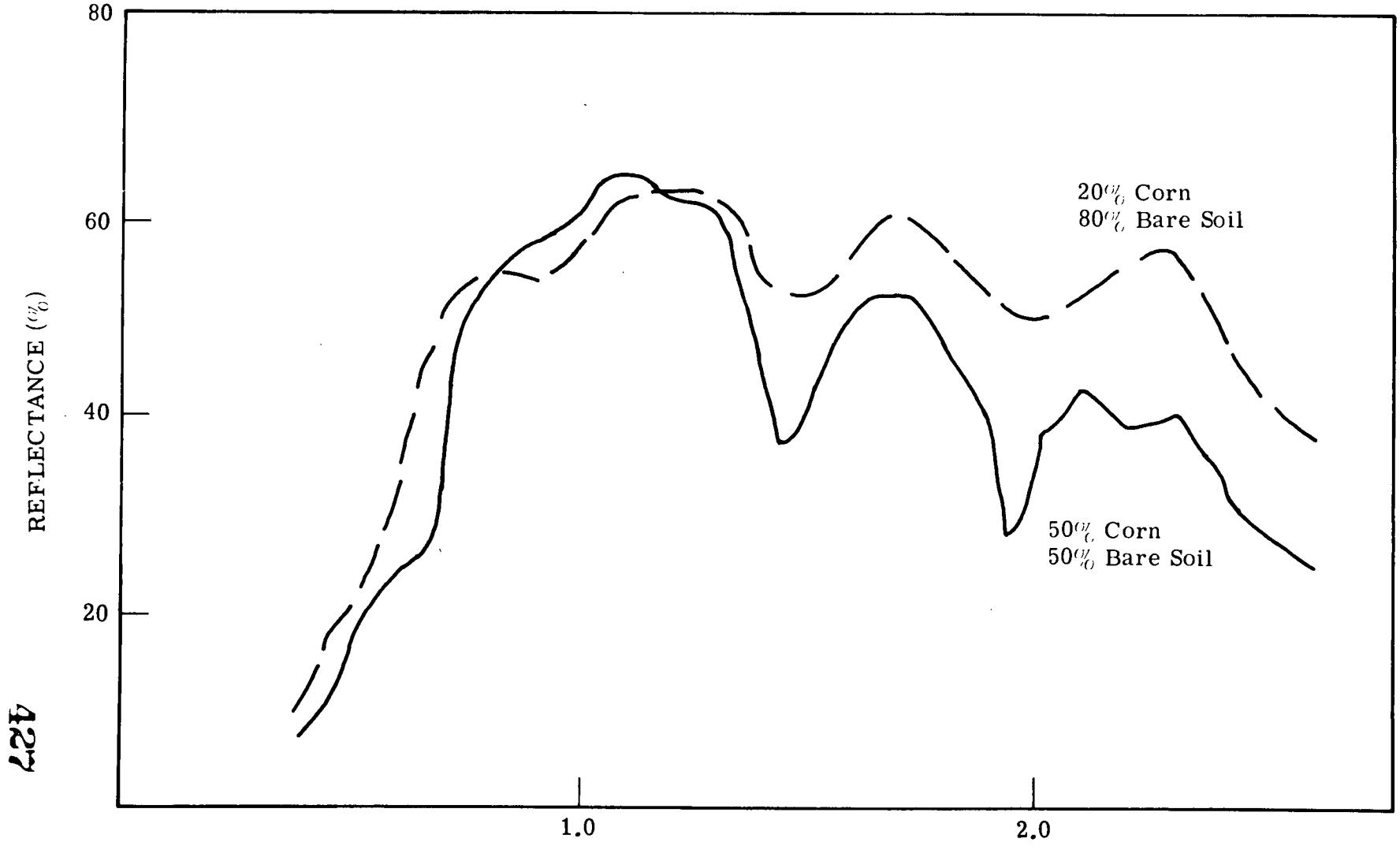
426



### REFLECTANCE SPECTRA

Figure 13

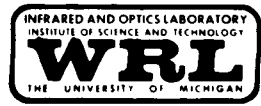




424

REFLECTANCE SPECTRA OF MIXTURES

Figure 14



CALCULATED ESTIMATES OF  
VEGETATIONAL COMPONENTS OF EXPERIMENTAL PLOTS

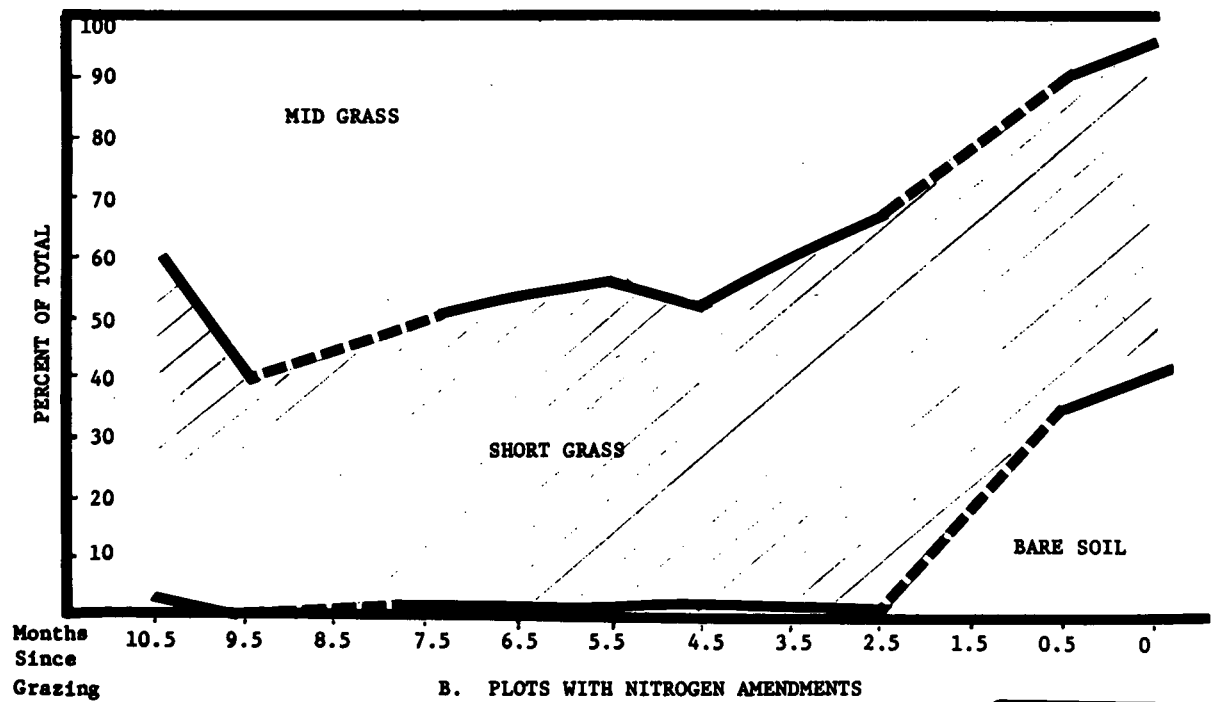
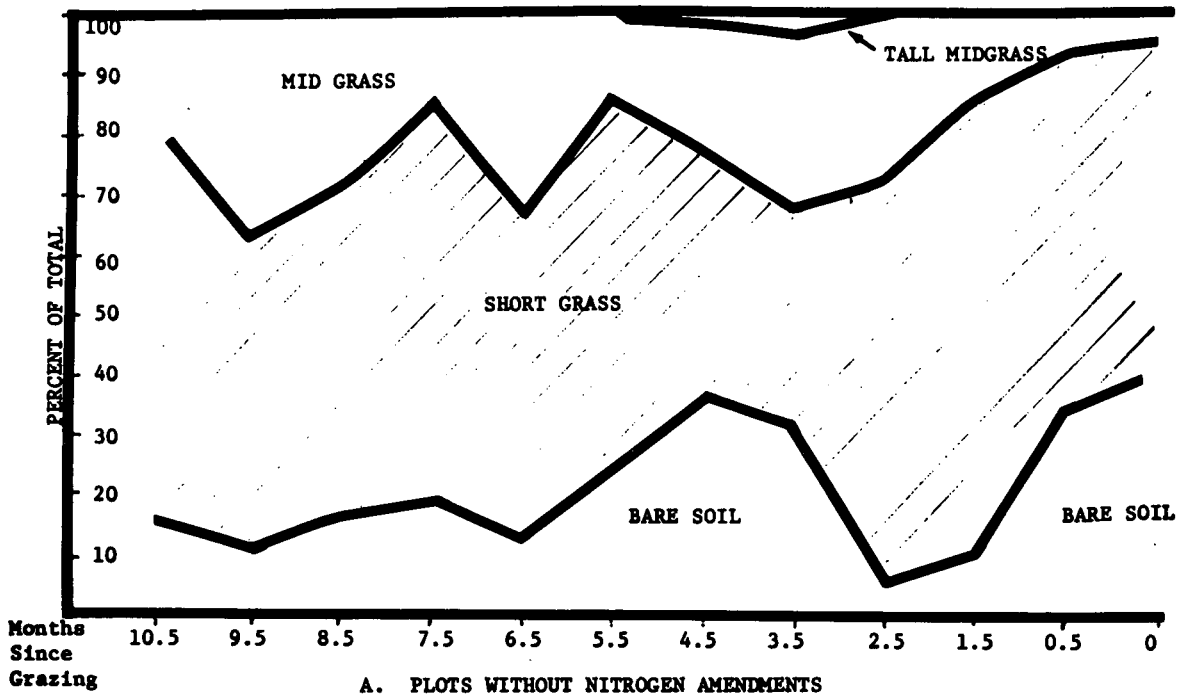
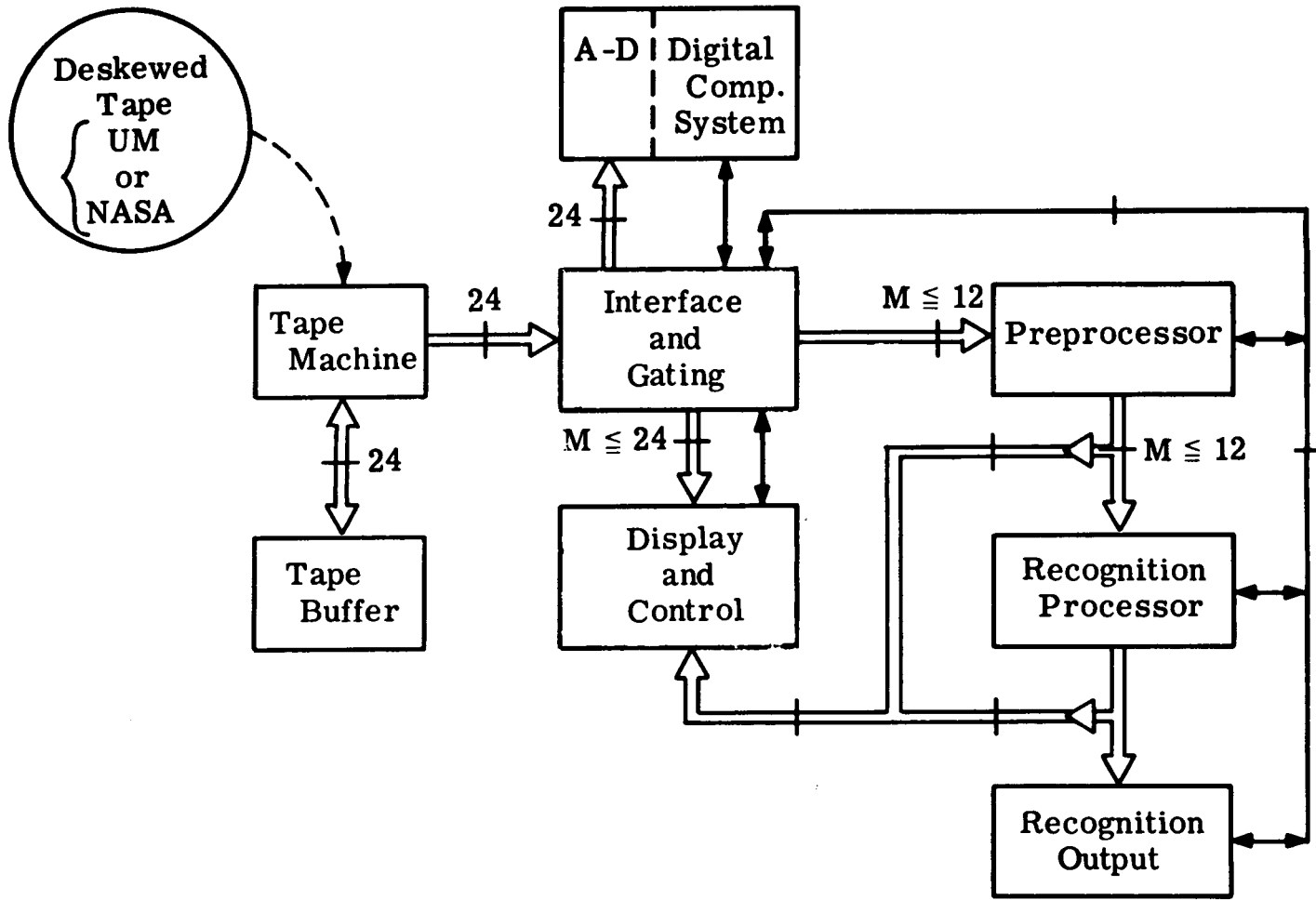

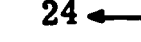



Figure 15

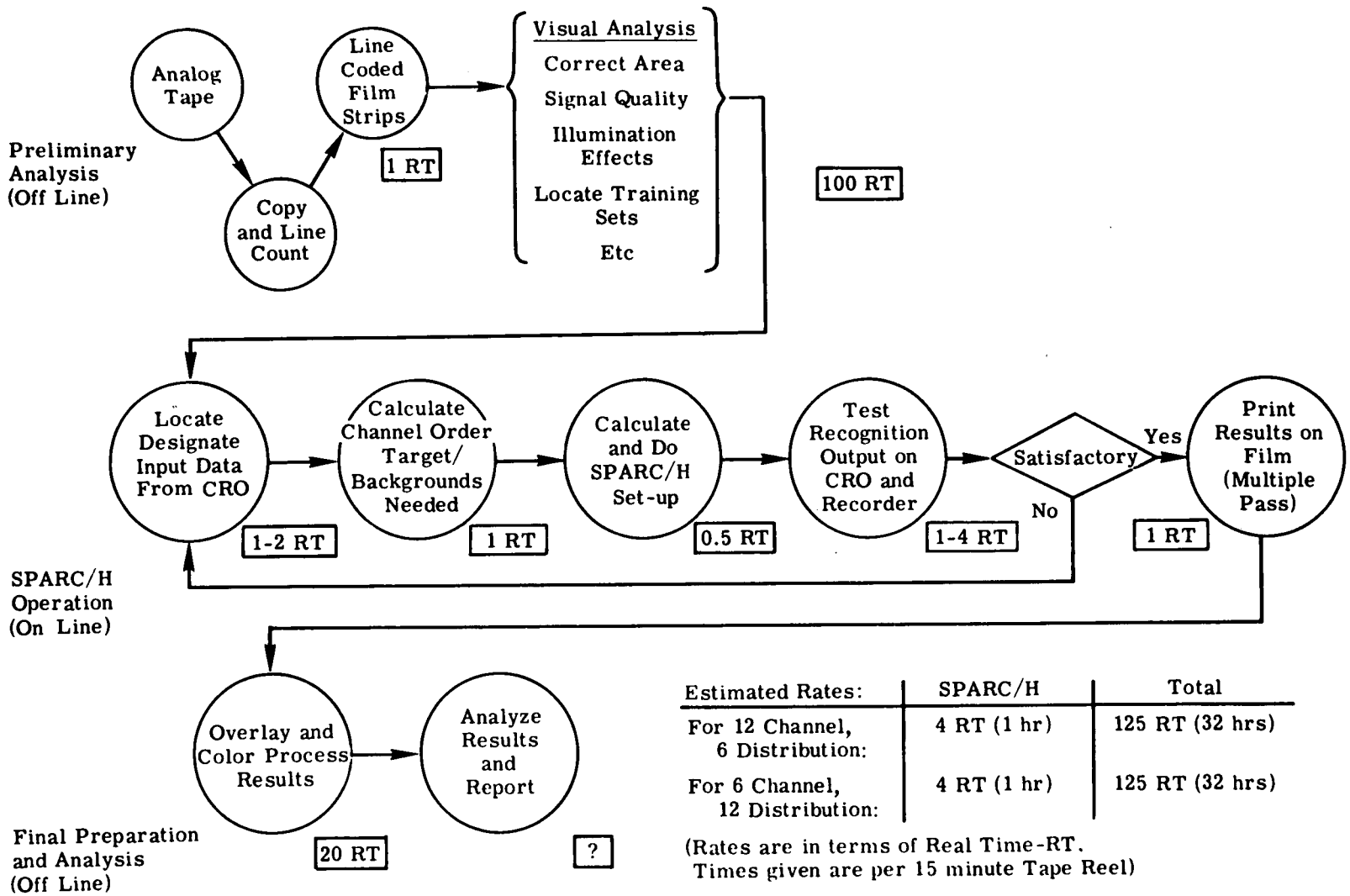




 Signal Flow  
 24 ← Number of Channels, M  
 → Control Lines, Multiple

429

# SPECTRAL ADAPTIVE RECOGNITION COMPUTER/HYBRID (SPARC/H)



## SPARC/H PROCESSING FLOW AND TIMING CHART

Figure 17

USER ORIENTED DATA PROCESSING  
AT THE UNIVERSITY OF MICHIGAN

by

Frederick J. Thomson  
Willow Run Laboratories  
The University of Michigan  
Ann Arbor, Michigan

INTRODUCTION

Half of the effort at The University of Michigan is directed towards data processing for various user application. This work has proven valuable in a number of directions. First, it has given us an opportunity to exploit the techniques of multispectral data processing that have been developed at Michigan on a wide variety of problems. Secondly, and perhaps more important, we have learned a great deal about types of problems that users encounter in interpreting multispectral data, and the knowledge gained in collaborating with the users has been a prime importance in directing the type of multispectral research in which we engage. The range of user applications have been large and in this past year we have dealt with 11 different users on quite dissimilar problems. In this paper I will not be able to cover in detail all of these investigations but I will discuss some that illustrate the general kinds of work that we have done at Michigan in the past year and the directions that user data processing of multispectral data are taking today. The remaining investigations are of equal interest and have been presented by various users at this meeting.

I would like to cover four scientific aspects of user data processing first: Signature extension and preprocessing, change detection, area measurement and geometric fidelity, and underwater feature recognition. To conclude I would like to summarize the kinds of processing services which we have developed at The University of Michigan and present a brief summary of the quantity of processing done during this past year.

SIGNATURE EXTENSION AND PREPROCESSING

Signature extension is a term which refers to the extension of the utility of a signature derived from a single training set to classify areas of the scene far removed from the training set. Because of the assumption in most processing that the spectral radiance signature of an object is



unique, changes in solar irradiance and other effects limit the scene area which can be processed with a given set of signatures. Signature extension is important to processing studies because frequently training is the only practical alternative to signature extension, the training phase of processing is time consuming, and the amount of data that can be processed with a given set of signatures is now becoming of limited value to investigators interested in broad area surveys.

One method of implementing signature extension is preprocessing. There are three basic preprocessing techniques which can be used - taking ratios of channels, dividing by or subtracting functions of scan angle, or the use of ancillary data such as the sun sensor. This is summarized in Figure 1. Various ratio preprocessing transforms which have been applied to data are shown in Figure 2. There are three basic types of ratio preprocessing transforms, the division of signals by the sum of all signals, the division of signals by adjacent signals, or dividing differences of signals by sums signals. Each of these ratio preprocessing techniques are able to correct for changes in irradiance and some are more effective than others when additive variations in path radiance are also present. In a paper by Dr. Smedes presented at this meeting, he discussed the application of ratio preprocessing transforms to a set of data collected in Yellowstone National Park in September 1967. The Yellowstone data were collected while flying in a canyon, so variations of solar irradiance occurred across the scan line. These variations prevented the signature from being extended even across the scan line, let alone along the flight line. Previous attempts to process this data ended in success only after as many as 12 training sets were used for each of 8 classes of material to be recognized to account for variation of irradiance with scan angle. The division by a function of scan angle preprocessing technique was also used for the Yellowstone data and its application is summarized in Figure 3. Figure 3 shows plots of the mean values and standard deviations of three materials as a function of scan angle for the Yellowstone data. Note that the mean value of each signature varies considerably across the scan line. Had we used only one signature from the left hand edge of the data, forest would have been misclassified as glacial till on the right hand edge of the data. By determining a function of scan angle which made the mean values of each category invariant with scan angle, and by dividing all data by this function, we arrived at the preprocessed data shown in Figure 4. In Figure 4, the preprocessed signatures are invariant with scan angle, thus suggesting that recognition using these signatures could be extended across the scan line. Preprocessing was carried out and reported by Dr. Smedes. The performance of the ratio preprocessing and the scan angle preprocessing were determined from analysis of recognition maps and found to be quite good. Most importantly, we used only 8 signatures to obtain each of these recognition maps, whereas previous work had used over 100 signatures to obtain maps of comparable quality. Digital processing time was cut by a factor of 12 through the use of only 1/12 as many signatures.

The third preprocessing technique, use of ancillary data, can be quite useful in compensating for variations of solar irradiance in long duration flights. An excellent example of the application of this technique will be discussed later in the North Dakota data processing discussion.

The digital recognition maps for the study performed by Dr. Smedes were printed in color. This was done by using different colored ribbons in our IBM 1401 page printer and running the paper through four times - once for each color. The maps are impressive because of the use of red, green, and blue in addition to black for portraying scene objects. This communicates effectively to the interpreter. They are also superior to previously hand colored versions because they can be produced by the computer rather than by human effort. An example of a color recognition map of Yellowstone data is shown in Figure 5. A legend also accompanies the figure.

#### AREA COUNTS AND CHANGE DETECTION

Both area counts and change detection are important to multispectral processing because they attempt to extract more useable information from the recognition process. For many applications, the percentage composition of the scene or area of a particular material maybe as important or more important to a user than the recognition map itself. For example in estimating the water resources of Everglades National Park, the first step might be to make a recognition map of aquatic plant species. By measuring the area of these plant species and knowing what range of water depth they grow in, an estimate of water volume can be made.

Similarly, change detection is important for many problems. By making recognition maps from data collected at two different times and comparing the maps, changes can be detected. Area counts help quantify the changes. Both change detection and area counts play important roles in the decision making process using remote sensing data as an input.

Both concepts are well illustrated by an extremely successful study performed for the Bureau of Sport Fisheries and Wildlife in Jamestown, North Dakota. The general problem is to estimate the migratory waterfowl productivity of the Great Plains area (including Canada) so that meaningful management procedures can be used. One of the ways of managing the migratory waterfowl population is through the setting of hunting limits and season. Hunting limits are set through consultation with United States and Canadian authorities in June or July of each year.

Estimates of waterfowl productivity are currently made by noting size, shape and number of ponds in sampling areas. This year, we used remote sensing techniques to obtain this estimate for one test area. We feel that our technique yielded more accurate data, at least as fast as the

previous airborne observer techniques. For this study, we used two samples of data. Data in May was used to assess water quantity important to nesting. Data in July determine those ponds productive of food. Areas of ponds and their perimeters are important measurements which allow the estimation of waterfowl. Areas are important because of the obvious relation to water quantity. Perimeter is important because nesting waterfowl require privacy. A pond of large perimeter will thus support more waterfowl than one of small perimeter, even if the pond areas are the same.

We automatically mapped ponds, their areas and their perimeters on May and July data sets collected at 4500 ft. 1.5 to 1.8 micron data were processed digitally. To obtain adequate pond recognition over the 120 mile flight line, preprocessing of the data was required. In this case, we divided all signals by the value of the sun sensor which measured ambient irradiance. This technique produced useable recognition of ponds with only one training set for the entire 120 mile run. The analysis showed that had preprocessing not been done, frequent training would have been necessary which would have slowed down the recognition process. Statistics and recognition maps were generated automatically by the computer and were in the hands of the managers within a month after the data were collected. Thus, they were well in time to influence this year's management effort.

Figure 6 and 7 show recognition maps of the same area made in May and July respectively. The two slides reveal that numerous small ponds present in May have dried up in July, and thus are not productive of food. To obtain a quantitative measure of water reduction, refer to Figures 8 and 9. These figures show areas, perimeters, and shape factors which are ratios of perimeters to square root of area normalized to one for a circle, are shown for each pond for May and July. This information was generated by the digital computer for each one mile segment of the 120 mile test area. At the end of each mile of data, a set of area and perimeter statistics were also automatically generated by the computer.

#### GEOMETRIC FIDELITY

There is a great potential for map generation using multispectral scanner data and automatic pattern recognition techniques. However, one important limitation is that scanner data is distorted. The scale is neither constant with the scan angle nor rectilinear. If the true potential of scanner data as a map source is to be realized, distortions must be reduced to acceptable levels. Fortunately, because the scanner data are recorded on tape, we have control over the production of pictorial output and can make some corrections electronically. Distortions in scanner data arise from two sources - scanning geometry and the variation in aircraft speed, heading, altitude and attitude. Scanning geometry distortions arise because the scanner covers the ground at a constant angular rate,

while in film reproduction the intensity modulated CRT beam is swept at a constant linear rate across the film. This combination yields an image which is compressed at the edges. Instead of a linear sweep on the CRT, we need a wave form proportional to the position of the instantaneous field of view on the ground. This waveform is  $\tan \theta$  where  $\theta$  is scan angle relative to the nadir. We generate such a waveform and use it to deflect the CRT spot thus removing scanner geometry distortion. At present, very little can be done about aircraft heading and speed variations during a run although potential corrections could be made if these parameters were known. Aircraft pitch, roll, and yaw are other quantities which can distort the scanner imagery. Corrections for roll are made on board the aircraft. Yaw corrections are also necessary to produce quality maps. A need for yaw corrections arise when aircraft is "crabbed" to maintain a given flight heading while flying in a cross-wind. Under such conditions, the scanner does not scan perpendicular to the flight direction and square corners are distorted as shown in the top photo of Figure 10. The solution is to rotate the CRT trace with respect to the film so that the geometry corresponds to the flight line-scan line geometry under which the data were collected. An example of this yaw correction is shown in the bottom half of Figure 10. Note that the square road intersections of the town at the top of the figure are distorted in the uncorrected video and correctly portrayed in the yaw corrected video. While it is not obvious from the video itself, both sets of data have had scan geometry distortions removed through the use of the  $\tan \theta$  sweep waveform and thus possess constant scale regardless of position in scene.

#### UNDERWATER FEATURE RECOGNITION

One of the major advances in the application of pattern recognition techniques to user data processing was the recognition of features on the bottom of Biscayne Bay. In this study, data collected at 6500 ft on 10 March 1970 over Biscayne Bay were processed to map classes of underwater vegetation likely to be affected by a thermal outfall from a power plant. This work has already been reported by Dr. Kolipinski of U.S. Geological Survey, Miami. What makes this study significant is that not only 6500 ft of air, but 10 to 15 ft of water lay between the objects being mapped and the aircraft. Apparently successful recognition of 8 categories were achieved, but only after the reflected energy from the water surface was removed by preprocessing. The reflected energy from the scene consists of reflection from underwater vegetation and from the water surface. The water surface reflection varied with scan angle as a result of the relative position of the sun and aircraft. This variation was removed by subtracting a function of scan angle determined by digital computer analysis. The optimum spectrometer channels for classifying the underwater vegetation were also determined from digital computer analysis. These channels were located in the blue, blue-green and orange regions of the spectrum, where the water is most

transparent. Near infrared channels useful for classifying terrestrial vegetation were useless for this study because the water is opaque at near infrared wavelengths. More work is required to make the recognition insensitive to water depths, or equivalently to extend vegetation signatures from shallow to deep water. This problem was averted in the present study by taking test areas in areas of uniform water depth.

#### QUANTITATIVE ASPECTS OF THE USER DATA PROCESSING PROGRAM

At the University of Michigan we have developed several techniques for analyzing multispectral data. We have classed these as Type I and Type II techniques, and these are summarized in Figures 11 and 12. Type I techniques are generally simple processing techniques applied to single channels of the multispectral data. The Type II processing techniques are more sophisticated processing techniques and are related to applications of pattern recognition to the data. Figures 13 and 14 illustrate the quantity of work completed during fiscal year 1970.

A list of users and applications is shown below:

<u>User</u>	<u>Organization</u>	<u>Application</u>
Orlo Crosby	USGS, Bismarck, North Dakota	Survey of Water Temperatures in Missouri River
A. E. Coker	USGS, Tampa, Florida	Survey of Phosphate Pollution in Tampa, Florida area
Milton Kolipinski	USGS, Miami, Florida	Survey of Underwater Vegeta- tion Features in Biscayne Bay
Kenneth Watson	USGS, Denver, Colorado	Reflectance Measurements and Classification of Rock Types
Herbert Hamm	Bureau of Recla- mation, Denver, Colorado	Survey of Saline Affected Areas in Irrigation Project in Moses Lake, Washington
William Percy	Oregon State U.	Studies of Ocean Temperature and Color Indicative of Nutrients and Fish.
Harry Smedes	USGS, Denver, Colorado	Classification of Glacial Terrain in Yellowstone National Park
Harvey Nelson	Bureau of Sport Fisheries & Wildlife Jamestown, N.D.	Survey of Wetlands for Water- fowl Production

Philip Weber	US Forest Service, Berkeley, Calif.	Recognition of Ponderosa Pine Beetle Attacked Trees in the Black Hills and Diseased Douglas Fir Trees in Oregon
Charles Olson	University of Mich. Ann Arbor, Mich.	Classification of Different Forest Species and Delineation of Root Rot Disease in Pine.
Robert Colwell	US Forest Service, Berkeley, Calif.	Classification of Forest and Brush Species at Bucks Lake, California

### CONCLUSION

The multispectral techniques have shown themselves capable of solving problems in a large number of user areas. The results obtained are in some instances quite impressive. As we review the picture today, we can make the following observations. In many instances, the multispectral detection of various phenomena is an empirical fact for which we have no or very little physical explanation today. It is fairly clear that in many instances with just a little more work, we should be able to put the detection process on a firmer intellectual foundation than we are able to do right now. To date, most of the user applications that have been addressed are exploratory in nature. The closest approximation to an operational situation that we have encountered so far is that of the Survey of Wetlands in North Dakota reported in this paper. It is very clear that a major step is the development of operational procedures for exploiting the multispectral techniques. The best starting point for this operational exploitation is in those areas where we have, of course, some experimental verification of the technique.

The signature extension techniques that have been developed have shown themselves to be useful in many instances. We should like to be able to report that the problem of signature extension is no longer with us, but we cannot. Progress has been made but it certainly is not complete. Future efforts should then consider unexplored areas mentioned above. First, we should begin to address very seriously using multispectral remotely sensed data for operational purposes and secondly, the problem of signature extension still remains with us, and while progress has been made, we must continue to work on this problem.

1. Channel Ratio Techniques
2. Divide by or Subtract a Function of Scan Angle
3. Use Ancillary Data (i.e. Sun Sensor)

Figure 1. Preprocessing Transforms

$$1. \frac{X_1}{\sum_{j=1}^{12} X_j}, \frac{X_2}{\sum_{j=1}^{12} X_j}, \dots, \frac{X_{11}}{\sum_{j=1}^{12} X_j}$$

$$2. \frac{X_2}{X_1}, \frac{X_3}{X_2}, \dots, \frac{X_{12}}{X_{11}}$$

$$3. \frac{X_2 - X_1}{X_2 + X_1}, \frac{X_3 - X_2}{X_3 + X_2}, \dots, \frac{X_{12} - X_{11}}{X_{12} + X_{11}}$$

Figure 2. Ratio Preprocessing Transforms

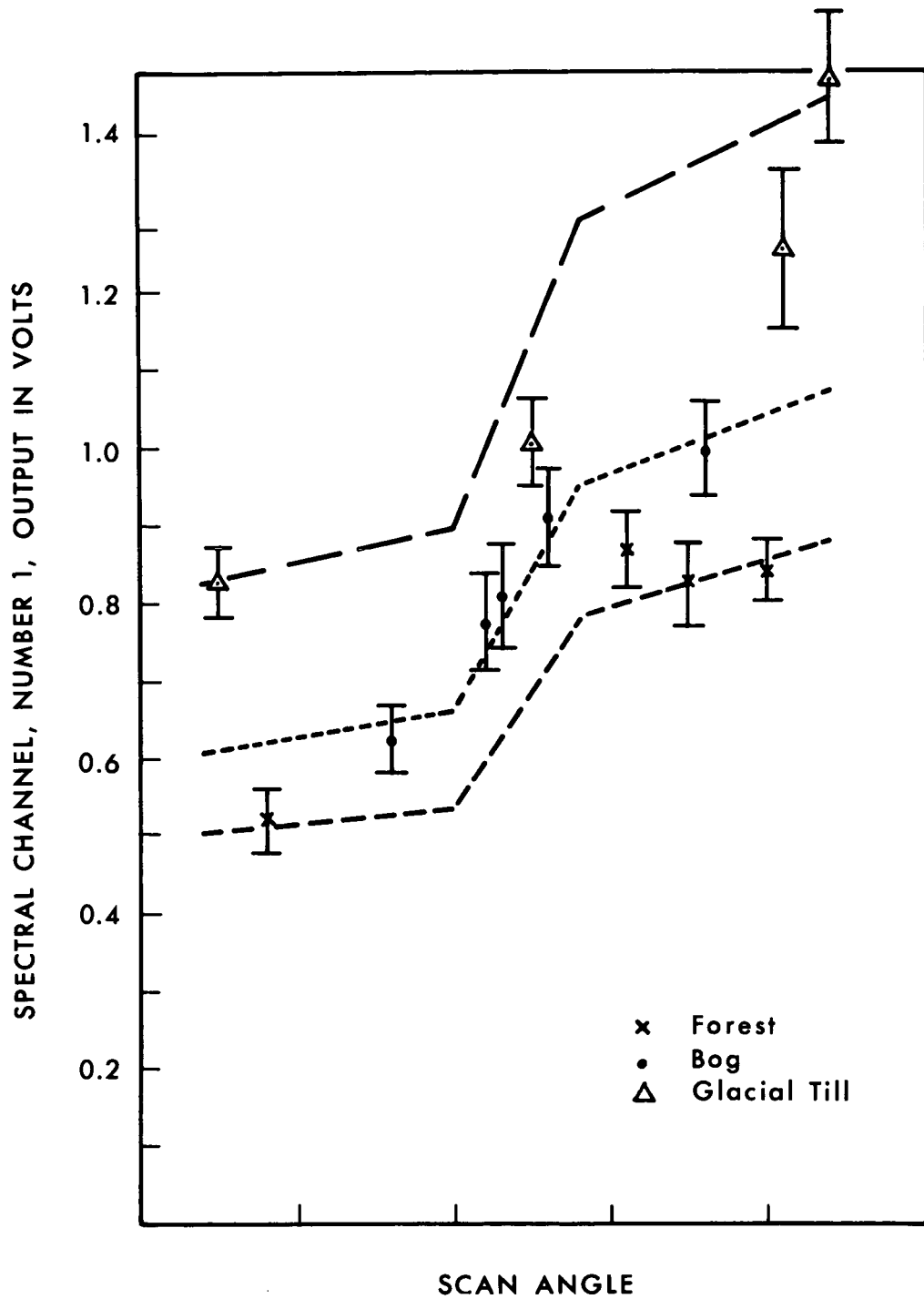


FIGURE 3. SPECTRAL CHANNEL OUTPUT VERSUS SCAN ANGLE FOR 3 MATERIALS SHOWING THE SCAN ANGLE FUNCTIONS



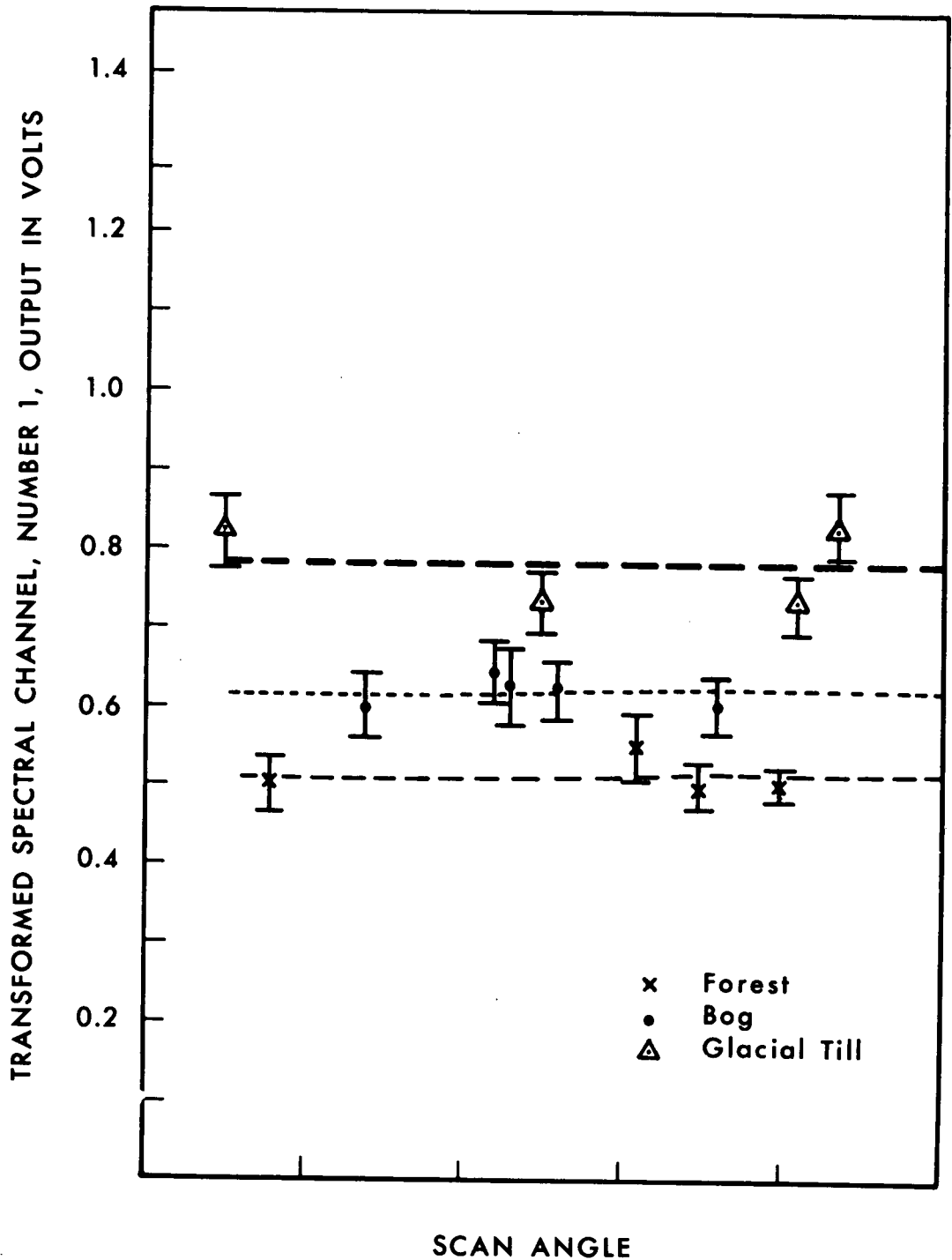
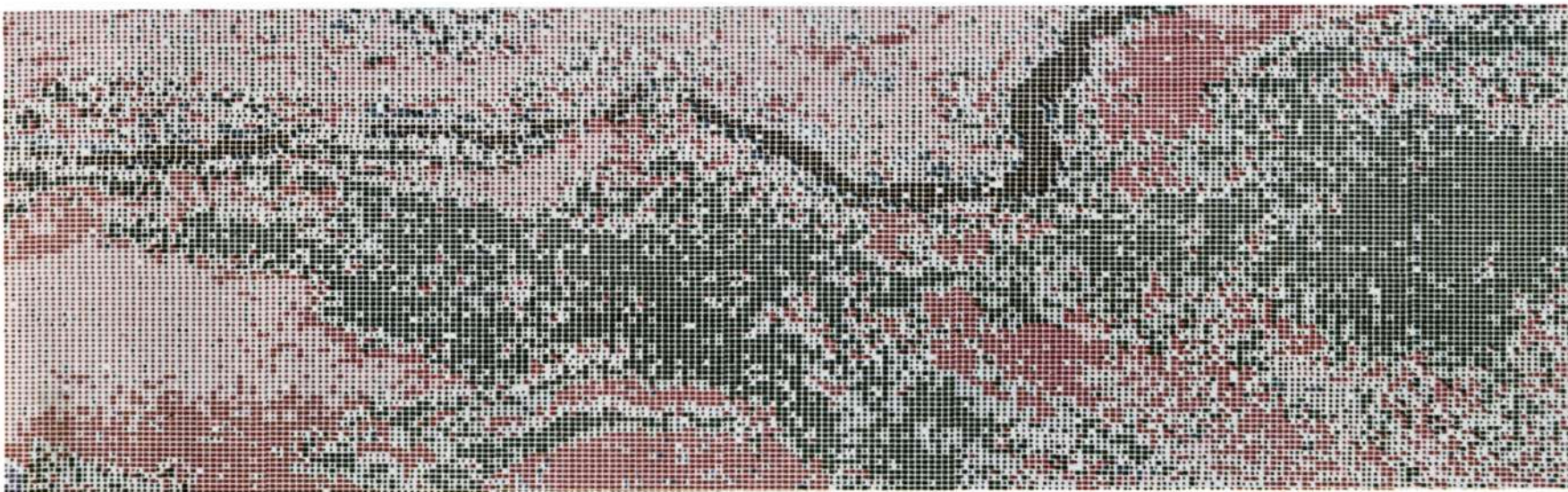


FIGURE 4. TRANSFORMED SPECTRAL CHANNEL OUTPUT VERSUS SCAN ANGLE FOR 3 MATERIALS SHOWING MEANS OF COMBINED SIGNATURES



COLOR CODE

Dark Blue.....Bedrock	Black.....Water
Light Blue.....Vegetated Rock Rubble	Medium Grey....Talus
Dark Green.....Forest	Light Grey.....Cloud
Light Green.....Bogs	Light Red.....Kame
White.....Not Classified	Dark Red.....Till

Figure 5. Color Coded Digital Recognition Map of a Portion of Yellowstone National Park Data Collected 9/19/67 at 1430 hrs.

442



FIGURE 6. TYPICAL DIGITAL COMPUTER GRAYMAP OF PONDS. WOODWORTH STUDY AREA, NORTH DAKOTA. Location over Clark Lake and Big Lake. 31 JULY 1970, 1013 hrs., Flight Line 1, 2 KFT., 1.5 - 1.8  $\mu$ m Data.





**FIGURE 7. TYPICAL DIGITAL COMPUTER GRAYMAP OF PONDS. WOODWORTH STUDY AREA, NORTH DAKOTA. Location over Clark Lake and Big Lake. 22 MAY 1970, 1105 hrs., Flight Line 1, 2 KFT., 1.5 - 1.8  $\mu$ m Data.**



443

# TYPICAL DIGITAL COMPUTER PRINTOUT OF POND STATISTICS. WOODWORTH STUDY AREA, NORTH DAKOTA.

ALTITUDE = 2100.FT VELOCITY = 207.FT/SEC SCAN RATE = 65.5 RPS  
RESOLUTION = 5.35 MRAD ONE SCANLINE IN 2. DIGITIZED NADIR AT  
POINT NO. 189 POINTS COUNTED IF VOLTAGE LIES BETWEEN 0 AND  
1.20 VOLTS NB = 0 NE = 1 SMTH = 5.62 FEET

SCAN LINE	POINT	AREA (ACRES)	PERIMETER (FEET)	SHAPE
18414	150	.119	306.734	1.063
18461	162	.279	418.794	.950
18475	192	.052	259.766	1.362
18487	231	.116	272.230	.959
18515	150	.328	456.598	.956
18563	190	.121	340.322	1.174
18565	172	.481	603.448	1.043
18569	226	1.528	1493.685	1.447
18620	130	.050	169.165	.904
18721	162	3.418	2254.672	1.461
18733	179	.067	239.502	1.107
18768	172	.072	271.878	1.213
18774	135	.502	584.780	.988
18815	248	10.515	6193.072	2.288
18872	135	.569	620.947	.986
18875	170	.730	932.161	1.307
18914	198	.360	494.842	.988
18929	130	.757	805.891	1.109
18998	239	.496	629.921	1.071

Computer Statistics from May 1970 Data



Figure 8

**TYPICAL DIGITAL COMPUTER PRINTOUT OF POND STATISTICS.  
WOODWORTH STUDY AREA, NORTH DAKOTA.**

ALTITUDE = 2015.FT VELOCITY = 204.FT/SEC SCAN RATE = 65.6 RPS  
RESOLUTION = 5.15 MRAD ONE SCANLINE IN 2. DIGITIZED NADIR AT  
POINT NO. 136 POINTS COUNTED IF VOLTAGE LIES BETWEEN 0 AND  
2.00 VOLTS NB = 1 NE = 1 SMTH = 53.84 FEET

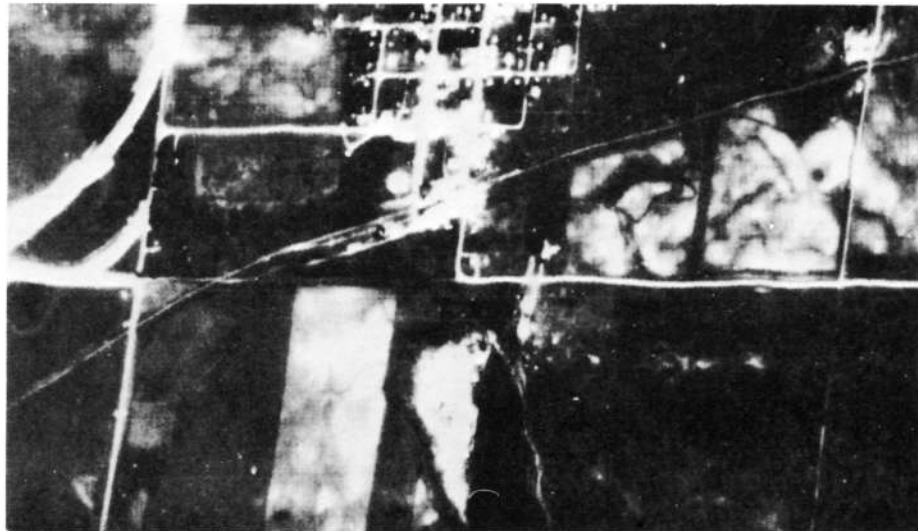
SCAN LINE	POINT	AREA (ACRES)	PERIMETER (FEET)	SHAPE
16256	203	.108	258.012	.941
16338	161	.055	237.148	1.215
16343	144	.269	443.305	1.024
16454	140	1.226	1055.163	1.142
16554	221	10.295	6011.876	2.241
16655	103	.356	557.124	1.118
16705	103	.510	604.893	1.015
16881	61	.210	403.672	1.053
17020	127	41.618	9186.915	1.706

Computer Statistics from July 1970 Data

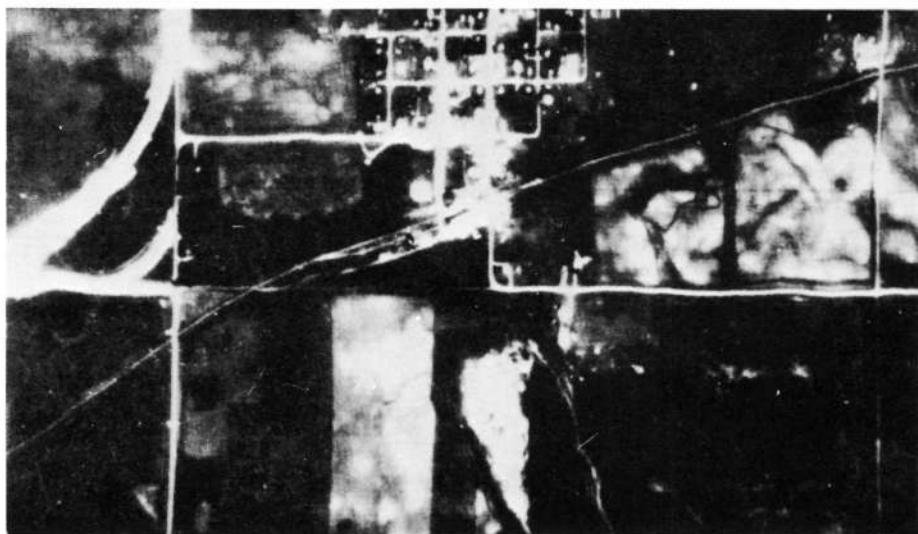
Figure 9



445

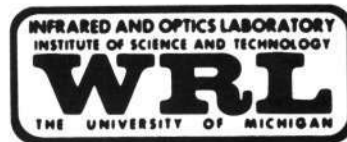


(a) Video with Yawed Geometry



(b) Video with Yaw Corrected Geometry

### COMPARISON OF TYPICAL YAWED AND YAW CORRECTED DATA



Imagery  
Contouring and Quantization  
False Color Films  
Digital Tape  
Canvas Panel Reflectance Measurements

Figure 11. TYPE I Processing Services

Optimum Channel Analysis  
Preprocessing Analysis  
Digital Recognition Map  
SPARC Recognition Map  
Signature Extraction

Figure 12. TYPE II Processing Services



Imagery ——— 2500 mi. Data  
Thermal Contouring and Quantization ——— 10 jobs  
Digital Tapes ——— 1 job  
Canvas Panel Reflectance Measurements ———2 jobs

Figure 13. TYPE I Work Completed - FY70

Optimum Channel Analysis——— 11 jobs  
Preprocessing Analysis ——— 6 jobs  
Digital Recognition Map ——— 8 jobs  
SPARC Recognition Map ——— 11 jobs  
Signature Extraction ——— 2 jobs

Figure 14. TYPE II Work Completed - FY70

THE APPLICATION OF AUTOMATIC RECOGNITION  
TECHNIQUES IN THE APOLLO IX SO-65 EXPERIMENT

by

R. B. MacDonald  
Laboratory for Applications of Remote Sensing  
Purdue University  
West Lafayette, Indiana

INTRODUCTION

Photographic materials can be viewed as a chemical detector of electromagnetic energy over certain wavelength regions. While film emulsions are notoriously difficult to control and calibrate, they do offer a means of measuring the spectral variations of reflected energy from a scene in addition to providing measurements of the spatial distribution of these energies. Either multiple emulsion films such as conventional color and color infrared or multiple camera and multiple lens camera systems employing different film filter combinations can be utilized to record energies in many multispectral bands over a spectral interval from approximately .4 to 1.0 micrometers.

A four-camera 70mm sensor system was carried by NASA Apollo IX. Researchers at Purdue University's Laboratory for Applications of Remote Sensing selected a simultaneously exposed four-frame set of photographic frames collected by Apollo IX of the Imperial Valley, California region. The primary objective of the analysis of these data was to study problems in analyzing multiband satellite photography of Earth's surface features using digital machine processing techniques. Specific objectives included the development of techniques for getting quantitative spectral measures from such photographic sensing materials and for data handling, storage and retrieval required to handle the four to five million numbers per band contained in each frame. The analysis described required various steps which fall into three major phases:

- data preprocessing
- training class and signature analysis
- automatic classification and result evaluation

The application objectives for this research were to determine which surface features could be identified with "ERTS-like" measurements collected with these photographic materials. Three categories of surface features in the southern California region were studied. These were crops, soils, and geological features. The spectral identifiability of

surface features is, in this case, dependent on the uniqueness of a spectral response of the various features in the three wavelength bands available from the photographs.

### DATA PREPROCESSING

The Apollo IX SO-65 experiment utilized four 70mm Hasselblad cameras having 80mm focal length lenses mounted together to view the same area. Film filter combinations were selected to obtain exposed frames in the green, visible red and reflective infrared portions of the spectrum. Three of the cameras contained black and white film and used filters to discriminate between the spectral bands. A fourth camera contained color infrared film which had dyes sensitive to approximately the same bands as the three black and white cameras. Thus, the experiment gathered image data in three bands by two methods. The approximate band sensed and the film data are listed in Table I.

Densitometric measurements were made over each frame with a 25 micron aperture at sampling intervals of 25 microns. This 25 micron area corresponded to a resolution element on the ground at nadir of 200 feet by 200 feet. The film density was measured using a linear scale, digitized, and recorded on magnetic tape for computer processing. The three multispectral black and white films were scanned using white light. The color infrared film was scanned sequentially using blue, green, and red filters and no filter in the white light path. In this fashion, seven representations of the frames were obtained on tape and consisted of a total of over 35 million density readings. A computer gray-scale printout of the white light scan of the color infrared frame is presented in Figure 1.

In order to analyze these data using multispectral pattern recognition programs, each of the raster scans must be registered in such a manner that each scene point is in geometric coincidence in all the scans. This image registration problem has been studied at LARS and a software system has been developed to register or "overlay" multiple images of the same scene. Following these procedures, the seven scans were brought into registration and a film data storage tape was compiled for subsequent analysis.

### TRAINING SAMPLE SELECTION

Several methods are in use at LARS for studying imagery to determine separable classes in given data. The statistical multispectral pattern analysis of LARSYSAA developed at LARS supplies several methods of class

selection. The system can compute the multidimensional first and second order statistics for up to 30 wavelength bands. These statistics are printed out in the form of histograms, correlation matrices, and coincident 3 sigma spectral plots. Any of these forms can be used to compute the pairwise separability between all classes. The analyzer can also be used to select the preferred set of wavelength bands to be used for classifications based on this divergence criteria. A third method of class separation utilizes clustering techniques to group image points around cluster centers in the multidimensional space such that the overall variance of the resulting sets is minimized. Visual histogram analysis and clustering were used to determine separable classes in the SO-65 imagery.

### AUTOMATIC CLASSIFICATION AND ANALYSIS

A synoptic feature analysis was made on a global scale over the entire 10,000 square mile area initially to develop a computer derived map of the following features: clouds, cloud shadow, water, rock, bare soil, sand, green vegetation and salt cliffs. Training data was obtained for the classes by visual inspection of the gray-scale pictorial print-outs and large prints of the film transparencies. Clustering was used to find subclasses of the global classes. Also, geological maps of the area were helpful in choosing training "fields" for rock and alluvial deposits. One can appreciate the accuracy of this analysis by inspecting the synoptic feature map shown in Figure 2. Every 6th point was processed and classified in this effort. At this resolution the only water discernible was in a portion of the Salton Sea. Also note that large deposits of salt were discernible on this synoptic map.

Next, SO-65 Test Site 15-A, commonly referred to as the Dogwood Area in the Imperial Valley, California region was classified into categories of vegetation, bare soil and water. The results of this classification are shown in Figure 3. Note the large 1/2 x 1 mile body of water correctly classified in the upper central portion of the figure. A quantitative assessment of the accuracy of this classification is shown in Table II.

The SO-65 Imperial Valley experiment included sufficient ground truth to permit LARS investigators to make a "greater detail" analysis of two selected areas. These were areas 15A, the Dogwood area and 15D, the McCabe Road area. Certain crop types such as carrots, lettuce and onions have very large percentages of soil background which were present in very small amounts and deleted for the study. The major cover types in the agriculture test site are barley, alfalfa, sugar beets, bare soil and salt flats. Water is present in very small quantities, but is easily distinguished and was included in the study.

Samples of data from each of the classes defined were selected and used for training the pattern classifier. The number of training samples used for each class is selected on the basis of previous experience performing similar classifications on other agricultural data. Test site 15A was represented by 66,600 data points and the training samples selected totaled 1132, or 1.7% of the total. The data run for Test Site 15B contained 27,300 points and 788 training samples for 2.8% of the total taken for this area. The statistics processor of the pattern classification system was used to compute the training statistics for each of the classes selected. These statistics consist of the means and covariance matrices to be used by the Gaussian maximum likelihood classifier.

Two methods of statistical pattern recognition were used to classify these points. One method classified each image point into one of the defined classes. The other classified an entire data field with one decision. A great advantage of the "per field classification scheme" is speed. A disadvantage is that the field coordinate must be determined and fed to the classifier before any classification can be performed. At least this is true unless an automatic boundary-finding algorithm can be derived. Such an algorithm has not yet been perfected. The per point classifier can classify any data without field boundaries being specified, but it is a time consuming process since every resolution element and image is classified individually. A color coded computer printout of the analysis results of the Dogwood Area is shown in Figure 4. The areas included in the small computer designated rectangles are the areas used for either training or test purposes. These particular printouts are the results of the per point classification of the Dogwood area. Inspection of the Dogwood Road results reveals that the accuracy for certain classes is relatively insensitive to the channels used. Bare soil and barley show relatively constant accuracy for all cases where two or more channels are used. The accuracy for sugar beets recognition was good for all four channels and the alfalfa performance was poor for all cases. Salt flats and water were recognized with high accuracy for all cases. An interesting result was the high accuracy achieved for some of the classifications using only one or two channels. The highest accuracy for barley, 82.1%, was achieved using only one channel. The peak for bare soil was near 100% using the green channel, the infrared channel and the visible red channel. Equal maximums for several channels were seen for alfalfa.

A color coded computer printout of the analysis of Test Site 15D, the McCabe Road area, is shown in Figure 5. It is interesting to note that in nearly all cases the per field classifier performed better than the per point classifier.

It was generally concluded on the basis of both classification results that general cover types are readily recognizable by three-band

multispectral photographic sensor and pattern classification system. More specific breakdowns of crop types are more difficult and in some cases impossible. These results were obtained, however, with uncalibrated photography having considerable overlap of the spectral bands, and probably containing other distortions in the spectral data. Improved photographic fidelity with more and better separated spectral bands could result in significantly better accuracies.

Soil scientists at LARS were interested in attempting to identify surface soils with these data. Soil type identification was pursued in an area near El Centro in the Imperial Valley. A 50-year-old soils map of the area is shown in Figure 6. The soils in this area are generally young, the surface soils and subsoils are very much alike. The material which forms the soil consists primarily of sediments deposited by the Colorado River, and local alluvium from the California coastal range of the Chocolate Mountains. There are 26 soils mapping units, most of these are named for major soil series that occur within each unit. The 26 mapping units are grouped into five major groups based on soil characteristics and qualities. These are:

- areas dominated by fine texture, very young soil
- areas dominated by medium and coarse texture, very young soils
- areas dominated by coarse and very coarse, very young soils
- areas dominated by young soils with line segregation in the subsoil
- areas dominated by miscellaneous land types

The following four soils types were distinguishable with the film data available:

- dune sand and sand dune designated by the letter D
- mellow land fine sandy loam designated ML
- Rositas fine sand designated Rf
- Holtville silty clay designated Hc
- Holtville silty clay loam designated Hs

A computer map of the El Centro region is shown in Figure 7. The areas of different soils are designated by the arrows.

Geologists at LARS are currently conducting investigations with these data to determine how well machine processing techniques work with multiband spectral data in producing geological maps.

In the area east of the Imperial Valley, clustering techniques were used to identify nine different geological materials:

- pre-Cambrian
- metasedimentary rocks
- granitic rocks
- tertiary volcanic rocks
- pleistocene volcanic rocks
- nondifferentiable slope material; this is unconsolidated slope material within each rock type as well as some older alluvium in the form of terraces and fans, all of which cannot be distinguished from each other

- alluvium; this is unconsolidated clay, silt, sand and gravel occurring primarily as valley fill and stream wash
- sand; windblown sand from nearby sand dunes
- river

Figure 8 shows a conventional geologic map of the area west of the Imperial Valley. A computer derived geological map is shown in Figure 9. Arrow 1 points out a clearly delineated contact between pre-Cambrian and tertiary rock. (Pre-Cambrian--color coded green, tertiary volcanic rocks--orange.) Arrow 2 indicates a contact between metasedimentary rocks (purple) and tertiary volcanic rock (orange). Since contacts are often places of weakness, they erode faster producing a valley along the contact. The printout indicates a valley (alluvium--gold and yellow) at the approximate location of contact. This could be used in distinguishing the contact itself. Arrow 3 points to where the printout indicates mostly slope material and alluvium with only a few classifications of actual rock. These classifications of rock, however, line up quite well with the ridge of mountain tops indicated on geologic maps. Here is where the actual rock outcrops occur. Arrow 4 indicates a sharp contact with metasediments and tertiary volcanics caused by salt. The printout shows sharp boundaries of tertiary volcanic. Arrow 5 indicates a very good classification between two volcanics. Both are mainly salt. The older is of the tertiary age (orange) and the younger is of pleistocene age (red). It should be noted that while these results indicate that the geologic features of the range are separable, they do not indicate that a specific rock type can be identified in any frame. Recognition of a specific rock type could be complicated by variability of service conditions, atmospheric conditions and other factors. The results of the study are generally encouraging. Good separability of many surface features were achieved and it is expected that large scale automatic surface features surveys can be performed using multiband photography.

#### ACKNOWLEDGEMENTS

The film data studied was scanned and digitized by Optronics International of Chelmsford, Massachusetts and by Fairchild Space and Defense Systems of Syosset, New York at no expense to Purdue University or NASA. Optronics scanned the black and white photographs and Fairchild performed color separation of the color infrared films as well as scanning the black and white photos. The cooperation of these industrial firms is greatly appreciated. The multiband Apollo IX photos of the SO-65 test site ground truth were obtained by NASA, Earth Resources Division, Manned Spacecraft Center, Houston, Texas. The U. S. Department of Agriculture supplied initial soils information and crops information for the study.

<u>Code</u>	<u>Film</u>	<u>Filter</u>	<u>Band</u>
A	SO-180 Ektachrome Infrared	Photar 15	.51-.89 micrometers
B	3400 Panatomic-X	Photar 58B	.47-.61 micrometers
C	SO-246 B/W Infrared	Photar 89B	.68-.89 micrometers
D	3400 Panatomic-X	Photar 25A	.59-.715

Table I. Film filter combinations used in SO-65 experiment



## Classification Summary by Test Classes

<u>Class</u>	<u>No. of Samples</u>	<u>Percent Correct</u>	<u>No. of Samples Classified Into</u>		
			<u>Vegetation</u>	<u>Bare Soil</u>	<u>Water</u>
Vegetation	544	96.3	524	20	0
Bare Soil	192	91.7	16	176	0
Water	72	100.0	0	0	72

Overall performance = 95.9%

Table II. Preliminary Classification Results



1 2 3 4 5 6 7 8 9 10 11 12 13 14 15 16 17 18 19 20 21 22 23 24 25 26 27 28 29 30 31 32 33 34 35 36 37 38 39 40 41 42 43 44 45 46 47 48 49 50 51 52 53 54 55 56 57 58 59 60 61 62 63 64 65 66 67 68 69 70 71 72 73 74 75 76 77 78 79 80 81 82 83 84 85 86 87 88 89 90 91 92 93 94 95 96 97 98 99 100

Figure 1

# Apollo 9 Computer Map of Imperial Valley Region



Clouds		Cloud Shadow	
Basalt		Vegetation	
Alluvium		Sand Dunes	

Figure 2

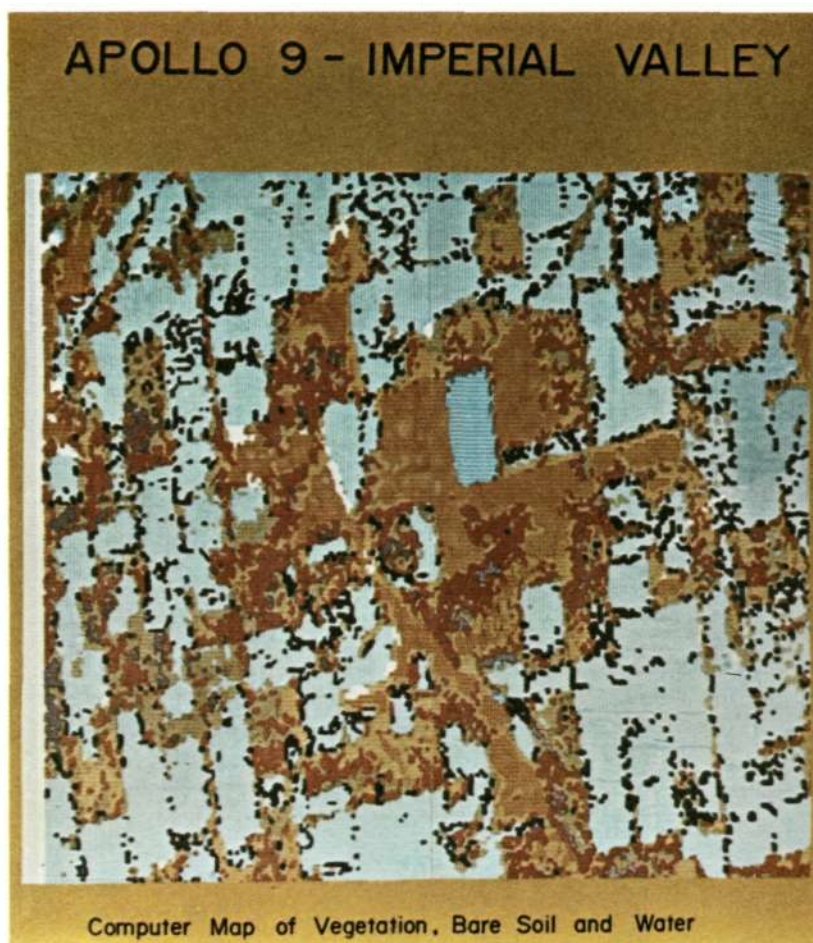


Figure 3

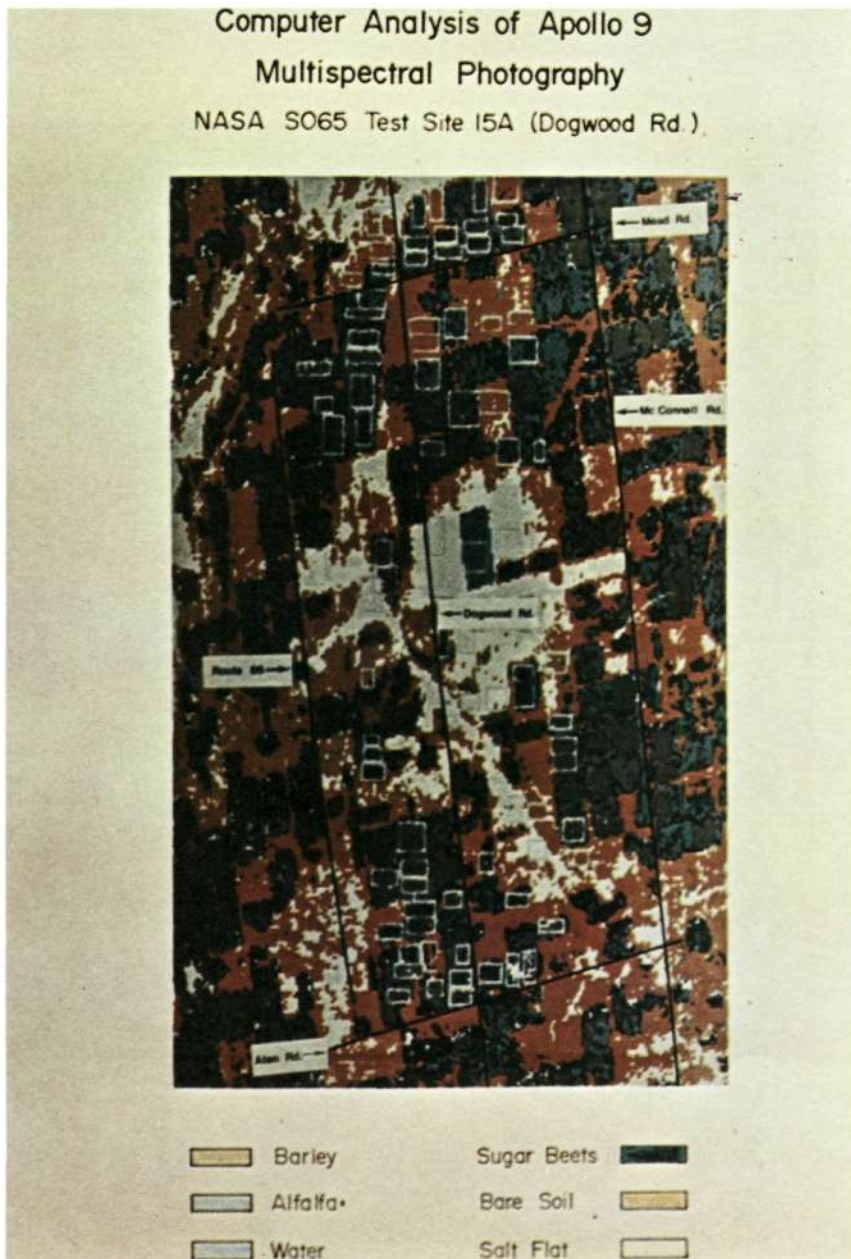


Figure 4



Figure 5

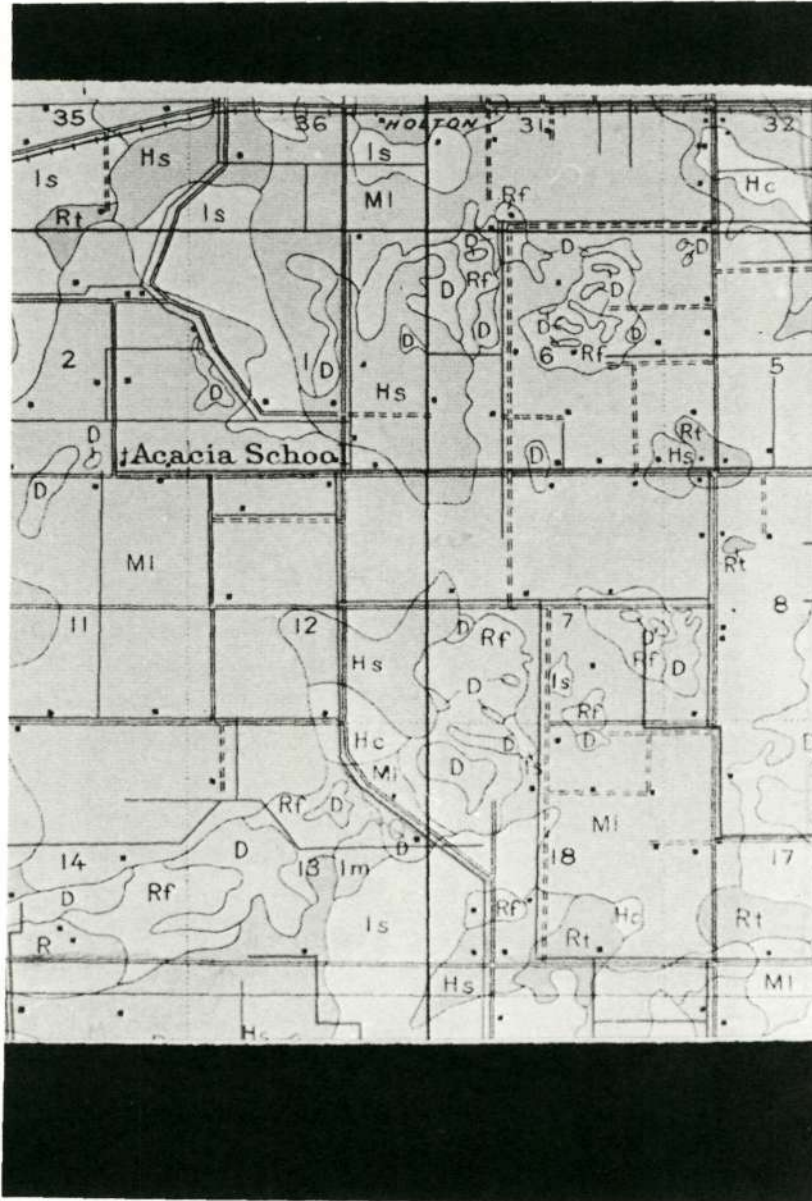


Figure 6



Figure 7



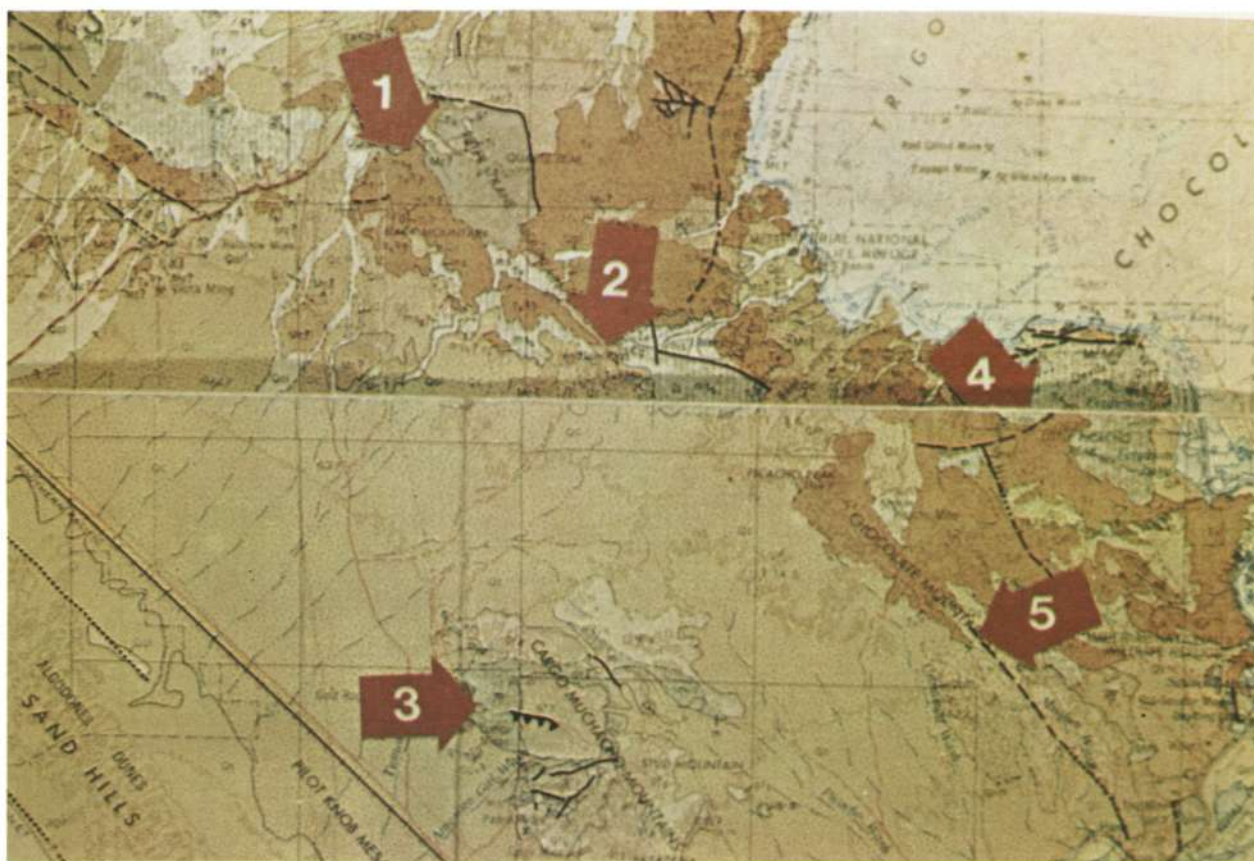


Figure 8



Figure 9

THE DEVELOPMENT OF MACHINE TECHNOLOGY PROCESSING FOR  
EARTH RESOURCE SURVEY

by

D. A. Landgrebe  
Laboratory for Applications of Remote Sensing  
Purdue University  
West Lafayette, Indiana

INTRODUCTION

Two earlier papers by R. B. MacDonald have described some of the research being pursued at LARS/Purdue directed toward the applications of remote sensing. The purpose of this presentation is to describe research in the development of new technology. Several projects to be discussed are of several years duration; current progress will be described in these cases. In addition, several new programs have begun and preliminary results will be presented.

THE REGISTRATION OF MULTISPECTRAL AND MULTITEMPORAL IMAGES

The first study to be described has to do with the registration of multispectral images. This work began several years ago and has passed through graded steps of increasing technological difficulty. The ultimate objective is to develop a capability for accurately aligning data in image form gathered from different parts of the spectrum and on different flight missions.

This first step in this process several years ago was to achieve the capability to register image data from two different sensors mounted aboard the same platform. Figure 1 serves to illustrate the problem. Shown is a printout from a channel of data in the visible portion of the spectrum (center) and data gathered at the same time but with a different scanner operating in the thermal region. A conventional panchromatic air photo is shown on the left for comparison. Registration accuracy to better than plus or minus 1 resolution element is desired.

Since the two scanners may be running at slightly different speeds, and creating other distortions of a local nature, a scheme which assures correct registration on both a global and local basis is necessary. The general approach chosen was to use two-dimensional correlation as a basis for finding points of correspondence in the two images. This approach provides the maximum flexibility which is required by a research situation as compared to an operational one. However, it quickly became apparent that images from widely separated parts of the spectrum may not correlate well since the spectral separation leads to fundamental differences in the data. It was found desirable to precede the correlation process by enhancing all the boundaries in both images and then correlating to the boundary-enhanced image.

Thus, the first useful system contained three steps: a boundary enhancement step; a two-dimensional correlation to determine the points of coincidence in the two images; and finally, the overlaying of the two data sets to form a new data set of dimensionality equal to the sum of the previous two.

The next step in the development of the system was to provide it with a measure of adaptability to the type of data being registered. The registration process utilizing two-dimensional correlation as a basis is clearly very scene-dependent. A different sized correlation window is required when registering data over an agricultural scene, for example, as compared to data from natural vegetation. Figure 2 shows the organization of the system after incorporating this capability. A means for estimating the complexity of the image in terms of the degree of difficulty in obtaining a proper two-dimensional correlation measure has been added to the system. This results in a picture complexity index from which the correlation window size is determined. Developments to this point were reported in this meeting a year ago (see reference 1).

Since that time, a number of additional capabilities have been added to the system. Chief among these has been the development of a capability for accomplishing rotation and scale change in the imagery. The current system diagram is shown in Figure 3 (see reference 2). The system now is organized to permit the overlay of two "slave" images onto a master. There is an opportunity to input scale and rotational corrections of a global nature manually into the system. After suitable buffering, the image boundary enhancement and complexity estimation step is next. Then follows the image correlation step in which the points of correspondence between the three images are determined. At this point the more precise local scale and rotational correction factors are determined and a capability for updating the global scale and rotation factors is provided. The final step is that of utilizing the scene correspondence points to achieve a single data tape on which have been properly registered the three previous images.

Two different methods of boundary enhancement techniques are available. Figure 4 shows examples of each. The simplest and computationally fastest means is a gradient technique utilizing the magnitude of the first difference of adjacent scene points to determine if a boundary exists. The result of such a computation is shown in the center of Figure 4. On the right is shown the result of using a clustering technique operating in a multivariant fashion to determine boundaries (see reference 3).

### The use of Temporal Information

The new capability which the modifications have provided enabled initial studies in the use of multi-temporal multi-spectral data analysis. Figure 5 shows printouts of single channels of the two data sets utilized. On the left is a printout of a channel of data from the June, 1969 mission. Due to a cross wind, an average yaw distortion of 11.7 degrees exists in the data. The August, 1969 data shown on the right contains very little yaw distortion. It is readily apparent from these two printouts that changes in the scene have taken place between June and August, and this provides a graphic example of the considerable scene dependence which exists in attempting to use two dimensional correlation directly for registration of images. Note in the June data that since the vegetation canopy does not fully cover the ground soil patterns are readily apparent in this display; by August this is no longer the case.

In the multi-temporal analysis experiment, a control classification was run utilizing the June data only. A classifier was trained using classes corn, soybeans, wheat and oats. The best four of the 12 channels of data were selected for this classification. Data from the August mission was registered onto the June data. The classification using the same classes, training, and spectral bands of this August data was then run for comparison. Next, the best four of the 8 channels (4 from June, the same 4 from August) were selected and the same classification was again carried out. The results of this experiment are shown in Figure 6. Note that the capability to discriminate between corn and soybeans does improve over that available from either of the data sets alone. It should also be noted that by the August mission all wheat and oats in the flightline had been harvested; these classes therefore did not exist by the time of that mission.

This classification test, while preliminary in nature, does tend to verify the expected increase in accuracy one should obtain by having multi-temporal data available. It seems reasonable to speculate that even greater accuracy should be possible if one permits oneself to select the best four of the total number of channels available (24 in this case) rather than constraining to the spectral bands which were favored for the June data set. The above procedure was used, however, in order to simu-

late the situation which might exist for a satellite sensor system in which the spectral bands to be used throughout must be selected a priori.

#### On the Value of Image Data Registration

There are at least four major reasons why image data registration is important. These are indicated in Figure 7. The desirability of registration in the case of multiple sensors has already been discussed. This was discussed within the context of visible and thermal data; however, the problem is similar in the case of data from the microwave portion of the spectrum. In general, each new part of the spectrum available in registered form should provide additional information about the contents of the scene.

The above example tended to illustrate the importance of the use of temporal information. However, not nearly enough experimentation has been possible to date in order to develop the full importance of this area.

A third reason for the importance of image data registration is that it permits the automatic correction of various types of distortion in image data. If a good quality image (from a photogrammetric standpoint) exists of an area, this image could be made to serve as a master upon which data from other sensors e.g. scanner, radar, television, etc. could be registered; in this fashion, rectification and geometric correction of all types could take place as a normal part of achieving multiband multi-temporal information.

Finally, the through-put rate for this type of information processing is limited as much as anywhere at points at which ground data and ancillary information must be merged into the multispectral image data stream itself. Data registration can, in many cases, tend to alleviate this difficulty. For example, in the case of an agricultural problem, one need only establish field boundaries etc. once during a growing season in order to have ground truth information referenced to the appropriate fields in this image data. Since the registration process establishes scene point coincidences in the images it established this same coincidence and referencing for all ground truth associated with given scene points. Thus, training sample coordinates need be selected only once during a season.

#### DIGITAL IMAGE DISPLAY SYSTEM

A second project underway for some time is the specification, design, procurement, and implementation of a digital image display system. A pacing item in the development of a capability to rapidly collect, ana-

lyze and disseminate information by remote sensing means is the capability for the human operator to rapidly interact with the image data stream and collate with it literal or other information from other sources. The purpose of the digital image display is to enable research into techniques to alleviate this limitation.

The need for such a system and the general outline of its specifications was first identified in March, 1966. After a long series of delays, the project was finally funded and a contract awarded for its construction by the IBM Federal Systems Division in August, 1969. The system has recently arrived on location at Purdue and is currently undergoing acceptance tests. It consists of three major elements: a control unit containing logic circuitry, interfacing circuitry, and a disk image buffer; the display console including a light pen and function keyboard for controlling software packages, and a photocopy unit used to generate hard copy versions of images being displayed.

Figure 8 shows a photograph of the photocopy unit (right) and display console (left). The display system provides an image of 768 elements and 577 lines with a 16-step grayscale and a 30-frame-per-second (with interlace) refresh rate. Figure 13 shows the output of image data produced by the photocopy unit. Upon final acceptance of the system from the manufacturer, work will begin on techniques for allowing the human operator to use very large quantities of remote sensing data.

#### DATA SYSTEMS PARAMETER STUDY

Figure 9 is a block diagram of a satellite-based remote sensing system. Shown are the major elements of such a system, such as the sensor, onboard processing and telemetry, ground processing and data reduction, and information consumption. In considering the design of such a system, it is immediately apparent that there are a great number of parameters to be chosen. Parameters such as the spectral and spatial resolution of the sensor, the detector signal-to-noise ratio, the type of telemetry, data compression scheme, etc. must all be selected.

Heretofore, research on individual elements of the system had not proceeded far enough to permit the consideration of overall performance relative to these parameters. It now appears, however, that this point has been reached. As a result, a data system parameter study has been defined. The approach to be used is to test the overall system sensitivity to various key parameters. Generally, the index of performance to be used is the pattern recognition classification performance on test data sets. Preliminary results in several of these parameter studies will now be described.

### Classification Sensitivity to Additive Noise

A parameter of considerable importance to the design of new sensor systems is the signal-to-noise ratio of the detector. For a sensor material of given sensitivity the signal-to-noise ratio of the data produced can generally be improved by degrading either the spectral or spatial resolution or both. However, data analysts are generally not anxious to see this done and a trade-off must be made. Quantitative information about desired signal-to-noise ratios for specific analysis tests has previously been scarce.

In order to increase the understanding of the necessary signal-to-noise ratio for various classification tests it was decided to carry out a single test classification on a data set to which varying amounts of noise have been added. Figure 10 shows a small portion of a scene from which the data was selected. Shown are a panchromatic air photo of the area and below it a printout of the original undegraded signal. Printouts of the same data with two different levels of noise added are shown on the right. Digital data of eight-bit precision was used. Thus, a gray scale of 256 possible steps is available. The magnitude of the noise (which was Gaussian and uncorrelated between channels) is measured in terms of the number of bins out of 256 per standard deviation.

The noise was generated using a software-implemented random number generator within the computer. It was decided to choose Gaussian noise, uncorrelated from spectral band to spectral band, as this most nearly approximates the type of noise generated within the sensor detector. Figure 11 is a classification of a segment of the data for the no-noise case and the two noise levels shown in Figure 10. The degradation of accuracy is visibly apparent.

The graph of Figure 12 summarizes the overall results for the study. This is a plot of the percent correct recognition for the classification task as a function of the magnitude of noise added to the data. The shapes of the curves which are in the form of the complement of the Gaussian error function could easily be predicted. It is also not surprising that the results for the training samples stayed consistently above the results for the overall test samples.

An interesting result can be seen from the two individual classes which are plotted. The data used for this test was of an agricultural scene in Tippecanoe County in June, early in the growing season. At this point in the season wheat is ready for harvest and, being golden brown at this stage, is a relatively easy class to separate from the rest of the scene. Thus, in the graph of Figure 12 the accuracy is high. More importantly at this point though, it degrades relatively



slowly. On the other hand, soybeans provides a much more challenging classification since the percent of ground cover at this stage of the season is very low. While the accuracy in the no-noise case is quite high, one sees that the additive noise quickly degrades this accuracy to a low value. These results tend to bear out the statement that as the signal-to-noise ratio degrades, the more difficult classifications will be affected most. That is, for simple classifications the signal-to-noise ratio is not too important; however, it becomes so for more difficult ones.

The classification used was a nine class classification. One would assume that in an extrapolation to the right, these curves would become asymptotic to chance performance which is 11 percent in this case. One can also consider an extrapolation of these curves to the left. This extrapolation should provide curves which become asymptotic to 100 percent accuracy. Since the original data did not have an infinite signal-to-noise ratio, it may be supposed that these curves provide an indication of the true original signal-to-noise ratio.

#### Data Compression based on Spatial Redundancy

The General Electric Company was awarded a contract some time ago by NASA to study the possibility of using data compression techniques on a sensor system of the type to be flown on the Earth Resources Technology Satellite. The techniques to be studied apparently are to be those based primarily on the fact that a great deal of redundancy exists in an image due to spatial correlation in the data. As a result of the application of efficient data compression techniques, it is possible to reconstruct the image transmitted to good but not perfect precision. It is, therefore, desirable to learn the degree to which the data compression technique will affect the ability of the data analyst to achieve good results.

It is desirable to determine these effects on both photointerpretative based analysis systems and pattern recognition (machine oriented) schemes. A co-operative program between LARS and GE was agreed upon in order to accomplish a portion of this evaluation. Test data was selected jointly by LARS and GE from among flightlines of data which had been flown by the Michigan scanner system and digitized at LARS. The data was provided to GE for the purpose of compressing and re-expanding it using compression algorithms of General Electric Company design. The four channels of the Michigan scanner system most nearly coinciding with the four channels of the ERTS multispectral scanner were to be used. After compression and re-expansion the data was returned to LARS and a test classification run upon it.

The joint study has now progressed to the point that the first compression algorithm has been tested. Figure 13 shows images generated from a small portion of the original data and the same data having been processed by the compression algorithm. The algorithm is a preliminary one for base line tests and is simply a procedure whereby only every fourth sample of each channel is transmitted. Intermediate points not transmitted are assumed on the ground to have been the same gray scale intensity as the last previously transmitted point in that spectral band.

Figure 14 shows the results of the test classification on the two different data sets. Also shown is the results of the classification of the same data but using the set of spectral bands which are preferred for this classification. Notice that the degradation provided by the compression as compared with the uncompressed data is not major. Full analysis of results must await the conclusion of the study including the use of other compression schemes. These will be reported in due course. However, some further comments about these results will be made after having reported the results of another data compression study in progress.

#### DATA COMPRESSION TECHNIQUES BASED ON SPECTRAL REDUNDANCY

A second data compression study has been underway for some time based on the use of the redundancy between spectral bands. This study is being conducted entirely by LARS. The point of departure of this study is somewhat different than the one previously described in that a larger number of spectral bands are assumed. An overview of the view point is contained in Figure 15. We see on the left a multispectral scanner sensor which produces data in  $M$  different channels. The technique here would be to design a data compression system which converts the  $M$  channels into  $N$  features,  $N < M$ . The original data could be recovered to within some prescribed accuracy by processing the data at this point through a reconstruction algorithm after which data analysis could take place.

However, imagery could be generated in each of the  $N$  features in exactly the same way that it could be generated in each of the  $M$  channels. In any case, the measure of the degree of compression in this case is the ratio of  $M$  to  $N$ .

The compression algorithm tested is a type based upon a Karhunen-Loeve expansion. It amounts, in fact, to a linear transformation in  $M$ -dimensional space and, more specifically, a linear transformation which is a rotation to principal co-ordinates. The same data and classifi-

cation was used to test this scheme as used in the LARS/GE Data Compression Study and the Additive Noise Study. The results of this classification are shown in Figure 16. The first line gives the results of the control classification, that is, classification directly on the original data.

When the 12 original channels were transformed and then half deleted so that only six features remained in the N-dimensional feature space, the accuracy of the classification did not change significantly. The test was repeated for a 12- to 3-dimensional transformation and again the accuracy was essentially unaffected. Not until all but two bands in feature space were deleted did the accuracy begin to seriously deteriorate. The percent of mean square difference between the reconstructed and the original image is shown on the right. These results have been judged to be very encouraging and the scheme is now being extended to include both spectral and spatial redundancy.

#### SOME COMMENTS ON SPECTRAL BAND SELECTION

Some of the results above raise some points that have to do with the relative importance of a band selection capability. Notice from Figure 14 that the overall classification accuracy for the preferred channels (i.e. the best of the 12 available) was approximately 90%. This is more than 10% higher than the performance figure for the same data but using the ERTS channels. Thus, one may say from the data analyst's viewpoint that being required to give up the capability to tailor the band selection to the particular classification being carried out is a more serious effect than accepting the degrading effects in the data due to a data compression algorithm. This can be seen and understood more clearly as follows:

Assume this case to be typical. Here, 12-channel data was available; the band limits of the particular bands are shown in Figure 17. The problem of band selection comes to finding the four best channels<sup>1</sup> of the 12 to use for the particular classification. The feature selection algorithm implemented in the LARSYSAA programming system computes the relative separability of each class pair for each possible four-tuple of spectral bands. The classes used in the test classification are shown on Figure 18. Beside each is indicated a single symbol used to designate that class in two following figures. Figure 19 shows the results of applying this algorithm to this classification task. The numbers on the right of this figure are the numbers indicating the relative separability of the class pairs. Class pairs are indicated by two symbols (SC for soybeans and corn, SW for soybeans and wheat) at the head of each of these columns. The four-

<sup>1</sup>A preliminary determination as to the number of channels to be used must, of course, be made. Four have been assumed.

tuple of features (spectral bands) are then rank-ordered based upon the average of these interclass separability measures. Thus, it can be seen that bands 1, 9, 11 and 12 were selected as the best feature set and bands number 6, 9, 11 and 12 which are the ones most nearly matching the ERTS channels are second.<sup>1</sup>

However, by using additional options available with the feature selection algorithm it is possible to further tailor the band selection to the classification task. Note that in Figure 19 some of the interclass pair separabilities are very large, indicating very obvious separability; on the other hand, other interclass separability measures are quite small. It would be desirable to select feature sets so as to increase the separability of the more difficult interclass pairs at the expense of the classes with the more obvious separability. In order to do this the feature selection algorithm has been provided with an option permitting the imposing of a maximum interclass separability measure which will be considered for the purpose of rank-ordering the four-tuples. Figure 20 shows the results of using a maximum of 200. Note that the preferred feature set now becomes 1, 6, 10 and 12 and that the ERTS simulated channels 6, 9, 11 and 12 become 55th in ranking.

The validity of this re-ranking is borne out in the difference in overall accuracy ultimately obtained in the two classifications. Approximately 90% for the preferred channels 1, 6, 10 and 12 as compared to approximately 80% for the ERTS channels 6, 9, 11 and 12.<sup>2</sup>

Thus, by being forced to a sub-optimum choice of spectral bands an overall 10% accuracy loss occurred and the increased loss in accuracy due to data compressions was only an additional 2 or 3 percent.

These results tend to suggest that the capability to make a proper selection of spectral bands from a large set may indeed be far more important than the effects of a perhaps lower signal-to-noise ratio, a data compression scheme, and conceivably other system parameters. As a matter of fact the scheme indicated in Figure 15 whereby in the spacecraft a scanner with many channels is operating but a compression algorithm reduces the dimensionality for transmission to earth may provide a more useful approach. Further investigations into this type of scheme are under way.

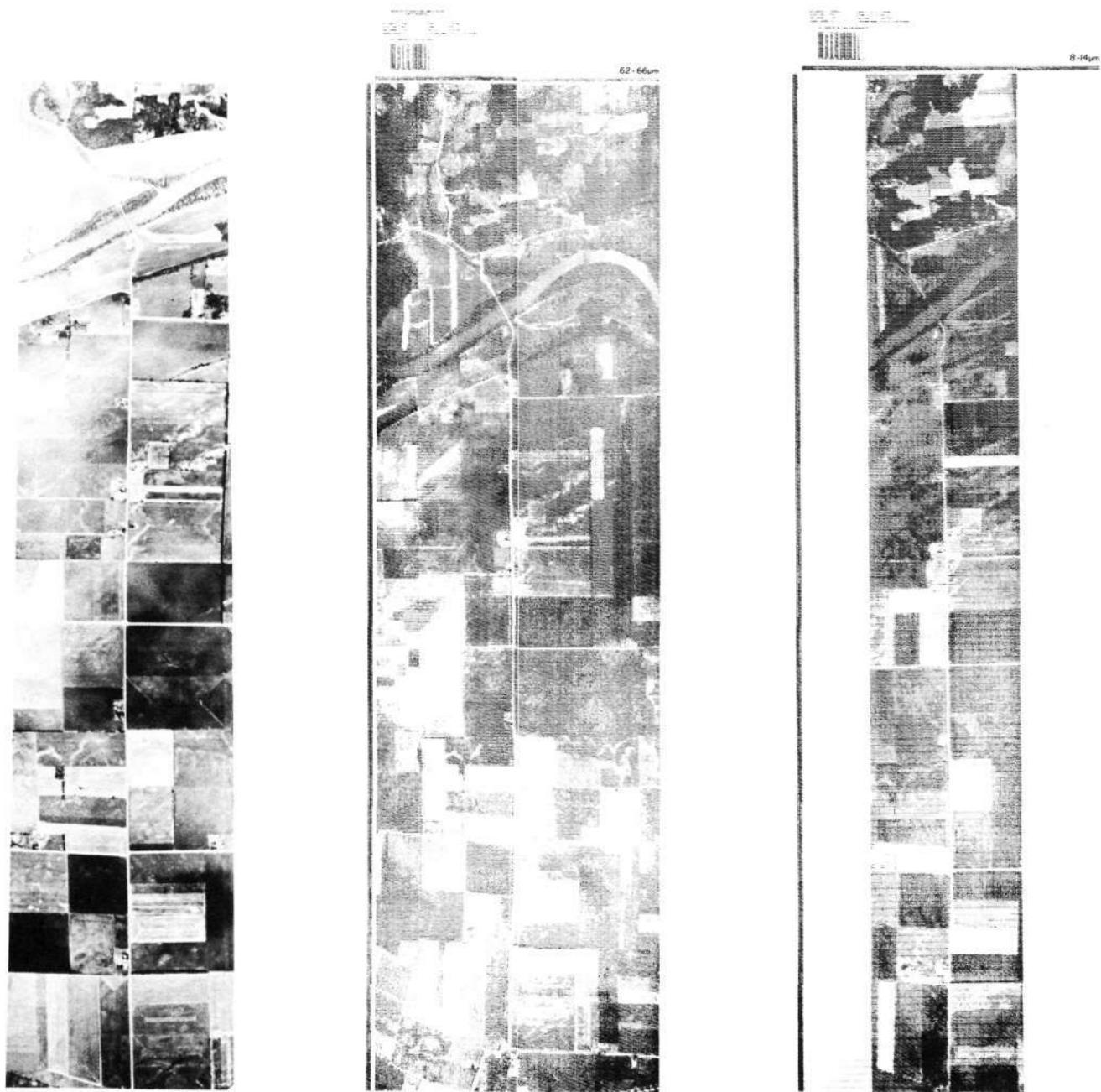
---

<sup>1</sup>In the case of an actual satellite however, channel 1 would probably not be as useful as it appears to be here, since it is well into the blue portion of the spectrum and from space there would be considerable blue scattering. These results tend to bear out the choice that the 4 ERTS spectral bands are generally a good set.

<sup>2</sup>From these results one might tend to conclude that the ERTS channels which are the best set of bands in general may be considerably sub-optimum in specific cases.

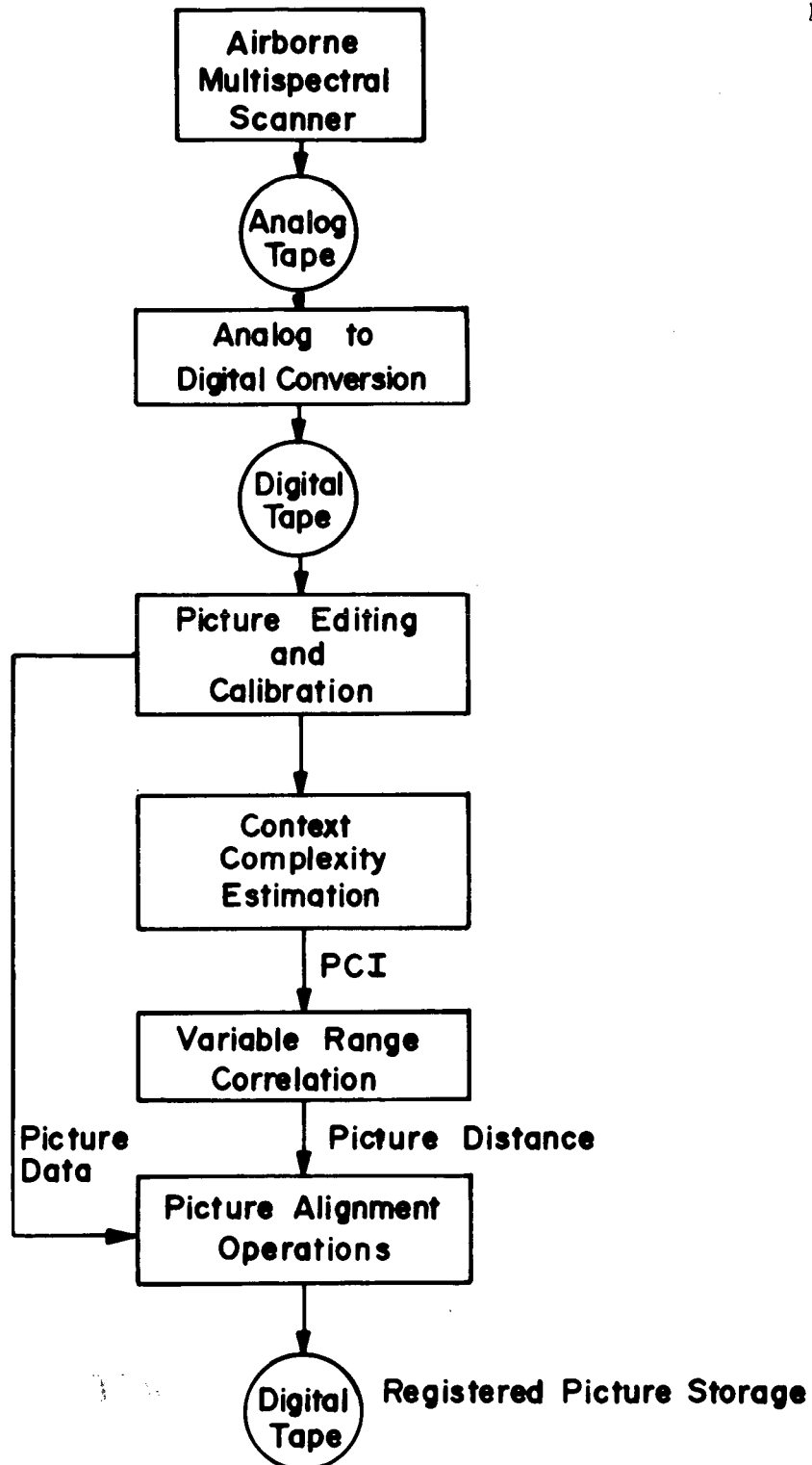
- Reference 1 - Anuta, P. E. "Digital Registration of Multispectral Video Imagery" Society of Photo-Optical Instrumentation Engineers Journal, Volume 7, Number 6, September 1969.
- Reference 2 - Anuta, P. E. "Spatial Registration of Multispectral and Multitemporal Digital Imagery Using Fast Fourier Transform Techniques", IEEE Transactions on Geoscience Electronics, Volume GE-8, Number 4, October 1970.
- Reference 3 - Wacker, A. G. and Landgrebe, D. A. "Boundaries in Multispectral Imagery by Clustering" 1970 IEEE Symposium on Adaptive Processes, December 7-9, 1970, University of Texas at Austin.

# Visible and Thermal IR Imagery



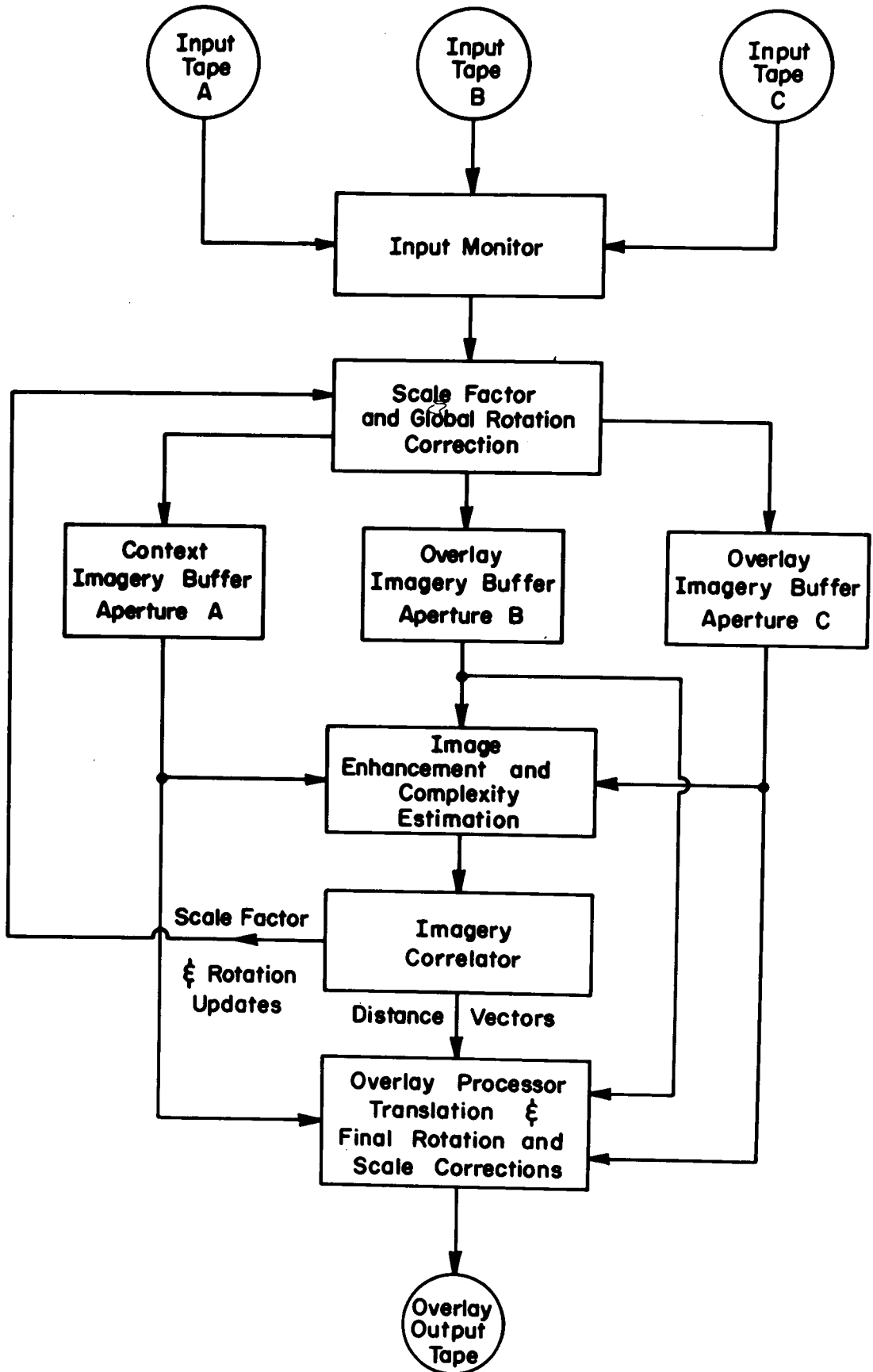
NOT REPRODUCIBLE

Figure 1



## ADAPTIVE MULTISPECTRAL PICTURE REGISTRATION SYSTEM

Figure 2

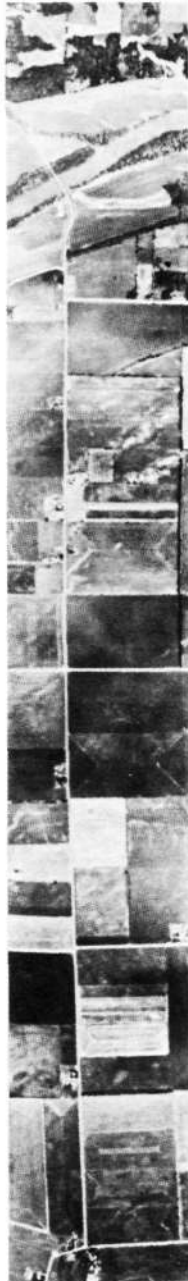


### DIGITAL IMAGERY REGISTRATION SYSTEM

Figure 3



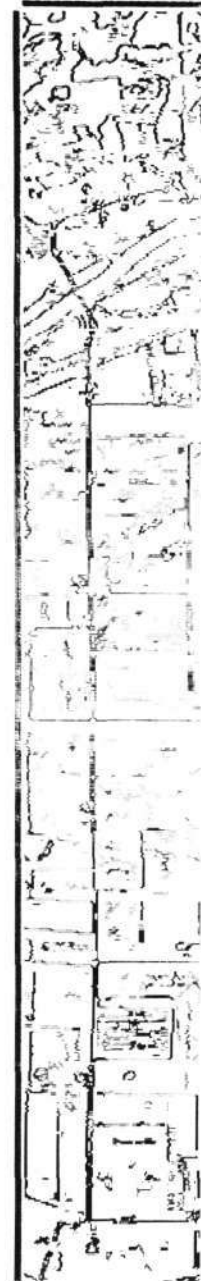
# Border Enhancement Techniques



Air  
Photo



Gradient  
Borders



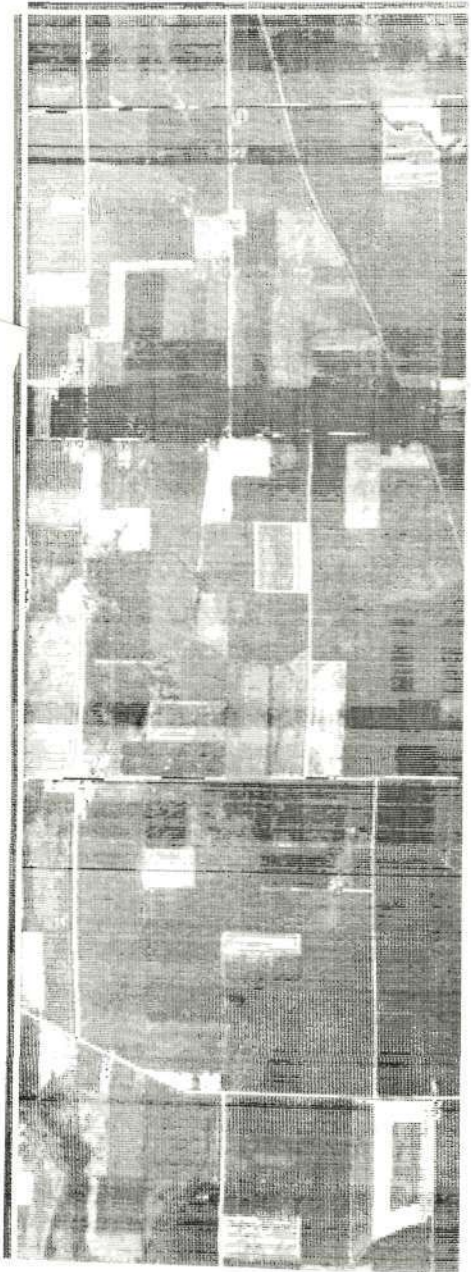
Cluster  
Borders

Figure 4



**June 1969**  
**11.7° Yaw Distortion**

**NOT REPRODUCIBLE**



**August 1969**  
**0° Yaw Distortion**

**Flightline PF24**  
**Altitude 5000 ft.**  
**Band .66-.72 microns**

**Example of Rotational Distortion in  
Multispectral Airborne Scanner Imagery**

MULTI-TEMPORAL ANALYSIS  
Scanner Data from June & August, 1969

PF24 Run 69004801

Test Field Classification Accuracy

		June (Ch 3,6,9,12)	August (3,6,9,12)	June/Aug. (6,9,12 June; 12 Aug.)*
	No. of Samples			
Corn	3281	80.2%	53.6%	86.4%
Soybeans	1738	83.3%	89.6%	91.8%
Wheat	396	71.5%	—	75.5%
Oats	693	78.1%	—	67.5%
OVERALL		80.3%	57.4%	85.8%
<u>Channel</u>	<u>Band</u>			
3	.52 - .55 $\mu$			
6	.62 - .66 $\mu$			
9	.80 - 1.0 $\mu$			
12	2.0 - 2.6 $\mu$			

\*Best 4 of the 8 Available by the  
Divergence Analyser

Figure 6

## Image Data Registration

- Non-single Aperature Sensors
- Temporal Information
- Distortion Correction
- Ground-Data Merge

Figure 7.

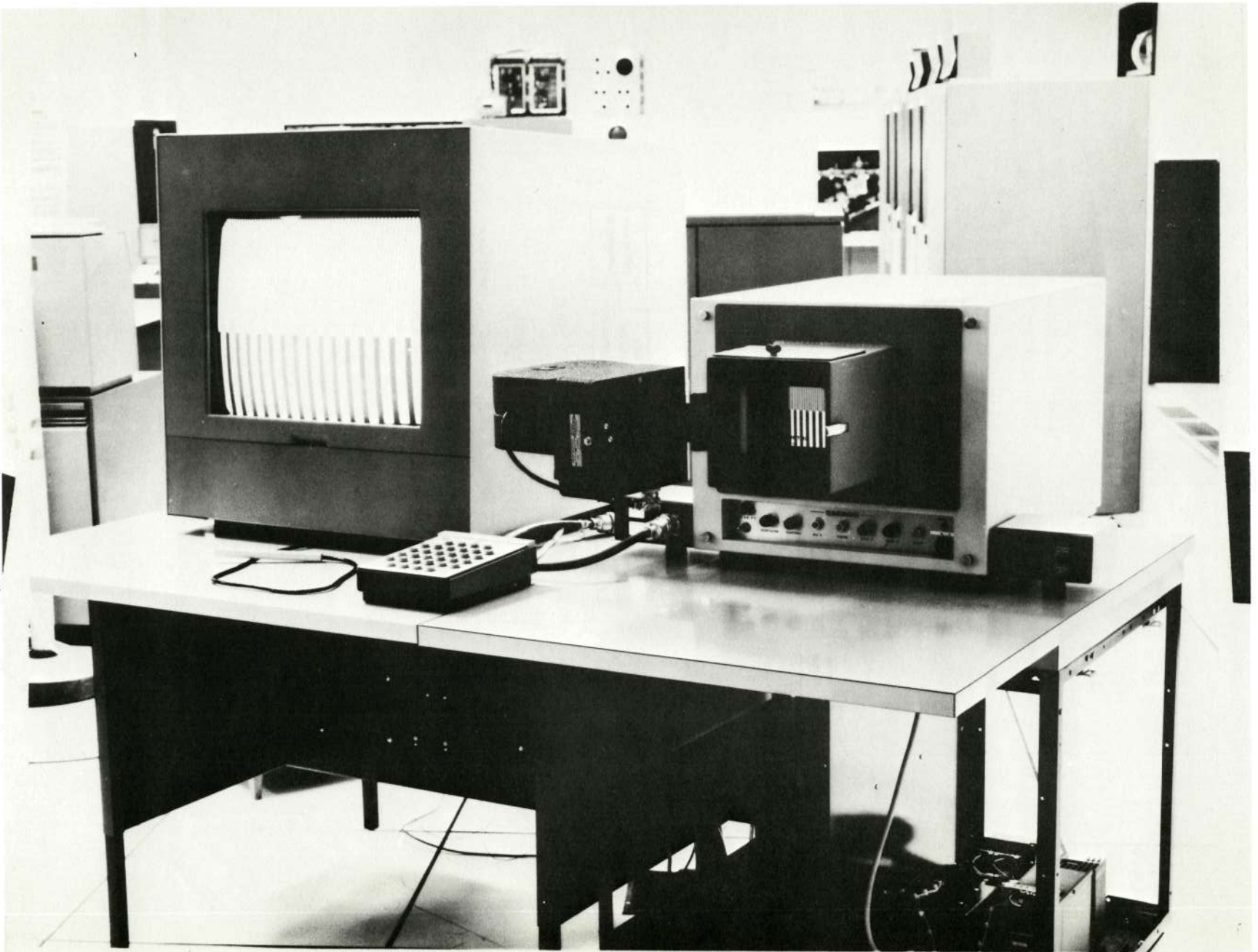


Figure 8

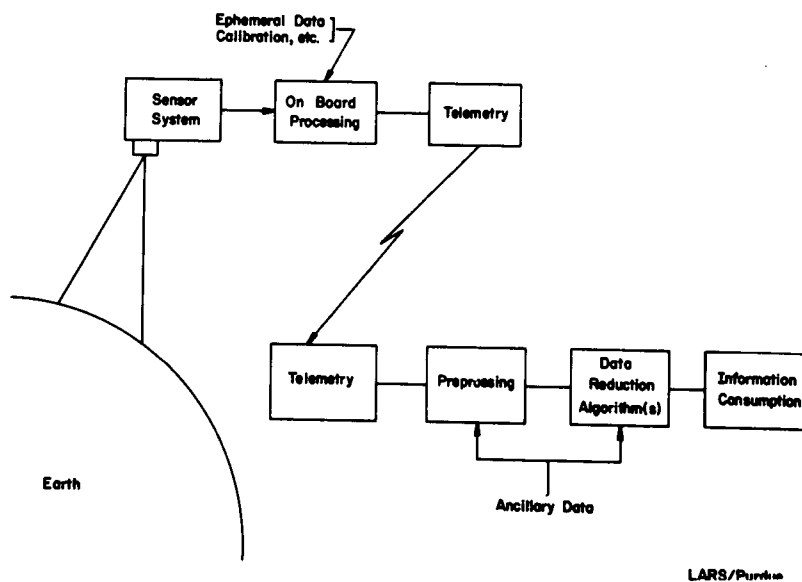
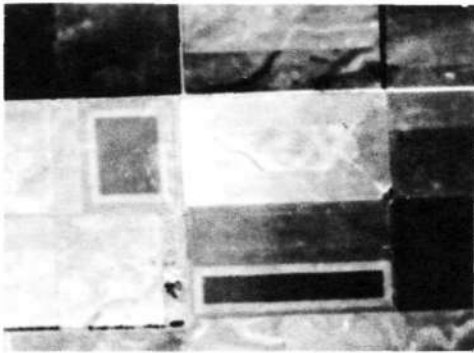


Figure 9

1957

# Data with Noise Added



Air Photo

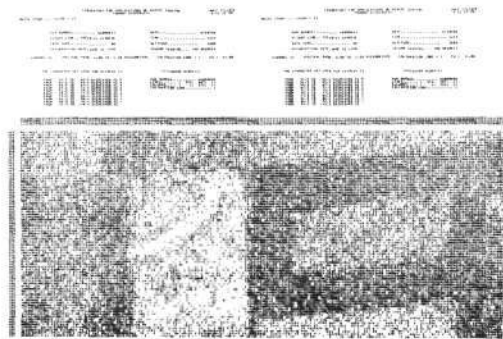


Sigma = 5

NOT REPRODUCIBLE



No Noise



Sigma = 15

Figure 10

# Classification Results, Wheat Only

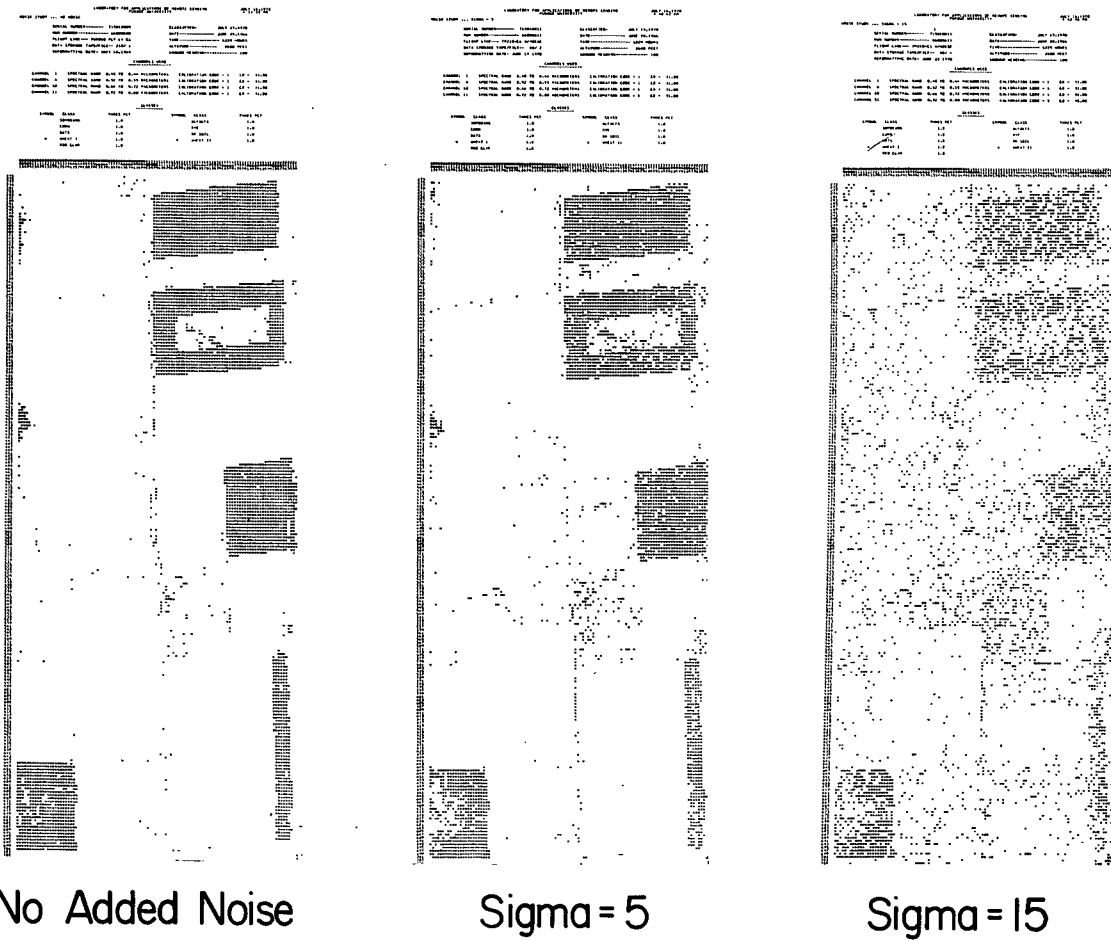


Figure 11



### Classification Performance vs Noise

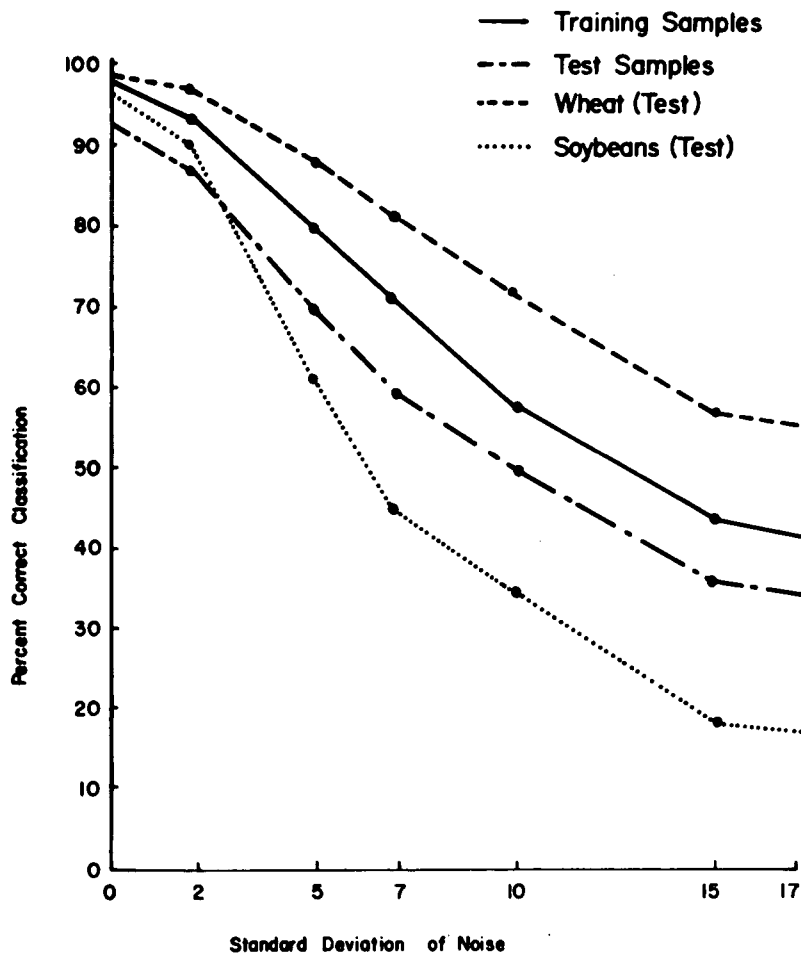
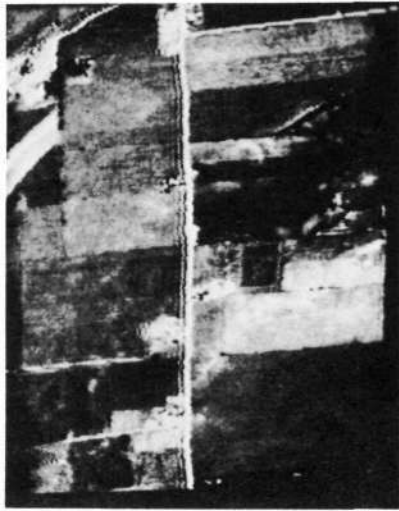
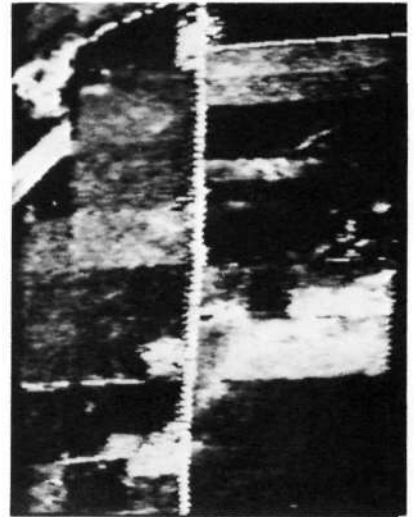


Figure 12

# GE/LARS Data Compression Study



Original Data



Compressed

GE/LARS Data Compression Study  
June 1966 CI Test Results

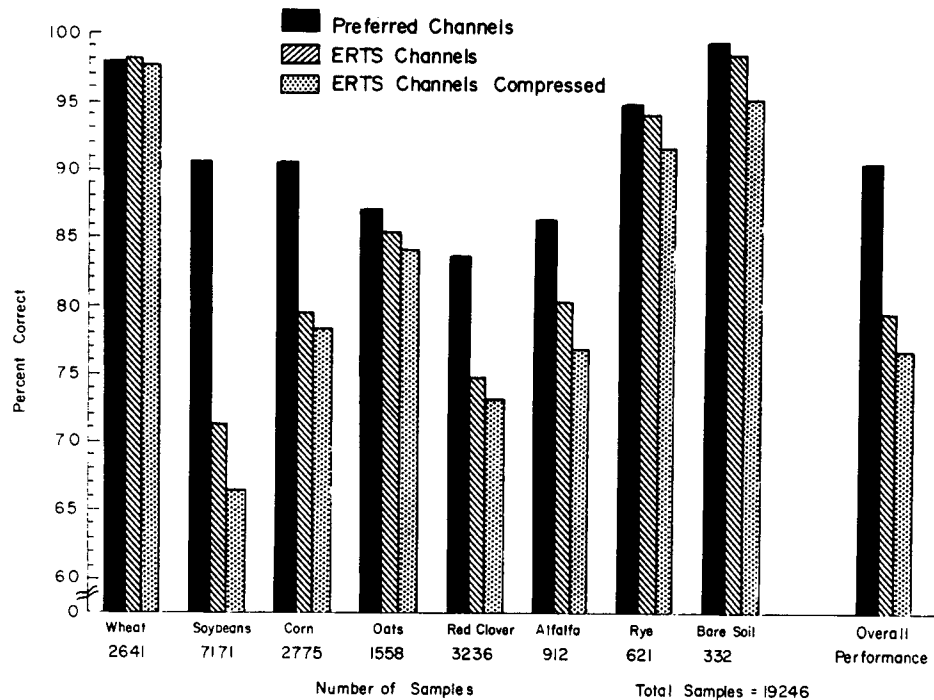


Figure 14

### MSS Data Compression Based on Spectral Correlation

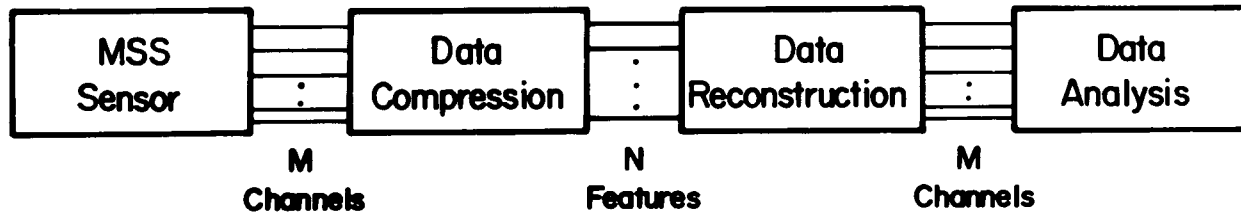


Figure 15

**MSS Data Compression  
Based on Spectral Correlation**

<u>Compression Ratio M/N</u>	<u>Overall Performance in %</u>	<u>Mean Square Error in %</u>
12/12	90.1	0
12/6	88.6	1.1
12/3	89.5	2.2
12/2	60.7	6.6

Spectral Bands for Classification: .40-.44, .52-.55, .66-.72  
and .80-1.0 $\mu$ m

Figure 16

## Spectral Band Selection

### Spectral Bands

1	.40-.44	7	.55-.58
2	.44-.46	8	.58-.62
3	.46-.48	9	.62-.66 -ERTS
4	.48-.50	10	.66-.72
5	.50-.52	11	.72-.80 -ERTS
6	.52-.55 ERTS	12	.80-1.00 -ERTS

Figure 17

## Spectral Band Selection

Classes	R - Red Clover
S - Soybeans	A - Alfalfa
O - Oats	W - Wheat 1
C - Corn	Y - Rye
M - Wheat 2	X - Bare Soil

Figure 18

Class Separability Measure  
(No Maximum)

Rank	Spectral Bands	Average Separability	Individual Class Separability				
			SC	SW	SA	WR	WY . . .
1	1, 9, 11, 12	444	25	190	188	620	58
-ERTS- 2	6, 9, 11, 12	428	26	177	299	630	208
3	2, 9, 11, 12	423	24	151	182	619	58
4	5, 9, 11, 12	420	.	.	.	.	.
5	8, 9, 11, 12	418	.	.	.	.	.
	.	.	.	.	.	.	.
	.	.	.	.	.	.	.
	.	.	.	.	.	.	.

Figure 19

495



Class Separability Measure  
(Maximum = 200)

Rank	Spectral Bands	Average Separability	Individual Class Separability				
			SC	SW	SA	WP	WY
1	1, 6, 10, 12	155	34	200	196	200	180
2	1, 6, 10, 11	154	34	200	192	200	183
3	1, 6, 9, 12	153	26	200	193	200	200
4	1, 6, 9, 11	153	27	200	190	200	200
	·	·	·	·	·	·	·
	·	·	·	·	·	·	·
-ERTS- 55	6, 9, 11, 12	145	26	177	200	200	200
	·	·	·	·	·	·	·
	·	·	·	·	·	·	·
	·	·	·	·	·	·	·
	·	·	·	·	·	·	·

Figure 20

REMOTE SENSING AT THE UNIVERSITY OF KANSAS  
IN RADAR SYSTEMS

by

Richard K. Moore  
Center for Research, Inc.  
University of Kansas  
Lawrence, Kansas

INTRODUCTION

Remote sensing research at The University of Kansas is a multidisciplinary effort involving the interaction of radar engineers, data processing engineers, and geoscientists who approach remote sensing as a systems problem. We believe that the interfaces between target-sensor interaction, sensor research, data processing, and geoscience user interpretation can best be solved by such a team effort. Figure 1 illustrates the remote sensing system as we view it.

Objects to be viewed are selected by the interpreters. The subject of target-sensor interaction is a most important one. This interaction determines the way in which the sensor views the object and consequently the way in which the interpreter can use the sensor for studying the object. Sensor development is another activity in the system. When the sensor produces images in multiple wavelengths or polarizations, or even at a single wavelength and polarization at multiple times, the images must be brought to congruence before they can be automatically processed with pattern recognition techniques. Multiple images almost demand automatic processing because of the difficulty for the human interpreter to relate one image to the other. Analog processing can be in almost real time, but digital processing permits great flexibility. We believe the digital techniques should be used to establish appropriate algorithms for particular data sets but that analog techniques should be then applied to processing the large mass of data. The data are useless to the interpreter unless displayed in an easily understood fashion; thus displays are an important part of the remote sensing system. Interpretation at any time after generation of the display requires the use of recorders, varying from a simple camera to an elaborate magnetic recording system. Automatic processing of data requires calibration throughout the system — unfortunately, this has not been widely used in remote sensing in the past. Interpreters should contribute significantly to the development and adjustment of the sensors, congruencers, processors, and displays since they are the ultimate users.

At The University of Kansas we engage in object-sensor interaction studies, in sensor development, and in image processing using both digital and analog pattern recognition techniques with displays ranging from computer printouts to color television screens. We have studied the congruencing problem but are not working on it. Our interpreters (geologists and geographers) interact closely with the engineers engaged both in the sensor development and the data processing equipment and technique development.

This paper confines itself to a discussion of our radar system research, including object-sensor interaction and sensor development. The papers by Kelly and Morain describe other aspects of our research.

### OBJECT-SENSOR INTERACTION

Table I summarizes the FY70 research at the University of Kansas in object-sensor interaction. Much of the theoretical work has been supported by the National Science Foundation and by the U. S. Army. Most of the experimental work reported here has been supported by NASA, but development of the radar spectrometer received both Army and NASA support.

Because of the limited time available, only the octave bandwidth spectral response experiment is reported here. Other activities listed have been or will be reported in technical reports, papers, and technical memoranda.

Spectral responses have been reported for decades over continuous bands in the visible and infrared regions. Microwave spectral response measurement however has consisted of separate widely spaced isolated wavelengths with each observation produced by a different radar or radiometer. Thus, assessment of the potential value of multi-wavelength or continuous-coverage microwave sensors has been seriously hampered because no data were available to illustrate the comparison between responses across continuous bands.

Spectral responses of remote sensing targets have been obtained over an octave bandwidth in the microwave region at The University of Kansas during the past year.<sup>1</sup> Figure 2 illustrates a normalized comparison of spectral responses in the optical-IR region with a comparable wavelength spread in the microwave region. The responses in the optical region govern the color; three typical ones are shown on the figure. The responses on the microwave region, therefore, determine a "microwave color" and three typical examples of these are shown in the figure. Clearly the variability in the microwave region is comparable with that

in the optical-IR region and "color" appears to be as valid a concept for microwaves as for the shorter wavelengths.

The absolute level of the microwave response varies from one object to another more than does the absolute level in the optical-IR region for typical illuminating angles. Thus, to show similarity, the curves presented had to be normalized by taking the mean response across the band as unity. The "error bars" shown on the microwave response are not caused by experimental error but rather are due to the inability to obtain sufficient bandwidth averaging. This subject is discussed later in connection with development of polypanchromatic radars.

The microwave region from 3.75 to 7.5 cm wavelength was chosen for the initial experiments because octave-bandwidth components are less readily available at shorter wavelengths. Extension of these responses to both shorter and longer wavelengths is contemplated, but shorter-wavelength equipment will work over smaller fractional bandwidths. The results will be particularly interesting, since most imaging radars used for remote sensing have operated at wavelengths of 3 cm or shorter.

### RADAR SYSTEMS RESEARCH

In addition to the object-sensor interaction studies, radar systems research has been conducted at The University of Kansas over the past year, and in fact since the conception of the NASA remote sensing program in 1964. Table II summarizes the activity in radar systems during the past year. Here we discuss primarily polypanchromatic radar development and the spacecraft imaging radar studies. Brief mention is made of the comparison between real and synthetic aperture operation of the DPD-2. Our extensive work in scatterometer systems analysis is not reported here although it has been documented. The paper by Dr. Krishen in this meeting describes some similar activities at MSC. Close liaison has been maintained between the work at Kansas and that at MSC on the scatterometer system.

### POLYPANCHROMATIC RADAR SYSTEM DEVELOPMENT

The potential of "radar color" has been demonstrated by the spectral response curves. To use this potential properly, however, requires adequate averaging of the radar return. Without such averaging each point in the return has an amplitude determined by one sample from a Rayleigh distribution and the result is a very speckled image.

The speckling comes about because of the use of coherent single frequency radiation.

The same sort of thing would happen if laser illumination were to be used in a still room for making photographs. Figure 3 illustrates this point. Three images are shown, one an air photo printed with white light, one an air photo printed from the same negative but with laser (monochromatic) light and one a radar like-polarized image of the same Imperial Valley area made with a typical monochromatic system. Note the speckled nature of the monochromatically printed air photo. This is due to phase interference caused by small irregularities within the negative. The comparable phase interference phenomenon occurs with radar. It too has a speckled image. Note that the radar does, however, show some features barely visible in the panchromatic photograph and invisible in the monochromatic photography. Presumably, if we were to make a panchromatic radar image of this area, speckle would disappear and the image would appear more like the panchromatic photography — within the limits imposed by the resolution of the radar.

The averaging that takes place and permits the panchromatic image to have smoother grey tones is because a broad band of frequencies is used and phase interference effects are removed by averaging on film of the responses at the different individual frequencies. With the radar one can hope to achieve this averaging either with a broad band or by other techniques. For instance, the azimuth resolution might be made better than needed and the degraded image would permit averaging together several cells of the fine-azimuth-resolution image. For a radar, averaging in frequency is equivalent to obtaining a finer range resolution than needed, with subsequent averaging together of the fine-range-resolution cells to obtain a poorer resolution with better grey scale rendition.

The effects of both frequency averaging and finer range resolution is demonstrated with Figure 4, using ultrasonic simulation.<sup>2</sup> The images shown were produced with ultrasonic waves in water at frequencies indicated. The wavelength for 1500 kHz ultrasonic waves in water is 1 mm. The top images were made with a pulse duration of 20  $\mu$ s at an angle of incidence of 30°; this gives a range resolution of 30 mm.

The target was made up to simulate a pattern of fields. Note that the small field projecting to the bottom is almost invisible in the monochromatic image and the large field projecting toward the bottom is invisible. In the panchromatic image, however, these fields show clearly and the grey scale in the larger fields is more uniform. For this image 16 independent samples are averaged per resolution element. The bottom pictures were made with a shorter pulse corresponding to a range resolution of 13.5 mm. With this finer resolution the eye is

able to distinguish the different characteristics of the small field projecting down, although it shows up better on the panchromatic image. The panchromatic image in this case is not improved as much relative to the monochromatic image because only about seven samples have been averaged for each point.

The frequency range occupied by a panchromatic image in Figure 4 has been divided into three parts to produce a color or "polypanchromatic" image. The image from each part of the spectrum was assigned a different primary color and the results were combined on the TV screen. Figure 5 shows this polypanchromatic image. The concept of radar color is shown by this picture, but the quality of the picture is lower than that of the panchromatic image from which it was derived because the amount of averaging for each cell was reduced by admitting only one-third the frequency sweep for a given component (single color) image. Thus the degree of speckle in each is mid-way between that of the monochromatic and panchromatic images of Figure 4.

The effect of using single frequencies without averaging is illustrated in Figure 6. These pictures were taken with the radar system used for determining the spectral response in Figure 2. The system was operated as a "B-scan radar" from a position atop a ten-story dormitory. In this format the vertical direction of the image is slant range and the horizontal direction is azimuth angle; consequently, close objects are spread across the image more than equal-width for objects that subtend a smaller angle.

Figure 6 shows three images made at single carrier frequencies less than 1 per cent separated. Careful examination of the images shows many differences and most of these differences are due to the phase interference phenomenon that causes speckle in monochromatic radar images. Figure 7 shows the same scene with a monochromatic and two panchromatic images. Especially striking is the filling in of the lines in the right hand part of the image on the panchromatic pictures. These lines are barriers in a parking lot and should be essentially continuous. Also notable is the shape of the structures in the center of the image. Some of them appear to have little shape in the monochromatic image but take on a clear shape in the panchromatic images.

Figure 8 shows the same thing at a higher frequency. Here the azimuth resolution is better because the same antenna was used as at 6.00 GHz. The difference in the parking lot is even more striking than before particularly for the wider bandwidth.

These illustrations clearly indicate the advantage of some sort of averaging and the fact that averaging in frequency can provide the desirable characteristic. With a real-aperture SLAR some azimuth averaging takes place automatically, but for a fine-resolution system

additional range averaging is needed to reduce speckle. With a synthetic aperture radar on the other hand, better azimuth averaging may well be possible. If so, it can be achieved without the additional power that may be required to obtain averaging in frequency.

The effect of averaging in frequency has been determined theoretically, and Figure 9 shows an example calculated from this theory. The ordinate is the variance of the received power, normalized to the square of the mean. Thus, at minimum bandwidth the variance is equal to the square of the mean. Examples are shown for range resolutions of 50 feet and 10 feet. To reduce the variance to 1 per cent (standard deviation to 10 per cent of the mean) bandwidth well in excess of 500 MHz is required for 50 foot resolution and 5 times as much bandwidth for 10 foot resolution.

The radar spectrometer was used to show this effect with returns from a grassy area as illustrated in Figure 10. The rapid fluctuations with frequency appearing in the 100 MHz curve are due to the phase interference phenomenon. Averaging with a bandwidth of 500 MHz removes most of these small-period fluctuations; presumably the remaining curve is reasonably representative of the actual mean scattering coefficient variation across the band. Note that even the 100 MHz curve represents averaging from about 2.5 independent samples and the fluctuation with this much averaging is significantly less than if the 40 MHz curve had been plotted!

Since the amount of bandwidth is limited in practical systems, and the fineness of azimuth resolution is also limited, some sort of trade-off may be necessary with radar systems for resource studies. The trade-off is between uniformity of grey tone for large homogeneous areas (and accuracy of grey tone for small objects) and resolution. Grey scale cannot be properly reproduced at the finest resolution, but degrading the resolution too far may be disastrous because boundaries or whole objects may be missed. This subject is receiving further study at The University of Kansas.

## SPACECRAFT IMAGING RADAR STUDY

Digital synthetic aperture processing on board a spacecraft has been considered in a preliminary study recently completed.<sup>3</sup> With present state of the art a digital processor for a spacecraft synthetic aperture radar appears prohibitively large both in space and in power. An adequate on-board processor may be possible by 1975, however, if the projections of this study are borne out.

A flexible computer program for simulating performance of real-aperture and synthetic-aperture radar systems was developed as part of this study. Results presented here are images printed out from this program. Application of the program to real images is prohibitively expensive; consequently, relatively simple contrived images are used in the example. Figure 11 shows three printouts from the program for a target consisting of two uniform elements with a boundary diagonally across the image. (1) is the "true image" whereas (2) and (3) show different contrasts in the output after synthetic aperture processing. The difference in appearance due to dynamic range of the output is an indication of the kind of problem that also exists with real radar images.

The simulated digital processor for spacecraft radar uses sub-aperture averaging to permit improved grey scale with reasonable resolutions for earth resource applications; it also reduces the amount of equipment and power required by the processor. Figure 12 illustrates the concept of subaperture processing. The largest possible synthetic aperture is the distance along the flight track during which the beam of the real antenna illuminates the desired ground object. If the synthetic aperture is "built" this long the resulting resolution, in theory, is half the length of the real antenna and the synthetic aperture radar is said to be "fully focussed." For a real antenna 4 meters long this would give an azimuth resolution of 2 meters, which would almost certainly be finer than desirable for a spacecraft system because of the vast quantity of data produced by such a fine resolution system. Thus it should be possible to average together some sizable number of the cells produced by the fully focussed processor. For the examples cited, 10 cells could be averaged together and give a 20 meter azimuth resolution.

Another way to achieve the same result involves a simpler digital processor. Portions of the available synthetic aperture are processed separately, the results stored until all processing is done, and then combined. Each subaperture has a length appropriate to the desired resolution. Thus, for the example cited 10 such subapertures would be possible. Figure 12 illustrates a system with 5 subapertures. The synthetic beam is squinted ahead for subapertures 1 and 2 and behind for subapertures 4 and 5. It is directly to the side only for subaperture 3. If only one subaperture were processed, the desired resolution (20 m for the example) would be obtained but the image would be highly speckled. The mean-to-standard deviation ratio for the image is improved by the square root of the number of independent samples averaged. Thus for the example in Figure 12, it is improved by the  $\sqrt{5}$  and for the example cited above with 10 subapertures the "speckle factor" (mean-to-standard deviation ratio) is improved by  $\sqrt{10}$ .



Figure 13 illustrates the effect of Rayleigh-distributed scattering for a monochromatic radar with subaperture processing and shows improvements due to averaging. Although the mean scattering cross section of the image shown as (1) in the figure is a constant on each side of the boundary the speckle is severe. (2) shows results for a processing technique giving an improvement of the  $\sqrt{5}$ . By using two separate channels with quadrature returns for each subaperture, the improvement in speckle is increased by  $\sqrt{2}$  and the result is shown in (3) in the figure. Clearly more averaging is needed to measure the mean value accurately, but the speckle has been greatly reduced by averaging.

As discussed earlier, the spacecraft radar system design involves a resolution-grey scale trade-off. To achieve better grey scale uniformity than that illustrated in the figure, resolution must be poorer (more subapertures must be used). If resolution is the important factor (as it may be for some types of problems), grey scale uniformity must suffer.

A projection was made for an electronic digital processor for spacecraft radar using assumptions about the possible electronic components available in 1975. Complementary-MOS devices are now becoming available, and it was assumed that availability of these devices would permit a storage unit with 10  $\mu$ W a bit. Subject to this assumption, the postulated radar is shown in Table III. Such a system is essentially that described in the example in the preceding paragraphs; it uses 10 subapertures rather than the 5 shown in Figure 12 and 13.

The average transmitter output power is 60 watts. The assumed transmitter draws a good deal more power from the spacecraft than 60 watts, however, and it transmits a high peak power probably in the 100's of kilowatts. The total drain for such a system, exclusive of the processor, may well exceed 300 watts. Nevertheless the total power consumption of processor and radar system would be well under 1 kW.

Such a system does not use panchromatic averaging. Panchromaticity would increase the power requirement significantly. Added center frequencies would also increase the power requirement but frequencies below 10 GHz could be added with less of a penalty than higher frequencies.

#### OPTIMUM DEPRESSION ANGLES FOR RADAR GEOLOGY<sup>4</sup>

The proper depression angle for a radar system depends upon the geometry of the terrain being imaged. In high mountains the phenomena of radar layover and shadowing make certain angles far more desirable than others. In flat country geologists would like to emphasize small

topographic differences and relatively small depression angles are called for. Application to agriculture, on the other hand, may call for larger depression angles.

Figure 14 shows the effect of different viewing angles across the swath of an imaging radar when a triangular mountain is to be imaged. At points 1 and 2 some layover exists; that is, the top of the mountain appears to be closer to the radar than the bottom, which in fact it is; but its ground distance is further than that to the bottom of the mountain. Thus, thought of in terms of a map, a radar picture is in error at these points because the top of the mountain appears in the wrong place. At angle 3 on the figure some shadow exists, and the front face of the mountain all appears at the same range even though it occupies different positions on the underlying plane. In 4 the shadow has been increased but the top and bottom of the mountains appear on the image in their correct ground-plane order, although with incorrect spacing. We are indeed fortunate that most mountains do not look like this one!

Figures 15 and 16 illustrate a map and a radar image of the same area in Alaska. This is a quite mountainous region and the result is considerable distortion at the inner edge of the image and considerable shadowing at the outer edge. Close examination of the image and the map illustrates the point.

Figure 16 was made with a "true ground range" presentation on the radar. With this type of presentation, the slant range measured by the radar is transformed prior to recording with a factor that would remove the distortion in a slant range presentation if the ground were flat. When the ground is mountainous, the net effect of the "true-ground-range" presentation is to make the image appear even more distorted than the slant-range image. The mountain peaks at the inner edge of Figure 16 show this point. In the "true-ground-range" presentation differences in slant range at the inner edge of the image are accentuated. When these are due to differences in height rather than to differences in distance along the ground this accentuates the height distortion as shown. Thus the use of "true-ground-range" presentation, while very helpful in flat terrain, may in fact be disadvantageous in mountains.

Some of these effects can also be seen in Figure 17 where two look angles about  $45^\circ$  apart were used to image the same area. In this case the slant-range presentation is used and the mountains in the near range do not appear as distorted as in Figure 16. Nevertheless they really are distorted and the differences are quite apparent by close examination of the two images. Furthermore, the effect of shadowing in the far range is severe. Some of the regions for which image A provides information are shadowed in B and conversely.

The study investigated the optimum radar depression angle for areas with different amounts of topographic expression. These results were compared with maps describing the relief in different parts of the world and optimum radar depression angle maps were prepared for the world as illustrated in Figures 18 and 19.

A relatively narrow range of depression angles is appropriate for some types of terrain. A radar system carried in an aircraft at moderate altitudes produces an image with a wide range of depression angles (typically from  $10^\circ$  or less to  $65^\circ$ ). A comparable radar carried at higher altitude, either in a very high altitude aircraft or preferably in a spacecraft, can achieve the same swath width but have a much narrower range of depression angles. Thus, the effects of layover and shadow from one side of the image to the other should be about the same, and the appropriate depression angle can be selected for the particular terrain being imaged. Consequently, it appears that radar should be used in spacecraft because this proper choice of the depression angle is permitted for the particular problem being studied; whereas such a choice is possible for an aircraft only over a very narrow swath.

#### MODIFICATION OF THE DPD-2 IMAGING RADAR

The modified DPD-2 imaging radar carried on the NASA/MSC aircraft was further modified at our request during the year to permit use of both real-aperture and synthetic-aperture imaging. Previous to this modification it had only had unfocussed synthetic-aperture capability. Little or no averaging is possible even though the resolution is relatively poor, as the unfocussed technique does not take full advantage of the available time that the target is illuminated by the real aperture of the antenna. It amounts to performing an aperture synthesis over one of the subapertures shown in Figure 12, and a relatively short one at that.

The DPD-2 has been flown in the Arctic within the past year by the U. S. Coast Guard; the version used for that purpose was a real aperture system. A logarithmic IF amplifier desirable for a real-aperture system had been removed from the military version when the system was converted for use by MSC. Although the military system used this amplifier for a different purpose, it was easy to replace the amplifier in the system and provide the capability of producing both real-aperture and synthetic-aperture images with the system at MSC. The results with the real aperture system are encouraging as indicated in the subsequent paper by Dr. Morain, although some problems still remain to be worked out for the particular unit at MSC.

A flight made during the year over the Garden City, Kansas, agricultural test site permitted comparison of the images with the real-

and synthetic-aperture systems on the MSC aircraft.<sup>5</sup> Figure 20 shows sample images from the two systems for the same terrain. Resolution on the synthetic-aperture system is considerably better than that for the real aperture, but the quality of the image is not as good because of the speckle in the grey scale due to insufficient averaging. The real-aperture system averages enough independent samples to produce a much better grey scale and consequently to permit better agricultural analysis.

For areas with smaller target units the synthetic-aperture system may be needed because of its finer resolution; however, for areas like that at Garden City, the real aperture system appears to give a better result because of improved averaging.

Other items in Table II will not be discussed at this time but reports are available.

### CONCLUSION

Demonstration that a spectral response across an octave bandwidth in the microwave region is as variable as the comparable response in the visible and infrared region is a major mile-stone and indicates the potential of polypanchromatic radar systems is analogous with that of color photography.

Averaging of the returns from a target element appears necessary to obtain a grey scale adequate for many earth-science applications of radar systems. This result can be obtained either by azimuth averaging or by the use of panchromatic techniques (range averaging). Improvement with panchromatic techniques has been demonstrated both with a land-based electromagnetic system and with an ultrasonic simulator. The advantage of the averaging achieved in azimuth with the real-aperture version of the DPD-2 when compared with the synthetic aperture version confirms the concept.

The study of optimum radar depression angles for geologic analysis leads to the conclusion that radars for geologic analysis should be carried in space or in very high altitude aircraft so that restricted ranges of depression angles can be used over relatively wide swaths. This is important because previous discussions have indicated that a radar could just as easily be carried in a moderate-altitude aircraft. This is certainly true for some applications but it appears not to be true for geologic analysis and other earth observation type analyses that must be conducted in hilly and mountainous terrain.

Other work at The University of Kansas is reported here by Kelly and by Morain. The interaction between the radar engineers, data processing engineers, and earth scientists at The University of Kansas is, we believe, most important. Each group benefits from the others comments, and the resulting combination is stronger than its individual components.

REFERENCES

1. Waite, W. P., "Broad-Spectrum Electromagnetic Backscatter," Ph. D. Thesis, University of Kansas, 1970, Also published as CRES Technical Report 133-17, August, 1970.
2. Thomann, G. C., "Panchromatic Illumination for Radar; Acoustic Simulation of Panchromatic Radar," Ph. D. Thesis, University of Kansas, 1970, Also published by NASA/MSC as CRES Technical Report 177-11, August, 1970.
3. Gerchberg, R. W., "Synthetic Aperture Radar and Digital Processing," Ph. D. Thesis, University of Kansas, 1970, Also published by NASA/MSC as CRES Technical Report 177-10, September, 1970.
4. MacDonald, H. C. and W. P. Waite, "Optimum Radar Depression Angles for Geological Analysis," published by NASA/MSC as CRES Technical Report 177-9, August, 1970.
5. Thomann, G. C. and T. James, "Real-Aperture/Synthetic-Aperture Image Comparison," to be submitted to IEEE Letter, Trans. on Aerospace and Electronics, University of Kansas, 1971.

TABLE I

RADAR SYSTEM RESEARCH

FY70

UNIVERSITY OF KANSAS

OBJECT-SENSOR INTERACTION

THEORY

ROUGH-SURFACE COMBINED PHYSICAL OPTICS-PERTURBATION MODEL

VOLUME-SCATTER AND 2-ROUGH SURFACE THEORY

APPLICATION OF VOLUME SCATTER TO ICE AND SNOW

PHYSICAL OPTICS MODEL APPLIED TO OCEAN RADIOMETRY

EXPERIMENT

OCTAVE-BANDWIDTH SPECTRAL RESPONSE

ULTRASONIC SIMULATION

SOIL-MOISTURE DIFFERENCE INDICATIONS ON SLAR IMAGES-NEAR RANGE

OLD SNOW DISTINGUISHED FROM NEW

RESTUDY AND SUMMARIZE OCEAN SCATTEROMETER DATA

APPLY PATTERN RECOGNITION TO 1967 ICE SCATTEROMETER DATA

MISSION SUPPORT - 119(OCEAN), 126(ICE), 130 AND 133

(AGRICULTURE)

## TABLE II

## RADAR SYSTEMS

## POLYPANCHROMATIC DEVELOPMENT

4-8GHz TESTS

ULTRASONIC SIMULATION

THEORY OF IMPROVEMENT BY AVERAGING

## SPACECRAFT IMAGING RADAR STUDY

DIGITAL SYNTHETIC APERTURE PROCESSOR

OPTIMUM DEPRESSION ANGLES SPECIFIED

SYSTEM FOR 1975 FLIGHT-SPECIFICATIONS

## AIRCRAFT IMAGING RADAR

SUPPORT FOR REAL-APERTURE MOD. TO DPD-2

POLYPANCHROMATIC RADAR SPECIFICATIONS

COMPARISON OF AVERAGING IN REAL AND SYNTHETIC-APERTURE RADARS

## SCATTEROMETER SYSTEMS

13. 3GHz SCATTEROMETER SYSTEM ERROR ANALYSIS

SCATTEROMETER DATA PROCESSING REQUIREMENTS

IMPROVED SCATTEROMETER CALIBRATION TECHNIQUES



TABLE III

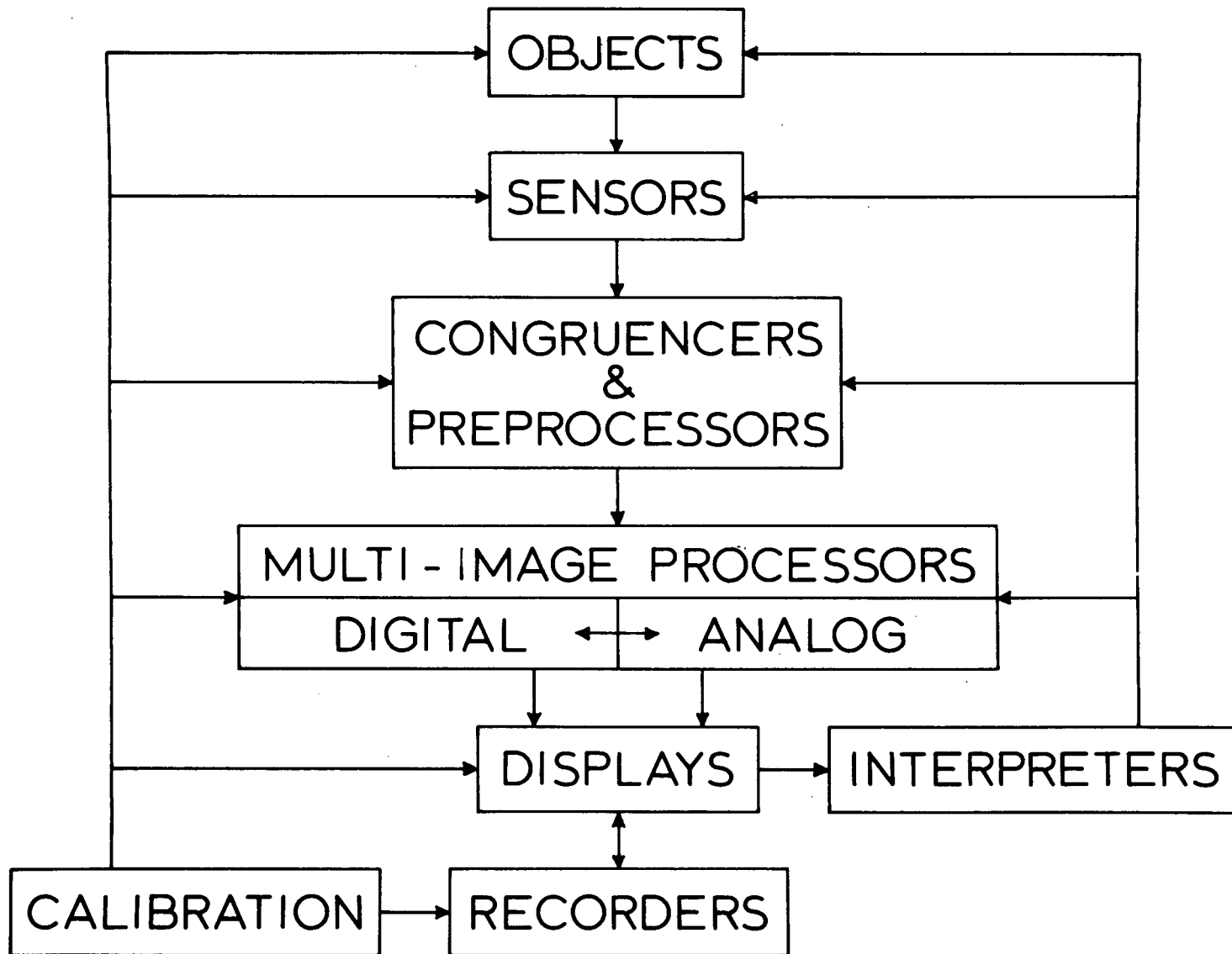
PROJECTED 1975 SYNTHETIC APERTURE  
SPACE RADAR WITH DIGITAL PROCESSING

- RADAR PARAMETERS -

SWATH	40km	ANTENNA LENGTH	4m
ALTITUDE	1080km	FREQUENCY	10 GHz
INCIDENT ANGLE	30°	RESOLUTION	30m
σ° RANGE	-20 TO +20 dB	AV. TRANS. POWER	60w

- PROCESSOR -

SUBAPERTURES	10	TOTAL POWER	200w
TOTAL STORAGE	4.8 MBITS	VOLUME	0.15m <sup>3</sup>
POWER TO STORAGE	48w	WEIGHT	30kg
(10μW/ BIT)			



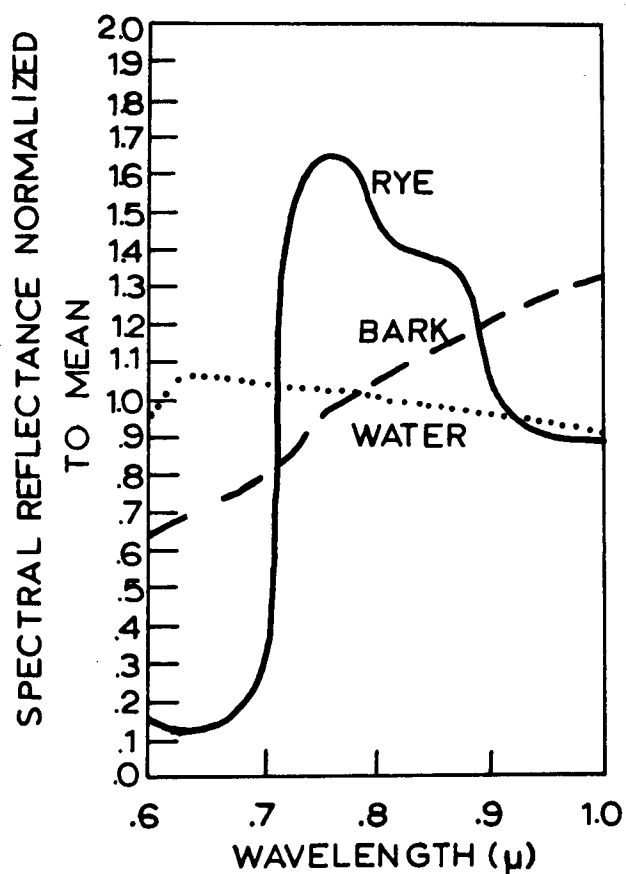
513

# THE REMOTE SENSING SYSTEM

Figure 1

# SPECTRAL RESPONSES OF OBJECTS OVER OCTAVE BANDWIDTHS

Optical-IR Region



Microwave Region

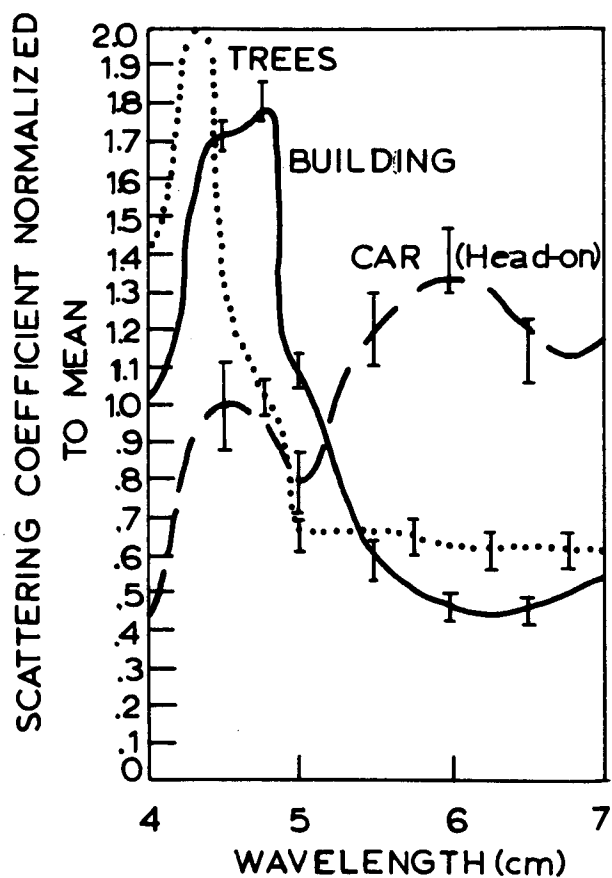
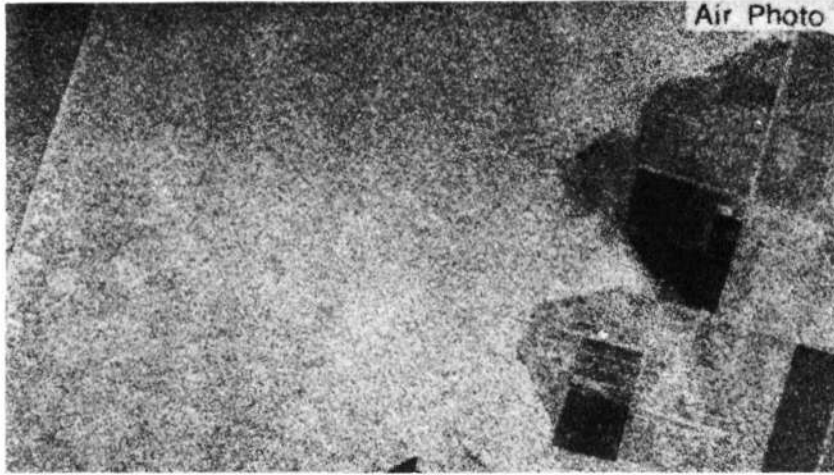


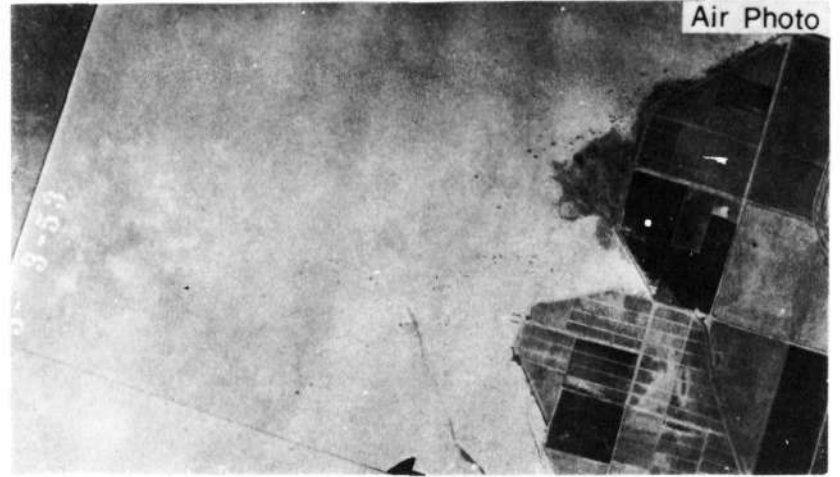
Figure 2

515

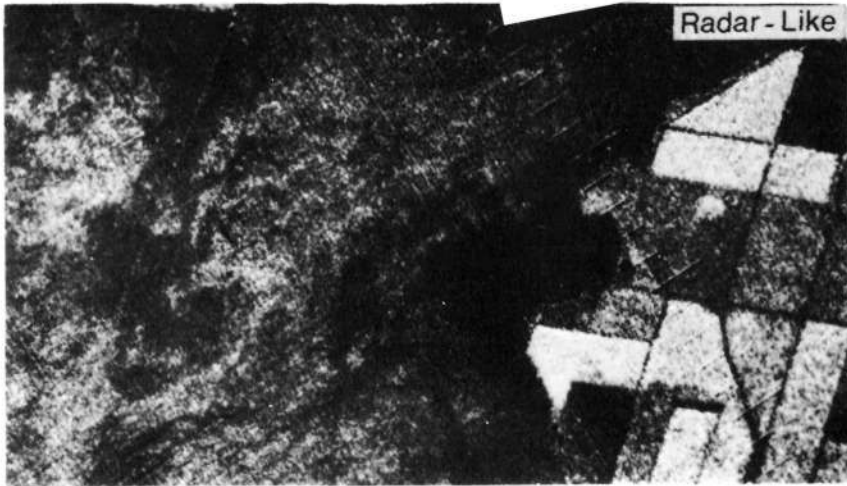


MONOCHROMATIC

NOT REPRODUCIBLE



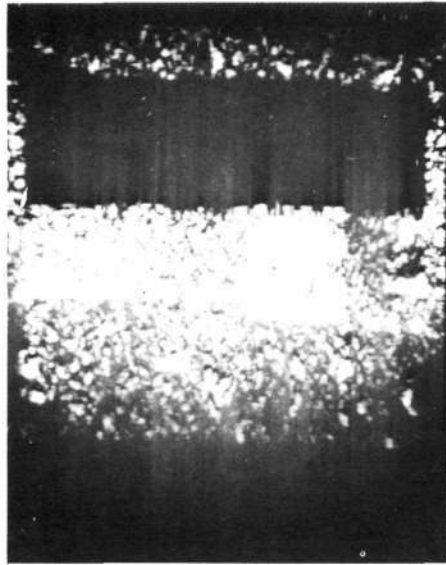
PANCHROMATIC



MONOCHROMATIC

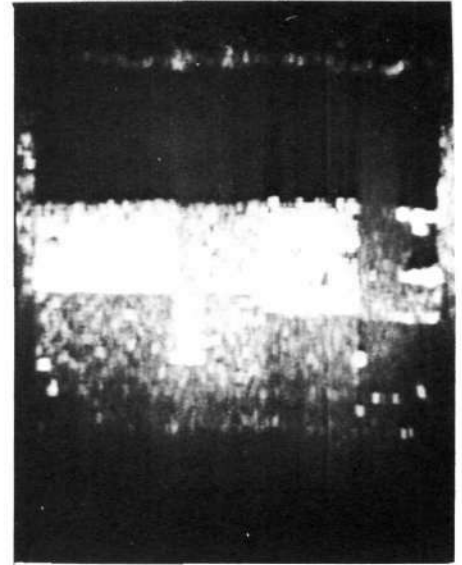
Figure 3

COMPARISON OF MONOCHROMATIC AND  
PANCHROMATIC AIR PHOTOS WITH  
MONOCHROMATIC RADAR IMAGE.



MONOCHROMATIC IMAGE

F = 1700 kHz



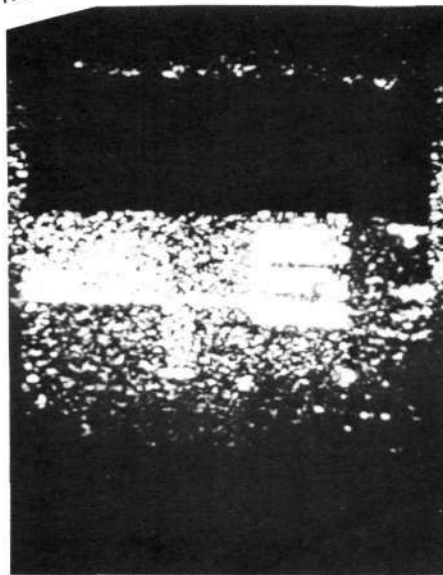
PANCHROMATIC IMAGE

F = 1200 - 2000 kHz

NOT REPRODUCIBLE

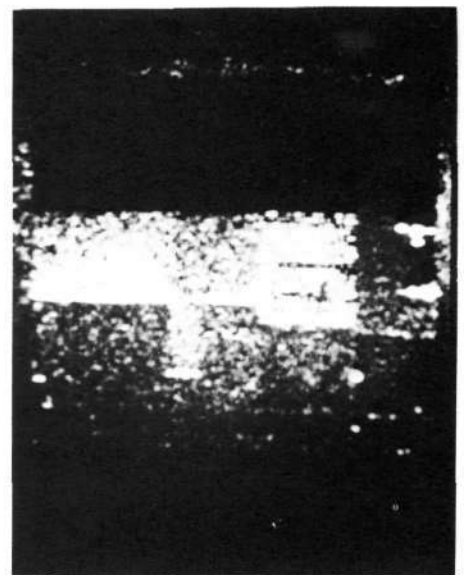
$\tau = 20 \mu\text{SEC.}$

$\theta \approx 30^\circ$



MONOCHROMATIC IMAGE

F = 1600 kHz



PANCHROMATIC IMAGE

F = 1200 - 2000 kHz

$\tau = 9 \mu\text{SEC.}$

$\theta \approx 31^\circ$

Figure 4

ACOUSTIC SIDE-LOOKING RADAR IMAGES OF AGRICULTURAL MODEL DEMONSTRATING IMPROVEMENT OF SENSING WITH PANCHROMATIC ILLUMINATION.

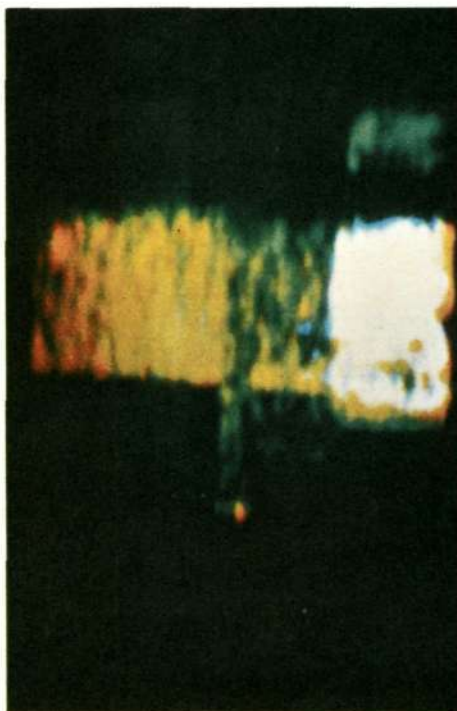
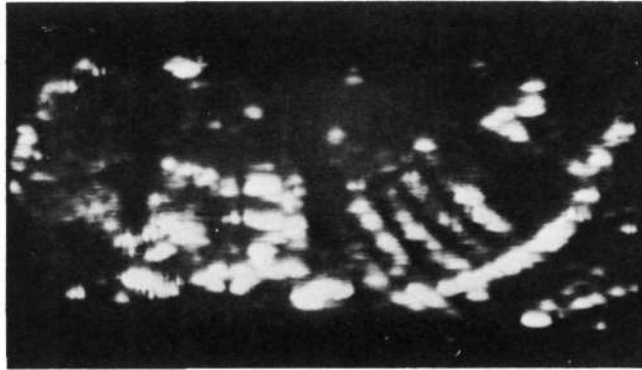
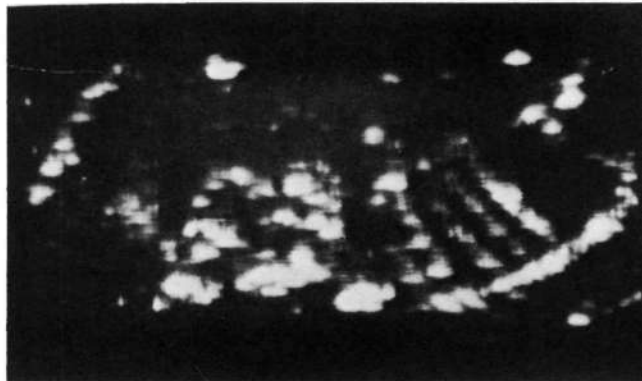


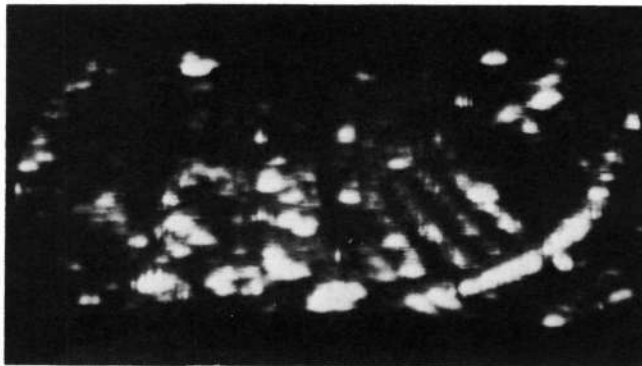
Figure 5. Ultrasonically simulated polychromatic radar image. Different colors indicate different materials distinguished by their spectral response.



(a)  $f = 6.00$  GHz

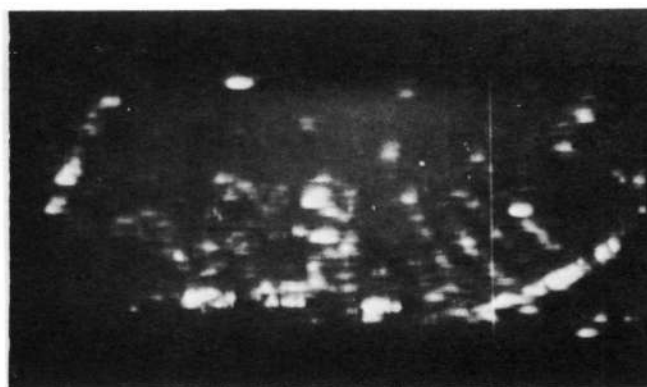


(b)  $f = 5.95$  GHz

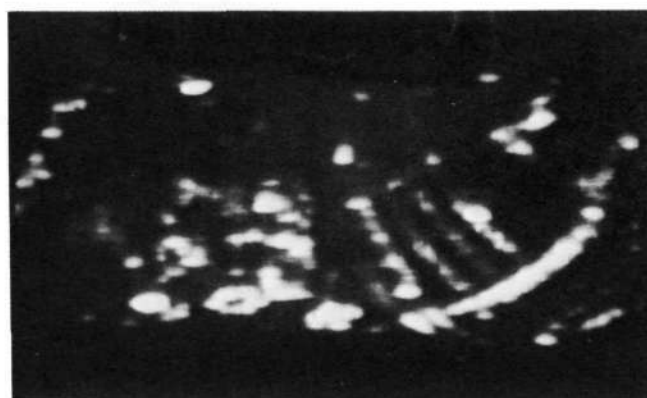


(c)  $f = 6.05$  GHz

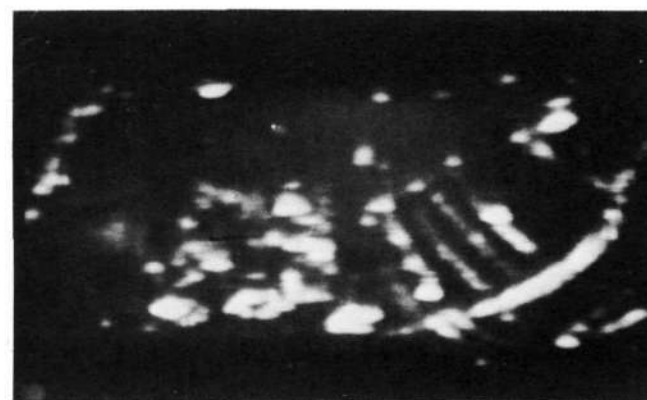
Figure 6. Monochromatic images taken at slightly different frequencies



(a) Monochromatic  $f = 6.00$  GHz



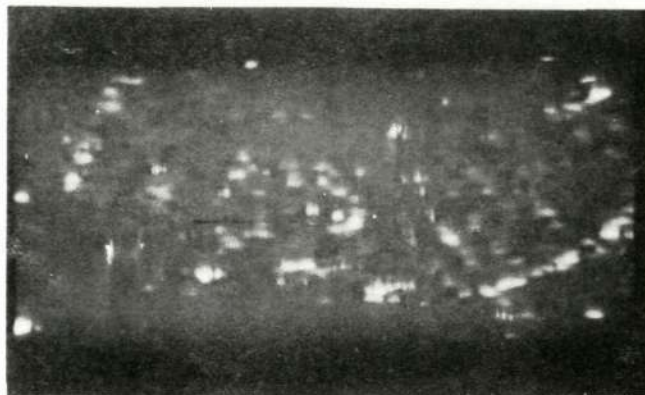
(b) Panchromatic  $f = 6.00 \pm 0.25$  GHz



(c) Panchromatic  $f = 6.00 \pm 0.50$  GHz

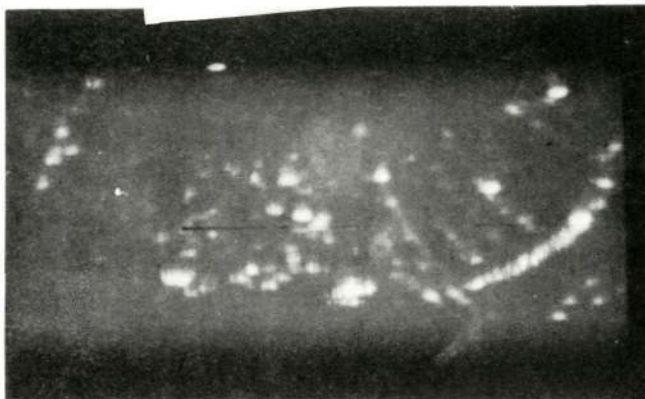
Figure 7. Comparison of monochromatic and panchromatic images



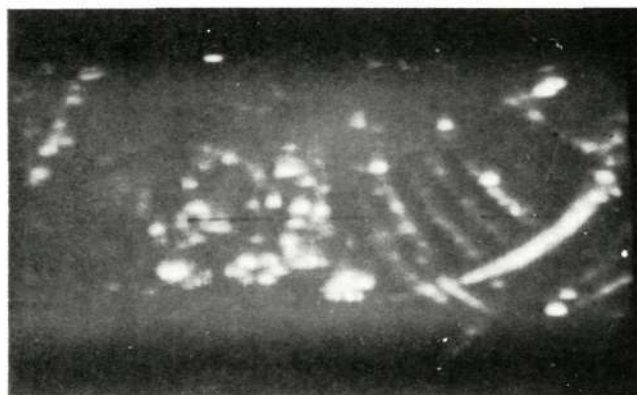


(a) Monochromatic  $f = 7.50$  GHz

NOT REPRODUCIBLE



(b) Panchromatic  $f = 7.50 \pm 0.25$  GHz



(c) Panchromatic  $f = 7.50 \pm 0.50$  GHz

Figure 8. Comparison of monochromatic and panchromatic images

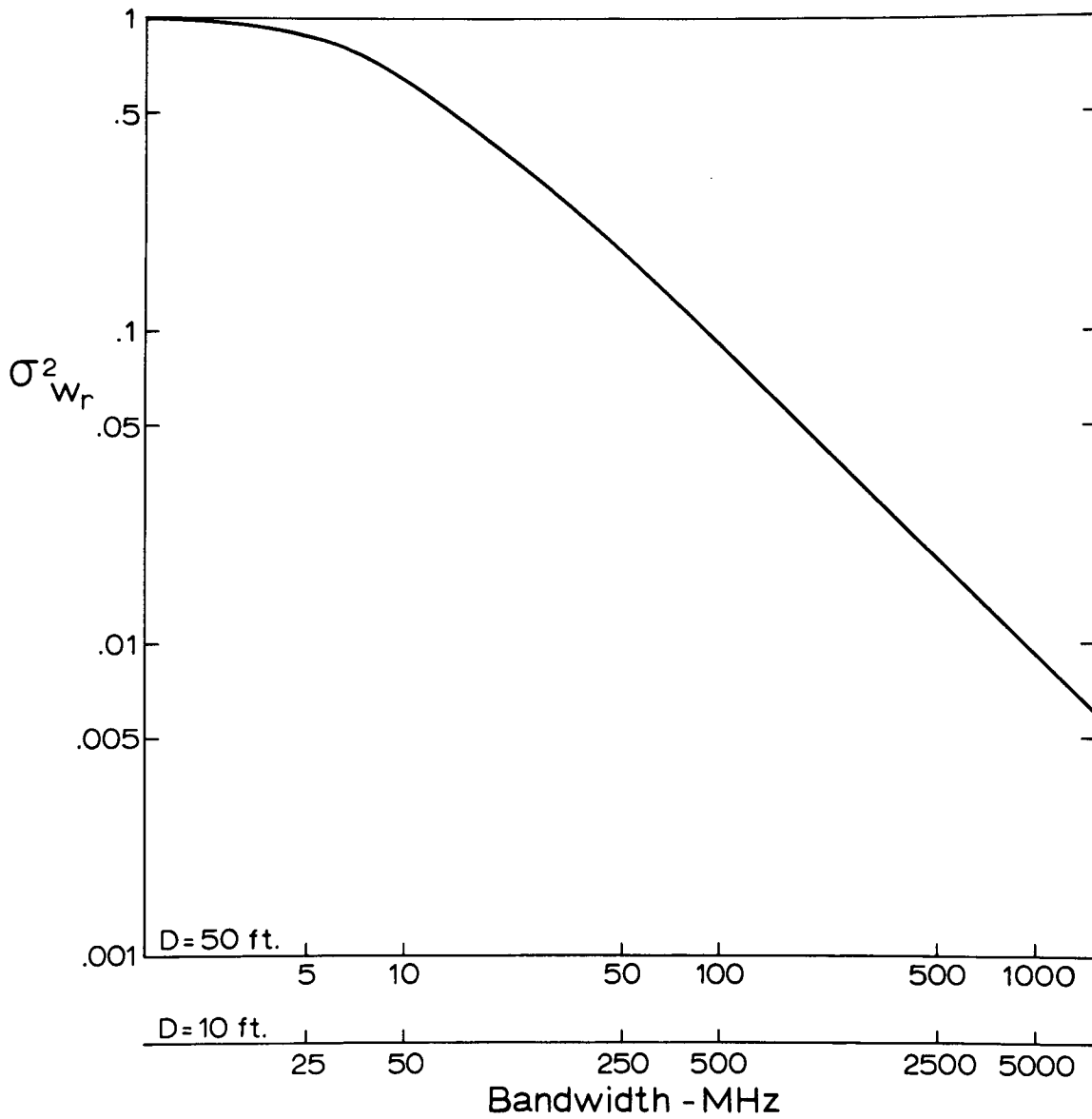


Figure 9. Variance of received power vs averaging bandwidth

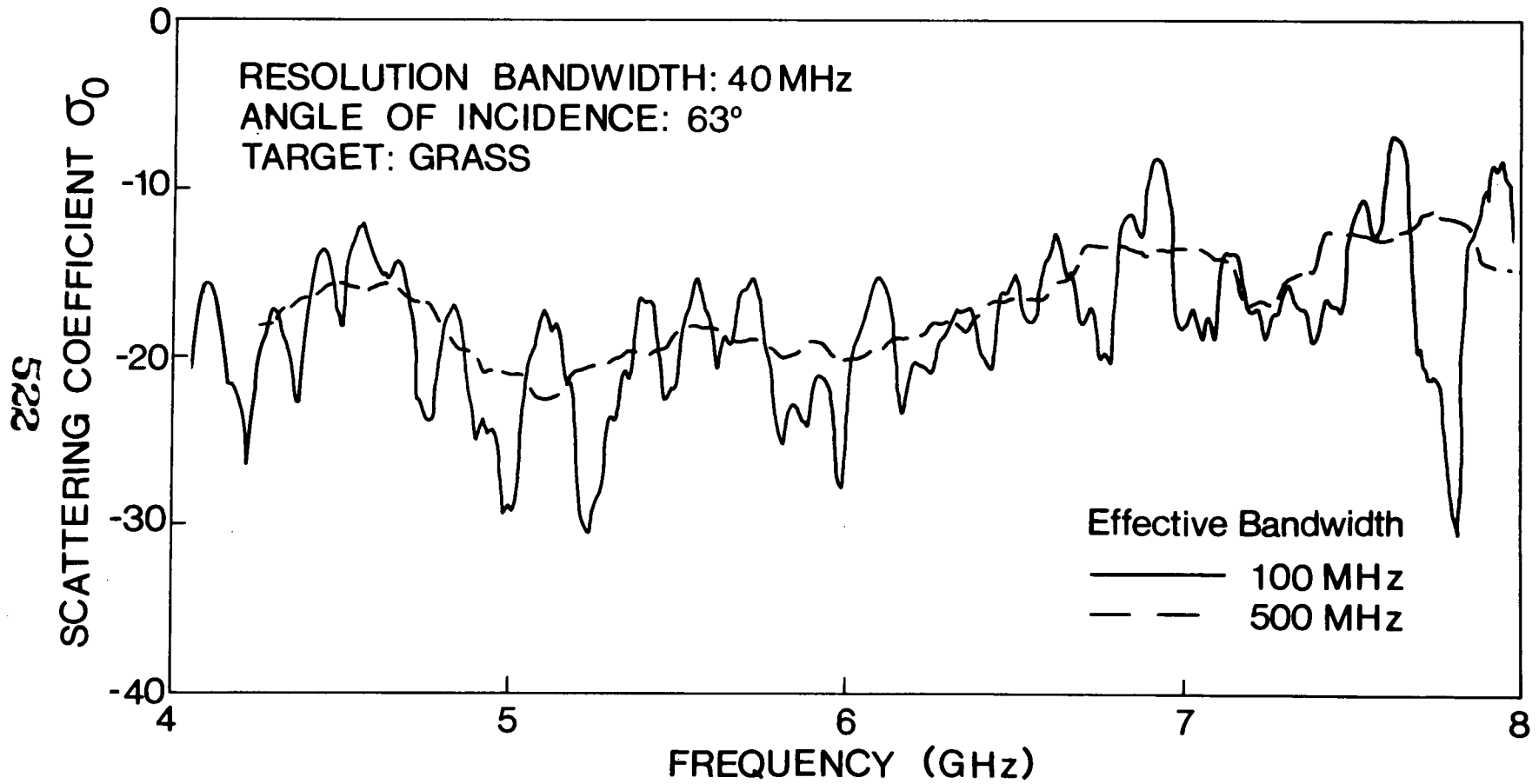
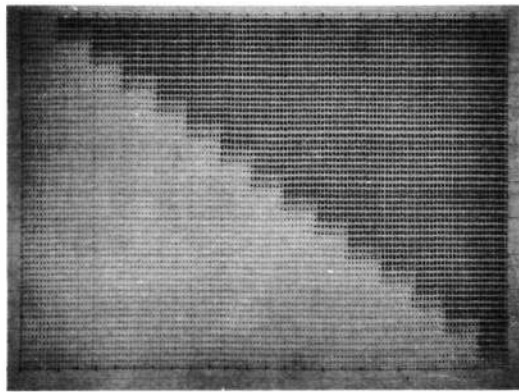
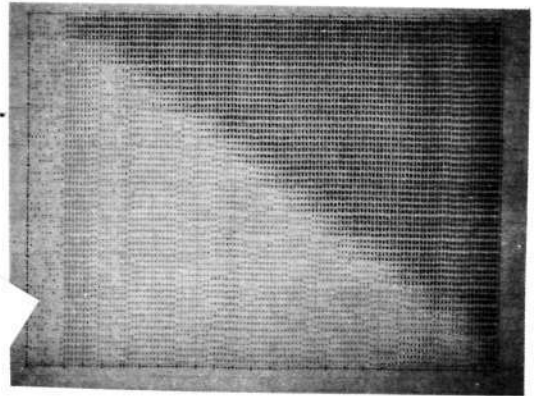


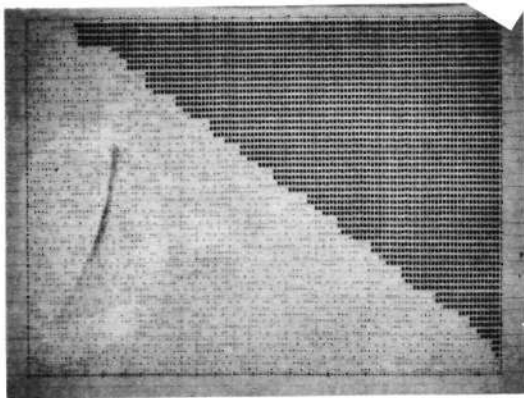
Figure 10. Example of fading that causes speckle in radar images



(1)



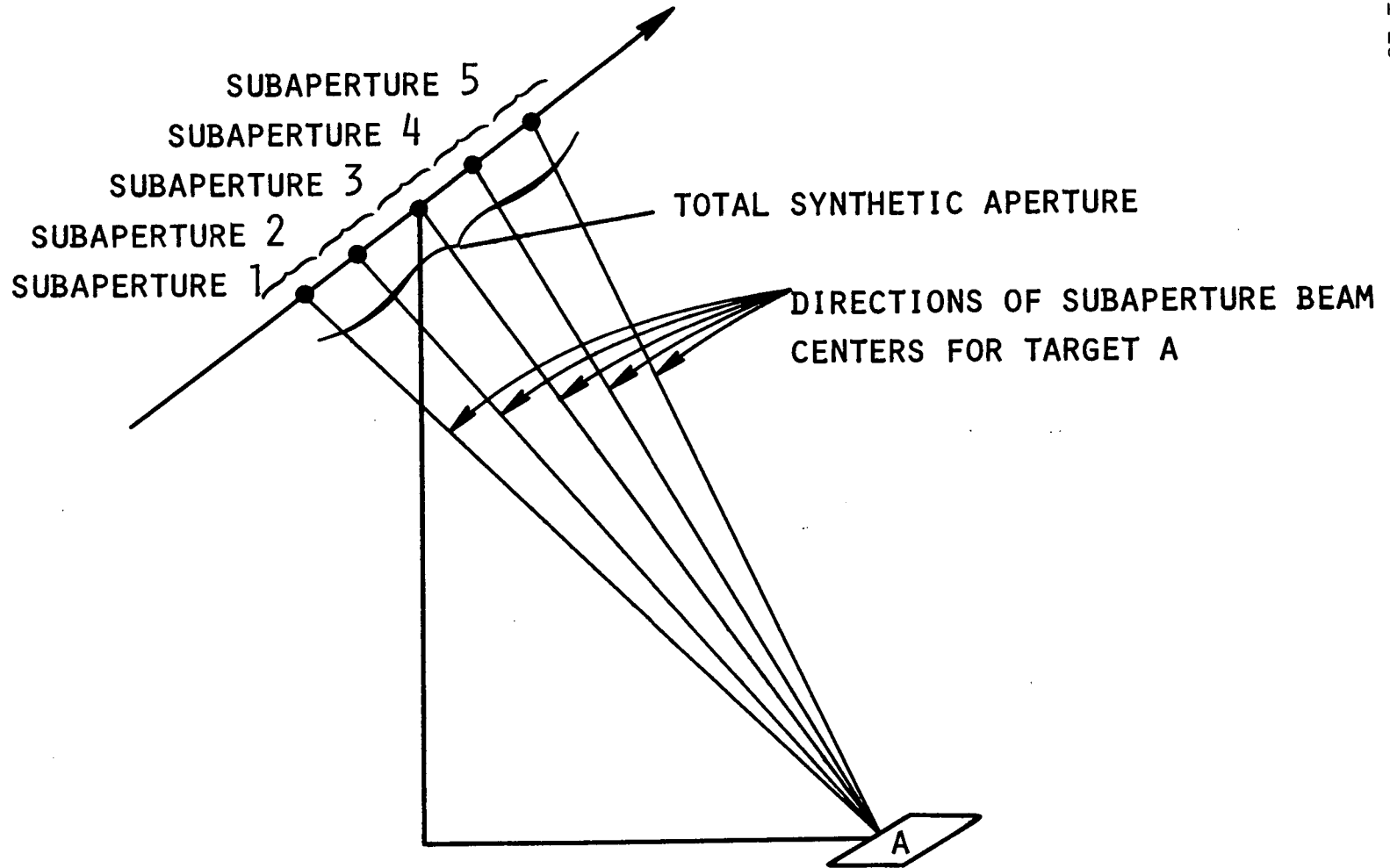
(2)



(3)

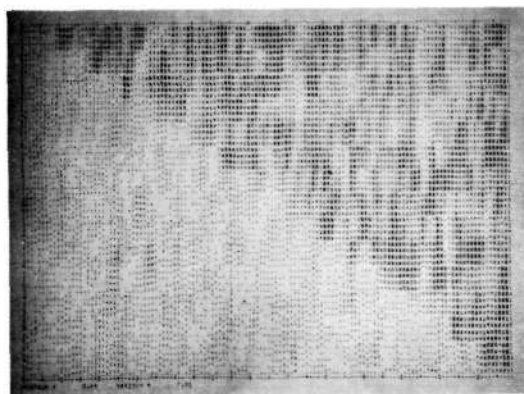
→  
Flight direction

Figure 11. Fully Focused synthetic aperture imaging over a boundary separating two fields whose non-statistically distributed scattering cross sections differ by 9.54 db. (1) "True" map of fields, (2) SAR image with dynamic range of display matched to image dynamic range, (3) SAR image with picture dynamic range much smaller than image range.

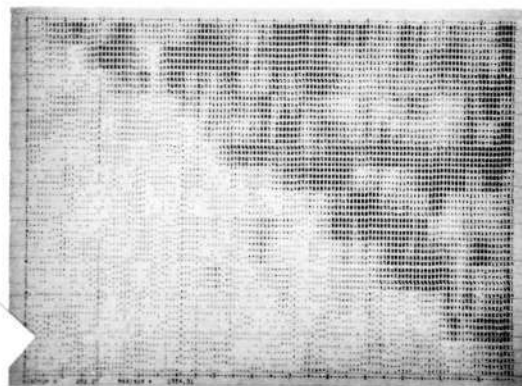


SYNTHETIC APERTURE DIVIDED INTO 5 SUBAPERTURES  
 THEORETICAL RESOLUTION 2.5X (REAL APERTURE)  
 IMAGE (MEAN/STD.DEV.) IMPROVED BY  $\sqrt{5}$

Figure 12. Use of multiple subapertures to improve grey scale

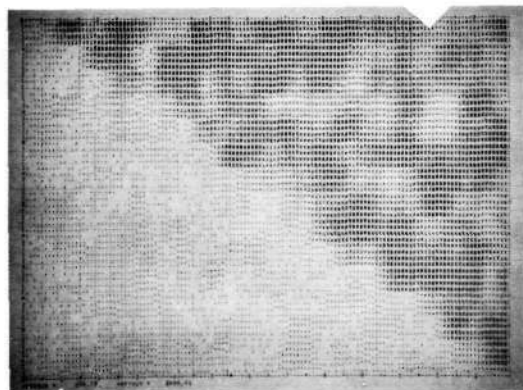


(1)



(2)

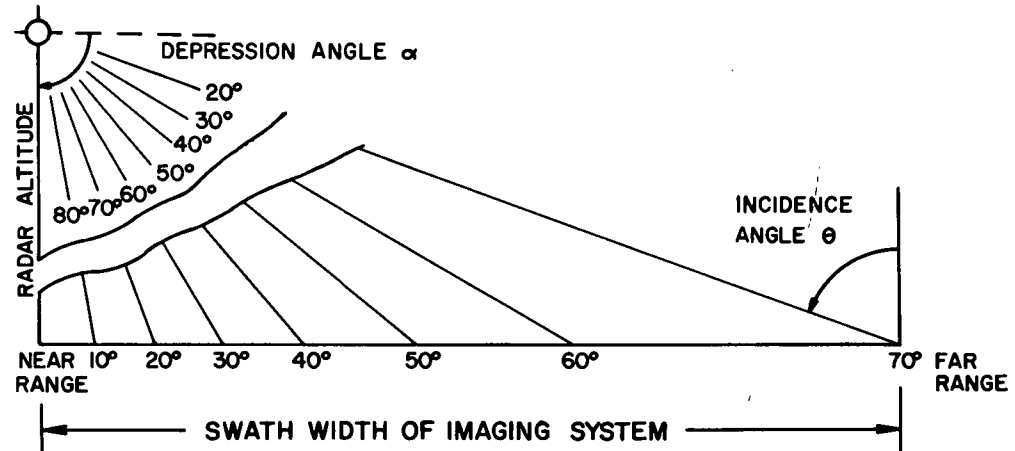
NOT REPRODUCIBLE



(3)

→  
Flight direction

Figure 13. (1) "True" map of Rayleigh distributed scattering cross sections for 2 fields whose differential scattering cross sections differ by 9.54 db —  $M/STD \approx \sqrt{3.6}$ ; (2) non-quadrature subaperture processing — 5 subapertures —  $M/STD \approx \sqrt{9.0}$ ; (3) quadrature subaperture processing — 5 subapertures —  $M/STD \approx \sqrt{18.0}$ .



526

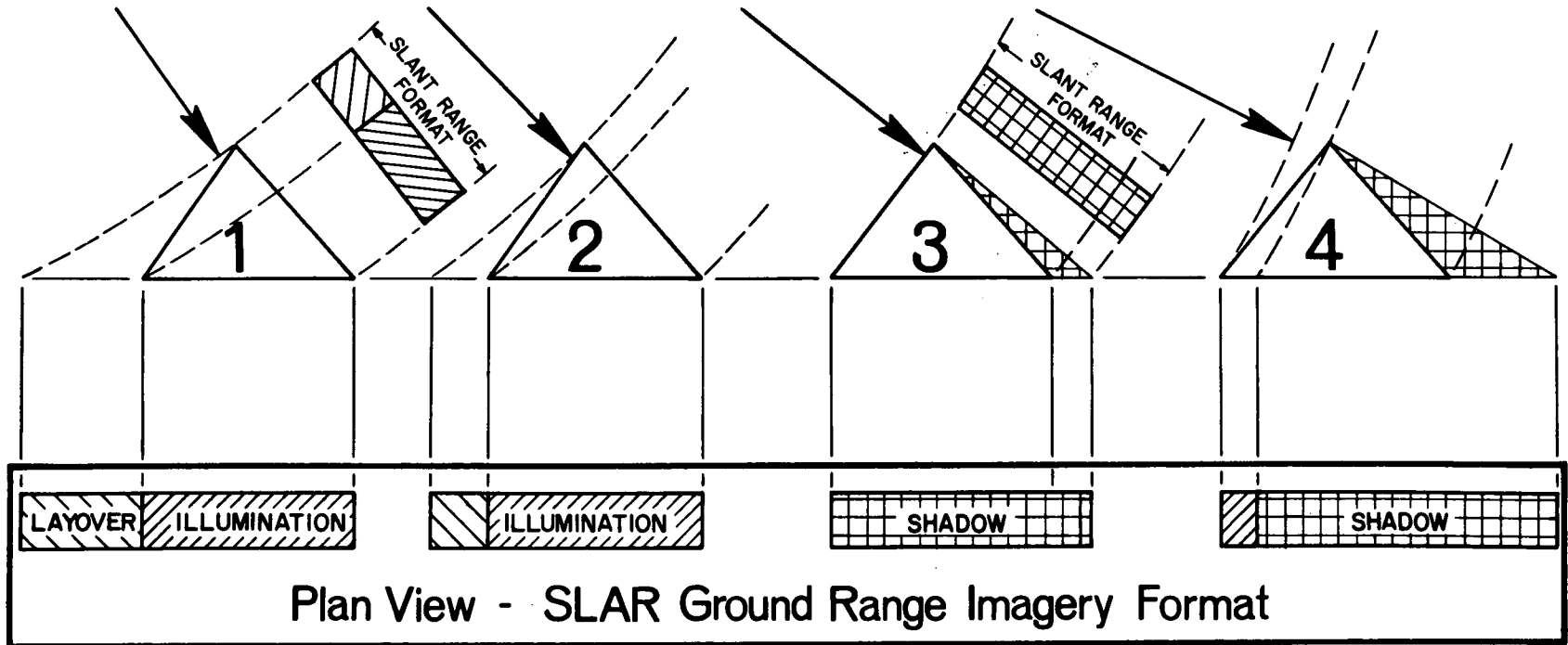
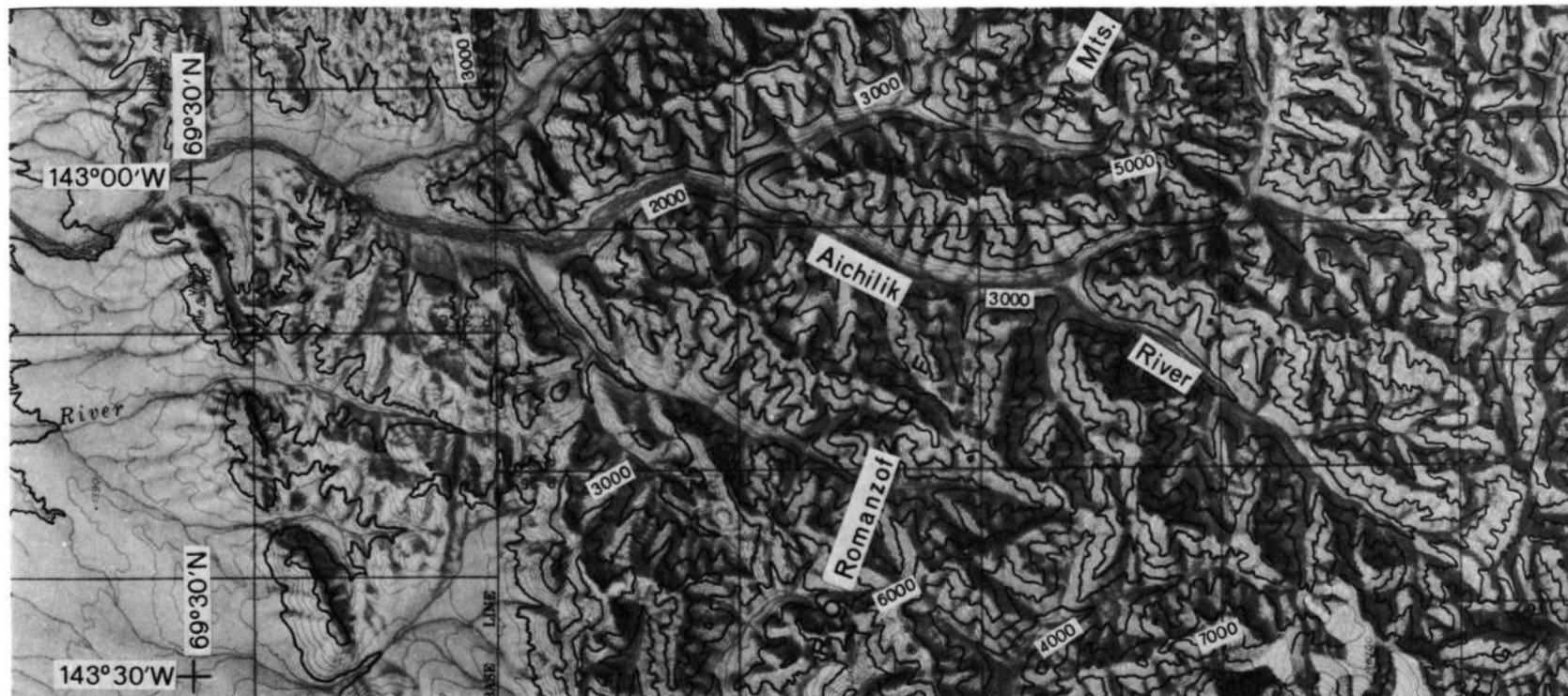


Figure 14. Radar shadow and layover vs angle

# AICHILIK RIVER AREA, ALASKA



527

NOT REPRODUCIBLE

Contour Interval 200 ft.  
Heavy Contour Interval 1000 ft.

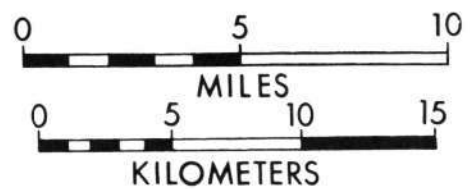
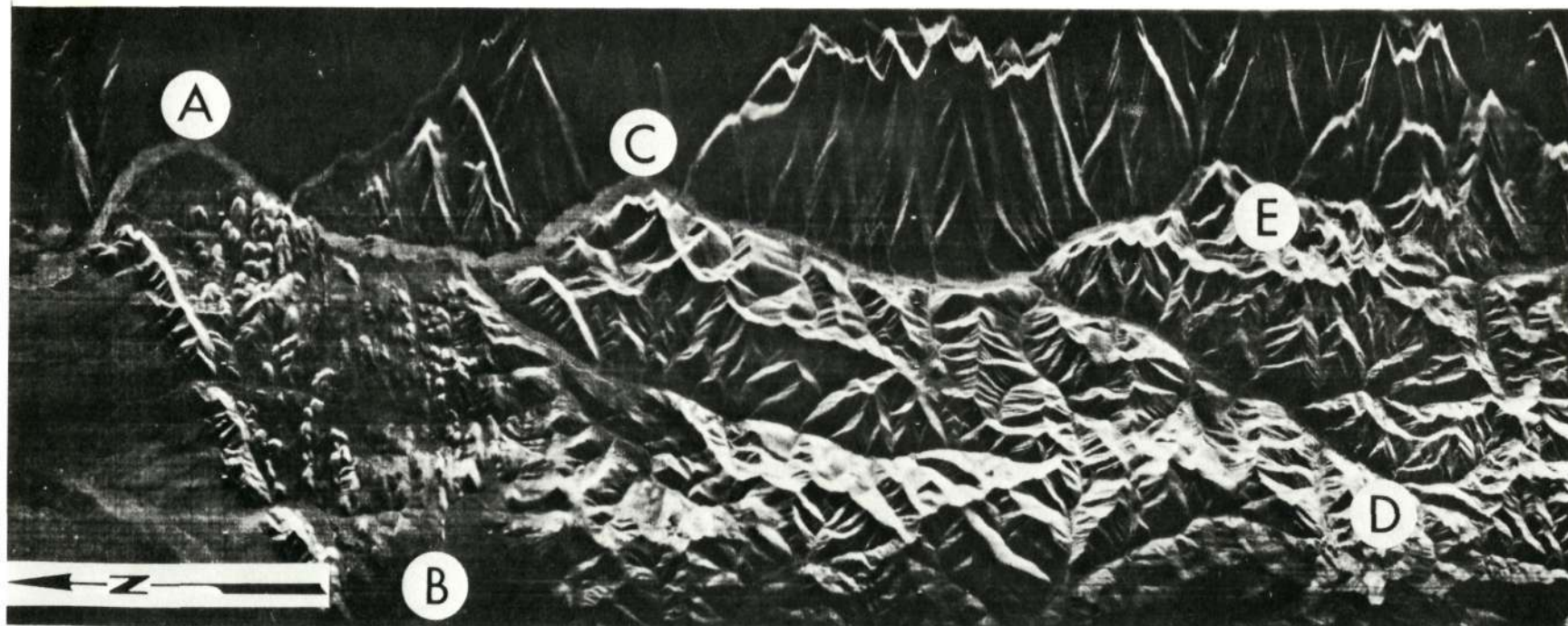


Figure 15. Contour map to go with figure 16





## GROUND RANGE RADAR



## AICHILIK RIVER AREA, ALASKA

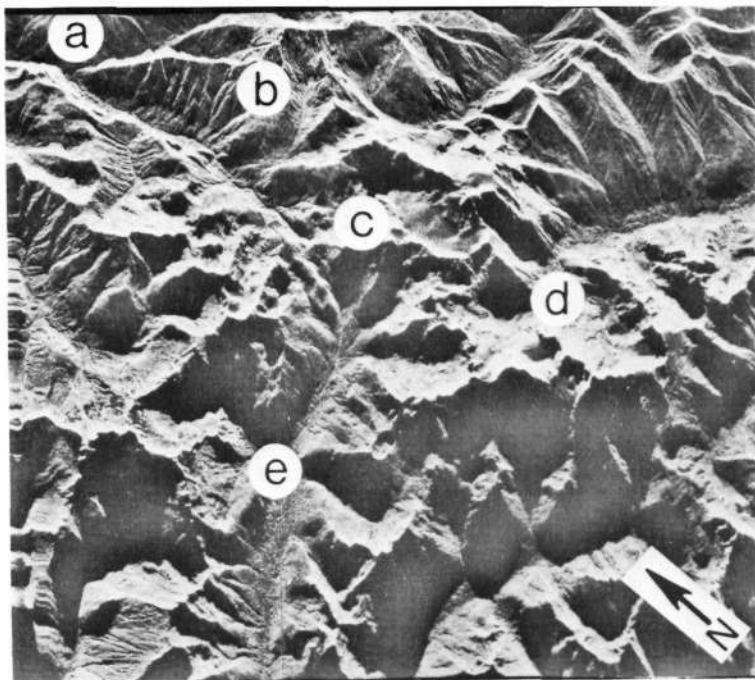
Figure 16. Example of "true ground range" presentation in mountainous terrain

# CASCADE GLACIER AREA, WASHINGTON



A

Near Range

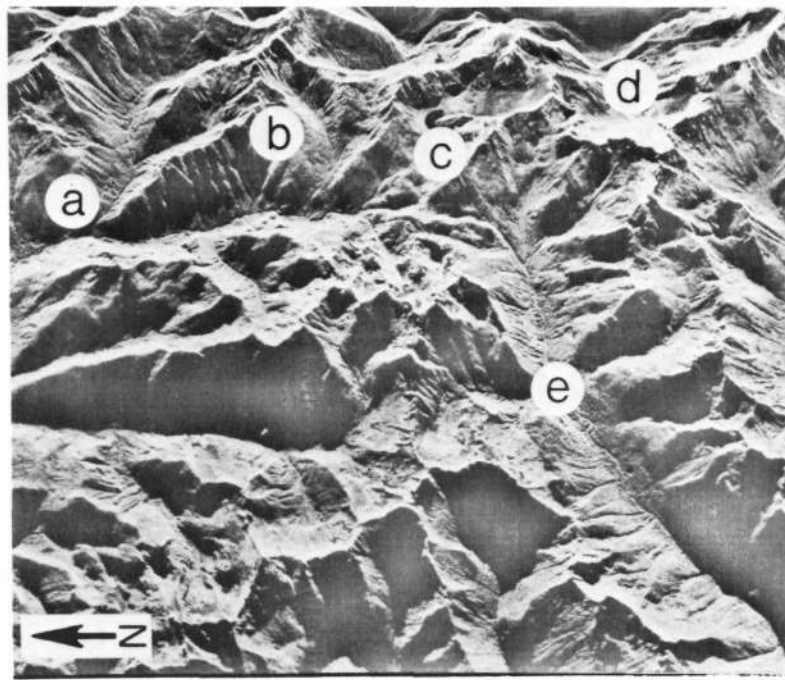


Far Range



B

Near Range



Far Range

0 5 Km

Approximate Scale

529

Figure 17. Illustration of radar layover and shadow using different look-angles for the same terrain and slant range presentation

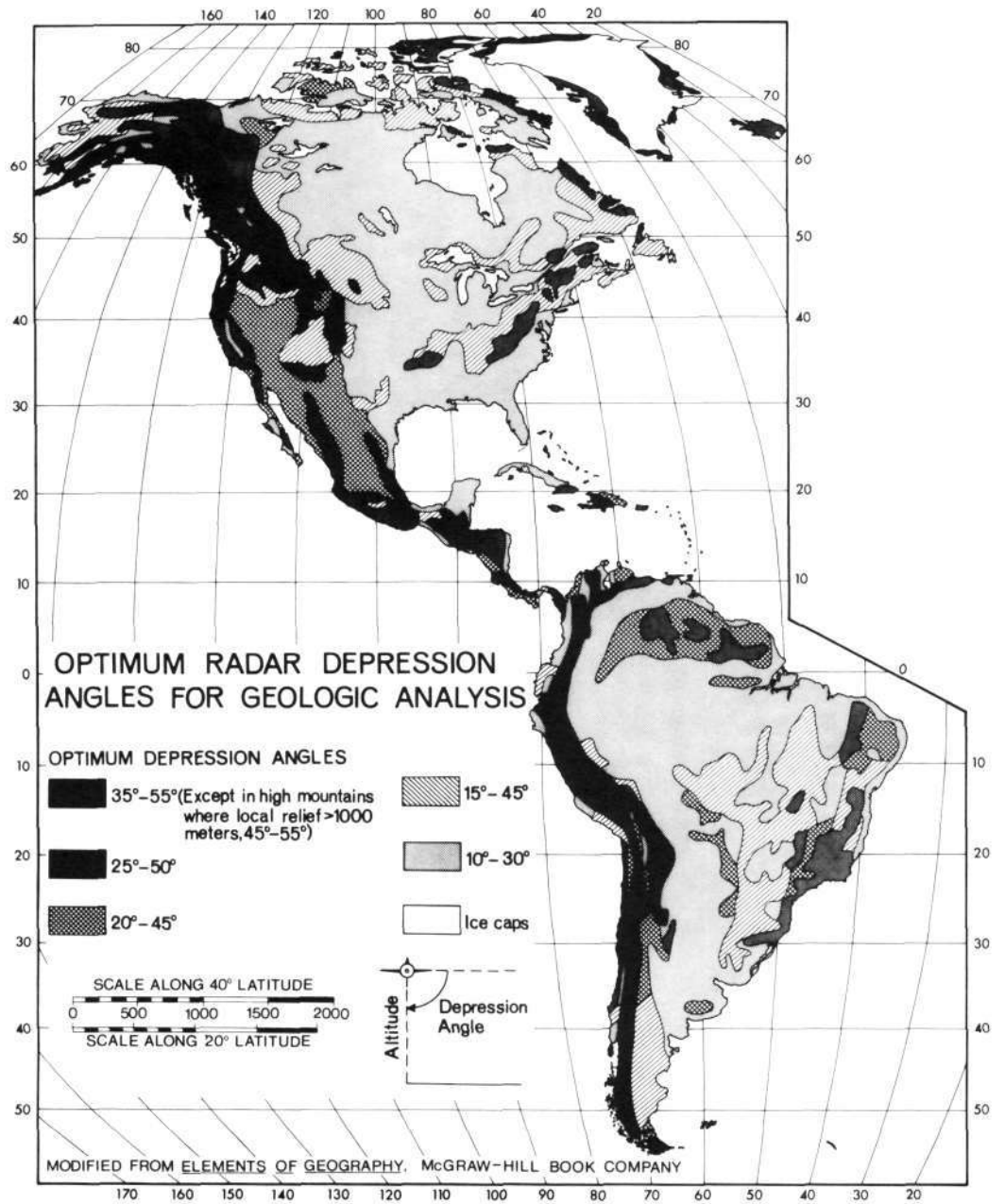


Figure 18

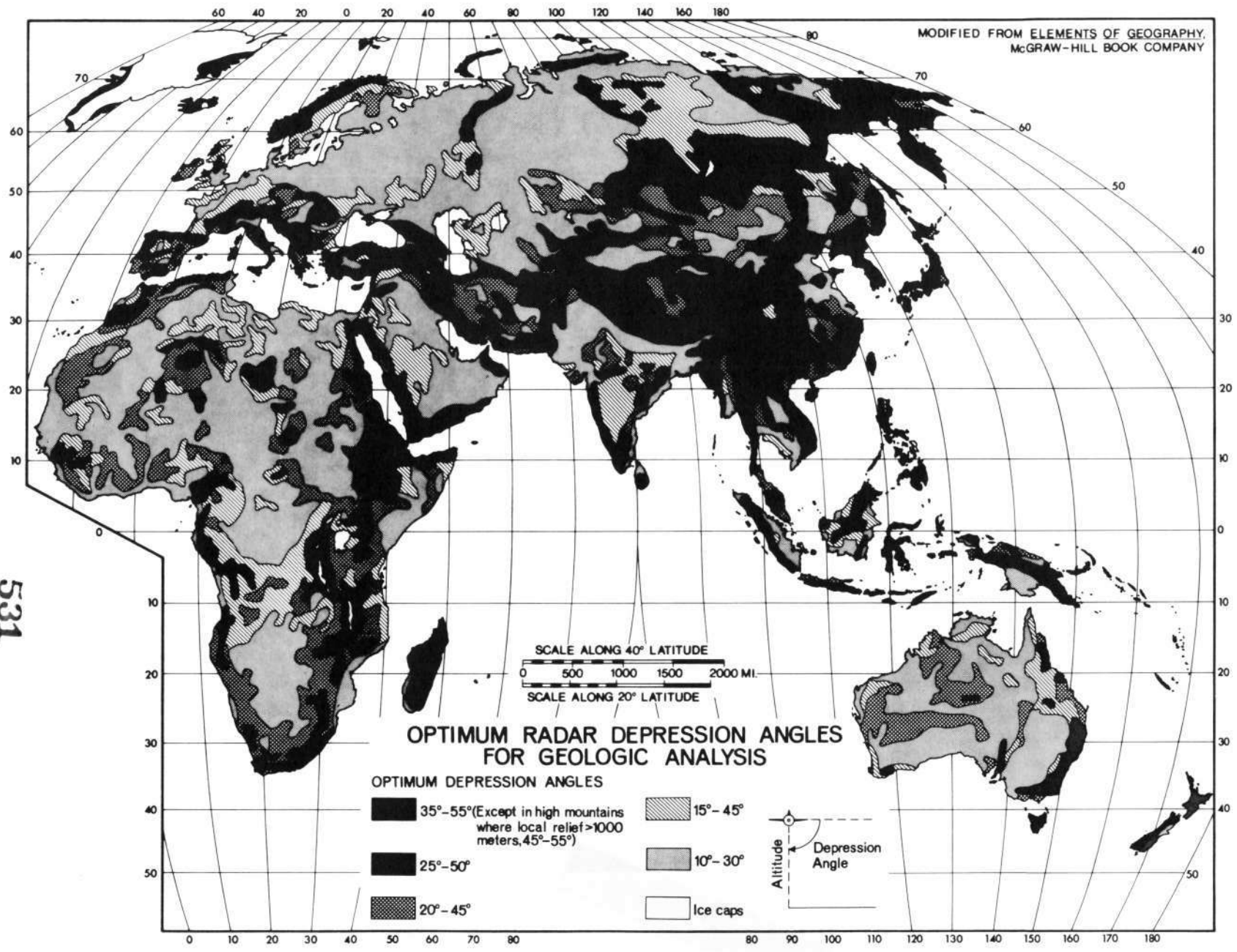
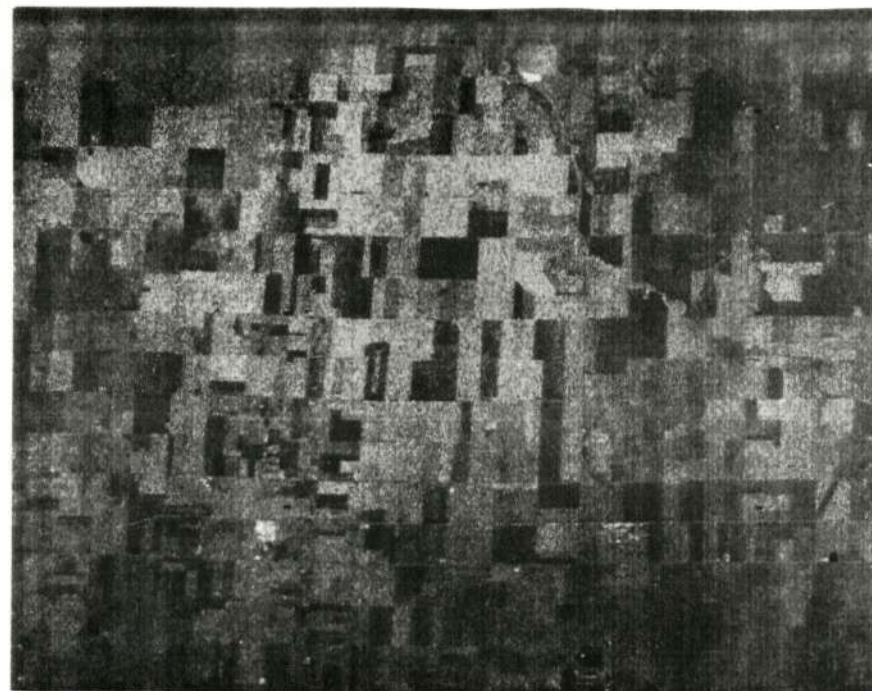
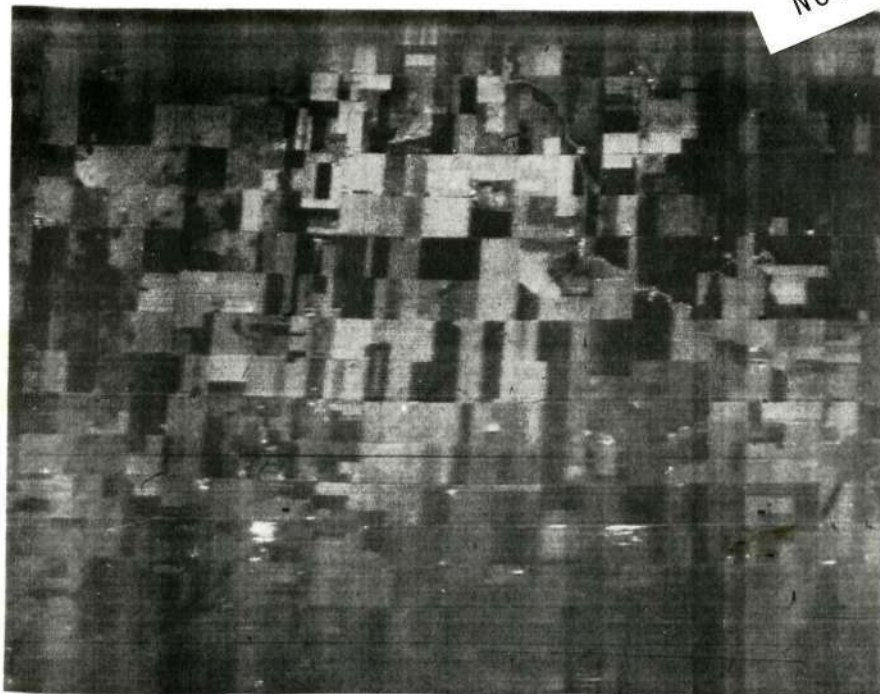


Figure 19

NOT REPRODUCIBLE



532

REAL

SYNTHETIC

41-36

COMPARISON OF REAL AND SYNTHETIC APERTURE DPD-2 IMAGES

GARDEN CITY, KANSAS 1970

Figure 20

## ADDENDUM

RESEARCH SUPPORTED BY NASA/MSC CONTRACT NAS 9-10261

Center for Research, Inc., University of Kansas

- \*"Multi-Image Pattern Recognition Ideas and Results," R. M. Haralick, Ph. D. Dissertation, CRES Technical Report 133-11, September, 1969.
- \*"A Novel Interface for a Man-Machine Display System," G. L. Kelly and J. A. Lucas, International Symposium on Man-Machine Systems, 8-12 September 1969, IEEE Conference Record No. 69C58-MMS.
- "Radar Sensing in Agriculture, A Socio-Economic Viewpoint," S. A. Morain, J. Holtzman, and F. Henderson, Presented at EASCON 1970. Also CRES Technical Report 177-14.
- "Cholame Area - San Andreas Fault Zone, California - A Study in SLAR," R. S. Wing, *Modern Geology*, vol. 1, 1970, pp. 173-186. Also CRES Technical Report 118-10.
- \*"Snowfield Mapping with K-Band Radar," W. P. Waite and H. C. MacDonald Remote Sensing of Environment, vol. 1, no. 2, 1970.
- \*"Effects of Roughness on Emissivity of Natural Surfaces in the Microwave Region," F. T. Ulaby and A. K. Fung, 1970 Southwest IEEE Conference.
- \*"Using Radar Imagery for Crop Discrimination: A Statistical and Conditional Probability Study," R. M. Haralick, F. Caspall, and D. S. Simonett, Remote Sensing of Environment, vol. 1, no. 2, 1970.
- \*"Interpretive and Mosaicking Problems of SLAR Imagery," A. J. Lewis and H. C. MacDonald, Remote Sensing of Environment, vol. 2.
- \*"The Apparent Temperature with Emissivity of Natural Surfaces at Microwave Frequencies," F. T. Ulaby, A. K. Fung, and S. Wu, March, 1970, CRES Technical Report 133-12.
- \*"Broad Spectrum Electromagnetic Backscatter," W. P. Waite, Ph. D. Dissertation, CRES Technical Report 133-17, 1970.
- \*"Worldwide Oceanic Wind and Wave Predictions Using a Satellite Radar Radiometer," R. K. Moore and W. J. Pierson, AIAA Technical Paper No. 70-310. Presented at AIAA Earth Resources Observations and Information Systems Meeting, March 2-4, 1970, Anapolis, Maryland.

- "Ground Return," Chapter 25 in: Radar Handbook, M. I. Skolnik, ed., R. K. Moore contributor, McGraw-Hill Book Co., New York, May, 1970.
- \*"Remote Sensing with Imaging Radar: A Review," D. S. Simonett, 1970, Commission VI- International Society of Photogrammetry Meeting, Dresden, Germany, Summer, 1970.
- \*"A High Speed Disc Memory and a Color Image Display for a Small Computer," J. Lucas, Ph. D. Dissertation, CRES Technical Report 133-20, August, 1970.
- \*"Spectral Reflectivity Data: A Practical Acquisition Procedure," D. D. Egbert, Master's Thesis, CRES Technical Report 133-21, November, 1970.
- "Technique for Producing a Pseudo-Three-Dimensional Effect with Monoscopic Radar Imagery," L. F. Dellwig, H. C. MacDonald, and J. N. Kirk, Photogrammetric Engineering, September, 1970.
- "Soil Moisture Detection with Imaging Radars" H. C. MacDonald and W. P. Waite, CRES Reprint 177-1, 1970.
- "Interface of PDP-15/20 and 201A1 Data Set," Parveen K. Gupta, Master's Thesis, September, 1970, University of Kansas, Electrical Engineering Department.
- "Radar Uses for Natural Resources Inventories in Arid Zones," S. A. Morain, Symposium in Mexico, November, 1970. In press — McGraw-Hill of Mexico.
- "An Analysis of RF Phase Error in the 13.3 GHz Scatterometer," G. A. Bradley, November, 1969, Technical Memorandum 177-1.
- "Mathematical Theory of Filtering Program," R. M. Haralick, December, 1969, Technical Memorandum 177-2.
- "Informal Log, 13.3 GHz Single-Polarized Scatterometer, 400 MHz Dual-Polarized Scatterometer, Mission 119, Argus Island, Bermuda, 19 January 1970 - 27 January 1970," G. A. Bradley, February, 1970, Technical Memorandum 177-4.
- "Principal Component Analysis," R. M. Haralick, April, 1970, Technical Memorandum 177-5.
- "Informal Log, Mission 126, Pt. Barrow, Alaska," G.A. Bradley, June, 1970, Technical Memorandum 177-6.
- "Frequency Averaging for Imaging Radars," G. C. Thomann, June, 1970, Technical Memorandum 177-7.

- "Informal Log, Mission 130, Garden City, Kansas," J. D. Young, May, 1970, Technical Memorandum 177-9.
- "Ninety-Day Mission Analysis Report, Mx 108, DPD-2, Side-Look Radar, Pisgah Crater, California," L. F. Dellwig, July, 1970, Technical Memorandum 177-10.
- "Correlated Averaging to Enhance Radar Imagery," Ralph W. Gerchberg, September, 1970, Technical Memorandum 177-11.
- "Analysis of Sea State Missions 20-60," J. Young, September, 1970, Technical Memorandum 177-12.
- "A Note on the Antenna Beamwidth Term Used in the Scatterometer Data Reduction Program," J. D. Young and G. A. Bradley, October, 1970, Technical Memorandum 177-13.
- "An Analysis of Methods for Calibrating the 13.3 GHz Scatterometer," G. A. Bradley, Technical Report 177-1.
- "Signal Analysis of the Single-Polarized 13.3 GHz Scatterometer," G. A. Bradley, May, 1970, Technical Report 177-2.
- "Image Textural Analysis by a Circular Scanning Technique," G. O. Nossaman, M. S. Thesis, June, 1970, Technical Report 177-3.
- "A Regional Study of Radar Lineaments Patterns in the Ouachita Mountains, McAlester Basin — Arkansas Valley, and Ozark Regions of Oklahoma and Arkansas," J. N. Kirk, June, 1970, Technical Report 177-4.
- "An Analysis of the Effects of Aircraft Drift Angle on Remote Radar Sensors," G. A. Bradley and J. D. Young, August, 1970, Technical Report 177-5.
- "Radar Lineament Analysis, Burning Springs Area, West Virginia — An Aid in the Definition of Appalachian Plateau Thrusts," R. S. Wing, W. K. Overbey, Jr., and L. F. Dellwig, July, 1970, Technical Report 177-6.
- "An Evaluation of Fine Resolution Radar Imagery to Making Agricultural Determinations," S. A. Morain, J. Coiner, August, 1970, Technical Report 177-7.
- "Optimum Radar Depression Angles for Geological Analysis," H. C. MacDonald and W. P. Waite, August, 1970, Technical Report 177-9.

---

\*Supported partially by NASA Contract NAS 9-10261, U. S. Army THEMIS Contract DAAK02-68-C-0089, or NOO Contract N60921-C-0221.



DATA PROCESSING AT THE UNIVERSITY OF KANSAS

By G. L. Kelly  
Center for Research, Inc.  
University of Kansas  
Lawrence, Kansas 66044

ABSTRACT

Because of the large amount of data contained in any image and the complexity of the types of information needed from images, a multifaceted approach to image processing is required. Such an approach should include provisions for (1) basic research to develop the theory and new algorithms to more effectively handle image processing problems, (2) a flexible computational facility to implement new ideas as well as one which can quantitatively evaluate old ideas, and (3) a near real-time piece of hardware to process and display many sets of images easily, economically, and quickly.

The University of Kansas has continually developed the ideas, image-discrimination enhancement, and combinations system, and the complementary "KANDIDATS" digital image-data system during the past 5 years. The idea is an analog-digital near real-time image-processing system to perform a wide variety of enhancements, measurements, and category discrimination on both single and multiple images. The categories, experimentally determined, can be displayed in different colors or textures.

The "KANDIDATS" is a software package consisting of a set of multi-image processing programs which include feature extraction, image-pattern recognition with a variety of decision rules, image-texture analysis, cluster-analysis congruencing, and various image display and editing capabilities.

## RECENT ADVANCES IN RADAR APPLICATIONS TO AGRICULTURE

by

Stanley A. Morain  
Center for Research, Inc.  
University of Kansas  
Lawrence, Kansas

INTRODUCTION

This report summarizes a series of studies now in progress at the remote sensing lab of the University of Kansas, Center for Research. These efforts comprise the geoscience interpretation portion of task 2.5\* of NASA contract NAS 9-10261. Specifically, results and discussion are presented for four studies grouped under the headings: New Approaches and Methodology; Advances in Radar/Agriculture; and Socio-Economic Considerations in Radar/Agriculture. Details of these studies are given in Morain and Coiner (1970), Morain, Holtzman and Henderson (1970), Morain (1970), Coiner and Morain (1970), and Henderson (1971).

RESULTS AND DISCUSSION

The investigations discussed below are diverse in strategy, methodology, and subject matter. They are based almost exclusively on human interpretations as preparation for future automatic data processing. Our guiding philosophy has been that automatic interpretation of such complex phenomena as those manifested in agricultural patterns, is premature until models are devised to direct the construction of algorithms. As Forrester (1970) explains "Computers are often being used for what the computer does poorly and the human mind does well. At the same time the human mind is being used for what the human mind does poorly and the computer does well. Even worse, impossible tasks are attempted while achievable and important goals are ignored (p.2)." We can approach a more realistic and efficient human/computer interface by creating interpretive models of human perception for subsequent, meaningful automation. Some of our more advanced studies, we feel, are nearing that stage.

---

\*Task 2.5: Applications and studies of Radar Scatterometers and Radar Imagers to Agriculture and Forestry.

At present all of our agricultural studies center on Garden City, Kansas (NASA Site 76). Two of these investigations are described as advances in approach and methodology while three contribute toward advancing radar/agriculture applications.

## NEW APPROACHES AND METHODOLOGY

Our ultimate goals in agricultural remote sensing in the active microwave are to, first, develop strategies to collect pertinent agricultural statistics exemplified by such measures as acres in production, acres in particular crops, harvested acres, or as input parameters for yield functions; and, second, to make recommendations regarding the parameters of a radar system specifically designed to collect agricultural data usable at several levels in the agricultural hierarchy—local county agents, state agricultural statisticians, and national Agricultural Research Service personnel. To place these goals into perspective we have pursued a new approach and revived a potentially powerful methodology. The first study summarized is an investigation into the information needs of farmers and county agents and an assessment of those needs in terms of radar sensing. The second is an attempt to design and implement radar interpretation keys.

### Basic Remote Sensing Needs in Agriculture

Until recently the information needs of users at primary levels in the agricultural hierarchy (farmers and county agents) have been largely neglected in studies of sensor applications. Yet it is at this level that many of our broadest claims for uses of remote sensor data are made. In July, 1970, data were collected in interviews with farmers and agricultural agents who were directly involved with the farmer. By working at the local level it was possible to determine some of the needs regarding land use and farming practices as perceived by these people. Three counties (Finney, Wichita and Grant) in the high plains of Western Kansas were selected to serve as a study area.

Methodology. - A transect of each county was selected to include a variety of land uses, agricultural practices, and large and small farm operations. One-hundred and twelve farmers located along these transects were interviewed and asked the following questions:

1. Which aspects of your farm and its operation would you like to know better but cannot now determine or predict?
2. What kinds of information might come from remote sensing experiments that would be of use to you?

3. If such information as periodic analyses of predicted crop yields, soil moisture content, or plant vigor were available, how would you use them on the farm?

In addition to individual farm operators, Soil Conservation Service (SCS), Agricultural Stabilization and Conservation Service (ASCS), and Agricultural Extension agents were interviewed and asked: "What information would improve your ability to aid farm operations and farm planning?" Responses to these questions were colored by each individual's perception of his environment and needs, but this is equally true for persons at regional and national levels in the hierarchy and certainly for those designing hardware. These perceptions at all levels, whether right or wrong, must be considered in order to 1) determine where information gaps lie; 2) to assign priorities to information needs; and 3) to develop rational remote sensing programs.

Results. - The list below is a small sample of responses considering the total number of farm types and operations in the United States. Problems paramount in other environments have not been determined but will surely have an impact on the potential usefulness of radar programs. In compiling responses to the questionnaires a decision was made to include only those answers most often given to avoid minor or singular requests. Those designated with an asterisk (\*) indicate possible radar applications. Clearly, many of the problems listed are not amenable to radar analysis or to radar analysis alone. It should be noted also that asterisks do not necessarily indicate the present capability of radar, but potential future ones as well. A complete defense of each present or future application is beyond the scope of this report; consequently a summary statement follows the listing of responses.

Typical responses to the first question were:

1. Proper fertilizer application — optimum time and amount
2. Knowledge of expected market prices early in the planting season
3. Which crops to plant and how many acres per crop
- \*4. More accurate irrigation guidelines - e.g., optimum time and duration
5. How to increase yields
- \*6. Early plant disease detection
7. Insect and disease elimination prior and/or subsequent to field infestation
8. How to cut operation costs

Replies to question two were:

- \*1. Prediction of pests and disease in crops
- \*2. Current field and crop conditions (see Morain and Coiner, 1970 for further details and references)

\*3. When and how much to irrigate

Frequent responses to question three were:

1. To increase profits
- \*2. For more efficient farm management
- \*3. To increase yields
- \*4. To detect and control disease and insects
- \*5. For farm planning
- \*6. To gain knowledge of soil fertility

Five local agricultural officials were asked, "What information would improve your ability to aid farm operations and farm planning?" Their most common replies were:

- \*1. Knowledge relating to the effect of irrigation water on soil, specifically on soil salinity
- \*2. Faster alerts on insect and disease epidemics
- \*3. A better overall picture of a farm than could be obtained by on-the-ground inspection. This included information on:
  - a) drainage and erosion
  - b) optimum land use versus actual use in relation to slope and conservation practices
  - c) better field and building arrangement
- \*4. Pollution control measures
- \*5. Degree of water weed infestation in irrigation ditches and larger water bodies.

These responses indicate that the radar remote sensing community has quite possibly overlooked a basic set of useful applications not specifically requiring crop identification. We have recognized but not yet taken full advantage of radar imagery's synoptic, all weather attributes. For example sequential monitoring by imagers or scatterometers using low incidence angles may prove useful in tracing crop moisture curves and suggesting optimum irrigation dates (responses 1-4; 2-3), harvesting dates, etc. Such applications would require a near continuous monitoring system. The capability for detecting moisture variation has already been shown by MacDonald and Waite (in press). Knowing what crops were in particular fields would not be as important as the  $\sigma^\circ$  vs T (time) for a fixed  $\Theta$ . Radar systems may also have a role in detecting those diseases which very quickly alter crop vigor or which result in defoliation (replies 1-6; 2-2; 3-4). Imagery would be required to monitor the spatial dimensions and directions of movement of these infestations (replies 2-1; 4-2), but scatterometry would be a useful addition for detecting "point" occurrences.

Lastly, a host of less critical needs could be addressed by radar sensors. Water weed infestation (responses 4-4; 4-5) in larger water bodies is certainly within the scope of present capabilities whether

caused by mere availability of water or eutrophication. Since water is a specular reflector with side-looking radars, the protuberance of any vegetational growth would increase  $\sigma^\circ$ . Such phenomena have already been observed for kelp beds off California and for swamps near Garden City and Horsefly Mountain.

When these kinds of information are combined, a better picture of farm operations on a regional scale may emerge. Regional outlooks on drainage and erosion, field sizes and arrangement, and irrigation dates may all lead to improved farm management schemes. As previously suggested, much of this could be done in the absence of field-by-field crop identifications.

### Design and Implementation of Radar Keys

The dichotomous key concept is not new. Prior to the introduction of numeric clustering methods, this approach was the most common for taxonomic purposes in botany and zoology; and even today it constitutes an important tool in these endeavors (Mayr, 1969, p. 277). In the field of photo interpretation, however, the use of keys is relatively new. They were first devised for use during and after World War II to enhance information extraction from aerial photography. Their widest popularity came during the decade following the Second World War, and several government agencies, including the Forest Service, remain heavily committed to them (Bigelow, 1963). Briefly, the dichotomous key may be defined as, "one in which...description assumes the form of a series of pairs of contrasting characteristics which permit progressive elimination of all but one object or condition of the group under consideration" (U.S. Navy, 1967, p. 57). By use of a binary choice method, it is possible to "key out" certain categories or entities which exist within a heterogeneous group.

Radar Keys in Agriculture. - The most valuable roles for radar sensors in agriculture appear to lie in their ability to 1) obtain synoptic, time-sequential data coverage; 2) perform crop segregation and identification tasks; 3) provide vital agricultural statistics; 4) monitor crop quality or stage of maturity; 5) monitor spatial diffusion of new crop introductions; and 6) provide partial but fundamental input to yield functions.

For agricultural determinations in the active microwave region we believe that interpretation keys will be useful for the following reasons:

1. Since backscattering cross-sections for any given crop type vary continuously as a function of:  $\sigma^\circ$

- a) system parameters (e.g. frequency, polarization, incidence angle, etc.)
- b) terrain parameters (e.g. moisture contents in plant and soil, soil texture, slope, etc.)
- c) agricultural practices (e.g. row spacing, frequency of irrigation, preference for particular varieties) and
- d) intervening variables such as past weather history, stage of growth and geographic location,

it seems desirable to adopt interpretation methods flexible enough to accommodate a mix of variables at any given time and locality.

2. In any full-fledged sensing program where agricultural statistics are required on a regional scale, it will be imperative that data interpretation take place at a local level, drawing on the knowledge and expertise of county agricultural agents cognizant of present and past conditions in their area. Logically, one of the quickest, most efficient and consistent methods employable for such interpretation would be based on simple dichotomous decisions.

3. The availability of an interpretation key may assist in the integration of information provided by radar into a larger data matrix consisting of aerial photos, ground collected data, and historical records. Conversely, the key may provide a method by which other sensor collected data, ground truth, and historical file data can be used in the interpretation of a radar image. The latter approach has already been applied in an analysis of vegetation at Yellowstone National Park (Hardy and Coiner, 1971).

4. The keys, though based initially on human perception and visual interpretation, can be readily automated into data processing algorithms. Thus, the man-machine interface, which is generally recognized as necessary in remote sensing systems, can be preserved. For reasons stated above, we believe that in the agricultural hierarchy the most effective point for such an interface is at the local (county) level.

Key Construction and Testing. - The format for dichotomous keys can be of two major types: a) a textual, unillustrated form; and b) a textual form supported by visual training aids. The latter is held to be more powerful. A number of preliminary agricultural and natural vegetation keys are being designed and tested. These represent three frequencies (X; Ka; and Ku-bands) for various times in the growing season. All are designed to determine crop types or crop conditions in the commercial grain farming economy of Western Kansas. For areas still in natural vegetation, keys intended to define major plant communities and ecological situations are under study. Our examples so far are drawn from studies at Horsefly Mountain, Oregon and Yellowstone National Park, Wyoming.

Tests of the keys produced to date are encouraging. In addition to providing a coherent and consistent means of interpretation, they seem to reveal a high correspondence between key format and interpreter success. For example, our ability to correctly identify crops using fine resolution X-band imagery was lower than expected, primarily because the design of the key itself was unnecessarily complex. In contrast, on Ku-band imagery having poor visual appearance, interpreters were highly successful, largely because the key was understandable. We have also found that illustrated keys are the most accurate. In some cases, up to 30% more correct identifications were achieved. Additional tests have pointed out that keys offer a range of user alternatives. From any given image, a host of keys can be prepared to yield data for particular interests, thereby allowing interpreters to by-pass unwanted information contained in the image.

In summary, our experience suggests that properly prepared keys increase the validity of interpretations and increase the range of image utility. Dichotomous keys may also solve the need for appropriate agricultural data at all levels in decision making from county through to state and federal agencies. Although the approach is only partially tested at present, interpretation keys seem to provide the best available method for conventional information extraction from SLAR imagery. Our future efforts will be in the areas of format improvement and automation.

## ADVANCES IN RADAR/AGRICULTURE

### Evaluation of Fine Resolution Radar Imagery

In this study, two techniques were used to interpret high resolution imagery\* of the Garden City test site. The first analysis was strictly a visual interpretation of the imagery. Its major objective was to explore possibilities for creating identification keys of crop types and states. Preliminary results have been extremely valuable in: 1) documenting the need for high resolution radar imagery in agriculture; 2) directing the aims of subsequent non-visual studies; 3) highlighting needs for improving terrain data collection; and 4) providing initial experience in the joint use of photographic and radar sensors for identifying crops.

---

\* Obtained October 1969 by the University of Michigan X-band system.



The second technique focused on extracting Quantalog spot densities from the X-1 resolution\* and investigating, through a set of categorization strategies, various ways of presenting the data. Film density values for the major land uses at Garden City were displayed in a series of scattergrams representing each of the grouping strategies. The order of presentation of the plots followed a logical sequence in attempting to spotlight the influence of particular terrain and system variables on crop optical densities. In the past (cf. Schwarz and Caspall, 1968; Haralick, et al., 1970), the scattergram method of data portrayal has often been used but never thoroughly evaluated for its worth in isolating the influence of particular variables. For a more complete discussion of the scattergrams see Morain and Coiner (1970).

Results indicate that the unconstrained plotting of all densities, irrespective of crop purity, incidence angle, etc. can distort the data and complicate its interpretation. Better segregation of crops in measurement space (HH vs. HV density) can be achieved if differences such as incidence angle, crop purity, row direction, stage of growth, and combinations of these, are taken into account. Nevertheless, spot densitometry derived from 2-polarization, single pass imagery will, by itself, rarely give unambiguous crop discrimination. Multiple "looks" throughout the growing season will be required if image tone is to be the only discriminant. Distinctions impossible to make in October may be quite possible earlier in the growing season or with a different frequency, polarization, incidence angle, or look direction. Both look direction and incidence angle are shown in this report to have significant effects on the return signal for particular crops.

Visual Interpretation. - The following paragraphs outline image appearances on a crop by crop basis. It is from such observations that visual interpretation keys are constructed. Only the more economically important crops are discussed.

**Sugar Beets:** By October, the sugar beet crop at Garden City is fully matured and ready for harvest. In healthy fields at this late date in the season, canopy shape and moisture content are probably the most important factors affecting radar backscatter. The most characteristic features of beet fields are their consistently high return and their tendency to strongly depolarize radar signals. They appear on both the HH and HV images in very light to light grey uniform tones. Only one field out of those compared had a conspicuously darker tone than the others. Whether this arose from image darkening by antenna pattern or an unhealthy (perhaps moisture stressed) field is uncertain. Degree of depolarization, as a discriminant, is at present only useful on individual passes of the aircraft where gain settings on the HV term can be assumed to be reasonably constant. Discrimination of sugar beets from

---

\*X-1 resolution refers to the best resolution presently obtainable.

its nearest appearing ally, maturing alfalfa, can often be accomplished using degrees of tone difference between polarizations. This appears to be possible, however, only up to a point in the alfalfa cycle; beyond that there is little difference between the HH-HV tones of these crops.

By using both the HH and HV polarizations and noting in particular the degree of tone shift and absence of within-field patterns, confusion with other crops can be largely overcome. In short, as was observed by Simonett, et al. (1967), sugar beets can be easily discriminated at this time of year on X-band imagery.

Sorghums: In 1969 sorghum as a category covered more acreage than any other crop present in the test site. It is not an especially well defined crop, however, since it includes forage sorghums exceeding six feet in height at one extreme and grain sorghums three to four feet high at the other. In addition, there are extreme differences in crop canopy and geometry between these sub-categories. In order to reduce this complexity, forage sorghum (mainly sudan) was separated from the grain subtype. Fields of grain sorghum were again subdivided depending upon whether the planting direction was orthogonal or parallel to the look direction. In the following discussion only grain sorghum is considered.

By early October grain sorghum is ready for harvest. The gross canopy geometry consists of two entities: a lower leaf stratum which is nearly continuous from any viewing angle; and an upper, more vertically oriented layer of emergent stalks and grain heads. Differences in tone from field to field are significant and from all evidence arise from differences in row direction. Specifically, we believe that differences in radar return this late in the growing season are associated mainly with the height of the head and the progress of ripening.\* When the signal is scattered from rows oriented perpendicular to the look direction, the major part of the return (at the higher incidence angles)\*\* may be coming directly from ripe grain heads. If the rows are oriented parallel to the look direction however, backscatter is more likely described as a complex interaction involving leaf, stalk, and head. Additional very detailed research on particular fields will have to be undertaken to firmly establish this relationship.

---

\*We have seen numerous fields on the Michigan imagery which appear to show differences in crop condition. Some of these differences are known to coincide with uneven ripening within fields which may in turn be a function involving plant and soil moisture as well as soil type.

\*\*In the Michigan system all incidence angles are  $\geq 69^\circ$ .

In general, sorghum fields ranged in tone from dark to light grey. Those with row directions orthogonal to the look direction were consistently darker in both polarizations than those planted with rows parallel to that direction. Grey scale variation from HH to HV showed little or no consistency regardless of row orientation. However, the HH to HV variation was somewhat less pronounced in those fields with rows perpendicular to the look direction. Tonal variations in fields of the same row direction and ripeness were also noted. Though we have no firm explanation for this phenomenon at present, we can be fairly confident that terrain parameters are a fundamental influence.

The difference in return related to row direction is more complicated than increase or decrease in return would suggest. In those fields with rows perpendicular to the incident signal, slight mottling in the illumination may arise. We believe these effects are related to local differences in crop height, moisture content, or degree of ripening (see also the discussion of K-band imagery by Simonett, et al., 1967).

Due to the broadness of the sorghum category and the range of reflectivities inherent in such a grouping, discovery of a completely unambiguous interpretation aid based on a single mission is not possible. Nonetheless, when one narrows the category to include only fields of grain sorghum with rows perpendicular to the line of flight (i.e., parallel to the incident signal), there is sufficient consistency of image tone and "texture" to suggest that interpretations using dichotomous keys should be fairly reliable. Sorghum fields, particularly on the HV, display a medium coarseness of texture which seems independent of the field's grey level. This texture and the within-field tone homogeneity are the best indicators for grain sorghum presently derivable from the Michigan imagery.

Wheat: By Fall, three broad types of winter wheat are recognizable in Western Kansas: 1) fields of recently planted and just emerging wheat—approximately 3" in height and covering a small percent of the ground; 2) developing wheat, planted in late August or early September, which by October is 6 to 8" in height and covers most of the ground; and 3) almost continuous volunteer regrowth from the preceding June harvest. The geometric similarity between fields of volunteer wheat and those with developing wheat higher than 3" dictates that these two types be considered as a single category.

Those fields which contained emergent wheat display mottled patterns within fields similar to those observed in sorghum. This spotty pattern varies from light grey to black and is characterized by a very fine "texture" in the light grey portions. These two attributes are most useful in discriminating emergent wheat. In contrast, those

fields with a more continuous cover and greater height, normally image in lighter tones. Equally important as discriminants, developing and volunteer wheat fields usually do not display evidence of cultivation patterns. In general, they have more uniform illumination and can occasionally be confused with sugar beets.

Neither of the wheat sub-categories varies substantially in tone from HH to HV except for the quadrants in emergent wheat in which the cultivation direction is orthogonal to the look direction. Both are subject to confusion with some types of fallow. However, discrimination can frequently be achieved between wheat and fallow on the basis of HH to HV variation. Fallow fields often appear mottled in the HV, while wheat normally does not.

Corn: This late in the growing season, corn is fully mature and is undergoing harvest. However, as is equally true of grain sorghum, delays in planting, timing of the final irrigation, and variations in ripening and drying rates all insure that minor differences (mainly in moisture status) exist between fields. By experience, farmers have learned to recognize when their field is uniformly dry enough to harvest and until that time arrives, the crop is left standing. Late in the season, then, one of the inherent characteristics of standing corn is non-uniformity within fields. A second defining attribute is height. Corn is normally the tallest crop encountered in Western Kansas, often reaching 8-10 feet. Its nearest rival is sudan grass—a type of forage sorghum occurring very infrequently.

Uniform, mature fields usually appear in medium grey tones, and much of the grey range arises from inhomogeneities (mottling) in both the HH and HV terms. Causes for these differences, appear to vary between polarizations. A comparison of the SLAR return with both Ekta-chrome and CIR failed to suggest a single source for the in-field variation, although in some cases the mottled tones could be related to suspected differences in the rate of crop maturation. Unlike sorghum, no overall trend in HH to HV shift could be derived.

Alfalfa: The crop cycle of alfalfa makes it a difficult crop to interpret. By October, fields may range in height from 6" to 24" and may be in any of several irrigation states. However, by splitting alfalfa into two sub-categories (under 12" and higher than 12"), it is possible to make fairly reliable distinctions.

Alfalfa less than 12" high (i.e., recently cut) images in dark grey to medium grey tones on the HH polarization. One of its most reliable features is the series of lineations which is always parallel to the longitudinal axis of the field. The cause of these is almost certainly associated with diking for flood irrigation. Another important

discriminant for this category is the tone shift from HH (dark) to HV (light), the trend being just opposite from that observed for other crop types. The increase in return on HV imagery might arise from the short, vertically oriented "stubble". To vertically polarized radar signals the field would appear, in analogous terms, as a short bristled brush, with a fairly high moisture content. Theroretically this phenomenon would be truer at high incidence angles than at low, and at the extreme (90° depression  $\lambda$ ), there should be no influence at all. Moisture must be an important factor because wheat stubble with the same basic geometry but lower moisture content gives lower returns than alfalfa. The moisture content of cut alfalfa averages 70-80 per cent, while wheat stubble is generally less than 10 per cent.

After alfalfa has grown to about 12" its appearance on HH imagery begins to be more uniform; that is, lineations begin to disappear.\* By the time the crop reaches full maturity (24"), complete homogeneity has been attained. Moreover, mature crops display little or no tone shift from HH to HV. We suspect the cause for these attributes lies in the density and uniformity of the alfalfa canopy as well as with the size and orientation of leaves.

Recently Tilled Fields: Recently tilled fields represent an easily distinguishable category. They nearly always appear as a uniform dark grey or black tone. This category includes those fields cultivated one to two weeks before the mission and observed at the time of field inspection as clean, vegetation free surfaces. Unfortunately, detailed data are lacking on the types of tillage operations performed or their effect on radar returns. Our reasoning at present is that operations like row harrowing, which completely turn the soil, tend to decrease backscatter more than disking. Recently tilled fields can be discriminated on the basis of their dark tone and similar appearance on both polarizations.

Crop Discrimination by Spot Densitometry. - Crop discrimination was attempted with the Garden City imagery using a Macbeth Quantalog spot densitometer. Spot densities were recorded on the HH and HV negatives of the X-1 resolution using a 1 mm aperture. Four strategies were then employed to see if the data spaces of particular crop categories could be separated from each other on the basis of their HH and HV film densities. These were as follows: 1) to plot the entire data set irrespective of field quality or viewing angle; 2) to plot the entire data set partitioned according to location (incidence  $\lambda$ ) on the imagery; 3) to plot selected, high quality fields irrespective of viewing angle; and 4) to plot selected fields partitioned according to location across the image.

\*This fact indicates that canopy penetration at X-band is almost non-existent. Once the crop is high enough to mask the diking, the lineations disappear.

Bearing in mind that the Michigan radar system utilizes a very narrow range of incidence angles (ca 16°) tables I-A and I-B list the kinds of crop separations achievable using strategies 2 and 4 above. When the HH-HV densities of all fields are arranged into incidence angle classes (table I-A) confusion arises in distinguishing many of the crops, particularly grain sorghum, wheat and alfalfa. By making an initial selection of high quality fields (table I-B) many of these ambiguities can be minimized. Moreover, there are sound theoretical and practical reasons for making such a selection. First it is axiomatic, though not 100 per cent true, that high quality, clean fields account for most of the yield for a particular crop; and second, in these early stages of model building, simplification of the problem is essential.

#### Agricultural Determinations from Fine Resolution Imagery

It should be noted that the Michigan imagery was obtained in early October, a suboptimum time in terms of crop calendars. Few crops are present this late in the season and those remaining are all on the down-slope side of their annual moisture curves. This results in reduced variance in terrain backscatter and greater difficulty in making determinations. While some determinations are possible using scattergram methods, the inability of the Michigan system to yield better results than the Westinghouse system (flown in September 1965) must be viewed in context of the cropping calendar.

The use of fine resolution imagery promises great improvement in our ability to accurately assess within-field variations. Aside from making interpretation keys, patterns resulting from differences in crop backscatter have given our first encouraging evidence that ripeness (or crop state) could be monitored through a function of crop moisture. From theoretical considerations we suspected this capability but, until the availability of fine resolution data, we had not actually observed the phenomenon.

The availability of fine resolution imagery has dramatically focused attention on the need for refining the collection of field data. We are now sure that factors such as crop purity, tillage patterns, soil type, crop moisture and a host of other variables must be studied in greater detail than heretofore necessary with coarser resolution systems. Some parameters must be better known in order to advance directly the preparation of interpretation keys; others because their influences are ultimately manifested in crop attributes used in the keys.

#### Comparison of Radar Systems for Agricultural Determinations

With this report we have to date prepared scattergrams from the imagery of three radar systems. Westinghouse AN/APQ-97 and NASA

DPD-2 imagery represent two separate frequencies in K-band; while the Michigan imagery is X-band. Since the data for all three were obtained over a one month period from September 4 to October 4,\* a brief comparison of their utility in distinguishing land use categories is in order. Data are also included from a fourth scattergram constructed from AN/APQ-97 imagery from July 1966 (Table II).

In making comparisons one must remember that different viewing angles and look directions are represented in each of the images and that the procedure for producing the plots was not standardized. For example, second generation negative transparencies were used for the Westinghouse analyses, but a positive transparency was used with the NASA data. Spot densitometry was used on the Michigan and NASA data, but line trace densities were taken from the Westinghouse imagery. We have no information on the relative merits of these various techniques.

More important differences occur in the plotting strategies. The Westinghouse data were plotted irrespective of viewing angle or field quality. NASA data from the DPD-2 attempted in a qualitative way to take viewing angle into account; and with the Michigan system both viewing angle and field quality were accounted for. General indications from Table II are listed below.

1. Fine resolution imagery exemplified by the Michigan system is not necessary or even particularly valuable in the late growing season solely as an aid to crop segregation by densitometry. Partly this may be due to uniformly low moisture status for all crops and of uncropped land at this time of year (see Schwarz and Caspall, 1968, p. 241).
2. At the opposite extreme (that is, uniformly high moisture status during the height of the growing season), fine resolution imagery would probably not be of great benefit over that from systems of coarser resolution in gaining optical density information. This is indicated by the fact that: a) both the July and October data compare favorably in relative information content; and b) the July and September 15 data from the same system differ markedly in their information. During the height of the growing season all crops have a high moisture status, consequently (in terms of crop dielectric properties) the influence of moisture on backscatter cannot be widely used as a discriminant.

---

\* Westinghouse AN/APQ-97 September 15, 1965; NASA DPD-2 September 4, 1969; and Michigan System October 4, 1969.

3. The data suggest that if only film density is used as a discriminant, optimum periods for crop segregation might occur in a narrow time interval around the middle of September when maximum differences exist in both moisture status and crop geometry; or in early May before the full complement of crop types enters the land use picture.
4. There might be sufficient frequency dependence between crops that a dual-polarized polypanchromatic radar flown in mid September could perform the task of crop discrimination. Alfalfa, which could not be isolated in two-space by Ka-band on September 15, was at least partially discriminable by Ku-band somewhat earlier in the season. If such contrasts were optimized, various training and prediction processes for automatically identifying crops might prove more successful. Unfortunately, it could be argued that mid-September is too late in the growing season to make very many useful economic predictions.

#### Radar Soil Mapping

Several investigators have reported on the scope for soil studies using radar imagery as a base. Simonett, for example, (1968) was able to distinguish four soil associations in Woods County, Oklahoma near the dry/subhumid boundary. These were largely restricted to uncultivated areas such as badlands, salt plains, floodplains and terraces. On adjacent cultivated land, soil texture patterns were masked by complex crop geometries and variable moisture patterns. Barr (1969) found that regional engineering soil types could be identified by inference combined with recognition of repetitive patterns. In his study it appeared that brute force systems yielded higher quality data than synthetic aperture radar, but given the present state-of-the-art in these type systems, this is not surprising. Since there was little penetration at the wavelengths used by Barr, the reflecting surface was found invariably to be the first surface intercepted by the signals. In desert regions in particular (an environment under investigation at Kansas) that surface is usually a combination of rock or bare soil and desert shrub. The low density of plants per unit area, together with a wide range of soil textures over short distances, leads one to suspect that significant soil information might be derived from the radar frequencies.

Figure 1 is a reproduction at original scale of Ka-band imagery  $\lambda = .8-.9$  cm obtained over Tucson in November, 1965. The valley region is devoted largely to irrigated agriculture and, as Simonett found in his studies in Oklahoma, the soil pattern is mostly obscured. Large areas on the alluvial fans and smaller areas along the valley



(particularly adjacent to the Santa Cruz River) reveal a pattern closely resembling that mapped by the USDA Soil Survey (Young, et al., 1931). Vegetation throughout the uncultivated area consists of Creosote bush (Larrea divaricata), scattered Mesquite (Prosopis juliflora) and Burweed (Haplopappus tenuisectus). It is improbable, therefore, that the patterns on the imagery are due to defineable plant communities. In Figure 2 boundaries have been delineated from the radar by combining information from the like (HH) and cross (HV) terms. Once delineated, the areas were categorized through reference to the pre-existing soil survey map compiled in 1931. A complete set of texture types including broken and stony land, coarse textured pebbly and sandy soils, silt loams, loams and clay loams resulted from this categorization. Highest returns on the imagery are observed for the stony and pebbly soils. These surfaces are apparently behaving as isotropic scatterers, perhaps because of the angularity of the sand grains comprising the surface and the comparability of their size to that of the transmitted wavelength. Generally, as texture becomes finer, radar return diminishes: loams, clays, and clay loams image as medium to dark grey tones, while silt loams image almost black. The apparent anomaly of silt loams imaging darker than clay loams in what is otherwise a consistent trend may be explained by the fact that, in this area, the Gila silt loam characteristically melts together to form a smooth surface reflecting the bulk of radar signals away from the receiver.

The patterns on Figure 2 can be compared with a simplified version of the USDA soil map illustrated in Figure 3. The major difference between them is that the cultivated area has expanded since 1931. Most of that expansion has involved soils of the Gila series. The overall correspondence in pattern is striking and suggests that interpreters knowledgeable about local soil-vegetation-topography relationships could produce reconnaissance or semi-detailed soil maps from radar. Much research still needs to be done, however, to define  $\sigma^{\circ}$  for various soil textures and conditions, as well as moisture contents, at specified frequencies and viewing angles.

Consistency of radar backscatter is, of course, an important issue in mapping any terrain phenomena. It is encouraging, therefore, that exactly the same texture/backscatter trend has been observed and mapped near Tule Mountain in the Trans-Pecos of southwest Texas. In this locality broken and stony land was separable on the basis of terrain texture and drainage patterns. Very gravelly loam, representing the Reeves series, imaged in medium gray tones, and, as texture became finer in the Ector and Rio Grande series, backscatter intensity diminished.

### Socio-Economic Considerations in Radar/Agriculture

For any sensor system time is a key discriminant. Research on the spectral reflectivities of plants has shown that instantaneous unique signatures are unlikely to exist and that time-sequential imaging may be required to identify crops (Haralick, et al., 1970; Park, 1969; Wiegand, et al., 1970). Basically there are two temporal frameworks in which to work: seasonal and year-to-year. Under both rubrics there exist within- and between-crop radar variations, but the economic and social implications attendant upon each are vastly different.

Between-Crop Seasonal Variations. - It is not, in fact, the ability of radar to collect useful information that stymies its wider application, but our ability to interpret the data. As Haralick, et al., (1970) point out, it will take a Herculean effort to create automatic data processing routines for crops whose spectral properties vary continuously in time and space. Wheat, the world's most important crop, is produced in scores of varieties under as many cultivation practices. Clearly, it is unrealistic to expect radar or any other sensor to provide interpretable agricultural data without knowing the nature or magnitude of within-crop geographic and phenologic variations. Basically, the problem reduces to knowing which radar and terrain parameters are critical in making accurate land use identifications. In searching for these we have overlooked one of the simplest, most useful aids to identification yet devised — the dichotomous key.

Provided imagery can be disseminated quickly enough for primary agencies to interpret the data in at least a sampling framework, improvement in statistics from crop reporting services could be realized. Bernstein and Cetron (1969) have indicated that techniques should be available for disseminating inventory information from large data banks by 1975. At present, data are gathered by an army of volunteer observers in coordination with regularly mailed questionnaires. By the end of the year, it is often true that acreages and yield predictions for wheat in the Great Plains are accurate to within 3 per cent. However, predictions prior to harvest are often gross estimations. It is not in improving accuracy for which radar holds great promise but in providing early estimates and in decreasing uncertainties inherent in the predictions.

Prompt and efficient interpretation of radar imagery generated at regular intervals throughout the growing season could dramatically improve such statistics as number of acres in particular crops, progress of harvest, number of acres harvested and others. All of these would result in better planning at the county and state level, even if the margin of improvement in accuracy were small.

Within-Crop Seasonal Changes. - The most important aspects of within-crop seasonal change are those subtle differences associated with crop quality or variety. Both are part of a complex yield function, the discerning of which lies at the foundation of agricultural reconnaissance. With the "Green Revolution" in progress in Asia (Wharton, 1969), it is imperative that both acreage and variety be considered in production estimates.

At present there is no evidence that radar, or any other sensor, can detect (at acceptable levels of confidence) differences between varieties, let alone identify them. There may be hope for some estimates, however, by using surrogates related to time (if some varieties ripen earlier or permit double or triple cropping) or space (if they occur in restricted localities) (Brown, 1968). Unlikely to be detected are small differences in  $\sigma^{\circ}$  arising from increased head size, longer stalks, or other geometric parameters. For the foreseeable future, it seems that radar's most valuable contribution to yield prediction rests largely with acreage calculations inserted into a more comprehensive yield function.

Crop quality information derivable by monitoring might be useful. As a parameter of the yield function, cause of poor quality is not important. It is sufficient to know simply that low quality fields are typically low yielders and should be weighted accordingly in making production predictions. However, if causes and effects can be related by using radar, tremendous economic benefits accrue. By following the rapid expansion of diseased areas or by tracing damage along storm tracks (both of which demand near all-weather capability), assessment of economic loss or preventive measures could be quickly made. The cost of monitoring would be small compared to the savings. In Kansas alone, loss of sorghum from aphid infestations, which spread across the state in two weeks, amounted to \$14,733,000 in 1968-69 (Kansas Board of Agriculture, 1970).

Year to Year Changes Between Crops. - The benefits of long term agricultural sensing have not been seriously considered. Land use histories compiled from data collected over the years and stored for rapid retrieval could be useful in developing production control measures. In higher echelons there is a tradition of juggling the amount of land planted to control surplus and deficit (Doll, et al., 1968). However, problems of cross compliance and input substitution have hindered any startling successes. By using automatic data processing, accurate regional histories and local land use trends could be mapped. Such projects are not possible today because historical records of field size, crop type, or production are not available. It would be highly desirable to trace diffusion rates and directions of new crops (varieties?) or

the development of farm-to-market road nets (Brown, 1968) and to follow the geographic spread of innovation such as the use of polyethylene protectors on sugar beet seedlings or the progress of land reform policies. Efficiency of production has been the keynote of 20th Century agriculture; yet, the policies instituted to achieve that efficiency are mostly based on aggregate\* statistics rather than detailed local data. Disaggregation may hold promise for substantially improving agricultural economic theory, and for this reason alone radars may prove their value by supplying synoptic coverage of any desired region.

Year to Year Change Within Crops. - The least studied aspect of agricultural surveillance, the gradual changes in crop reflectivities over the years, may ultimately be the most important in aiding plans for world food supplies and production, since these indicate the spread of the "Green Revolution" or improvements in crop vigor. Most of the increase relates to gradually improving yields, which leads us to agree with Pendleton (1970) that the concept of a "yield plateau" is a myth. Increasingly, man must rely on greater production from each acre to feed expanding populations. The best mechanism for doing this is by creating better varieties and engaging in other forms of input substitution; namely, fertilizer application, irrigation, etc. We are quite uncertain how radar will prove economically beneficial, but certainly a most worthy pursuit would be to explore the numerous possibilities.

#### In Future

We have attempted in this brief summary to place into socio-economic perspective a number of possible applications and benefits of radar sensing in agriculture. Some of these applications (e.g., cultivated land inventories and selected crop acreages) should be realizable within a few years with continued research and technological advances. Others are further down the research road and others, yet, may never be achievable. Even though firm cost/benefit ratios are not yet calculable, we are convinced of the economic desirability of using radar to obtain basic agricultural statistics. At this point, however, society demands that we address even more pervasive social and political questions. We are already near enough to attempting some of the stated capabilities (perhaps five years) that fears are surfacing regarding attitudes among the farming community and among foreign peoples and governments toward the unseen and all-seeing sensor. Exceedingly complex legal and social problems will attend agricultural monitoring programs, and it is time we anticipate these issues.

---

\*Aggregate statistics refer to averages rather than individual values. See for example, Grunfeld and Griliches, 1960.

## REFERENCES

- Barr, D. J., 1969, "Use of Side-Looking Airborne Radar (SLAR) Imagery for Engineering Soil Studies," U. S. Army Engineer Topographic Laboratories, Fort Belvoir, Virginia, Tech. Report 46-TR, project 4A62350IA854.
- Bernstein, G. B. and M. J. Cetron, 1969, "SEER: A Delphic Approach Applied to Information Processing," Technological Forecasting 1(1):33-54.
- Bigelow, G. F., 1963, "Photographic Interpretation Keys - A Reappraisal," Photogrammetric Engineering, 29(6):1042-1051.
- Brown, L. R., 1968, "The Agricultural Revolution in Asia," Foreign Affairs, 46(4): 688-698.
- Coiner, J. C. and S. A. Morain, 1970, "Image Interpretation Keys to Support Analysis of SLAR Imagery," summary of paper submitted for presentation at the 7th International Symposium on Remote Sensing of the Environment, University of Michigan, Ann Arbor, 4 pp. (typescript)
- Doll, J. P., V. J. Rhodes and J. G. West, 1968, Economics of Agricultural Production, Markets, and Policy, Homewood, Ill.: Richard D. Irwin, Inc., 557 pp.
- Forrester, J. W., 1970, "Counterintuitive Behavior of Social Systems," Testimony for the Subcommittee on Urban Growth of the committee on Banking and Currency, House of Representatives, document #D-1383-1, October 7, 1970, 27 pp. (typescript)
- Grunfeld, Y., and Z. Griliches, 1960, "Is Aggregation Necessarily Bad?" Review of Economics and Statistics, 42(1): 1-13.
- Haralick, R. M., F. Caspall and D. S. Simonett, 1970, "Using Radar Imagery for Crop Discrimination: A Statistical and Conditional Probability Study," Remote Sensing of Environment 1, pp. 131-142.
- Hardy, N. and J. C. Coiner, 1971, "Vegetation Mapping with Side-Looking Airborne Radar: Yellowstone National Park," (in preparation)

- Henderson, F. M., 1971, "Agriculture and Remote Sensing in Western Kansas: A Survey of Land Use Practices in Finney County," University of Kansas, Center for Research, Inc., RSL, Tech. Memo. 177-17, 15 pp.
- Kansas Board of Agriculture, 1970, 52nd Annual Report of Kansas Agriculture (for the reporting period 1968-69.)
- MacDonald, H., and W. Waite, (In press), "Soil Moisture Detection with Imaging Radars."
- Mayr, Ernst, 1969, Principles of Systematic Zoology, New York: McGraw-Hill, Inc.
- Morain, S. A., 1970, "Radar Uses for Natural Resource Inventories in Arid Zones," First World Symposium on Arid Zones, Mexico City, November 9-12, Proceedings to be published by McGraw-Hill of Mexico.
- Morain, S. A., J. Holtzman and F. Henderson, 1970, "Radar Sensing in Agriculture: A Socio-Economic Viewpoint," Convention Record Electronic and Aerospace Systems (EASCON'70), published by IEEE, pp. 280-287.
- Morain, S. A. and J. Coiner, 1970, "An Evaluation of Fine Resolution Radar Imagery for Making Agricultural Determinations," CRES Tech. Report 177-7, 35 pp.
- Park, A. B., 1969, "Remote Sensing of Time Dependent Phenomena," in Proceedings of the 6th Symposium on Remote Sensing of Environment, University of Michigan, Ann Arbor, pp. 1227-1236.
- Pendleton, J. W., 1970, "Advances in Crop Cultural Practices," Agronomy Abstracts, American Society of Agronomy, Abstract of a paper presented at the annual meeting, Tucson, August 23-27.
- Schwarz, D. E. and F. Caspall, 1968, "The Use of Radar in the Discrimination and Identification of Agricultural Land Use," The 5th International Symposium on Remote Sensing of Environment, University of Michigan, Ann Arbor, pp. 233-248.
- Simonett, D. S., et al., 1967, "The Potential of Radar as a Remote Sensor in Agriculture: 1. A Study with K-band Imagery in Western Kansas," CRES Report 61-21, Center for Research, Inc., University of Kansas, Lawrence, 13 pp.

- Simonett, D., 1968, "Potential of Radar Remote Sensors as Tools in Reconnaissance, Geomorphic, Vegetation and Soil Mapping," Trans. 9th International Congress of Soil Science, vol. IV, paper 29, Adelaide, Australia.
- U.S., Navy Department, 1967, "Image Interpretation Manual," vol. I, (NAVAIR 10-35-685), section 3-9, Image Interpretation Keys, pp. 56-62.
- Wharton, C. R. Jr., 1969, "The Green Revolution: Cornicopia or Pandora's Box," Foreign Affairs, 47: 464-476.
- Wiegand, C. L., R. W. Learner, A. H. Gerbermann and D. A. Weber, 1970, "Comparison of Multibase and Multiemulsion Photography for Identifying Crop and Soil Conditions from Space," American Society of Photogrammetry, Technical papers from the 36th annual meetings, March 1-6, 1970, pp. 496-511.
- Young, F. O., A. T. Sweet, T. W. Glassey and E. N. Poulson, 1931, "Soil Survey of the Tucson Area Arizona," USDA Bureau of Chemistry and Soils, Series 1931, no. 19, 60 pp.

TABLE I-A SEGREGATION OF CROP GROUPS ON THE  
BASIS OF RADAR RETURN AND VIEWING ANGLE  
(All Fields)

	Low Radar Return	Medium Radar Return	High Radar Return
Low Incidence	Bare	Grain Sorghum, Corn, Wheat	Sugar Beets, Alfalfa
Medium Incidence	Bare	Grain Sorghum, Weeds	Wheat, Alfalfa, Sugar Beets
High Incidence	Bare, Wheat	Wheat, Alfalfa	Grain Sorghum, Sugar Beets, Corn

TABLE I-B SEGREGATION OF CROP GROUPS ON THE  
BASIS OF RADAR RETURN AND VIEWING ANGLE  
(Selected Fields)

	Low Radar Return	Medium Radar Return	High Radar Return
Low Incidence	Bare	Grain Sorghum, Corn	Sugar Beets, Alfalfa
Medium Incidence	Bare	Grain Sorghum	Sugar Beets, Alfalfa
High Incidence	Bare	Grain Sorghum, Wheat, Corn	Alfalfa



TABLE II. PERCENT CROP SEGREGATION\*ON SCATTERGRAMS AS A  
FUNCTION OF RADAR FREQUENCY AND DATE IN THE GROWING SEASON

Date and Radar System	7/66	9/4/69	9/15/65	10/69
	Westinghouse AN/APQ-97 Ka-Band	NASA DPD-2 Ku-Band	Westinghouse AN/APQ-97 Ka-Band	Michigan X-Band
Wheat	Not present	- - -	- - -	} 77
Grain Sorghum	} 82 (cropped)	- - -	69	
Corn		28	92	
Alfalfa		50	- - -	} 64
Sugar Beets	92	- - -	97	
Bare Ground	91**	90	83	91

\* Calculated as a percent of all fields comprising the fractional codes, NOT as a fraction of all fields of a given crop type. For example, grain sorghum on Westinghouse imagery for September 1965 comprised 69 per cent of all crops contained in the data space bounded by an upper and lower hyperplane, but almost 95 per cent of all grain sorghum fields plotted on the scattergram occurred within that data space. In other words, while most of the sorghum fields occur within a fairly well defined data space, they cannot be unambiguously discriminated from a host of other crops.

\*\* Including wheat stubble.

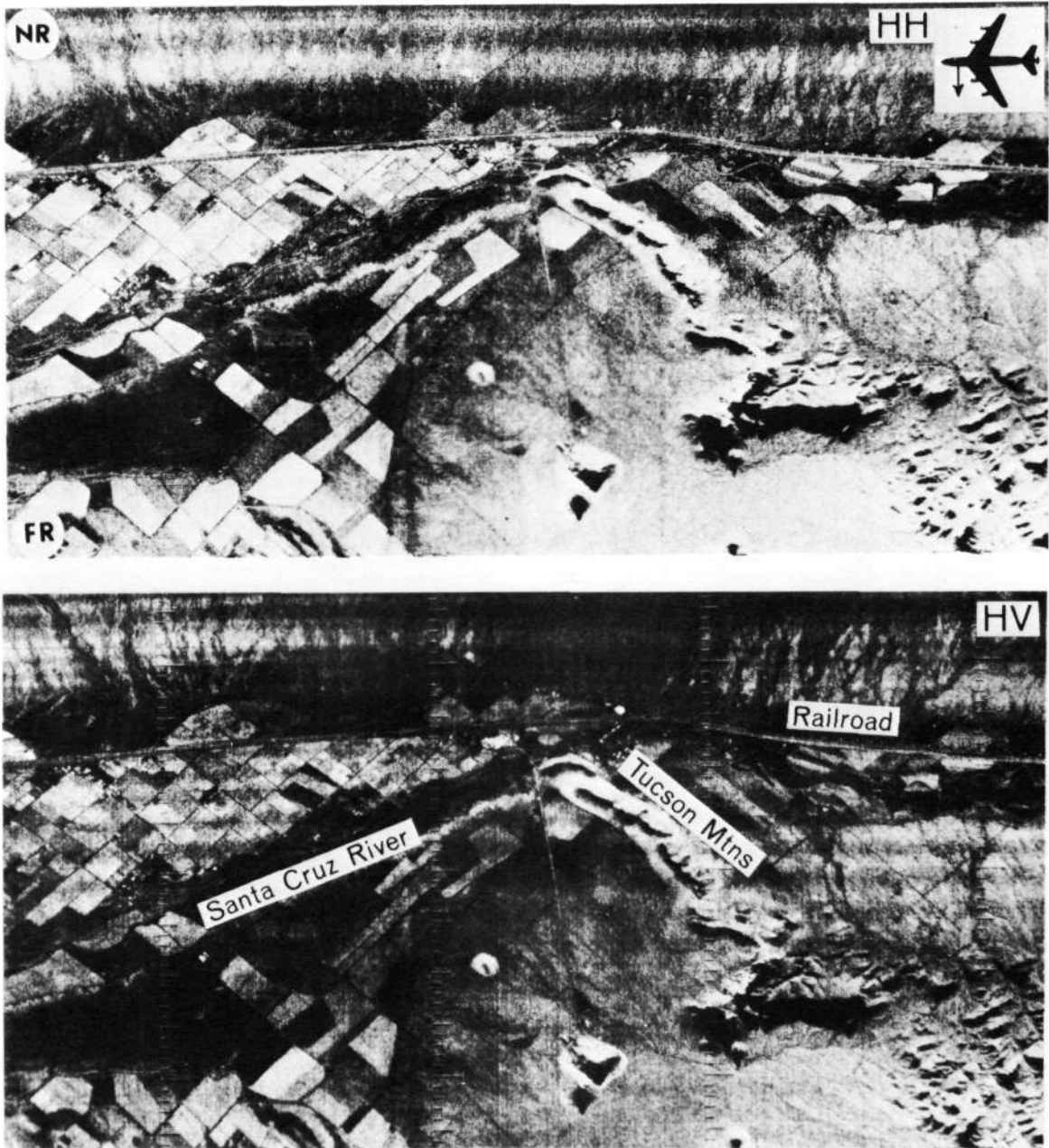


Figure 1. K-band radar imagery near Tucson, Arizona. Note soil patterns revealed on alluvial fans surrounding Tucson Mtns. and on slopes north of railroad line. Pattern in valley is partly obscured by agriculture.

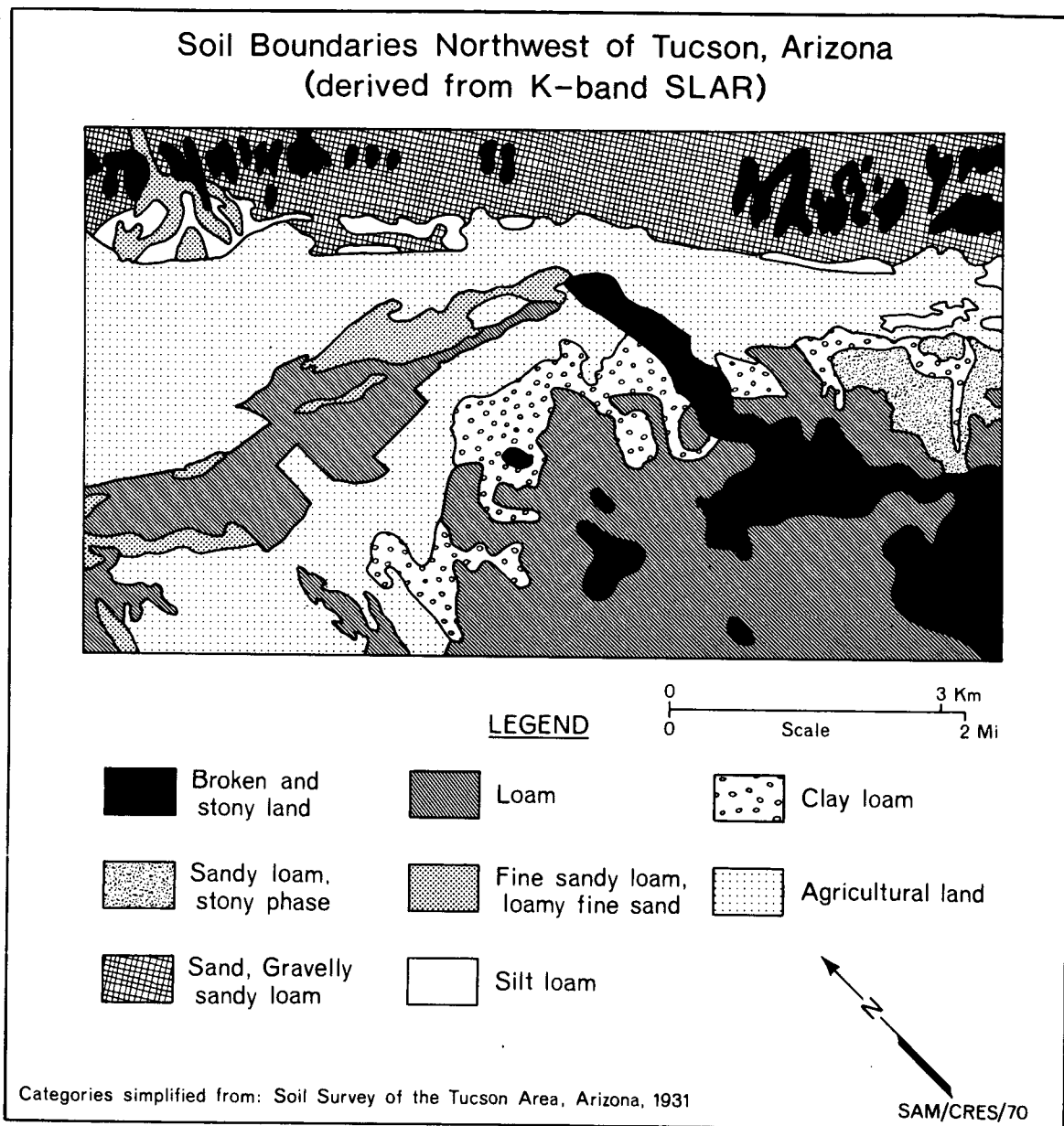


Figure 2.

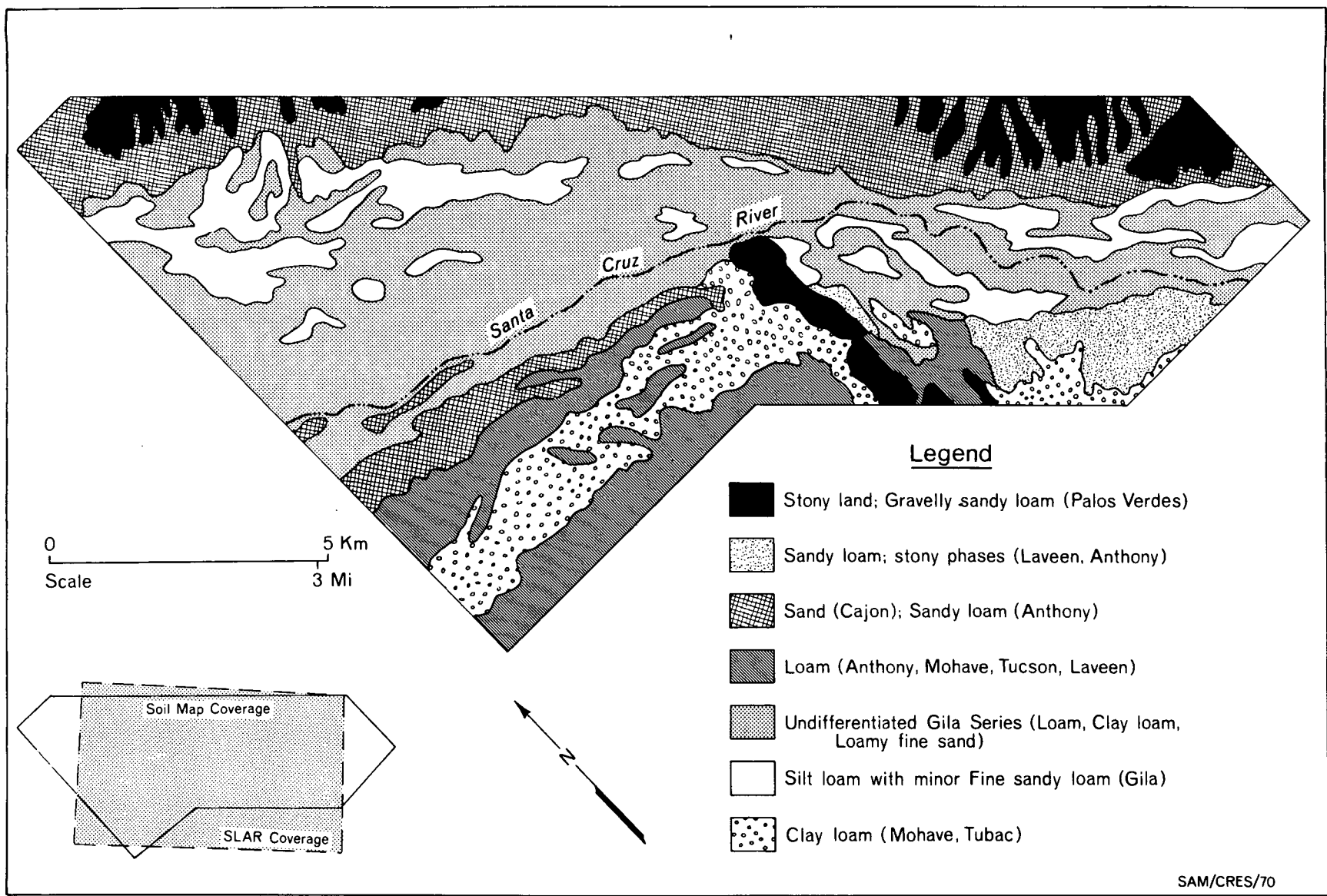


Figure 3. Soil types of the Tucson region simplified from USDA Soil Survey Map of 1931.

## INTERACTIVE DISPLAY/GRAPHICS SYSTEMS

## FOR REMOTE SENSOR DATA ANALYSIS

by

W. G. Eppler, D. L. Loe, and E. L. Wilson  
Lockheed Electronics Company  
Houston, Texas 77058

and

S. L. Whitley and R. J. Sachen  
Manned Spacecraft Center  
Houston, Texas 77058

INTRODUCTION

Using a color-television display system and interactive graphics equipment on-line to an IBM 360/44 computer, investigators at the Manned Spacecraft Center have developed a variety of interactive displays which aid in analyzing remote sensor data. This paper describes how such interactive displays are used to:

- 1) Analyze data from a multispectral scanner.
- 2) Develop automatic pattern recognition systems based on multispectral scanner measurements.
- 3) Analyze data from non-imaging sensors such as the infrared radiometer and microwave scatterometer.

DESCRIPTION OF DISPLAY/GRAPHICS SYSTEM

The work described in this report was performed in the computer laboratory of the Manned Spacecraft Center Information System Division. This laboratory includes a Digital Television Display System (DTDS) and a Grafacon tablet on-line to an IBM 360/44 digital computer.

## HARDWARE

The DTDS consists of eight channels of recirculating memory each capable of storing a complete 729-line television frame. The system hardware includes a symbol library which makes it possible to display the various alphanumeric characters at any specified location within the frame as in Figures 9 - 13.

The intensity at each raster point within the frame is encoded in the recirculating memory using a single binary bit; i.e., each raster point is either on with full intensity or completely off. In order to obtain a gray scale the frame is divided into cells each of which can have a different number of raster points intensified. For example, in Figure 2 the intensity variation (in each color) was obtained by dividing the frame into 160 x 111 cells each having 5 x 5 raster points. The intensity of each cell is set by controlling the number (0 to 25) of intensified raster points. The various 5 x 5 dot matrices are stored as special symbols in the hardware symbol library.

Another important component of the DTDS hardware is the vector generator. This unit takes as its input the display coordinates of two points and automatically generates the display coordinates of all points on the straight line connecting them. This feature is used in forming the displays shown in Figures 17 - 19.

The display device used for all of the color photographs presented in this paper is the precision color monitor shown schematically in Figure 1. It consists of three cathode ray tubes having red, green and blue phosphors; each tube (i.e., color) is intensified by a separate channel of recirculating memory. The images on the three tubes are superimposed and projected onto a ground-glass viewing screen by a combination of mirrors, dichroic filters and a projection lens. Accurate registration of the three images is maintained by various electronic (e.g., deflection gain and centering) and mechanical (e.g., mirror alignment) adjustments.

Another output device connected to the DTDS is the Xerox hard-copy machine. It is used for copying black-and-white alphanumeric and graphic displays such as Figures 9, 10 and 19.

The user communicates graphical and alphanumeric information to the computer by way of a Grafacon tablet and a keypack, respectively. The Grafacon tablet is a device which 30 times per second transmits to the computer the instantaneous coordinates of

a pen held by the investigator. The tablet is 10 in. on a side and the coordinates are quantized to 0.01 in. As explained later, the operator uses the Grafacon pen to define certain areas and intervals of interest; for example, see Figures 3, 4, 17 and 18. The keypack, similar to a typewriter keyboard, contains all of the alphanumeric symbols. It is used to assign numbers to the areas and intervals of interest in Figures 3, 4, 17 and 18.

## SOFTWARE

All of the programs used to generate the displays reported in this paper were written in FORTRAN IV. This was possible because the DTDS system is supported by an extensive software package consisting of many FORTRAN-callable assembler language subroutines (Reference 1).

## DISPLAYS USED TO ANALYZE MULTISPECTRAL SCANNER DATA

### INTRODUCTION

The multispectral scanner collects radiant energy from a small area (i.e., resolution cell) on the ground and separates it into spectral components in each of twelve wavelength bands between  $0.40\mu$  and  $1.00\mu$ . The instantaneous output signals are recorded and subsequently converted to numbers in the range 0-255 by an analog-to-digital conversion process.\* The instantaneous field-of-view is scanned rapidly across the flight-line by a rotating mirror; the data is sampled at 222 points within each scan line. Successive scan lines are displaced along the flight line by the forward motion of the aircraft. The result is that multispectral scanner measurements are specified (i.e., referenced) on the basis of three independent variables: 1) scan line, 2) sample within a scan line, and 3) channel number.

---

\*The multispectral scanner data presented in this paper was processed by the Laboratory for Applications of Remote Sensing (LARS) at Purdue University. In addition to the multispectral scanner data, LARS also provided the ground truth information necessary to conduct pattern recognition studies.

## COLOR DISPLAY OF MULTISPECTRAL SCANNER DATA

Figure 2 is a photograph taken from the Digital Television Display System color monitor showing an approximately natural-color picture of the ground scene as reconstructed from the multispectral scanner data. This display consists of Lines 1 to 160 in the horizontal direction and Samples 1 to 111 in the vertical direction; this represents an area  $2/3 \times 1/2$  mi. on Purdue Flight Line C-1 flown on June 26, 1966.

At each display cell the intensity of the blue, green, and red is set according to the multispectral scanner outputs at that particular Line and Sample in Channels 2, 6 and 10 (i.e., radiance measured at that particular ground cell in the spectral ranges  $0.44-0.46\mu$ ,  $0.52-0.55\mu$ , and  $0.66-0.72\mu$ , respectively). For each of the three different colors the user can specify the intensity (one of 16 levels) associated with any multispectral scanner output (in the range 0-255). The user can also associate any one of the twelve multispectral scanner channels with each of the three colors; in this way a variety of "false-color" displays can be generated.

The necessary annotation data is included as an integral part of the display. For example, the following information is recorded in the top line of Figure 2:

- 1) The blue, green, and red intensities depend on Channels 2, 6, and 10, respectively.
- 2) The data is from Purdue Flight Line C-1 flown on 26 June 1966.
- 3) The display consists of Lines 1-160 and Samples 1-111 in steps one.\*

## INTERACTIVE METHOD FOR ENTERING GROUND-TRUTH INFORMATION

One of the most important functions which an investigator

---

\*The program also has a provision for displaying every other Line and/or every other Sample.



must perform in analyzing remote sensor data is to put ground-truth information into the computer. The Digital Television Display System is well-suited to this requirement in that it 1) displays a complete frame rather than a single scan line at a time, 2) is available immediately rather than requiring film processing, and 3) is responsive to on-line keyboard and graphical input devices.

In processing multispectral scanner data it is necessary to put into the computer certain training and/or test fields (Reference 2). These are areas where the material classification (e.g., crop-type) is known from a ground-truth survey. In the interactive system developed at the Manned Spacecraft Center the investigator uses a Grafacon pen to outline fields he recognizes in the natural or false-color display shown in Figure 2.

Movement of the Grafacon pen causes a corresponding line to be displayed on the monitor. Using this display, the investigator moves the pen so as to outline the field of interest.\* Once the boundary has been closed the computer responds by erasing the enclosed field from the display. The investigator then uses the keypack to type in the field number designation for this area.

The investigator is assisted in the interactive dialog with the system by computer-generated instructions displayed in the upper-left corner of the frame (e.g., see Figure 3). The table on the next page gives the sequence of instructions and the investigator's response. A short 16 mm color movie (NASA/MSC # S-70-370 available from the authors) shows the procedure used to set into the computer the boundaries of several different fields.

Figure 4 shows the result of outlining all fields within the frame. Here all areas (except roads) have been erased from the display leaving only the boundaries and associated field numbers. This information is also printed out in the form of a Xerox hard-copy for permanent documentation.

---

\*It should be emphasized that the fields can have any shape and orientation; for example, see Figure 3.

Computer-Generated Instruction	Investigator's Response
OUTLINE A FIELD	Use the Grafacon pen to outline the area of interest.
DRAW BOUNDARY AGAIN	Outline the area again, this time making sure to <u>close</u> the boundary.
POSITION FIELD NUMBER	Use the Grafacon pen to point to the place in the erased area where the field number should be displayed.
TYPE FIELD NUMBER	Use the keypach to type in the number associated with the outlined area.

#### GROUND-TRUTH MAP

The boundary information shown in Figure 4 is recorded on magnetic tape and used in subsequent processing to derive a ground-truth map in computer-readable form. This is a magnetic tape giving the material-type at every point (i.e., Line-Sample combination) within the outlined areas.

To obtain the ground-truth map the investigator only needs to specify (in the form of data cards) the material-type to be associated with each field number.\* Using an algorithm described in Reference 3, the computer automatically "fills in" the outlined fields with the designated material-types and records the result on magnetic tape. In this way a ground-truth tape was prepared for the entire flight line and is available from the authors.

---

\*In the case of the data presented here (Purdue Flight Line C-1, June 26, 1966) the necessary information resulted from a ground-truth survey conducted by the Laboratory for Applications of Remote Sensing.

Figure 5 is a color coded ground-truth map formed by displaying Lines 1 to 160 and Samples 1 to 111 of the ground-truth tape. In this figure the colors red, green, yellow, and blue represent areas of soybean, wheat, oats, and bare soil, respectively. The white areas are fields where no crop-type designation was available.

#### COMPUTER DERIVED LAND-USE MAP

Using algorithms described in the next section the computer processes the multispectral scanner data to determine automatically what material is present within each resolution element. This determination is based on data from several (e.g., four) channels at any given point.

The computer-derived results are displayed in the form of a color coded land-use map such as Figure 6. In this display the color assigned to a given point (i.e., Line-Sample combination) depends on the crop-type derived by the computer. As in Figure 5 the colors red, green, yellow and blue represent areas of soybean, wheat, oats, and bare soil, respectively.

#### ERROR MAP

By comparing Figures 5 and 6 it can be seen that the computer derived results generally agree with the actual ground-truth. To facilitate this comparison an error map display was developed. This is a presentation showing the correct crop-type (as its own distinctive color) at every point where the computer derived classification is incorrect; areas correctly classified (and white areas where no crop-type designation was available) are left blank. Figure 7 is an error map which shows the differences between Figures 5 and 6.

#### DISPLAYS USED FOR PATTERN RECOGNITION RESEARCH

##### INTRODUCTION

The term "pattern recognition" is often applied to the various computer-based methods by which material-type classifications are derived automatically from multispectral scanner measurements. The

pattern recognition process can be explained by reference to Figure 8. Here a point in the three-dimensional vector space represents the tip of a measurement vector having as its components the measured outputs from three spectral bands at a single resolution cell on the ground. The pattern recognition process is based on the fact that measurement vectors for different materials tend to cluster in different regions of measurement space. Pattern recognition systems operate in two stages:

- 1) The multidimensional measurement space is partitioned into non-overlapping regions associated with each type of material. The regions may be described analytically (Reference 2) or prestored in computer memory (Reference 4).
- 2) The measurement vector for each resolution cell is analyzed to determine which region it occupies in measurement space.

The displays shown in Figures 9 - 16 were developed to aid in the design of such pattern recognition systems.

#### MULTIDIMENSIONAL HISTOGRAM

In order to observe the clustering of measurements from a given material it is helpful to plot in three-dimensional space the measurement vectors of all resolution cells inside the training fields for that material; this is shown in Figure 8. It is possible to present this same information in two dimensions by plotting only those points which fall within a specified slice (i.e., range of values) in the third dimension. For example, in Figure 8 a training sample having the value  $x$  in Channel X, the value  $y$  in Channel Y, and a value in the range  $z_1$  to  $z_2$  in Channel Z is plotted at the point  $(x, y)$ . A multidimensional histogram for a given material is formed by counting the number of training samples at the point  $(x, y)$  and in the range  $z_1$  to  $z_2$ .

Figure 9 is a multidimensional histogram for soybean. This type of display is a quantitative version of the "Color-Space" plot described by Holter (Reference 5). At any point in the Channel 1 - Channel 9 plane is given the number of soybean training samples which are in the range 151 to 158 for Channel 11 and the range 179 to 186 for Channel 12. The material-type and the Channel 11 - Channel 12 slice are specified at the top of the display. The

range\* of values in Channel 1 and in Channel 9 are displayed on the horizontal and vertical axes, respectively.

Figure 10 is a histogram for corn plotted over the same range in Channels 1 and 9 and for the same slice in Channels 11 and 12. From Figures 9 and 10 it can be seen\*\* that multispectral scanner measurements from corn lie above and to the right of measurements from soybean. The computer-based pattern recognition system to be described next uses this as a basis for discriminating between soybean and corn.

### CLASSIFICATION SPACE

As explained previously, pattern recognition involves partitioning the measurement space into non-overlapping regions associated with each material-type. A common analytic method for deriving the classification space assumes a Gaussian probability density function and employs a maximum-likelihood decision rule.

Equation (1) gives the probability that Material  $i$  gave rise to the given measurement vector  $X$ .

$$P_i(X) = \frac{1}{(2\pi)^{N/2} |K_i|^{1/2}} \cdot \exp[ -1/2(X - M_i)^T K_i^{-1} (X - M_i) ] \quad \text{Eq. (1)}$$

where:

$P_i$  = Probability density function for the  $i^{\text{th}}$  material  
 $X$  = Measurement vector for a particular ground cell  
 $N$  = Number of channels used  
 $M_i$  = Mean vector for the  $i^{\text{th}}$  material  
 $K_i$  = Covariance matrix for the  $i^{\text{th}}$  material

---

\*The display provides only 16 points along the horizontal and vertical axes; however, each point can represent any integer number of multispectral scanner units. For example, in Figures 9 and 10 each point represents a cell 3 x 3 multispectral scanner units in the Channel 1 - Channel 9 plane.

\*\*The arrows in Figures 9 and 10 point to the same position in the Channel 1 - Channel 9 plane. These arrows were inserted for the convenience of the reader and are not part of the computer-generated display.

The mean vector  $M_i$  and the covariance matrix  $K_i$  which appear as parameters in Equation (1) are evaluated from the training samples of Material  $i$ . These are measurements from resolution cells inside training fields similar to the ones outlined in Figure 4.

The maximum-likelihood decision rule classifies a given sample as Material  $i$  if the probability of Material  $i$  computed from Equation (1) is higher than the probability of any other material. However, it is sometimes preferable to assign a sample to the category "Unknown" rather than misclassify it. This is accomplished by the parameters  $L$  and  $D$  in the decision rule given by Equation (2).

CLASSIFY THE GIVEN GROUND CELL AS MATERIAL  $i$  IF:

$$\begin{aligned} P_i(X) &\geq L \cdot P_j(X) \text{ and} \\ 1/2 (X-M_i)^T K_i^{-1} (X-M_i) &\leq D \end{aligned} \quad \text{Eq. (2)}$$

where:

$L$  = Likelihood ratio

$D$  = Threshold distance

Here a sample is classified as Material  $i$  only if the following two conditions are met:

- (1) The probability of Material  $i$  must be at least  $L$  times greater than the probability of the second most likely material.
- (2) The normalized distance between the measurement vector and the mean vector for Material  $i$  must be less than  $D$ .

Displays were developed to study the effect of  $L$  and  $D$  on the classification space.

Figures 11 - 16 are classification space displays. For specific values in Channels 11 and 12 they show at each point in the Channel 1 - Channel 9 plane the material-type derived from Equations (1) and (2). To facilitate comparison with the multidimensional histograms the range of values in Channel 1 and in Channel 9 are the same as for Figures 9 and 10. Also the specific values for Channels 11 and 12 (i.e., 154 and 182, respectively) are in the middle of the Channel 11 - Channel 12 slices.

Figure 11 shows the classification space for the case  $L = 1$

and  $D = 1000$ ; this corresponds to the maximum-likelihood decision rule. In this display the letters S, C, O, R, W, and Y represent soybean, corn, oats, red clover, wheat and rye, respectively. Figure 12 shows the case  $L = 5$  and  $D = 1000$ . Here no classification is made unless the probability of the most likely material is at least five times the probability of the second most likely material. The result is that regions on the boundaries between different materials are classified as "Unknown" (i.e., no classification is made). Figure 13 shows the case  $L = 1$  and  $D = 15$ . Here no classification is made if the measurement vector is further than the specified distance from the mean vector. In four-dimensional measurement space a threshold setting of  $D=15$  excludes the correct classification less than 1% of the time.

In Figure 14 the region of measurement space associated with soybean is represented by the yellow area\* for the case  $L = 1$  and  $D = 10$ . The effect of increasing the threshold distance to  $D = 20$  is to expand the soybean region to include the red area below and to the left. The reason the expansion is not symmetrical will be discussed in connection with Figure 16.

Figure 15 is a composite display formed by superimposing the multidimensional histogram for soybean (see Figure 9) on the soybean classification region. It can be seen that almost all the samples are correctly classified because they fall within the soybean region. Shown in red are the number of soybean samples which would be incorrectly classified as some other crop-type or classified as "Unknown".

Figure 16 is a composite display formed by superimposing the multidimensional histogram for corn (see Figure 10) on the soybean classification region. Shown in yellow are the number of corn samples which would be incorrectly classified as soybean. From this figure it can be seen that expansion of the soybean classification region upward and to the right would result in many corn samples being misclassified as soybean. This is the reason for the asymmetrical expansion of the soybean region in Figure 14 when the threshold distance was increased from 10 to 20.

---

\*This area is equivalent to the area cut out from the classification mask in the "light-pencil" technique for pattern recognition developed at the University of Michigan (Reference 5).

DISPLAYS USED TO ANALYZE NON-IMAGING SENSOR DATA

## INTRODUCTION

Unlike the multispectral scanner, many sensors produce output signals which cannot be displayed in the form of imagery such as Figure 2. This limitation results from the fact that they a) have very poor resolution and/or b) provide only a line scan over the ground scene. Non-imaging sensors currently used in the Earth Resources program include the infrared radiometer, infrared spectrometer, microwave radiometer and microwave scatterometer.

In order to analyze data from these non-imaging sensors it is helpful to display their output signals in spatial registration with ancillary imagery of the ground scene. References 3 and 6 describe a method for producing computer-generated transparencies which are superimposed over aerial photographs to show the exact sensor boresight path and the resulting output signals. Using these overlays an analyst can a) determine the sensor response for various materials which can be recognized from the photograph and/or b) identify the material which gave rise to any given sensor response.

This overlay approach has been extended to permit on-line interactive analysis using the Digital Television Display System. The black and white aerial photograph (e.g., a 9 x 9 in. RC8 camera frame) is scanned by a closed-circuit television camera and the resulting video signal is presented on the green tube of the precision color monitor. The computer-generated graphics showing the sensor boresight path and the output signals are displayed on the red tube. The two displays are superimposed\* and projected onto the ground-glass viewing screen as shown in Figure 1. Using the Grafacon pen and the keypack on-line to the computer the analyst can define flight path intervals over which the computer processes the sensor data. This approach will be explained by reference to infrared radiometer and microwave scatterometer data.

---

\*The magnification and alignment of the closed-circuit television camera are carefully maintained so that the resulting image on the monitor is in exact spatial registration with the computer-generated graphics.



## INFRARED RADIOMETER

The green part of Figure 17 is the closed-circuit television presentation of RC8 Frame 4419 taken during Mission 102. It shows an island (actually a spoil sand bank) adjacent to the intracoastal waterway south of Corpus Christi, Texas; the surrounding dark areas are cloud shadows. The red part of Figure 17 is computer-generated graphics showing the sensor boresight path\* and resulting output signal from the infrared radiometer. From this display it is apparent that the path of the sensor passed directly over the island and that the island was significantly warmer than the surrounding water.

The analyst interacts with the display by defining certain intervals along the sensor boresight path. He does this by using the Grafacon pen to point to the beginning and ending points of each interval. The computer responds by displaying a short mark across the sensor path at the selected position; six such points define three different intervals in Figure 17. After the analyst signals that he has set in all intervals of interest the system responds by computing the average sensor signal over each interval. The three average temperatures are displayed across from their corresponding intervals in Figure 17.

## MICROWAVE SCATTEROMETER

Figure 18 shows the boresight paths and output signals for four different look-angles of the microwave scatterometer. The look-angles (displayed in the upper-left corner) are 2, 5, 10, and 20 degrees forward from nadir. Sigma Zero, the reflectance coefficient for each look-angle, is plotted in spatial registration with the ground scene. It is apparent from this display that the reflectance coefficient increases as the beam passes over the island.

As before, the analyst interacts with the display by using the Grafacon pen to define intervals along the sensor path. In the case of the microwave scatterometer, however, the computer responds by

---

\*References 3 and 6 describe in detail how the sensor boresight path (relative to aerial photographs) is computed using aircraft guidance and navigation data recorded in flight.

displaying the average value of reflectance coefficient for all four look-angles in each interval. For example, in Interval #1 the average reflectance coefficients are -6, -16, -33, and -37 decibels for look-angles of 2, 5, 10, and 20 degrees, respectively.

The system also produces a Xerox hard-copy showing a graph of the reflectance coefficient versus look-angle for each interval. Figure 19 gives the microwave scatterometer signatures for the three intervals defined in Figure 18. Such displays can be used to determine whether the signatures are different enough to permit discrimination between materials of interest.

### CONCLUSIONS

An interactive display/graphics system has been developed for remote sensor data analysis. This system has the following advantages over other systems being used currently:

- 1) It displays digital data in color a full frame at a time.
- 2) The display is available immediately because no photographic processing is involved.
- 3) It permits the analyst to interact with the display and the data processing.

The display system has been used in the following applications:

- 1) Natural and false color displays of multispectral scanner data.
- 2) Ground-truth and land-use maps.
- 3) Multidimensional histograms and classification-space plots for pattern recognition research.
- 4) Displays showing non-imaging sensor data in spatial registration with ancillary imagery.
- 5) Microwave scatterometer signatures.

The interactive graphics capability has been used for the following purposes:

- 1) To define training and test fields by setting into the computer boundaries and ground-truth information.
- 2) To define intervals along the boresight paths of non-imaging sensors.

The development of such systems has considerable programmatic importance in that they make it possible to analyze large quantities of remote sensor data in a short time.

REFERENCES

1. "Basic Display Access Method for Interactive Terminals--User's Document," Information Systems Division Internal Note MSC-01625, Manned Spacecraft Center, Houston, Texas, May 1970.
2. K. S. Fu, D. A. Landgrebe, and T. L. Phillips, "Information Processing of Remotely Sensed Agricultural Data," Proceedings of the IEEE, Vol. 57, No. 4, pp. 639-653, April 1969.
3. W. G. Eppler and R. D. Merrill, "Relating Remote Sensor Signals to Ground-Truth Information," Proc. IEEE, Vol. 57, No. 4, pp. 665-675, April 1969.
4. W. G. Eppler, C. A. Helmke, and R. H. Evans, "Table Look-Up Approach to Pattern Recognition," Proc. 7th Symp. on Remote Sensing of Environment (University of Michigan, Ann Arbor), May 1971.
5. Marvin R. Holter, "Research Needs: The Influence of Discrimination, Data Processing, and System Design," Chapter 9 in Remote Sensing with Special Reference to Agriculture and Forestry, National Academy of Sciences, Washington, D. C., 1970, pp. 372-374.
6. W. G. Eppler, "Accuracy of Determining Sensor Boresight Position During Aircraft Flight-Test," Proc. 6th Symp. on Remote Sensing of Environment (University of Michigan, Ann Arbor), pp. 205-225, October 1969.

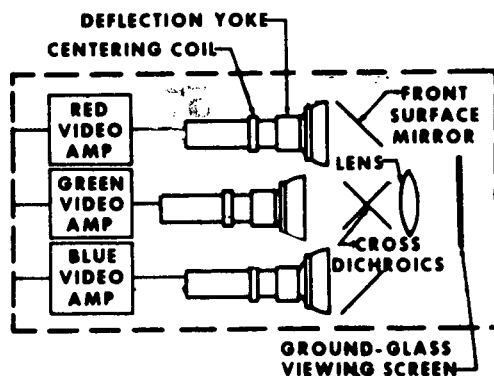


Figure 1.-Schematic diagram of precision color monitor.

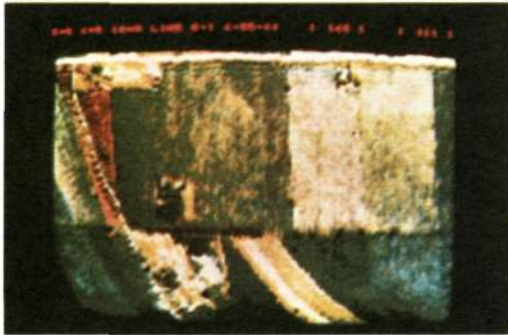


Figure 2.- Natural-color display of multispectral scanner data.

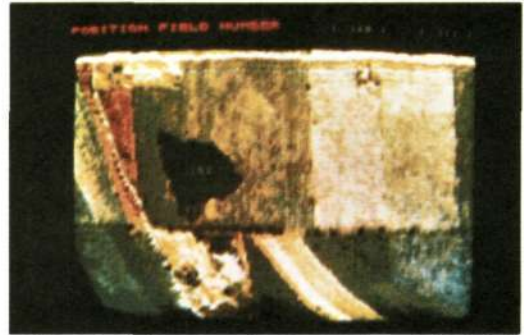


Figure 3.- Interactive method for entering ground-truth areas.

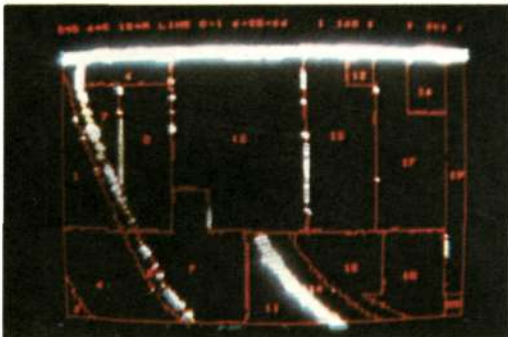


Figure 4.- Completed boundaries for ground-truth areas.



Figure 5.- Display showing color coded ground-truth map.

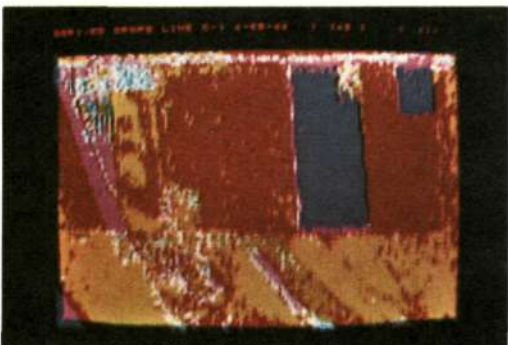


Figure 6.- Display showing computer derived land-use map.



Figure 7.- Errors in the computer derived land-use map.

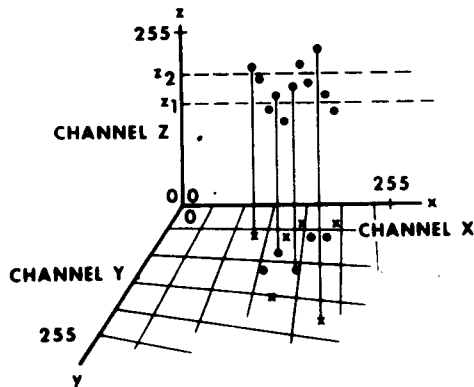


Figure 8.- Multispectral scanner data represented as points in three-dimensional measurement space.

580

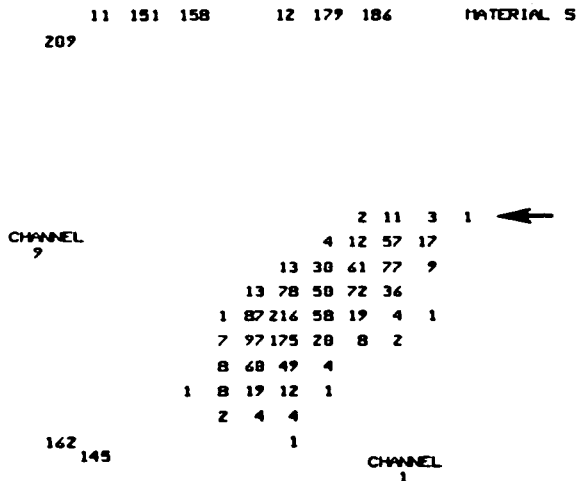


Figure 9.- Multidimensional histogram for soybean.

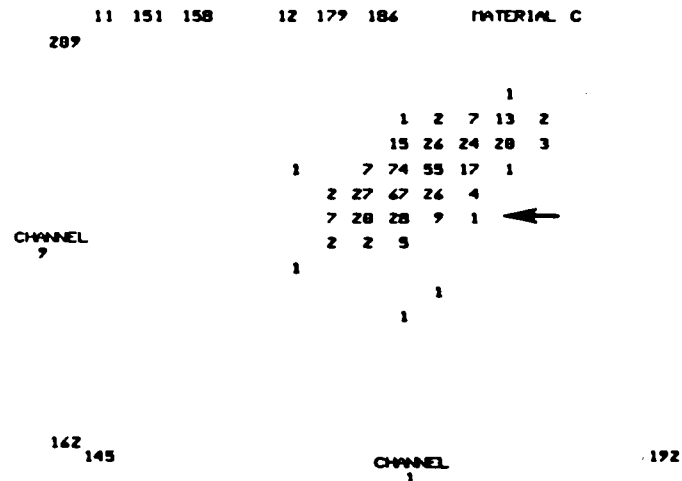


Figure 10.- Multidimensional histogram for corn.

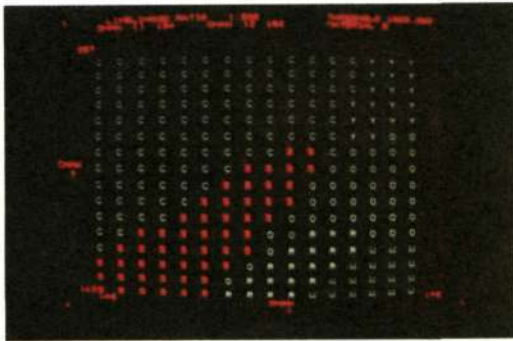


Figure 11.- Classification space derived using L=1.0 and D=1000.

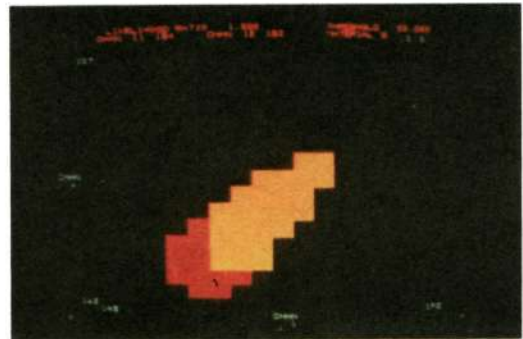


Figure 14.- Areas classified as soybean for D=10 and D=20.

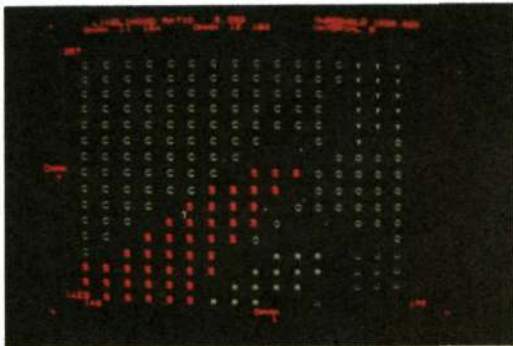


Figure 12.- Classification space derived using L=5.0 and D=1000.

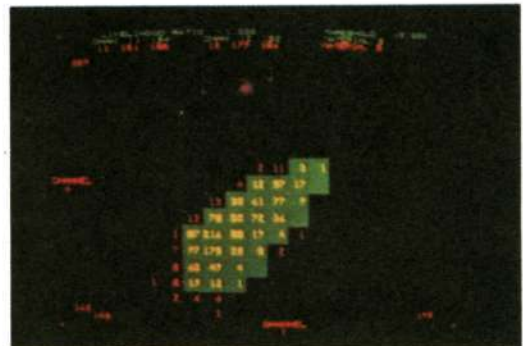


Figure 15.- Soybean histogram on area classified as soybean.

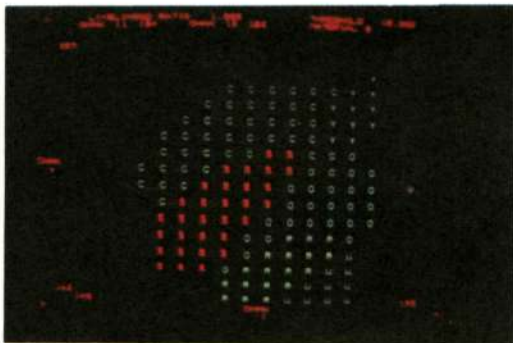


Figure 13.- Classification space derived using L=1.0 and D=15.

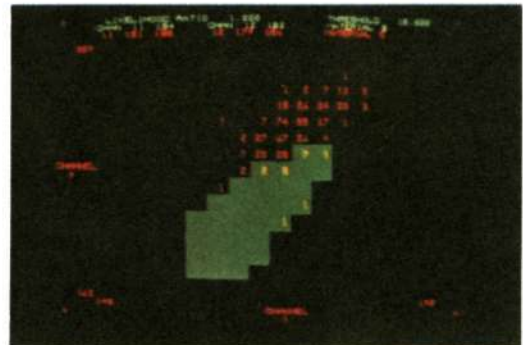


Figure 16.- Corn histogram on area classified as soybean.

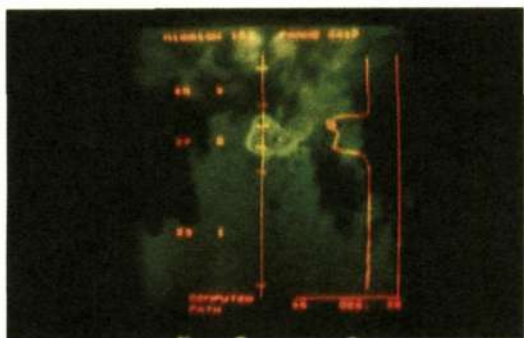


Figure 17.- Boresight path and sensor return for infrared radiometer.

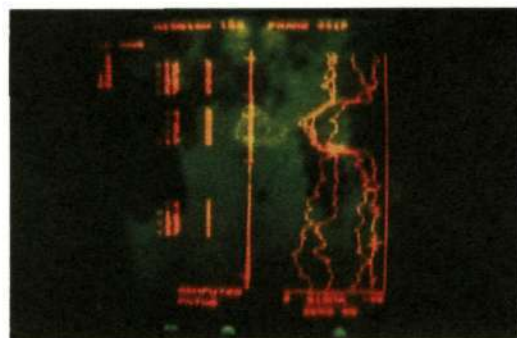


Figure 18.- Boresight path and sensor return for microwave scatterometer.

MISSION 102 SITE 175 FLIGHT FCF 3 LINE 2 FRAME 4419

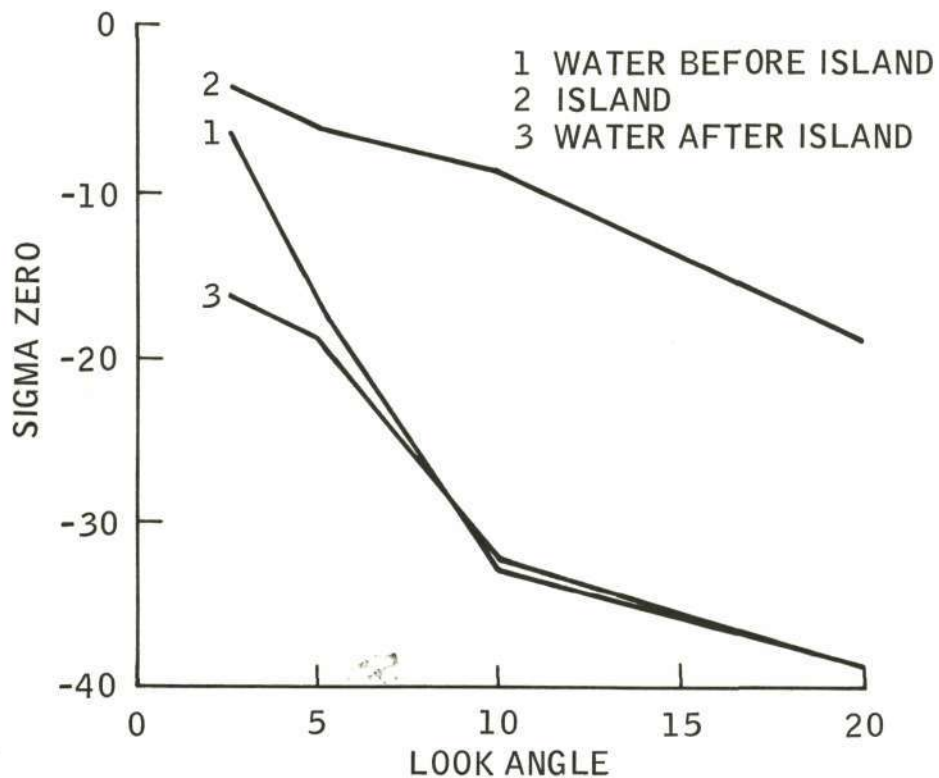


Figure 19.- Microwave scatterometer signatures for three different flight-path intervals.

## RESULTS OF SCATTEROMETER SYSTEMS ANALYSIS

FOR NASA/MSC EARTH OBSERVATION

SENSOR EVALUATION PROGRAM

by

K. Krishen, N. Vlahos, O. Brandt  
Earth Observation Division  
Lockheed Electronics Company

and

G. Graybeal  
NASA/MSC Earth Observation Division

November 1970

ABSTRACT

Radar scatterometers have applications in the NASA/MSC Earth Observation Aircraft Program. Over a period of several years, several missions have been flown over both land and ocean. In this paper a systems evaluation of the NASA/MSC 13.3 GHz Scatterometer System is presented. The effects of phase error between the scatterometer channels, antenna pattern deviations, aircraft attitude deviations, environmental changes, and other related factors such as processing errors, system repeatability, and propeller modulation, were established. Furthermore, the reduction in system errors and calibration improvement was investigated by taking into account these parameter deviations. Typical scatterometer data samples are presented.

ACKNOWLEDGMENTS

The work reported in this paper was supported by NASA/MSC under contract NAS 9-5191. The hardware test data were provided by the Telecommunications Systems Division of NASA/MSC. The cooperation of J. Fisher and J. Skipworth (Computation and Analysis Division) in processing and analysis of test tape data is appreciated.



## INTRODUCTION

The airborne 13.3-GHz Single Polarized Scatterometer is currently used by the NASA/MSC Earth Observation Division to investigate its use for the following applications:

- Study of wind fields and resulting sea waves; the dependence of radar scattering cross section ( $\sigma_o$ ) on parameters such as local wind velocity, significant wave height, and sea spectrum
- Discrimination of arctic ice types
- Study characteristics of the earth's surface in order to determine and catalog reflectivity data for various types of land areas for geoscience investigations.

These studies are aimed at correlating surface composition and shape with backscattering cross sections as a function of incident angle, polarization, and frequency.

The 13.3-GHz scatterometer is a continuous-wave doppler radar system, designed to measure reflectivity per unit area as a function of the angle of incidence ( $\theta$ ). The scatterometer antenna illuminates a fan-shaped area (approximately  $120^\circ$  along the aircraft flightpath), and the data is gathered for vertical-transmit, vertical-receive polarization states only. As a result of the forward motion of the aircraft, doppler frequency shifts are introduced and the signal returned by a ground resolution cell can be retrieved by bandpass filtering at the corresponding doppler frequencies.

Several scatterometer missions have been flown by NASA/MSC over several years. In the process of data interpretation and correlation from various missions and scatterometers, several problem areas were evident. These problems were related to the scatterometer hardware parameter evaluation, the data processing, and the antenna pattern parametric evaluation. Consequently, a systems evaluation was undertaken within the Earth Observation Division at MSC for the 13.3-GHz Single Polarized System. In this paper a review of the results of this evaluation is presented.

SENSOR TEST EVALUATION

A circuit diagram of the 13.3-GHz system is shown in Figure 1. A functional and equipment description of the system is contained in reference 1. To define the terminology used in this paper, a brief description of the system follows.

The radar-frequency energy is radiated by an antenna which has a wide fore-and-aft beam and a narrow transverse beam (Figure 2). The returned energy may be separated using the doppler equation as a function of incidence angle

$$f_d = \frac{2V}{\lambda} \sin \theta \quad (1)$$

where

V = aircraft ground velocity

$\lambda$  = wavelength of the transmitted power

$\theta$  = angle of incidence.

The returned energy is received from all angles of incidence simultaneously and is divided equally into two channels, one of which is 90° out of phase with the other. The data for each channel, detected by a direct-to-audio technique, are amplified and recorded on an FM tape recorder. The fore-and-aft beam data are separated by use of a sign sensing technique (reference 2). To calibrate the system a ferrite modulator is used to provide an absolute power reference level of the transmitted signal. The  $\sigma_0$  versus  $\theta$  information is obtained by subtracting known system losses and aircraft attitude and velocity factors and comparing the remainder with a reference signal level.

The radar cross section per unit area is given by the equation

$$\sigma_0(\theta) = \frac{P_R}{P_T} \frac{2(4\pi)^3}{\lambda^3} \cdot \frac{Vh^2}{\Delta f_d} \cdot \frac{1}{\int_{-\psi_1}^{\psi_2} G_T(\psi)_\theta G_R(\psi)_\theta d\psi} \quad (2)$$

where

$P_T$  = transmitted power

$P_R$  = power received in the doppler window defined by  $\Delta f_d$

$G_T, G_R$  = transmitting antenna and receiving antenna gain, respectively, as a function of  $\theta$  (incident angle), and  $\psi$  (cross track angle)

$h$  = altitude of the aircraft.

Equation (2) may be rearranged for computer calculations as

$$\sigma_0(\theta) = RC + 20 \log h + 10 \log V + 20 \log \frac{E_i}{E_r} + 10 \log \frac{BW_R}{BW_i} + R(D) - G_0^2 F'(\theta) + Z(\theta) \quad (3)$$

where

$RC$  = radar offset constant

$h$  = aircraft height

$E_i$  = average radar data at  $i$ th filter

$E_r$  = average reference data

$BW_i$  = bandwidth of  $i$ th filter

$R(D)$  = system rolloff

$Z(\theta)$  = any system errors  $f(\theta)$  which can be determined

$G_0^2 F'(\theta)$  = two-way antenna gain

$BW_R$  = reference bandwidth

The radar offset constant (RC) is computed from the following equation

$$RC = 10 \log_{10} 2(4\pi)^3 + FMC - 10 \log_{10} P_T - 30 \log_{10} \lambda \quad (4)$$

where

FMC = ferrite modulator constant.

As a result of the time element involved in the data gathering program, several factors can contribute to a change in the scatterometer system. As a consequence an investigation of mission-to-mission consistency and repeatability of the scatterometer data was undertaken. In this section a summary of the hardware test results in connection with the consistency and repeatability study is presented.

#### KLYSTRON POWER

In the process of checking the klystron power output for missions 70 and 88, it was found that the quoted output klystron power for these two missions was 1.6 watts and 2.1 watts, respectively. However, in the program for computing the scattering cross section, a power of 1.5 watts was assumed for both missions. To reflect correct transmitted power the previously processed data for mission 88 was adjusted by 1.5 dB. For the succeeding missions two new klystrons were obtained by NASA/MSD (S/Ns 235 and 251). Environmental testing also was conducted on both klystrons where the ambient air temperature was taken between 0° F to 100° F with the klystron body temperature varying from 30° F to 130° F. Figure 3 shows results wherein the output power is reasonably constant for these klystrons at 31.3 dBm (S/N 235) and 31.6 dBm (S/N 251). The long term frequency shift is approximately 26 MHz.

#### FERRITE MODULATOR

The ferrite modulator was tested for temperature stability. The ferrite modulator, measured over a temperature range of 0° F to 200° F, was found constant. The recently measured value of the ferrite modulator constant is -125.72 dB, while the value measured 2 years ago was -127.7 dB. The proper ferrite modulator constant was reflected in the radar offset constant for mission 119 and subsequent missions.

## WAVEGUIDE INSERTION LOSSES

The 13.3-GHz system was tested for insertion losses in the waveguide plumbing. These losses, shown in Table I, determine the power levels. Adjustments in the radar offset constant, reflecting the latest loss measurements, indicate good consistency of the values of these losses.

TABLE I.- WAVEGUIDE INSERTION LOSSES

13.3-GHz Single Polarized Scatterometer Waveguide Insertion Loss Test Data (reference Figure 1):

Receiver antenna (1) to diode mixer (5): 3.3 dB  
 Receiver antenna (1) to diode mixer (6): 3.6 dB  
 Klystron (2) to transmit antenna port (3): 0.5 dB  
 Klystron (2) to diode mixer port (6): 37.4 dB  
 Klystron (2) to diode mixer port (5): 36.5 dB

## ANTENNA BORESIGHT

To process data from missions 88 and 70, the 13.3-GHz scatterometer antenna was originally boresighted down (fore beam down) by 3° from the NP3A aircraft centerline. In reviewing the recent boresight data it was noted that the antenna was boresighted down by only 1.5° (fore beam down). The computer program therefore was modified to reflect the 1.5° boresight alignment.

## PROPELLER MODULATION

Propeller modulation was noticed at 20,000-foot altitude on the NP3A aircraft. The frequency spectrum of the propeller modulation corresponds to about 42° to 60° angle of incidence for an aircraft speed of 200 knots. With the present klystron, the effect of propeller modulation is not serious at altitudes below 5,000 feet for high sea states. Further editing of the effect of propeller modulation can be achieved by properly selecting the doppler frequencies in this interference band.

## ROLLOFF CONSTANT CURVES

The 13.3-GHz Single Polarized Scatterometer System's amplifier's four attenuators were checked for frequency response. This resulted in new rolloff curves for use in the computer processing program. Figure 4 shows a comparison of previous and newly measured values. The new rolloff constants have to be taken for all missions succeeding mission 88.

## ANTENNA PATTERN MEASUREMENTS

The 13.3-GHz Single Polarized Scatterometer System was designed and fabricated in early 1965 and adopted by the NASA Apollo Program to determine lunar reflectivity characteristics by overflying selected test sites. The system was a breadboard design with emphasis placed upon relative rather than absolute measurements. The antenna measurements were made on a two-way basis using a CV-240 aircraft mockup. At the termination of the lunar reflectivity program, this sensor was installed on board the NP3A and the CV-240 aircraft for Earth Resources studies. The data for all sea state missions after mission 60 were collected aboard the NP3A aircraft.

In reviewing the data from missions 70 and 88 (with CV-240 mockup patterns), some anomalies were observed in the power spectral density plots (return versus doppler shift). It was recommended that patterns with the NP3A mockup be utilized in the data reduction program. Further study of the data from missions 70 and 88 indicated that in order to reduce errors in scattering cross section, additional antenna pattern data would be required. The CV-240 mockup measurements were made for a long track of  $\pm 70^\circ$  at  $1^\circ$  intervals on the principal axis only, and the cross track data was taken every  $10^\circ$  along the principal axis (reference 1). New antenna patterns with the NP3A mockup were obtained on a better range (0.1 dB accuracy in measurement). These patterns, obtained in September 1969, were made for  $\pm 70^\circ$ , every  $0.2^\circ$  on the long track and in the cross track ( $\psi$ ,  $\pm 10^\circ$ ) in increments of  $0.5^\circ$  out to  $\pm 3^\circ$  and  $1^\circ$  increments from  $\pm 3^\circ$  to  $\pm 10^\circ$ .

Figure 5 illustrates the differences in antenna patterns. The value of  $G_{0F}^2(\theta)$  is calculated with 3 dB beamwidth points (reference 1). "Old  $G_{0F}^2(\theta)$ " refers to the CV-240 mockup pattern given in reference 1; "Redop 1" refers to patterns obtained with the NP3A mockup with no change in radome configuration; and "Redop 1 modified" (used in all missions after mission 88) refers to patterns with the NP3A mockup after the antenna was cleaned and a new radome was fabricated.

Differences up to 5 dB are indicated in the antenna gain values. The study of antenna pattern integration into the processing program (in the next section) shows that the elaborate new antenna gain measurements have made it possible to reduce the errors in scattering cross section resulting from insufficient antenna gain values.

#### TAPE RECORDER ADJUSTMENTS

A test was conducted on the Ampex FR-1900 Tape Recorder in the Data Techniques Laboratory, recording on tracks 2 and 4. The results showed an azimuth adjustment of  $\pm 14$  microseconds at 30-ips tape speed. This means that the azimuth adjustment on this tape recorder can shift the phase relationship between channel 1 and channel 2 by about  $\pm 50^\circ$  at 10 kHz. An analysis of phase error between channels 1 and 2 (see next section) shows that this phase shift contributes a significant error to the scattering cross-section values. The results of the FR-1900 study made it clear that a means of adjusting the Computation and Analysis Division (CAD) playback tape recorders azimuth verniers to a zero phase reference was necessary.

Measurements on the 13.3-GHz system showed that the land and sea filters were matched and that the only significant skew or phase error was caused by the tape recorder record head alignment. A test tape was made on board the NP3A aircraft. A sweep oscillator output was fed into the 13.3-GHz system at the preamplifier output location (Figure 1). The signal (a 12-kHz sine wave and a sine sweep from 500 Hz to 12 kHz) passed through the sea/land filters and postamplifiers, and was recorded on the Ampex AR-1600 tape recorder.

This tape was analyzed in the Data Techniques Laboratory. The results showed that the phase error increased linearly with frequency and that it could be nulled with the reproduce tape recorder azimuth adjust. Based on this study, a method of adjusting the CAD tape recorders for a zero phase error was outlined. The method consists of recording an in-phase 10-kHz sine wave on the two channels and while monitoring these channels with a dual beam oscilloscope at the playback station, adjusting the azimuth control of the playback recorder for an in-phase condition (reference 3). This adjustment assures that no phase shift is introduced into the audio and recording portion of the 13.3-GHz Scatterometer System.

## SYSTEMS PERFORMANCE EVALUATION

During the evaluation of the systems performance, three areas appeared for further study. The first area was related to the inconsistencies in the previously reported circuit configurations. This is particularly important in separating the fore and aft beam data. The results of a study leading to the correct circuit configuration of the 13.3-GHz system is described. The second area was related to the effects of a phase shift error in the RF portion of the system. The third area of study was to investigate various methods for integrating the antenna pattern in the calculation of the scattering cross section.

### CIRCUIT CONFIGURATION FOR SIGN SENSING

Inconsistencies in the documentation of 13.3-GHz Single Polarized Scatterometer System configuration presented a task in determining fore and aft beam data. In particular, the following uncertainties were encountered:

- Which channel has the calibration signal?
- Which channel is phase-shifted by 90°?
- Is the phase shift leading or lagging?

One of the procedures developed to ascertain the correct fore and aft beam separation was the simulated doppler test. A positive or a negative doppler signal of 1 kHz was produced (Figure 6) by controlling the direction of rotation and speed of the motor. The doppler signals developed were at 13.3 GHz ( $\pm 1$  kHz) and of constant amplitude. The (+) sign corresponds to the fore-beam data and the (-) sign to the aft-beam data.

The data sequence consisted of 2 minutes of a positive 1-kHz doppler signal, followed by a period when the drive power was turned off, causing the positive 1-kHz signal to decrease in frequency to 0 Hz. Further, the preceding sequence was repeated with the motor drive reversed, thereby simulating negative 1 kHz, followed by a decreasing frequency signal to 0 Hz. The data were recorded on a magnetic tape. The data were processed using an analog processing procedure to check the power spectral density of the recorded signal.

The tape was processed utilizing the CAD digital computer program (reference 2). Figure 7 shows positive 1-kHz signal in the fore beam,



and Figure 8 shows the negative 1-kHz signal in the aft beam. It was concluded that the program was producing the correct doppler data. The fore beam data resulted from positive doppler and the aft beam from negative doppler, as the case should be. Furthermore, the calibration was on channel 1. At this time a problem arose as to the correct phase shift between channels 1 and 2. Further investigation into hardware plumbing using X-rays was conducted. The following conclusions were made:

- The phase shift was not introduced through the local oscillator
- The phase shift was introduced in the 3 dB coupler (Figure 9)
- The signal in channel 1 lags the channel 2 signal by 90°.

These conclusions are reflected in Figures 1 and 9.

#### PHASE SHIFT ERRORS

In validating the NASA/MSR 13.3-GHz Single Polarized Scatterometer data, it is essential that the influence of the system on the data be completely formulated. The phase shift between channels 1 and 2 is an important parameter of this system. The fore and aft beam data can be separated accurately if the amplitudes of the signals are equal for channels 1 and 2 before data processing and the phase difference between the two is 90°. However, there are several possible reasons why this phase difference can vary from 90°. The possible sources of error are (Figure 9):

1. Hybrid coupler output may not have 90° phase shift
2. Ferrite modulator error could be caused by temperature changes
3. Possible local oscillator phase difference at the input to the channels
4. Mixers and amplifiers could give unequal phase shift in the two channels
5. Tape recorders phase shift could be introduced through nonalignment.

The phase shift errors resulting from amplifiers, filters, and tape recorders have been checked and present no problem (see previous section). In the following paragraphs the errors in scattering cross section due to any phase shift errors in the RF portion of the system will be derived. The calculated values have been compared with measured values.

#### Mathematical Analysis of the RF Phase Shift

The received signals from fore and aft beam scattering at a particular angle of incidence are assumed to be, respectively

$$\begin{aligned} \sqrt{2} A_+(\omega_d, t) \cos [(\omega_T + \omega_d)t + \alpha(\omega_d, t)] \\ \sqrt{2} A_-(\omega_d, t) \cos [(\omega_T - \omega_d)t + \beta(\omega_d, t)] \end{aligned} \quad (5)$$

where

$\omega_T$  = the transmitter frequency

$\pm\omega_d$  = the doppler shift corresponding to fore and aft beam at a particular angle of incidence

$\alpha(\omega_d, t)$  = the transit phase shift introduced by the rough surface in the fore beam

$\beta(\omega_d, t)$  = the transit phase shift introduced by the rough surface in the aft beam

The output in channels 1 and 2 (Figure 9) is

$$\begin{aligned} \text{channel 1 (F}_1\text{)} &= k[A_+ \sin(\omega_d t + \alpha) + A_- \sin(-\omega_d t + \beta)] \\ \text{channel 2 (F}_2\text{)} &= k[A_+ \cos(\omega_d t + \alpha) + A_- \cos(-\omega_d t + \beta)] \end{aligned} \quad (6)$$

where

$k = 1/2[\text{channel transfer function/gain}]$ .

The value of  $A_+$  and  $A_-$  can be obtained by taking Fast Fourier Transform (FFT) of equation (6). After a few manipulations the values of  $A_+$  and  $A_-$  are given by

$$\begin{aligned} A_+^2 &= k^2 [\{\text{Re } f_1 - \text{Im } f_2\}^2 + \{\text{Re } f_2 + \text{Im } f_1\}^2] \\ A_-^2 &= k^2 [\{\text{Re } f_1 + \text{Im } f_2\}^2 + \{\text{Re } f_2 - \text{Im } f_1\}^2] \end{aligned} \quad (7)$$

where

$\text{Re } f_1$  is the real part of the FFT of channel 1

$\text{Im } f_2$  is the imaginary part of the FFT of channel 2, etc.

Now, the total RF phase shift between the two channels is assumed to be

$$(90 + \theta_m + \theta_e)$$

where  $\theta_m$  is the phase difference due to ferrite modulator, and  $\theta_e$  the total error due to other sources. The signal in channel 1 is mixed with  $\cos(\omega_T t + \theta_m)$  while the channel 2 signal is mixed with  $\cos(\omega_T t)$ . The resultant output at the end of channels 1 and 2 is, respectively

$$F_{1e} = k[A_+ \sin(\omega_d t + \theta_e + \alpha) + A_- \sin(-\omega_d t + \theta_e + \beta)] \quad (8)$$

$$F_{2e} = k[A_+ \cos(\omega_d t + \alpha) + A_- \cos(-\omega_d t + \beta)]$$

The FFT of equation (8), ignoring the negative frequency terms, yields

$$f_{1e} = \frac{k}{2} \left[ \left\{ A_+ \sin(\theta_e + \alpha) + A_- \sin(\theta_e + \beta) \right\} + j \left\{ A_+ \cos(\theta_e + \alpha) - A_- \cos(\theta_e + \beta) \right\} \right] \delta(\omega_d) \quad (9)$$

$$f_{2e} = \frac{k}{2} \left[ \left\{ A_+ \cos \alpha + A_- \cos \beta \right\} + j \left\{ A_- \sin \beta - A_+ \sin \alpha \right\} \right] \delta(\omega_d)$$

As a result of phase error, the values of fore and aft beam data are different from  $A_+$  and  $A_-$ . Consequently, the value of fore and aft beam signal is assumed to be, respectively

$$\begin{aligned} \sqrt{2} X_+(\omega_d, t) \cos [(\omega_T + \omega_d)t + m(\omega_d, t)] \\ \sqrt{2} X_-(\omega_d, t) \cos [(\omega_T - \omega_d)t + n(\omega_d, t)] \end{aligned} \quad (10)$$

The following equation can be obtained from equations (9) and (10)

$$\begin{aligned} X_+ \cos m &= \frac{k}{2} [A_+ \cos \alpha + A_- \cos \beta + A_+ \cos (\theta_e + \alpha) \\ &\quad - A_- \cos (\theta_e + \beta)] \\ X_+ \sin m &= \frac{k}{2} [A_+ \sin (\theta_e + \alpha) + A_- \sin (\theta_e + \beta) - A_- \sin \beta \\ &\quad + A_+ \sin \alpha] \\ X_- \cos m &= \frac{k}{2} [A_+ \cos \alpha + A_- \cos \beta - A_+ \cos (\theta_e + \alpha) \\ &\quad + A_- \cos (\theta_e + \beta)] \\ X_- \sin m &= \frac{k}{2} [A_+ \sin (\theta_e + \alpha) + A_- \sin (\theta_e + \beta) + A_- \sin \beta \\ &\quad - A_+ \sin \alpha] \end{aligned} \quad (11)$$

The following values can be obtained from equation (11)

$$\frac{X_+}{A_+} = \left[ \frac{1}{2} + \frac{P^2}{2} + \frac{P}{2} \cos (\alpha + \beta) + \left( \frac{1}{2} - \frac{P^2}{2} \right) \cos \theta_e - \frac{P}{2} \cos (\alpha + \beta + 2\theta_e) \right]^{1/2} \quad (12)$$

$$\frac{X_-}{A_-} = \left[ \frac{1}{2} + \frac{1}{2P^2} + \frac{1}{2P} \cos (\alpha + \beta) + \left( \frac{1}{2} - \frac{1}{2P^2} \right) \cos \theta_e - \frac{1}{2P} \cos (\alpha + \beta + 2\theta_e) \right]^{1/2}$$

where

$$P = \frac{A_-}{A_+}$$

The error in the radar cross section is  $20 \log_{10} (X_+/A_+)$  and  $20 \log_{10} (X_-/A_-)$ , for fore and aft beam, respectively.

#### Discussion of Theoretical Results

The values of  $20 \log_{10} \frac{X_+}{A_+}$  and  $20 \log_{10} \frac{X_-}{A_-}$  were calculated on a computer (reference 4). The values of  $P$  were taken as 0.01, 0.1, 0.8, 1.0, 10.0, and 100.0. This corresponds to a range of difference of -40 dB to +40 dB between the fore and aft data. Values of  $\theta_e$  were taken as 2.0°, 4.0°, 6.0°, 8.0°, and 10.0°;  $(\alpha+\beta)$  were varied between 0° and 360° in 5° steps. Table II summarizes the results, giving the values of maximum errors. The value of  $(\alpha+\beta)$ , at which the maximum error occurs, is also given in the table. The following conclusions can be drawn from the computed results presented in Table II:

1. The value of maximum error increases as  $\theta_e$  increases and is dependent on the value of  $(\alpha+\beta)$ .

TABLE II.- MAXIMUM VALUE OF ERROR FOR SELECTED PARAMETERS

$\theta_e$ , deg	P	$(\alpha+\beta)$ , deg	$20 \log_{10} \left( \frac{X_+}{A_+} \right)$	$20 \log_{10} \left( \frac{X_-}{A_-} \right)$
2.0	0.01	90	0.00019	8.769
2.0	0.01	270	-0.0028	-2.535
2.0	0.1	90	0.0138	1.395
2.0	0.1	270	-0.0164	-1.666
2.0	0.8	90	0.119	0.186
2.0	0.8	270	-0.12339	-0.1928
2.0	1.0	90	0.14889	0.14889
2.0	1.0	270	-0.15400	-0.15400
2.0	10.0	90	1.395	0.0138
2.0	10.0	270	-1.666	-0.0164
2.0	100.0	90	8.76	0.0001918
2.0	100.0	270	-2.5	-0.002838
4.0	.01	85	-0.00226	13.04
4.0	.01	265	-0.008326	7.926
4.0	0.1	85	0.0249	2.596
4.0	0.1	265	-0.03567	-3.735
4.0	0.8	85	0.2339	0.365
4.0	0.8	265	-0.2513	-0.3929
4.0	1.0	85	0.2928	0.2928
4.0	1.0	265	-0.3139	-0.3139
4.0	10.0	85	0.2596	0.02498
4.0	10.0	265	-3.7353	-0.03567
4.0	100.0	85	13.043	-0.00226
4.0	100.0	265	7.926	-0.00836
6.0	0.01	85	-0.007361	15.8926
6.0	0.01	265	-0.016464	12.5374
6.0	0.10	85	0.03348	3.6479
6.0	0.10	265	-0.05754	-6.4581
6.0	0.80	85	0.3447	0.539159
6.0	0.80	265	-0.38387	-0.60031
6.0	1.0	85	0.4317	0.4317
6.0	1.0	265	-0.4794	-0.4794

TABLE II.- MAXIMUM VALUE OF ERROR FOR  
SELECTED PARAMETERS (Concluded).

$\theta_e$ , deg	P	$(\alpha+\beta)$ , deg	$20 \log_{10} \left( \frac{X_+}{A_+} \right)$	$20 \log_{10} \left( \frac{X_-}{A_-} \right)$
6.0	10.0	85	3.6479	0.03348
6.0	10.0	265	-6.4581	-0.0575
6.0	100.0	85	15.8926	-0.007361
6.0	100.0	265	12.537	-0.016464
8.0	0.01	85	-0.01511	18.032
8.0	0.01	260	-0.02725	15.53
8.0	0.1	80	0.03930	4.5827
8.0	0.1	260	-0.082097	-10.4168
8.0	0.8	80	0.45134	0.70627
8.0	0.8	260	-0.52087	-0.8151
8.0	1.0	80	0.5655	0.5655
8.0	1.0	260	-0.6504	-0.6504
8.0	10.0	80	4.5827	0.03905
8.0	10.0	260	-10.41	-0.08209
8.0	100.0	80	18.032	-0.01511
8.0	100.0	260	15.532	-0.02725
10.0	0.01	80	-0.02551	19.74
10.0	0.01	260	-0.0407	17.75
10.0	0.1	80	0.0425	5.4263
10.0	0.1	260	-0.10944	-18.0867
10.0	0.8	80	0.5544	0.8683
10.0	0.8	260	-0.66337	-1.0390
10.0	1.0	80	0.6953	0.6953
10.0	1.0	260	-0.828	-0.828
10.0	10.0	80	5.426	0.0425
10.0	10.0	260	-18.08	-0.1094
10.0	100.0	80	19.7459	-0.02551
10.0	100.0	260	17.57	-0.04071

2. The value of the error in radar cross section increases as the value of  $P$  becomes small or large compared to 1.0; for example,  $\theta_e = 2.0^\circ$  and  $P = 0.01$ , a maximum error of 8.769 dB can result in the aft beam data.
3. In case the fore and aft data are nearly equal ( $P = 1.0$ ), the maximum error in the value of fore and aft radar scattering cross sections (for  $\theta_e$  up to  $10^\circ$ ) is either 0.695 or -0.828 depending on the value of  $(\alpha+\beta)$ .
4. A computer search was made in order to find the value of maximum error for each value of  $\theta_e$ . This revealed that the value of error in  $\sigma_0$  (fore beam) tends toward -97.95 dB ( $X_+ \rightarrow 0$ ) for the following values of  $\theta_e$ ,  $(\alpha+\beta)$ , and  $P$ .

$\theta_e^\circ$	$(\alpha+\beta)^\circ$	$P$	$X_+/A_+$
1	269.0	114.588	0.2859E - 03
2	268.0	57.29	0.1566E - 03
3	267.0	38.19	0.729E - 04
4	266.0	28.6362	0.555E - 04
5	265.0	22.9037	0.578E - 04
6	264.0	19.0811	0.1265E - 04
7	263.0	16.35	0.3747E - 04
8	262.0	14.300	0.2288E - 04
9	261.0	12.7062	0.2080E - 04
10	260.0	11.4300	0.2677E - 04

Similar results can be obtained for the aft beam case.

5. The error in phase shift due to the ferrite modulator  $\theta_m$  does not affect the radar cross sections.



Comparison of the Theoretical Results  
with Experimental Results

An experimental test was conducted to obtain the value of errors experimentally. The value of the phases was chosen at each frequency so that  $\alpha = \beta = 0$ . The value of  $P$  and  $\theta_e$  can be selected arbitrarily. For the sake of comparison,  $90^\circ$  phase shift is taken as reference on the abscissa in Figure 10. The value of  $P$  is zero, since at this frequency only fore beam data was taken. The computed value of  $X_+/A_+$  for the preceding values of parameters is

$$\frac{X_+}{A_+} = \sqrt{\frac{1 + \cos \theta_e}{2}}$$

The calculated value of  $20 \log_{10} \frac{X_+}{A_+}$  compares extremely well with Figure 10 (of course,  $\theta_e = 0$  corresponds to the  $90^\circ$  point or the no-error point in Figure 10).

Remarks on Phase Error Study

The field scattered by a rough surface at a given point (in a given direction) is necessarily the sum of elementary waves in mutual phase interference. It can be shown that  $\alpha$  and  $\beta$  are uniformly distributed in the range of  $-\pi$  to  $\pi$  (reference 5). Furthermore,  $A_-$  and  $A_+$  are Rayleigh distributed, implying that the maximum errors in the fore and aft scattering cross sections are governed by a probability distribution. Thus, there is a finite probability that the radar cross section has the maximum errors given in Table II.

For the return from sea surfaces, past experimental data and theoretical calculations have shown that the ratio of fore and aft radar cross section is within  $\pm 6$  dB (reference 6). This then would give the value of  $P$  within 0.5 to 2.0. Now, from the calculated values of the maximum error, it can be shown that a maximum error of  $-0.75$  dB can be encountered for the aft or fore beam data, in case  $\theta_e = 4^\circ$ .

It then can be concluded that for the data gathered over ocean, the phase shift error  $\theta_e$  should be maintained to within  $4^\circ$ .

## ANTENNA PATTERN STUDY AND PARAMETRIC EVALUATION

In the data processing plan corresponding to a certain resolution cell geometry (Figure 2), two parameters ( $G_0^2 F'(\theta)$  and  $BW_i$ ) are needed. The antenna gain  $G_0^2 F'(\theta)$  has been calculated in the past as follows:

The maximum value of the product  $G_T(\psi)_\theta G_R(\psi)_\theta$  at any long track angle  $\theta$  is given by  $G_0^2 F(\theta)$ . The integral in equation (2) is evaluated as

$$\int_{-\psi_1}^{\psi_2} G_T(\psi)_\theta G_R(\psi)_\theta d\psi = G_0^2 F(\theta) \cdot \psi(\theta) = G_0^2 F'(\theta) \quad (13)$$

where  $\psi(\theta)$  is the beamwidth between two 3-dB down points at a long track angle  $\theta$ .

To calculate the bandwidths of the filters (the old version of the CAD program), the beamwidth was assumed constant ( $2.5^\circ$ ) and the 3-dB down points symmetrically located with respect to  $\psi = 0$  angle (Figure 11a).

A study of the latest antenna patterns revealed the following factors (reference 7):

1. It is desirable to have all patterns on a digital tape so that the plan for data processing could automatically choose appropriate values of the antenna gain at each incident angle.
2. In order to account for variation of gain along track, a finer grid of the gain along track should be taken. Additionally, the data for  $\sigma_0$  versus  $\theta$  curves should be processed corresponding to those angles where the two-way gain (along track) does not change very rapidly.
3. The maximum gain need not necessarily be on the prime axis. The limits on the skewness of the maximum gain curve should be considered.
4. For patterns where the cross-track beamwidth varies, a variable beamwidth should be included in the computer program.

5. Excessive side-lobes certainly play an important role in the degradation of the final data; therefore, the influence of the side lobes should be considered.
6. The antenna gains are a function of the angles  $\theta$ ,  $\psi$ . Consequently, when the aircraft parameters change, the gain toward a fixed direction changes; thus it is important to consider roll, pitch, drift, and vertical velocity of the aircraft.

To study the preceding factors computer programs were developed. A tape first was generated on which two-way gains were recorded. The tape was generated by multiplying the antenna gains of the transmitting and receiving antennas. The beamwidths, bandwidths, and antenna gains were computed from the tape using computer programs. The values for two-way antenna patterns were taken in increments of  $0.2^\circ$  in the long track angle. The results (reference 8) are summarized below.

#### Redop 1 Modified Antenna Patterns

The effect of Redop 1 modified antenna patterns is demonstrated by computing the factor  $10 \log_{10} \left( \frac{1}{BW_i} \right)$  and  $G_0^2 F'(\theta)$ . The value of  $(BW_i)$  is given by Figures 11b and 11c

$$BW_i \approx \frac{2VL}{\lambda h} \cos^3 \theta \cos \frac{\Delta\theta}{2} \quad (14)$$

First, the value of  $BW_i$  was calculated using the old pattern (reference 1) values and the parameters

$$h = 3000 \text{ feet}$$

$$V = 200 \text{ knots}$$

The area illuminated for each resolution cell = 22,500 square feet. Then, using the same parameters as before, Redop 1 modified patterns were used for calculation of equation (14). The results are shown in Figure 12.

The beamwidth  $\psi(\theta)$  and gain  $G_0^2 F'(\theta)$  are shown in Figures 13 and 14. These computations were completed as outlined in equation (13). These figures outline the significant differences between the old pattern and the Redop 1 modified.

### Long Track Antenna Gain Variations

In order to study the effect of long track antenna gain variation and side-lobe effects, three types of integrations were performed:

The 3-dB Summation Method.- In this case the maximum value of two-way gain ( $G_0^2 F(\theta)$ ) was determined at an angle  $\theta$ . From  $G_0^2 F(\theta)$  dB, a 3-dB value was subtracted. Two values of  $\psi$  ( $\psi_1$  and  $\psi_2$ ) were determined where gain equaled ( $G_0^2 F(\theta) - 3$  dB). The 3-dB summation beamwidth is defined by

$$\psi_{3s}(\theta) = \frac{\sum_{\psi_1}^{\psi_2} G_0^2 F(\theta) f(\theta, \psi) \Delta\psi}{G_0^2 F(\theta)} \quad (15)$$

In equation (15),  $G_0^2 F(\theta)$  is expressed in numerical value and not in dB. The increments are taken as  $0.5^\circ$ . The gain corresponding to this beamwidth is given by

$$\left[ G_0^2 F'(\theta) \right]_{3s} = G_0^2 F(\theta) + \psi_{3s}(\theta) \quad (16)$$

where quantities are expressed in dB.

Summation Method.- A rearrangement of equation (2) led to the following result

$$\sigma_0(\theta, \psi = 0) = \frac{2P_r V(4\pi)^3 h^2}{P_T G_0^2 f(\theta) \lambda^3 \Delta f_d \int_{\psi} f(\theta, \psi) f_{\sigma}(\theta, \psi) d\psi} \quad (17)$$

where

$$f_{\sigma}(\theta, \psi) = \frac{\sigma_0(\theta, \psi)}{\sigma_0(\theta, \psi = 0)}$$

For a constant incidence angle approximation, all points on a constant doppler have incidence angles equal to  $\theta$  at the point where the doppler line crosses  $\psi = 0$ . Based on the above assumption

$$\int_{\psi} f(\theta, \psi) f_{\sigma}(\theta, \psi) d\psi = \int_{\psi} f(\theta, \psi) d\psi \approx \psi(\theta)_S$$

The above equation can be written as

$$\psi(\theta)_S = \sum f(\theta, \psi) \Delta\psi \quad (18)$$

An equivalent expression of equation (18) used to evaluate the "equivalent" beamwidth  $\psi(\theta)_S$  from the tabulated results is given by

$$\psi(\theta)_S = \frac{\sum G_0^2 F(\theta) f(\theta, \psi)}{G_0^2 F(\theta)} \Delta\psi \quad (19)$$

where the summation is taken over  $-10^\circ \leq \psi \leq 10^\circ$ .

Since by definition  $G_0^2 F'(\theta)$  is the product of the two-way antenna gain times the integral of the port-starboard beamwidth for any incidence angle, the two-way gain is computed as follows

$$\left[ G_0^2 F'(\theta) \right]_S = G_0^2 F(\theta) \cdot \psi(\theta)_S \quad (20)$$

In equations (19) and (20) the quantities are taken in numerical value.

Cumulative Power at 95 Percent.- The following analysis was conducted to determine the overall effect of the antenna side-lobes on resolution (reference 8):

- Evaluate the total area under the curve (as shown in Figure 15a) as a function of cross-track angle  $\psi$  for angular lengths  $\pm\Delta\psi$  at each incident angle  $\theta$ .
- From the digital results of the computed two-way cross-track antenna gains given for incidence angles of  $-70 \leq \theta \leq +70^\circ$  and cross-track angles of  $-10 \leq \psi \leq +10^\circ$ , the specific two-way beamwidth can be calculated as follows:
  - (1) For specific  $\theta$  convert the digital cross-track gains which are given for  $\pm\psi$  values up to  $10^\circ$  to their decimal representation; i.e.,  $N = 10^{\text{dB}/10}$ .
  - (2) Integrate the energy area obtained using the converted  $N$  values by using Romberg's integration technique. See Figure 15a for an illustrative ideal example of the areas to be integrated.
- Plot the areas found by the above integrations. (Plot: Percent of Cumulative Cross-Track Beam Power vs Cross-Track Angle.)
- Normalize the values with the maximum value (Figure 15b).
- From the above plot determine the two-way beamwidth value  $\psi(\theta)_c$  at 95 percent power point.
- Find  $G_0^2 F'(\theta)$  using the new calculated two-way beamwidth values; i.e.,  $G_0^2 F'(\theta) = G_0^2 F(\theta) + \psi(\theta)_c$  in dB.

The results of the computer-generated programs are summarized in Figures 16 and 17. These graphs can be utilized in the CAD computer processing plan. The selection of angles at which  $\sigma_0$  should be computed also can be made on the basis of these graphs.

#### Aircraft Parameters

Errors caused by aircraft parameter changes (vertical velocity, roll, pitch, and yaw) can be introduced into the processed data. Examples are given below to illustrate this point.

Vertical Velocity.- First, it is assumed that the aircraft has a ground speed (horizontal)  $V$  of 200 knots. With the following parameters, incident angle  $\theta$  is calculated

$$h = 3000 \text{ feet}$$

$$L, \text{ length in long track of} \\ \text{each resolution cell} = 150 \text{ feet}$$

As a second step, in addition to the preceding aircraft parameters, a vertical velocity  $V_z$  of 10 knots is assumed. The incident angle corresponding to the new parameters is given by

$$\theta_1 = \sin^{-1} \left[ \frac{\lambda f_d}{2V} \right] + \tan^{-1} \left[ \frac{V_z}{-V} \right] \quad (21)$$

If the antenna gain is not taken at  $\theta_1$  angle in the presence of vertical velocity, the error caused by improper antenna gain is

$$G_0^2 F'(\theta_1) - G_0^2 F'(\theta)$$

This error is listed in Table III.

Roll.- The effect of roll (Figure 18) is to change the incident angle to

$$\theta_2 = \cos^{-1} \left[ \cos \theta \cos \xi \right] \quad (22)$$

First, we assume the parameters are given in the example above (vertical velocity = 0). Then a roll ( $\xi$ ) of  $4^\circ$  is introduced and  $\theta_2$  is calculated. The error caused by improper gain inclusion in the processing plan is

$$\left[ G_0^2 F'(\theta) - G_0^2 F'(\theta_2) \right]$$

TABLE III.- VERTICAL VELOCITY ERROR

<u><math>\theta</math></u> (Fore beam, degrees)	<u><math>\theta_1</math></u>	<u>Error due to</u> <u><math>V_z = 10</math> knots</u> <u>(dB)</u>
2.5	-0.36	0.69
5.0	2.1	0.65
10.0	7.1	1.78
15.0	12.1	0.25
20.0	17.1	1.50
25.0	22.1	0.50
30.0	27.1	1.97
35.0	32.1	1.70
40.0	37.1	1.62
45.0	42.1	0.51
50.0	47.1	1.90
55.0	52.1	1.50
60.0	57.1	0.37



Table IV presents these errors

TABLE IV.- ERROR CAUSED BY ROLL OF 4°

$\theta$ (Fore beam, degrees)	$\theta_2$	Error due to $\xi = 4^\circ$
2.5	4.71	0.59
5.0	6.4	0.38
10.0	10.76	0.42
15.0	15.51	0.27
20.0	20.38	0.11
25.0	25.29	0.25
30.0	30.24	0.23

Pitch and Yaw.- Pitch variations can be treated in the same manner as roll variations. In the present processing program the pitch corrections are taken automatically. Yaw errors are minor for small yaw changes over water. Procedures for taking into account roll and vertical velocity are being investigated. However, MSC is attempting to screen the flight parameter data and not process data where these parameters are excessive.

## DATA PROCESSING

Scatterometer data can be processed by either analog or digital processing programs. There are several advantages in processing the data on a digital computer. In the past, questions have been raised as to the consistency between analog and digital processed data. A review of analog and digital programming capabilities was undertaken to investigate all anomalies. A summary of the results follows:

### TEST TAPE STUDY

A test tape was generated using analog equipment with known amplitudes. The data recorded consisted of a basic 400 Hz square wave complete with harmonics on one track of the test tape and the same signal shifted by 90° (lagging) on the second track. This tape was processed with both analog and digital equipment. The filter bandwidths were chosen properly (reference 9). For frequencies (harmonics) up to 2 kHz (5th harmonic), good comparison between analog and digital results was observed. The differences at higher frequencies were attributed to the azimuth alignment of the tape recorder read heads. The alignment error was eliminated later by introducing an adjustment routine.

Further study was done using another tape (reference 10). The signals recorded on the tape were made similar to the scatterometer return from a typical ocean surface. It was shown that a change of 4.24 dB was introduced by hamming the data on the digital computer. The digitally generated tape was converted to analog data and processed by analog equipment. The analog and digital results compared very well.

### NOISE FLOOR LEVEL

In the process of comparing analog and digital filtered data, it was noted that the analog processing presented a noise floor of -70 dB while the digital filtering could produce no better than -55 dB (Figure 19). An investigation revealed that some of the high-frequency noise was being folded back into the data in the digital filtering. Additionally, the data were not being processed properly to realize full resolution of the calibration signal versus data. The program now has equipment and procedures incorporated to reduce these effects. The change incorporated was the utilization of Redcor filters to reduce the high-frequency noise power component. The amplification

of data to band edge enabled increased resolution of the data. Data now processed with digital equipment present a noise floor near -70 dB (Figure 20).

#### Effect of Gain Variations

In reviewing past data (Flight 6, Mission 88) it was found that a large change in reference signal had taken place with a channel gain change in the system. Furthermore, it was found that the reference signal was not being continuously monitored in the computer program. Thus, a jump in the data was noticed corresponding to the gain change. Two steps were taken to alleviate this problem:

- The data processing program monitors both data and reference signal throughout a given flight line.
- A gain change should be avoided during a given flight line.

In reviewing Mission 88, Flight 6 data after the program modification, it was apparent that no jump in the data because of channel gain change existed.

#### Data Averaging Errors

In reviewing the past processed data it was noticed that the computer program was computing the statistical average of  $\sigma_0$  by averaging the dB values rather than the numerical value  $N$  of the scattering cross section. To correct this, first the value of scattering cross section was calculated as a number, then averaged, and the average was expressed in dB.

#### Aircraft Parameter Errors

In the program for processing the data, proper values of  $h$ ,  $V$ ,  $V_z$  must be taken for each instant of time. As an example, if  $V$  changes by 10 knots, the bandwidth of the filters changes. This is illustrated in Figure 21 for the following parameters:

$$V_1 = 200 \text{ knots}$$

$$V_2 = 210 \text{ knots}$$

$$\Delta\theta \text{ (constant)} = 3^\circ$$

$$h = 3000 \text{ feet}$$

where  $V_1, V_2$  are the aircraft velocity and  $\Delta\theta$  the resolution cell angle. Similarly, altitude and vertical velocity ( $V_z$ ) changes can cause errors in the processed data. In the processing plan currently used, altitude, aircraft velocity  $V$  and pitch variation are properly accounted for.

REFERENCES

1. Scatterometer Data Analysis Program, Final Report, No. 57667-2, Ryan Aeronautical Company, September 1967.
2. Program Documentation, Scatterometer Filter Program (FILT13), Program Q605, Project 4610, prepared for Computation and Data Analysis Division, NASA/MSC, February 1970.
3. Jordan, L., Interdepartmental Communication, LEC No. 71-015-PCN-97, to G. Graybeal, May 1970.
4. Krishen, K., Interdepartmental Communication, LEC No. 71-015-PCN-109, to G. Graybeal, June 1970.
5. Beckmann, P. and Spizzichino, A.; The Scattering of Electromagnetic Waves From Rough Surfaces; The MacMillan Company, New York, 1963.
6. Krishen, K., Saturation of  $\sigma_0$  With Increasing Wind Velocity, Technical Report No. 649D.21-007, Lockheed Electronics Company, Houston, August 1969.
7. Krishen, K., Definition of Scatterometer Antenna Problems and Possible Approaches to Data Processing, Technical Report No. 649D.21.011, Lockheed Electronics Company, Houston, December 1969.
8. Vlahos, N. and Kell, T., Study of Antenna Patterns and Parametric Evaluation for 13.3-GHz Single Polarization Radar Scatterometer, Technical Report No. 649D.21.030, Lockheed Electronics Company, Houston, November 1970.
9. Vlahos, N., Analysis of Analog vs Digital Filtering Techniques as Applied to Radar Scatterometry, Technical Report No. 649D.21.032, Lockheed Electronics Company, Houston, July 1970.
10. Krishen, K., Preliminary Evaluation of Computation and Analysis Division (CAD) 13.3-GHz Single Polarized Scatterometer Data Processing Program, Interdepartmental Communication, LEC No. 78-015-PCN-06, to B. Baker (NASA/MSC), October 1970.

613

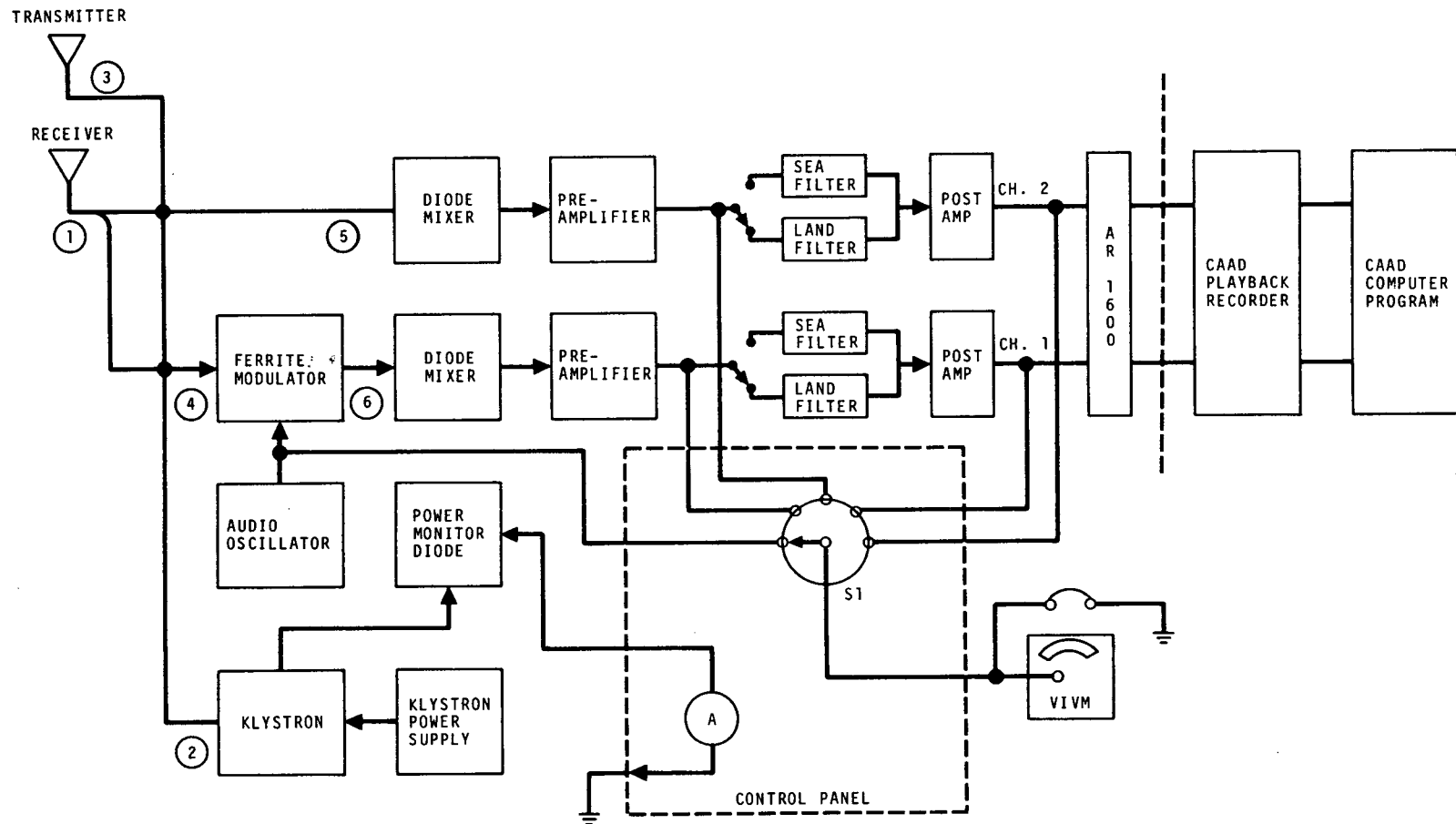


Figure 1. - 13.3 GHz scatterometer system block diagram.

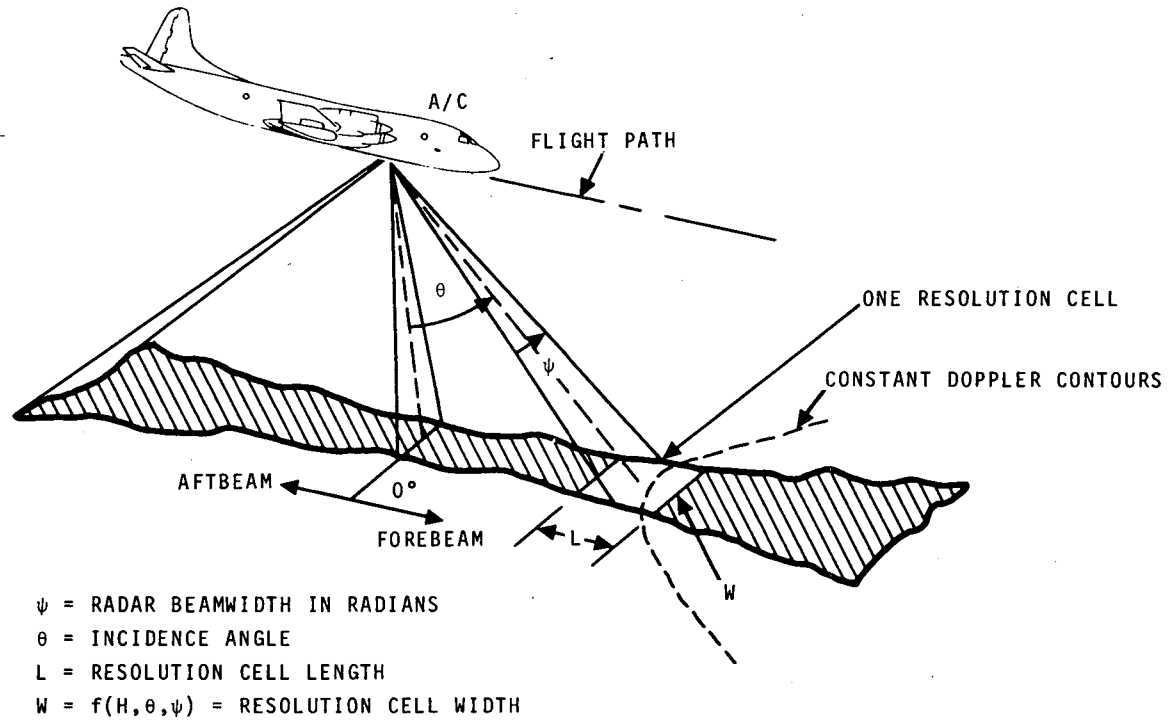


Figure 2. - 13.3 GHz scatterometer, resolution cell geometry.

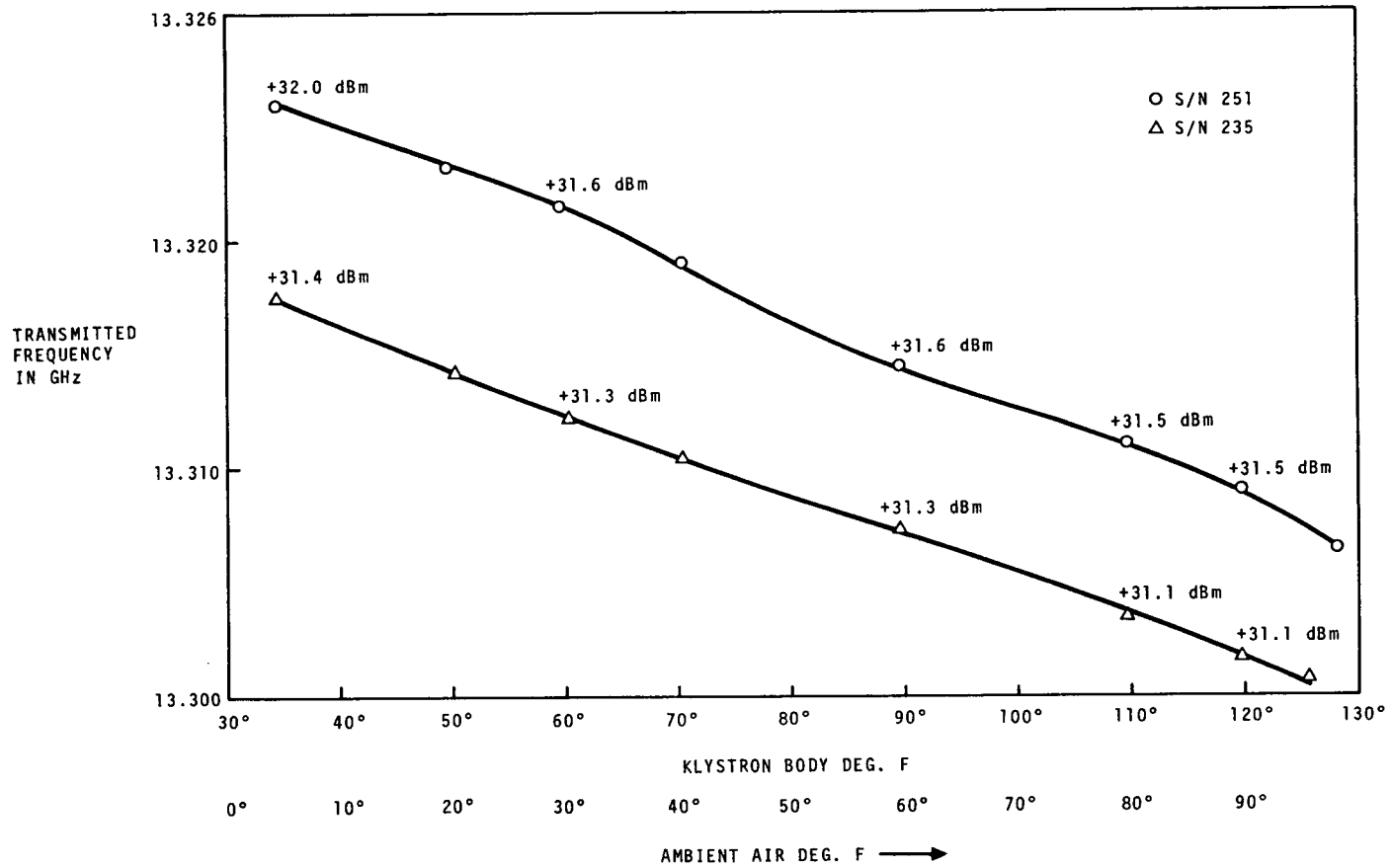


Figure 3. - Klystron temperature stability



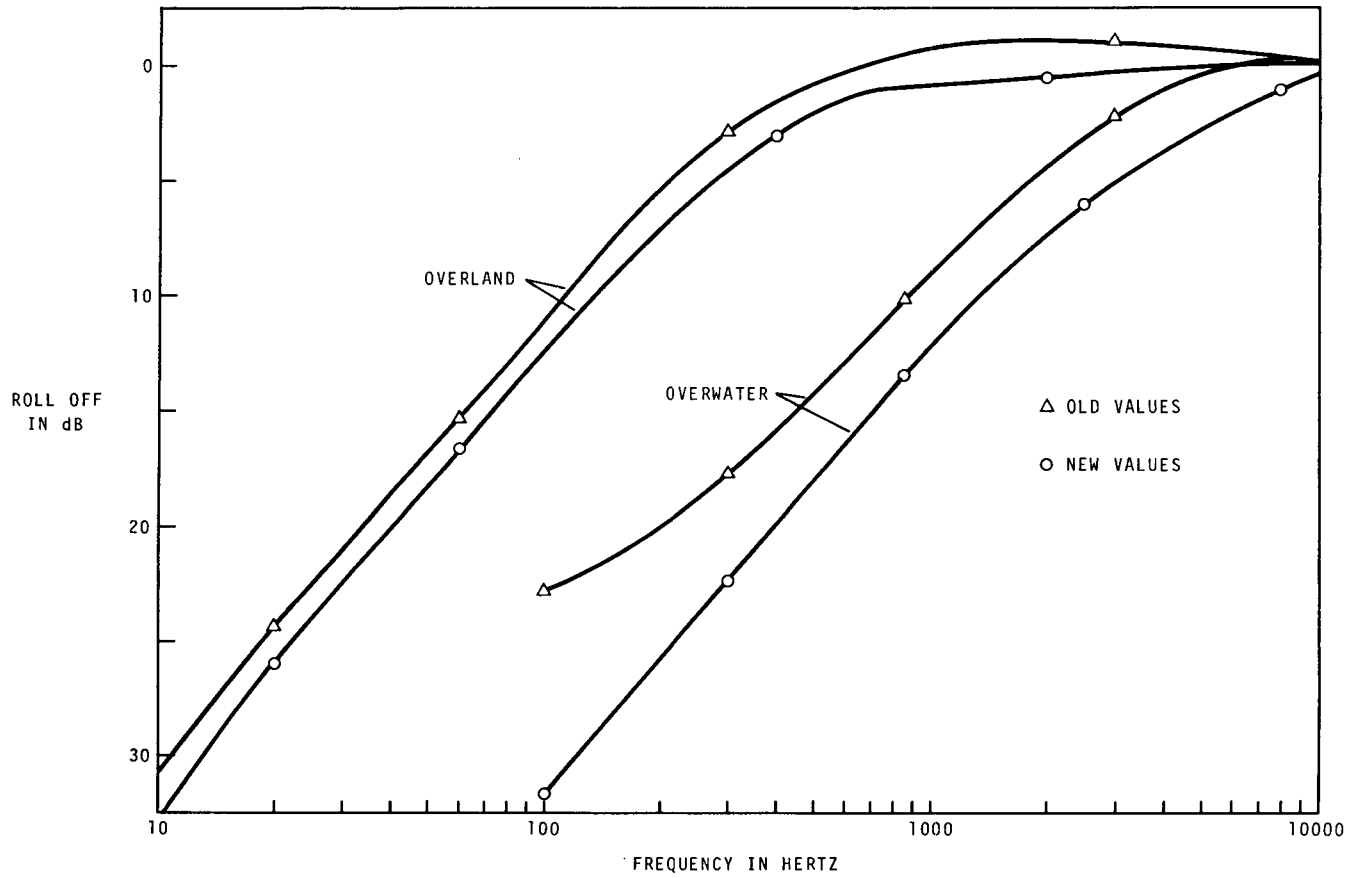


Figure 4. — Rolloff values for 13.3 GHz scatterometer.

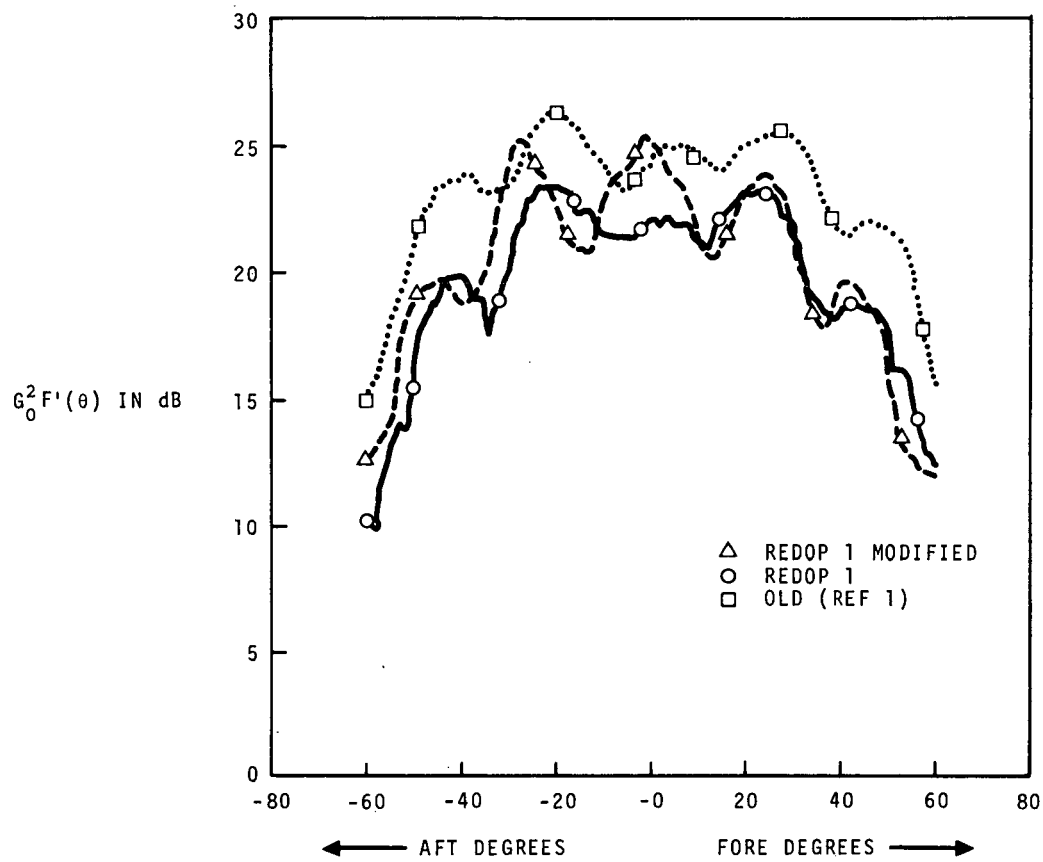


Figure 5. —  $G_0^2 F'(\theta)$  values with 3dB beamwidth.

618

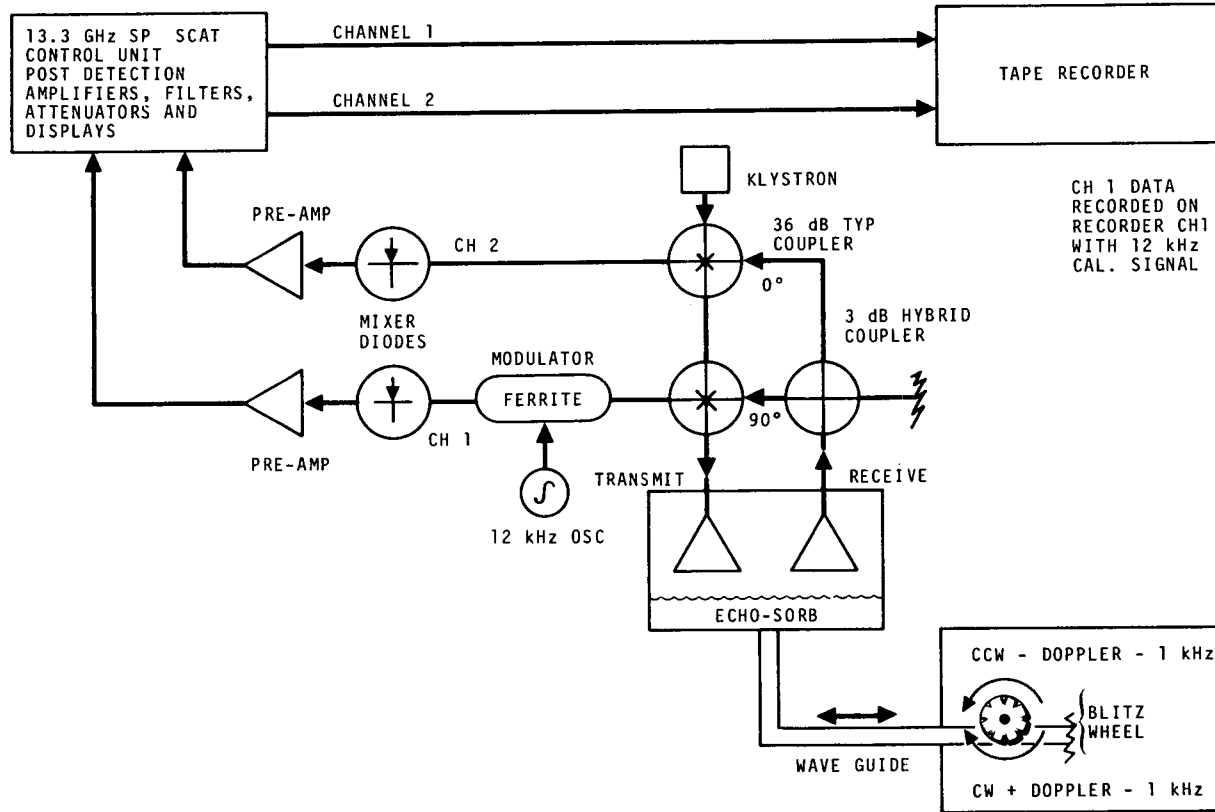


Figure 6. - 13.3-GHz Single Polarized Scatterometer blitz wheel test.

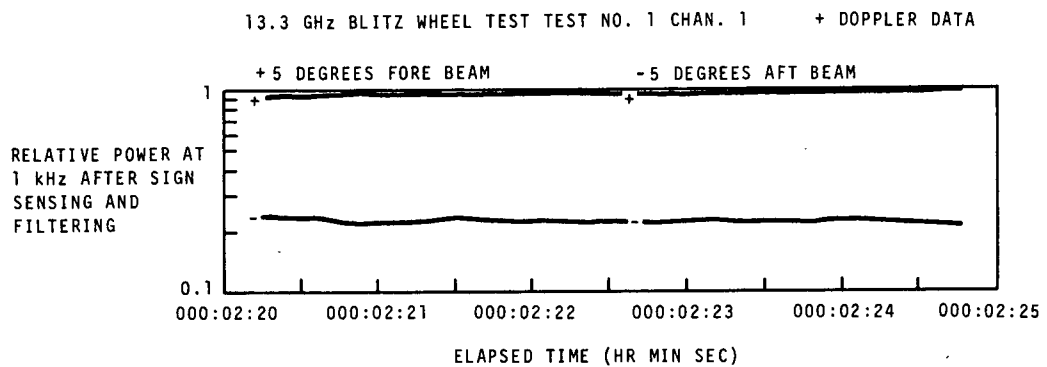


Figure 7. — Digital program output of the blitz wheel test.

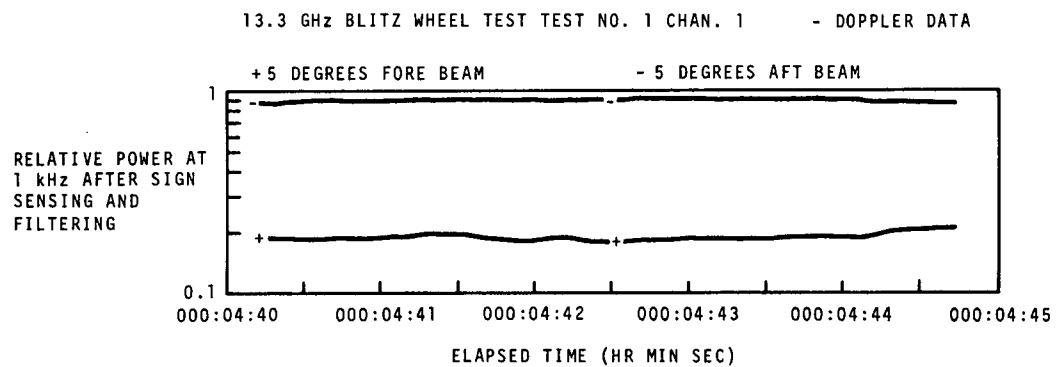


Figure 8. — Digital program output of the blitz wheel test.

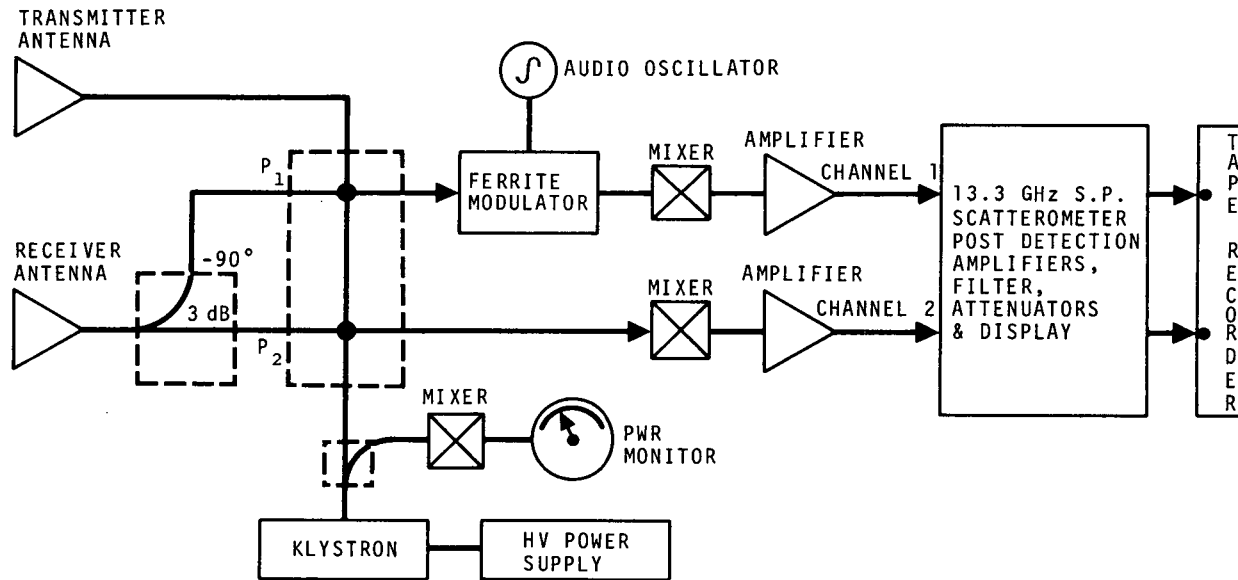


Figure 9. - 13.3 GHz single polarized scatterometer diagram showing channel phase shift.

621

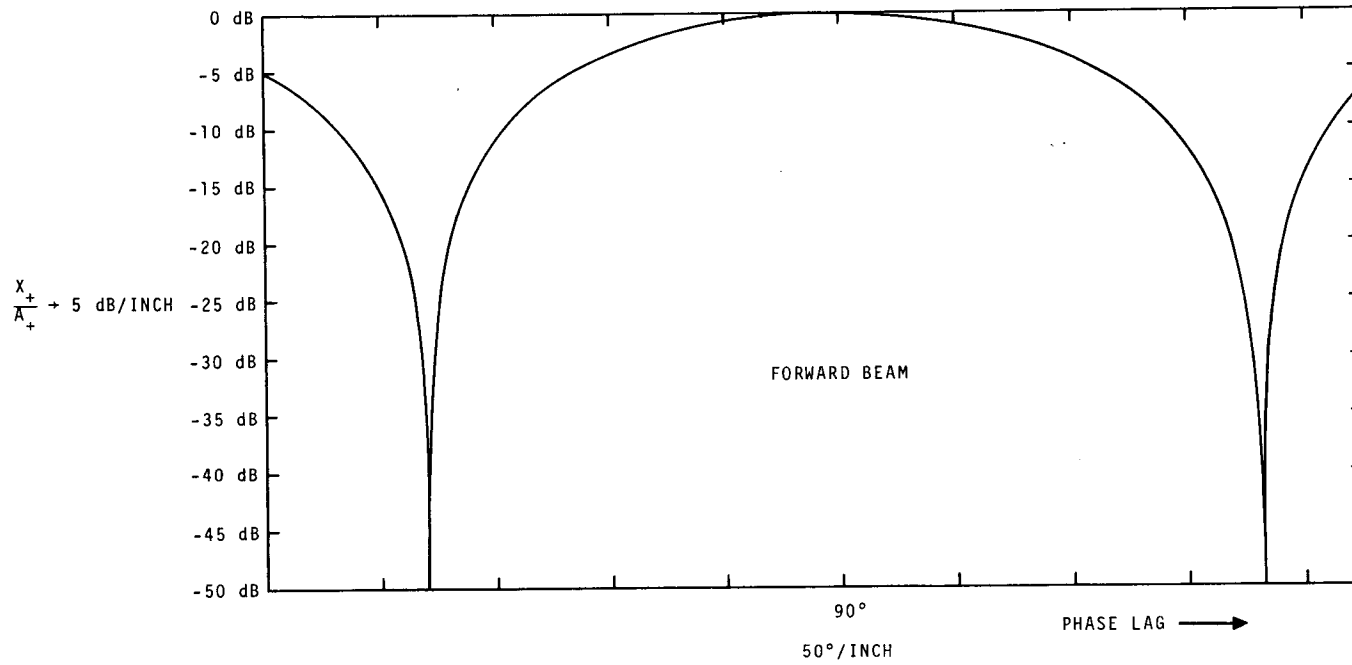


Figure 10. — Experimental results of phase shift study.

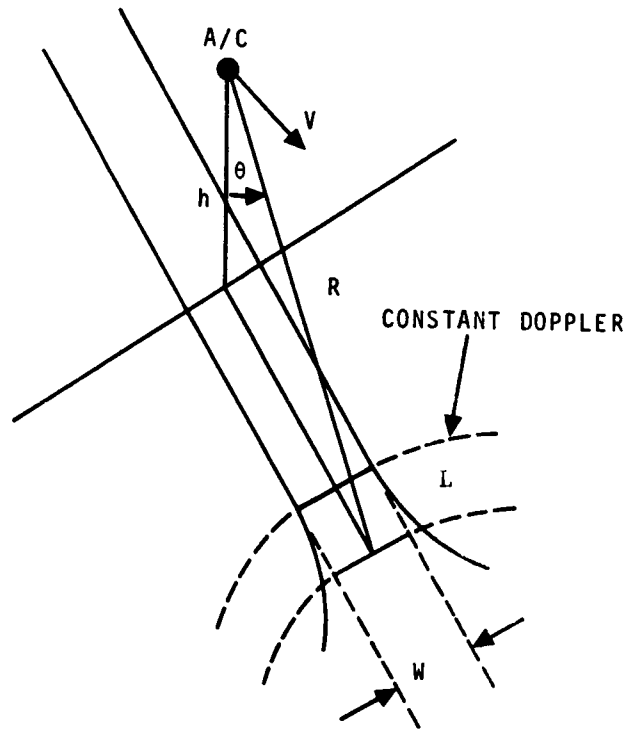


Figure 11a. - Resolution cell geometry.

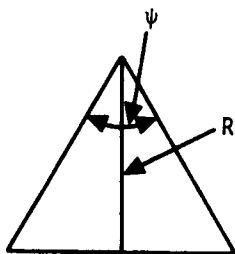


Figure 11b. - Cross track geometry.

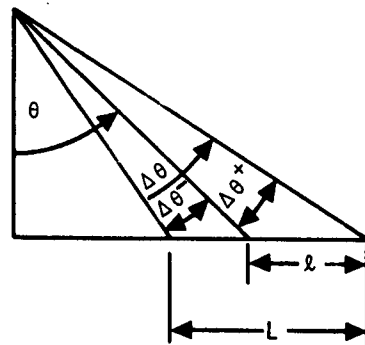


Figure 11c. - Along track geometry.

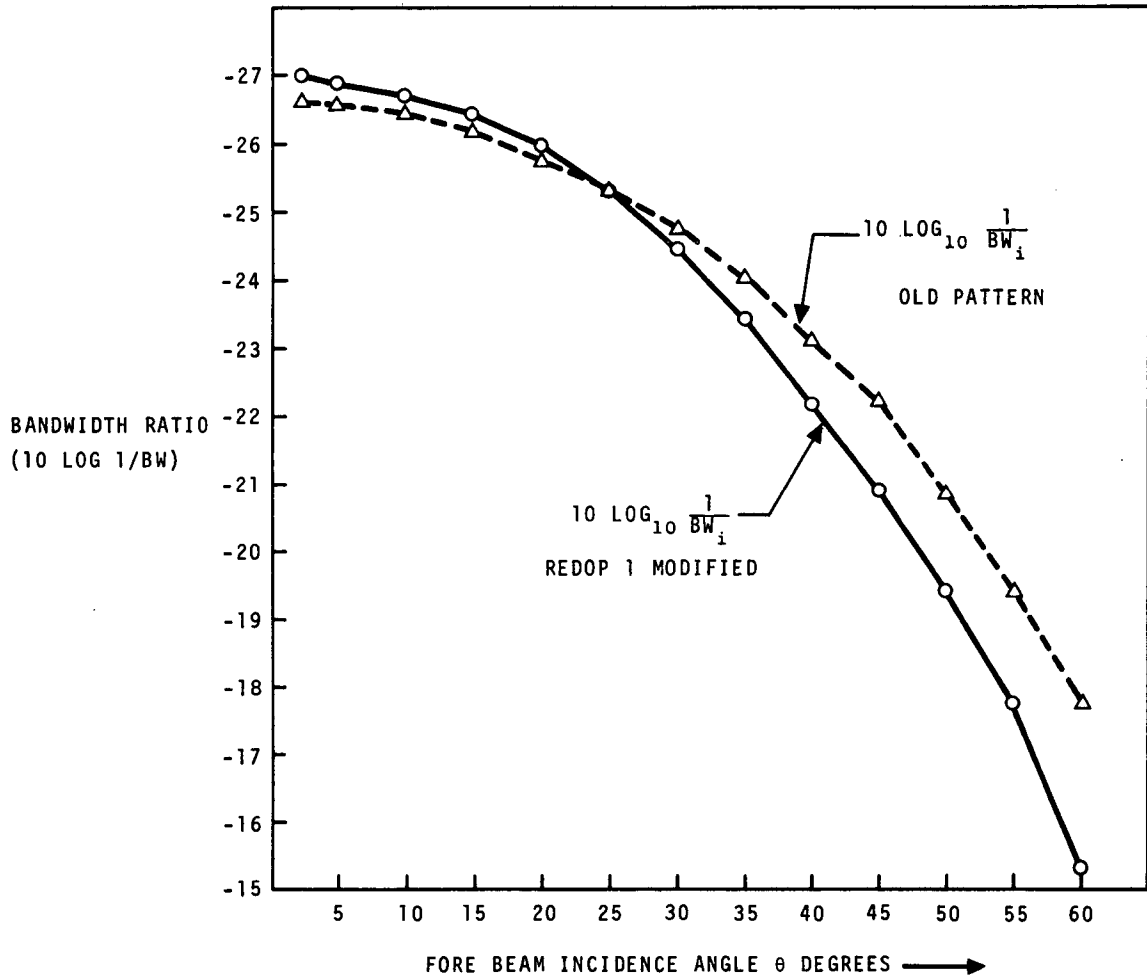


Figure 12. - Cross-section ratio of bandwidths.



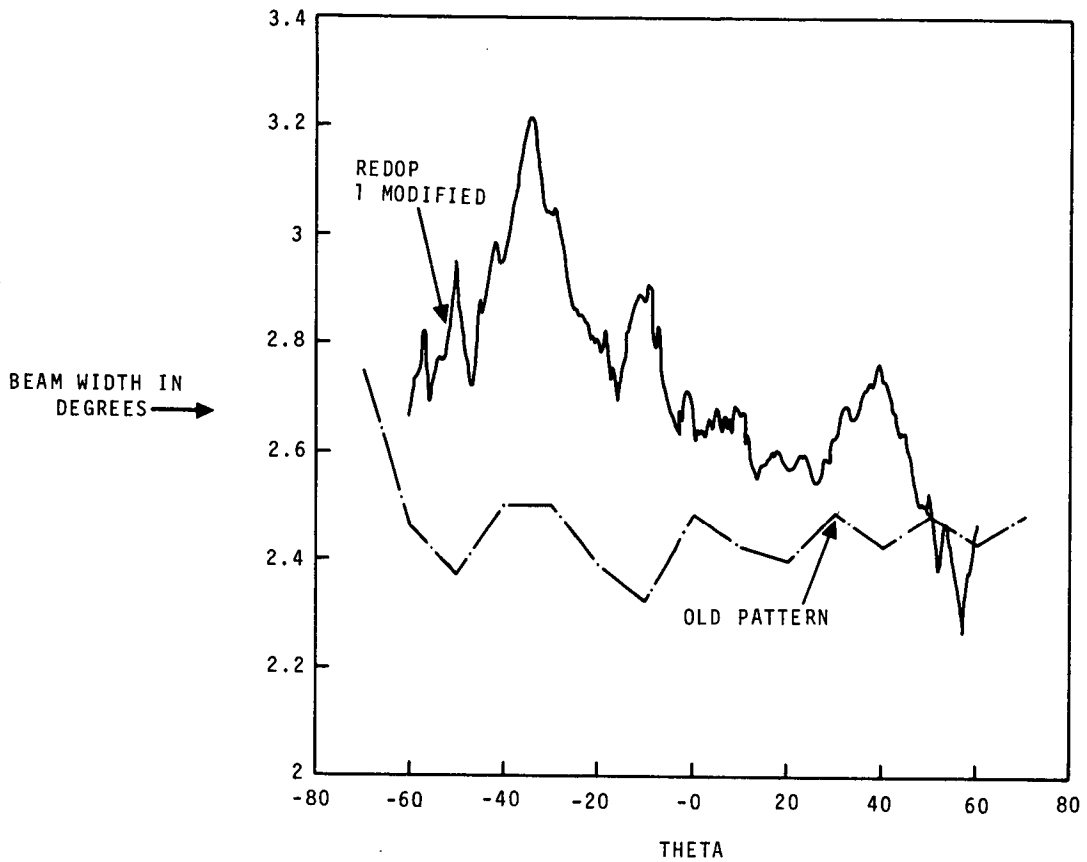


Figure 13. - Comparison of old and Redop 1 modified beamwidths computed according to equation (13).

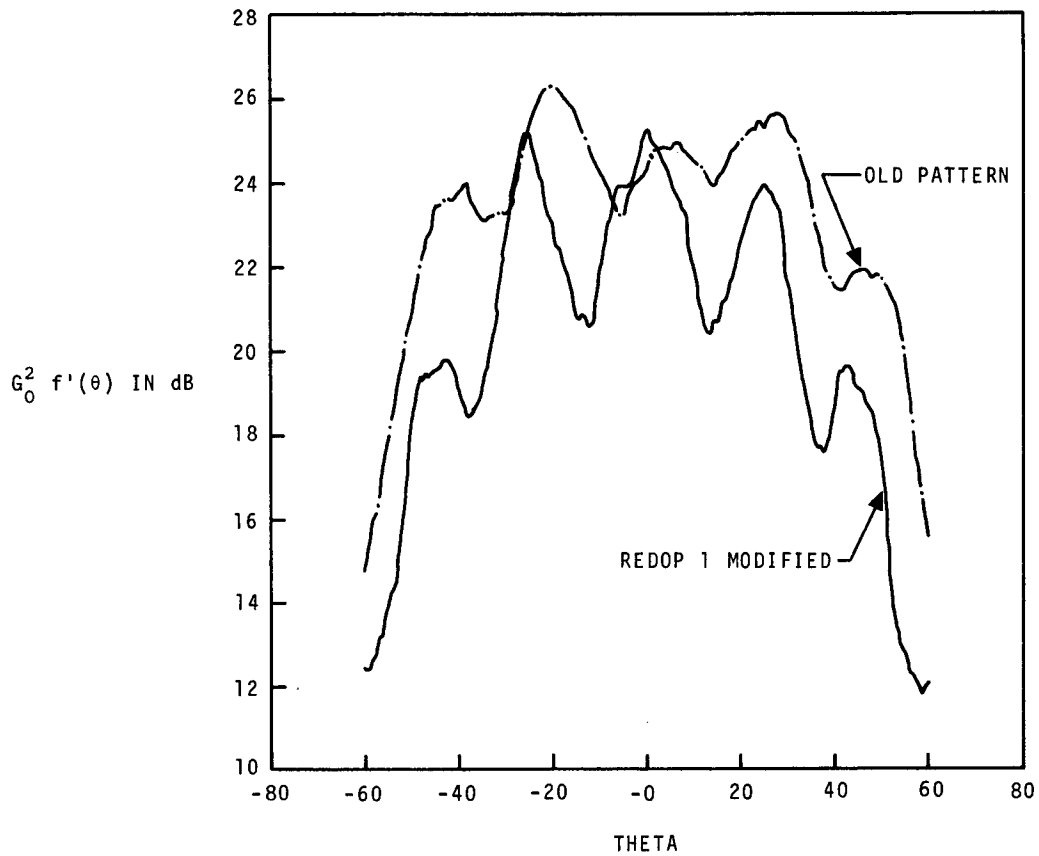


Figure 14. - Comparison of antenna gains  $G_0^2 F'(\theta)$  of old and Redop 1 modified antenna patterns computed according to equation (13).

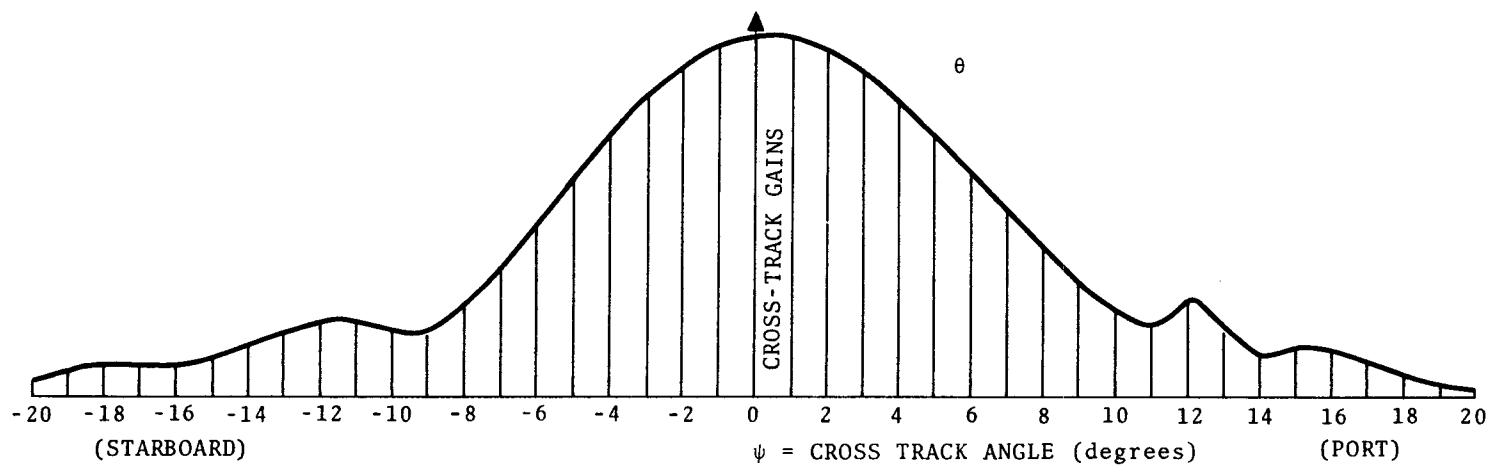


Figure 15a. — Area of total transmitted/received antenna energy

626

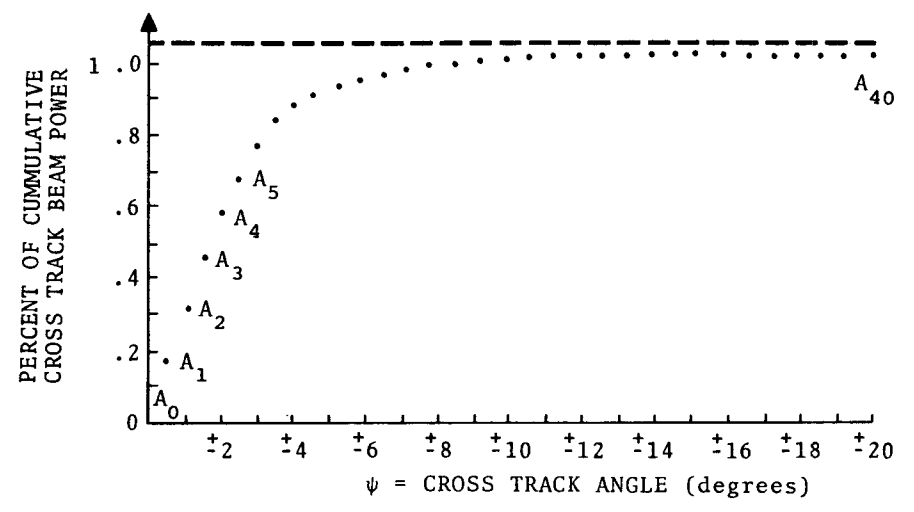


Figure 15b. — Cumulative probability (percent of total power)

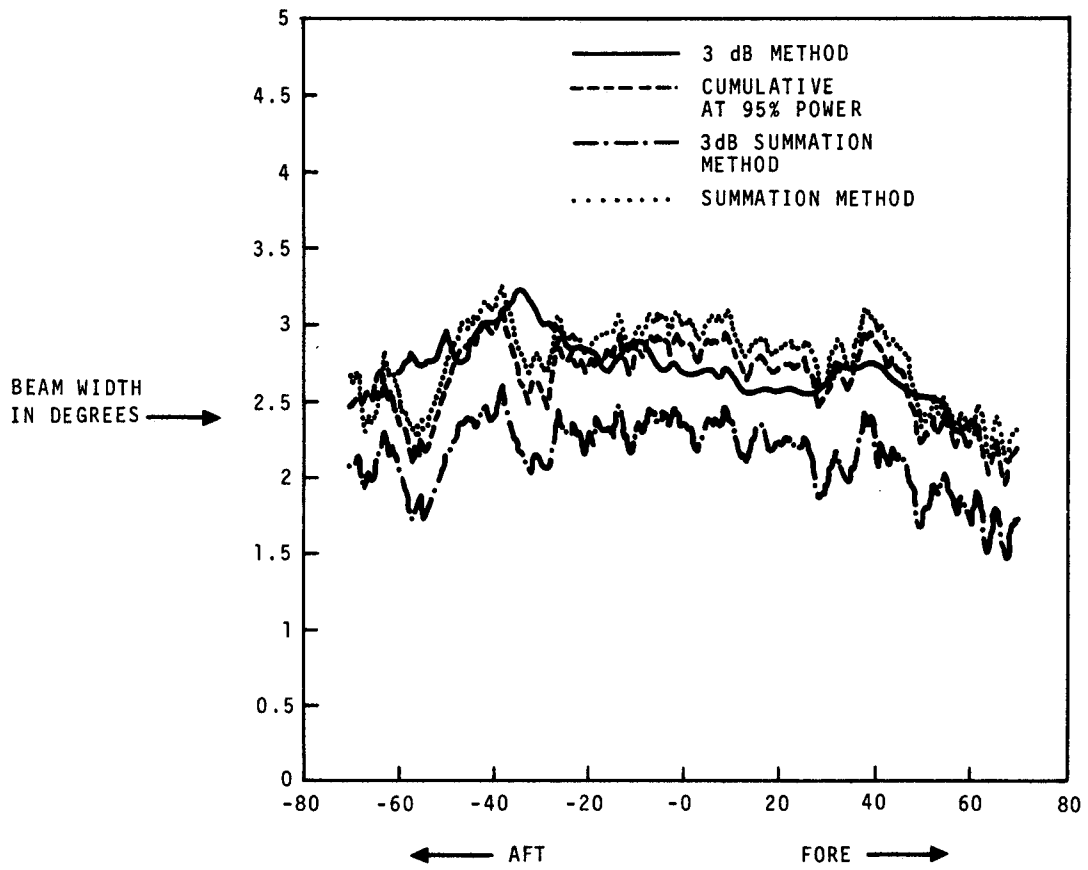


Figure 16. - The value of beamwidth using various methods for Redop 1 modified antenna patterns.

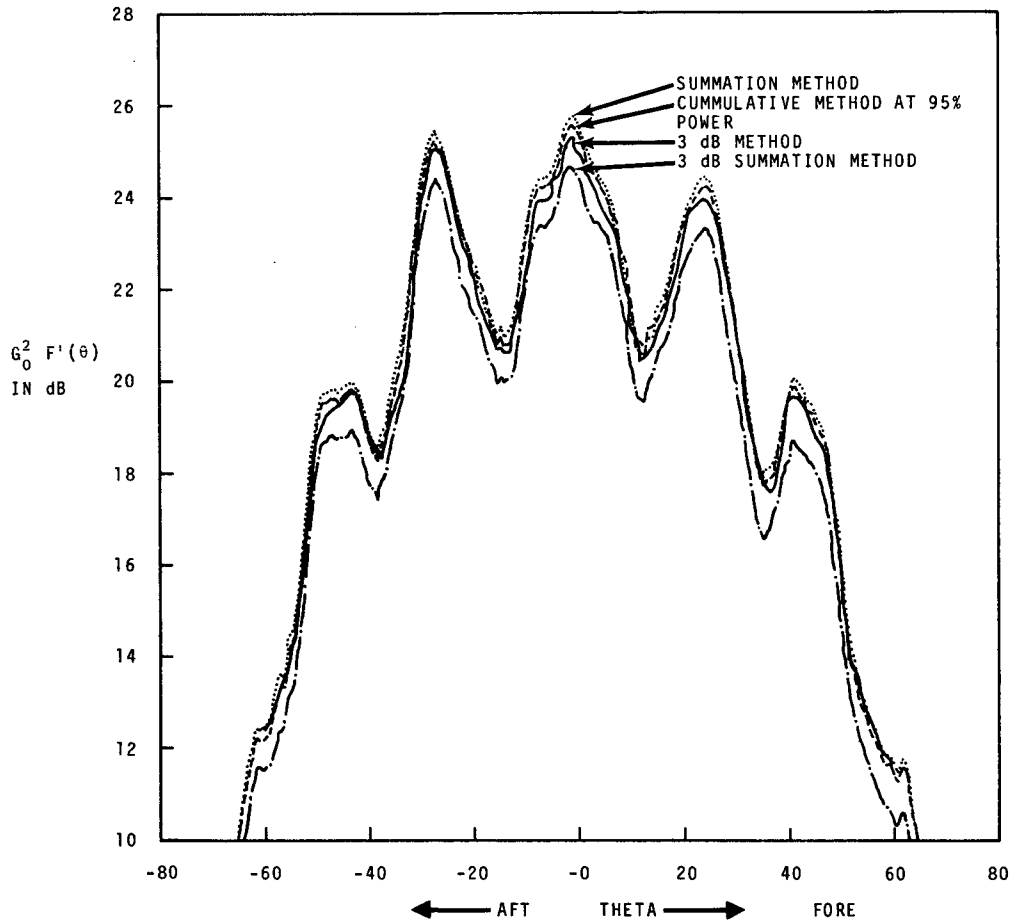
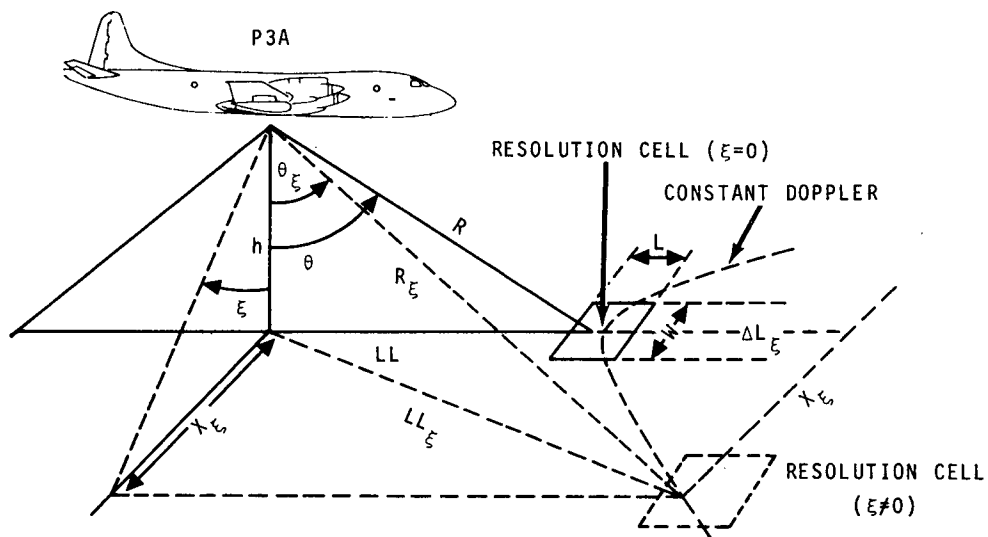


Figure 17. — The value of  $G_0^2 F'(\theta)$  using various methods for Redop 1 modified antenna patterns



- $\epsilon$  = ROLL ANGLE
- $\theta_\epsilon$  = NEW INCIDENCE ANGLE IN THE PRESENCE OF ROLL ANGLE
- $R$  = SLANT RANGE FROM ANTENNA TO RESOLUTION CELL CENTER
- $R_\epsilon$  = SLANT RANGE FROM ANTENNA TO RESOLUTION CELL CENTER WITH ROLL ANGLE
- $W$  = RESOLUTION CELL WIDTH
- $L$  = RESOLUTION CELL LENGTH
- $LL$  = LOCATION OF RESOLUTION CELL
- $LL_\epsilon$  = DISTANCE AWAY FROM FLIGHT LINE
- $\Delta L_\epsilon$  = ALONG TRACK DISPLACEMENT

Figure 18. — Resolution cell geometry in the presence of roll variation

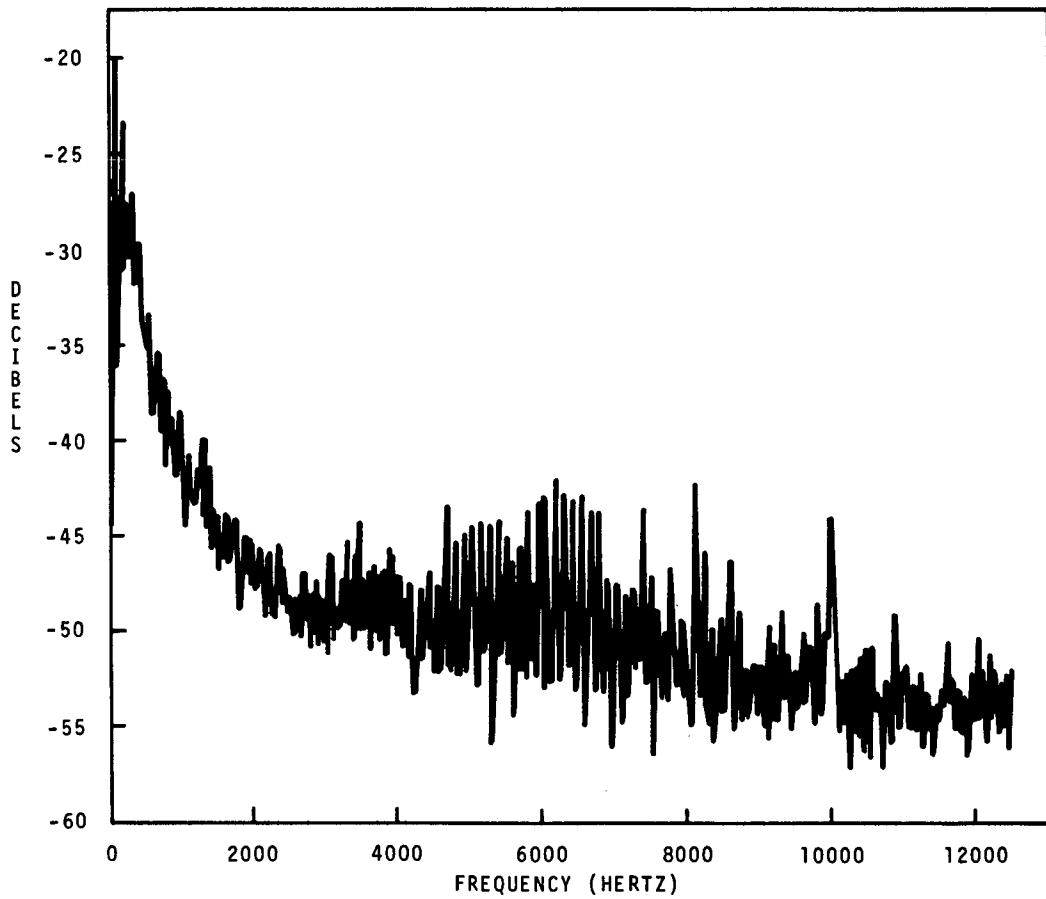


Figure 19. - Typical digital computer processed data plot (PSD) for Mission 119 (FCF) before program change.

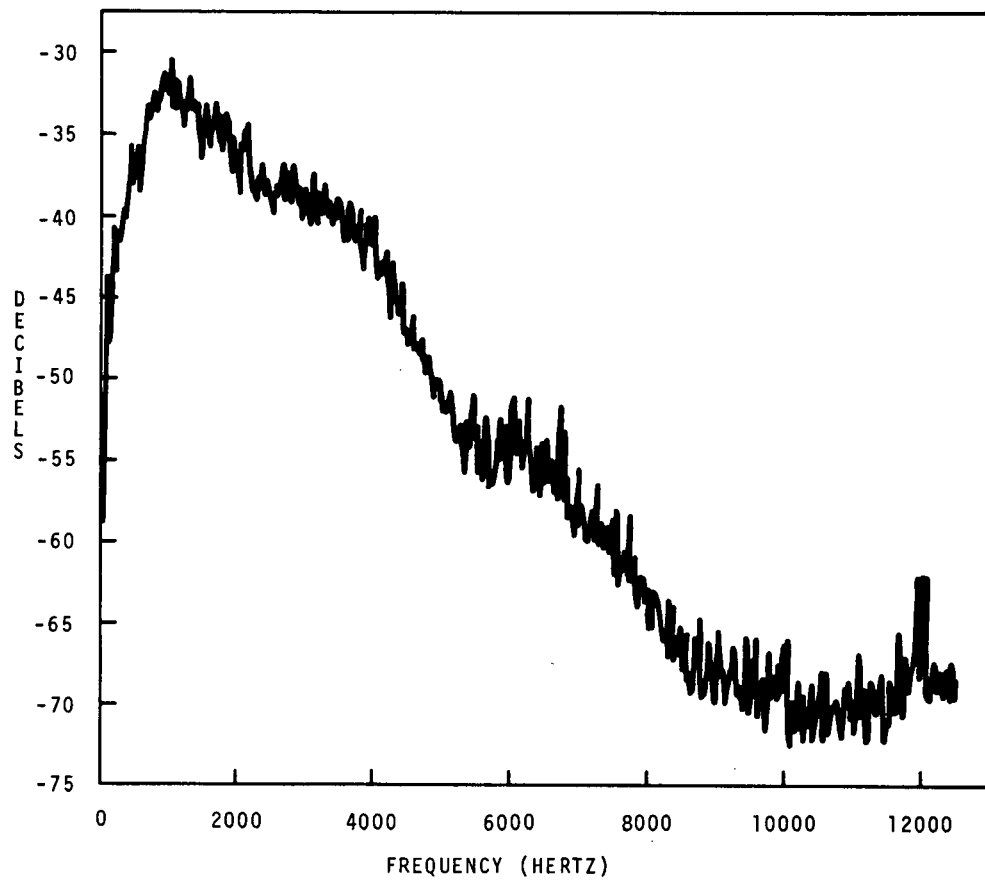


Figure 20. - Typical digital computer processed data plot (PSD) for Mission 119 after program change.



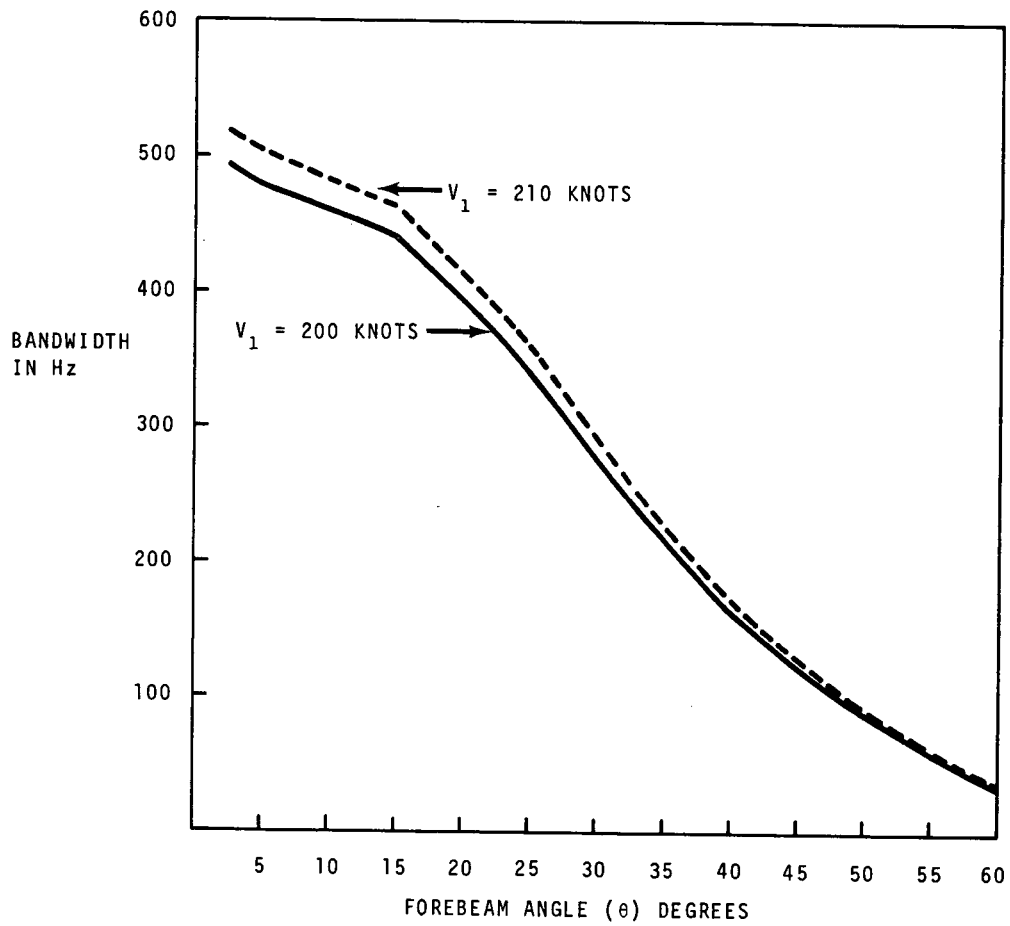


Figure 21. — Change in filter bandwidth due to change in aircraft velocity

PHENOMENOLOGICAL APPROACH  
TO SCATTEROMETER DATA INTERPRETATION

by

F. E. Alzofon  
Lockheed Electronics Company  
Houston Aerospace Systems Division  
Houston, Texas

ABSTRACT

This paper proposes a graphic method of analyzing radar scatterometer sea clutter data leading to linear relations between scattering cross sections and tan angle of incidence of the radiation. This relation permits formulation of simple analytic relations without reference to the ocean surface spectrum. Parameters introduced depend on the wavelength of the incident radiation and its polarization, and on wind and sea states. The simplicity of the expressions derived suggests a corresponding simplicity in the physical mechanism of radar sea clutter return.

INTRODUCTION

The complicated character of expressions derived in the theories of the analysis of scattering of electromagnetic waves from rough surfaces has been mentioned frequently (e.g., references 1 and 2). As a consequence, physical interpretation of the theories' predictions is difficult, and approximations must be made if explicit and useful results are required (references 2 and 3). Applied to ocean scatterometry, these theories often begin with doubtful assumptions about the nature of the ocean's surface and with Kirchhoff's approximation; thus, even the complicated initial results of the theory are questionable.

The history of physical research demonstrates that insight into the nature of physical processes can be gained by beginning with the experimental data (rather than with electromagnetic field theory as in reference 1, for example) and attempting to find simple relations between the experimental parameters. These relations then become the basis of a provisional and uncomplicated theory featuring the trends and correlations summarized in the empirical expressions; this procedure permits a minimum number of assumptions about the physical mechanisms involved. Consequently, there is more certainty about whatever details of the physical processes are assumed in order to derive the theory. Such a theory is characterized as "semi-empirical" or "phenomenological", since the experimental data is of primary importance and the theoretical structure is taken to follow from this, rather than the converse. Although the validity of the theory is no greater than that of the data available, the value of this approach has been amply demonstrated in many connections: one outstanding example is the discovery of the Balmer series in spectroscopy, later the basis of the Bohr theory of the hydrogen atom. Another example is met in the study of radioactive decay, where a theory had to be constructed to explain an observed exponential decay law. In both the above cases, plotting the data against log-log scales to obtain a linear variation was found to be a useful device in data analysis.

In the analysis of scatterometer data from several sources, the writer has found that a considerable simplification in description of the data can be obtained by plotting the data against log-log scales in the tradition mentioned above. Since the data do not include measures of precision or accuracy, the latter technique will appear, in effect, as a mode of fitting the data by lines or curves of regression. It is found that simple analytic expressions can be derived inductively from the data so displayed, and since the data is dependent on wind and ocean conditions, analysis of relations between these factors appears possible by the technique suggested. Again, the expressions are only as accurate as the data from which they were derived.

Relations between scattering cross section, angle of incidence, wavelength of incident radiation, and wind velocity can be derived in the manner described.

#### ASSUMPTIONS

The following discussion relates only to radar return from the ocean surface.

Several alterations were made in the usual method of representing scatterometer data; these were made to conform the more customary physical kind of approach emphasized above.

1. The scattering cross section per unit area  $N$  of the ocean's surface was used, rather than the derived quantity  $\sigma_0$  measured in decibels. The latter quantities are related by

$$\sigma_0 = 10 \log_{10} N \quad (1)$$

A major reason for using  $N$  rather than  $\sigma_0$  lies in the fact that relation (1) implies a distortion of the scale of the cross section when  $N$  is less than unity, and hence may lead to incorrect interpretation of the physical character of the ocean surface.

2. To a first approximation, as suggested by Beckman and Spizzichino (reference 4) and by Spetner and Katz (reference 5), we assume that the scattering cross section for radar return from the ocean surface is a function of the radiation's angle of incidence  $\theta$  through the function  $\tan \theta$  alone. Reference 5 arrives at the latter conclusion by assuming that wave facets specularly reflect energy back to the receiver.
3. In order to expose any dependence of  $N$  on a power of the argument  $\tan \theta$ , the experimental data for  $N$  versus  $\tan \theta$  are plotted on logarithmic scales.

The value of the assumptions will depend on the simplicity and fruitfulness of the conclusions derived from them.

RESULTS

By replotting two typical curves from Figure 18.4, p. 406, reference 4, we obtain Figure 1. It is seen that two straight line segments are obtained; for each such segment

$$N \propto (\tan \beta_0 / \tan \theta)^m \quad (2)$$

( $m > 0$  and  $\tan \beta_0$  is a mean ocean wave slope). The validity of the straight line approximation for one of the segments over more than three decades of variation in  $N$  (for  $\theta$  between approximately  $15^\circ$  and  $45^\circ$ ) testifies to the remarkable persistence of the dependence (2) for fixed  $m$  and  $\sigma_0$ . Indeed, the linear relation is independent of any choice of  $\tan \beta_0$ ; for simplicity we would write, for example

$$N \propto (1/\tan \theta)^m \quad (3)$$

Once having obtained the hoped-for linear relation, this property of the data can be utilized in a variety of ways:

1. Each straight line segment illustrates a dependence on  $\theta$  through the function  $\tan \theta$  alone. Hence the manner in which radar energy is reflected back to the receiver, assumed by Spetner and Katz (assumption 2 above), gains credibility.
2. Attention is focused on features of the straight lines such as slopes and intercepts; indeed we can readily use the straight line law (insofar as it is found to continue to be valid) for data smoothing and rejection.
3. The sharp change in straight line behavior at the angles shown indicates a similar rapid change in the reflectivity properties of the ocean surface for these angles.
4. We need no prior knowledge of the structure of the ocean surface to pursue this mode of analysis.

5. Another implication of Figure 1 for other theories is a contradiction to a deduction of Beckman and Spizzichino (reference 4, p. 405, formula 9). The text asserts that

$$N \propto e^{-(\tan \theta / \tan \beta_0)^2} \quad (4)$$

or (in decibels)

$$\sigma_0 \propto -(\tan \theta / \tan \beta_0)^2 \log_{10} e \quad (5)$$

provided that the population of ocean wave slopes is represented by a Gaussian distribution. But relation (4) contradicts relation (2), since (2) implies that

$$N \propto (1/\tan \theta)^m \quad (6)$$

or (in decibels)

$$\sigma_0 \propto -m \log_{10} \tan \theta \quad (7)$$

Thus, we deduce from experimental evidence exhibited in the manner suggested herein that the population of the ocean wave slopes is not described by a Gaussian distribution over a range of angles from about  $10^\circ$  to  $70^\circ$ . The directness of this analysis is an argument for its adoption.

The validity of relations (2) and (3) is verified by data derived from other experimenters, although it is found that the exponent  $m$  may depend on the wavelength of the radiation. For example, in Figure 2 (reference 6) we display the variation with wavelength of the scattered radiation's energy (vertically polarized in both transmission and reception). There is a remarkable constancy of slopes in the straight line segments exhibited for small angles of incidence (about  $10^\circ$  to about  $30^\circ$ ), but the slopes ( $-m$ ) of the line segments vary monotonically in a well-defined manner with wavelength between  $30^\circ$  and  $85^\circ$ . The latter variation is indicated in Figure 3. Since no limits for the precision of the measurements were given in the reports consulted, the curve was interpolated

midway between points to indicate the average trend. An independent verification of at least one point on the curve in Figure 3 is obtained from the averaged curve of  $N$  versus  $\tan \theta$  derived from observations of sea clutter at 13.3 GHz for vertically polarized radiation made by the National Aeronautics and Space Administration (Manned Spacecraft Center, Houston). The slope of a corresponding line segment agrees with the prediction of the curve in Figure 3.

The behavior of the scattering cross section  $N$  for horizontally polarized and received radiation is radically different than for vertically polarized radiation, but the fundamental feature of the straight line variation pointed out above remains (Figure 4).

The effect of wind speed variation is indicated in Figure 5 (reference 7). It is seen that the straight line remains a reasonable approximation for the variation of  $N$  with  $\tan \theta$  for 8 to 12 knot winds, as well as for 46 to 48 knot winds. In the latter case, for a smaller percent variation in wind speed, the points adhere more closely to the straight line than for the former case. It appears that variation in wind speed leads to a displacement of the straight lines parallel to the abscissa in the representation adopted. This feature agrees with an asserted dependence of the scattering cross section  $N$  upon a power of the wind speed (reference 4, p. 413).

#### CONCLUSIONS

1. The persistence of the function dependence [relation (2) or (3)] argues a similar persistence of the physical mechanism causing it, and resultant simplicity of any physical model corresponding to the mechanism.
2. That the linear behavior of the plotted data is preserved for both vertically and horizontally polarized radiation suggests that the physical mechanism is similar in both cases.
3. The ability of the analysis described earlier to deliver useful results without prior knowledge of the nature of the ocean surface (e.g., as in the approximate analyses reported in reference 8, depending on various hypotheses about the ocean surface) suggests its usefulness.
5. Variation in wind speed (other factors remaining unchanged) is reflected in a translation of the linear graphs parallel to one another and to the abscissa on which  $\tan \theta$  is plotted.

5. Theories based on electromagnetic field theory and an assumed structure for the ocean surface must agree with the empirical relations derived wherever the latter are valid.

#### SUMMARY

We have shown (in accord with historical precedent in the development of physical theory) how the introduction of suitable alterations in the scale of plots of experimental values of radar sea clutter cross section versus angle of incidence can result in simplified linear representation of the data. In turn, the latter results suggest a similar simplicity in analysis of the physical mechanism leading to the observed sea clutter return. A variety of conclusions are drawn which indicate the usefulness of the approach and the value of further investigations using this technique.



REFERENCES

1. Rice, S. E., "Reflection of Electromagnetic Waves from Slightly Rough Surfaces", *Comm. Pure Appl. Math.*, Vol. 4, pp. 351-378, 1951.
2. Fung, A. K., *Scattering Theories and Radar Return*, CRES Report No. 48-3, The University of Kansas, Center for Research, Inc., Engineering Science Division, Lawrence, Kansas, May 1965.
3. Semenov, B., "An Approximate Calculation of Scattering of Electromagnetic Waves from a Slightly Rough Surface", *Radio Engineering and Electronics Physics (IEEE)*, Vol. 11, pp. 1179-1187, August 1966.
4. Beckmann, P. and A. Spizzichino, *The Scattering of Electromagnetic Waves from Rough Surfaces*, The MacMillan Company, New York, 1963.
5. Spetner, L. M., and I. Katz, "Two Statistical Models for Radar Terrain Return", *IEEE Trans. Antennas and Prop.*, Vol. AP-8, pp. 242-246, May 1960.
6. Daley, J. C., J. T. Ransone, J. A. Burkett, and R. J. Duncan, *Sea Clutter Measurements on Four Frequencies*, Naval Research Laboratory, Washington, D. C., NRL Report 6806, 29 November 1968.
7. Guinard, N. W. and J. C. Daley, *An Experimental Study of a Sea Clutter Model*, Naval Research Laboratory, to be published by the Naval Oceanographic Office as part of the Proceedings of the NASA/Navy Microwave Review Meeting, June 16, 1969.
8. Chia, R. C., *The Theory of Radar Scatter from the Ocean*, Technical Report 112-1, The University of Kansas, Center for Research, Inc., Remote Sensing Laboratory, Lawrence, Kansas, October 1968.

1	51	101	151	201	251	301	351	401	451	501	551	601	651	701
2	52	102	152	202	252	302	352	402	452	502	552	602	652	702
3	53	103	153	203	253	303	353	403	453	503	553	603	653	703
4	54	104	154	204	254	304	354	404	454	504	554	604	654	704
5	55	105	155	205	255	305	355	405	455	505	555	605	655	705
6	56	106	156	206	256	306	356	406	456	506	556	606	656	706
7	57	107	157	207	257	307	357	407	457	507	557	607	657	707
8	58	108	158	208	258	308	358	408	458	508	558	608	658	708
9	59	108	159	209	259	309	359	409	459	509	559	609	659	709
10	60	110	160	210	260	310	360	410	460	510	560	610	660	710
11	61	111	161	211	261	311	361	411	461	511	561	611	661	711
12	62	112	162	212	262	312	362	412	462	512	562	612	662	712
13	63	113	163	213	263	313	363	413	463	513	563	613	663	713
14	64	114	164	214	264	314	364	414	464	514	564	614	664	714
15	65	115	165	215	265	315	365	415	465	515	565	615	665	715
16	66	116	166	216	266	316	366	416	466	516	566	616	666	716
17	67	117	167	217	267	317	367	417	467	517	567	617	667	717
18	68	118	168	218	268	318	368	418	468	518	568	618	668	718
19	69	119	169	219	269	319	369	419	469	519	569	619	669	719
20	70	120	170	220	270	320	370	420	470	520	570	620	670	720
21	71	121	171	221	271	321	371	421	471	521	571	621	671	721
22	72	122	172	222	272	322	372	422	472	522	572	622	672	722
23	73	123	173	223	273	323	373	423	473	523	573	623	673	723
24	74	124	174	224	274	324	374	424	474	524	574	624	674	724
25	75	125	175	225	275	325	375	425	475	525	575	625	675	725
26	76	126	176	226	276	326	376	426	476	526	576	626	676	726
27	77	127	177	227	277	327	377	427	477	527	577	627	677	727
28	78	128	178	228	278	328	378	428	478	528	578	628	678	728
29	79	129	179	229	279	329	379	429	479	529	579	629	679	729
30	80	130	180	230	280	330	380	430	480	530	580	630	680	730
31	81	131	181	231	281	331	381	431	481	531	581	631	681	731
32	82	132	182	232	282	332	382	432	482	532	582	632	682	732
33	83	133	183	233	283	333	383	433	483	533	583	633	683	733
34	84	134	184	234	284	334	384	434	484	534	584	634	684	734
35	85	135	185	235	285	335	385	435	485	535	585	635	685	735
36	86	136	186	236	286	336	386	436	486	536	586	636	686	736
37	87	137	187	237	287	337	387	437	487	537	587	637	687	737
38	88	138	188	238	288	338	388	438	488	538	588	638	688	738
39	89	139	189	239	289	339	389	439	489	539	589	639	689	739
40	90	140	190	240	290	340	390	440	490	540	590	640	690	740
41	91	141	191	241	291	341	391	441	491	541	591	641	691	741
42	92	142	192	242	292	342	392	442	492	542	592	642	692	742
43	93	143	193	243	293	343	393	443	493	543	593	643	693	743
44	94	144	194	244	294	344	394	444	494	544	594	644	694	744
45	95	145	195	245	295	345	395	445	495	545	595	645	695	745
46	96	146	196	246	296	346	396	446	496	546	596	646	696	746
47	97	147	197	247	297	347	397	447	497	547	597	647	697	747
48	98	148	198	248	298	348	398	448	498	548	598	648	698	748
49	99	149	199	249	299	349	399	449	499	549	599	649	699	749
50	100	150	200	250	300	350	400	450	500	550	600	650	700	750